

Stokes Polarimetric Imaging and Applications to Novel Materials

Jie Gou

Institute for Materials Research

Joule Physics Laboratory

School of Sciences, Engineering, and Environment

University of Salford

Salford, UK

Submitted in Partial Fulfilment of the Requirements of the Degree of
Doctor of Philosophy, December 2019

Contents

Acknowledgement i

Abbreviations: The symbols in thesis ii

Abstract vi

Chapter 1

Introductory 1

Chapter 2

The description of polarization 7

2.1 Description of polarization 7

2.1.1 Maxwell's equation 7

2.1.2 Stokes representation 11

2.2 Representation of polarization 15

2.2.1 Mueller calculus 15

2.2.2 Jones Calculus 16

2.2.3 Transformation between Jones Matrix and Mueller Matrix 17

2.2.4 The propagation equation for the Stokes parameters 18

2.3 Summary 19

Reference 19

Chapter 3

Literature review 21

3.1 Stokes polarimetry 21

3.2 Stokes polarimetric microscope 22

3.3 Research material system 24

3.3.1 Micropipe in SiC 24

- 3.3.2 Pin hole 26
- 3.3.3 Liquid crystal 27
- 3.3.4 Nanograter 29
- 3.4 The aim of the research 31**
- 3.5 Summary 33**

Reference 33

Chapter 4

Stokes polarimetry 39

- 4.1 Introduction 39**
- 4.2 The PEM 39**
- 4.3 Methodology of Stokes polarimetry 40**
 - 4.3.1 The configuration of experiment 41
- 4.4 The method of acquire six special polarization 48**
- 4.5 Calibration 48**
 - 4.5.1 Experiment of calibration 48
 - 4.5.2 Data analysis method of calibration 52
 - 4.5.2.1 Nonlinear regression 52
 - 4.5.3 Elliptical polarization 53
 - 4.5.4 Calibration result 60
 - 4.5.4.1 Weight factor in the calibration 60
 - 4.5.4.2 The effect of temperature on the measurement of Stokes parameters 60
 - 4.5.4.3 Current effect to the calibration matrix 69
 - 4.5.4.4 The effect of the filter wavelength on the calibration matrices 70
 - 4.5.4.5 The effect of monochromaticity on the calibration matrix 72
 - 4.5.4.6 Comparison of the test interval of the angles on the calibration matrix 73
- 4.6 Summary 75**

Reference 75

Chapter 5 Stokes polarimetry microscope -- computerized automation in image acquisition and the identification of best operational conditions 77

5.1 Experiment 77

- 5.1.1 Experimental set-up 78
- 5.1.2 The 12- channel signal extraction 79
- 5.1.3 The six-channel signal recovery method 80

5.2 The computerization of the image acquisition 81

- 5.2.1 The Switch of the channels 82
- 5.2.2 The design logic of the program 83
- 5.2.3 The comparison of the 7 versions of program 85

5.3 The optimisation of the microscope operation 89

- 5.3.1 Reflection on the surface of polarimeter 89
- 5.3.2 Rainbow on the image of depolarization 89
- 5.3.3 Situation without a condenser 90
- 5.3.4 Situation with a condenser 94
- 5.3.5 Comparison between uncoated polarizer and the antireflection polarizer 98
- 5.3.6 Comparison of the laser light source and the LED light source 99
- 5.3.7 Boundary behaviour of the image of the elliptical angle 101

5.4 Summary 102

References 102

Chapter 6

Research of Anisotropy in SiC 104

6.1 experimental results on optical bench 104

- 6.1.1 Experiment 1—Rotation of polarizer without adjustment the Stokes polarimeter 104

6.2 The imaging of the micropipe defects using the OPTIMUM microscope 105

- 6.2.1 Experiment 2 – observation the micropipes using the Stoked polarimetric microscope 105
- 6.2.2 Image of double micropipe in focus position 106
- 6.2.3 Image of the double micropipe at different focus position 110
- 6.2.4 Image of single micropipes in focus position 120
- 6.2.5 Image of single micropipe in different focus positions 124
- 6.2.6 Additional defects 131

6.3 Summary 135

Reference 136

Chapter 7 Investigation of the polarisation characteristics of light in the vicinity of a pinhole 138

7.1 The experiment 138

- 7.1.1 The experiment of pinhole 138

7.2 Results and discussion 139

- 7.2.1 Airy-like pattern from a circular aperture 139
- 7.2.2 Mapping of the polarization parameter before the pin hole 150
- 7.2.3 The situation in front of and behind the pinhole 153

7.3 Theory model 159

- 7.3.1 The model of the scattering at a pin hole 159

7.4 Summary 161

Chapter 8

Liquid crystal droplets 162

8.1 Experiment 162

- 8.1.1 The detail of four liquid crystal sample 162

8.2 Results and discussions 165

- 8.2.1 Sample1 165
- 8.2.2 Sample 2 170

- 8.2.3 Sample3 176
- 8.2.4 Sample4 181
- 8.2.5 The movement of liquid crystal 186

8.3 Summary 188

Reference 189

Chapter 9

Research of the nanograters 190

9.1 Experiment 190

- 9.1.1 Experiment of nanograter 190

9.2 Results and discussion 195

- 9.2.1 Polarizer rotation experiment 195
- 9.2.2 Sample rotation experiment with the protrusions facing the light source 213
- 9.2.3 sample rotation experiment with the protrusions facing the camera 235
- 9.2.4 The optical axis of polarizer perpendicular to the axis of the nanograter 254
- 9.2.5 The axis of polarizer parallel to the axis of the nanograter 259
- 9.2.6 The influence of the angle of the protrusion to the polarization patterns 265
- 9.2.7 Other types of nanograter 275
 - 9.2.7.1 Rectangle shape 275
 - 9.2.7.2 Square shape 277
 - 9.2.7.3 Flower shape 279

9.3 Summary 283

Reference 284

Chapter 10

Summarize and future work 285

Appendix A 288

A.1 Calibration experiment -- Alignment 288

Appendix B: Optical component extraction deduction 289

B.1 Mueller matrix of different optical component 289

- B.1.1 Mueller Matrix of linear birefringence 290
- B.1.2 Mueller Matrix of circular birefringence sample 290
- B.1.3 Mueller Matrix for a linear dichroism material 290
- B.1.4 Mueller Matrix of a circular dichroism material 291
- B.1.4 Mueller Matrix of the property of depolarization 292

B.2 Deduction of the effective optical parameters 292

- B.2.1 Testing method 293
- B.2.2 Situation without regard to depolarization 293
- B.2.3 Situation with regard to depolarization 297
- B.2.4 Acquisition of the Mueller matrix of a sample 304

Reference 307

List of figures and tables

Figure 2.1.2.1 Poincaré representation of the state of polarization of a monochromatic wave.....	13
Figure 2.1.2.2 The polarization ellipse of an elliptical polarization.	14
Figure 3.3.3.1 The chiral nematic state of liquid crystal	27
Figure 3.3.4.1 The surface current loop response to different electric field	30
Figure 4.3.1.1 The configuration of the experimental set up.....	42
Figure 4.3.1.2 the angle of the optical axis of optics referenced to the laboratory coordinate(Guan et al., 2010).....	42
Figure 4.5.1.1 Experimental set-up for calibration of the system.....	51
Figure 4.5.3.1 The trace of the end of the Stokes vector in 3D graphic, when rotate the polarizer from 0° to 180° at retarder angle $\rho = 65^\circ$	55
Figure 4.5.3.2 the trace of the end of the Stokes vector on Poincaré sphere, when rotate the polarizer from 0° to 180° , at different retarder angles: (a) $\rho = 0^\circ$; (b) $\rho = 45^\circ$; (c) $\rho = 90^\circ$; (d) $\rho = 135^\circ$	57
Figure 4.5.3.3 the 3D image of the trace of the end point of the Stokes vectors on Poincaré sphere when changing the retarder angle from 0° to 180° when the polarizer angle is 45°	58
Figure 4.5.3.4 The trace of the end of the Stokes vector on Poincaré sphere, when rotate the retarder from 0° to 180° , at different retarder angles: (a) $\theta = 0^\circ$; (b) $\theta = 45^\circ$; (c) $\theta = 90^\circ$; (d) $\theta = 135^\circ$	59
Figure 4.5.4.1 The representation of the Stokes parameters on Poincaré sphere for circular polarization under fixed retarder angle of 65° tested at different temperature: (a) 23°C , (b) 22.6°C , (c) 22.1°C , (d) 21.8°C , (e) 21.5°C , (f) 21.3°C using the calibration parameters at 22.6°C	63

Figure 4.5.4.2 The Stokes parameters for linear polarization tested at different temperatures: (a)23°C, (b)22.6°C, (c)22.1°C, (d)21.8°C, (e)21.5°C, (f)21.3°C using the calibration parameters at 22.6 °C.....	64
Figure 4.5.4.3 The Stokes parameters for circular polarization at different angle of view [(a) 3D imagine, (b) projection image on plane of U and V, (c) projection image on plane of Q and U] under fixed polarization angle of 45° tested at different temperatures: 23°C, 22.6°C, 22.3°C, 21.8°C, 21.5°C, 21.3°C using the calibration parameters at 22.6 °C.....	67
Figure 4.5.4.4 The variation of the calibration parameters $k_1, k_2, k_3, k_4, k_5, k_6, k_7,$ and k_8 to the calibration temperature, under different test configurations: (a) polarizer is at 45° and (b) retarder is at 65°	68
Figure 4.5.4.5 the signal acquired at 84kHz of PEM2	74
Figure 4.5.4.6 the signal acquired at 100kHz of PEM1	74
Figure 4.5.4.7 signal acquired by PEM1 at 50kHz	75
Figure 5.1.1.1 The diagram of the Stokes polarimetry microscope.....	78
Figure 5.1.2.1 The calibration curve of the linear polarization (a) and the elliptical polarization (b) calculated through twelve channel method.....	80
Figure 5.1.3.1 The calibration curve for, a linear polarization (a), and an elliptically polarization (b), calculated through six channel method.....	81
Figure 5.2.1.1 The control code of the time unit in version 1 and version 2	83
Figure 5.2.1.2 The control code of the time unit in version 3 to version 7.....	83
Figure 5.2.2.1 the flow chart of the main structure of the program: the version I (a); the version II (b); the version III (c)	84
Figure 5.2.3.1 The front panel of the version 4 of the microscope controlling program.	86
Figure 5.2.3.2 The front panel of the version 6 of the microscope controlling program.	87

Figure 5.2.3.3 the front panel of the version 7 of the microscope controlling program ..	88
Figure 5.2.3.4 The situation of the front panel after the running process	89
Figure 5.3.3.1 The profile of the normalized depolarization without a condenser using the different focus distance light source: (a) 1f1 position with a divergent light beam; (b) 4f3 position with a parallel light beam; c) 18f1 position with a convergent beam	91
Figure 5.3.3.2 The depolarization profile image of the whole image in special position	92
Figure 5.3.3.3 The diagram of second reflection of the light source.	93
Figure 5.3.3.4 The slope of depolarization with a covered filter in two situations: (a) without a condenser in the light path; (b) with a collimator in the light path.....	94
Figure 5.3.4.1 the relationship between the polarization angle and the rainbow background on the image of normalized depolarization.....	95
Figure 5.3.4.2 The best picture quality acquired at last experiment (with an antireflection polarizer): (a) image of depolarization; (b) image of normalized depolarization; c) image of elliptical angle; (d) image of azimuth angle; (e) image of normalized Stokes parameter Q; (f) image of normalized Stokes parameter U; (g) image of normalized Stokes parameter V; (h) image of the intensity.....	97
Figure 5.3.5.1 the image of normalized depolarization of the scale plate using: normal polarizer (a); antireflection polarizer (b).....	99
Figure 5.3.6.1 The pattern of the normalized depolarization of eclogite sample: measured using the laser light source (a); and measured using the LED light source (b).....	100
Figure 5.3.7.1 the image of the elliptical angle on the circle age structures: pinhole (a); liquid crystal droplet (b).....	102
Figure 6.1.1.1 the normalized stokes parameter V/I changed with the polarization angle for different Sn ion irradiation dose.	104
Figure 6.2.1.1 the laboratory coordinate showing on the image of the microscope	106

Figure 6.2.2.1 Image of contrast of the Stokes parameters on double micropipe: (a) Intensity, (b) Stokes parameter Q , (c) Stokes parameter U , (d) Stokes parameter V	107
Figure 6.2.2.2 The image of (a) normalized depolarization, (b) normalized Stokes parameter Q/I , (c) normalized Stokes parameter U/I , and (d) normalized Stokes parameter V/I on a double micropipe.	108
Figure 6.2.2.3 The contrast image of (a) the elliptical angle χ , (b) the azimuth angle ψ , (c) the retardation of phase δ , and (d) the $\sin\delta$ on a double micropipe.....	109
Figure 6.2.3.1 The mapping of the intensity of the double micropipe in different focus position.....	110
Figure 6.2.3.2 The mapping of Stokes parameter Q of the double micropipe in different focus position.....	111
Figure 6.2.3.3 Stokes parameter of the double micropipe in different focus positions .	112
Figure 6.2.3.4 Stokes parameter V of the double micropipe in different focus positions	113
Figure 6.2.3.5 The mapping of elliptical angle χ of the double micropipe in different focus positions	114
Figure 6.2.3.6 The mapping of azimuth angle ψ of the double micropipe in different focus position.....	115
Figure 6.2.3.7 the mapping of normalized Stokes parameter Q/I of the double micropipe in different focus position	117
Figure 6.2.3.8 normalized Stokes parameter V/I of the double micropipe at different focus positions	118
Figure 6.2.3.9 normalized depolarization of double micropipe in different focus positions	119
Figure 6.2.4.1 Image of contrast of the Stokes parameters at a single micropipe: (a)	

Intensity, (b) Stokes parameter Q , (c) Stokes parameter U , (d) Stokes parameter V	121
Figure 6.2.4.2 The image of at a single micropipe (a) normalized depolarization dP/I , (b) normalized Stokes parameter Q/I , (c) normalized Stokes parameter U/I , and (d) normalized Stokes parameter V/I	122
Figure 6.2.4.3 The contrast image of at a single micropipe (a) the elliptical angle χ , (b) the azimuth angle ψ , (c) the retardation of phase δ , and (d) the $\sin(\delta)$	123
Figure 6.2.5.1 The overlapping image of the mapping of the intensity of the single micropipe	124
Figure 6.2.5.2 The overlapping image of the mapping of the phase difference δ of the single micropipe.....	125
Figure 6.2.5.3 The mapping of the intensity of the single micropipe at different focus position.....	126
Figure 6.2.5.4 The mapping of Stokes parameter Q of the single micropipe in different focus positions	126
Figure 6.2.5.5 The mapping of Stokes parameter U of the single micropipe in different focus positions	127
Figure 6.2.5.6 The mapping of Stokes parameter V of the single micropipe in different focus positions	127
Figure 6.2.5.7 The mapping of azimuth angle ψ of the single micropipe in different focus positions	128
Figure 6.2.5.8 the mapping of $\sin(\delta)$ of the single micropipe in different focus positions	129
Figure 6.2.5.9 The mapping of normalized Stokes parameter Q/I of the single micropipe in different focus positions.....	129
Figure 6.2.5.10 The mapping of normalized Stokes parameter U/I of the single	

micropipe in different focus positions	130
Figure 6.2.5.11 The mapping of normalized Stokes parameter V/I of the single micropipe in different focus positions	130
Figure 6.2.5.12 The mapping of normalized depolarization IdP/I of the single micropipe in different focus positions.	131
Figure 6.2.6.1 Image of contrast of the Stokes parameters at three micropipe: (a) Intensity, (b) Stokes parameter Q , (c) Stokes parameter U , (d) Stokes parameter V	132
Figure 7.1.1.1 (a) the SEM picture of the pinhole used in the experiment; (b) the image of Q measured by Stokes Polarimetric microscope.	139
Figure 7.2.1.1 The configuration of the pinhole experiment	140
Figure 7.2.1.2 The Airy-like pattern of I for the pinhole after focus position: (a) $0 \mu\text{m}$, (b) $1 \mu\text{m}$, (c) $2 \mu\text{m}$, (d) $3 \mu\text{m}$, (e) $4 \mu\text{m}$, (f) $5 \mu\text{m}$	141
Figure 7.2.1.3 The Airy-like pattern of Q for the pinhole after focus position: (a) $0 \mu\text{m}$, (b) $1 \mu\text{m}$, (c) $2 \mu\text{m}$, (d) $3 \mu\text{m}$, (e) $4 \mu\text{m}$, (f) $5 \mu\text{m}$	141
Figure 7.2.1.4 The Airy-like pattern of U for the pinhole after focus position: (a) $0 \mu\text{m}$, (b) $1 \mu\text{m}$, (c) $2 \mu\text{m}$, (d) $3 \mu\text{m}$, (e) $4 \mu\text{m}$, (f) $5 \mu\text{m}$	142
Figure 7.2.1.5 The Airy-like pattern of V for the pinhole after focus position: (a) $0 \mu\text{m}$, (b) $1 \mu\text{m}$, (c) $2 \mu\text{m}$, (d) $3 \mu\text{m}$, (e) $4 \mu\text{m}$, (f) $5 \mu\text{m}$	143
Figure 7.2.1.6 The Airy-like pattern of χ for the pinhole after focus position: (a) $0 \mu\text{m}$, (b) $1 \mu\text{m}$, (c) $2 \mu\text{m}$, (d) $3 \mu\text{m}$, (e) $4 \mu\text{m}$, (f) $5 \mu\text{m}$	144
Figure 7.2.1.7 The Airy-like pattern of ψ for the pinhole after focus position: (a) $0 \mu\text{m}$, (b) $1 \mu\text{m}$, (c) $2 \mu\text{m}$, (d) $3 \mu\text{m}$, (e) $4 \mu\text{m}$, (f) $5 \mu\text{m}$	144
Figure 7.2.1.8 The Airy-like pattern of δ for the pinhole after focus position: (a) $0 \mu\text{m}$, (b) $1 \mu\text{m}$, (c) $2 \mu\text{m}$, (d) $3 \mu\text{m}$, (e) $4 \mu\text{m}$, (f) $5 \mu\text{m}$	145
Figure 7.2.1.9 The Airy-like pattern of $\sin(\delta)$ for the pinhole after focus position: (a) 0	

μm , (b) 1 μm , (c) 2 μm , (d) 3 μm , (e) 4 μm , (f) 5 μm	145
Figure 7.2.1.10 The Airy-like pattern of I_dP/I for the pinhole after focus position: (a) 0 μm , (b) 1 μm , (c) 2 μm , (d) 3 μm , (e) 4 μm , (f) 5 μm	146
Figure 7.2.1.11 The Airy pattern of Q/I for the pinhole after focus position: (a) 0 μm , (b) 1 μm , (c) 2 μm , (d) 3 μm , (e) 4 μm , (f) 5 μm	146
Figure 7.2.1.12 The Airy-like pattern of U/I for the pinhole after focus position: (a) 0 μm , (b) 1 μm , (c) 2 μm , (d) 3 μm , (e) 4 μm , (f) 5 μm	147
Figure 7.2.1.13 The Airy-like pattern of V/I for the pinhole after focus position: (a) 0 μm , (b) 1 μm , (c) 2 μm , (d) 3 μm , (e) 4 μm , (f) 5 μm	147
Figure 7.2.1.14 The Airy-like pattern of $ E_x $ for the pinhole after focus position: (a) 0 μm , (b) 1 μm , (c) 2 μm , (d) 3 μm , (e) 4 μm , (f) 5 μm	148
Figure 7.2.1.15 The Airy-like pattern of $ E_y $ for the pinhole after focus position: (a) 0 μm , (b) 1 μm , (c) 2 μm , (d) 3 μm , (e) 4 μm , (f) 5 μm	148
Figure 7.2.1.16 The Airy pattern of real part of E_y for the pinhole after focus position: (a) 0 μm , (b) 1 μm , (c) 2 μm , (d) 3 μm , (e) 4 μm , (f) 5 μm	149
Figure 7.2.1.17 The Airy pattern of imaginary part of E_y for the pinhole after focus position: (a) 0 μm , (b) 1 μm , (c) 2 μm , (d) 3 μm , (e) 4 μm , (f) 5 μm	149
Figure 7.2.2.1 The contrast image of (a) the elliptical angle χ , (b) the azimuth angle ψ , (c) the retardation of phase δ , and (d) the $\sin(\delta)$	151
Figure 7.2.2.2 Image of contrast of the Stokes parameters on pinhole: (a) Intensity, (b) Stokes parameter Q, (c) Stokes parameter U, (d) Stokes parameter V.	152
Figure 7.2.2.3 The modulus of the electric field with reference to the laboratory coordinate.....	152
Figure 7.2.2.4 The electric field along y-axis: (a) real part and (b) the imaginary part.	153
Figure 7.2.3.1 The mapping of I for the pinhole: (a) the object plane behind the pinhole; (b) the object plane on the pinhole; (c) the object plane in front of the pinhole....	153

Figure 7.2.3.2 The mapping of Q for the pinhole: (a) the object plane behind the pinhole; (b) the object plane on the pinhole; (c) the object plane in front of the pinhole.... 154

Figure 7.2.3.3 The mapping of U for the pinhole: (a) the object plane behind the pinhole; (b) the object plane on the pinhole; (c) the object plane in front of the pinhole.... 154

Figure 7.2.3.4 The mapping of V for the pinhole: (a) the object plane behind the pinhole; (b) the object plane on the pinhole; (c) the object plane in front of the pinhole;... 155

Figure 7.2.3.5 The mapping of IdP/I for the pinhole: (a) the object plane behind the pinhole; (b) the object plane on the pinhole; (c) the object plane in front of the pinhole..... 155

Figure 7.2.3.6 The mapping of U/I for the pinhole: (a) the object behind plane the pinhole; (b) the object plane on the pinhole; (c) the object plane in front of the pinhole..... 156

Figure 7.2.3.7 The mapping of Q/I for the pinhole: (a) the object behind plane the pinhole; (b) the object plane on the pinhole; (c) the object plane in front of the pinhole..... 156

Figure 7.2.3.8 The mapping of V/I for the pinhole: (a) the object plane behind plane the pinhole; (b) the object plane on the pinhole; (c) the object plane in front of the pinhole..... 156

Figure 7.2.3.9 The mapping of χ for pinhole (a) the object plane behind plane the pinhole; (b) the object plane on the pinhole; (c) the object plane in front of the pinhole..... 157

Figure 7.2.3.10 The mapping of ψ for the pinhole: (a) the object plane behind plane the pinhole; (b) the object plane on the pinhole; (c) the object plane in front of the pinhole..... 157

Figure 7.2.3.11 The mapping of δ for the pinhole: (a) the object plane behind plane the pinhole; (b) the object plane on the pinhole; (c) the object plane in front of the pinhole..... 157

Figure 7.2.3.12 The mapping of $|Ex|$ for the pinhole: (a) the object plane behind plane

the pinhole; (b) the object plane on the pinhole; (c) the object plane in front of the pinhole.....	158
Figure 7.2.3.13 The mapping of $ E_y $ for the pinhole: (a) the object plane behind plane the pinhole; (b) the object plane on the pinhole; (c) the object plane in front of the pinhole.....	158
Figure 7.2.3.14 The mapping of $\text{Re}(E_y)$ for the pinhole: (a) the object plane behind plane the pinhole; (b) the object plane on the pinhole; (c) the object plane in front of the pinhole	159
Figure 7.2.3.15 The mapping of $\text{Im}(E_y)$ for the pinhole: (a) the object plane behind plane the pinhole; (b) the object plane on the pinhole; (c) the object plane in front of the pinhole	159
Figure 7.3.1.1 The interaction of the polarization at the edge of pin hole.....	160
Figure 8.1.1.1 The chemical component of the E7 liquid crystals.....	163
Figure 8.1.1.2 the molecular structure of the chiral solution S1011.....	163
Figure 8.1.1.3 The structure of PVA	163
Figure 8.1.1.4 The structure of glycerol.....	164
Figure 8.2.1.1 Image of contrast of the Stokes parameters on LCD sample1: (a) Intensity, (b) Stokes parameter Q, (c) Stokes parameter U, (d) Stokes parameter V.	165
Figure 8.2.1.2 The contrast image of (a) the elliptical angle χ , (b) the azimuth angle ψ , (c) the retardation of phase δ , and (d) the $\sin(\delta)$ on LCD sample1.....	166
Figure 8.2.1.3 The image of (a) normalized depolarization, (b) normalized Stokes parameter Q/I , (c) normalized Stokes parameter U/I , and (d) normalized Stokes parameter V/I on LCD sample1.....	167
Figure 8.2.1.4 The modulus of the electric field of the LCD sample1 with reference to the laboratory coordinate (a) E_x and (b) E_y	168

Figure 8.2.1.5 The electric field of the LCD sample1 along y-axis: (a) real part and (b) the imaginary part.	168
Figure 8.2.1.6 The modulus of the electric field of the LCD sample1 with reference to the polarizer coordinate: (a) modulus of electric field along x_1 , (b) modulus of electric field along y_1 , and (c) the retardation of phase δ_1	169
Figure 8.2.2.1 the structure of the sample2.....	170
Figure 8.2.2.2 Image of contrast of the Stokes parameters on LCD sample 2 : (a) Intensity, (b) Stokes parameter Q, (c) Stokes parameter U, and (d)Stokes parameter V.	171
Figure 8.2.2.3 The contrast image of (a) the elliptical angle χ , (b) the azimuth angle ψ , (c) the retardation of phase δ , and (d) the $\sin(\delta)$ on LCD sample2.....	172
Figure 8.2.2.4 The image of (a) normalized depolarization, (b) normalized Stokes parameter Q/I , (c) normalized Stokes parameter U/I , and (d) normalized Stokes parameter V/I on LCD sample2.	173
Figure 8.2.2.5 The modulus of the electric field of the LCD sample2 with reference to the laboratory coordinate (a) x-axis and (b) y-axis.....	173
Figure 8.2.2.6 The modulus of the electric l field of the LCD sample 2 with reference to the polarizer coordinate: (a) modulus of electric field along x_1 , (b) modulus of electric field along y_1 , and (c) the retardation of phase δ_1	174
Figure 8.2.2.7 The contrast image of (a) the elliptical angle χ , (b) the azimuth angle ψ , (c) the retardation of phase δ , and (d) the $\sin(\delta)$ at another position of LCD sample2.	175
Figure 8.2.2.8 Image of contrast of the Stokes parameters on another position of LCD sample2 : (a) Intensity, (b) Stokes parameter Q, (c) Stokes parameter U, and (d) Stokes parameter V.....	176
Figure 8.2.3.1 the structure of sample 3.....	177
Figure 8.2.3.2 Image of contrast of the Stokes parameters on LCD sample3 : (a)	

Intensity, (b) Stokes parameter Q, (c) Stokes parameter U, and (d) Stokes parameter V.....	177
Figure 8.2.3.3 The contrast image of (a) the elliptical angle χ , (b) the azimuth angle ψ , (c) the retardation of phase δ , and (d) the $\sin(\delta)$ on LCD sample3.....	178
Figure 8.2.3.4 The image of (a) normalized depolarization, (b) normalized Stokes parameter Q/I , (c) normalized Stokes parameter U/I , and (d) normalized Stokes parameter V/I on LCD sample3.....	179
Figure 8.2.3.5 The modulus of the electric field of the LCD sample 3 with reference to the laboratory coordinate (a) x-axis and (b) y-axis.....	180
Figure 8.2.3.6 The electric field of the LCD sample1 along y-axis: real part (a) and the imaginary part (b).	180
Figure 8.2.3.7 The modulus of the electric field of the LCD sample3 referenced to the polarizer coordinate: (a) modulus of electrical field along x_1 -axis, (b) modulus of electrical field along y_1 -axis, and (c) the retardation of phase δ_1	181
Figure 8.2.4.1 The contrast image of (a) the elliptical angle χ , (b) the azimuth angle ψ , (c) the retardation of phase δ , and (d) the $\sin(\delta)$ on LCD sample 4.....	182
Figure 8.2.4.2 Image of contrast of the Stokes parameters on LCD sample4 : (a) Intensity, (b) Stokes parameter Q, (c) Stokes parameter U, and (d) Stokes parameter V.....	183
Figure 8.2.4.3 The image of (a) normalized depolarization dP/I , normalized Stokes parameters (b) Q/I , (c) U/I , and (d) V/I on LCD sample4.....	184
Figure 8.2.4.4 The modulus of the electric field of the LCD sample4 referred to the laboratory coordinate (a) x-axis and (b) y-axis.....	184
Figure 8.2.4.5 The electric field of the LCD sample4 along y-axis: (a) real part and (b) the imaginary part.	185
Figure 8.2.4.6 The modulus of the electric field of the LCD sample4 referred to the polarizer coordinate: (a) modulus of electric field along x_1 , (b) modulus of	

electrical field along y_1 , and (c) the retardation of phase δ_1	186
Figure 8.2.5.1 The mapping of I for the LCD sample2 tested in different time intervals, when the polarization azimuth angle sited at 128° and sample stage sited in 147° , sample number: (a) 0s, (b) 1s, (c) 2s, (d) 3s, (e) 4s, (f) 5s, (g) 6s, (h) 7s, (i) 8s	187
Figure 8.2.5.2 The mapping of IdP for the LCD sample2 tested in different time intervals, when the polarization azimuth angle sited at 128° and sample stage sited in 147° , sample number: (a) 0s, (b) 1s, (c) 2s, (d) 3s, (e) 4s, (f) 5s, (g) 6s, (h) 7s, (i) 8s	188
Figure 9.1.1.1 The configuration of the experiment: (a) the sample stage 3 mounted on the microscope; (b) the sample stage 3	191
Figure 9.1.1.2 The number of the nanograter samples.....	192
Figure 9.1.1.3 the diagram of the polarization coordinate and the laboratory coordinate	192
Figure 9.2.1.1 The mapping of I for the nanograter tested at different polarization angles reference to the laboratory coordinate	197
Figure 9.2.1.2 The mapping of Q for the nanograter tested at different polarization angles reference to the laboratory coordinate.	198
Figure 9.2.1.3 The mapping of U for the nanograter tested at different polarization angles reference to the laboratory coordinate.	199
Figure 9.2.1.4 The mapping of V for the nanograter tested at different polarization angles reference to the laboratory coordinate.	200
Figure 9.2.1.5 The mapping of IdP/I for the nanograter tested at different polarization angles reference to the laboratory coordinate.	201
Figure 9.2.1.6 The mapping of Q/I for the nanograter tested at different polarization angles reference to the laboratory coordinate.	202
Figure 9.2.1.7 The mapping of U/I for the nanograter tested at different polarization	

angles reference to the laboratory coordinate.	203
Figure 9.2.1.8 The mapping of V/I for the nanograter tested at different polarization angles reference to the laboratory coordinate.	204
Figure 9.2.1.9 The mapping of χ for the nanograter tested at different polarization angles reference to the laboratory coordinate.	205
Figure 9.2.1.10 The mapping of ψ for the nanograter tested at different polarization angles reference to the laboratory coordinate.	206
Figure 9.2.1.11 The mapping of δ for the nanograter tested at different polarization angles reference to the laboratory coordinate.	207
Figure 9.2.1.12 The mapping of $\sin(\delta)$ for the nanograter tested at different polarization angles reference to the laboratory coordinate.	208
Figure 9.2.1.13 The mapping of $ Ex $ for the nanograter tested at different polarization angles reference to the laboratory coordinate.	209
Figure 9.2.1.14 The mapping of $ Ey $ for the nanograter tested at different polarization angles reference to the laboratory coordinate.	210
Figure 9.2.1.15 The mapping of $\text{Re}(Ey)$ for the nanograter tested at different polarization angles reference to the laboratory coordinate.	211
Figure 9.2.1.16 The mapping of $\text{Im}(Ey)$ for the nanograter tested at different polarization angles reference to the laboratory coordinate.	212
Figure 9.2.2.1 The configuration of the polarization and the nanograter: (a) polarization along the symmetrical plane of the nanograter; (b) polarization perpendicular to the symmetrical plane of the nanograter. (c) the SEM image of the nanograter.	214
Figure 9.2.2.2 The mapping of I for the nanograter sited at angles: (a) 58° , (b) 148° , (c) 238° , (d) 328° , (e) 102° , (f) 192°	215
Figure 9.2.2.3 The mapping of Q for the nanograter sited at angles reference to the laboratory coordinate: (a) 58° , (b) 148° , (c) 238° , (d) 328° , (e) 102° , (f) 192°	216

Figure 9.2.2.4 The mapping of U for the nanograter sited at angles: (a) 58° , (b) 148° , (c) 238° , (d) 328° , (e) 102° , (f) 192°	217
Figure 9.2.2.5 The mapping of V for the nanograter sited at angles: (a) 58° , (b) 148° , (c) 238° , (d) 328° , (e) 102° , (f) 192°	218
Figure 9.2.2.6 The mapping of dP/I for the nanograter sited at angles: (a) 58° , (b) 148° , (c) 238° , (d) 328° , (e) 102° , (f) 192°	219
Figure 9.2.2.7 The mapping of Q/I for the nanograter sited at angles: (a) 58° , (b) 148° , (c) 238° , (d) 328° , (e) 102° , (f) 192°	220
Figure 9.2.2.8 The mapping of U/I for the nanograter sited at angles: (a) 58° , (b) 148° , (c) 238° , (d) 328° , (e) 102° , (f) 192°	221
Figure 9.2.2.9 The mapping of V/I for the nanograter sited at angles: (a) 58° , (b) 148° , (c) 238° , (d) 328° , (e) 102° , (f) 192°	222
Figure 9.2.2.10 The mapping of elliptical angle χ for the nanograter sited at angles: (a) 58° , (b) 148° , (c) 238° , (d) 328° , (e) 102° , (f) 192°	223
Figure 9.2.2.11 The mapping of azimuth angle ψ for the nanograter sited at angles: (a) 58° , (b) 148° , (c) 238° , (d) 328° , (e) 102° , (f) 192°	224
Figure 9.2.2.12 The mapping of δ for the nanograter sited at angles: (a) 58° , (b) 148° , (c) 238° , (d) 328° , (e) 102° , (f) 192°	226
Figure 9.2.2.13 The mapping of $\sin(\delta)$ for the nanograter sited at angles: (a) 58° , (b) 148° , (c) 238° , (d) 328° , (e) 102° , (f) 192°	227
Figure 9.2.2.14 The mapping of $ Ex $ for the nanograter sited at angles: (a) 58° , (b) 148° , (c) 238° , (d) 328° , (e) 102° , (f) 192°	228
Figure 9.2.2.15 The mapping of $ Ey $ for the nanograter site at: (a) 58° , (b) 148° , (c) 238° , (d) 328° , (e) 102° , (f) 192°	229
Figure 9.2.2.16 The mapping of $Re(Ey)$ for the nanograter sited at angles (a) 58° , (b) 148° , (c) 238° , (d) 328° , (e) 102° , (f) 192°	230

Figure 9.2.2.17 The mapping of $Im(Ey)$ for the nanograter sited at angles: (a) 58° , (b) 148° , (c) 238° , (d) 328° , (e) 102° , (f) 192°	231
Figure 9.2.2.18 The mapping of $ Ex1 $ for the nanograter sited at angles: (a) 58° , (b) 148° , (c) 238° , (d) 328° , (e) 102° , (f) 192°	232
Figure 9.2.2.19 The mapping of $ Ey1 $ for the nanograter sited at angles: (a) 58° , (b) 148° , (c) 238° , (d) 328° , (e) 102° , (f) 192°	233
Figure 9.2.2.20 The mapping of δ_1 for the nanograter sited at angles: (a) 58° , (b) 148° , (c) 238° , (d) 328° , (e) 102° , (f) 192°	234
Figure 9.2.3.1 The mapping of I for the nanograter protrusion facing to the camera, when the polarizer sited at 122° : (a) 34° , (b) 124° , (c) 214° , (d) 304°	236
Figure 9.2.3.2 The mapping of Q for the nanograter protrusion facing to the camera, when the polarizer sited at 122° : (a) 34° , (b) 124° , (c) 214° , (d) 304°	237
Figure 9.2.3.3 The mapping of U for the nanograter protrusion facing to the camera, when the polarizer sited at 122° : (a) 34° , (b) 124° , (c) 214° , (d) 304°	238
Figure 9.2.3.4 The mapping of V for the nanograter protrusion facing to the camera, when the polarizer sited at 122° : (a) 34° , (b) 124° , (c) 214° , (d) 304°	239
Figure 9.2.3.5 The mapping of IdP/I for the nanograter protrusion facing to the camera, when the polarizer sited at 122° : (a) 34° , (b) 124° , (c) 214° , (d) 304°	240
Figure 9.2.3.6 The mapping of Q/I for the nanograter protrusion facing to the camera, when the polarizer sited at 122° : (a) 34° , (b) 124° , (c) 214° , (d) 304°	241
Figure 9.2.3.7 The mapping of U/I for the nanograter protrusion facing to the camera, when the polarizer sited at 122° : (a) 34° , (b) 124° , (c) 214° , (d) 304°	242
Figure 9.2.3.8 The mapping of V/I for the nanograter protrusion facing to the camera, when the polarizer sited at 122° : (a) 34° , (b) 124° , (c) 214° , (d) 304°	243
Figure 9.2.3.9 The mapping of χ for the nanograter protrusion facing to the camera, when the polarizer sited at 122° : (a) 34° , (b) 124° , (c) 214° , (d) 304°	244

Figure 9.2.3.10 The mapping of ψ for the nanograter protrusion facing to the camera, when the polarizer sited at 122° : (a) 34° , (b) 124° , (c) 214° , (d) 304°	245
Figure 9.2.3.11 The mapping of δ for the nanograter protrusion facing to the camera, when the polarizer sited at 122° : (a) 34° , (b) 124° , (c) 214° , (d) 304°	246
Figure 9.2.3.12 The mapping of $\sin(\delta)$ for the nanograter protrusion facing to the camera, when the polarizer sited at 122° : (a) 34° , (b) 124° , (c) 214° , (d) 304°	247
Figure 9.2.3.13 The mapping of $ Ex $ for the nanograter protrusion facing to the camera, when the polarizer sited at 122° : (a) 34° , (b) 124° , (c) 214° , (d) 304°	248
Figure 9.2.3.14 The mapping of $ Ey $ for the nanograter protrusion facing to the camera, when the polarizer sited at 122° : (a) 34° , (b) 124° , (c) 214° , (d) 304°	249
Figure 9.2.3.15 The mapping of $Re(Ey)$ for the nanograter protrusion facing to the camera, when the polarizer sited at 122° : (a) 34° , (b) 124° , (c) 214° , (d) 304°	250
Figure 9.2.3.16 The mapping of $Im(Ey)$ for the nanograter protrusion facing to the camera, when the polarizer sited at 122° : (a) 34° , (b) 124° , (c) 214° , (d) 304°	251
Figure 9.2.3.17 The mapping of $Ex1$ for the nanograter protrusion facing to the camera, when the polarizer sited at 122° : (a) 34° , (b) 124° , (c) 214° , (d) 304°	252
Figure 9.2.3.18 The mapping of $Ey1$ for the nanograter protrusion facing to the camera, when the polarizer sited at 122° : (a) 34° , (b) 124° , (c) 214° , (d) 304°	253
Figure 9.2.3.19 The mapping of $\delta1$ for the nanograter protrusion facing to the camera, when the polarizer sited at 122° : (a) 34° , (b) 124° , (c) 214° , (d) 304°	254
Figure 9.2.4.1 The mapping of I for the nanograter protrusion facing to (a)the camera, (b) the light source, when $P \perp A$, polarizer sited at 122°	255
Figure 9.2.4.2 The mapping of $Ex1$ for the nanograter protrusion facing to (a) the camera, (b) the light source, when $P \perp A$, polarizer sited at 122°	255
Figure 9.2.4.3 The mapping of $Ey1$ for the nanograter protrusion facing to (a) the camera, (b) the light source, when $P \perp A$, polarizer sited at 122°	256

Figure 9.2.4.4 The mapping of δ_1 for the nanograter protrusion facing to (a) the camera, (b) the light source, when $P \perp A$, polarizer sited at 122°	256
Figure 9.2.4.5 The mapping of semi-major axis of the polarization a for the nanograter protrusion facing to (a)the camera, (b) the light source, when $P \perp A$, polarizer sited at 122°	256
Figure 9.2.4.6 The mapping of semi-major axis of the polarization b for the nanograter protrusion facing to (a) the camera, (b) the light source, when $P \perp A$, polarizer sited at 122°	257
Figure 9.2.4.7 The mapping of IdP for the nanograter protrusion facing to (a) the camera, (b) the light source, when $P \perp A$, polarizer sited at 122°	257
Figure 9.2.4.8 The mapping of $Im(Ey)$ for the nanograter protrusion facing to (a)the camera, (b) the light source, when $P \perp A$, polarizer sited at 122°	258
Figure 9.2.4.9 The mapping of χ for the nanograter protrusion facing to (a)the camera, (b) the light source, when $P \perp A$, polarizer sited at 122°	258
Figure 9.2.4.10 The mapping of ψ for the nanograter protrusion facing to (a)the camera, (b) the light source, when $P \perp A$, polarizer sited at 122°	259
Figure 9.2.5.1 The mapping of I for the nanograter protrusion facing to (a) the camera, (b) the light source, when $P \parallel A$, polarizer sited at 122°	260
Figure 9.2.5.2 The mapping of Ex_1 for the nanograter protrusion facing to (a) the camera, (b) the light source, when $P \parallel A$, polarizer sited at 122°	260
Figure 9.2.5.3 The mapping of Ey_1 for the nanograter protrusion facing to (a) the camera, (b) the light source, when $P \parallel A$, polarizer sited at 122°	261
Figure 9.2.5.4 The mapping of δ_1 for the nanograter protrusion facing to (a) the camera, (b) the light source, when $P \parallel A$, polarizer sited at 122°	261
Figure 9.2.5.5 The mapping of semi-major axis of the polarization a for the nanograter protrusion facing to (a) the camera, (b) the light source, when $P \parallel A$, polarizer sited at 122°	262

Figure 9.2.5.6 The mapping of semi-minor axis of the polarization b for the nanograting protrusion facing to (a) the camera, (b) the light source, when $P\parallel A$, polarizer sited at 122° 262

Figure 9.2.5.7 The mapping of IdP for the nanograting protrusion facing to (a) the camera, (b) the light source, when $P\parallel A$, polarizer sited at 122° 263

Figure 9.2.5.8 The mapping of $Im(Ey)$ for the nanograting protrusion facing to (a) the camera, (b) the light source, when $P\parallel A$, polarizer sited at 122° 263

Figure 9.2.5.9 The mapping of χ for the nanograting protrusion facing to (a) the camera, (b) the light source, when $P\parallel A$, polarizer sited at 122° 264

Figure 9.2.5.10 The mapping of ψ for the nanograting protrusion facing to (a) the camera, (b) the light source, when $P\parallel A$, polarizer sited at 122° 264

Figure 9.2.6.1 The SEM image of the U-shape nanograting with different angles.266

Figure 9.2.6.2 The mapping of I for the nanograting that protrusion in different angles: (a) 5.6° , (b) 27.2° , (c) 40° , (d) 80° , (e) 90° , (f) 116.3° , (g) no protrusions, when $P\parallel A$, polarizer sited at 122° and sample stage sited in 148° 266

Figure 9.2.6.3 The mapping of Q for the nanograting that protrusion in different angles: (a) 5.6° , (b) 27.2° , (c) 40° , (d) 80° , (e) 90° , (f) 116.3° , (g) no protrusions, when $P\parallel A$, polarizer sited at 122° and sample stage sited in 148° 267

Figure 9.2.6.4 The mapping of U for the nanograting that protrusion in different angles: (a) 5.6° , (b) 27.2° , (c) 40° , (d) 80° , (e) 90° , (f) 116.3° , (g) no protrusions, when $P\parallel A$, polarizer sited at 122° and sample stage sited in 148° 267

Figure 9.2.6.5 The mapping of V for the nanograting that protrusion in different angles: (a) 5.6° , (b) 27.2° , (c) 40° , (d) 80° , (e) 90° , (f) 116.3° , (g) no protrusions, when $P\parallel A$, polarizer sited at 122° and sample stage sited in 148° 268

Figure 9.2.6.6 The mapping of dP/I for the nanograting that protrusion in different angles: (a) 5.6° , (b) 27.2° , (c) 40° , (d) 80° , (e) 90° , (f) 116.3° , (g) no protrusions, when $P\parallel A$, polarizer sited at 122° and sample stage sited in 148° 268

Figure 9.2.6.7 The mapping of Q/I for the nanograter that protrusion in different angles:
(a) 5.6° , (b) 27.2° , (c) 40° , (d) 80° , (e) 90° , (f) 116.3° , (g) no protrusions, when
P||A, polarizer sited at 122° and sample stage sited in 148° 269

Figure 9.2.6.8 The mapping of U/I for the nanograter that protrusion in different angles:
(a) 5.6° , (b) 27.2° , (c) 40° , (d) 80° , (e) 90° , (f) 116.3° , (g) no protrusions, when
P||A, polarizer sited at 122° and sample stage sited in 148° 269

Figure 9.2.6.9 The mapping of V/I for the nanograter that protrusion in different angles:
(a) 5.6° , (b) 27.2° , (c) 40° , (d) 80° , (e) 90° , (f) 116.3° , (g) no protrusions, when
P||A, polarizer sited at 122° and sample stage sited in 148° 269

Figure 9.2.6.10 The mapping of χ for the nanograter that protrusion in different angles:
(a) 5.6° , (b) 27.2° , (c) 40° , (d) 80° , (e) 90° , (f) 116.3° , (g) no protrusions, when
P||A, polarizer sited at 122° and sample stage sited in 148° 270

Figure 9.2.6.11 The mapping of ψ for the nanograter that protrusion in different angles:
(a) 5.6° , (b) 27.2° , (c) 40° , (d) 80° , (e) 90° , (f) 116.3° , (g) no protrusions, when
P||A, polarizer sited at 122° and sample stage sited in 148° 270

Figure 9.2.6.12 The mapping of δ for the nanograter that protrusion in different angles:
(a) 5.6° , (b) 27.2° , (c) 40° , (d) 80° , (e) 90° , (f) 116.3° , (g) no protrusions, when
P||A, polarizer sited at 122° and sample stage sited in 148° 270

Figure 9.2.6.13 The mapping of $\sin\delta$ for the nanograter that protrusion in different
angles: (a) 5.6° , (b) 27.2° , (c) 40° , (d) 80° , (e) 90° , (f) 116.3° , (g) no protrusions,
when P||A, polarizer sited at 122° and sample stage sited in 148° 271

Figure 9.2.6.14 The mapping of Ex for the nanograter that protrusion in different angles:
(a) 5.6° , (b) 27.2° , (c) 40° , (d) 80° , (e) 90° , (f) 116.3° , (g) no protrusions, when
P||A, polarizer sited at 122° and sample stage sited in 148° 271

Figure 9.2.6.15 The mapping of Ey for the nanograter that protrusion in different angles:
(a) 5.6° , (b) 27.2° , (c) 40° , (d) 80° , (e) 90° , (f) 116.3° , (g) no protrusions, when
P||A, polarizer sited at 122° and sample stage sited in 148° 272

Figure 9.2.6.16 The mapping of $Re(Ey)$ for the nanograter that protrusion in different

angles: (a) 5.6°, (b) 27.2°, (c) 40°, (d) 80°, (e)90°, (f) 116.3°, (g) no protrusions, when P A, polarizer sited at 122° and sample stage sited in 148°	272
Figure 9.2.6.17 The mapping of $Im(Ey)$ for the nanograter that protrusion in different angles: (a) 5.6°, (b) 27.2°, (c) 40°, (d) 80°, (e)90°, (f) 116.3°, (g) no protrusions, when P A, polarizer sited at 122° and sample stage sited in 148°	272
Figure 9.2.6.18 The mapping of $Ex1$ for the nanograter that protrusion in different angles: (a) 5.6°, (b) 27.2°, (c) 40°, (d) 80°, (e)90°, (f) 116.3°, (g) no protrusions, when P A, polarizer sited at 122° and sample stage sited in 148°	273
Figure 9.2.6.19 The mapping of $Ey1$ for the nanograter that protrusion in different angles: (a) 5.6°, (b) 27.2°, (c) 40°, (d) 80°, (e)90°, (f) 116.3°, (g) no protrusions, when P A, polarizer sited at 122° and sample stage sited in 148°	273
Figure 9.2.6.20 The mapping of $\delta1$ for the nanograter that protrusion in different angles: (a) 5.6°, (b) 27.2°, (c) 40°, (d) 80°, (e)90°, (f) 116.3°, (g) no protrusions, when P A, polarizer sited at 122° and sample stage sited in 148°	274
Figure 9.2.6.21 The mapping of a for the nanograter that protrusion in different angles: (a) 5.6°, (b) 27.2°, (c) 40°, (d) 80°, (e)90°, (f) 116.3°, (g) no protrusions, when P A, polarizer sited at 122° and sample stage sited in 148°	274
Figure 9.2.6.22 The mapping of b for the nanograter that protrusion in different angles: (a) 5.6°, (b) 27.2°, (c) 40°, (d) 80°, (e)90°, (f) 116.3°, (g) no protrusions, when P A, polarizer sited at 122° and sample stage sited in 148°	274
Figure 9.2.6.23 The mapping of dP for the nanograter that protrusion in different angles: (a) 5.6°, (b) 27.2°, (c) 40°, (d) 80°, (e)90°, (f) 116.3°, (g) no protrusions, when P A, polarizer sited at 122° and sample stage sited in 148°	275
Figure 9.2.7.1 SEM image of rectangle nanograter: (a) sample: 20, (b) sample 34, (c)sample 36.....	276
Figure 9.2.7.2 The mapping of $ Ex1 $ for the nanograter that protrusion in different direction, when the polarization azimuth angle sited at 122° and sample stage sited in 148° : (a) sample 20, protrusion along the azimuth angle of polarization ($P \parallel A$);	

(b) sample 34, no protrusion; (c) sample36, protrusion perpendicular to the azimuth angle of polarization ($P \perp A$).....	276
Figure 9.2.7.3 The mapping of $ E_{y1} $ for the nanograter that protrusion in different direction, when the polarization azimuth angle sited at 122° and sample stage sited in 148° : (a) sample 20, $P \parallel A$; (b) sample 34, no protrusion; (c) sample36, $P \perp A$	277
Figure 9.2.7.4 The mapping of δ_1 for the nanograter that protrusion in different direction, when the polarization azimuth angle sited at 122° and sample stage sited in 148° : (a) sample 20, $P \parallel A$; (b) sample 34, no protrusion; (c) sample36, protrusion perpendicular to the azimuth angle of polarization $P \perp A$	277
Figure 9.2.7.5 SEM image of (a) sample 24, (b) 25 and (c) 26	278
Figure 9.2.7.6 The mapping of $ E_{x1} $ for the square-nanograter that protrusion in different angles, when the polarization azimuth angle sited at 122° and sample stage sited in 148° , sample number: (a) 24, (b) 25, c) 26	278
Figure 9.2.7.7 The mapping of $ E_{y1} $ for the square-nanograter that protrusion in different angles, when the polarization azimuth angle sited at 122° and sample stage sited in 148° , sample number: (a) 24, (b) 25, (c) 26.....	279
Figure 9.2.7.8 The mapping of δ_1 for the square-nanograter that protrusion in different angles, when the polarization azimuth angle sited at 122° and sample stage sited in 148° , sample number: (a) 24, (b) 25, c) 26	279
Figure 9.2.7.9 SEM image of flower-shape nanograter, sample number: (a) 13, (b) 14 (c) 15, (d) 19.....	280
Figure 9.2.7.10 The mapping of $ E_{x1} $ for the nanograter that protrusion in different angles, when the polarization azimuth angle sited at 122° (sample stage sited in 146° for sample 13, 14, 15 and 148° for sample 19), sample number: (a) 13, (b) 14 (c) 15, (d) 19	281
Figure 9.2.7.11 The mapping of $ E_{y1} $ for the nanograter that protrusion in different angles, when the polarization azimuth angle sited at 122° (sample stage sited in	

146° for sample 13, 14, 15 and 148° for sample 19), sample number: (a) 13, (b) 14
(c) 15, (d) 19282

Figure 9.2.7.12 The mapping of δ_1 for the nanograter that protrusion in different angles,
when the polarization azimuth angle sited at 122° (sample stage sited in 146° for
sample 13, 14, 15 and 148° for sample 19), sample number: (a) 13, (b) 14 (c) 15,
(d) 19.....283

List of tables

Table 4.5.1.1 The values of Bessel function at 2.405 rad and 3.0536rad	49
Table 4.5.4.1 The calibration parameter of the LED source with 6 channel (S3, S4, S5, S6, S11, and S12) method: the comparison on the differential ratio of γ_4 , $\gamma_1 = \gamma_2 = \gamma_3 = 1$	60
Table 4.5.4.2 Calibration parameters at different temperatures, the elliptical polarization is acquired under the retarder at 65°	61
Table 4.5.4.3 calibration parameters at different temperatures, the elliptical polarization is acquired under the polarizer at 45°	62
Table 4.5.4.4 The maximum value of Stokes parameters U and V under different room temperatures, using the same calibration matrix K under 22.6°C	67
Table 4.5.4.5 absolute error and relative error of maximum Stokes parameters U and V at temperature variation of 0.4°C and 1.3°C	68
Table 4.5.4.6 The comparison of the calibration parameters tested at different LED current with 660nm filter.	70
Table 4.5.4.7 the comparison of the calibration parameter tested with different wavelength filter using 670nm retarder at the same drive current (400mA) of the LED.....	70
Table 4.5.4.8 the relative error produced by using different filter , filter (660nm) and the filter (670nm). The light source driving current is 400mA and retarder wavelength is 670nm.....	71
Table 4.5.4.9 The calibration comparison on the Stokes polarimetric microscope between the situation with and without a filter.	72
Table 4.5.4.10 calibration parameters tested at different increment of angle in twelve channel method.	73

Table 5.2.2.1 Comparison of the time used in the running of three program versions	85
Table 5.2.2.2 the parameters of the camera setting in two program when selecting the same special area of the CCD.	85
Table 5.2.3.1 Comparison of seven version developed on LabVIEW environment.....	86
Table 6.2.1.1 The experiment of the AlGaN/GaN/SiC on microscope.....	106
Table 6.2.6.1 The figures of intensity of defects 3, 4 and 5 at different focus position.	133
Table 6.2.6.2 The figures of Stokes parameter V of defects 3, 4 and 5 at different focus position.....	134
Table 6.2.6.3 The figures of azimuth angle ψ of defects 3, 4 and 5 at different focus position.....	135
Table 7.1.1.1the experiment of pinhole conducted using the microscope	139
Table 7.2.1.1 The exposure time of the images took at six planes (a-f).....	140
Table 8.1.1.1 The experiment parameter on liquid crystal droplet polarization observation.....	162
Table 9.1.1.1 the experiment of nanograter performed on the microscope: “ \neg ” means the protrusion of the nanograter facing the light source; “ \dashv ” means the protrusion of nanograter is facing the camera	194
Table 9.2.2.1 The configuration of the axis of polarizer (P) and the axis of nanograter (A).....	214
Table 9.2.3.1the configuration of the sample stage rotation experiment—the protrusion facing to the camera.	235
Table 9.2.5.1 The table of showing the visible part and the invisible part in the image of Physical quantity (‘ \neg ’ represent the U-shape hole; ‘ \dashv ’ represent the protrusion)	265
Table 9.2.6.1 The name of the samples and the relevant angles	265

Acknowledgement

At the end of my thesis, I am going to acknowledge my two supervisor Tiehan Shen and Heather Yates, providing me a chance to study in UK. I am going to thank you my colleague Grenville Jones for the thesis revision, Jorge Luis Romas Angulo for the guiding in the experiment, and Huda Alzahrani for the discussion.

I want to say thank you to my supervisor Tiehan Shen. His requirement of repeating the experiment is the most impression to me. At the beginning, I felt frustrated for repeating the experiment. But later, I find it is important and repeat the experiment by myself. In the way of exploring the truth in science, the repeatability is important before publishing, because the reason behind the phenomenon is not easily to be found. The sceptical spirit is the origin of knowledge. I am going to say thank you to Mike Clegg, Bruce Lucie for the support on technique in the experiment. I am going to say thank you to my English teacher Maggi for research methodology introduction, and Amanda for my written English improvement.

I am going to say thank you to my family, my mother, my father, my husband and my daughter. They accompany with me in UK for three years of my PhD life. They give me a support in spirit and encourage me when I meet any frustration. I want to say thank you to my every friend in UK, who provide me a help in need and make my life in UK abundant.

I am going to acknowledge my foundation supporter, China Scholarship Council, supporting my study in UK. I am going to acknowledge University of Salford, providing my tuition fee for my PhD study.

Abbreviations: The symbols in thesis

α	Angle between an optical axis of retarder and x-axis
β	Angle between an optical axis of analyser and x-axis
θ	Angle of the optical axis of polarizer in laboratory coordinate
δ	Retardation of a phase
μ	Phase retardance of linear birefringence
ν	Orientation angle of linear birefringence
γ	Optical rotation angle of linear birefringence
θ_d	Optical rotation angle of linear dichroism
D	Linear dichroism
R	Circular dichroism
p_1, p_2, p_3	Component of polarize in Q, U, and V direction
d_1, d_2, d_3	Component of diattenuation of Q, U, and V
e_1, e_2, e_3	Component of depolarization in Q, U and V direction
E	the electric vector
B	magnetic induction
D	electric displacement
H	magnetic vector
j	Free carrier density passing the surface
ρ	electric charge density
σ	specific conductivity
ε	electric permittivity
μ	magnetic permeability
ω	the circular frequency of the plane wave
k	the wave vector
k	The value of wave vector

z	the position of light analyzed in z axis
ϕ	Absolute phase of a plane wave
ϕ_x	Absolute phase of a plane wave along x-axis
ϕ_y	Absolute phase of a plane wave along y-axis
$I_{0^\circ}, I_{45^\circ}, I_{90^\circ}, I_{135^\circ}$	the intensity of the linear polarization along the $0^\circ, 45^\circ, 90^\circ, 135^\circ$
I_r	the intensity of right-hand circular polarization
I_l	the intensity of left-hand circular polarization
I, Q, U, V	Stokes parameters
I_{dP}/I	Normalized depolarization
$Q/I, U/I, V/I$	Normalized Stokes parameters
χ	ellipticity angle
ψ	azimuth angle
ndP	Degree of depolarization
I_{dp}	The intensity of depolarization
P	electric polarization induced by the electromagnetic wave
M_B	magnetic polarization induced by the electromagnetic wave
a	length of semi-major axis of polarization ellipse
b	length of semi-minor axis of polarization ellipse
I	Intensity of light
J	Jones matrix
$\sigma_i (i = 0, 1, 2, 3)$	Pauli operator
ψ_J	Jones vector
S	Stokes vector
Ψ_M	Stokes vector
ϵ_r	Relative electric permittivity

χ_r	Electric susceptibility
Ω_1	Frequency of photo elastic modulator one
Ω_2	Frequency of photo elastic modulator two
\mathbf{M}_{cb}	Mueller matrix of circular birefringence
\mathbf{M}_{lb}	Mueller matrix of linear birefringence
\mathbf{M}_{ld}	Mueller matrix of linear dichroism
\mathbf{M}_{cd}	Mueller matrix of circular dichroism
Λ	The extinction angle of the wave plate
\mathbf{M}_s	The Mueller matrix of a sample
$[\boldsymbol{\epsilon}_r]$	The permittivity tensor
$[\boldsymbol{\epsilon}_r']$	The real part of the permittivity tensor
$[\boldsymbol{\epsilon}_r'']$	The imaginary part of the permittivity tensor
ω_a	The rotating angular frequency of the analyzer
φ_s	The orientation angle of the specimen
ϑ	The rotation angle between the polarization coordinate and laboratory coordinate
$ E_x $	The modulus of electric field along x-axis
$ E_y $	The modulus of electric field along y-axis
δ	The phase difference between x-axis and y-axis
δ_1	The phase difference between x1-axis and y1-axis
$ E_{x1} $	The modulus of electric field along x1-axis
$ E_{y1} $	The modulus of electric field along y1-axis
P	The optical axis of a polarizer
A	The symmetric axis of the nanograter
C	The angle between the polarization direction and the circular normal
XOY	The laboratory coordinate
X ₁ OY ₁	The polarization coordinate

Abstract

In this thesis, a dual photo elastic modulator-based Stokes polarimetric method for polarization measurement is described, which forms the basis of the operation of a prototype polarimetric microscope. The operational characteristics of the microscope have been characterized in this study and optimized. The polarimetric imaging technique has been applied to the study of four material systems, namely, micropipe defects in SiC, a pinhole, liquid crystal droplets, and nanograting structures. The thesis includes ten chapters, which provide the description of polarization, literature review of the research, the methodology of the Stokes polarimetry and its calibration, computer automation of the measurements and the characterization and the optimization of the performance of the Stokes polarimetric microscope, a detailed study of the polarimetric images of micropipes and their strain fields in SiC wafers, a pinhole in a metallic film, and the polarization characteristics of liquid crystal droplets, the polarization characteristics of plasmonic nanograting structures on gold film.

This polarization state is sensitive to the structure of a material. Under the assumption of a plane wave, the local electrical field is obtained. This microscope realizes mapping the full polarization states in area widefield setting with high sensitivity and good spatial resolution under a single optical setup. A set of experimental parameters, such as the ambient temperature, light source construction, and polarization angle setting, have been optimized; as well as, the optical alignments, data analysis method, and image acquisition program implemented to provide an efficient operation of the microscope. The mapping of the polarization parameter provides a new way to research the characteristics of material; It also provides vector data for understanding the behavior of the interaction between light and materials. The work demonstrates that the Stokes polarimetric imaging method is useful and may have potential applications in a wide range of research fields.

Chapter 1 **Introductory**

Light is an electromagnetic wave, which is described through the Maxwell equations. The solution of the Maxwell equation is a sinusoidal wave in two orthogonal directions which perpendicular to the propagation of the light. Light is a transverse wave. The phase difference of the light includes the information of birefringence which reflects the matter structure when a light interacted with the matter. The measurement method of the polarization is called the Stokes polarimetry.

The Stokes polarimetry is used to measure the Stokes parameters of the polarized light. The Stokes parameters are a set of the difference of the intensity detected in special orientation angles reference to the laboratory coordinate; so, the Stokes polarimetry is proceeding in a laboratory coordinate. Technically, the detection of the polarization of light is based on the detection of the intensity. The Stokes parameter describe the state of polarization entirely, no matter the partially polarized light or completely polarized light.

The set-up of the Stokes polarimetry is Dual-Photo Elastic Modulator (PEM) Stokes polarimeter, which includes two PEMs, one analyzer, and an intensity detector. In theory, every optics is represented as a Mueller matrix, and the effect of dual-PEM Stokes polarimetry to a polarized light is the product of the Mueller matrix of the three optics. In practical, the configuration of the optical axis of the three optics (PEM1, PEM2, and Analyser) is setting in special angles (0° , 45° , 22.5°). Under the settings, the K matrix, which connect the experiment signal and the Stokes parameters, is diagonalized. Using the Fourier transformation, the signal of the Stokes parameters is divided into the four parts, which is three AC signal detected with three lock-in amplifier and one DC signal detected with a picometer. The principle of dual-PEM Stokes polarimetry is described in Guan's paper.

Based on dual-PEM Stokes polarimetry. I found optimum operational settings of the dual-

PEM Stokes polarimetry. It includes: firstly, the sample stage should be separated to the Stokes polarimeter (including two PEMs, one analyzer, and one detector) ; secondly, the position of the sample stage is fixed in every measurement; thirdly, the position of the retarder is fixed in light path; fourthly, the set-up should be settled on a stage with the less vibration; the room temperature should be controlled in 22.1°C to 22.6°C; fifthly, the monochromaticity make the measurement more accurate; sixthly, the driven current of the light source should be fixed during the calibration process and the measurement process.

Our group established a dual-PEM based Stokes polarimetric microscope, which using the dual-PEM Stokes polarimetry on to a microscope. The Stokes polarimetry imaging technique is the research focus of my PhD thesis. It includes a program developing that control the timing unit and the camera automatically, using the LabVIEW environment. Also, I have found its optimum operation polarizer setting so as to minimize the artifacts which are most likely due to stray lights in the microscope introduced by the insertion into the optical path of additional optical devices. I developed a set of jigsaw washer (the thickness is 1mm, 2mm, 5mm, 10mm, 20mm, 50mm) to control the parallel and adjust the distance between the optics freely, that makes the adjustment of the equipment more efficiency. I developed a method to adjust the parallel light which is very important on the microscope because an unparallel light can produce the stray light when the light reflected on the surface of the optics, which used for imaging. An image of the depolarization with a flat uniform background is acquired for the first time on our equipment.

Using the Stokes polarimetry microscope, four special system is researched to evaluate the microscope: i) a pinhole, to verify the operation of the imaging system can acquire a good spatial resolution, ii) micropipe defects, to prove the micro strain distribution can be detected using the Stokes polarimetry microscope, iii) liquid crystal droplets, to prove the interface in

the liquid crystal droplet can be detected using the polarization imaging technique, iv) nanograter structures, to show that it is possible to relate the polarization information obtained to the local electric vector field distributions, with a plane wave incidence assumption.

Based on the research on the four different type of sample , we verified that the polarimetric microscope can provide a polarimetric imaging; we identified an optimum polarizer setting, enable polarization information being obtained at pixel level with good image spatial resolution (Using the LED light source and optimized the light path of the microscope and optimum calibration prerequisite, the resolution reached $1 \mu\text{m}$ for the first time); with a plane wave incidence assumption, experimental observations may be directly comparable to future theoretical modelling; we proved that the polarimetric image can reflect the inner boundary of a sample.

The thesis includes the Stokes polarimetry imaging technique and its application. A Stokes polarimetric microscope is established and characterized using four material system with different structures, for example micropipe, pinhole, nanograter, and liquid crystal. Based on Stokes polarimetric microscope, the mapping of the polarization parameters is acquired. Using the relationship between the parameters of the polarization description, many other parameters beside the Stokes parameters, electrical field and the phase difference, is deduced.

All the thesis includes ten chapters.

Firstly, the fundamental knowledge about the description of polarization is introduced in chapter two: such as, Maxwell equations, Mueller calculus, Jones calculus, the transformation between Jones calculus and Mueller calculus. The interaction between the matter and the light is described carefully.

Chapter three summarize the research background of the four-measurement system that introduced to evaluate the microscope, such as micropipe, pinhole, liquid crystal droplet, and nanograter. Micropipe is a kind of defect with big strain in the silicon carbide, which is good example to show the strain characterization function of the Stokes polarimetric microscope. The pinhole is a simplest round structure and is a good example to prove the resolution of the microscope and the polarized light diffraction. Only scattering happens when the light passing through the pinhole. Pinhole is a good example to characterize the effect produced by the scattering process. The four kind of liquid crystal droplet are a ball shaped structure in general with different inner structure inside of the ball. It is a good example to prove the priority of the inner structure detection function with the polarimetric microscope. The nanograter is a three-dimensional scattering structure with a splitting resonance ring. It adjusts the electromagnetic wave with scattering process in special direction. Except the nanograter system, the circle boundary condition is the common point of the micropipe, pinhole, liquid crystal, that introduce a fourfold structure on the image of the Stokes parameters.

Chapter four introduces the experimental technique of Stokes polarimetry: including theory; experimental setup; the calibration process; the effect of the temperature and light source wave front and the monochromaticity to the calibration matrix.

Chapter five introduce a Stokes polarimetry microscope. Some developed technique is introduced: including the controlling software development, the alignment of the microscope, the method of acquiring a uniform background, and the method of acquiring a parallel light. An illumination configuration increases the resolution of the microscope much than that before and acquired a uniform background. A uniform background of depolarization is only existed at a special polarization angle cross with the analyser.

Chapter six introduce the research of the micropipe using Stokes polarimetric microscope. The micro strain distribution near to the micropipe is detected through Stokes polarimetric microscope sharply. Micropipe is a three-dimensional structure, only the position near to the focus plane can be see clearly.

Chapter seven demonstrate the polarization mapping of a pinhole. The variation of the polarization after passing a pinhole, is from the scattering of the edge of the pinhole. The Stokes parameter because of the pure edge scattering effect is shown in this chapter. Also, the Airy-like pattern of the Stokes parameters is detected at different focus position on the microscope. The image of the normalized Stokes parameters is in bad quality because of big scattering around the edge of the pinhole, which makes the intensity, as a denominator, at that position very small.

Chapter eight demonstrate the Stokes parameter image of four kind of liquid crystal droplets. Beside the shape of the liquid crystal droplet detected with the intensity signal, the inner structure inside the liquid crystal is detected with the Stokes parameter signal, through using Stokes polarimetry microscope. The process of the light interacted with the liquid crystal droplet is a refractive process, the variation of the polarization is not only because of the edge inside of liquid crystal but also because of the refractive index.

Chapter nine demonstrate the mapping of the nanograter, which is another scattering system like the pinhole, but in three-dimension. The phase difference of the electrical field is measured. The electrical field varies with the relative angle between the polarization and the nanograter alignment. The nanograter can modulate the electromagnetic wave for its splitting resonance ring structure. The electrical field around the nanograter is obtained, assuming the inner light is a plane wave. When the azimuth angle of polarization is along with axis of symmetry of the nanograter, a special electrical field distribution (heart shape) is acquired.

Chapter ten summarize the thesis and shows the future work. The Stokes polarimetric microscope is established and running automatically. The best calibration parameters are acquired in the optimum alignment. The Stokes polarimetric microscope is useful to measure the micro strain around a micropipe in silicon carbide, and it can detect the inner structure of a liquid crystal droplet. In the phenomenon produced by the edge scattering, the direction of the edge is sensitive to the polarization variation. The timing unit need to improve further to measure the intensity signal accurately.

In Appendix, the method of acquiring a Mueller matrix of a sample in experiment is stated; the method of extracting polarization parameters through Mueller Matrix is introduced, too.

Chapter 2 The description of polarization

This chapter presents a description of the state of polarization of light and the related mathematical method. Details of the matrix inversion technique to determine the optical characteristic of the sample relevant to the measurement of polarization with Stokes polarimetry are also presented.

2.1 Description of polarization

2.1.1 Maxwell's equation

Light is part of the electromagnetic radiation spectrum, and is described by Maxwell's equations (Born & Wolf, 1959). The Maxwell equations in continuous medium can be written as follows,

$$\nabla \times \mathbf{H} - \frac{\partial \mathbf{D}}{\partial t} = \mathbf{j}, \quad (2.1.1.1)$$

$$\nabla \times \mathbf{E} + \frac{\partial \mathbf{B}}{\partial t} = 0, \quad (2.1.1.2)$$

$$\nabla \cdot \mathbf{D} = \rho, \quad (2.1.1.3)$$

$$\nabla \cdot \mathbf{B} = 0. \quad (2.1.1.4)$$

\mathbf{E} is the electric vector, \mathbf{B} is magnetic induction, \mathbf{D} is electric displacement, \mathbf{H} is magnetic vector, \mathbf{j} is free carrier density passing through the surface, ρ is electric charge density.

When an electromagnetic wave propagates through a substance, the material equations need to be considered. The simplest form is shown below in the situation of a homogeneous and isotropic material.

$$\mathbf{j} = \sigma \mathbf{E}. \quad (2.1.1.5)$$

$$\mathbf{D} = \varepsilon \mathbf{E} \quad (2.1.1.6)$$

$$\mathbf{B} = \mu \mathbf{H} \quad (2.1.1.7)$$

where, σ is conductivity, ϵ is electric permittivity, μ is magnetic permeability.

Electromagnetic radiation is a transverse wave, with the field \mathbf{E} and \mathbf{H} perpendicular to the direction of propagation, hence,

$$\mathbf{E} \cdot \mathbf{s} = \mathbf{H} \cdot \mathbf{s} = 0. \quad (2.1.1.8)$$

Here, \mathbf{s} denotes a unit vector in the direction of propagation of the light, which is along the z axis in Cartesian coordinates. The electric field of a linear polarized light beam along x-axis and y-axis, which are solutions of electromagnetic wave equation, are described by equations 2.1.1.9 and 2.1.1.10 (Kliger, Lewis, & Randall, 1990, p.91). We consider the nature of the curve which the end point of the electric vector describes at a typical point in space; this curve is the locus of the point whose coordinates $(\mathbf{E}_x, \mathbf{E}_y)$ are

$$\mathbf{E}_x = \mathbf{E}_x^0 \cos(\tau + \phi_x) = E_x^0 \sin(\omega t - kz + \phi_0) \mathbf{i}, \quad (2.1.1.9)$$

$$\mathbf{E}_y = \mathbf{E}_y^0 \cos(\tau + \phi_y) = E_y^0 \sin(\omega t - kz + \phi_0 + \delta) \mathbf{j} \quad (2.1.1.10)$$

The direction of polarization is the direction of the electric vector. Where, τ denotes the variable part of the phase factor, $\tau = \omega t - \mathbf{k} \cdot \mathbf{r}$, \mathbf{k} is the wave vector, whose magnitude is the wave number k ; $k = \frac{\omega}{c}n$, ω is the angular frequency of the plane wave; n is the refractive index of a media; c is the velocity of light; the orientation of \mathbf{k} is along z-axis; \mathbf{i} and \mathbf{j} are unit vectors along the x and y axes respectively; ϕ_0 is a constant specifying its absolute phase; E_x^0 is the magnitude of the electric field along x-axis; E_y^0 is the magnitude of the electric field along y-axis; t is the time at given point; and z is a point along z-axis; δ is the phase difference between ϕ_y and ϕ_x .

For an elliptically polarized plane wave propagating along z-axis in an isotropic media with refractive index n , the electric field is given by (Allia, P. , Oldano, C., and Trossi, 1988)

$$\mathbf{E} = \text{Re}[(E_x \mathbf{i} + E_y \mathbf{j}) \exp i(kz - \omega t)] \quad (2.1.1. 11)$$

Where, Re means the “real part of” and $E_x = a \exp(i\phi_0)$, $E_y = b \exp(i(\phi_0 + \delta))$.

where, the plane of polarization is the plane containing the electric vector and the direction of propagation.

The interaction of matter and field through polarization \mathbf{P} and magnetization \mathbf{M} of the material, is given by,

$$\mathbf{D} = \varepsilon_0 \mathbf{E} + \mathbf{P}, \quad (2.1.1. 12)$$

$$\mathbf{B} = \mu_0 (\mathbf{H} + \mathbf{M}_B) \quad (2.1.1. 13)$$

Here, \mathbf{P} is called the electric polarization induced by the electromagnetic wave passing through a medium and \mathbf{M}_B is the magnetic polarization induced by the electromagnetic wave passing through a medium.

In homogeneous, linear and isotropic matter

$$\mathbf{P} = \chi \varepsilon_0 \mathbf{E}. \quad (2.1.1. 14)$$

$$\chi = \varepsilon_r - 1 \quad (2.1.1. 15)$$

where, χ is the electric susceptibility, ε_r is the relative permittivity.

Solid matter is made of atoms, especially for the crystal, that are arranged in special lattice which depends on the crystal class. “The response \mathbf{P} in a solid is not necessarily parallel to the excitation as in gas or liquid (Huard, 1997, p.39)”. Then the relative permittivity and electric susceptibility are relative permittivity tensor $[\varepsilon_r]$ and electric susceptibility tensor $[\chi]$.

These are related through the relation

$$[\varepsilon_r] = [I] + [\chi], \quad (2.1.1. 16)$$

Each term of the tensor $[\varepsilon_r]$ is related to the terms of the tensor $[\chi]$ by the relation

$$\epsilon_{rij} = \delta_{ij} + \chi_{ij}, (i, j = 1, 2, 3), \quad (2.1.1. 17)$$

Where, δ_{ij} is Kronecker symbol ($\delta_{ij} = 1$ if $i = j$ and 0 if $i \neq j$). Tensor $[\epsilon_r]$ contains nine terms and only six of them are independent (Huard, 1997, p.39). “Moreover, in loss-free media and depending on the crystal class, the number of independent terms may still be reduced (Huard, 1997, p.39)”.

For non-absorbent material (Huard, 1997, p. 40), $\epsilon_{rij} = \epsilon_{rji} = \epsilon_{rji}^* = \epsilon_{rij}^*$ and ϵ_{rji}^* are the Hermite of ϵ_{rij} and ϵ_{rji} . Only birefringence will be considered in a case of non-absorption media. In a proper reference system, the $[\epsilon_r]$ is a real, diagonal tensor (Huard, 1997, p.41). Considering a non-magnetic media, with magnetic permeability constant μ_0 , the refractive index is related to the electric permittivity, $\epsilon_{ri} = n_i^2$, $i = x, y, \text{ or } z$. According to $[\epsilon_r]$, media is classified as isotropic media ($\epsilon_{rx} = \epsilon_{ry} = \epsilon_{rz}$), uniaxial anisotropic media ($\epsilon_{rx} = \epsilon_{ry} \neq \epsilon_{rz}$), and biaxial anisotropic media (Huard, 1997, p.42)($\epsilon_{rx} \neq \epsilon_{ry} \neq \epsilon_{rz}$).

However, in the case of absorbent media, the dichroism is going to be considered as well as birefringence. The $[\epsilon_r] = [\epsilon_r'] + i[\epsilon_r'']$ (Huard, 1997, p.65). Where, $[\epsilon_r']$ is a real tensor related with the birefringence; $[\epsilon_r'']$ is an imaginary tensor related to the dichroism.

Considering a complex refractive index \hat{n} , $\hat{n} = \nu + i\kappa$, $\hat{n}^2 = \epsilon_r$, Where, the ν is the refractive index and κ is the extinction index (Huard, 1997, p.65).

According to the definition in table B.1.1, for the linear birefringence, $\delta = 2\pi(n_s - n_f)l/\lambda$; for circular birefringence, $\gamma = 2\pi(n_- - n_+)l/\lambda$; for the linear dichroism, $D = 2\pi(\mu_s - \mu_f)l/\lambda$; for circular dichroism(Pham & Lo, 2012), $R = 2\pi(\mu_- - \mu_+)l/\lambda$; where, l is the thickness of the material; λ is the wavelength of the test light beam; n_s and n_f are the refractive index along slow axis and fast axis; μ_s and μ_f are the absorption coefficient of slow axis and fast axis; n_+ and n_- represents refractive index of right circular polarization

and left circular polarization; μ_+ and μ_- represents the absorption coefficient of right circular polarization and left circular polarization.

Based on the statement above, the relationship between phase shift δ and anisotropy of the optical birefringence ($n_s - n_f$) are established.

The polarization of the light is represented through Jones Matrix and Mueller Matrix. The waves that satisfy Maxwell's equations are transverse, hence there are different ways for the electric field (or magnetic field) to vibrate -- different ways of vibration resulting in different states of polarization of electromagnetic wave. Polarization is defined by the electric field. For plane polarized light, the electric field oscillates in only one direction. Polarization happens when light interacts with matter. The quantities of polarization and magnetization represent the influence of matter on the electromagnetic field (Born & Wolf, 1959). In the simplest case, for linear optical response of homogeneous and isotropic material, the interaction of light and media can be introduced through the polarization and magnetization of the materials. Boundaries and anisotropic materials may change the state of polarization of light as it traverses through the medium.

In other words, the properties of the internal electric field \mathbf{E} and magnetic field \mathbf{H} in matter are related to the polarization properties because of the interaction of the light and matter; so, the measurement of polarization is the key to analyze the information of the internal \mathbf{E} and \mathbf{H} of matter. The research presented focus on the study of the polarization state of light as it interacts with novel material.

2.1.2 Stokes representation

Polarization state of light can be described by Stokes parameters, (I, Q, U, V). The parameters were introduced by George Stokes in 1852. They are defined as (Bashara, 1989;

Huard, 1997, p.24)

$$I = I_{0^\circ} + I_{90^\circ} = I_{45^\circ} + I_{135^\circ} = I_r + I_l, \quad (2.1.2.1)$$

$$Q = I_{0^\circ} - I_{90^\circ} \quad (2.1.2.2)$$

$$U = I_{45^\circ} - I_{135^\circ} \quad (2.1.2.3)$$

$$V = I_r - I_l \quad (2.1.2.4)$$

where, I_{0° , I_{45° , I_{90° , I_{135° are, respectively, the intensity of the linear polarization along the 0° , 45° , 90° , 135° , with respect to x-axis of the laboratory coordinate, respectively; I_r is the intensity of right-hand circular polarization; and, I_l is the intensity of left-hand circular polarization.

Stokes parameters can be used to describe not only totally polarized light, but also partially polarized light. $Q/I = S_1$, $U/I = S_2$, and $V/I = S_3$ are the coordinates along **x**, **y**, and **z** axes on the Poincaré sphere(Huard, 1997,p.25), shown in Fig. 2.1.2.1. In Fig. 2.1.2.1, I_p equals one; χ is ellipticity angle; and Ψ is azimuth angle.

Q , U , and V are polarization components along x-axis, y-axis, z-axis in the Poincaré Sphere (Huard, 1997, p.25), which is shown in Fig. 2.1.2.1. Any fully polarization state is represented as a point on Poincaré Sphere. The linear polarization is represented by points in the equatorial plane ($V = 0$); the right-handed circular polarization is represented by the north pole ($Q = U = 0, V = I$); the left-handed circular polarization is represented by the south pole ($Q = U = 0, V = -I$); and elliptical polarization is represented all other points on the Poincaré Sphere. Partially polarized light is a point inside the Poincaré sphere.

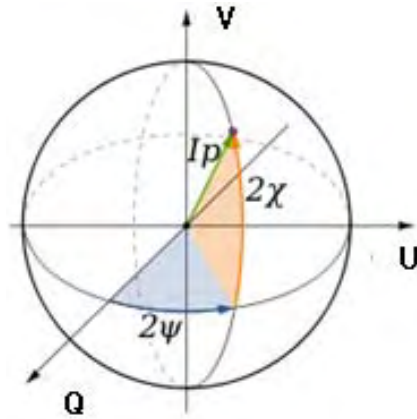


Figure 2.1.2.1 Poincaré representation of the state of polarization of a monochromatic wave.

For totally polarized light, the Stokes parameters obey the relationship below.

$$I^2 = Q^2 + U^2 + V^2 \quad (2.1.2.5)$$

For partial polarized light, the Stokes parameters obey the relationship below.

$$I^2 > Q^2 + U^2 + V^2 \quad (2.1.2.6)$$

The retardation of phase of a polarization is represented as

$$\delta = \text{atan} \left(\frac{V}{U} \right) \quad (2.1.2.7)$$

Retardation of a phase δ is an important physical quantity, defining the state of polarization of the light. The polarization status is classified through the retardation: where, $\delta = 0^\circ$ or $\delta = 180^\circ$ represents linear polarization; $\delta = 90^\circ$ or $\delta = -90^\circ$ represents the circular polarization; $-90^\circ < \delta < 0$ represents left-handed elliptical polarization; $0 < \delta < 90^\circ$ represents right-handed elliptical polarization.

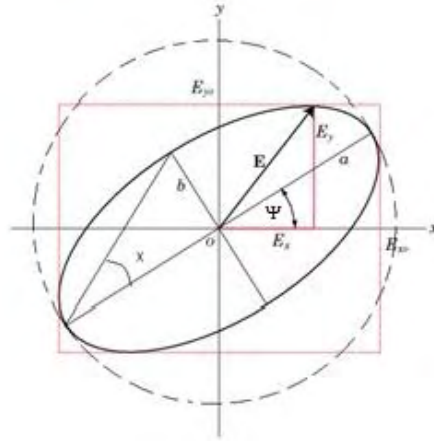


Figure 2.1.2.2 The polarization ellipse of an elliptical polarization.

The state of polarization can be fully described by the Stokes parameters. The relations between the components of polarization are shown on the ellipse on Fig. 2.1.2.2. Given the four Stokes parameters, all polarization characteristics may be derived. For instance, the intensity of depolarization, I_{dp} , can be evaluated by

$$I_{dp} = \sqrt{I^2 - (Q^2 + U^2 + V^2)} \quad (2.1.2.8)$$

The degree of depolarization, ndP is shown below

$$ndP = I_{dp}/I \quad (2.1.2.9)$$

The ellipticity angle, χ , is given by

$$\chi = \frac{1}{2} \sin^{-1} \left(V / \sqrt{Q^2 + U^2 + V^2} \right) \quad (2.1.2.10)$$

The azimuth angle Ψ is deduced by

$$\Psi = \frac{1}{2} \tan^{-1}(U/Q) + \vartheta, \vartheta = \begin{cases} 0, & -45^\circ < 2\Psi < 45^\circ \\ \frac{\pi}{2}, & 45^\circ < 2\Psi < 135^\circ \\ \pi, & 135^\circ < 2\Psi < 225^\circ \\ \frac{3\pi}{2}, & 225^\circ < 2\Psi < 315^\circ \end{cases} \quad (2.1.2.11)$$

According to the calibration result, to be explained in Chapter 2, ϑ added here is to make sure the azimuth angle calculated through the Stokes parameter corresponds to the azimuth angle of the polarization in Laboratory coordinate.

2.2 Representation of polarization

2.2.1 Mueller calculus

The Stokes parameters are readily measurable in the experiment; while, the Jones vectors represented plane wave more directly. Both Jones representation and Mueller representation are used in this thesis to connect experiment with the theory. So, I introduce both Mueller representation and Jones representation in this section and next section.

The Stokes parameters can be represented in vector format. The status of a light beam before interaction with a sample is represented as $[I \quad Q \quad U \quad V]^T$ and the status of a light after interacted with a sample is represented as $[I' \quad Q' \quad U' \quad V']^T$. The relationship between these two vectors is shown as a formula

$$\Psi_M' = \begin{bmatrix} I' \\ Q' \\ U' \\ V' \end{bmatrix} = \mathbf{M} \begin{bmatrix} I \\ Q \\ U \\ V \end{bmatrix} = \mathbf{M} \Psi_M \quad (2.2.1.1)$$

where, the matrix \mathbf{M} is a 4×4 matrix, which is called the Mueller matrix and Ψ_M is Stokes vector. The Mueller matrix is used to represent the effect of the sample or optical components on a beam of light. It is used to describe not only a totally polarized light, but also a partially polarized light. The Stokes vector is

$$\mathbf{S} = \boldsymbol{\psi}_M = \begin{pmatrix} I \\ Q \\ U \\ V \end{pmatrix} = \begin{pmatrix} a^2 + b^2 \\ a^2 - b^2 \\ 2ab\cos\delta \\ 2ab\sin\delta \end{pmatrix} \quad (2.2.1.2)$$

where, a is the semi-major axis of polarization ellipse; b is the semi-minor axis of polarization ellipse shown in Fig. 2.1.2.2; and, δ is the retardation of phase.

According to equation (2.1.2.10) and (2.2.1.2), the relationship between ellipticity angle χ and retardation of phase δ is acquired

$$\chi = \frac{1}{2} \sin^{-1} \left(\frac{2ab\sin\delta}{a^2 + b^2} \right) \quad (2.2.1.3)$$

2.2.2 Jones Calculus

In addition to Stokes representation, an alternative representation of polarized light is the Jones representation and Jones Matrix. The Jones representation is another way to represent polarized light, related to the electrical field of a light, which is easy to relate with the Maxwell equations. The status of a light beam before interaction with a sample is represented as $\boldsymbol{\psi}_J$ and the status of a light beam after interaction with a sample is represented as $\boldsymbol{\psi}'_J$. The relationship between these two vectors is shown as a formula

$$\boldsymbol{\psi}'_J = \mathbf{J}\boldsymbol{\psi}_J \quad (2.2.2.1)$$

where, \mathbf{J} is the Jones Matrix, and $\boldsymbol{\psi}_J$ is the Jones vector.

Reference equation 2.1.1.8 and 2.1.1.9, the Jones vector represents the solution of plane wave directly, which is

$$\boldsymbol{\psi}_J = \begin{pmatrix} E_x \\ E_y \end{pmatrix} = e^{i\phi} \begin{pmatrix} a \\ be^{i\delta} \end{pmatrix} \quad (2.2.2.2)$$

where, a is length of semi-major axis of polarization ellipse; b is length of semi-minor axis of

polarization ellipse shown in Fig. 2.1.2.2; δ is the retardation of phase between two orthogonal directions, x-axis and y-axis. In detail, $e^{i\phi}$ represented by equation 2.1.4.3.

$$e^{i\phi} = e^{i\omega t - i\mathbf{k}\cdot\mathbf{z} + i\phi_x} \quad (2.2.2.3)$$

where, $e^{i\omega t}$ is the time-dependent term, $e^{i\mathbf{k}\cdot\mathbf{z}}$ is the space dependent term, ϕ_x is absolute phase along x-axis. ω is the circular frequency of the plane wave; t is the time of light propagation; \mathbf{k} is the wave vector; \mathbf{z} is the position of light analyzed in z axis.

2.2.3 Transformation between Jones Matrix and Mueller Matrix

The knowledge of the transformation between Jones Matrix and Mueller Matrix is useful to establish the relationship between the experiment and theory. Sometimes we need the matrix for different optical components to do the calculation.

The Mueller matrix \mathbf{M} corresponding to Jones matrix \mathbf{J} is given by (Iam-Choon Khoo, 1988)

$$\mathbf{M} = \mathbf{T}(\mathbf{J} \otimes \mathbf{J}^*) \mathbf{T}^{-1} \quad (2.2.3.1)$$

Where

$$\mathbf{T} = \begin{pmatrix} 1 & 0 & 0 & 1 \\ 1 & 0 & 0 & -1 \\ 0 & 1 & 1 & 0 \\ 0 & i & -i & 0 \end{pmatrix}, \mathbf{T}^{-1} = 0.5 \begin{pmatrix} 1 & 1 & 0 & 0 \\ 0 & 0 & 1 & -i \\ 0 & 0 & 1 & i \\ 1 & -1 & 0 & 0 \end{pmatrix} \quad (2.2.3.2)$$

And \otimes is Kronecker product, \mathbf{J}^* is the Hermite matrix to matrix \mathbf{J} .

$$\mathbf{J} \otimes \mathbf{J}^* = \begin{pmatrix} J_{11}J_{11}^* & J_{11}J_{12}^* & J_{12}J_{11}^* & J_{12}J_{12}^* \\ J_{11}J_{21}^* & J_{11}J_{22}^* & J_{12}J_{21}^* & J_{12}J_{22}^* \\ J_{21}J_{11}^* & J_{21}J_{12}^* & J_{22}J_{11}^* & J_{22}J_{12}^* \\ J_{21}J_{21}^* & J_{21}J_{22}^* & J_{22}J_{21}^* & J_{22}J_{22}^* \end{pmatrix} \quad (2.2.3.3)$$

The relationship between Stokes parameters and Jones Vectors can be written as

$$\Psi_{Mi} = \Psi_{\mathbf{J}}^+ \sigma_i \Psi_{\mathbf{J}}, i = 0,1,2,3. \quad (2.2.3.4)$$

Where Ψ_{Mi} are the Stokes parameters, Ψ_J is the column matrix representing the Jones vector, $\Psi_J^+ = (E_x^*, E_y^*)$ is its adjoint, and

$$\sigma_0 = \begin{pmatrix} 1 & 0 \\ 0 & 1 \end{pmatrix}, \sigma_1 = \begin{pmatrix} 1 & 0 \\ 0 & -1 \end{pmatrix}, \sigma_2 = \begin{pmatrix} 0 & 1 \\ 1 & 0 \end{pmatrix}, \sigma_3 = \begin{pmatrix} 0 & -i \\ i & 0 \end{pmatrix} \quad (2.2.3.5)$$

The operator σ_i ($i = 0, 1, 2, 3$) in equation 2.2.3.5 is the Pauli operator(Cloude, 1986)

2.2.4 The propagation equation for the Stokes parameters

The status of polarization of a light beam, Stokes parameters, may change when the light goes through an optical component.

The propagation equation for the Stokes parameters is (Iam-Choon Khoo, 1988, p.348)

$$\frac{dI}{dz} = 0, \quad \frac{d}{dz} \begin{pmatrix} Q \\ U \\ V \end{pmatrix} = \begin{pmatrix} 0 & -\Omega_3 & \Omega_2 \\ \Omega_3 & 0 & -\Omega_1 \\ -\Omega_2 & \Omega_1 & 0 \end{pmatrix} \begin{pmatrix} Q \\ U \\ V \end{pmatrix},$$

$$\text{or} \quad \frac{d\mathbf{S}}{dz} = \boldsymbol{\Omega} \times \mathbf{S} \quad (2.2.4.1)$$

$$\mathbf{H} = \frac{1}{2} \sum_{i=0}^3 \Omega_i \sigma_i \quad (2.2.4.2)$$

Where $\boldsymbol{\Omega}$ is the vector of components Ω_1, Ω_2 and Ω_3 referred to the Poincaré's space in which the vector \mathbf{S} has been defined as (Q, U, V) , z is the direction of the propagation of light, \mathbf{H} is the propagation matrix. The evolution of the Stokes parameters of polarization is described through equation (2.2.4.2).

For uniaxial medium with optical axis orthogonal to z -axis and without optical activity, the transmission matrix \mathbf{H} is real, $\Omega_3 = 0$. This means $\boldsymbol{\Omega}$ lies in the (Q, U) plane of the Poincaré sphere, and $\mathbf{S}^\pm = \text{const} \cdot \boldsymbol{\Omega}$ corresponds to linearly polarized waves, which are extraordinary and ordinary waves. For an optically active isotropic medium, $\Omega_1 = \Omega_2 = 0, \Omega_3 \neq 0$, the

eigenfunctions of the electromagnetic wave, propagating without changing their polarization, are circularly polarized in opposite directions.

For an optically active anisotropic medium, Ω has, in addition to Ω_3 , a component in the (Q , U) plane of the Poincaré sphere, which is zero only for light propagating along an optical axis. The eigenfunction of the electromagnetic wave is elliptically polarized.

In all the above considered cases, a vector S which is not parallel to Ω rotates, with increasing z , around Ω in such a way that its terminal point describes a circle on the Poincaré's sphere. In the case $\Omega = 0$, which correspond to an isotropic medium without optical activity, S is a constant vector, any wave propagates without changing its polarization state (Iam-Choon Khoo, 1988, p.349).

2.3 Summary

This chapter introduce the theory related to the polarization characterization. The polarization of light describes the vibration plane of the electromagnetic wave. The polarization is described through Stokes calculus and Jones calculus. The Mueller matrix and the Jones matrix, which describe the interaction between the matter and the light, can transform between each other. Also, the anisotropy can change the polarization. This basic knowledge is useful to understand the research in the follow chapters.

Reference

Allia, P. , Oldano, C., and Trossi, L. (1988). Linear optics: matrix methods. In *Physics of Liquid Crystalline Materials: based on lectures delivered at the summer school on the physics of liquid crystals* (p. 339). Italy: Gordon and Breach Science Publisher.

Azzam, R. M. A., & Bashara, N. M. (1988). *Ellipsometry and Polarized Light*. North-Holland:

Elsevier Science Publisher.

Born, M., & Wolf, E. (1959). *Principles of Optics* ((7th (expa). Cambridge University Press.

Cloude, S. R. (1986). Group theory and polarisation algebra. *Optik(Stuttgart)*, 75, 26–36.

Huard, S. (1997). *Polarization of light*. (G. Vacca, Ed.). Paris: John Wiley & Sons, Masson.

Iam-Choon Khoo, F. S. (1988). *Physics of Liquid Crystalline Materials*. (F. S. Iam-Choon Khoo, Ed.), *Based on Lectures Delivered at the Summer School on the Physics of Liquid Crystals*. Bra, Italy: Gordon and Breach Science Publisher.

Kliger, D. S., Lewis, J. W., & Randall, C. E. (1990). *Polarized light in optics and spectroscopy*. London: Academic Press.

Pham, T.-T.-H., & Lo, Y.-L. (2012). Extraction of effective parameters of turbid media utilizing the Mueller matrix approach: study of glucose sensing. *Journal of Biomedical Optics*, 17(9), 97002.

Chapter 3 Literature review

This chapter introduces the research background of the Stokes polarimetry and microscopy based on the Stokes polarimetry. The research background of the four materials used for characterizing the Stokes polarimetric microscope is introduced either.

3.1 Stokes polarimetry

Quantitative determination of the full state of polarization using Stokes parameters, known as Stokes polarimetry, usually requires four separate experimental measurements using one photo elastic modulator. The use of two photo elastic modulators enables the measurements to be conducted simultaneously in a single optical arrangement. This section outlines a brief literature review on Stokes polarimetry.

The Stokes parameters describe the information of a light beam accurately, such as phase, intensity, polarization angle, and ellipticity angle; so, the measurement of the Stokes parameters is meaningful. One PEM method to measure the Stokes parameters, stated in Liu's thesis(Y. Liu, 2005), need much time to finish the measurement, for four steps needed to determine the Stokes parameters. Guan derived a theory of dual photoelastic modulator system to measure the stokes parameters of an arbitrary beam (Guan, Liu, Shen, & Jones, 2008); which can determine the Stokes parameters through one measurement. In the polarization imaginary process, the Stokes parameters mapping distribution is measured in one time. A time unit technology is used in the polarization imaginary system. The development of the acquirement speed in the experiment expand the application range of Stokes polarimetry technology, such as the measurement of the moving particles.

As a part of measurement, calibration is the crux. Before the acquirement of the Stokes parameter, a calibration process is needed. The simplest one is linear regression on one PEM

Stokes polarimetry(Guan et al., 2008); later, the nonlinear optimization method is developed for convenient (Cook, 2010). Paul Cook's thesis(Cook, 2010) introduced the calibration of the linear polarization part carefully; however, the circular polarization calibration part is indistinct. The calibration of circular polarization is important for the Stokes parameter V that related with the birefringence directly; also, the accuracy measurement of the Stokes parameter Q, U, and V, is the prerequisite to obtain a depolarization accurately. Based on the importance of measuring the Stokes parameter V, Calibration method is improved in my thesis. The improvement of calibration includes the circular polarization calibration, quick data acquirement, and data analysis. Till now, the quickest speed of doing the calibration is two hours measurement and two hours analysis. In my experiment, I find the calibration parameter is sensitive to the room temperature and the wave front of the light source, especially the Stokes parameter V. The detail is going to be discussed in chapter 4.

3.2 Stokes polarimetric microscope

The Stokes polarimetric microscope has been developed by Optimum Imaging Ltd. The design principle is published by a patent priority filing (GB201411478D0, T. H. Shen and P. J. Cook.) which incorporate a dual PEM Stokes polarimeter in a widefield microscope. The polarimetric signals are recovered at the pixel level using a numerical algorithm. Polarimetric parameters are then computed to form images, for instance, of ellipticity angle contrast. The microscope is also referred to as the Optimum microscope.

In essence, a dual PEM Stokes polarimeter described in (refer to section 3.1) is inserted in the 'infinite space' of an Olympus IX71 biological microscope. The current implementation of the phase sensitive detection at the pixel level is achieved by a combination of a hardware electronic timing unit, which provides the modulation to the source intensity phase locked to the reference signal from the two PEMs for signal accumulation, and signal extraction with

software algorithms.

Since the microscope is a single channel implementation of the design, 12 channels of images are required for recovering the signals at the three reference frequencies with zero and quadrature phase differences. It is also possible to operate at 6 channels so that the signals at the quadrature phase difference with respect to the reference are not obtained. It has been found that the electronic timing device in use has a limited frequency response so that at the high reference frequency, the phase setting between zero and quadrature cannot be correctly obtained. As a result of the issue, for all the practical work described in this thesis, only the 6-channel implementation is used.

The development of the microscope is to detect the morphology information of the sample. A kind of polarization signal, birefringence, includes the information of the phase shift makes the observation of the phase shift to be realized.

Phase contrast microscopy invented by Frits Zernike (Zernike, 1955) can detect the birefringence of the sample, which can transfer the phase shift into the brightness changes in the image. Birefringence is also observed by measuring the light intensity transmitted through the sample when viewed between two crossed polarizers used by Harley (Max Born and Emil Wolf, 1959, p.472). Another way to measure birefringence is the rotating polarizer method developed by Glazer (Wood & Glazer, 1980). The rotating polarizer method increases the intensity of the signal compared with the method of two crossed polarizers. Stokes polarimetry imaging method is based on the two photo elastic modulators method (Guan, Cook, Jones, & Shen, 2010; Guan et al., 2008) developed by Guan et al. to characterize the polarization information (such as Stokes parameters, phase difference) into a contrast image. Applying this method to a microscope is the innovation point of our experiment.

We can understand the difference of these three technologies through their test principles:

1. For the two crossed polarizer methods, the principle of the measurement is according to the formula $I = I_0 \sin^2 2\varphi \sin^2 2\delta$. (where, φ is the angle between polarizer and an allowed vibration direction in the crystal. δ is the phase shift, I is the intensity after interacted with the sample, I_0 is the intensity of the background);
2. For the rotating polarizer method, the principle of the measurement is based on the formula $I = I_0/2[1 + \sin 2(\omega_a t - \varphi_s) \sin \delta]$. (where, ω_a is the rotating angular frequency of the analyzer, φ_s is the orientation angle of the specimen, and δ is the phase shift, I is the intensity of the light after interacted with the sample, I_0 is the intensity of the background);
3. In Stokes polarimetry method, Stokes parameters are detected through the Stokes polarimeter (introduced in Chapter 4), the shift of phase is calculated through $\delta = \text{atan}(V/U)$, Which is absolutely different from the first two method. The Stokes parameters U and V are acquired through PEM modulation process.

Comparing the formula of the method 1 and method 2, the power of $\sin \delta$ from 2 change to 1, that means the signal of the phase shift increase because the original signal is acquired through the comparison of the intensity.

3.3 Research material system

3.3.1 Micropipe in SiC

The anisotropy, a physics property in media produced through the asymmetry of the inner structures introduces many new physical phenomena: optical anisotropy, acoustic anisotropy, and double axis stress. Optical anisotropy, represented as a producing of polarization, is a phenomenon happens when the light going through an anisotropic matter in which the velocity of the light is anisotropic; acoustic anisotropy, similar with the polarization, is produced because the velocity of the sound is a tensor for the different density in different

directions; double axis stress, a stress produced because of the anisotropy of the strain produced through the lattice mismatch in matter, is another phenomenon of the anisotropy. The common thing of three physics phenomena is the two axes existed in matter: the fast axis and the slow axis. The fast axis and slow axis are introduced because of the anisotropy of the structure in media; and the velocity along fast axis is faster than that along the slow axis, is the origin of these phenomenon. Based on these relationship shows above, the structure anisotropy of a media, as well as the strain in it, can be characterized through the method of optical polarization, which is described through Stokes vector and can be acquired accurately in the laboratory of us.

Silicon carbide is an attractive semiconductor nowadays, for its band gap wide (2.4-3.3eV), high thermal conductivity, high temperature stability(Presser, Loges, & Nickel, 2008). It is a material used for the MOSFET. Micropipe is a kind of macro-defect in silicon carbide, which is hollow tube-like structures with diameter from $0.1\mu m$ to $5\mu m$ (V. Presser, A. Loges, 2008). The centre of the micropipe is a screw dislocation, the radius of the micropipe increases with the Burgers vector(Ouisse, Chaussende, & Auvray, 2009; Presser et al., 2008). The birefringence measurement is a method of the detection of the defects without the damage. Presser indicated that only the tilted pipes (compared with the c-axis) can be observed through the polarization microscopy for 60 years(Presser et al., 2008). Ming et al summarized the birefringence topography of the defects(Ming & Ge, 1990) and indicated that the birefringence image of the edge dislocation and screw dislocation is different. Also, the shape of the birefringence pattern is changed with the rotation of the polarizer and analyser in the two crossed polarizer measure system (Ming & Ge, 1990). The birefringence is observed on a microscope with a pair of polarizers which are orthogonal to each other(Ming & Ge, 1990). Ouisse use the microscopy developed by Glazer(Wood & Glazer, 1980) to measure the micropipe in 6H-SiC(Hoa, Ouisse, & Chaussende, 2012). In the measurement of Ouisse, the

retardance is calculated through the formula of rotating polarizer method listed in last section. Based on Glazer method, the centre of the birefringence is blank in the Ouisse 's paper(Hoa et al., 2012, 2014; Ouisse et al., 2009). Based on the technique listed above, the micropipe is detected through the microscope without damage the sample. However, the detail of the micropipe is not available through the technique listed above. A new technique called Stokes polarimetry microscope is used in our thesis, that give the detail information of a micropipe which is not parallel to the optical axis. In this thesis, the micropipe in a silicon carbide is researched on our homemade Stokes polarimetry microscope. The strain around a micropipe is detected by the microscope.

3.3.2 Pin hole

Diffraction happens after a light passing through a pinhole. It has been researched for centuries(Wang, Yang, Li, Chen, & Bai, 2018). Many approximations used in the calculation of the patterns. The diffraction pattern of a pinhole is calculated through Fraunhofer diffraction in far field and Fresnel diffraction in near field. Technically, the diffraction of the light is a vector wave and it obey the Helmholtz equation. Also, the light interact with material around the pinhole for it is an electromagnetic wave. When we use a polarized light as a light source of the pinhole diffraction, we can observe the vector field diffraction pattern. Polarization information is a vector information; and, the polarimetry microscope is powerful to measure vector field of the electromagnetic wave near to the sample. Due to a pinhole is the simplest scattering system; and its diffraction have been researched in theory(Stratton & Chu, 1939) and experiment(Raman, 1959). However, the vector field of the pinhole is rarely be reported. The accuracy calculation of the vector diffraction pattern of a pinhole is still a problem nowadays(Deng & Li, 2000). Using our polarimetric microscope, it is easy to acquire the vector field around a pinhole. The information of the vector field near to the pinhole provides a reference information for the relevant calculations. When the focus

position of the microscope is sited behind the pinhole, a diffraction pattern of the pinhole is observed. In this thesis, the Stokes parameters of a diffraction pattern of a pinhole is obtained through our homemade Stokes polarimetric microscope.

3.3.3 Liquid crystal

Liquid crystal is a distinct soft matter material used in photonics, because of their birefringence and high susceptibility to external stimuli that can affect their internal structure (Mur, 2016). Liquid crystals combine the physical and optical properties of both liquids and solids (Cooper, n.d.). The liquid crystal has some degree of the orientational and positional order, although it flows like liquids. Especially, the elongated, rod-like molecular structure can lead to some interesting optical properties of solids, such as birefringence. Liquid crystal also reacts predictably to an electric current, which enables the control of light passage. Due to these properties, liquid crystals are used in liquid crystal displays (Mur, 2016). Cholesteric liquid crystals are also known as chiral nematic liquid crystals. They organize in layers with no positional ordering within layers, but a director axis which varies with layers. The variation of the director axis tends to be periodic in nature. The structure of chiral nematic liquid crystals is shown in Fig. 3.3.3.1.

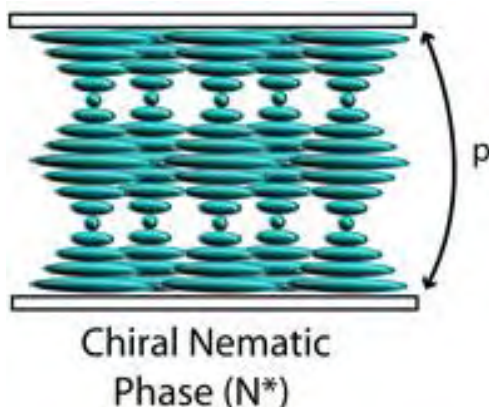


Figure 3.3.3.1 The chiral nematic state of liquid crystal

In chiral crystal state, liquid crystal forms a bandgap for visible light, that is a resonance

cavity for the laser. Based on this theory, liquid crystal is used on liquid crystal lasers(Humar & Muševič, 2010)(Mur, 2016). Like a crystal, liquid crystal can form a Photonic band gap that is rely on the marshalling sequence of the liquid crystal molecules. This pitch¹(p shown in Fig. 3.3.3-1) of a liquid crystal determines the wavelength of light which is reflected (Bragg Reflection). A pitch can be modified through the dopant concentration, a shift of wavelength from 370nm to 680 nm is reported(Mur, 2016). The liquid crystal droplet will confine the liquid crystal molecules in spherical, which can generate certain lasing mode(Humar & Muševič, 2010). The configuration of the liquid crystal inside the droplet can depend on the size and the shape of the droplet, surface anchoring and applied external field. Optical properties of liquid crystals are highly influenced by the director field. Different configuration of director field in spherical crystal droplet include bipolar, radial, toroidal, and axial(Mur, 2016). The configuration of the liquid crystal is characterized by the polarization microscope. Yoshioka et al. reported the heat-flux-driven rotation of the cholesteric droplets.(Yoshioka & Araoka, 2018) .The topological state of cholesteric liquid crystal droplet include five types under the polarising microscope: cross pattern, twisted cross pattern, U-shape pattern, figure-eight pattern, and tumbleweed-like streak pattern(Yoshioka & Araoka, 2018). The topological diagram of cholesteric droplet are observed by polarising microscopy Chiral nematic liquid crystal possess a variety of orientation structures so that difference topological defects are possible due to their confined envelop(Krakhalev et al., 2017). So, the polarization measurement is sensitive to detect the topological structure of the liquid crystal. Liquid crystal has the significance signal of the birefringence, it is an ideal sample to be observed on our microscope, for our Stokes polarimetric microscope can

¹ The period of this variation (the distance over which a full rotation of 360 °is completed) is known as the pitch in liquid crystal. The pitch is the p in Fig. 3.3.3.1.

measure the full information if the polarization.

3.3.4 Nanograter

Periodical structure in mesoscopic (100nm-1 μ m) influences the propagation of light. Opal is a natural meta material which can modulate the light because of its periodic structure of silica spheres. These spheres which diameters are between 150nm to 300nm produce the internal colour by causing the interference and diffraction of light passing through the microstructure of the opal. The reason is the periodic change of the electrical permittivity (ϵ) and magnetic permeability (μ) can modulate electromagnetic wave. The electric permittivity and the magnetic permeability of light in dielectric material and metal are very different. The electric permittivity is a complex number $\epsilon_f = \epsilon - i\frac{\sigma}{\omega}$ in metal, where i represents the imaginary part, σ is the conductivity of the metal, ω is the angular frequency of the electromagnetic field, ϵ is the real part of the electric permittivity. A damping on amplitude of vibration and a delay of the phase usually happen when a light interacts with a metal, that is, the reasons why the metals are not transparent. While the electric permittivity of a dielectric is a real number. Because of the difference of electric permittivity and magnetic permeability, the Poynting vector is kept a constant in dielectric material and no energy loss happens in the process; however, the Poynting vector in metal is a function of propagation depth and phase and the light is easy to produce the damping of amplitude and a delay of phase. According to the difference, many kind of metal-dielectric metamaterials are researched (Kivshar, 2014). It can be divided into two categories, one is SRR-based style and the other is multilayer-based style, such as hyperbolic material(Wei et al., 2016), perfect lens(Pendry, 2000), which is a kind of two dimensional (2D) metamaterial. SSR-based style (three dimensional meta materials) are the U-shaped resonator (Xiong, Meng, et al., 2013). SSR-based style is a kind of antenna in mesoscale mounted on a flat metal film periodically, Xiong's group found it can absorb and reflect polarized light in orthogonal directions (Xiong, Hu, Peng, Wang, & Jiang, 2013). The

reason for that is U-shaped resonator can produce induce local current which generates a magnetic dipole. The oscillating electric current radiates an electromagnetic wave. The absorption happens when the phase of the reflected light is opposite to that of the radiated electromagnetic wave. Meanwhile, the absorption happens when light polarized direction parallel to the surface of the U-shape structure, shown in Fig. 3.3.4.1b.

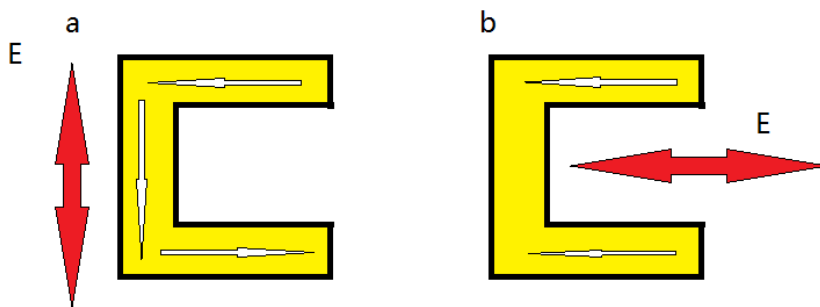


Figure 3.3.4.1 The surface current loop response to different electric field

Based U-shaped structure, another kind of Vertical U-shape split ring resonators (nanograter) are fabricated (Cui et al., 2015). Nanograter is a kind of three dimensions (3D) metamaterials (MMs) developed by focused ion beam (Z. Liu et al., 2016). Nanograter is similar to the splitting ring resonance (SRR) but in three dimensions. SRR is becoming a research focus recently because of its novel modulation to the propagation of the light, such as electromagnetic invisibility, negative refraction, super resolution. A selectively absorption to polarized light is existed in the SRR metamaterials. A relation between absorption ratio and wavelength is characterized by an absorption spectrometer. The prediction of metamaterial begins in 1968 by Veselago (Veselago, 1968). From the negative electric permittivity are existed in meta material proved by John Pendry (Pendry, 2000), many kinds of meta materials are designed in recent twenty years. The style can be divided into three categories (Kivshar, 2014): they are nonlinear arrays of magnetic meta-atoms SRR (Kivshar, 2014), wire metamaterials (fishnet structures) (Valentine et al., 2008) and metal-dielectric layered

materials(Chebykin, Orlov, Simovski, Kivshar, & Belov, 2012). A series of new optical properties, such as negative index, super-resolution, and invisibility stimulate scientist interests to manipulate the light.

In this thesis, the nanograter is measured by our Stokes polarimetric microscope. The vector field of the light manipulated by the nanograter is shown here. The electrical field around the nanograter is also measured.

3.4 The aim of the research

Polarization is a vector information; so, the polarimetry microscope is powerful to measure the vector field of the electromagnetic wave near to the sample. The mapping polarization image can be measured through our polarimetry microscope, such as Stokes parameters, elliptical angle, depolarization, and azimuth angle. The Mueller matrix of a sample can be deduced with the Stokes parameters of a polarization before and after interacted with the sample.

There is a common thing among the micropipe, pinhole, and the liquid crystal droplet, that is a round boundary existed in their structures. Comparing the vector field of the three structure helps to understand the effects produced by the round boundary restrictions to the polarization.

A pinhole is the simplest scattering system. Although its diffraction has been researched in theory and experiment, the research of the pinhole through the Stokes polarimetric microscope can provide the information of the vector field diffraction which is rarely be reported. It helps to complete the theory of the tiny hole diffraction in near vector field. The purpose of the work on pinhole has two folds – 1) illustration that the local polarization states, hence the complex field vector (assuming a plane wave, normal incidence) may be

experimentally determined. 2) a comparison of ‘out of focus’ characteristics between the intensity image and the polarimetric images.

The findings are shown below:

1) we can measure them quite well in the vicinity up to tens of microns away from the pinhole and broadly in line with what are known in literatures.

2) the ‘decay’ in the signals are comparable and hence the ‘depth of focus’ would be expected in a similar manner.

The investigation on the effect of defects (micropipes) on the local strains, hence the optical anisotropy contains two parts: The first is trying to obtain the information on the Mueller matrix of the samples (birefringence, dichroism, and depolarization of the sample), assuming the samples are homogeneous over the measurement area; the effort is a partial success as the variation of strain on a local scale has been found to be a major obstacle for obtaining consistent results. The second part of the study is to address the local variation of optical anisotropy using the recently developed Optimum microscope, which has been met with better success.

The liquid crystal is sensitive to the polarization due to its anisotropy in shape and alignment. A birefringence is existed in liquid crystal. The liquid crystal droplet is a sphere. The inner structure of a liquid crystal droplet can be detected with the Stokes polarimetry microscope. Four type of liquid crystal droplet are researched in this thesis.

Due to a kind of nonlinear metamaterial (nanograting) is response to electrical field along two orthogonal direction (the azimuth angle of polarization) in different way; the research using the polarimetry microscope to measure the polarization information around the nanograting is interesting and important.

3.5 Summary

This chapter introduces the literature review of the Stokes polarimetry and the Stokes polarimetric microscope. The Stokes polarimetric microscope can provide a vector information image to research the anisotropy structure with a birefringence. Also, the research background of the four material systems, micropipe, pinhole, liquid crystal and nanograting, are introduced to characterize the microscope respectively. The Stokes polarimetry signal is strong in micropipe, liquid crystal and nanograting. The pinhole is researched to prove that the signal detected by the microscope is near to the focus plane.

Reference

Born, M., & Wolf, E. (1959). *Principles of Optics* (7th (expa). Cambridge University Press.

Chebykin, A. V, Orlov, A. A., Simovski, C. R., Kivshar, Y. S., & Belov, P. A. (2012). Nonlocal effective parameters of multilayered metal-dielectric metamaterials. *Physical Review B*, 86(11), 115420. Retrieved from internal-pdf://physrevb.86.115420-2352140546/PhysRevB.86.115420.pdf

Cook, P. (2010). *A study of focussed ion beam patterned thin magnetic films with soft X-ray and Magneto-optical microscopy*. School of Computing, Sciences and Engineering. University of Salford, Salford.

Cooper, J. (n.d.). *Compositional Analysis of Merck E7 Liquid Crystal Intermediates Using UltraPerformance Convergence Chromatography (UPC 2) with PDA Detection*. Manchester, UK. Retrieved from <https://www.waters.com/webassets/cms/library/docs/720004814en.pdf>

Cui, A., Li, J., Shen, T. H., Xia, X., Li, Z., Gong, Z., ... Liu, Z. (2015). Directly Patterned Substrate-

free Plasmonic “Nanograter” Structures with Unusual Fano Resonances. *Light: Science & Applications*, 4, e308. Retrieved from <http://internal-pdf//> (compressed)

Isa_2015_81-2616775936/ (compressed) Isa_2015_81.pdf

Deng, X., & Li, G. (2000). The vector theory and its scalar approximation of the diffraction at a plane aperture in the far-field. *Journal of Hefei University of Technology*, 23, 999–1002.

Guan, W., Cook, P. J., Jones, G. A., & Shen, T. H. (2010). Experimental determination of the Stokes parameters using a dual photoelastic modulator system. *Applied Optics*, 49, 2644. Retrieved from http://internal-pdf//48_Guan_2010_Appl Optics-3168858373/48_Guan_2010_Appl Optics.pdf

Guan, W., Liu, Y., Shen, T. H., & Jones, G. A. (2008). The measurement of the Stokes parameters: A generalized methodology using a dual photoelastic modulator system. *Journal of Applied Physics*, 103(4), 43104. Retrieved from <internal-pdf://228.60.152.103/Guan2008.pdf>

Ho, L. T. M., Ouisse, T., & Chaussende, D. (2012). Critical assessment of birefringence imaging of dislocations in 6H silicon carbide. *Journal of Crystal Growth*, 354, 202–207.

Ho, L. T. M., Ouisse, T., Chaussende, D., Naamoun, M., Tallaire, A., & Achard, J. (2014). Birefringence Microscopy of Unit Dislocations in Diamond. *Crystal Growth Design*, 14, 5761–5766.

Humar, M., & Mušević, I. (2010). 3D microlasers from self-assembled cholesteric liquid-crystal microdroplets. *Optics Express*, 18(26), 26995–27003.

<https://doi.org/10.1364/OE.18.026995>

Kivshar, Y. S. (2014). Tunable and nonlinear metamaterials: toward functional metadevices.

Ad. Nat. Sci. Nanosci. Nanotechnol, 5, 013001. Retrieved from

iopscience.iop.org/article/10.1088/2043-6262/5/1/013001/pdf

Krakhalev, M. N., Gardymova, A. P., Prishchepa, O. O., Rudyak, V. Y., Emelyanenko, A. V, Liu,

J.-H., & Zyryanov, V. Y. (2017). Bipolar configuration with twisted loop defect in chiral

nematic droplets under homeotropic surface anchoring. *Scientific Reports*, 7(1), 14582.

<https://doi.org/10.1038/s41598-017-15049-6>

Liu, Y. (2005). *A study of magnitic ultra thin films on GaAs and optically excited spin injection*.

University of Salford.

Liu, Z., Gong, Z., Li, H., Xia, X., Shen, T. H., Li, J., ... Cui, A. (2016). Saptially oriented plasmonic

“nanograter” structures. *Scientific Reports*, 6, 28764.

<https://doi.org/doi:10.1038/srep28764>

Ming, N., & Ge, C. (1990). Direct Observation of Defects in Transparent Crystals by Optical

Microscopy. *Journal of Crystal Growth*, 99, 1309–1314.

Mur, U. (2016). *Materials for soft matter photonics*. Ljubljana. Retrieved from

[http://mafija.fmf.uni-](http://mafija.fmf.uni-lj.si/seminar/files/2015_2016/Materials_for_soft_matter_photonics.pdf)

[lj.si/seminar/files/2015_2016/Materials_for_soft_matter_photonics.pdf](http://mafija.fmf.uni-lj.si/seminar/files/2015_2016/Materials_for_soft_matter_photonics.pdf)

Ouisse, T., Chaussende, D., & Auvray, L. (2009). Micropipe-induced birefringence in 6H silicon

carbide. *Journal of Applied Crystallography*, 43, 122–133.

Pendry, J. B. (2000). Negative Refraction Makes a Perfect Lens. *Physical Review Letters*,

85(18), 3966–3969. Retrieved from internal-pdf://physrevlett.85.3966-2386984193/PhysRevLett.85.3966.pdf

Presser, V., Loges, A., & Nickel, K. G. (2008). Scanning electron and polarization microscopy study of the variability and character of hollow macro-defects in silicon carbide wafers. *Philosophical Magazine*, 88, 1639–1657. Retrieved from <http://www.informaworld.com>

Raman, C. V. (1959). *CAUSTICS FORMED BY DIFFRACTION AND THE GEOMETRIC THEORY OF DIFFRACTION PATTERNS*. Retrieved from <https://www.ias.ac.in/article/fulltext/seca/049/06/0307-0317>

Stratton, J. A., & Chu, L. J. (1939). Diffraction Theory of Electromagnetic Waves. *Physical Review*, 56, 99–107.

Valentine, J., Zhang, S., Zengraf, T., Ulin-Avila, E., Genov, D., Bartal, A. G., & Zhang, X. (2008). Three-dimensional optical metamaterial with a negative refractive index. *Nature*, 455(18), 376. Retrieved from [http://internal-pdf//ContentServer\(1\)-1311171074/ContentServer\(1\).pdf](http://internal-pdf//ContentServer(1)-1311171074/ContentServer(1).pdf)

Veselago, V. . (1968). The electrodynamics of substances with simultaneously negative values of ϵ and μ . *Soviet Phys Uspekhi*, 10(4), 509. Retrieved from internal-pdf://pu3699-3271102209/pu3699.pdf

Wang, C., Yang, Y., Li, Y., Chen, Y., & Bai, J. (2018). Characterization of the pinhole diffraction based on the waveguide effect in a point diffraction interferometer. *Applied Optics*, 57, 781–787.

Wei, D., Harris, C., Bomberger, C. C., Zhang, J., Zide, J., & Law, S. (2016). Single-material

semiconductor hyperbolic metamaterials. *Optics Express*, 24(8), 8735–8745.

<https://doi.org/10.1364/oe.24.008735>

Wolf, E. (2007). *Introduction to the theory of coherence and polarization*. Cambridge University Press.

Wood, I. G., & Glazer, A. M. (1980). Ferroelastic Phase Transition in BiVO₄. I. Birefringence Measurement using the Rotating-Analyser Method. *Journal of Applied Crystals*, 13, 217–233.

Xiong, X., Hu, Y.-H., Peng, R.-W., Wang, M., & Jiang, S.-C. (2013). Structured Metal Film as a perfect Absorber. *Advanced Materials*, 25, 3994. Retrieved from [http://internal-pdf//Xiong_et_al-2013-Advanced_materials_\(Deerfield_Beach,_Fla.\)-3847774208/Xiong_et_al-2013-Advanced_materials_\(Deerfield_Beach,_Fla.\).pdf](http://internal-pdf//Xiong_et_al-2013-Advanced_materials_(Deerfield_Beach,_Fla.)-3847774208/Xiong_et_al-2013-Advanced_materials_(Deerfield_Beach,_Fla.).pdf)

Xiong, X., Meng, C., Jiang, S.-C., Hu, Y.-H., Peng, R.-W., Wang, M., & Xue, Z.-H. (2013). Polarization-dependent perfect absorbers/reflectors based on a three-dimensional metamaterial. *Physical Review B*, 88, 115105. Retrieved from <internal-pdf://physrevb.88.115105-2301948416/PhysRevB.88.115105.pdf>

Yoshioka, J., & Araoka, F. (2018). Topology-dependent self-structure mediation and efficient energy conversion in heat-flux-driven rotors of cholesteric droplets. *Nature Communications*, 9(1), 432. <https://doi.org/10.1038/s41467-018-02910-z>

Zernike, F. (1955). How I Discovered Phase Contrast. *Science*, 121 (3141), 345–349. <https://doi.org/DOI: 10.1126/science.121.3141.345>

Chapter 4 Stokes polarimetry

4.1 Introduction

Stokes polarimetry is a method to measure the Stokes parameters. The set-up of the optical parts of the Stokes polarimeter includes two photo elastic modulators (PEM), one analyser, and one detector. As a part of Stokes parameter measurement, calibration is the crux. A calibration process is needed before the measurement of the Stokes parameters. The calibration of circular polarization is important for the Stokes parameter V which relates to the birefringence directly; also, the accurate measurement of the Stokes parameters Q , U , and V , is the prerequisite to obtain a depolarization accurately. Based on the importance of measuring the Stokes parameter V , calibration method is improved in this thesis. The improvement of calibration includes the circular polarization calibration, quick data acquirement, and data analysis. Till now, the quickest speed of doing the calibration is two hours measurement and two hours calculation. In my experiment, I find the calibration parameter, especially the Stokes parameter V , is sensitive to the room temperature and the wave front of the light source.

Also, the principle of the dual Stokes polarimetry deduced from the theory is stated. Every optical element is treated as a Mueller matrix. The PEM is treated as a retarder with a birefringence.

4.2 The PEM

Photo elastic modulator (PEM) is a light modulated device made of fused quartz which is vibrated in a frequency of ultrasonic wave to produce a standing wave in a quartz crystal (“Photoelastic Modulation Principles of Operation - Hinds Instruments,”). A PEM includes a controller, an optical head and an electronic head (“Photoelastic Modulation

Principles of Operation - Hinds Instruments,"). The electronic head generates a highly precise sinusoidal function for the optical head. The optical head is an octagonal fused silica (a half wave resonant bar) bonded to two quartz piezoelectric transducers, which are driven by the electronic circuit and vibrate at a fixed frequency to compress and stretch the bar. The frequency of the transducer is tuned to the natural frequency of the bar. This resonance modulation results in highly sensitive polarization measurements. The fundamental vibration of the silica is along its longest dimension. The frequency of the photo elastic modulator head is a constant (In our experiment, two photo elastic modulators with frequency of 47 kHz and 42 kHz are adopted.). Practically, a standing wave produced by the resonance in quartz crystal, producing an anisotropy of density in fused quartz, means the velocity of the light propagation is different in different direction, because the velocity of a light is a function of the density.

“The PEM produces an oscillating signal at a special frequency to modulate the modulus of the intensity; and afterwards, the amplitude of the oscillating signal is monitored by a lock-in amplifier.” (Guan, Cook, Jones, & Shen, 2010). On account of its high sensitivity, wide spectral range and high precision phase modulation, the PEM has figured prominently in a wide range of physical measurements (Liu, 2005) . Based on a series of calculation and analysis of the signal at different oscillation frequency, the detection of the Stokes parameters is realized.

4.3 Methodology of Stokes polarimetry

The photo elastic modulators manufactured by HINDS. The advantage of dual PEM polarimetry is all four Stokes parameters are measured simultaneously, thus the polarization state of light is completely characterized.

4.3.1 The configuration of experiment

The configuration of dual polarimetric setup is shown in Fig. 4.3.1.1. To acquire a stable representation of the measurement, the Sample rotation stage and the quarter waveplate next to the sample rotation stage are mounted separately. The part of the laser source includes Polarizer, slit quarter waveplate and laser are mounted together on a stage. The other part of the Polarimeter include a photo diode, analyzer, PEM1, and PEM2 are mounted together as a whole thing. We can get circular polarization when we put in a quarter waveplate and set a special angle. We can get a linear polarization when we remove the quarter waveplate.

During our experiment, the sample stage is adjusted to make the surface of the sample perpendicular to the direction of the light propagation. And the sample rotation stage can rotate to adjust the optical axis of the sample.

Figure 4.3.1.2 shows the configuration of the optical axis of PEM1, PEM2, and analyzer in laboratory coordinates: α is the angle between PEM1 and laboratory coordinates; β is the angle of the optical axis of analyzer in laboratory coordinate; the optical axis of PEM2 is along the x-axis of laboratory coordinate in the Stokes polarimetry system(Guan et al., 2010).

The final intensity detected by the photo diode is transferred into a potential signal by a photo diode before sending into a pre-amplifier. The potential signal multiplied by pre-amplifier includes two parts, DC signal and AC signal. DC signal is monitored by an electrometer, while AC signal is tuned by lock-in amplifiers to produce harmonic signal(Guan et al., 2010).

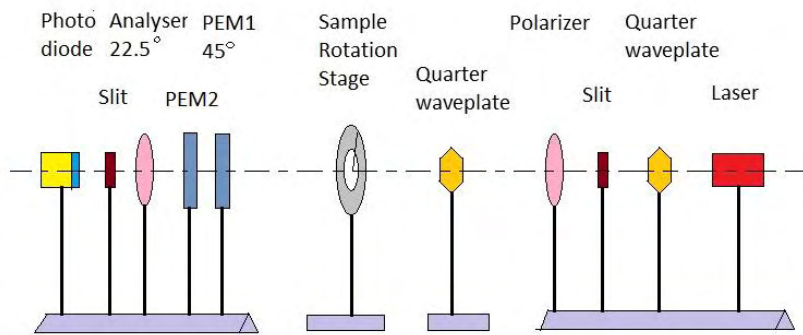


Figure 4.3.1.1 The configuration of the experimental set up

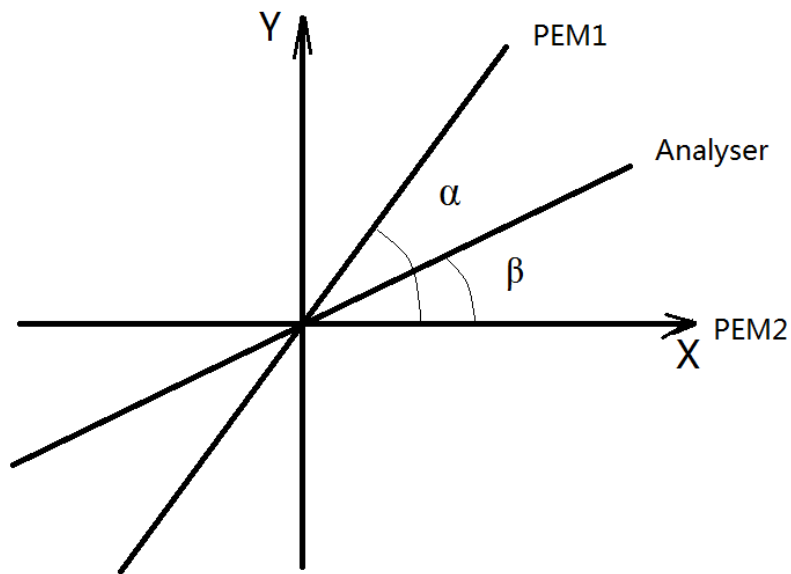


Figure 4.3.1.2 the angle of the optical axis of optics referenced to the laboratory coordinate(Guan et al., 2010).

Then the intensity signal of modulated signal is decomposed into four parts S_{DC} , S_Q , S_U , and S_V , which are tested by one voltmeter and three lock-in amplifiers.

The meter readings acquired by the electrometer and lock-in amplifiers are transferred into a computer. The GPIB socket (IEEE488.2) is used to connect the instrument and computer. The

meter reading of the four equipment is transferred into the computer through a controlling program written on LabVIEW.

Based on the formula (B.1.1.1), the Mueller Matrices of PEM1, PEM2 used in the experiment are shown as matrices M_1 , M_2 , and respectively in below.

M_1

$$= \begin{pmatrix} 1 & 0 & 0 & 0 \\ 0 & \cos(4\alpha) \sin^2\left(\frac{\delta_1}{2}\right) + \cos^2\left(\frac{\delta_1}{2}\right) & \sin(4\alpha) \sin^2\left(\frac{\delta_1}{2}\right) & -\sin(2\alpha) \sin(\delta_1) \\ 0 & \sin(4\alpha) \sin^2\left(\frac{\delta_1}{2}\right) & -\cos(4\alpha) \sin^2\left(\frac{\delta_1}{2}\right) + \cos^2\left(\frac{\delta_1}{2}\right) & \cos(2\alpha) \sin(\delta_1) \\ 0 & \sin(2\alpha) \sin(\delta_1) & -\cos(2\alpha) \sin(\delta_1) & \cos(\delta_1) \end{pmatrix} \quad (4.3.1.1)$$

$$M_2 = \begin{pmatrix} 1 & 0 & 0 & 0 \\ 0 & 1 & 0 & 0 \\ 0 & 0 & \cos(\delta_2) & \sin(\delta_2) \\ 0 & 0 & -\sin(\delta_2) & \cos(\delta_2) \end{pmatrix} \quad (4.3.1.2)$$

According to the Mueller matrix of a linear polarizer(Huard, 1997), the Mueller Matrix of the analyzer in the experimental set up is described through matrix M_3 .

$$M_3 = \frac{1}{2} \begin{pmatrix} 1 & \cos(2\beta) & \sin(2\beta) & 0 \\ \cos(2\beta) & \cos^2(2\beta) & \cos(2\beta)\sin(2\beta) & 0 \\ \sin(2\beta) & \cos(2\beta)\sin(2\beta) & \sin^2(2\beta) & 0 \\ 0 & 0 & 0 & 0 \end{pmatrix} \quad (4.3.1.3)$$

Here, $\delta_1 = \delta_{10} \sin(\Omega_1 t)$ is the retardation of phase produced by PEM1, δ_{10} is the amplitude of the retardation of PEM1 and Ω_1 is the modulating frequency of PEM1. $\delta_2 = \delta_{20} \sin(\Omega_2 t)$ is the retardation of phase produced by the PEM2, δ_{20} is the amplitude of the retardation of PEM2 and Ω_2 is the modulating frequency of PEM2.

The polarization states before and after the Stokes polarimeter are represented as

$(I \ Q \ U \ V)^T$ and $(I' \ Q' \ U' \ V')^T$, respectively. The effect of dual Stokes polarimetry

on a polarization can be described as a product of the three Mueller matrices, the following

relationship was obtained:

$$\begin{pmatrix} I' \\ Q' \\ U' \\ V' \end{pmatrix} = M_3 M_2 M_1 \begin{pmatrix} I \\ Q \\ U \\ V \end{pmatrix} \quad (4.3.1.4)$$

Equation (4.3.1.4) is used to describe the effect of the dual PEM Stokes polarimeters to the light going through it.

Multiplying out equation 4.3.1.4, the total intensity can be measured by the photo detector collected and enlarged with a preamplifier. Using the standard expansions of Bessel Functions shown in equation 4.3.1.5 and 4.3.1.6, a Fourier transformation to make the signal to be measured by the lock-in amplifier and ammeter in laboratory, shown in 4.3.1.7.

$$\begin{aligned} \sin(\delta_i) &= \sin[\delta_{i0} \sin(\Omega_i t)] \\ &= 2J_1(\delta_{i0}) \sin(\Omega_i t) + 2J_3(\delta_{i0}) \sin(2\Omega_i t) + 2J_5(\delta_{i0}) \sin(4\Omega_i t) + \dots \\ &= 2 \sum_{n=0}^{\infty} J_{2n+1}(\delta_{i0}) \sin((2n+1)\Omega_i t) \end{aligned} \quad (4.3.1.5)$$

$$\begin{aligned} \cos(\delta_i) &= \cos[\delta_{i0} \sin(\Omega_i t)] \\ &= J_0(\delta_{i0}) \sin(\Omega_i t) + 2J_2(\delta_{i0}) \sin(2\Omega_i t) + 2J_4(\delta_{i0}) \sin(4\Omega_i t) + \dots \\ &= J_0(\delta_{i0}) \sin(\Omega_i t) + 2 \sum_{n=1}^{\infty} J_{2n}(\delta_{i0}) \cos(2n\Omega_i t) \end{aligned} \quad (4.3.1.6)$$

Here, $i = 1$ and 2 indicate the index for PEM1 and PEM2.

$$\begin{aligned}
I' = & \frac{1}{2}I + \frac{1}{2}Q\cos^2(2\alpha) \cos(2\beta) + \frac{1}{4}U\sin(4\alpha) \cos(2\beta) \\
& + \left[\frac{1}{2}Q\sin^2(2\alpha) \cos(2\beta) - \frac{1}{4}U\sin(4\alpha) \cos(2\beta) \right] J_0(\delta_{10}) \\
& + \left[\frac{1}{4}Q\sin(4\alpha) \sin(2\beta) + \frac{1}{2}U\sin^2(2\alpha) \sin(2\beta) \right] J_0(\delta_{20}) \\
& - \left[\frac{1}{4}Q\sin(4\alpha) \sin(2\beta) - \frac{1}{2}U\cos^2(2\alpha) \sin(2\beta) \right] J_0(\delta_{10})J_0(\delta_{20}) \\
& - V\sin(2\alpha) \cos(2\beta)J_1(\delta_{10}) \sin(\Omega_1 t) \\
& + V\cos(2\alpha) \sin(2\beta)J_1(\delta_{10})J_0(\delta_{20}) \sin(\Omega_1 t) \dots \\
& + \left[Q\sin^2(2\alpha) \cos(2\beta) - \frac{1}{2}U\sin(4\alpha) \cos(2\beta) \right] J_2(\delta_{10}) \cos(2\Omega_1 t) \\
& + \left[\frac{1}{2}Q\sin(4\alpha) \sin(2\beta) + U\sin^2(2\alpha) \sin(2\beta) \right] J_2(\delta_{20}) \cos(2\Omega_2 t) \\
& - \left[\frac{1}{2}Q\sin(4\alpha) \sin(2\beta) - U\cos^2(2\alpha) \sin(2\beta) \right] J_2(\delta_{10})J_0(\delta_{20}) \cos(\Omega_1 t) \\
& - \left[\frac{1}{2}Q\sin(4\alpha) \sin(2\beta) - U\cos^2(2\alpha) \sin(2\beta) \right] J_0(\delta_{10})J_2(\delta_{20}) \cos(\Omega_2 t) \\
& + [Q\sin(2\alpha) \sin(2\beta) - U\cos(2\alpha) \sin(2\beta)]J_1(\delta_{10})J_1(\delta_{20}) \cos(\Omega_1 + \Omega_2) t \\
& + [Q\sin(2\alpha) \sin(2\beta) - U\cos(2\alpha) \sin(2\beta)]J_1(\delta_{10})J_1(\delta_{20}) \cos(\Omega_1 - \Omega_2) t \\
& + V \sin(2\beta) J_2(\delta_{10})J_1(\delta_{20}) \sin(2\Omega_1 + \Omega_2) t \\
& + V \sin(2\beta) J_2(\delta_{10})J_1(\delta_{20}) \sin(2\Omega_1 - \Omega_2) t \\
& + V\cos(2\alpha) \sin(2\beta)J_1(\delta_{10})J_2(\delta_{20}) \sin(2\Omega_2 + \Omega_1 t) \\
& - V\cos(2\alpha) \sin(2\beta)J_1(\delta_{10})J_2(\delta_{20}) \sin(2\Omega_2 - \Omega_1 t) \\
& + \dots \dots \dots \quad (4.3.1.7)
\end{aligned}$$

According to (4.3.1.7), the intensity of the light is decomposed into four signals: one direct current signal and three alternating current signals based on the frequencies Ω_1 ; $2\Omega_1$; and $2\Omega_2$.

For easier analysis, we put $\delta_{10} = \delta_{20} = \frac{2\pi}{\lambda}(0.383\lambda) = 2.4808rad$, because at this point, $J_0(\delta_{10}) = J_0(\delta_{20}) = 0$, which make the formula simpler.

To simplify this equation, we use some constant to represent the coefficient in equation

4.3.1.7. Then the formula 4.3.1.8 is obtained:

$$\begin{aligned}
I' = & k_1I + k_2Q + k_3U - k_8V \sin(\Omega_1t) + [k_4Q - k_5U] \cos(2\Omega_1t) + [k_6Q + k_7U] \cos(2\Omega_2t) \\
& + [Q\sin(2\alpha) \sin(2\beta) - U\cos(2\alpha) \sin(2\beta)]J_1(\delta_{10})J_1(\delta_{20}) \cos(\Omega_1 + \Omega_2) t \\
& + [Q\sin(2\alpha) \sin(2\beta) - U\cos(2\alpha) \sin(2\beta)]J_1(\delta_{10})J_1(\delta_{20}) \cos(\Omega_1 - \Omega_2) t \\
& + V \sin(2\beta) J_2(\delta_{10})J_1(\delta_{20}) \sin(2\Omega_1 + \Omega_2) t \\
& + V \sin(2\beta) J_2(\delta_{10})J_1(\delta_{20}) \sin(2\Omega_1 - \Omega_2) t \\
& + V\cos(2\alpha) \sin(2\beta)J_1(\delta_{10})J_2(\delta_{20}) \sin(2\Omega_2 + \Omega_1t) \\
& - V\cos(2\alpha) \sin(2\beta)J_1(\delta_{10})J_2(\delta_{20}) \sin(2\Omega_2 - \Omega_1t) + \dots \quad (4.3.1.8)
\end{aligned}$$

The relationship of equation (4.3.1.9) is obtained if the higher order items of equation 4.3.1.8 can be neglected.

$$\begin{aligned}
I' = & k_1I + k_2Q + k_3U - k_8V \sin(\Omega_1t) \\
& + [k_4Q - k_5U] \cos(2\Omega_1t) + [k_6Q + k_7U] \cos(2\Omega_2t) \quad (4.3.1.9)
\end{aligned}$$

The four independent relationships established through picking up those terms. The relationship between the signals and the Stokes parameters is determined. Four signals are direct current I_{dc} , harmonic signals associated with Ω_1 , $2\Omega_1$, $2\Omega_2$ respectively. Then, the signals got by photodiode are distinguished into four parts. The I, Q, U and V are acquired through the four signals.

In practice, the theoretical signal is not equal to the actual signals detected by the detector, according to the experiment. So, the relationship between theoretical signal and actual signal is as shown below:

$$\begin{aligned}
I_{dc} &= c_{dc}S_{dc}, \\
I_{QU1} &= c_{QU1}S_{QU1}, \\
I_{QU2} &= c_{QU2}S_{QU2}, \\
I_V &= c_VS_V,
\end{aligned} \quad (4.3.1.10)$$

Then we can establish the relation between actual signal and Stokes parameter(Guan et al.,

2010):

$$\begin{pmatrix} S_{dc} \\ S_{QU1} \\ S_{QU2} \\ S_V \end{pmatrix} = \begin{pmatrix} g_1 & g_2 & g_3 & 0 \\ 0 & g_4 & g_5 & 0 \\ 0 & g_6 & g_7 & 0 \\ 0 & 0 & 0 & g_8 \end{pmatrix} \begin{pmatrix} I \\ Q \\ U \\ V \end{pmatrix} = G \begin{pmatrix} I \\ Q \\ U \\ V \end{pmatrix} \quad (4.3.1.11)$$

The matrix G can be obtained through the process of calibration. Then we can get the Stokes parameters through the straightforward inversion of G, which is matrix K shown below.

$$\begin{pmatrix} I \\ Q \\ U \\ V \end{pmatrix} = \begin{pmatrix} k_1 & k_2 & k_3 & 0 \\ 0 & k_4 & k_5 & 0 \\ 0 & k_6 & k_7 & 0 \\ 0 & 0 & 0 & k_8 \end{pmatrix} \begin{pmatrix} S_{dc} \\ S_{QU1} \\ S_{QU2} \\ S_V \end{pmatrix} = K \begin{pmatrix} S_{dc} \\ S_{QU1} \\ S_{QU2} \\ S_V \end{pmatrix} \quad (4.3.1.12)$$

When we choose the configuration of $\alpha = 45^\circ$, $\beta = 22.5^\circ$, $k_2 = k_3 = k_5 = k_6 = 0$, the matrix G is diagonalized. then the equation (4.3.1.9) can be simplified as follows:

$$\begin{aligned} I' = & \frac{1}{2}I - V \frac{\sqrt{2}}{2} J_1(\delta_{10}) \sin(\Omega_1 t) + Q \frac{\sqrt{2}}{2} J_2(\delta_{10}) \cos(2\Omega_1 t) + U \frac{\sqrt{2}}{2} J_2(\delta_{20}) \cos(2\Omega_2 t) \\ & + Q \frac{\sqrt{2}}{2} J_1(\delta_{10}) J_1(\delta_{20}) \cos(\Omega_1 + \Omega_2) t + Q \frac{\sqrt{2}}{2} J_1(\delta_{10}) J_1(\delta_{20}) \cos(\Omega_1 - \Omega_2) t \\ & + V \frac{\sqrt{2}}{2} J_2(\delta_{10}) J_1(\delta_{20}) \sin(2\Omega_1 + \Omega_2) t \\ & + V \frac{\sqrt{2}}{2} J_2(\delta_{10}) J_1(\delta_{20}) \sin(2\Omega_1 - \Omega_2) t + \dots \dots \quad (4.3.1.13) \end{aligned}$$

The matrix K is diagonalized when the higher order item in 4.3.1.12 was neglected.

By measurement of the DC signal, first harmonic signal of PEM1, the second harmonic signal of PEM1, and the second harmonic signal of PEM2, the Stokes parameters I (DC), V (Ω_1), Q ($2\Omega_1$) and U ($2\Omega_2$) can be deduced respectively from these measurements. I' expansion has many terms containing I, Q, U, and V. By measuring the DC component, all ac signals averaged over a period. The signals with frequencies Ω_1 , $2\Omega_1$, $2\Omega_2$ (related with the

V, Q, and U, respectively), are selected by three lock-in amplifiers. The four relationships (relationships between the experiment signal and the Stokes parameters) is established. We calculated matrix K through the nonlinear-regression method, which is called calibration.

4.4 The method of acquire six special polarization

The configuration of the experiment on the bench is shown in Fig. 4.3.1.1. The method of acquiring six special polarization is shown here.

To measure the Mueller matrix of a sample, six special polarization is needed. The detail is in Appendix B. Linear polarization is easy to acquire through the rotation of the polarizer: set the fast axis at 0° , 45° , 90° , and 135° . The acquisition of the circular polarization follows the steps below.

1. We cross the polarizer with respect to the analyzer to acquire an extinction; and mark the angle of the polarizer to be 0° (reference coordinate).
2. Insert the quarter waveplate between the polarizer and analyzer to get an extinction.
3. Note the angle of the quarter waveplate Λ and remove the quarter waveplate.
4. When we need the circular polarization, just put the retarder in and set the angle of quarter wave plate to be $\Lambda+45^\circ$ (clockwise rotate polarizer 45°) and $\Lambda-45^\circ$ (anticlockwise rotate polarizer 45°) to acquire a right handed circular polarization and left handed circular polarization respectively.

4.5 Calibration

4.5.1 Experiment of calibration

Normally, the DC signal and amplitude of harmonic signal are chosen by the lock-in amplifier. Another way to acquire the DC signal and amplitude of harmonic signal is the equivalent algorithm timing unit. In the system using the equivalent algorithm, two methods

are used to acquire the four signals: one is the twelve channels method; and another is the six channels method. The two method are going to be explained in chapter 5.

The calibration is determined after aligning the optical parts and the electronic part of the Stokes polarimetry. The retardation is the parameter on the PEM setting. All the parameters of the equipment should not change after the calibration.

The values of Bessel function at special retardation point 2.405 rad and 3.053 rad are shown in Table 4.5.1.1.

Table 4.5.1.1 The values of Bessel function at 2.405 rad and 3.0536rad

retardation	J_0	J_1	J_2	J_3	J_4	J_5	J_6	J_7
2.405 rad	0	0.5191	0.4318	0.199	0.0648	0.0164	0.0034	0.0006
3.053 rad	-0.278	0.3188	0.4835	0.3185	0.1392	0.0463	0.0125	0.0029

In our experiment, the retardation chosen is 0.486λ , when the $\delta_{10} = \delta_{20} = \frac{2\pi}{\lambda}(0.486\lambda) = 3.0536 \text{ rad}$. The value of Bessel function shows in table 4.5.1.1. Under the configuration of $\alpha = 45^\circ$ and $\beta = 22.5^\circ$, the intensity is represented as

$$\begin{aligned}
I' = & \frac{1}{2}I + \left[\frac{1}{2}Q \cos(2\beta) \right] J_0(\delta_{10}) + \left[\frac{1}{2}U \sin(2\beta) \right] J_0(\delta_{20}) - V \cos(2\beta) J_1(\delta_{10}) \sin(\Omega_1 t) \cdots \\
& + [Q \cos(2\beta)] J_2(\delta_{10}) \cos(2\Omega_1 t) + [U] J_2(\delta_{20}) \cos(2\Omega_2 t) \\
& + [Q \sin(2\beta)] J_1(\delta_{10}) J_1(\delta_{20}) \cos(\Omega_1 + \Omega_2) t \\
& + [Q \sin(2\beta)] J_1(\delta_{10}) J_1(\delta_{20}) \cos(\Omega_1 - \Omega_2) t \\
& + V \sin(2\beta) J_2(\delta_{10}) J_1(\delta_{20}) \sin(2\Omega_1 + \Omega_2) t \\
& + V \sin(2\beta) J_2(\delta_{10}) J_1(\delta_{20}) \sin(2\Omega_1 - \Omega_2) t
\end{aligned} \tag{4.5.1.1}$$

A calibration process is used to establish the relationship (Matrix K in equation 4.3.1.12) between the collected signals and the Stokes parameters. The calibration of the dual-PEM

polarimeter was done after the alignment of the optical components. The DC signal is collected through a picometer; the signal of Q and U are obtained through the double frequency oscillation of the PEM1 and PEM2; the signal of V is acquired through the fundamental frequency of PEM1. The orientation angle of polarization changed through rotation of the polarizer and the retarder, the S_I , S_Q , S_U , and S_V are recorded through the computer. During the configuration of $\alpha = 45^\circ$, $\beta = 22.5^\circ$, the matrix k is diagonalized and the parameters k_4 , k_6 , k_7 are acquired by the four states calibration method(Guan, 2007). Based on the solver function in Excel, a nonlinear calibration method(Cook, 2010), which is more accurate and not rely on the diagonalized matrix, was adopted in the experiment.

The frequency of PEM 1 is 47.065 kHz and the frequency of PEM 2 is 42.055 kHz. The input reference frequencies of the three lock-in amplifiers are 94.12 kHz (2F), 84.11 kHz (2F), and 47.07 kHz (F) in the experiment.

The experimental set up of calibration for dual-PEM Stokes polarimetry microscope is shown on Fig. 4.5.1.1. Every optics settled parallel with the jigsaw washers, shown in Fig.4.5.1.1. The thickness of washers is 1mm, 2mm, 5mm, 10mm, 20mm, and 50mm. The washes are combing used together to acquire different distance between the two optics. A parallel light is acquired through adjust the distance between the lens on the light source. A filter is mounted to increase the monochromaticity of the light. A scotch tape is settled to increase the homogeneity of the light. A linear polarization is acquired through a polarizer. A circular polarization is obtained when the optical axis of a linear polarizer cross with the optical axis of the retarder (quarter waveplate). A Stokes polarimeter is sited under the sample stage. The intensity at every pixel obtained by a camera is sent into a computer.

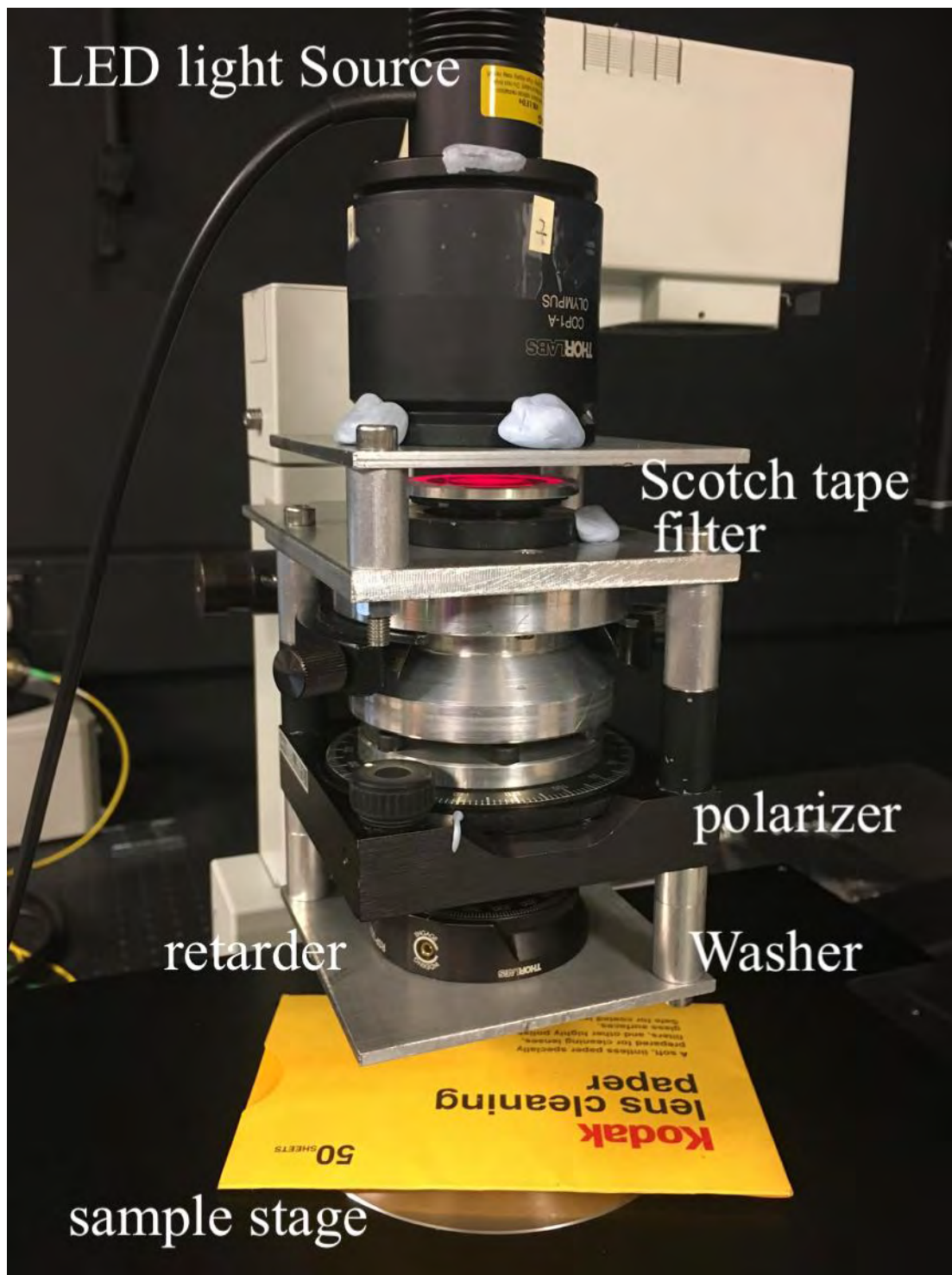


Figure 4.5.1.1 Experimental set-up for calibration of the system

A linear polarized light in different angle is used to do the calibration. To acquire k8, a quarter wave plate for 670 nm is mounted between the polarizer and the PEM1 to acquire an elliptical polarization.

4.5.2 Data analysis method of calibration

4.5.2.1 Nonlinear regression

In practice, it's not easy to make sure the setting angles of PEMs and the analyzer are accurate; and a more accurate non-linear calibration method is adopted (Cook, 2010). In the non-linear calibration process, many polarizations are measured to acquire more data point that make the regression more reliable. Linear polarizer at different orientation angles are used after the laser has been tuned into a circular polarization through a quarter wave plate (retarder). The purpose of this process is to make sure the intensity of the polarization at different orientation angles is uniform and grade of polarization is a few parts permillage. In this case, the passing axis of the polarizer sited after a circular polarizer (quarter wave plate) is rotated. The angle between the passing axis of the polarizer and the fast axis of the PEM2 (x-axis of the laboratory coordinate) is noted as θ_t . The angle of polarizer θ_t is varied from 0° to 180° in incremental angle of 10° . An elliptical polarization is obtained through putting a quarter wave plate between polarizer and PEM1. The matrix K can be got through a random number fitting method, executed by computer iteration on solver on the Excel software, to make sure the $\lim_{\tau} \sigma = I^2 - Q^2 - U^2 - V^2 = 0$, here τ is the cycle index. Four error values should be close to zero when the constants are correctly fitted, they are as follows (Cook, 2010):

$$\varepsilon_{1i} = \gamma_1(I_i^2 - I_{pi}^2)^2 = \gamma_1 I_{dpi}^4 \quad (4.5.2.1)$$

$$\varepsilon_{2i} = \gamma_2\left(\frac{I_i^2}{I_{pi}^2} - 1\right)^2 = \gamma_1 \frac{I_{dpi}^4}{I_{pi}^4} \quad (4.5.2.2)$$

$$\varepsilon_{3i} = \gamma_3\left(\frac{Q_i}{I_i} - \cos(2\theta_t)\right)^2 + \gamma_3\left(\frac{U_i}{I_i} - \sin(2\theta_t)\right)^2 \quad (4.5.2.3)$$

$$\varepsilon_{4i} = \gamma_4 \left(\left| \frac{V_i}{I_i} \right| - |\sin(2(\theta_t - \rho))| \right)^2 + \gamma_4 \left(\frac{\sqrt{U_i^2 + Q_i^2}}{I_i} - |\cos(2(\theta_t - \rho))| \right)^2 \quad (4.5.2.4)$$

$$I_{pi}^2 = Q_i^2 + U_i^2 + V_i^2 \quad (4.5.2.5)$$

Here $\gamma_1, \gamma_2, \gamma_3, \gamma_4$ are scaling factors, ρ is the angle between the fast axis of quarter waveplate and the x-axis of laboratory coordinate. To make sure the calibration parameters converge to the same value in different initial value. In Cook's thesis (Cook, 2010), the influence of initial value of $\gamma_1, \gamma_2, \gamma_3$, is discussed and the value of $\gamma_1, \gamma_2, \gamma_3$ is chosen to make sure the convergence of the regression. In my experiment, $\gamma_1 = \gamma_2 = \gamma_3 = 1$. The convergence of ε_{total} can be very well and not influenced by the initial parameter of the K matrix when the equipment is in good alignment. ε_{4i} is based on the wavelength of the retarder match the wavelength of the light, because the circular polarization is only available in this situation.

In the iteration process, we should keep ε_{total} near to 0, ε_{total} is shown below:

$$\varepsilon_{total} = \varepsilon_{1t} + \varepsilon_{2t} + \varepsilon_{3t} = \sum_{i=1}^m \varepsilon_{1i} + \sum_{i=1}^m \varepsilon_{2i} + \sum_{i=1}^m \varepsilon_{3i} + \sum_{i=1}^m \varepsilon_{4i} \quad (4.5.2.6)$$

Here, m is the number of polarizations adopted in the calibration process.

Matrix K shown in equation (4.3.1.12) is obtained through the process of calibration.

Both the calibration, on the optical bench system measured with the lock-in amplifier and that on the microscope measured with the equivalent algorithm, use the non-linear regression method.

4.5.3 Elliptical polarization

The calibration experiment is used to establish the relationship between actual signals and Stokes parameters. A proper alignment is the basement of the right calibration parameters.

The process of alignment is shown in Appendix A.1. The configuration of the calibration is shown in Fig. 4.5.1.1. A linear calibration and circular calibration are done separately. The retarder (waveplate) is installed between the polarizer and PEM1, in the process of doing the elliptical calibration. The linear polarization calibration has been stated in Cook's thesis (Cook, 2010); I state the elliptical polarization calibration here for an accurate measurement of Stokes parameter V.

It is a bit complex to acquire a circular polarization, the circular polarization is got when the angle between the axis of the polarizer and retarder equals 45° . In the calibration experiment, there are two ways to acquire the elliptical polarization: one is fixing the retarder and rotating the polarizer; and the other is fixing the polarizer and rotating the retarder.

In our experiment, a linear polarizer and a quarter waveplate are used to acquire a circular polarization. According to the Appendix B in (Kliger, Lewis, & Randall, 1990), the Mueller Matrix of a quarter wave plate is shown in formula (4.5.3.1)

$$M_{\text{qw}} = \begin{pmatrix} 1 & 0 & 0 & 0 \\ 0 & \cos^2(2\rho) & \sin(2\rho)\cos(2\rho) & -\sin(2\rho) \\ 0 & \sin(2\rho)\cos(2\rho) & \sin^2(2\rho) & \cos(2\rho) \\ 0 & \sin(2\rho) & -\cos(2\rho) & 0 \end{pmatrix} \quad (4.5.3.1)$$

where, the ρ represents the angle of the optical axis with the x-axis of the laboratory coordinate.

The Stokes parameter vector of a linear polarization after a polarizer, whose optical axis is aligned at an angle θ reference to the laboratory coordinate, is represented as a vector $(1 \ \cos 2\theta \ \sin 2\theta \ 0)^T$. When the linear polarization light comes through a quarter waveplate whose optical axis represented as an angle of ρ reference to the laboratory coordinate, the Stokes parameter vector represented as \mathbf{S}_r ,

$$\begin{aligned}
\mathbf{S}_r &= M_{qw} \begin{pmatrix} 1 \\ \cos 2\theta \\ \sin 2\theta \\ 0 \end{pmatrix} = \begin{pmatrix} 1 & 0 & 0 & 0 \\ 0 & \cos^2(2\rho) & \sin(2\rho) \cos(2\rho) & -\sin(2\rho) \\ 0 & \sin(2\rho) \cos(2\rho) & \sin^2(2\rho) & \cos(2\rho) \\ 0 & \sin(2\rho) & -\cos(2\rho) & 0 \end{pmatrix} \begin{pmatrix} 1 \\ \cos 2\theta \\ \sin 2\theta \\ 0 \end{pmatrix} \\
&= \begin{pmatrix} 1 \\ \cos(2\rho) \cos(2\rho - 2\theta) \\ \sin(2\rho) \cos(2\rho - 2\theta) \\ \sin(2\rho - 2\theta) \end{pmatrix} \quad (4.5.3.2)
\end{aligned}$$

Consider two situations: fix the retarder and rotate the polarizer; and fix the polarizer and rotate the retarder. These are designated case 1 and 2, respectively.

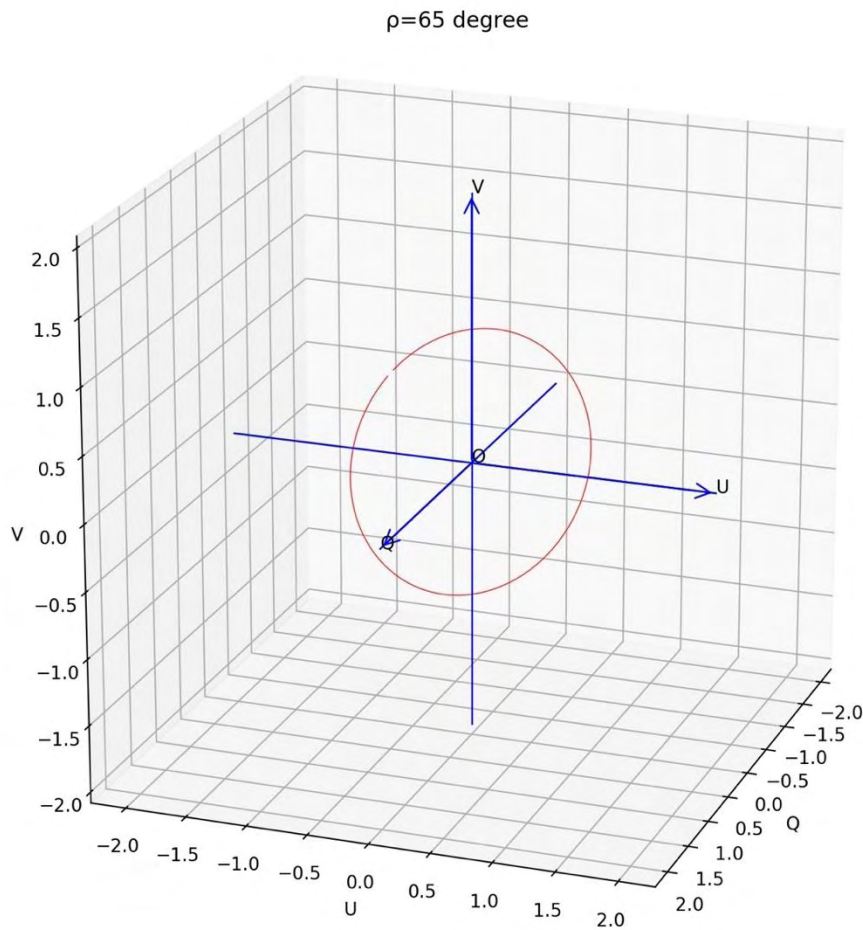


Figure 4.5.3.1 The trace of the end of the Stokes vector in 3D graphic, when rotate the polarizer from 0° to 180° at retarder angle $\rho = 65^\circ$

Case 1: keep the retarder fixed and rotate the polarizer: $\rho = \text{const}$; and $\theta = (0^\circ - 180^\circ)$.

the trace of the end of the Stokes vector on Poincaré sphere is a big circle on Poincaré sphere, shown in Fig. 4.5.3.1, which across the south point and the north point of Poincaré sphere.

We discuss the simplest four configurations shown below:

1. When $\rho = 0^\circ$, then $\mathbf{S}_r = \begin{pmatrix} 1 \\ \cos(2\theta) \\ 0 \\ -\sin(2\theta) \end{pmatrix}$
2. When $\rho = 45^\circ$, then $\mathbf{S}_r = \begin{pmatrix} 1 \\ 0 \\ \sin(2\theta) \\ \cos(2\theta) \end{pmatrix}$
3. When $\rho = 135^\circ$, then $\mathbf{S}_r = \begin{pmatrix} 1 \\ 0 \\ \cos(2\theta) \\ -\sin(2\theta) \end{pmatrix}$
4. When $\rho = 90^\circ$, then $\mathbf{S}_r = \begin{pmatrix} 1 \\ \cos(2\theta) \\ 0 \\ \sin(2\theta) \end{pmatrix}$

The trace of the polarization after the retarder in case 1 is shown in Fig. 4.5.3.2.

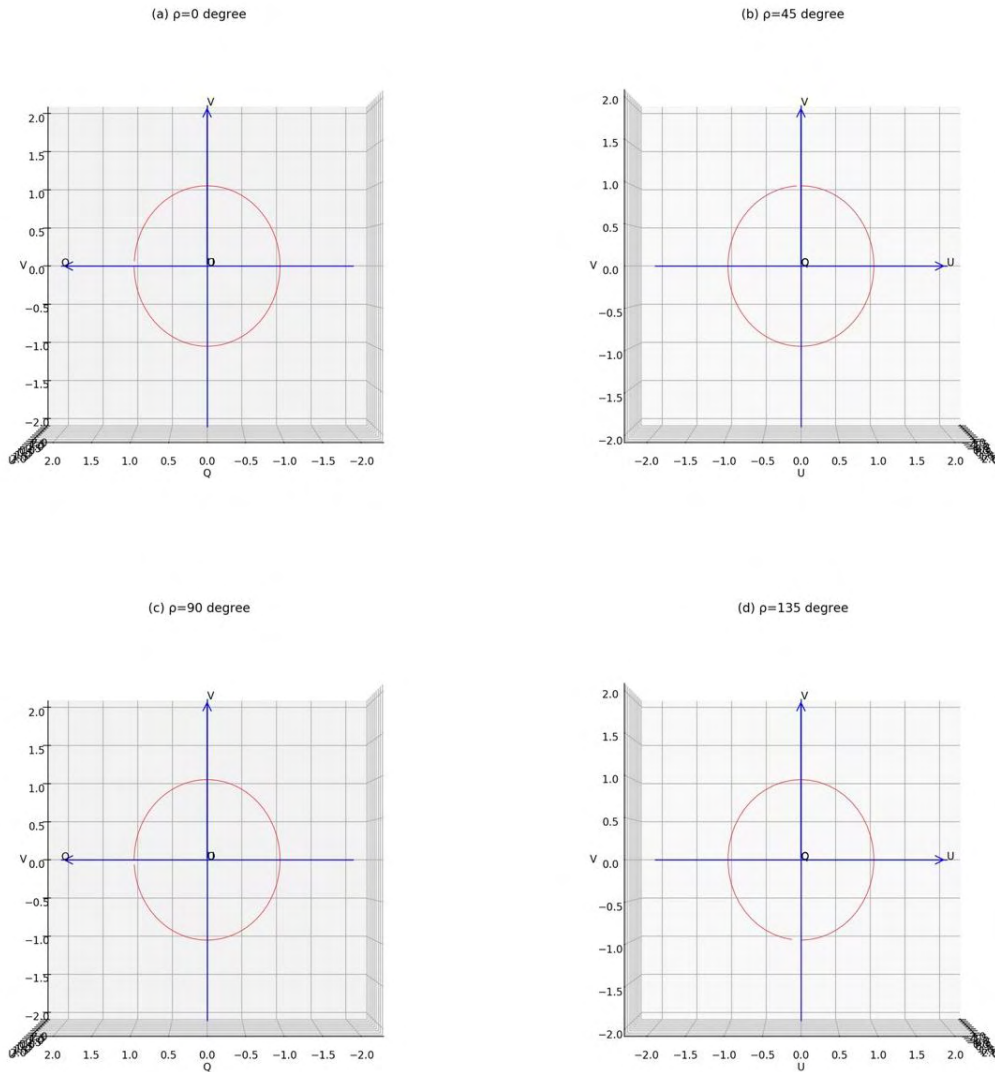


Figure 4.5.3.2 the trace of the end of the Stokes vector on Poincaré sphere, when rotate the polarizer from 0° to 180° , at different retarder angles: (a) $\rho = 0^\circ$; (b) $\rho = 45^\circ$; (c) $\rho = 90^\circ$; (d) $\rho = 135^\circ$

Case 2: keep the polarizer fixed and rotate the retarder: $\theta = const$; and $\rho = (0^\circ - 180^\circ)$.

The trace of the end of the Stokes vector on Poincaré sphere is a special curve on Poincaré sphere, shown in Fig.4.5.3.3, which across the south point, the north point, and the equator on Poincaré sphere.

$\theta=45$ degree

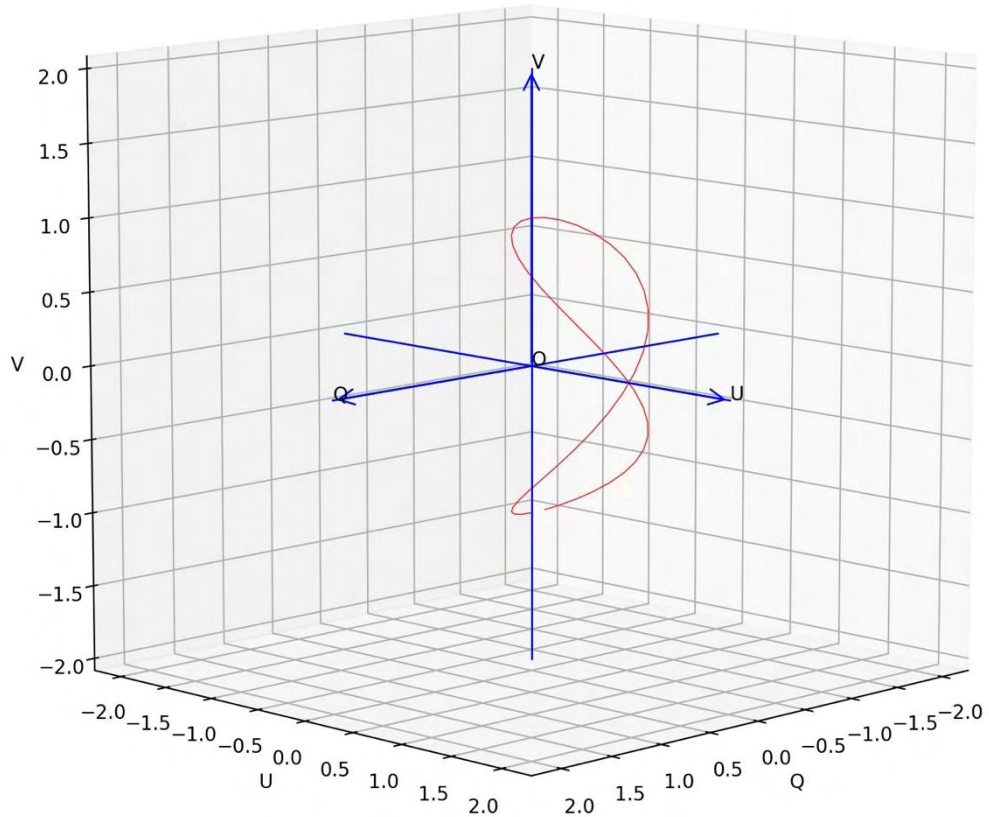


Figure 4.5.3.3 the 3D image of the trace of the end point of the Stokes vectors on Poincaré sphere when changing the retarder angle from 0° to 180° when the polarizer angle is 45° .

We discuss the simplest four configurations shown below:

1. When $\theta = 0^\circ$, then $\mathbf{S}_r = \begin{pmatrix} 1 \\ \cos(2\rho)\cos(2\rho) \\ \sin(2\rho)\cos(2\rho) \\ \sin(2\rho) \end{pmatrix}$
2. When $\theta = 45^\circ$, then $\mathbf{S}_r = \begin{pmatrix} 1 \\ \cos(2\rho)\cos(2\rho) \\ \sin(2\rho)\cos(2\rho) \\ -\sin(2\rho) \end{pmatrix}$
3. When $\theta = 90^\circ$, then $\mathbf{S}_r = \begin{pmatrix} 1 \\ \cos(2\rho)\cos(2\rho) \\ \sin(2\rho)\cos(2\rho) \\ \sin(2\rho) \end{pmatrix}$

4. When $\theta = 135^\circ$, then $\mathcal{S}_r = \begin{pmatrix} 1 \\ -\cos(2\rho)\cos(2\rho) \\ -\sin(2\rho)\cos(2\rho) \\ \sin(2\rho) \end{pmatrix}$

The trace of the end of the Stokes vector of the polarization after the retarder in case 2 is shown in Fig. 4.5.3.4.

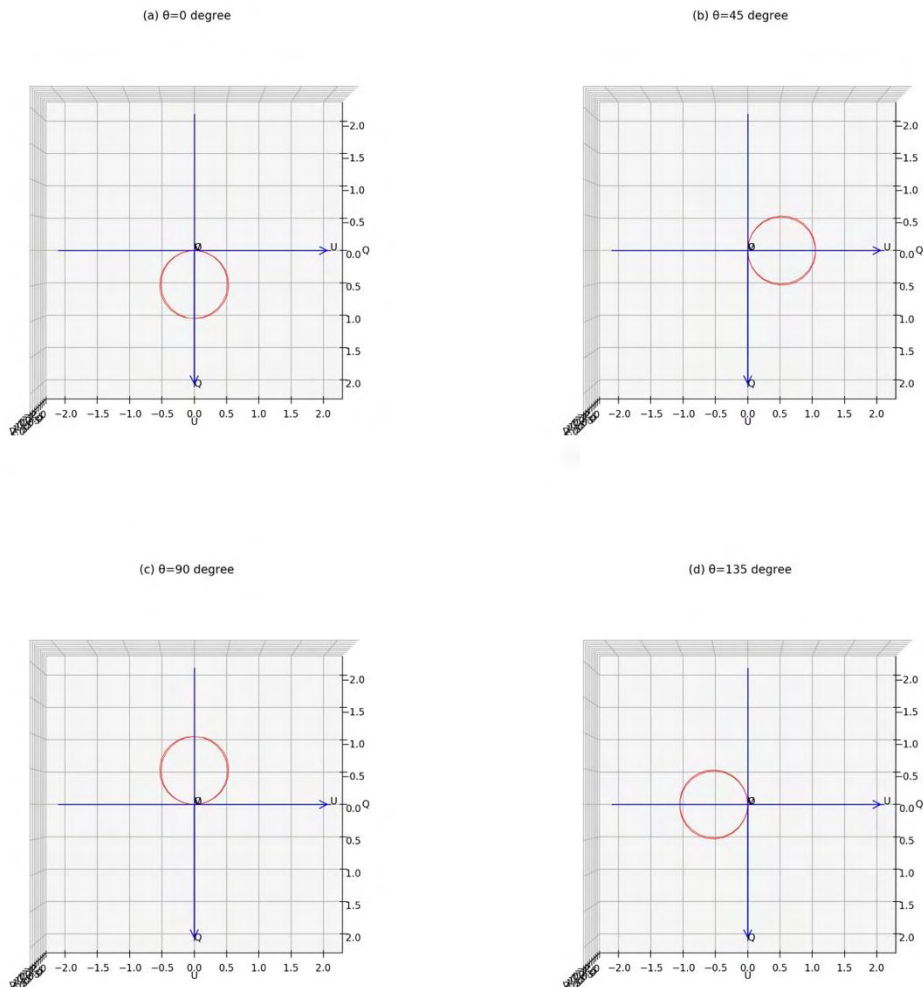


Figure 4.5.3.4 The trace of the end of the Stokes vector on Poincaré sphere, when rotate the retarder from 0° to 180° , at different retarder angles: (a) $\theta = 0^\circ$; (b) $\theta = 45^\circ$; (c) $\theta = 90^\circ$; (d) $\theta = 135^\circ$

In summary, the method used to attain the elliptical polarization in the two case is different.

The trace of the end of the Stokes vector on Poincaré sphere is also different. The two methods are identical to the calibration but deduced different curves. In our experiment, the

test is done when $\rho = 65^\circ$ and $\theta = 45^\circ$; the trace of the polarization in 3D Poincaré sphere after the retarder is shown in Fig. 4.4-2 and Fig. 4.4-4, respectively.

4.5.4 Calibration result

4.5.4.1 Weight factor in the calibration

According to the equation 4.5.2.2 to equation 4.5.2.4, the weight factor of calculation of the fourth error γ_4 is discussed in this section. In the calibration process of elliptical polarization, keeping the angle of retarder ρ to be a constant ($\rho = 65^\circ$) and rotating the polarizer, ε_{4t} is considered in the calibration. Table 4.5.4.1 shows calibration parameter of the LED source using 6 channel method with different weight factor of γ_4 . From table 4.5.4.1, γ_4 is not a dominant parameter in the process of calibration; so, in most calibration, we set γ_4 to be zero and ignore it.

Table 4.5.4.1 The calibration parameter of the LED source with 6 channel (S3, S4, S5, S6, S11, and S12) method: the comparison on the differential ratio of γ_4 , $\gamma_1 = \gamma_2 = \gamma_3 = 1$

γ_4	0	1	0.1
k_1	1	1	1
k_2	0.33362878	0.33363727	0.33362991
k_3	-6.4664483	-6.4669231	-6.4664968
k_4	2.3841937	2.38263873	2.3840346
k_5	3.47867617	3.44020227	3.47484097
k_6	-0.581882	-0.5876728	-0.5824586
k_7	13.3599652	13.3437633	13.3583404
k_8	1.75606593	1.75661201	1.75612785
ε_{1t}	0.03683115	0.0368312	0.03682664
ε_{2t}	0.28895661	0.28989602	0.28901579
ε_{3t}	1.72E-02	1.68E-02	1.72E-02
ε_{4t}	-----	5.45E+00	5.45E-01
ε_{total}	0.34303393	5.79611419	0.88838696

4.5.4.2 The effect of temperature on the measurement of Stokes parameters

PEM is sensitive to the temperature. The normalized Stokes parameter V under the same sequence of the variation of the temperature. The variation of the room temperature is about

2°C over 24 hours; so, keeping the stable of the room temperature is important. The variation of the temperature may produce an error on the measurement of the Stokes polarimeters. To clarify the influence of the temperature on the Stokes parameter measurement, calibration under different temperature is done in the system of the Stokes polarimetric microscope.

The calibration parameters under five different room temperatures, shown in Table 4.5.4.2 and Table 4.5.4.3 are measured to find a suitable temperature regime of doing the experiment. From table 4.5.4.2 and table 4.5.4.3, the calibration parameter is stable between 22.1°C and 22.6°C.

Table 4.5.4.2 Calibration parameters at different temperatures, the elliptical polarization is acquired under the retarder at 65°

Temperature (°C)	21.3	21.5	21.8	22.1	22.6	23
k_1	1	1	1	1	1	1
k_2	0.825295	0.818964	0.793202	0.806342	0.807120	0.816797
k_3	-0.429385	-0.434175	-0.433474	-0.436373	-0.436121	-0.446456
k_4	2.089706	2.099021	2.097920	2.145031	2.149179	2.197265
k_5	-0.449445	-0.451311	-0.440221	-0.463483	-0.454554	-0.474884
k_6	0.273516	0.279134	0.277612	0.282740	0.285535	0.284613
k_7	3.723577	3.738653	3.756446	3.807487	3.811786	3.871728
k_8	3.765930	3.691535	3.090881	2.982916	2.953434	2.826086
ε_{1t}	0.015741	0.034330	0.015382	0.032401	0.049497	0.069008
ε_{2t}	0.003128	0.006265	0.002865	0.005177	0.007432	0.007252
ε_{3t}	0.000614	4.98E-04	4.48E-04	1.04E-03	7.81E-04	1.12E-03
ε_{total}	0.019482	0.0410	0.0187	0.0386	0.05771	0.07738

In theory, the situation of the calibration and the measurement should be exactly the same to keep the accuracy of the measurement. In practice, the set-up of the calibration and the measurement is different. Of course, the calibration and the measurement can't be done at the same time. The variation of the environment temperature influences the accuracy of the measurement. It's very important to keep the temperature in a small variation range. Using the calibration parameter of one temperature to calculate the Stokes parameters measured at different temperature can help to find a reliable temperature range of the measurement.

Table 4.5.4.3 calibration parameters at different temperatures, the elliptical polarization is acquired under the polarizer at 45°

Temperature (°C)	21.3	21.5	21.8	22.1	22.6	23
k_1	1	1	1	1	1	1
k_2	0.820240	0.818741	0.795740	0.806907	0.806141	0.816514
k_3	-0.42663	-0.42148	-0.42953	-0.44801	-0.44689	-0.44404
k_4	2.089499	2.098183	2.097910	2.142456	2.145591	2.196268
k_5	-0.44643	-0.46012	-0.44738	-0.46579	-0.45868	-0.46323
k_6	0.275279	0.274966	0.273749	0.282557	0.284859	0.289715
k_7	3.727160	3.743279	3.752759	3.823937	3.835210	3.862457
k_8	3.633819	3.774747	3.060242	2.968449	2.900989	2.832062
ε_{1t}	0.066309	0.019679	0.029634	0.059362	0.085347	0.072348
ε_{2t}	0.012468	0.003932	0.005272	0.007406	0.009831	0.008433
ε_{3t}	5.86E-04	5.98E-04	4.89E-04	1.08E-03	9.28E-04	9.92E-04
ε_{total}	0.079364	0.024209	0.035395	0.067846	0.096106	0.081773

Figure 4.5.4.1 shows the Stokes Parameters tested at different temperatures using the same calibration parameters tested at 22.6°C. The Stokes parameter V is strongly influenced by the test temperature: 21% of decrease under the temperature decrease of 1°C; 4% of increase with the temperature increase of 0.4°C. A stable test temperature range shown by the experiment is from 22.1°C to 22.6°C.

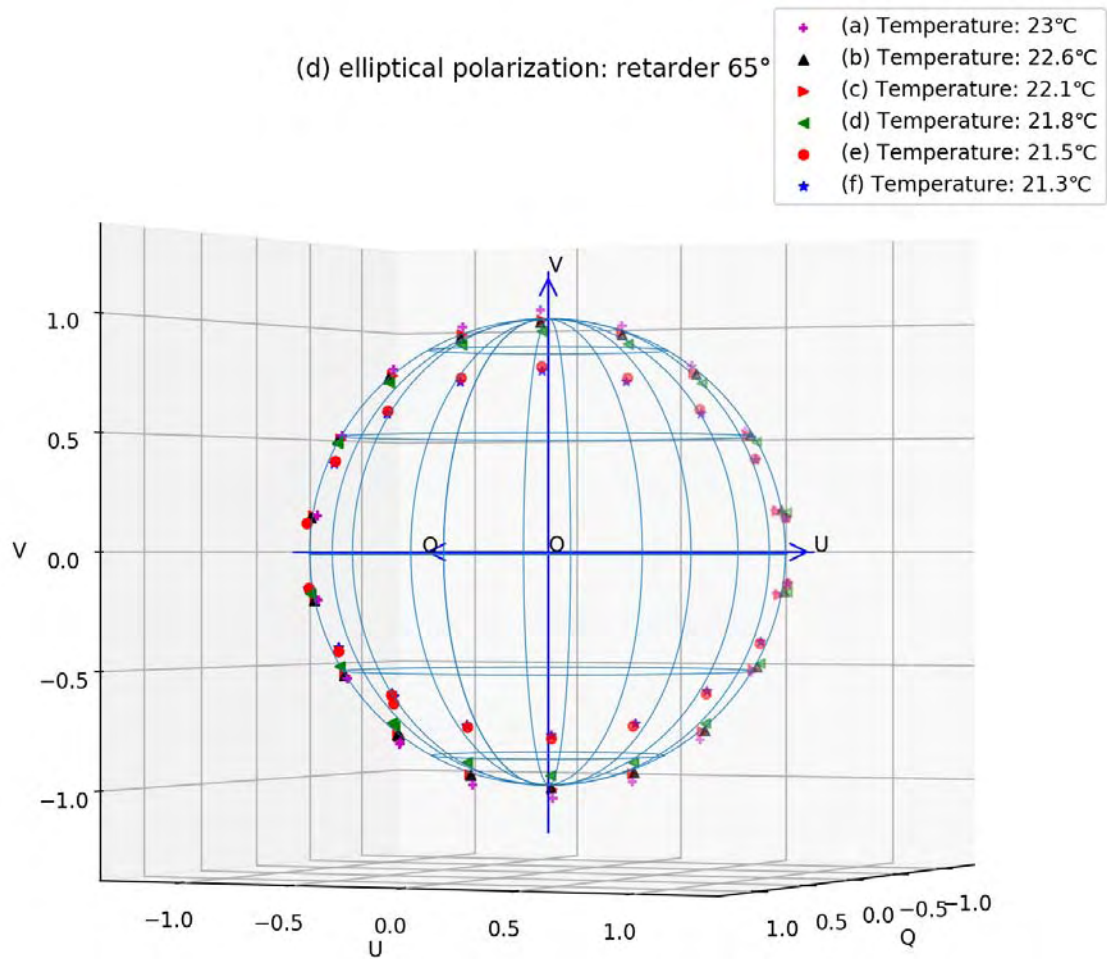


Figure 4.5.4.1 The representation of the Stokes parameters on Poincaré sphere for circular polarization under fixed retarder angle of 65° tested at different temperature: (a) 23°C , (b) 22.6°C , (c) 22.1°C , (d) 21.8°C , (e) 21.5°C , (f) 21.3°C using the calibration parameters at 22.6°C

However, the linear polarization is not sensitive to the variation of the temperature, shown in Fig. 4.5.4.2. The Stokes parameter Q decreases slightly under the increase of temperature: Q shows 1.8% of decrease under the increase of temperature of 0.4°C ; Q is 3.8% of increase under the decrease of the temperature of 1.3°C . The Stokes parameter U decrease slightly under the increase of the temperature: U is 1.2% of decrease under the increase of temperature of 0.4°C ; U is 2.7% of increase under the decrease of the temperature of 1.3°C .

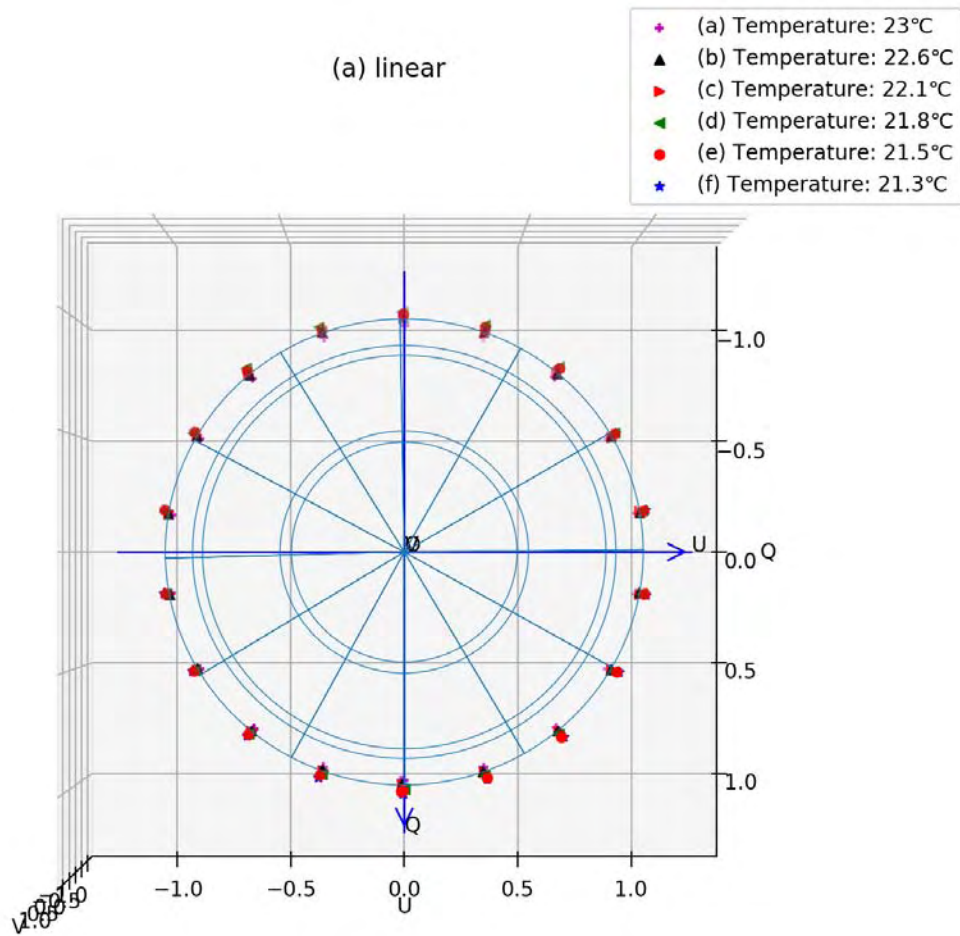
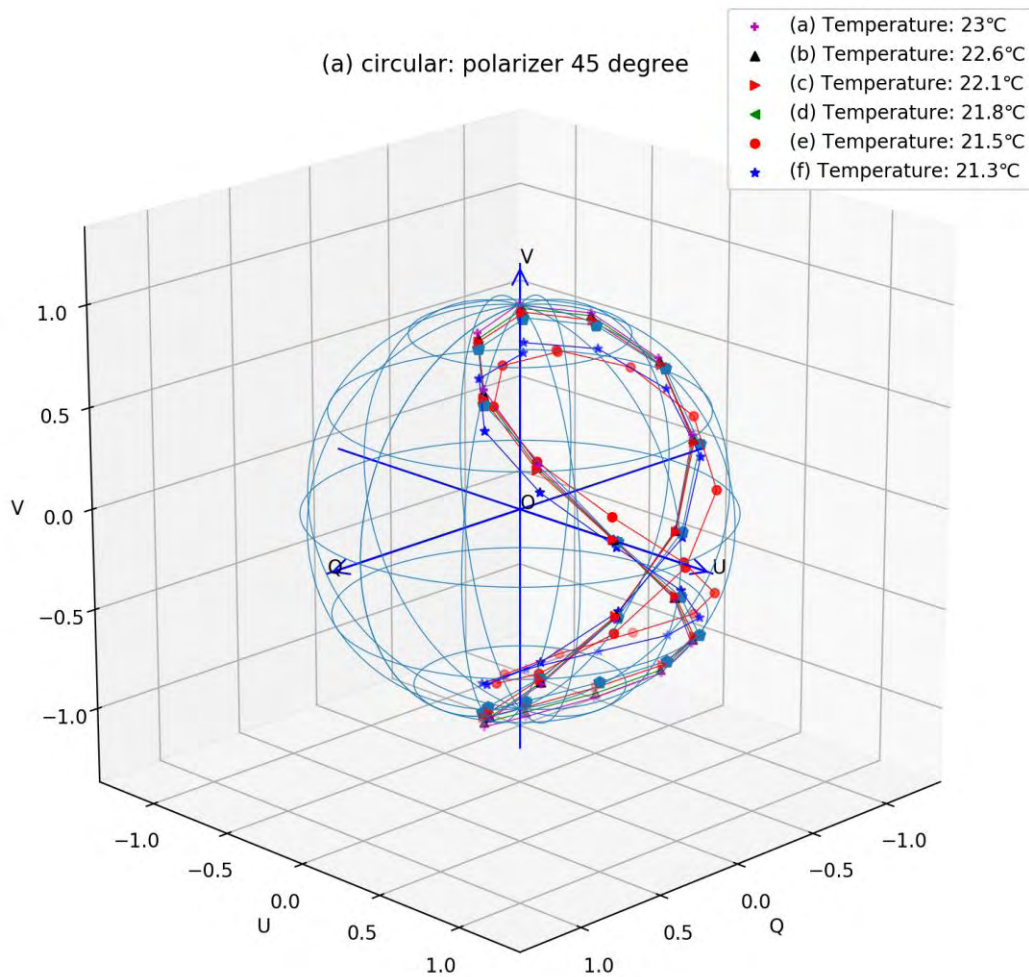


Figure 4.5.4.2 The Stokes parameters for linear polarization tested at different temperatures: (a)23°C, (b)22.6°C, (c)22.1°C, (d)21.8°C, (e)21.5°C, (f)21.3°C using the calibration parameters at 22.6 °C

The variation of the Stokes parameters of an elliptical polarization acquired through rotation of the retarder, shows on Fig. 4.5.4.3. Figure 4.5.4.3a is the 3D image. The shape of the experimental curve is similar to the theoretical calculation shown on Fig. 4.5.3.3. From Fig. 4.5.4.3b, the Stokes parameter V decreases under the decrease of the temperature, while, the Stokes parameter U increases under the decrease of the temperature. The Stokes parameter Q is shifted towards the direction of -Q with the decrease of the temperature, shown in Fig.

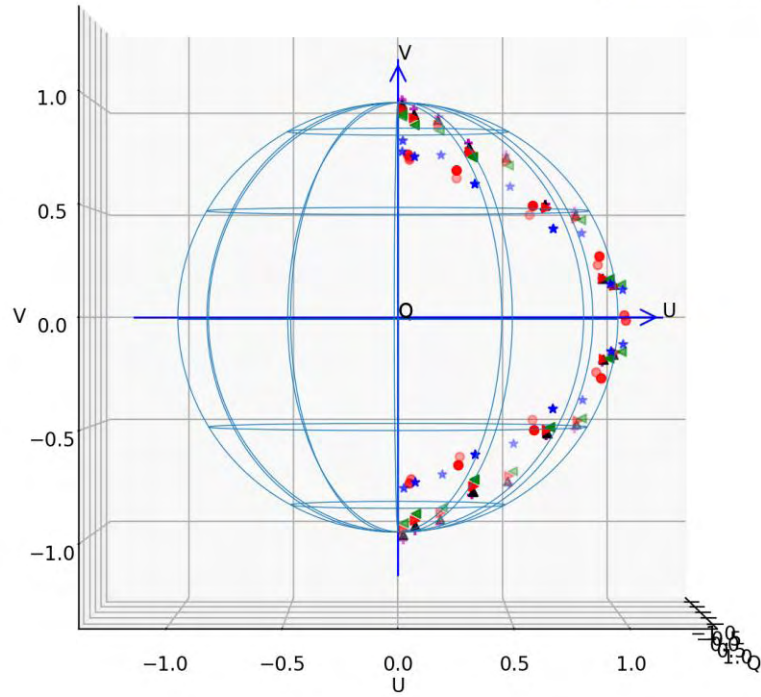
4.5.4.3c. The difference of the calibration temperature and the measurement temperature can make the Stokes parameter tested does not remain on the Poincaré's sphere; while, that move to inside or outside the Poincaré's sphere. Furthermore, the pure polarization may be shown as a partially polarization because of the application of calibration parameter measured under a not right temperature.

So, keeping the temperature stable during the experiment and using the right temperature calibration parameter is the key for the accurate characterization.



(b) circular: polarizer 45 degree

- ✦ (a) Temperature: 23°C
- ▲ (b) Temperature: 22.6°C
- ▶ (c) Temperature: 22.1°C
- ◀ (d) Temperature: 21.8°C
- (e) Temperature: 21.5°C
- ★ (f) Temperature: 21.3°C



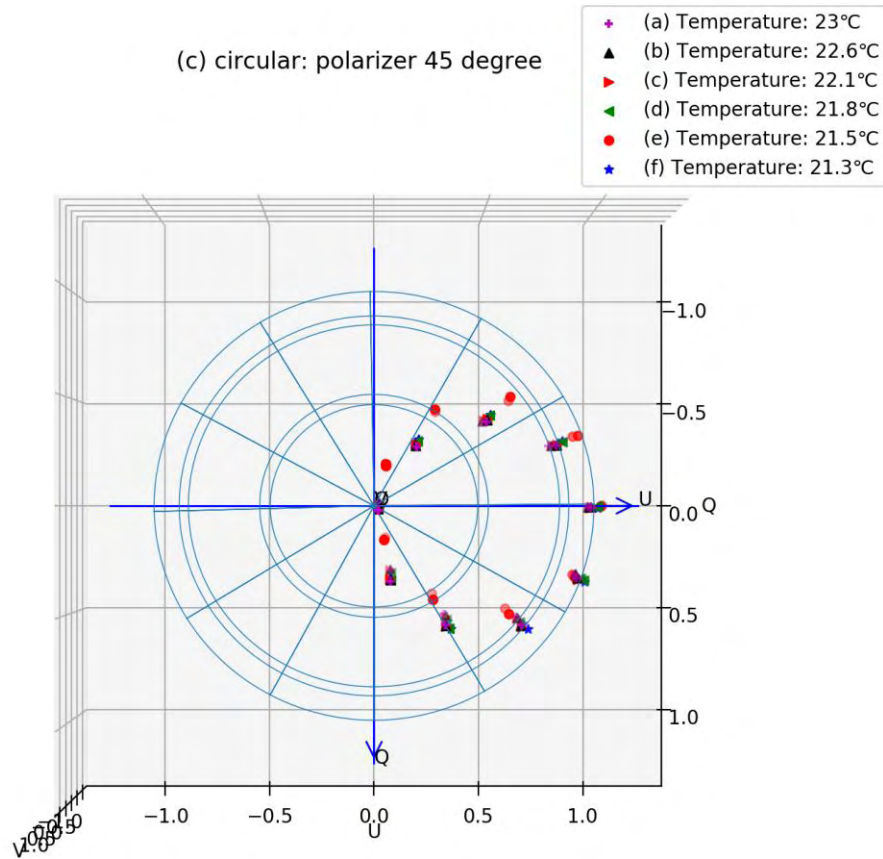


Figure 4.5.4.3 The Stokes parameters for circular polarization at different angle of view [(a) 3D imagine, (b) projection image on plane of U and V, (c) projection image on plane of Q and U] under fixed polarization angle of 45° tested at different temperatures: 23°C, 22.6°C, 22.3°C, 21.8°C, 21.5°C, 21.3°C using the calibration parameters at 22.6 °C.

Table 4.5.4.4 The maximum value of Stokes parameters U and V under different room temperatures, using the same calibration matrix K under 22.6°C.

Temperature (°C)	U_{\max}	V_{\max}
23	0.9875	1.01
22.6	0.98	0.98
21.3	1.02	0.77

Table 4.5.4.5 absolute error and relative error of maximum Stokes parameters U and V at temperature variation of 0.4 °C and 1.3°C

Temperature difference (°C)	dU_{\max}	dV_{\max}	dU_{\max}/dT	dV_{\max}/dT
0.4	-0.0015	0.03	-0.00375	0.075
1.3	-0.04	0.21	-0.03077	0.161

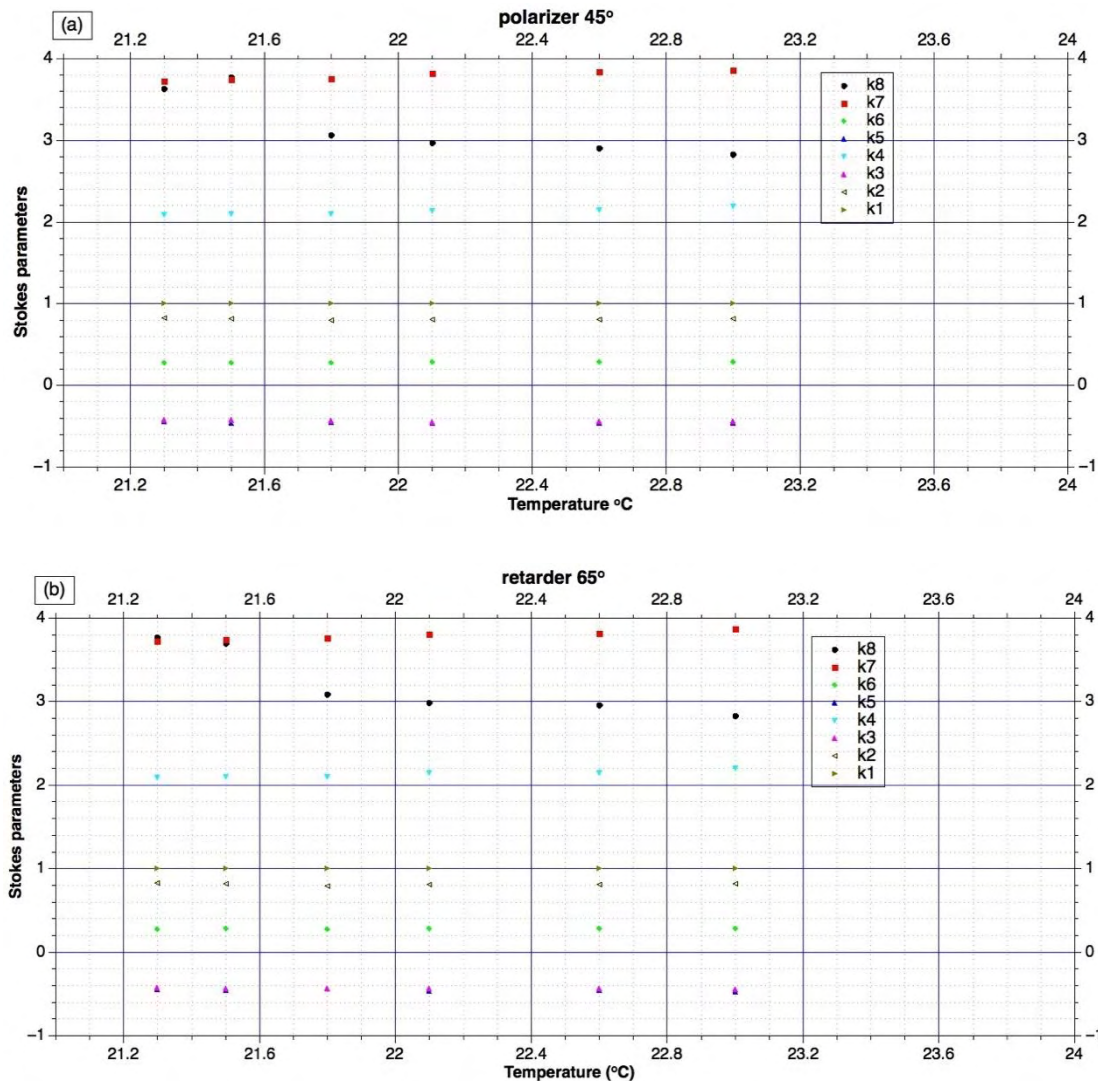


Figure 4.5.4.4 The variation of the calibration parameters $k_1, k_2, k_3, k_4, k_5, k_6, k_7,$ and k_8 to the calibration temperature, under different test configurations: (a) polarizer is at 45° and (b) retarder is at 65°

Table 4.5.4.4 shows the maximum value of Stokes parameters U and V under $21.3^\circ\text{C}, 22.6^\circ\text{C}, 23^\circ\text{C}$, calculated using the calibration parameter under 22.6°C . Based on this, the error of temperature variation around 0.4°C and 1.3°C is calculated, shown in Table 4.5.4.5. From

Table 4.5.4.5, the room temperature variation of 0.4°C makes the error in V of 7.5%. The measurement of linear polarized light is not as strict as that on the elliptical polarized light, the room temperature variation on 1.3°C makes the error of 3.1% in U.

Figure 4.5.4.4a compared the calibration parameter acquired under different temperatures, at the configuration of fixing the polarizer at 45° and rotating the retarder. The calibration parameter k_8 is strongly influenced by the variation in temperature. A suitable test temperature should lie between 22.1°C and 22.6°C. Figure 2.4-10b shows the calibration parameters acquired under different temperatures, with the configuration of fixing the retarder at 65° and rotating the polarizer. The variation is similar to Fig. 2.4-10a; so, the method of acquiring the circular polarization is not influenced by the calibration parameters.

In summary, temperature is a very sensitive condition for the experiment. The variation of the temperature can produce a relative error around 0.375% for Stokes parameter U and 7.5% for Stokes parameter V when the variation of temperature is within 0.4°C. Larger temperature variation produces a great error. the variation of the temperature can produce a relative error around 3.077% for Stokes parameter U and 16.1% for Stokes parameter V when the variation of temperature is within 1.3°C. According to the experiment, a more stable temperature range, 22.1°C to 22.6°C, is suitable to do experiment in order to avoid the error arising from the variation of the temperature.

4.5.4.3 Current effect to the calibration matrix

The calibration parameters change very much with the drive current of the LED. Table

4.5.4.6 compares the calibration parameters tested at different drive currents of the LED.

Every calibration parameter strongly influenced by the drive current of the LED. So, it is very important to keep the drive current of the source the same during the measurement and the calibration process.

Table 4.5.4.6 The comparison of the calibration parameters tested at different LED current with 660nm filter.

drive current	104mA	104mA	400mA	400mA
670nm retarder	retarder 65°	polarizer 45°	retarder 65°	polarizer 45°
Temperature (°C)	22.3	22.3	22.3	22.3
k_1	1	1	1	1
k_2	0.59474312	0.59614547	0.79944091	0.80132288
k_3	-0.312358	-0.3101647	-0.4503723	-0.4488464
k_4	1.75434194	1.75616876	2.20076337	2.19973518
k_5	-0.3069869	-0.3086612	-0.4661182	-0.469393
k_6	0.22446946	0.22344232	0.30885216	0.30729587
k_7	2.6580261	2.65563444	3.9744122	3.97647766
k_8	2.27827764	2.2983657	2.98041251	2.9824212
ε_{1t}	0.3612712	0.59046311	0.12514279	0.14374952
ε_{2t}	0.00461015	0.00773862	0.00690742	0.00782706
ε_{3t}	0.00134587	1.25E-03	7.96E-04	8.33E-04
ε_{total}	0.36722722	0.5994474	0.13284616	0.15240971

4.5.4.4 The effect of the filter wavelength on the calibration matrices

Table 4.5.4.7 shows the comparison of the influence of the filter wavelength at the same drive current of the LED (400mA). The wavelength of the retarder is 670nm. The convergence is better in the situation using the 670nm filter than that using 660nm filter. The 660nm filter is used for high intensity output of the LED light source.

Table 4.5.4.7 the comparison of the calibration parameter tested with different wavelength filter using 670nm retarder at the same drive current (400mA) of the LED

Filter chosen	660nm	660nm	670nm	670nm
Geometry configuration	retarder at 65°	polarizer at 45°	retarder at 65°	polarizer at 45°
Temperature (°C)	22.3	22.3	22.1	22.1
k_1	1	1	1	1
k_2	0.79944091	0.80132288	0.80634187	0.80690654
k_3	-0.4503723	-0.4488464	-0.4363731	-0.4480133
k_4	2.20076337	2.19973518	2.14503125	2.14245597
k_5	-0.4661182	-0.469393	-0.4634834	-0.4657941
k_6	0.30885216	0.30729587	0.2827399	0.28255678
k_7	3.9744122	3.97647766	3.80748683	3.82393709
k_8	2.98041251	2.9824212	2.98291605	2.96844904
ε_{1t}	0.12514279	0.14374952	0.03240131	0.05936162
ε_{2t}	0.00690742	0.00782706	0.0051775	0.00740569
ε_{3t}	7.96E-04	8.33E-04	1.04E-03	1.08E-03

ε_{total}	0.13284616	0.15240971	0.03862103	0.06784598
-----------------------	------------	------------	------------	------------

The difference of wavelength of the filter produces an error shown in table 4.5.4.8. The difference of wavelength produces an error 2.5%, 8.8%, and 4.3% to the calibration parameter k_4 , k_6 , and k_7 shown in Table 4.5.4.8. Stokes parameters Q and U are strongly influenced by the choice of the wavelength, for Q is dependent with the k_4 and k_5 ; and U is dependent with the k_6 and k_7 . While, the error of the calibration parameter k_8 is very small, which is within 0.1% for the rotating polarizer (retarder 65°) method and 0.46% for rotation of the retarder method (polarizer 45°). So, the wavelength chosen does not produce a big error to the measurement of Stokes parameter V which is relevant on k_8 . The relative error of k_3 (3%) using rotating polarizer method is much different from that (0.2%) using rotating retarder method, shown in Table 4.5.4.8.

Table 4.5.4.8 the relative error produced by using different filter, filter (660nm) and the filter (670nm). The light source driving current is 400mA and retarder wavelength is 670nm.

	relative error	
	retarder at 65°	polarizer at 45°
670nm retarder		
source current	400mA	400mA
k_1	1	1
k_2	-0.0085951	-0.0069439
k_3	0.03157441	0.00185772
k_4	0.02564876	0.02638263
k_5	0.00566866	0.00769668
k_6	0.08827792	0.08388229
k_7	0.04290094	0.03911089
k_8	-0.0008396	0.00469584

The influence of the current may be explained by the difference of the shape of wave front of the intensity under different drive currents. The height of the pulse of the light intensity is different, although the period is different. That makes different shape of the front of the light

pulse. The wave front chosen by filter 660nm is different from the wave front chosen by the filter 670nm. So, the errors shown in Table 4.5.4.8 exists. This order of the magnitude of the error is acceptable to do the measurement. We chose 660nm filter in the situation of increasing the intensity.

4.5.4.5 The effect of monochromaticity on the calibration matrix

The calibration parameters measured on the Stokes polarimetric microscope. The other optical setting is same, but in the two situations: with a filter covered by a scotch tape and without a filter covered with a scotch tape. The scotch tape can prevent the mirror reflection from the surface of the filter. The working current of the LED light source is 400mA. The filter increased the monochromaticity. The calibration matrix K is shown in Table 4.5.4.9. ϵ_{total} is smaller in the situation with a filter than that in the situation without a filter. The situation with a filter is the best calibration we have obtained.

Table 4.5.4.9 The calibration comparison on the Stokes polarimetric microscope between the situation with and without a filter.

	without filter			with filter		
	polarizer 45°	retarder 65°		polarizer 45°	retarder 65°	
		$\gamma_4 = 1$	$\gamma_4 = 0$		$\gamma_4 = 1$	$\gamma_4 = 0$
k_1	1	1	1	1	1	1
k_2	0.2092673	0.2074199	0.2074145	0.2122284	0.2177296	0.21772651
k_3	-2.20633	-2.2014794	-2.2013796	-2.3644821	-2.3724368	-2.3724427
k_4	2.4977149	2.5000255	2.5003110	2.7561998	2.7548650	2.75467118
k_5	0.99045711	0.9857056	0.9841226	1.3853479	1.3838578	1.38417161
k_6	-0.5419384	-0.5452004	-0.5463411	-0.8154092	-0.8167409	-0.8165331
k_7	4.6296085	4.6332038	4.6356422	4.8335046	4.8389402	4.83895942
k_8	1.6179447	1.6218813	1.6197493	1.6092152	1.6041688	1.60442641
ϵ_{1t}	0.0043165	0.0030530	0.0030027	7.8062E-05	8.4593E-05	8.4618E-05
ϵ_{2t}	0.0101958	0.0070421	0.0069046	0.0027987	0.0030413	0.00304199
ϵ_{3t}	0.0201648	0.0202402	0.0203432	0.0006438	6.04E-04	0.00060248
ϵ_{4t}		5.3292880			5.34E+00	
ϵ_{total}	0.0346771	5.3596232	0.0302505	0.0035206	5.3482781	0.00372908

4.5.4.6 Comparison of the test interval of the angles on the calibration matrix

A series of tests was done to acquire a set of more accurate calibration parameters, one is the change of the number of the data. The data point was collected at angles in different interval of angles. Table 4.5.4.10 shows the calibration matrix K measured with the angle intervals in 10° , 5° , 2° .

Table 4.5.4.10 calibration parameters tested at different increment of angle in twelve channel method.

Calibration in different depth	10°	5°	2°
k_1	1	1	1
k_2	0.4151712	0.42957818	0.35181403
k_3	-0.2926271	-0.1908937	-0.3887469
k_4	1.66779577	1.68498509	1.59720765
k_5	-0.2805359	-0.2995648	-0.3773759
k_6	0.2097901	0.22759809	0.20464706
k_7	2.84104073	2.95744701	2.74867656
k_8	2.59036343	2.5675225	2.55897749
ε_{1t}	0.024638	0.03043611	0.02778696
ε_{2t}	0.08099658	0.09900998	0.0922023
ε_{3t}	0.01451597	0.01328985	0.00433309
ε_{total}	0.12015054	0.14273595	0.12432235

Technically, the calibration tested at small intervals of angle should be more accurate than the big intervals of angle, for more test samples used to do the fitting. The abnormal phenomenon shown in table 4.5.4.10 is from an error of the hardware, which is shown in Fig. 4.5.4.6. The signal at 100kHz is not symmetric at the zero point, which is from the selection error of the signal choice on the test device. While, the signal at 84kHz shown in Fig. 4.5.4.5 and 50kHz shown in Fig. 4.5.4.7 are symmetric to the zero point, which is the right signal.

We chose six channel method in later experiments after we found out the problem. The timing unit has not reached a better situation at the moment.

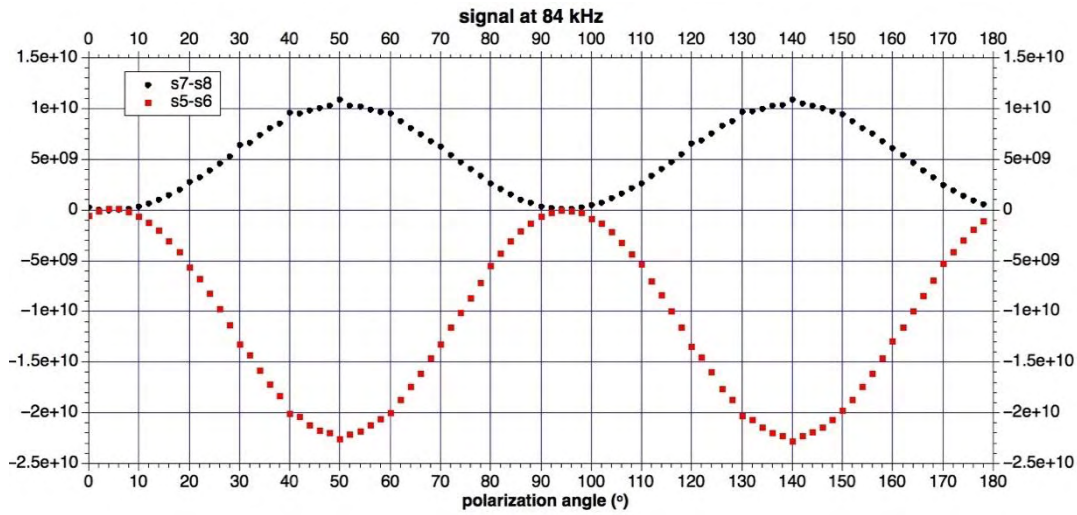


Figure 4.5.4.5 the signal acquired at 84kHz of PEM2

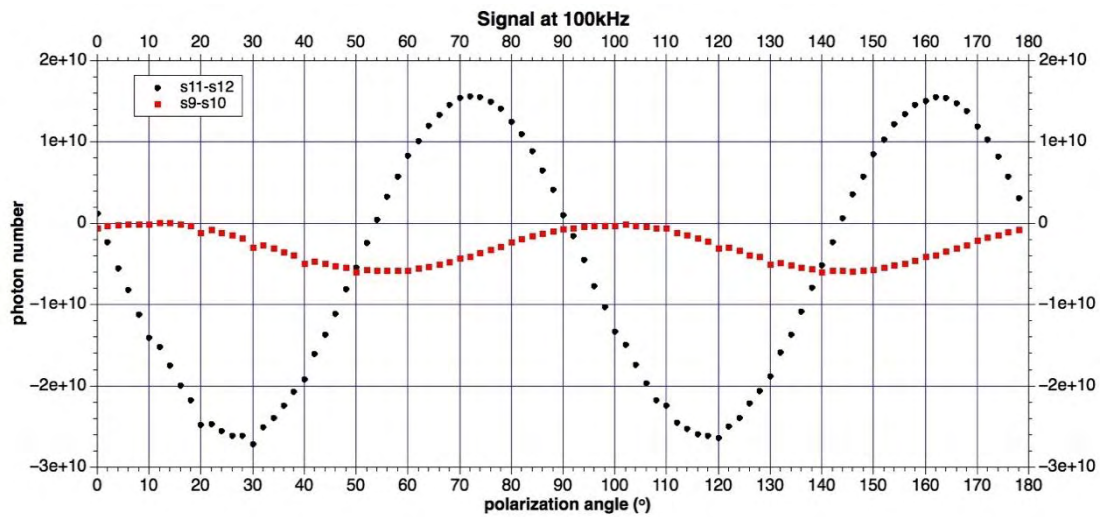


Figure 4.5.4.6 the signal acquired at 100kHz of PEM1

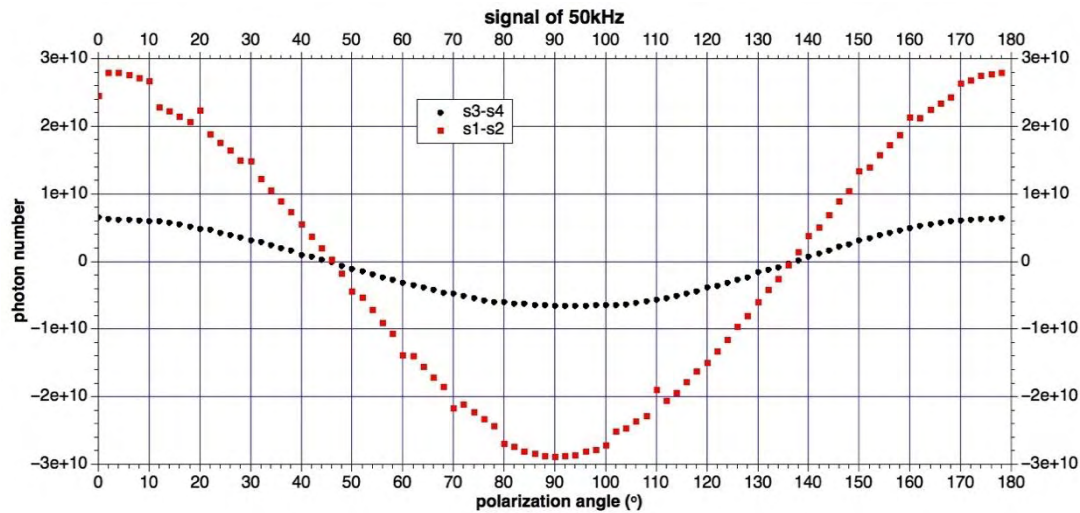


Figure 4.5.4.7 signal acquired by PEM1 at 50kHz

4.6 Summary

In this chapter, the principles of Stokes polarimetry are introduced. The calibration is discussed carefully. Despite the linear regression method, a nonlinear regression method is introduced to solve the calibration matrix. Elliptical polarization calibration is acquired through two ways: rotation of the polarizer and rotation of the retarder. At the same configuration, the calibration parameter k_8 is sensitive to the ambient temperature. A stable temperature region of the measurement is between 22.1°C to 22.6°C. The calibration matrix K is sensitive to the drive current of the LED and the matching of the optical components. The convergence of the calibration depends on good alignment and the monochromaticity of the light source. From the research above, a reasonable measurement needs five prerequisites: keeping room temperature between 22.1°C to 22.6°C, keeping the LED driving current constant, using the matching optical components, maximizing monochromaticity of the light, and doing a careful alignment. Calibration can be used to check the problem of the hardware equipment. Ten degrees interval is accurate enough to acquire a reasonable calibration matrix.

Reference

- Cook, P. (2010). *A study of focussed ion beam patterned thin magnetic films with soft X-ray and Magneto-optical microscopy*. School of Computing, Sciences and Engineering. University of Salford, Salford.
- Guan, W. (2007). *Ultra thin films on semiconductor substrates: growth, magneto-optical characteristics and spin injection*. University of Salford, Salford.
- Guan, W., Cook, P. J., Jones, G. A., & Shen, T. H. (2010). Experimental determination of the Stokes parameters using a dual photoelastic modulator system. *Applied Optics*, 49, 2644. Retrieved from http://internal-pdf//48_Guan_2010_Appl Optics-3168858373/48_Guan_2010_Appl Optics.pdf
- Guan, W., Liu, Y., Shen, T. H., & Jones, G. A. (2008). The measurement of the Stokes parameters: A generalized methodology using a dual photoelastic modulator system. *Journal of Applied Physics*, 103(4), 43104. Retrieved from internal-pdf//228.60.152.103/Guan2008.pdf
- Huard, S. (1997). *Polarization of light*. (G. Vacca, Ed.). Paris: John Wiley & Sons, Masson.
- Kliger, D. S., Lewis, J. W., & Randall, C. E. (1990). *Polarized light in optics and spectroscopy*. London: Academic Press.
- Liu, Y. (2005). *A study of magnetic ultra thin films on GaAs and optically excited spin injection*. University of Salford.
- Photoelastic Modulation Principles of Operation - Hinds Instruments, from <https://www.hindsinstruments.com/knowledge-center/technology-primer/pem-photoelastic-modulation/principles-of-operation/>

Chapter 5 Stokes polarimetry microscope -- computerized automation in image acquisition and the identification of best operational conditions

The Stokes polarimetric microscope has been developed by Optimum Imaging Ltd. The design principle is protected by a patent priority filing (GB201411478D0, T. H. Shen and P. J. Cook.) which incorporate a dual PEM Stokes polarimeter in a widefield microscope. The polarimetric signals are recovered at the pixel level using a numerical algorithm. Polarimetric parameters are then computed to form images, for instance, of ellipticity angle contrast. The microscope is also referred to as the Optimum microscope.

In essence, a dual PEM Stokes polarimeter described in (refer to a previous chapter and the literature review chapter) is inserted in the ‘infinite space’ of an Olympus IX71 biological microscope. The current implementation of the phase sensitive detection at the pixel level is achieved by a combination of a hardware electronic timing unit, which provides the modulation to the source intensity phase locked to the reference signal from the two PEMs for signal accumulation, and signal extraction with software algorithms.

Since the microscope is a single channel implementation of the design, 12 channels of images are required for recovering the signals at the three reference frequencies with zero and quadrature phase differences. It is also possible to operate at 6 channels so that the signals at the quadrature phase difference with respect to the reference are not obtained. It has been found that the electronic timing device used has a limited frequency response so that at the high reference frequency, the phase setting between zero and quadrature cannot be correctly obtained. As a result of this issue, for all the practical work described in this thesis, only the 6-channel implementation is used.

5.1 Experiment

5.1.1 Experimental set-up

Based on the Stokes polarimeter, a Stokes polarimetric microscope is established. In practice, a Stokes polarimeter is installed on a microscope to acquire the signals of the Stokes parameters. The camera of the microscope detected the signal. PEM1 and PEM 2 are connected with a timing unit to collect the signals of three frequencies (50kHz, 100 kHz and 84kHz). The diagram of the equipment is shown in Fig. 5.1.1.1.

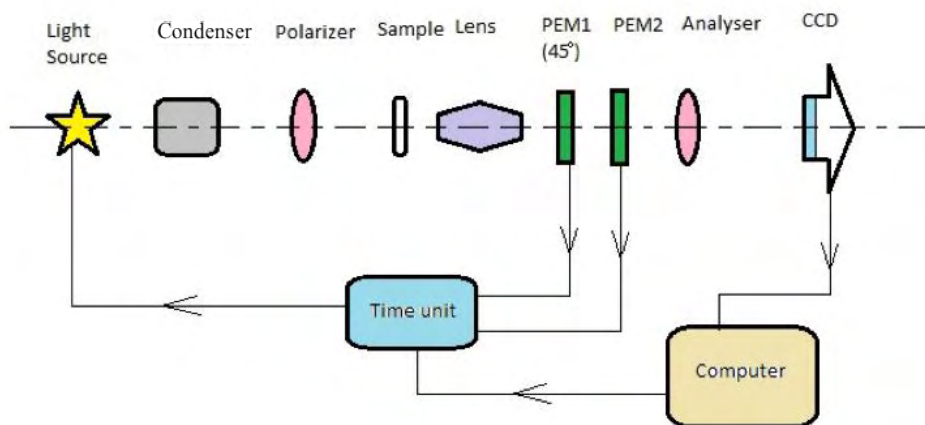


Figure 5.1.1.1 The diagram of the Stokes polarimetry microscope

The computer connects with the timing unit and sends a command to the timing unit to change the working frequency of the time unit. The timing unit controls the intensity of the light source. The images under different working frequencies captured by the Andor Zyla 5.5 camera are sent to the computer. After the calculation and analyses, the images including the information of Stokes parameters are acquired.

The image capture process is controlled by a program developed based on the LabVIEW software. The program sends a command to the time unit firstly, and grabs an image secondly, then saves as a picture document. The involvement of the program controlling is to

make sure the process of the test is more convenient and efficient. In the process of data collection, 12-channel method and 6-channel method are adopted in our experiment which is going to be introduced later.

5.1.2 The 12- channel signal extraction

Equations (5.1.2.1) to (5.1.2.4) are used to obtain the four signals at each pixel for the 12-channel method.

$$S_{dc} = \frac{S_1 + S_2 + S_3 + S_4 + S_5 + S_6 + S_7 + S_8 + S_9 + S_{10} + S_{11} + S_{12}}{6} \quad (5.1.2.1)$$

$$S_{50} = \sqrt{(S_1 - S_2)^2 + (S_3 - S_4)^2} \quad (5.1.2.2)$$

$$S_{84} = \sqrt{(S_5 - S_6)^2 + (S_7 - S_8)^2} \quad (5.1.2.3)$$

$$S_{100} = \sqrt{(S_9 - S_{10})^2 + (S_{11} - S_{12})^2} \quad (5.1.2.4)$$

Where, S_i, \dots, S_{12} are the phase locked accumulated intensity signals at each pixel. The first four signals are phase locked to the fundamental frequency $1F_1$ of PEM1, the second four to the first harmonic frequency $2F_2$ of PEM2, and the last four to the first harmonic frequency $2F_1$ of PEM1. For the PEMs with frequencies of 50kHz, 84kHz, 100kHz, the calibration curve is shown in Fig. 5.1.2.1. From Fig. 5.1.2.1, we can find the curve q is discontinuous when the polarizer is at 45° and 135° . That is because an error in the timing unit mentioned earlier. The details of the signal at frequency 100kHz is shown in Fig. 4.5.4.6. The angle between signal s_9-s_{10} and $s_{11}-s_{12}$ is not 90° . According to Fig. 4.5.4.6, the angle between s_9-s_{10} and $s_{11}-s_{12}$ is 73° . However, the effect is only observable when P_1 close to zero. Since the calibration procedure can automatically adjust the phase factor in the phase sensitive signal recovery, so the 6-channel method is used for most of the experimental work, which is detailed in the next section.

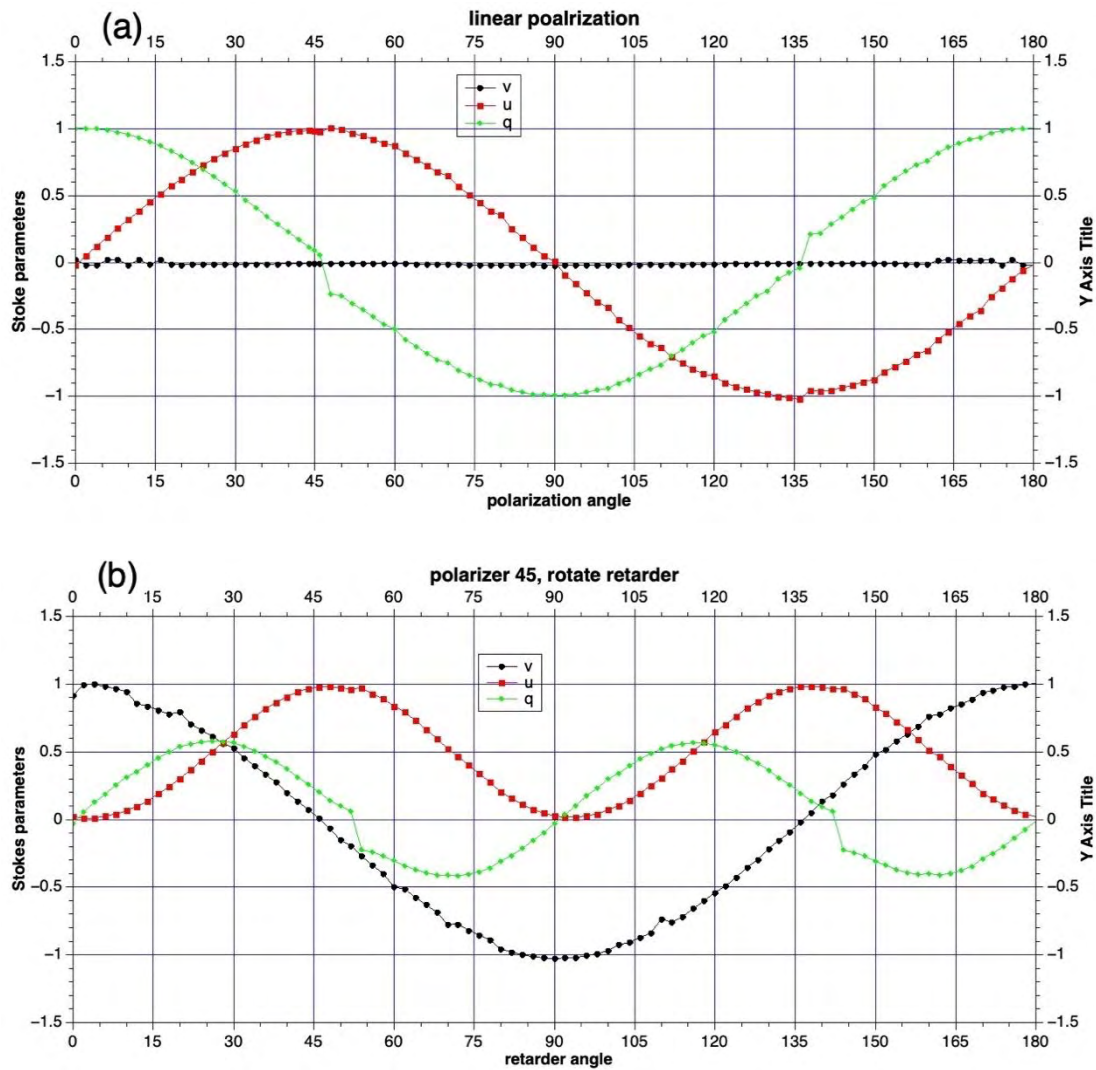


Figure 5.1.2.1 The calibration curve of the linear polarization (a) and the elliptical polarization (b) calculated through twelve channel method.

5.1.3 The six-channel signal recovery method

To avoid the problem discussed in section 5.1.2, the six-channel method is used to obtain the signals of different frequency.

In the six-channel method, the formulae needed to calculate the signal of S_{dc} , S_{50} , S_{84} , and S_{100} are shown as follows,

$$S_{dc} = \frac{S_1 + S_2 + S_5 + S_6 + S_{11} + S_{12}}{3} \quad (5.1.3.1)$$

$$S_{50} = \frac{S_1 - S_2}{0.94888} \quad (5.1.3.2)$$

$$S_{84} = -\frac{S_5 - S_6}{0.8912} \quad (5.1.3.3)$$

$$S_{100} = -\frac{S_{11} - S_{12}}{0.9950} \quad (5.1.3.4)$$

The calibration results are shown in Fig. 5.1.3.1. The discontinuities in Fig. 5.1.2.1 are removed.

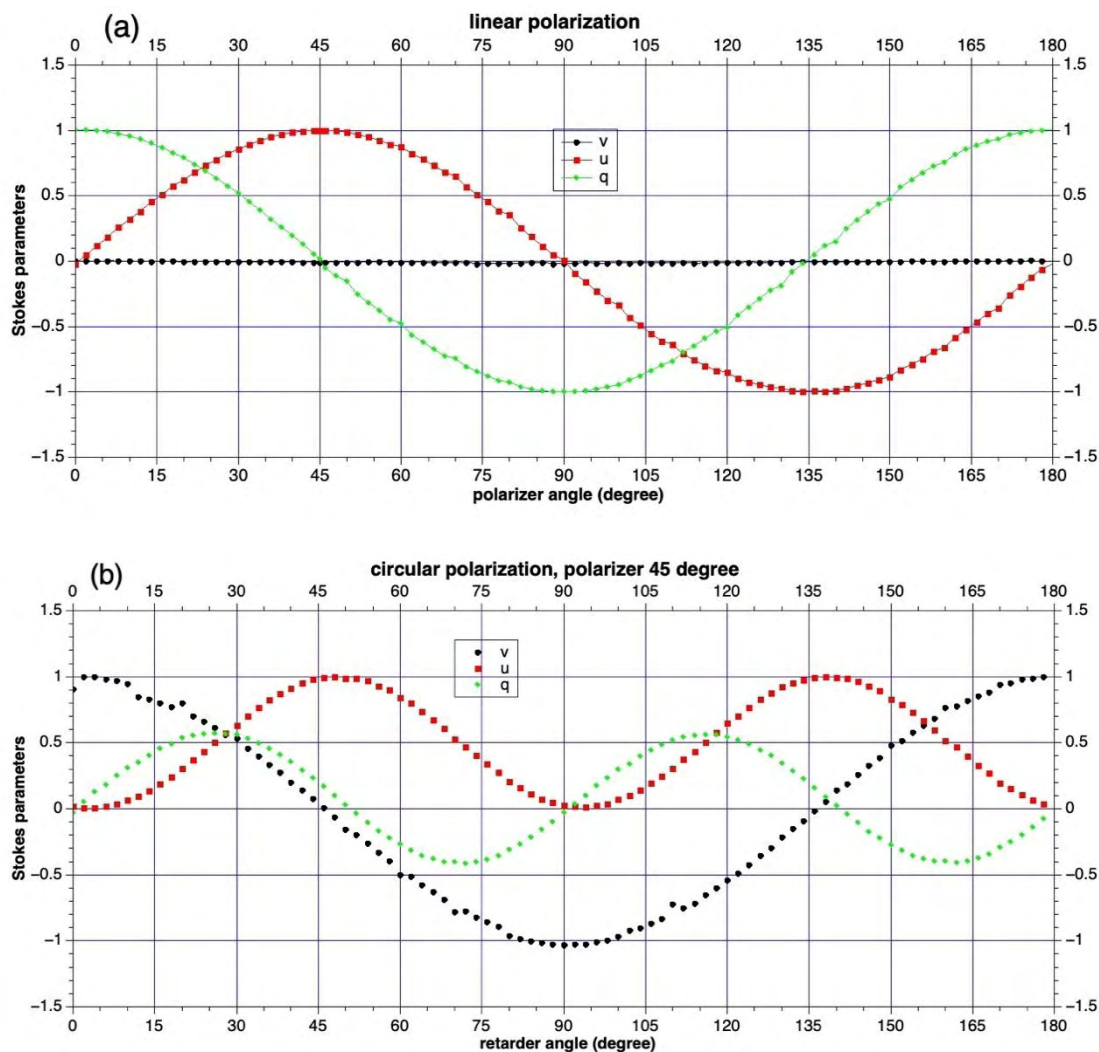


Figure 5.1.3.1 The calibration curve for, a linear polarization (a), and an elliptically polarization (b), calculated through six channel method

5.2 The computerization of the image acquisition

The camera used with the microscope, supports the programming based on the LabVIEW

development platform with underlying Andor SDK3 Software Development Kit. LabVIEW is a graphic programming environment product from National Instruments, which is a convenient tool for developing control software for scientific instrumentation. The related programming method is stated in this section.

5.2.1 The Switch of the channels

To acquire the images at different channels, the situation of the set-up is switched from channel-1 to channel-12. The change of the channels is realized by a timing unit. A command from a computer, is sent to the timing unit to generate a pulse signal with special frequency that controls the light source of the microscope. The data collection of the measurement realized through the process of changing channels, taking the pictures in different channels, and saving the pictures, sequentially. After the timing unit switched from channel-1 to Channel-12, twelve pictures in different situations are obtained for the analysis in future.

The timing unit is connected with a computer through an USB 'COM port', which is a series port operated with a baud rate 19200 bit/s. The control command is based on the Virtual Instrument Software Architecture (VISA) function. The VISA command is an ASCII ("NI-VISA Overview," 2018) string. The VISA command is not affected by the method of the physical connection between the computer and the equipment, such the Serial port, GPIB card, Enter net, or USB.

The program of controlling the timing unit is shown in Fig. 5.2.1.1 and 5.2.1.2. The first method shown in Fig. 5.2.1.1 can be used in a loop and returned a symbol after the successful change of the channel. We use the second method shown in Fig. 5.2.1.2 in later version of the controlling program, which is simple and not return a symbol after the successful change of the channel, but the speed increased.

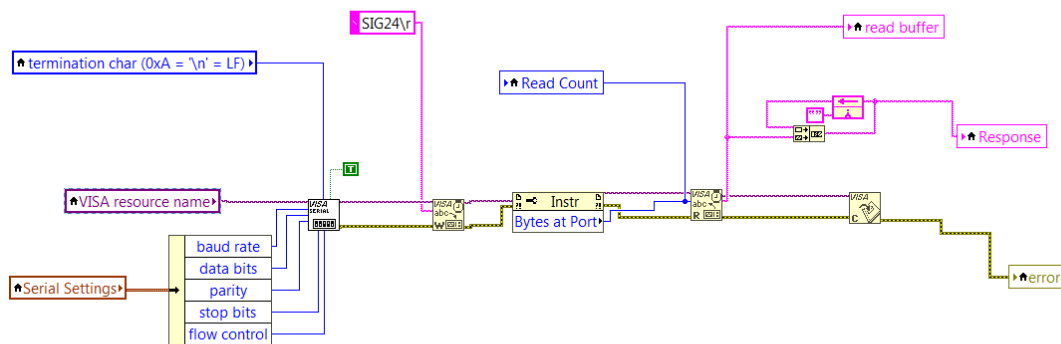


Figure 5.2.1.1 The control code of the time unit in version 1 and version 2

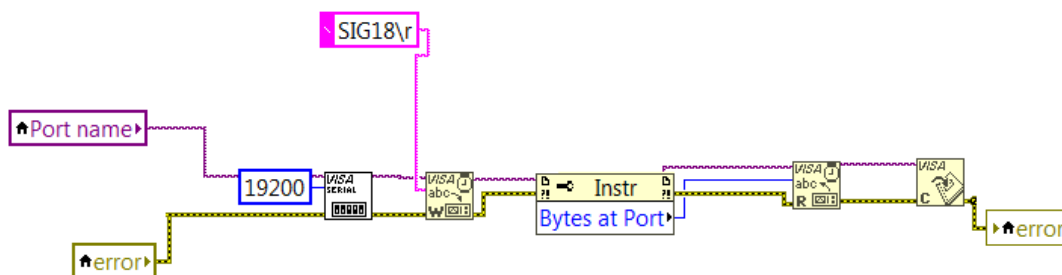


Figure 5.2.1.2 The control code of the time unit in version 3 to version 7

5.2.2 The design logic of the program

For increasing the speed, the images are saved in a buffer during the process of image acquisition. The space of one image with 2160*2560 pixel is 8323072 bytes. A circular buffer

is used for the Andor camera. The size of the buffer distribution equals the product of the number of accumulations and the bytes of the space of one image. After the distribution of the space, the data of the images taken by the camera are sent into the buffer one by one. The data are output into a file document from a buffer, after all the buffer are saved images, which is a two-dimensional matrix. The intensities are accumulated at every pixel through the matrix superposition. Basically, three main structures were used in the program development. The flowchart is shown in Fig. 5.2.2.1.

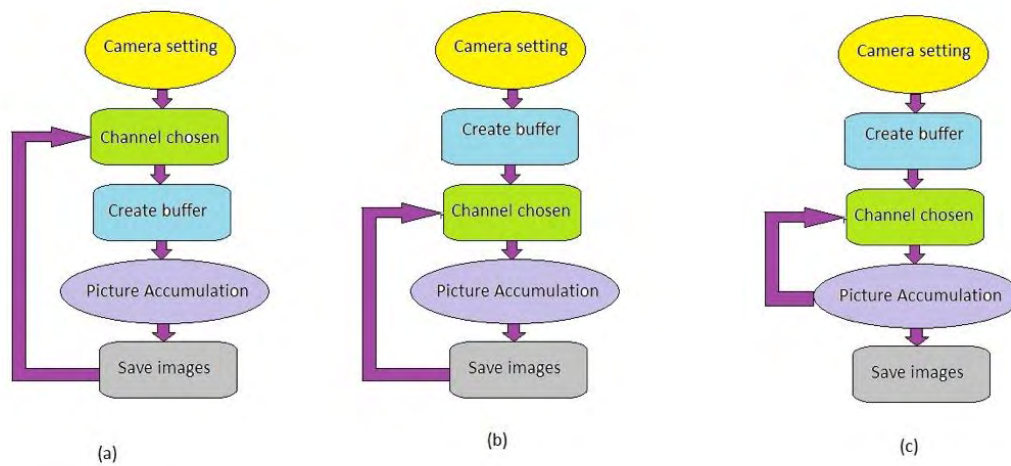


Figure 5.2.2.1 the flow chart of the main structure of the program: the version I (a); the version II (b); the version III (c)

The speed of image acquisition of the three flow charts in Fig. 5.2.2.1, is shown in table 5.2.2.1. The version 1 creates a buffer at every time of changing the channel, it is suitable for the situation that needs for more accumulation. The version 2 and version 3 create one buffer at a time, it is limited by the physical buffer of the computer, but the speed increase because it saves the time of creating the buffers. The version 3 make the data acquisition process and the data saving process be executed separately, hence increasing the actual image acquisition speed.

Table 5.2.2.1 Comparison of the time used in the running of three program versions

Accumulation number	Version 1	Version 2	Version 3
10	48s	38s	31s
100	75s	71s	55s
300	157s	150s	141s
500	230s	219s	206s

To increase the speed, choosing a small interested area in the full-scale image to take photos, increase the speed of the microscope efficiently. The parameter setting comparison in the LabVIEW developing kit and the Andor solis program are shown in Tab. 5.2.2.2. The AOI-Bottom and the AOI-Top indicate a same position on the full-scale image. The parameters shown in Table 5.2.2.2 represented as the same area on the whole image. The data input into a buffer firstly and output later from a buffer later. The sequence of input and output is inversed. Because of the difference of the sequence between the input and output, some data acquired through our LabVIEW program is a reversal image of the image acquired through the Andor solis program, which is the default program of the Andor Zyla camera.

Table 5.2.2.2 the parameters of the camera setting in two program when selecting the same special area of the CCD.

Andor Solis	Parameters	Labview	Parameters
AOI-Height	500	AOI-Height	500
AOI-Bottom	900	AOI-Top	900
AOI-Width	500	AOI-Width	500
AOI-Left	1000	AOI-Left	1000

5.2.3 The comparison of the 7 versions of program

Totally, seven versions of the controlling program are developed, the benefits are shown in Tab. 5.2.3.1.

Table 5.2.3.1 Comparison of seven version developed on LabVIEW environment

Version number	buffer creation times	Accumulation number	channel number	Benefit	new function 1	new function 2
1	12	6000	12	more accumulation		
2	1	500	12	more efficiency		
3	1	500	12	Higher resolution		
4	1	500	12, 6, 2	Overlapping, area selection	channel selection	
5	1	500	12, 6, 2	Overlapping area selection	channel selection	setting checking
6	1	500	12, 6, 2	Overlapping, area selection	channel selection	ten set of data collection
7	1	500	12, 6, 2	Overlapping, area selection	special channel selection	ten set of data collection

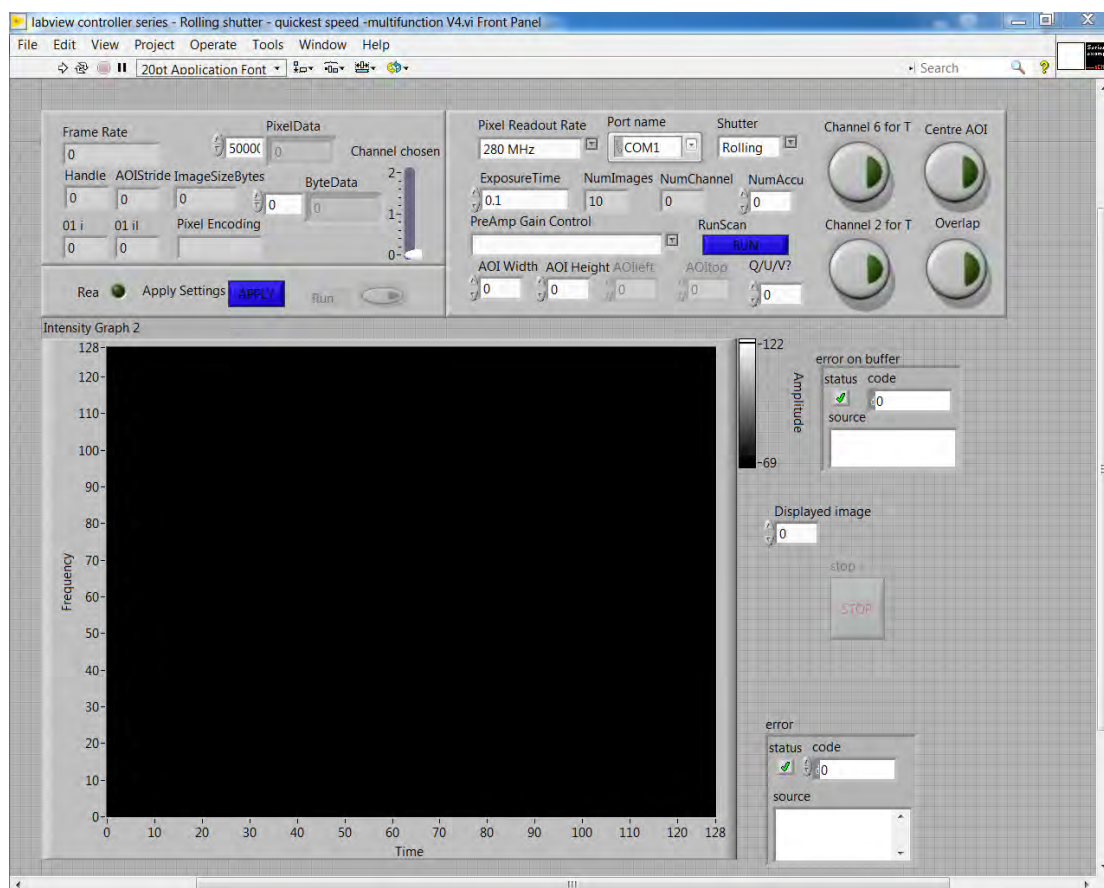


Figure 5.2.3.1 The front panel of the version 4 of the microscope controlling program
Version 1 suitable for the situation of big accumulation numbers. Version 2 is quicker than

version 1 for saving the time of create buffer, but it only can do around 6000 pictures in total for 12 channels. Version 3 set the image acquisition process and image output process separately. It increases the speed of the image acquisition. Based on the version3, version 4 increase a function of channel chosen and area chosen. The turning on mode of Center AOI, shown in Fig. 5.2.3.1, can increase the speed of the image acquisition. The turning on mode of overlap, shown in Fig. 5.2.3.1 can increase the speed of the image acquisition, too.

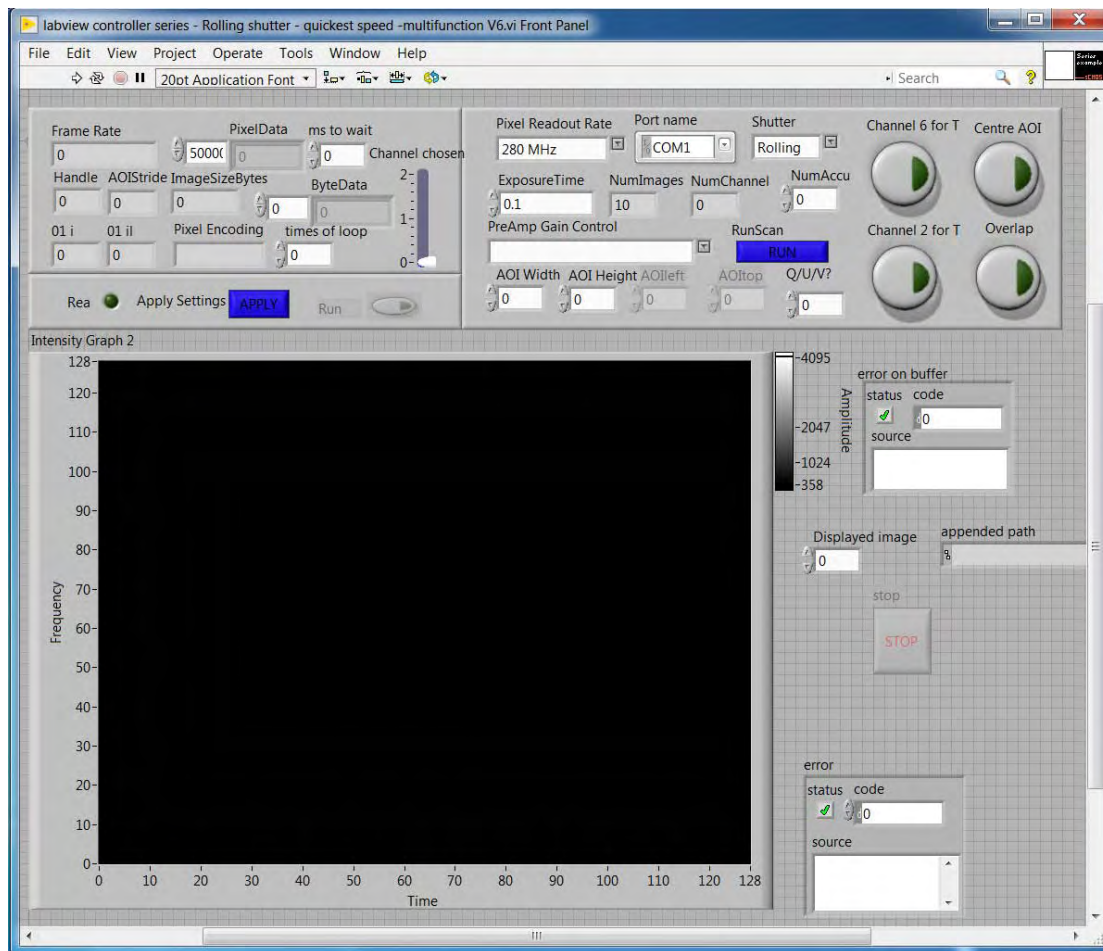


Figure 5.2.3.2 The front panel of the version 6 of the microscope controlling program
Version 6 is used for acquiring ten sets of images at the setting time intervals, the front panel is shown in Fig.5.2.3.2.

Figure 5.2.3.3 is the front panel of the version 7 for the microscope controller. Based on the front panel on the version 6, Version 7 have another function of the channel chosen in a

special channel. For example: In 2 channel mode, the program usually outputs the signals from channel 1 and channel 2 when the number of V channel is 0; the user can also choose from the signals channel 3 and channel 4 when the number of V channel is 1. The choice of the U channel and Q channel is in the same principle.

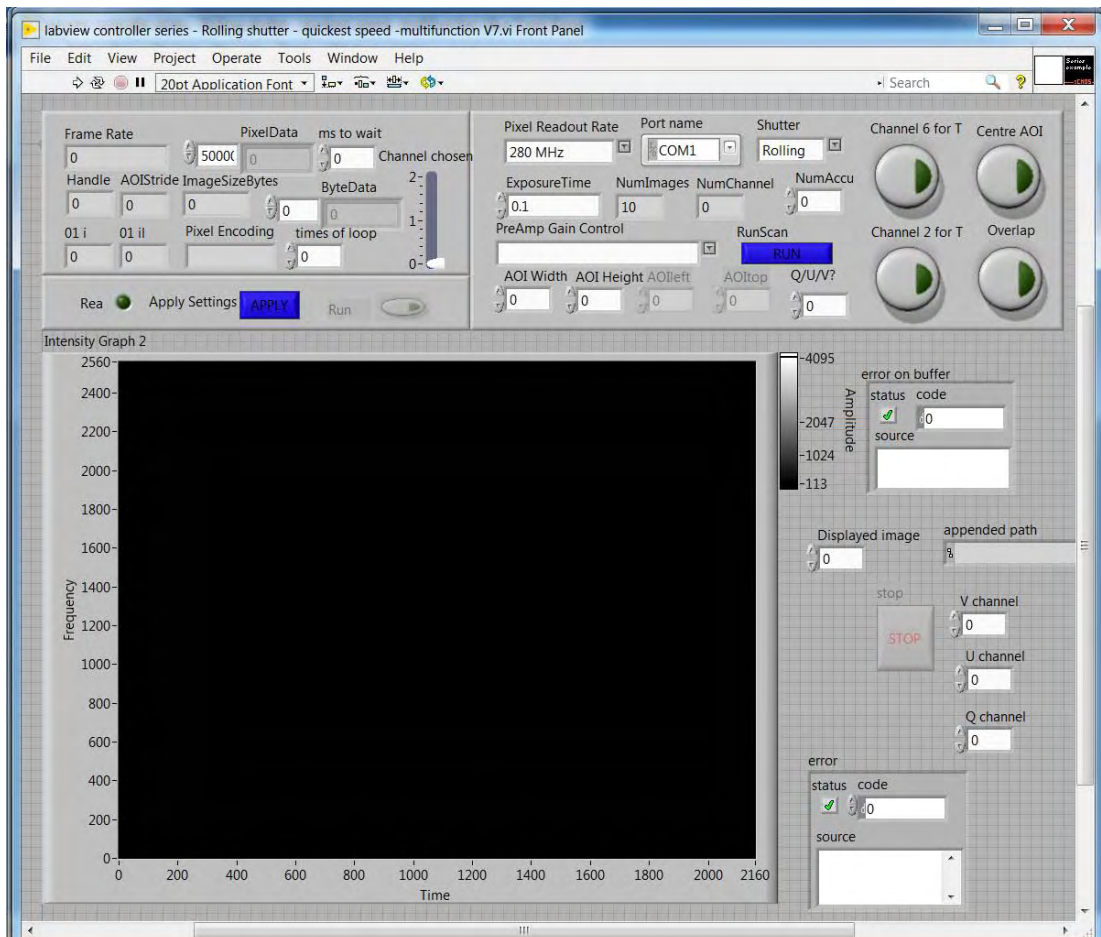


Figure 5.2.3.3 the front panel of the version 7 of the microscope controlling program

Figure 5.2.3.4 is the situation of the program after taking one set of images for a full scale.

The quickest speed is 100 frames per second for a 2160*2560 pixels images. The highest speed is only available when the image area is very small and siting in the centre of the image. That is because the CCD acquires the signal pixel by pixel. Fewer pixels means a saving of time. The quickest speed is 1639.87 frames per second for 128*128 pixels image.

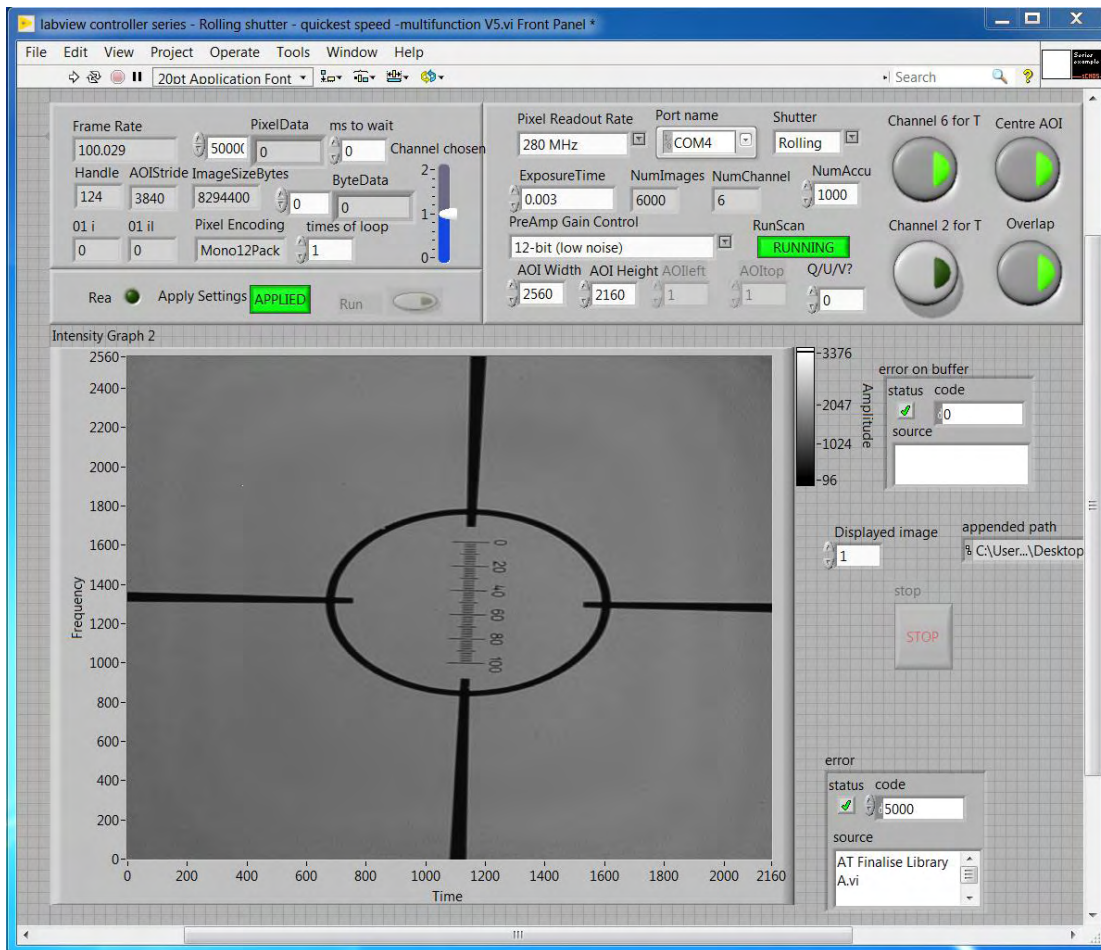


Figure 5.2.3.4 The situation of the front panel after the running process

5.3 The optimisation of the microscope operation

5.3.1 Reflection on the surface of polarimeter

A ‘rainbow’ is a large variation of background in the form of part of a circular band. It looks like a ‘rainbow’ only when a false colour representation is used. The rainbow problem always existed on the image, especially in the image of the ellipticity angle and azimuth angle. We found it is from the multireflection of the photo elastic modulator and the analyser. It has been removed by tilting the photo elastic modulators and the analyser slightly, to make sure the image of the reflection and the image itself not overlapped.

5.3.2 Rainbow on the image of depolarization

A rainbow background variation in depolarization image was found to be still present after

tilt the PEMs and the analyzer, however such feature can be completely suppressed when the polarizer is orthogonal to the analyzer, suggesting it is likely to be a stray light issue, which is minimum in the cross-polarizer geometry. Depolarization include the information of three Stokes parameters, such as Q, U, and V. It is more complex than the elliptical angle and the azimuth angle because it include the information of the Q, U, and V. Mei et al. indicate that, the distribution of polarimetric properties of a Gaussian Schell-model beam, over transverse beam cross-section, is non uniform on propagation even though it is typically uniform in the source plane (Z. Mei, Korotkova, & Shechepakina, 2013). According to Mei's theory , the state of polarization in the center of the beam and the fringe of the beam is different. Only the polarization state at the centre of the beam is kept the same on the process of propagation of the light beam(Z. Mei et al., 2013). On the microscope, the light source is a surface light source. To keep the background of the depolarization image in uniform must set the area of the light source cover the area of the image, firstly. The second prerequisite is keeping the light beam to be parallel beam. The third prerequisite is the sample stage must be perpendicular to the light beam. The experiment is conducted on this situation.

5.3.3 Situation without a condenser

I did a set of experiments on the microscope without a condenser to find the reason for the nonuniform background.

1. Light source

The Stokes microscope is built on a framework of a normal microscope. The light beam is reflected by a mirror to change the direction of propagation of the beam for 90° before it projects on the sample stage. The maintenance of a parallel light beam is very important in this process, because the diameter of the light beam keeps the same situation after the propagation direction is changed. To acquire a parallel light beam, a mark of one, two, three, and four is written on the double side of the screw on the LED source, which can mark the

distance of the two LED lenses accurately. For example, the smallest distance between the two lenses record as $1f_1$; after the lens rotated one circle, the distance between the two lenses record as $2f_1$. The divergence of the light beam is adjusted through changing the distance between two lenses on the LED light source. The background of the depolarization is measured in different distance between the lenses as shown in Fig. 5.3.3.1. we can find a valley between 2000 and 2500 pixels on the profile of the background, that is the position with a nonuniform position of the background. The difference between the maximum value of normalized depolarization and the minimum value of normalization for position $18f_1$ keeps around 0.9, and that for position $1f_1$ keeps around 0.6. The position of the valley shifted outward when the distance between the two lenses increase. The distance marked $4f_3$ is a position output a parallel light beam. In the position marked $18f_1$, the trend of the curve is decreased from left to right, no valley existed on the image.

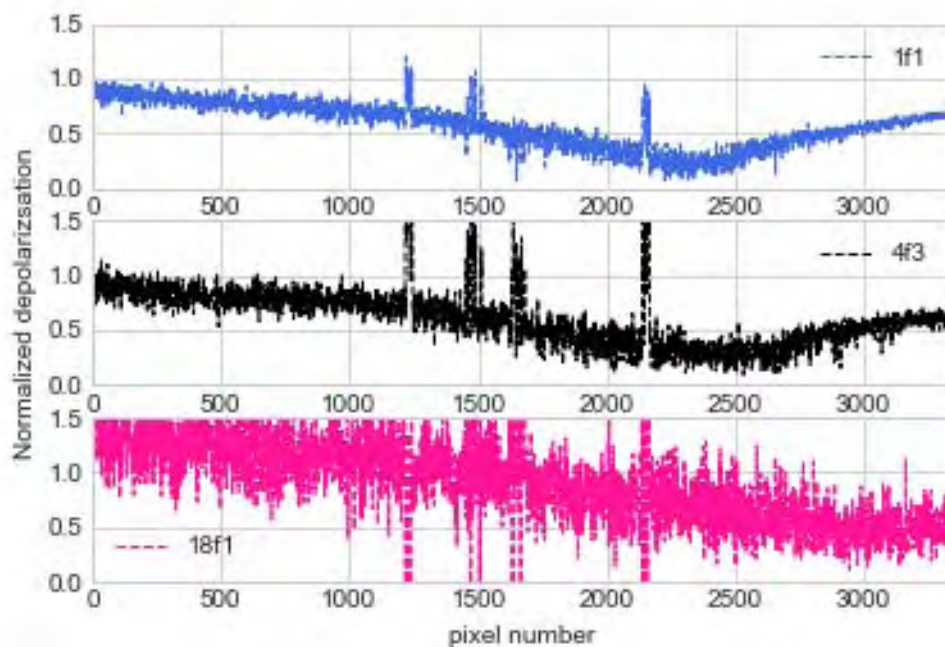


Figure 5.3.3.1 The profile of the normalized depolarization without a condenser using the different focus distance light source: (a) $1f_1$ position with a divergent light beam; (b) $4f_3$ position with a parallel light beam; (c) $18f_1$ position with a convergent beam

The valley is from a reflection of the light when the light beam is a divergent beam, which is reflected and overlapped on the original light source. The distribution of the original light and the reflected light is different because it divergent and travels different distance. The divergent light beam change into a convergent light beam because of the increase of the distance between the two lenses.

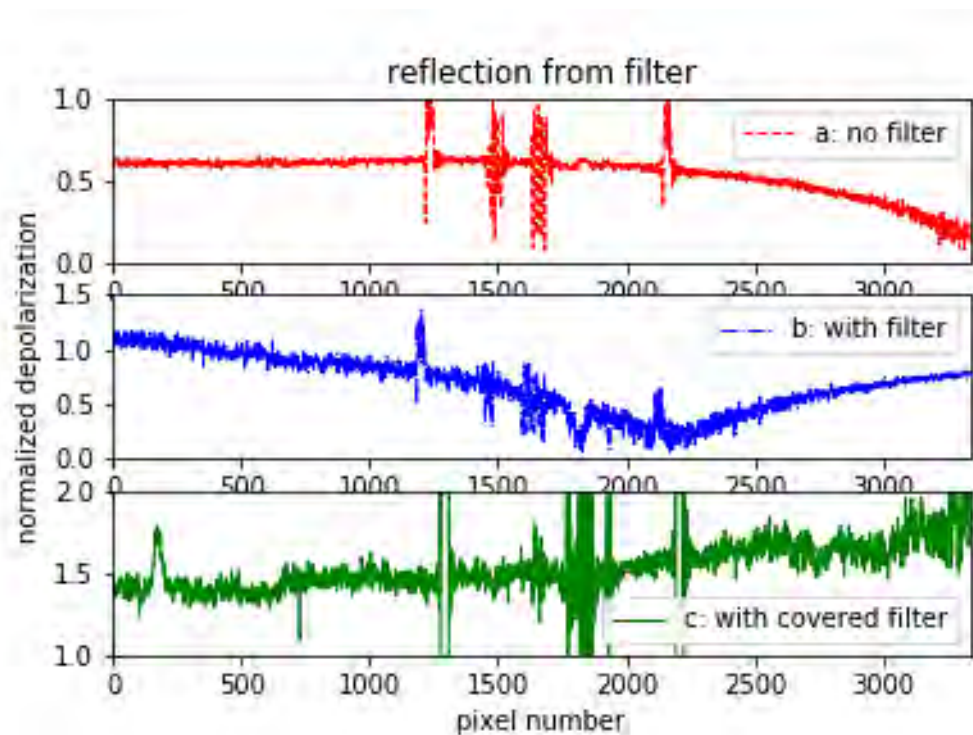


Figure 5.3.3.2 The depolarization profile image of the whole image in special position

Figure 5.3.3.2 compares the situation with and without a filter, and with a covered filter. The valley is from a mirror reflection on a band filter facing the light source overlapped on the light source, shown in Fig. 5.3.3.3. The valley existed in curve b in Fig. 5.3.3.2 is from the reflection on the surface of the filter, which is looks like a mirror. Because the reflected light overlapped on the original light, the light source comprised two parts: the original light and the reflected light, which state of polarization distribution is different in radius(Z. R. Mei, 2010). According to Mei's theory, the distribution of the polarization of a Gaussian Schell-model beam varies with the distance of propagation and with the radius of the light beam.

The overlapping produces a nonuniform of the polarization from the light source. The propagation distance from the light source directly and the secondary reflection light to the sample surface is different. To keep the radius of the beam of the light the same, I adjust the distance between the LED chip and the lens before LED ($4f_3$ position), to make sure the light in use to be a parallel light. The diffuse reflection shown in Fig. 5.3.3.2c, the valley disappeared, but the difference of the normalized depolarization image from one side to another side is still existed which is 0.6.

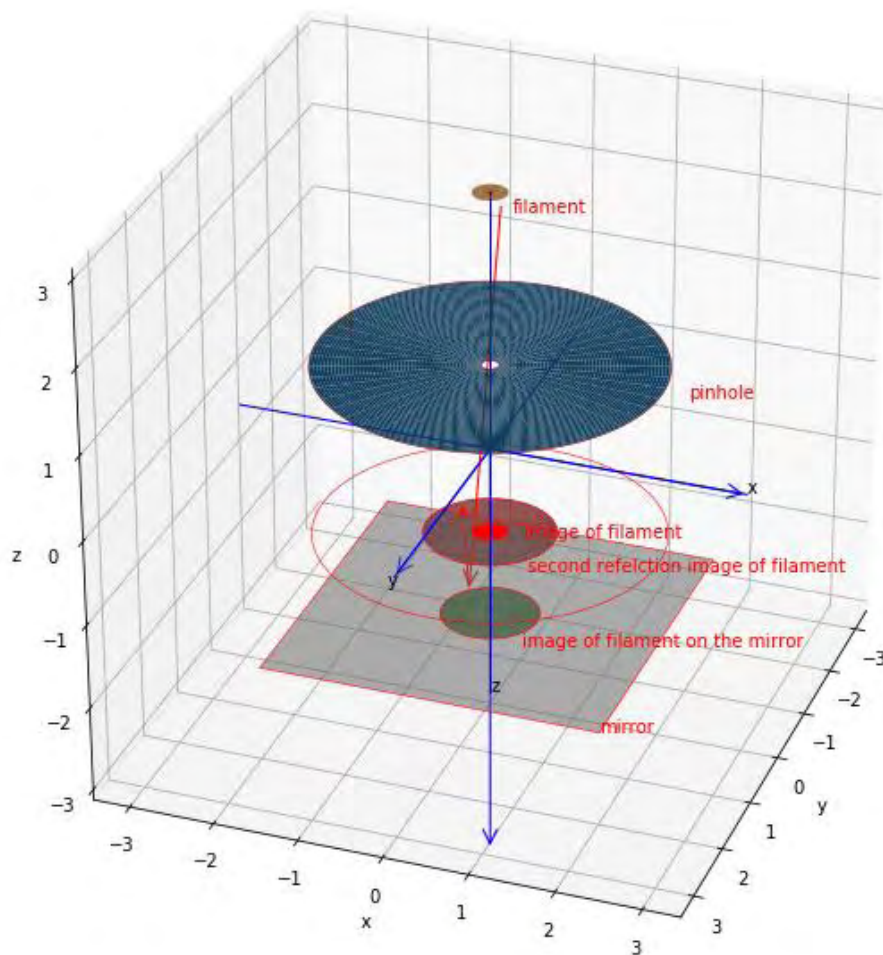


Figure 5.3.3.3 The diagram of second reflection of the light source.

Figure 5.3.3.3 is a drawing to explain the double composition of the light source. An image of

the filament is acquired after its passing through a pinhole, is doubled if a mirror is sited under the image position. Apparently, the surface of the sample reflects the light, although it is only part of light for a transparent light. The tilt of the mirror can make the image of the filament and the second reflection image of filament be not coaxial.

Using the covered filter, the situation with a condenser and without a condenser is shown in Fig. 5.3.3.4. The condenser converges the light and makes the situation more complex because the diameter of the light beam is adjusted by the condenser and more reflection produced on the surface of the lens on condenser.

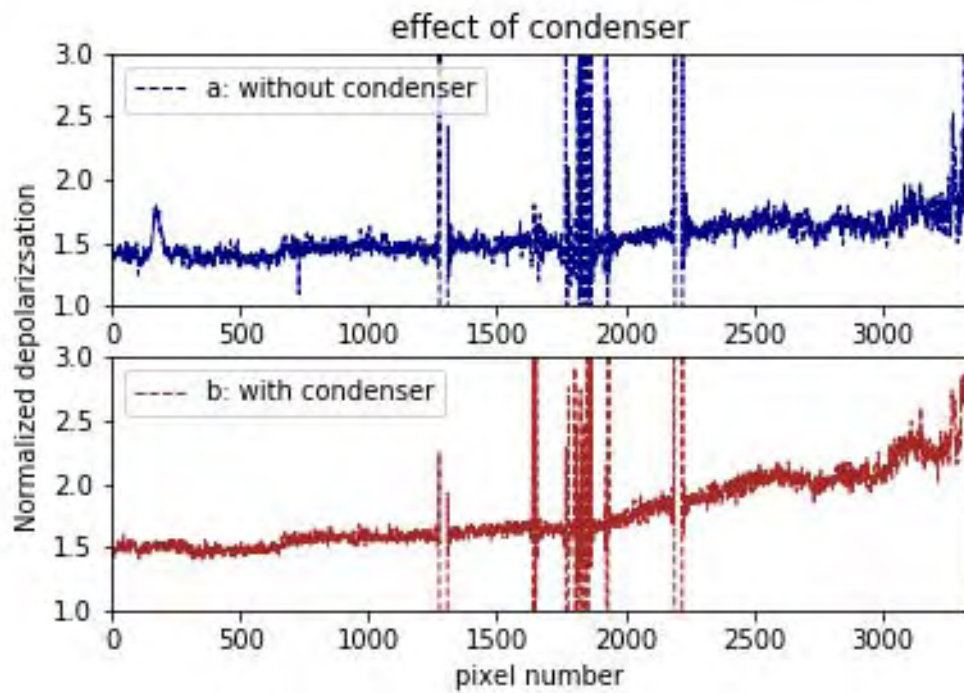


Figure 5.3.3.4 The slope of depolarization with a covered filter in two situations: (a) without a condenser in the light path; (b) with a collimator in the light path.

To remove the slope on Fig. 5.3.3.4 curve b, a polarizer rotation experiment is done and introduced in next section.

5.3.4 Situation with a condenser

A condenser is a most important device on the microscope to increase the intensity of the

light which goes into the objective lens. It used on the microscope to increase the resolution of the image. It can focus a light from the light source into a lens. In the process of the focusing a light, the light is converging. The light from the edge of the condenser to the focusing point may reach Brewster angle. The polarization status may be changed during the reflection process. That reflected light goes back to the source and reflected back again as a part of the light source. This reflected light produces the rainbow pattern background of the depolarization image. Fortunately, the reflection at an angle bigger than Brewster angle is polarized. This means that it can be eliminated by placing the polarizer at a special polarization angle.

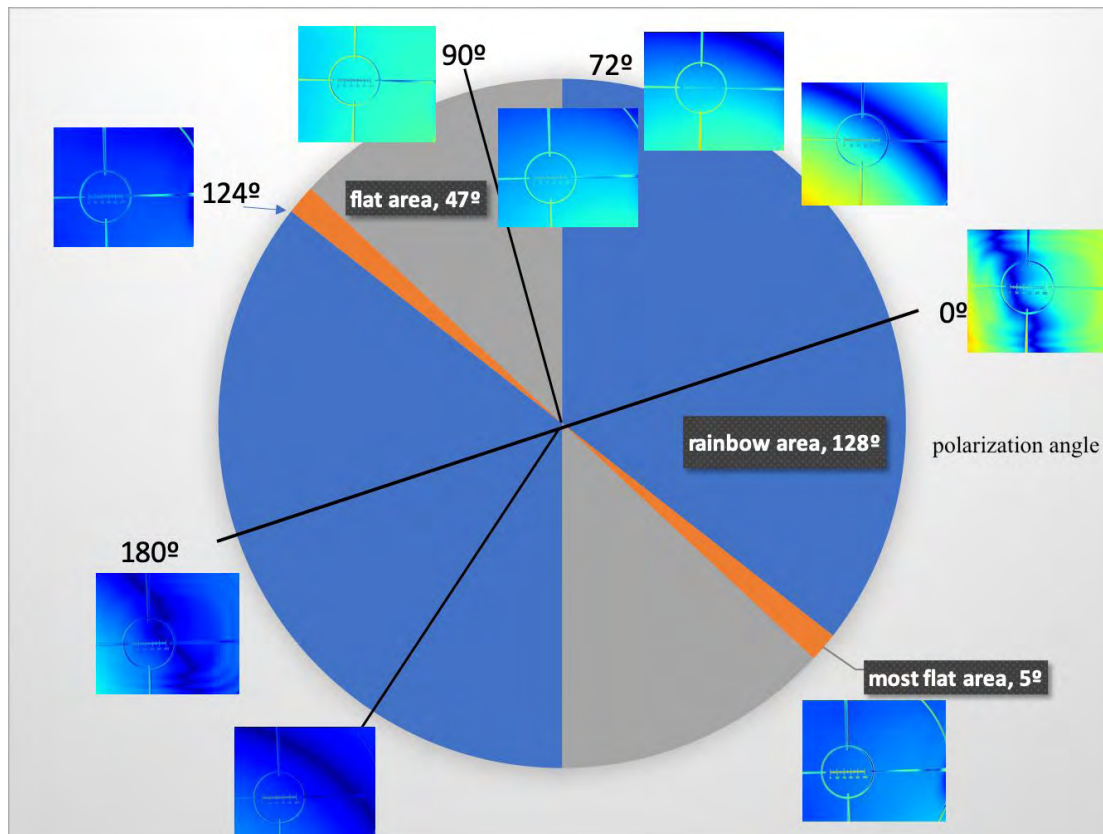


Figure 5.3.4.1 the relationship between the polarization angle and the rainbow background on the image of normalized depolarization

Figure 5.3.4.1 shows the non-uniform background (rainbow) on the depolarization image is disappeared at special polarization angle (119°-124°). That position is exactly the position

that the optical axis of polarizer crosses the optical axis of analyzer. Based on this, we can acquire a flat image, without a rainbow, of the normalized depolarization from 72° to 124° . The flattest image for normalized depolarization and the azimuth angle should be measured at $120^\circ \pm 2^\circ$ (azimuth angle reference to the laboratory coordinate).

To acquire a better resolution of the image, the polarization angle used in my experiment is 119° , where a best depolarization image and an azimuth angle image is obtained, shown in Fig. 5.3.4.2.

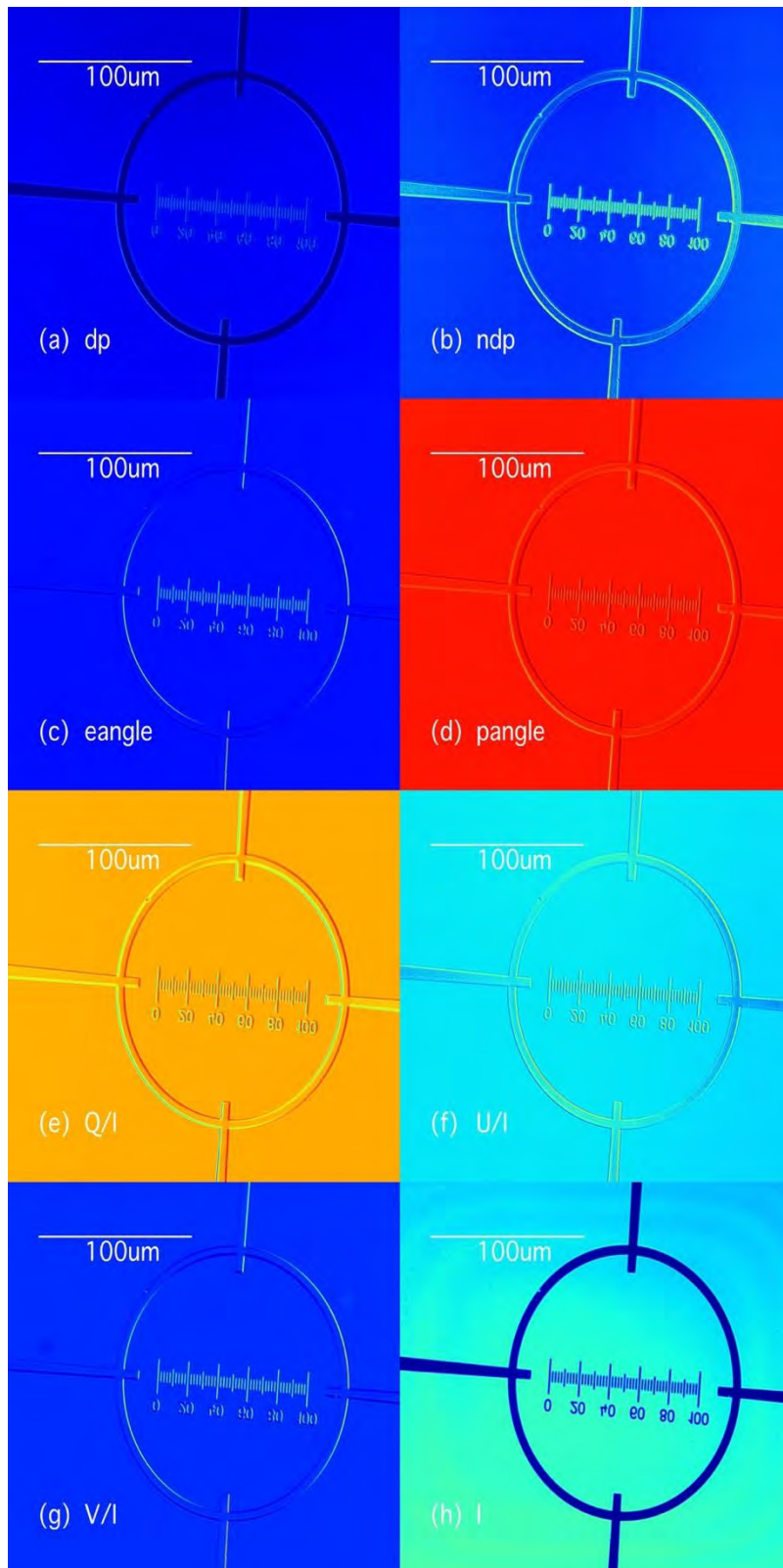
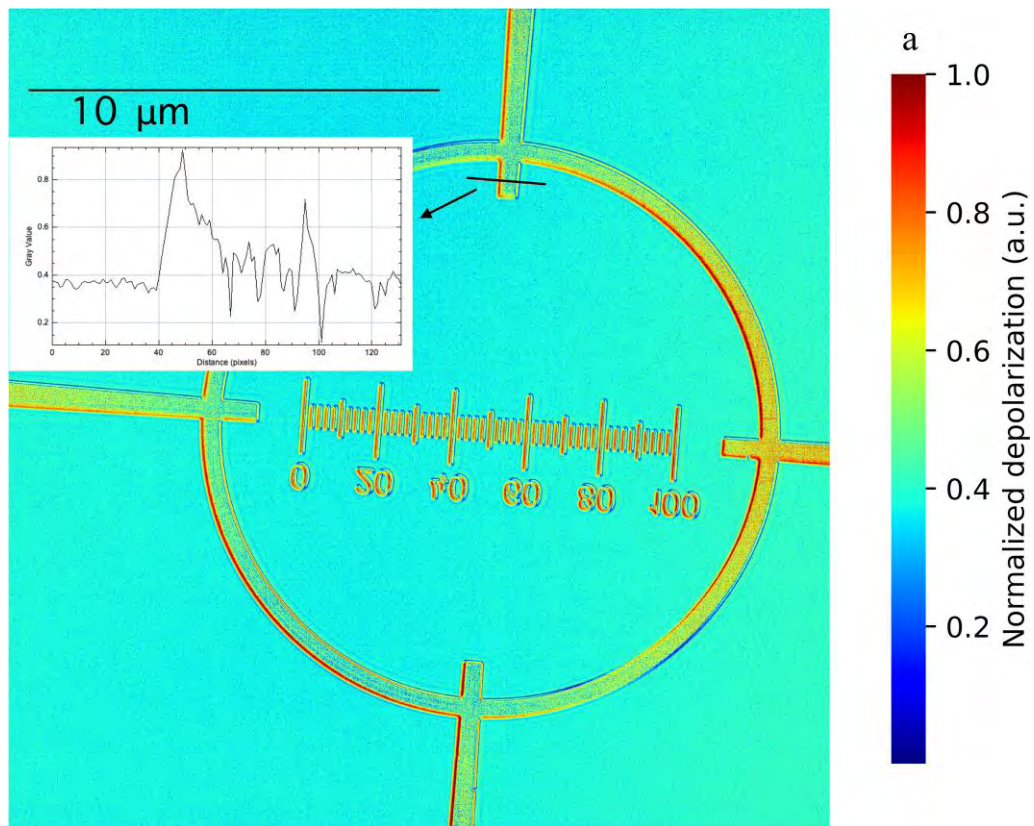


Figure 5.3.4.2 The best picture quality acquired at last experiment (with an antireflection polarizer): (a) image of depolarization; (b) image of normalized depolarization; (c) image of elliptical angle; (d) image of azimuth angle; (e) image of normalized Stokes parameter Q; (f) image of normalized Stokes parameter U; (g) image of normalized Stokes parameter V; (h) image of the intensity

5.3.5 Comparison between uncoated polarizer and the antireflection polarizer

The antireflection polarizer can increase the resolution of the image, shown in. Fig. 5.3.5.1.

The inset is the profile of the image along the line in black. Figure 5.3.5.1a shows the situation with a normal polarizer. Figure 5.3.5.1b shows the situation with an antireflection polarizer. The resolution increased after using the antireflection polarizer. However, the edge in the image seems more significant in the image using the antireflection polarizer.



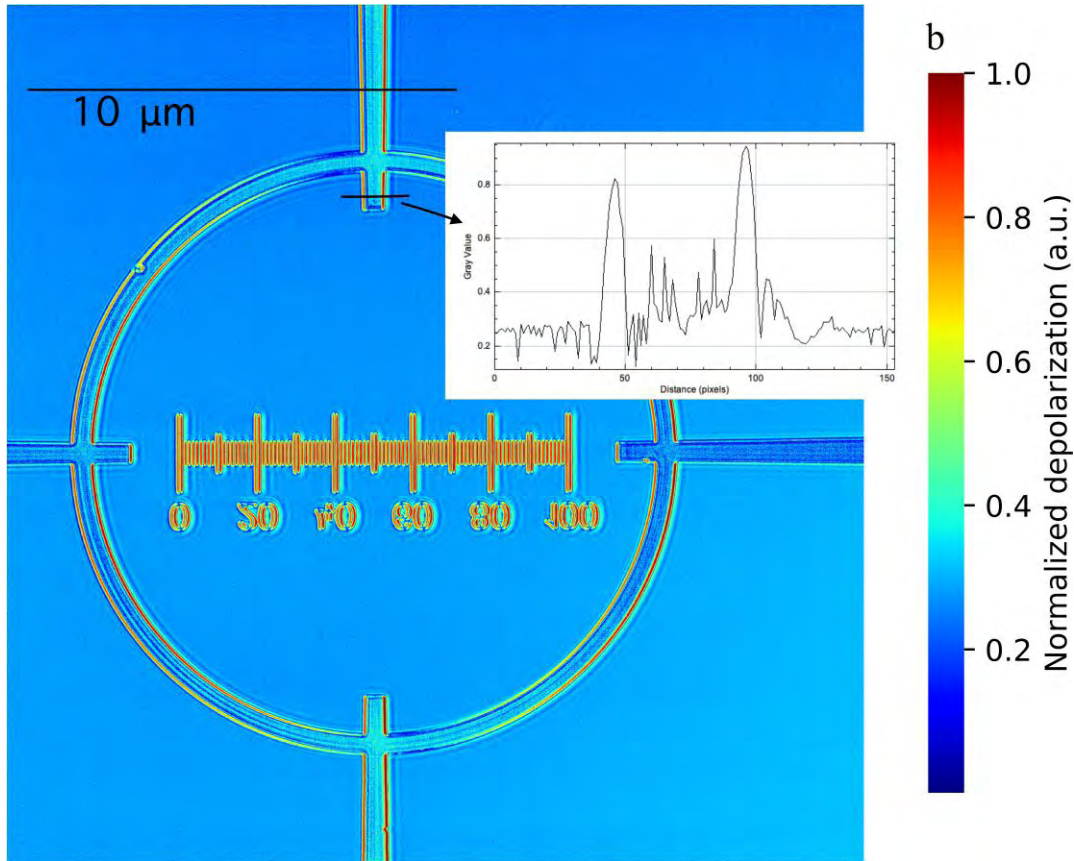


Figure 5.3.5.1 the image of normalized depolarization of the scale plate using: normal polarizer (a); antireflection polarizer (b)

This proved that the reflection on the surface of the polarizer is one reason for the deterioration in resolution of the microscope.

5.3.6 Comparison of the laser light source and the LED light source

The using of the LED light source improves the quality of the image significantly. Figure 5.3.6.1 is the image of normalized depolarization of the eclogite sample, a mineral, took under the laser light source (Fig. 5.3.6.1a) and the LED light source (Fig. 5.3.6.1b). The resolution of the image increases significantly after using the LED light source.

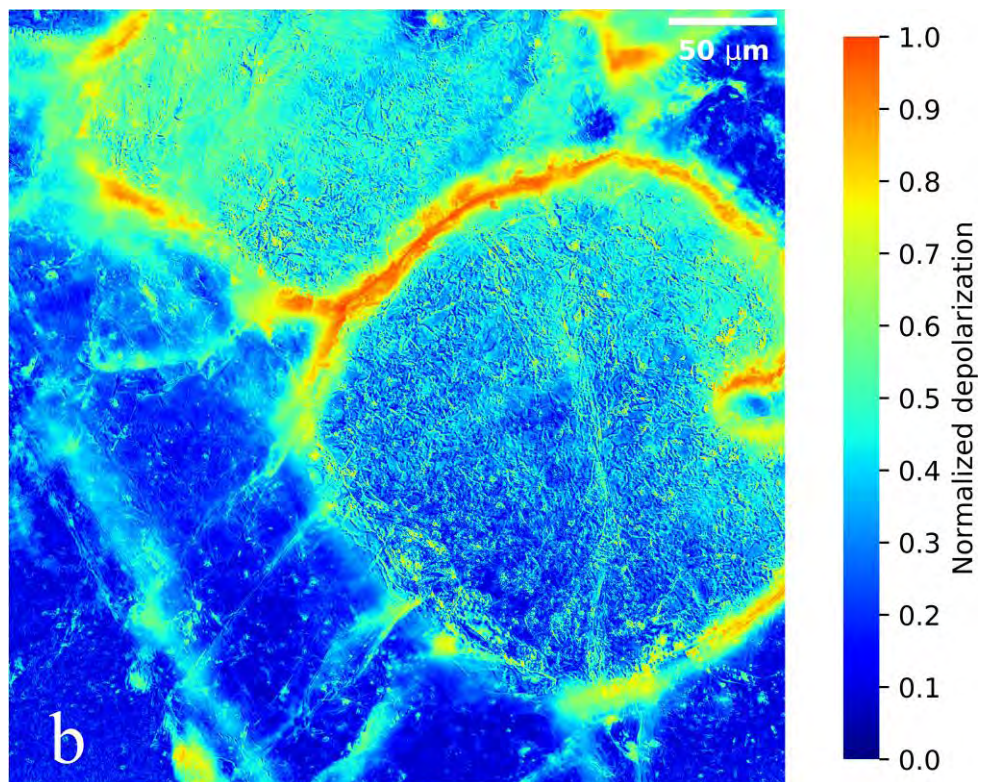
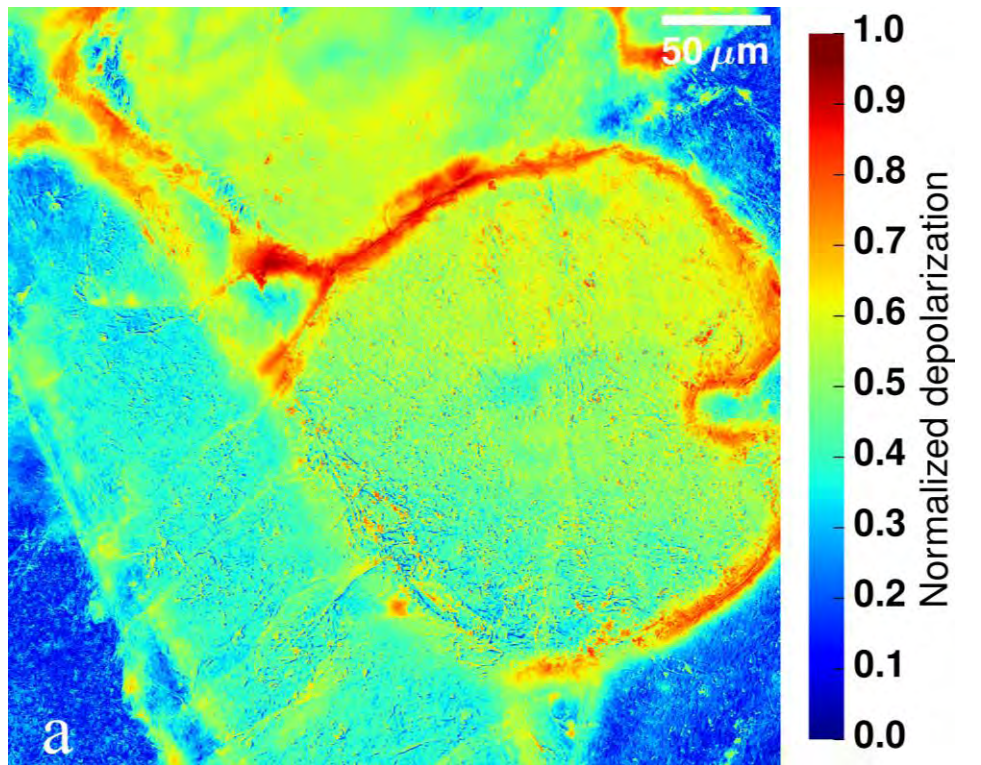
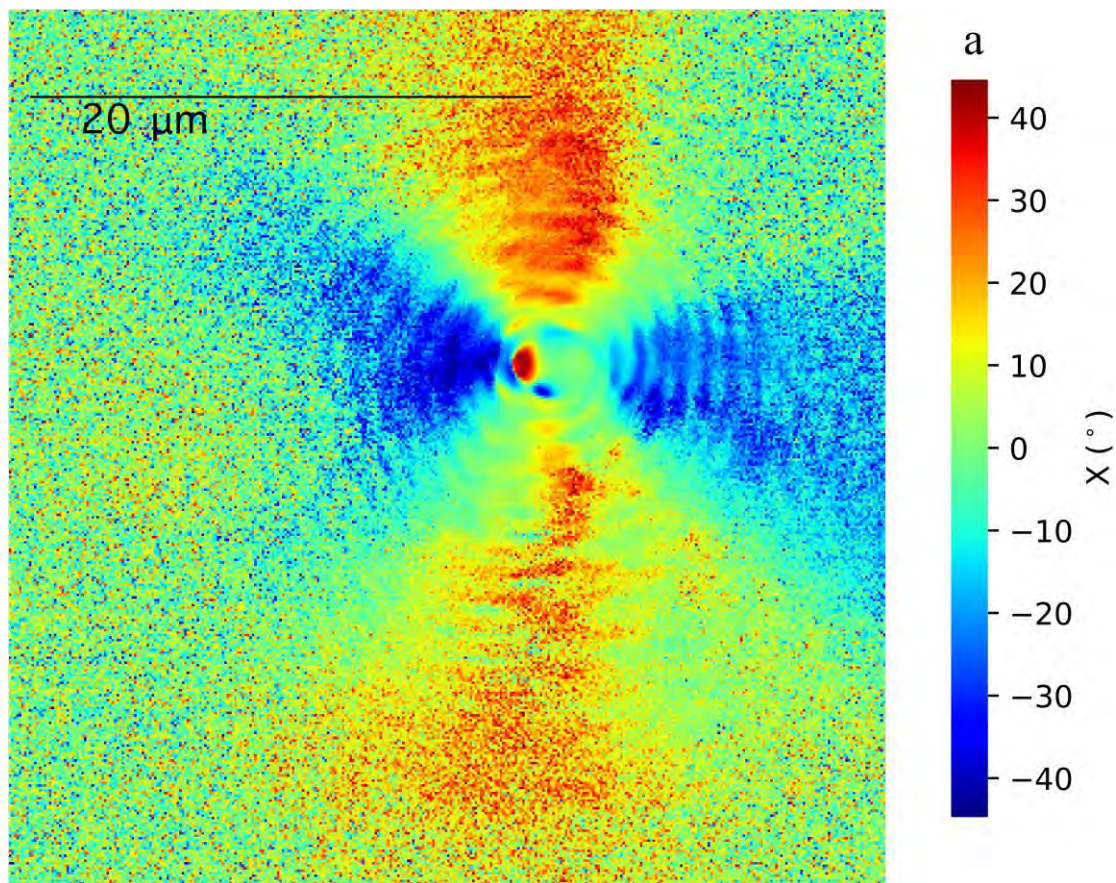


Figure 5.3.6.1 The pattern of the normalized depolarization of eclogite sample: measured using the laser light source (a); and measured using the LED light source (b)

5.3.7 Boundary behaviour of the image of the elliptical angle

The common factor of a pinhole and the liquid crystal is the round shape of the age. The angle distribution of the elliptical angle is positive and negative alternately around the circle age. The line of demarcation between the positive value and the negative value is exactly along the optical axis of the polarizer or perpendicular to the optical axis of the polarizer. The structure of the elliptical polarization pattern is the fourfold symmetry structure, shown in Fig. 5.3.7.1. The image on the pinhole, Fig. 5.3.7.1a, is in bad quality because of only scattering process in this process. The image of the liquid crystal droplet, Fig. 5.3.7.1b, is in good quality because both the refractive process and the scattering process happens in this process.



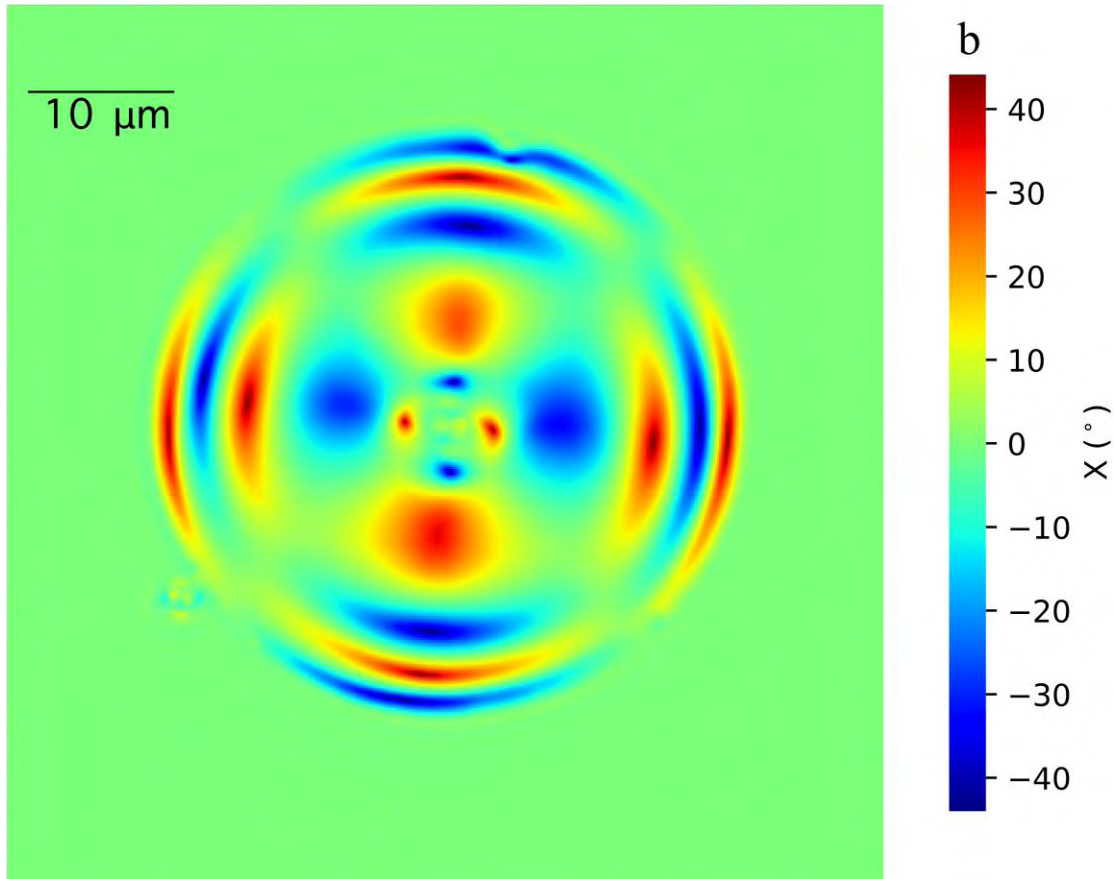


Figure 5.3.7.1 the image of the elliptical angle on the circle age structures: pinhole (a); liquid crystal droplet (b)

5.4 Summary

In this chapter, the in-house Stokes polarimetric microscope is introduced. The twelve-channel and the six-channel signal recover are introduced. The programing of the data acquisition is introduced. For obtain a uniform background image, several solutions are adopted, such as using parallel light, setting the special polarization angle. To increase the resolution, the antireflection polarizer and the LED light source is used. The image quality in the pure scattering process is as good as that in the refractive process.

References

Born, M., & Wolf, E. (1959). *Principles of Optics* (7 ed.): Cambridge University Press.

Glazer, I. G. W. a. A. M. (1980). Ferroelastic Phase Transition in BiVO₄. I. Birefringence Measurement using the Rotating-Analyser Method. *Journal of Applied Crystals*, 13, 217-233.

Guan, W., Cook, P. J., Jones, G. A., & Shen, T. H. (2010). Experimental determination of the Stokes parameters using a dual photoelastic modulator system. *Applied Optics*, 49, 2644.

Guan, W., Jones, G. A., Liu, Y., & Shen, T. H. (2008). The measurement of the Stokes parameters: A generalized methodology using a dual photoelastic modulator system. *Journal of Applied Physics*, 103(4), 043104.

Modulation. (2018). Wikipedia. Retrived from https://en.wikipedia.org/wiki/Modulation#Analog_modulation_methods

NI-VISA Overview. (2018). National Instrument. Retrived from <http://www.ni.com/tutorial/3702/en/>

Shen, T., & Cook, P. J. (2014). United States Patent No. <https://patents.google.com/patent/US20180058934A1/en>: U. o. S. E. Ltd.

Zernike, F. (1955). How I Discovered Phase Contrast. *Science*, 121 (3141), 345-349.
doi:DOI: 10.1126/science.121.3141.345

Chapter 6 Research of Anisotropy in SiC

6.1 experimental results on optical bench

6.1.1 Experiment 1—Rotation of polarizer without adjustment the Stokes polarimeter

The sample used in the experiment is the commercial sample from Cree company, c-plane 4H-SiC with an epilayer of GaN/AlGaN. The crystal structure is hexagonal. I measured Stokes parameters of the laser light after passing through a sample on the bench shown in Fig 4.3.1.1. The polarizer rotates on its own axis during the process of measurement. The sample with Sn ion irradiation is measured, and the result is shown in Fig. 6.1.1.1.

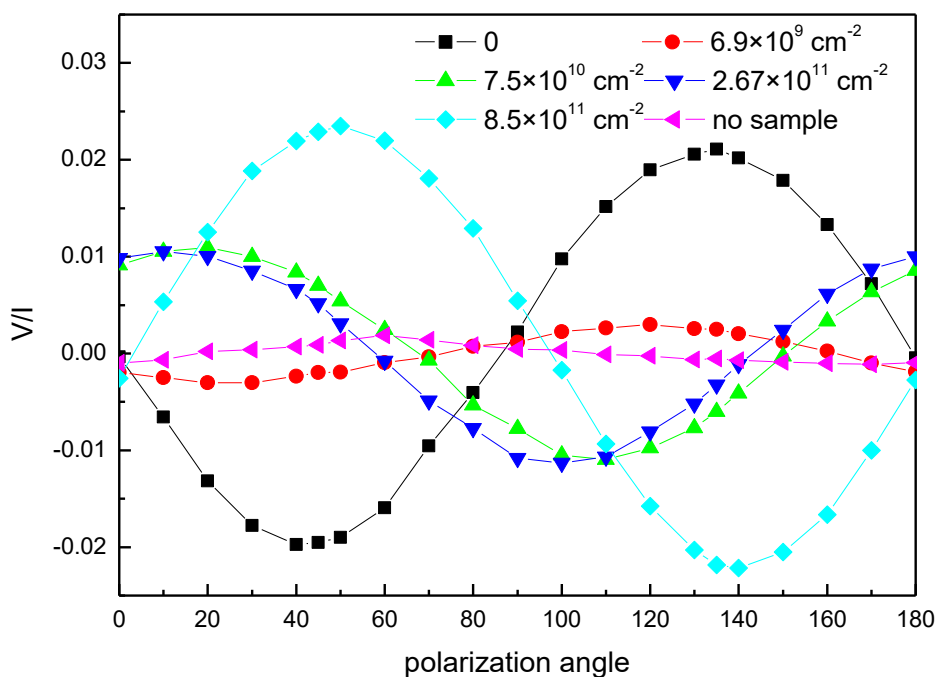


Figure 6.1.1.1 the normalized stokes parameter V/I changed with the polarization angle for different Sn ion irradiation dose.

Figure 6.1.1.1 refers to the Stokes parameter V/I tested with different linear polarization light.

Slight birefringence is detected through the increase of V . The signal V/I is not zero and the

results follow the rotation of polarizer. If the plane of the polarizer is not perpendicular to the light path, the laser may project on the different area of the sample. The sample may not uniform, shown in how the extent of birefringence of the sample (V/I) changes with different polarization angle. To detect the non-uniformity of the sample, the Stokes polarimetric microscope is used, and the result is listed in next section. In the first few steps of rotation of the sample, the results follow the rotation of an effective uniaxial optical axis.

6.2 The imaging of the micropipe defects using the OPTIMUM microscope

Through the experiment on the optical bench in section 6.1, we know some slight birefringence existed in the AlGaN/GaN//4H-SiC film. To measure the distribution of birefringence carefully, Stokes polarimetric microscope is used to measure the polarization. In this experiment, we find a set of defects that exist in the SiC substrates. There is micropipe, a kind of tube shape defect found in semiconductors. In my experiment, five defects are observed, one twisted double micropipe and the others are the single micropipe. All the micropipes can't be seen in one focus position.

6.2.1 Experiment 2 – observation the micropipes using the Stoked polarimetric microscope

Both laser and LED light sources are used to measure the micropipe in the SiC. We only discuss the experiment using LED source, which is in good resolution. Table 6.2.1.1 shows the experimental situation.

To acquire a flat background, the polarizer is set at in a special angle 120° with reference to the laboratory coordinate, the configuration of the orientation on the image is shown in Fig. 6.2.1.1. The x-axis shown on Fig. 6.2.1.1 is zero degree in the laboratory coordinate.

Table 6.2.1.1 The experiment of the AlGaIn/GaN/SiC on microscope

date	Sample	light source	lens	Item	Experiment configuration
20180724	0	LED	40X	Micropipe	focus changing
20180725	Background	LED	40X	Micropipe	focus changing
20180726	0	LED	40X	five defects	
20181011	0	LED	40X	Micropipe	three p angle
20190207	0	LED	40X	Micropipe	
20190208	0	LED	40X	Micropipe	

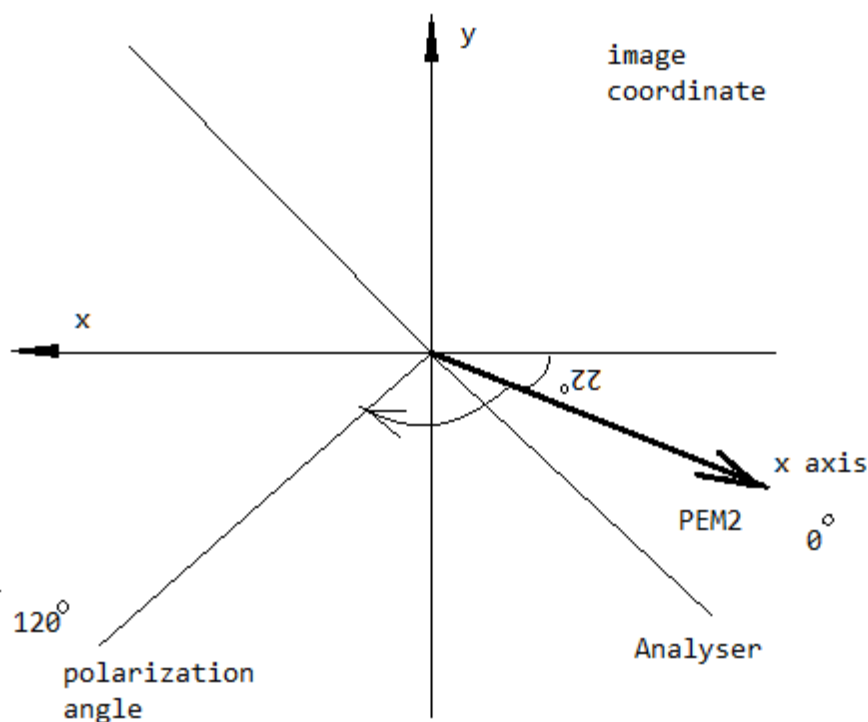


Figure 6.2.1.1 the laboratory coordinate showing on the image of the microscope

6.2.2 Image of double micropipe in focus position

Figure 6.2.2.1 is the image of Stokes parameters of a double micropipe. Figure 6.2.2.1a, the image of the intensity, give out the diameter of one micropipe, $4.5\mu\text{m}$; and, the area around the big hole is another micropipe, which cannot be focused well in this focus plane. Stokes parameter Q and U are negative outside the micropipe, but remain positive in the hole of the micropipe, shown in Fig. 6.2.2.1b and 6.2.2.1c. Stokes parameter V varies apparently in a big

area, about $128\mu\text{m}$, shown in Fig. 6.6.2.1d. The response area to Stokes parameter V ($128\mu\text{m}$) is much bigger than that in images using Q , U and I , which is about $10\mu\text{m}$, shown in Fig. 6.2.2.1a.

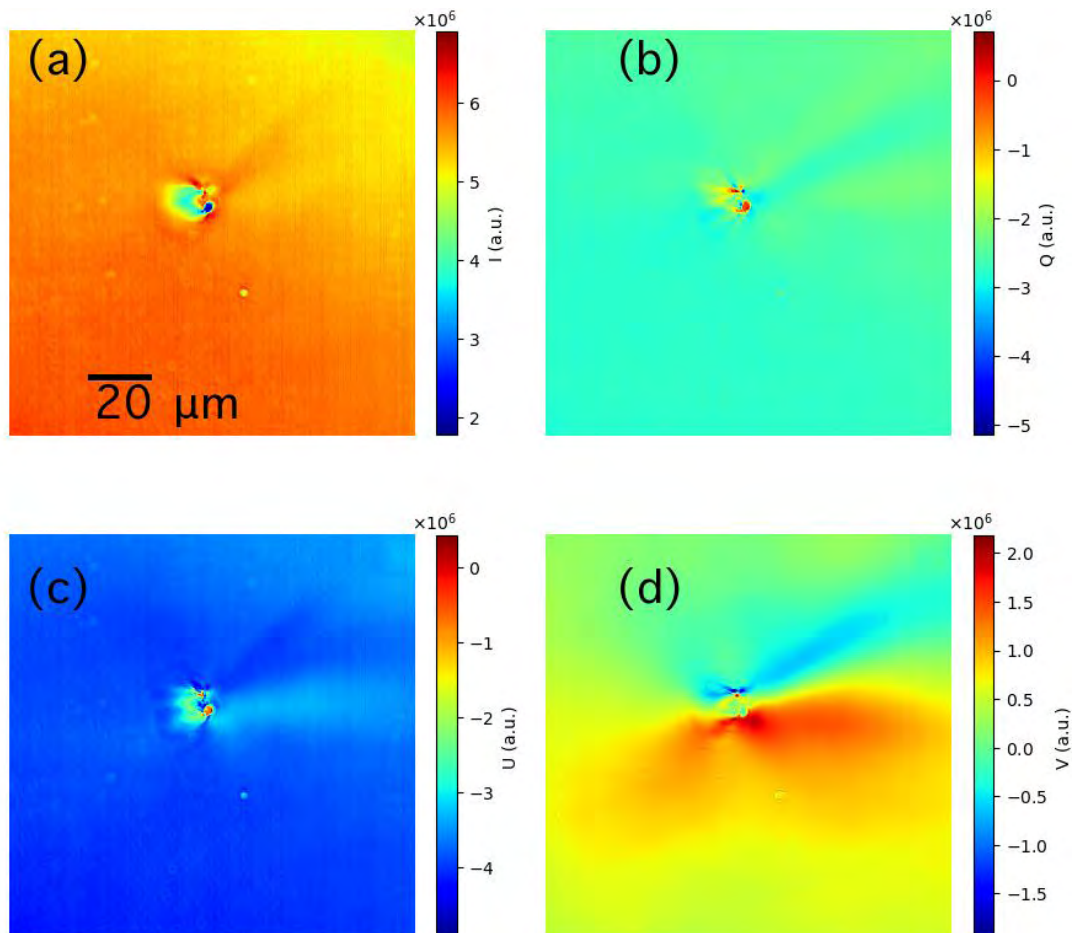


Figure 6.2.2.1 Image of contrast of the Stokes parameters on double micropipe: (a) Intensity, (b) Stokes parameter Q , (c) Stokes parameter U , (d) Stokes parameter V .

Figure 6.2.2.2 shows the normalized polarization parameters. Figure 6.2.2.2a shows that a strong depolarization (0.97) existed in the position of the hole. The depolarization is small outside the micropipe but still around 0.5. The normalized Stokes parameter Q/I , shown in Fig. 6.2.2.2b, remains around -0.5 in the normal area but positive in the area of the hole. The normalized Stokes parameter U/I , shown in Fig. 6.2.2.2c, keeps around -0.7 in the normal area but -0.4 in the area of the hole. The normalized Stokes parameter V/I , shown in Fig.

6.2.2.2d, keeps around -0.2 in the upper area of the image but 0.1 in the lower area of the image. The positive part and the negative part are divided along the direction of the polarization.

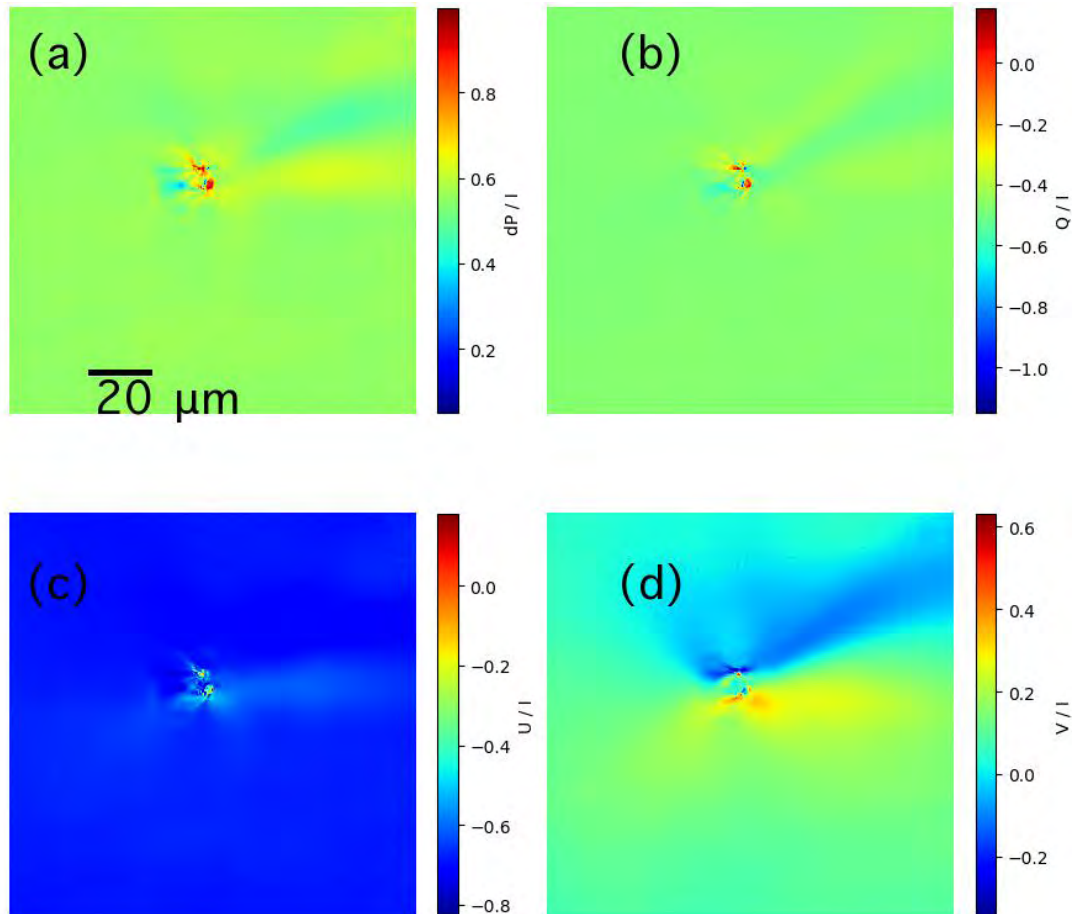


Figure 6.2.2.2 The image of (a) normalized depolarization, (b) normalized Stokes parameter Q/I , (c) normalized Stokes parameter U/I , and (d) normalized Stokes parameter V/I on a double micropipe.

Figure 6.2.2.3a shows the elliptical angle X varies between -10° and 10° . The azimuth angle Ψ shown in Fig. 6.2.2.3b keeps 120° in the area outside of the micropipe, which is same as the azimuth angle of the polarization; While, the azimuth angle decreases to 50° at a special edge of the micropipe. The surrounding area of the micropipe exist anisotropy on structure which produce a retardation of phase δ , shown in Fig. 6.2.2.3c, that varies between -30° and 30° . The contrast image in $\sin(\delta)$ in Fig. 6.2.2-3d looks clearer than δ in Fig. 6.2.2.3c.

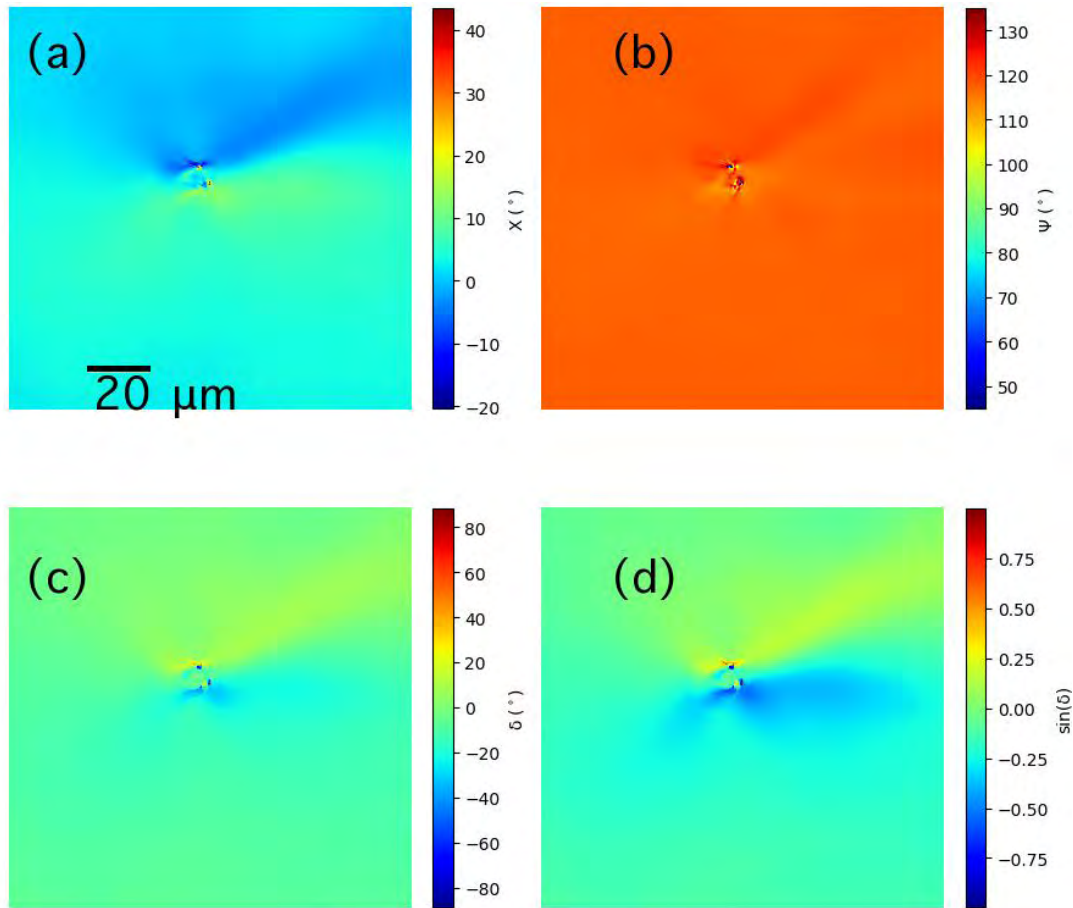


Figure 6.2.2.3 The contrast image of (a) the elliptical angle χ , (b) the azimuth angle ψ , (c) the retardation of phase δ , and (d) the $\sin(\delta)$ on a double micropipe..

This section introduces a set of images of a double micropipe acquired at one particular position. The Stokes parameters are acquired at the beginning, other parameters are deduced based on the Stokes parameters. The Stokes parameters are near to zero inside the hole. The Stokes parameters change at the edge of the hole: Q and U decrease (2×10^6 a.u. and 2×10^6 a.u. respectively), and V increases (2×10^6 a.u.). The normalized depolarization in the hole is near to 1, the mapping of depolarization has three tails (the depolarization varies between 0.4 and 0.6) on the left side of the hole.

6.2.3 Image of the double micropipe at different focus position

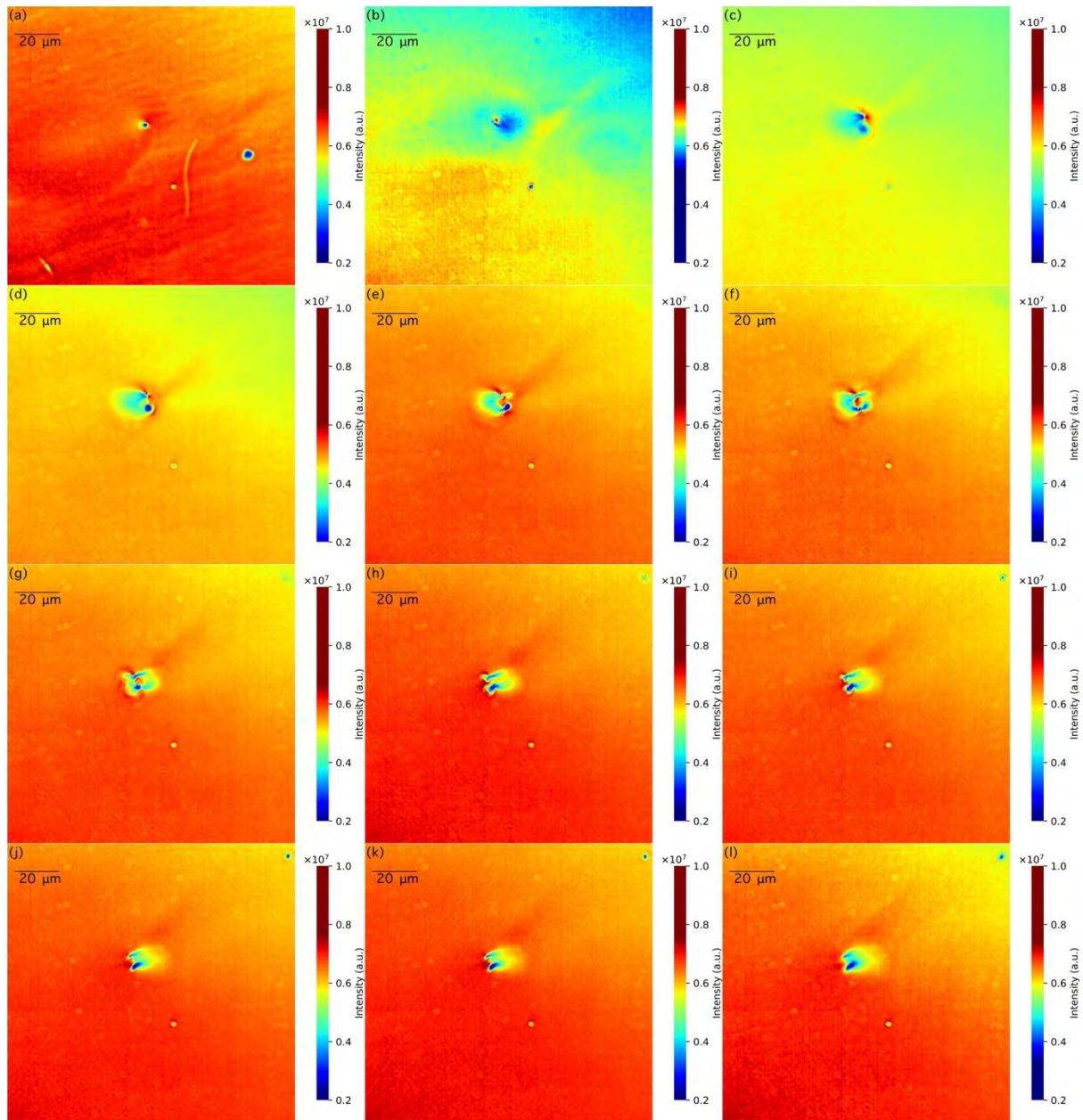


Figure 6.2.3.1 The mapping of the intensity of the double micropipe in different focus position

The micropipe is a kind of defect that distributed within a certain focus position. So, a set of focus position is used to observe the micropipe. In this section, all the pictures marked with the same letter are taken in the same position at one time.

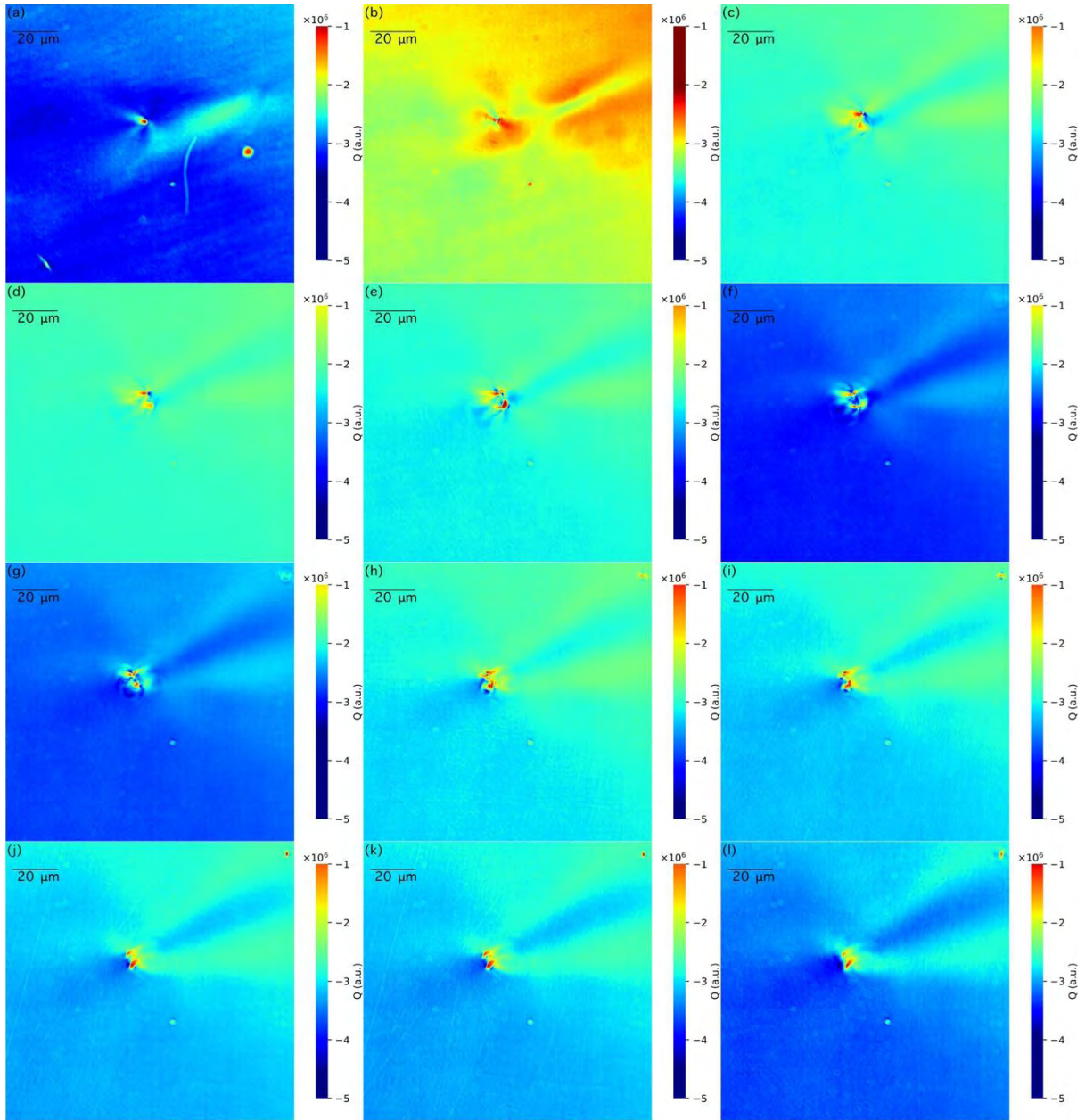


Figure 6.2.3.2 The mapping of Stokes parameter Q of the double micropipe in different focus position

Figure 6.2.3.1 shows the image of the intensity of the double micropipe in different focus positions. It is a structure of two micropipes twisted together. Figure 6.2.3.1a, 6.2.3.1c, and 6.2.3.1d shows a position with a bigger hole which is nearly perpendicular to the surface of the sample. While in other positions, shown from 6.2.3.1h to 6.2.3.1l, the micropipe is tilted to the surface of the sample. The Fig. 6.2.3.1f and 6.2.3.1g show a position that the micropipe are twisted.

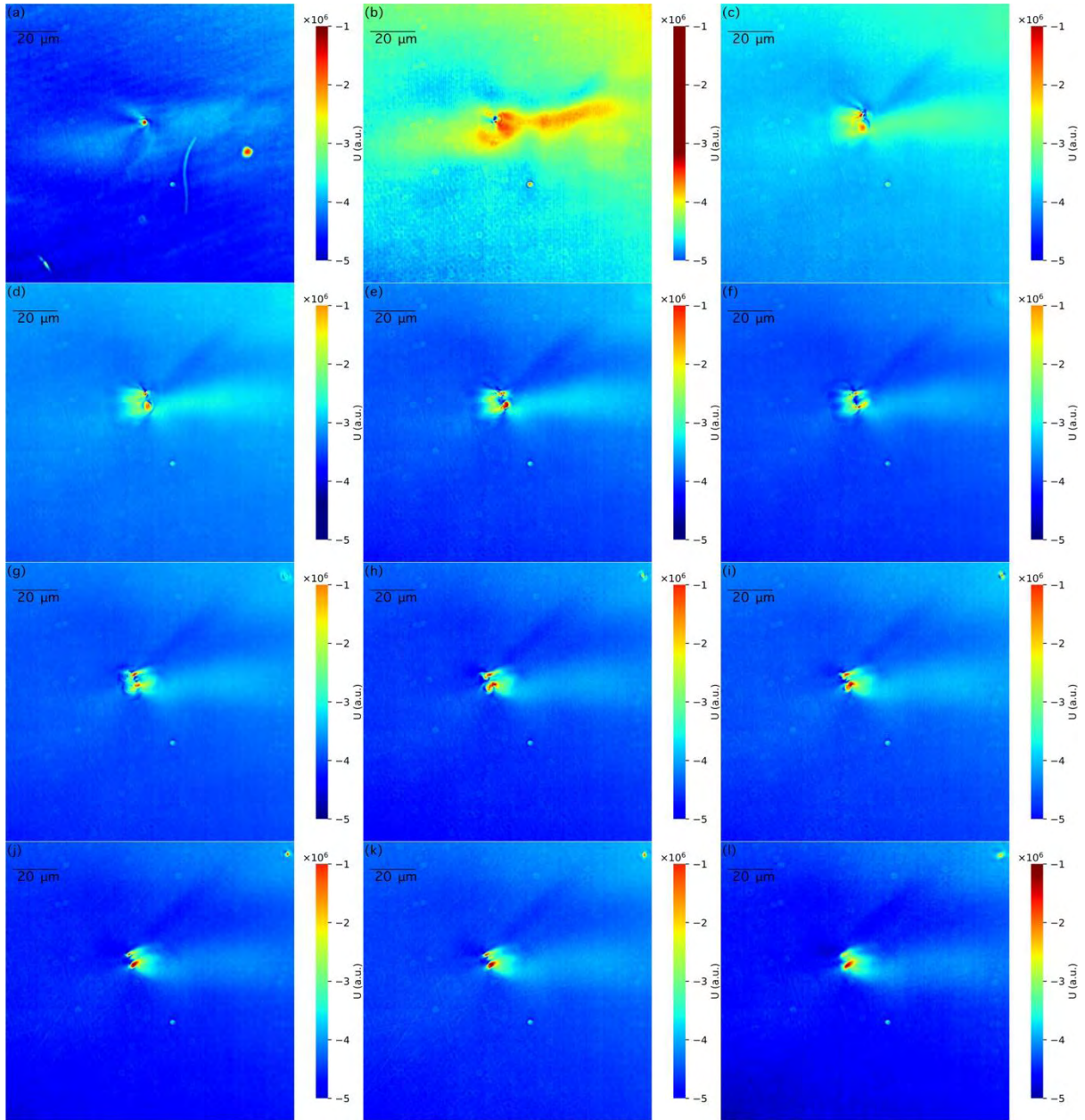


Figure 6.2.3.3 Stokes parameter of the double micropipe in different focus positions

Figure 6.2.3.2 is the image of the Stokes parameter Q of the double micropipe in different depth. Stokes parameter Q is a negative number in all the pictures. The value of Q in the hole (around -0.5×10^6 a.u.) is bigger than that in surrounding areas (around -2.5×10^6 a.u.). The range of the U is small (about 2.5×10^6 a.u.) in the twist position, shown in Fig. 6.2.3.2f and Fig. 6.2.3.2g.

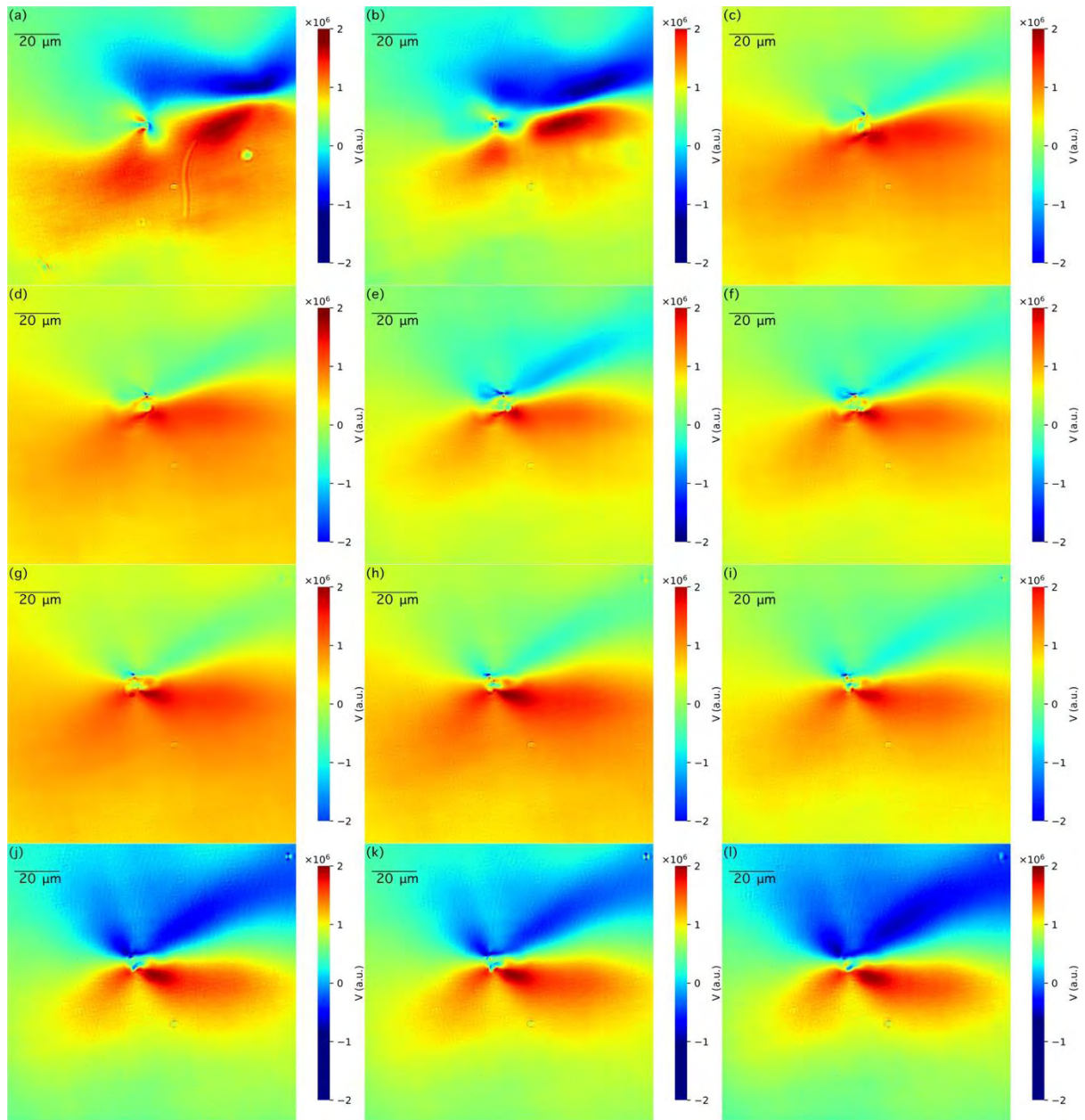


Figure 6.2.3.4 Stokes parameter V of the double micropipe in different focus positions

Figure 6.2.3.3 shows the mapping of the Stokes parameter U , which is a negative value in most area of the images. The value of U in the position of the hole (about 0) is bigger than the surrounding areas (about -4.5×10^6 a.u.). In the position shown in Fig. 6.2.3.3f and Fig. 6.2.3.3g, two lobes (shown in colour of green) with a lower value of U existed in left side and right side of the hole position (shown in red). In other positions, shown from 6.2.3.3h to 6.2.3.3i, only a lobe existed on the right side of the hole. While in Fig. 6.2.3.c and 6.2.3.d, only a lobe existed on the left side of the hole.

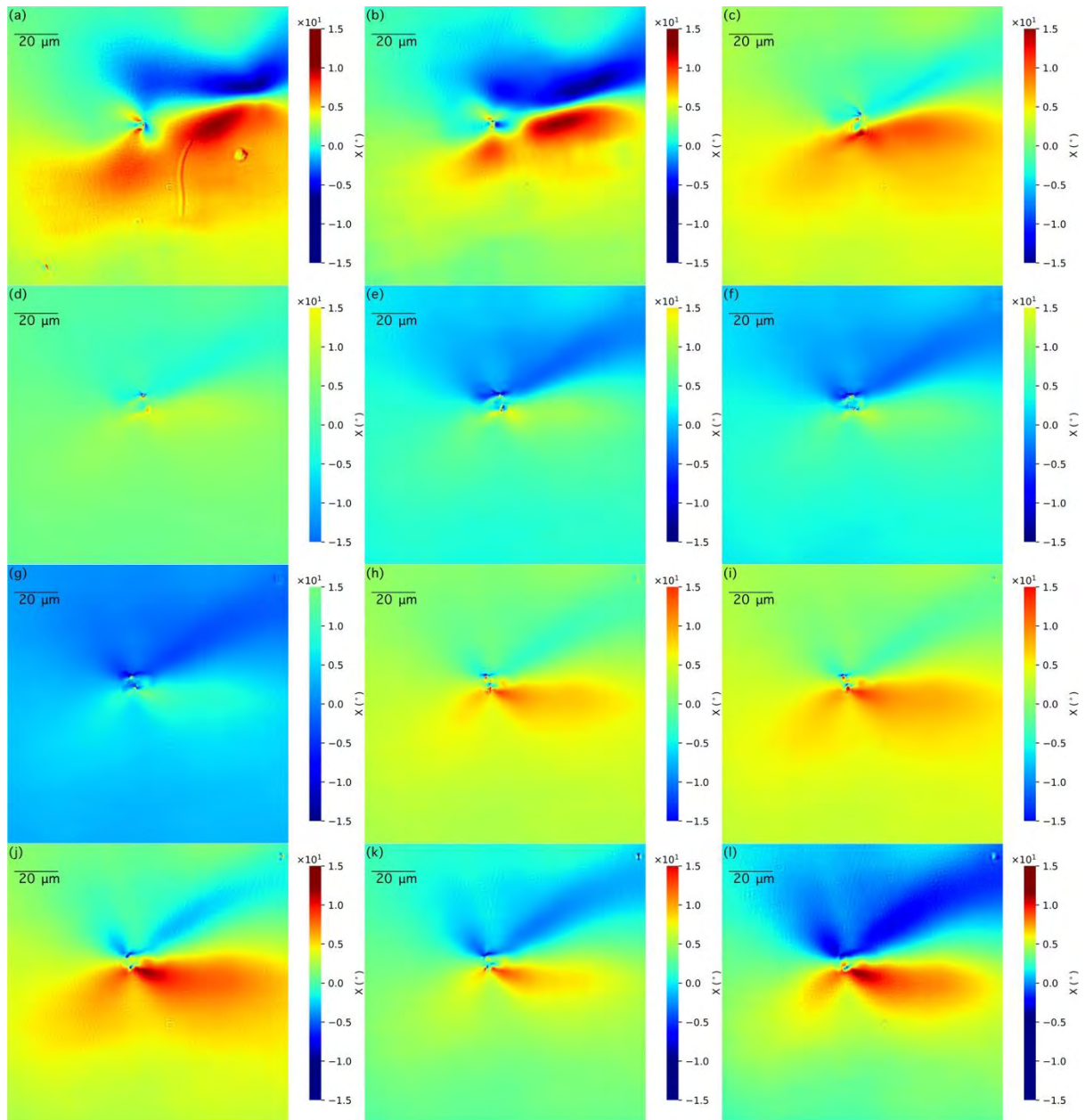


Figure 6.2.3.5 The mapping of elliptical angle χ of the double micropipe in different focus positions

Figure 6.2.3.4 is the image of Stokes parameter V at different depths. Stokes parameter V is related to the properties of anisotropy of the structure. V varies between a positive value (about 2×10^6 a.u.) and a negative value (about -2×10^6 a.u.) in all the images. In the positions shown in Fig. 6.2.3.4a and 6.2.3.4b, a sharp change (from -1×10^6 a.u. to 2×10^6 a.u.) exists in the area surrounding the micropipe. In the position of a big hole, shown in Fig. 6.2.3.4c and 6.2.3.4d, the value of V is about 0 in the position of big hole, while is about -2.5×10^6 a.u. at

the hole vanishing point. The variation of the surrounding area is small in Fig. 6.2.3.4c and 6.2.3.4d. Figure 6.2.3.e shows a twisted position of the micropipe

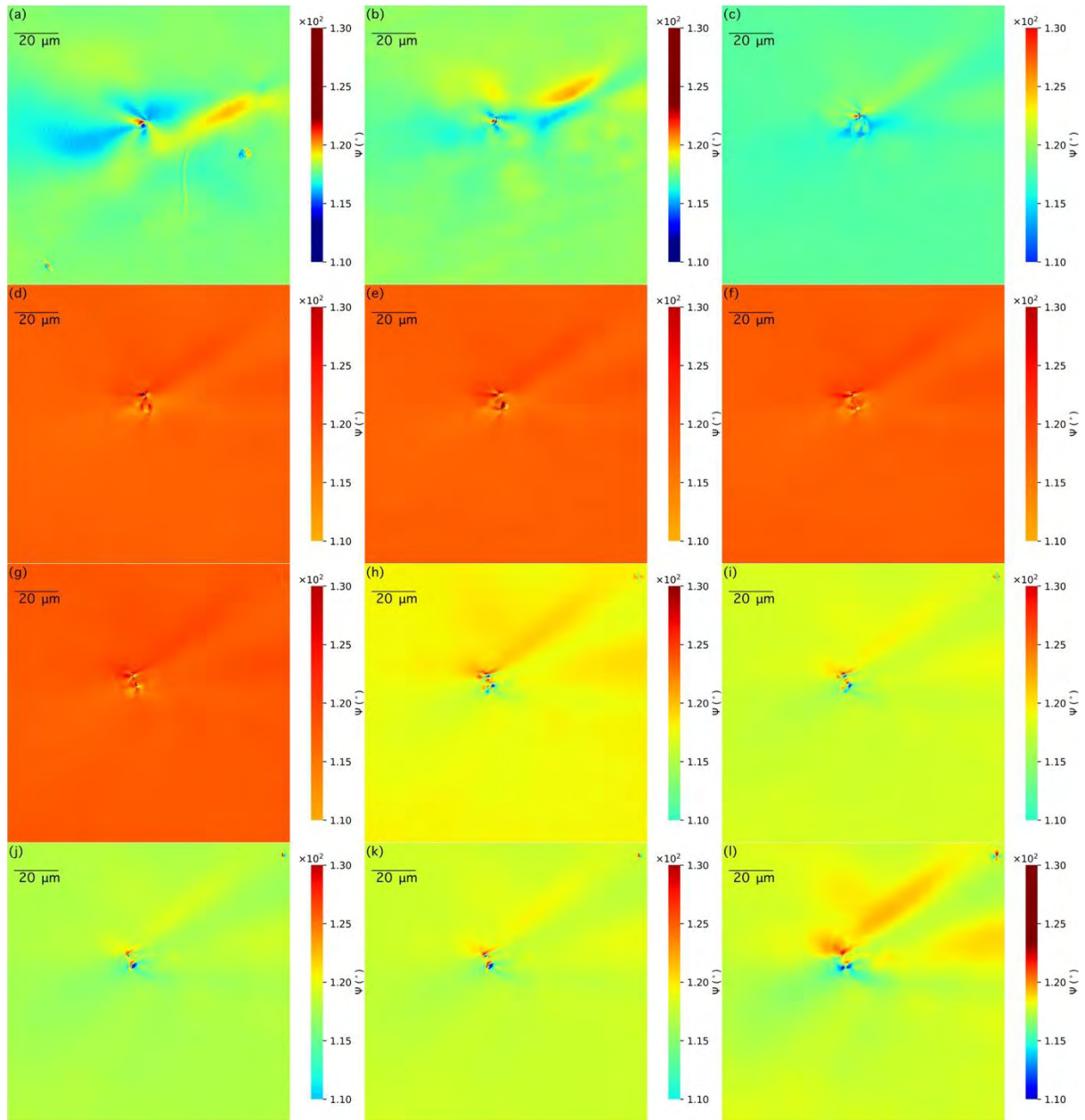


Figure 6.2.3.6 The mapping of azimuth angle ψ of the double micropipe in different focus position

Figure 6.2.3.5 is the image of the elliptical angle χ of the micropipe at different focus positions. The variation in Fig. 6.2.3.5 is similar to the variation in Fig. 6.2.3.4 because both V and χ are related to the anisotropy of the structure. The elliptical angle χ reaches -30° in

Fig. 6.2.3.5d, in a vanishing point position of a hole, reference to Fig. 6.2.3.1d. while in the position of a big hole, it is only 0° . The position at the boundary of the big hole is about 30° . The variation of the surrounding area is about 15° shown in Fig. 6.2.3.5a, 6.2.3.5i to 6.2.3.5l. At the twisted position, shown from Fig. 6.2.3.5e to Fig. 6.2.3.5g, the variation reaches 40° . Apparently, the azimuth angle is sensitive to the tilt angle of the tube wall of the micropipe.

Figure 6.2.3.6 show the mapping of the azimuth angle of the double micropipe at different focus positions. The azimuth angle of the probing polarization is at 120° . The azimuth angle is rotated a little (about 2°) in the position of the micropipe, shown in Fig. 6.2.3.6. In Fig. 6.2.3.6j and Fig. 6.2.3.6k, at the position shown in blue and red colour together is two boundaries of the micropipe, reference to Fig. 6.2.3.1j and Fig. 6.2.3.1k. At the vanishing point position of a micropipe shown in Fig. 6.2.3.6d, the azimuth angle is about 50° . While in the position of a big hole nearly perpendicular to the sample surface, shown in Fig. 6.2.3.6d, the azimuth angle is about 115° .

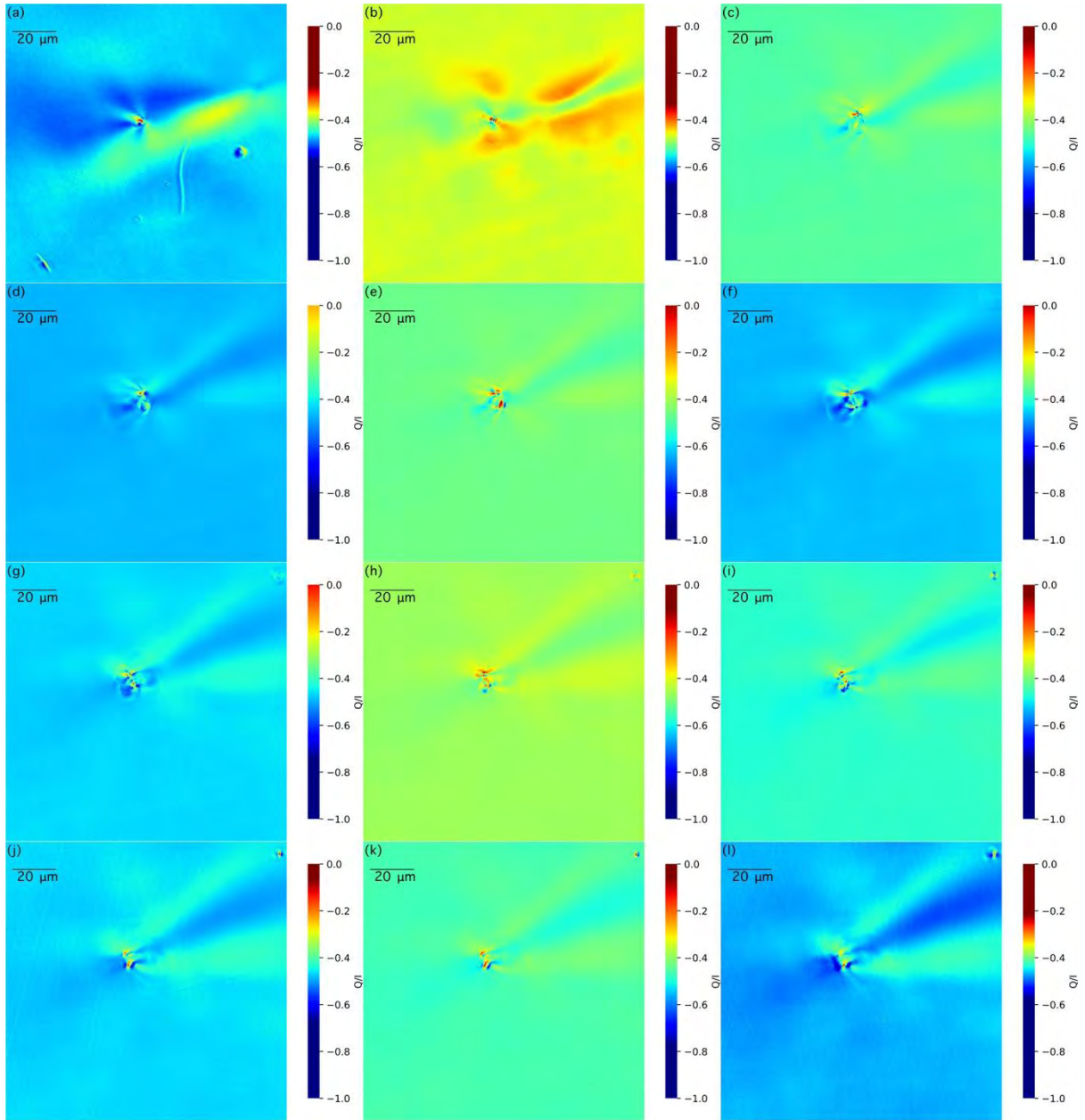


Figure 6.2.3.7 the mapping of normalized Stokes parameter Q/I of the double micropipe in different focus position

Figure 6.2.3.7 shows the normalized Stokes parameter Q/I for the double micropipe at different positions. The variation of the Q/I in Fig. 6.2.3.7a, Fig. 6.2.3.7a, and Fig. 6.2.3.7l, is about 0.3. While in other images, from Fig. 6.2.3.7c to Fig. 6.2.3.7k, the variation of that is about 0.6 to 0.9. In Fig. 6.2.3.7d, a three-lobe structure exists at the tail of the vanishing point position and a maximum value and a minimum value of the Q/I are sited at the vanishing point position.

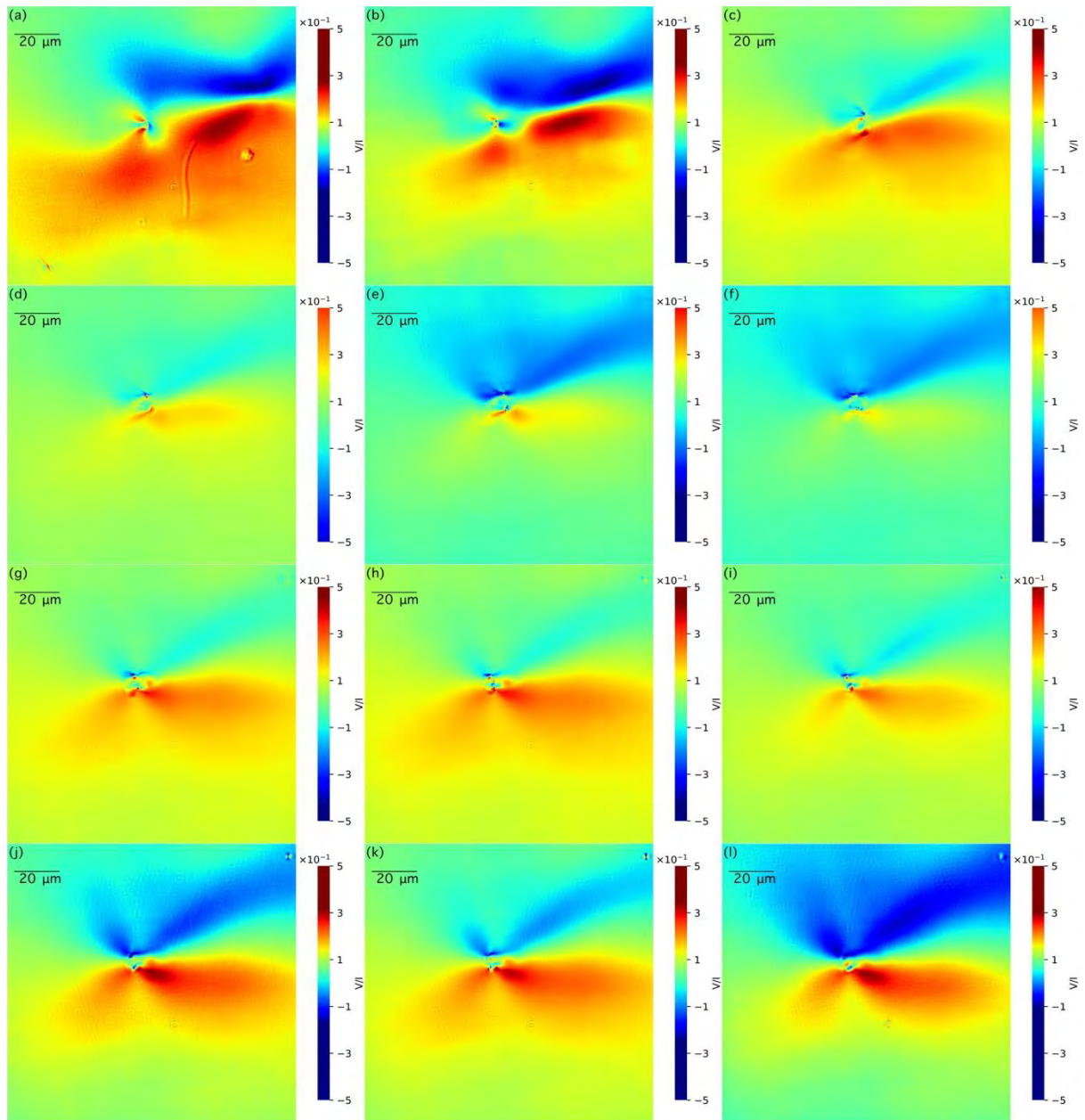


Figure 6.2.3.8 normalized Stokes parameter V/I of the double micropipe at different focus positions

Figure 6.2.3.8 is the mapping of the normalized Stokes parameter V/I in different focus positions. In the twist position shown in Fig. 6.2.3.8e and Fig. 6.2.3.8f, the variation of V/I is about 0.8. A sharp variation existed at the vanishing point position in Fig. 6.2.3.8d; while, the V/I in the position of the big hole, in Fig. 6.2.3.8c, is 0 and the V/I in the surrounding area of the hole is about 0.3.

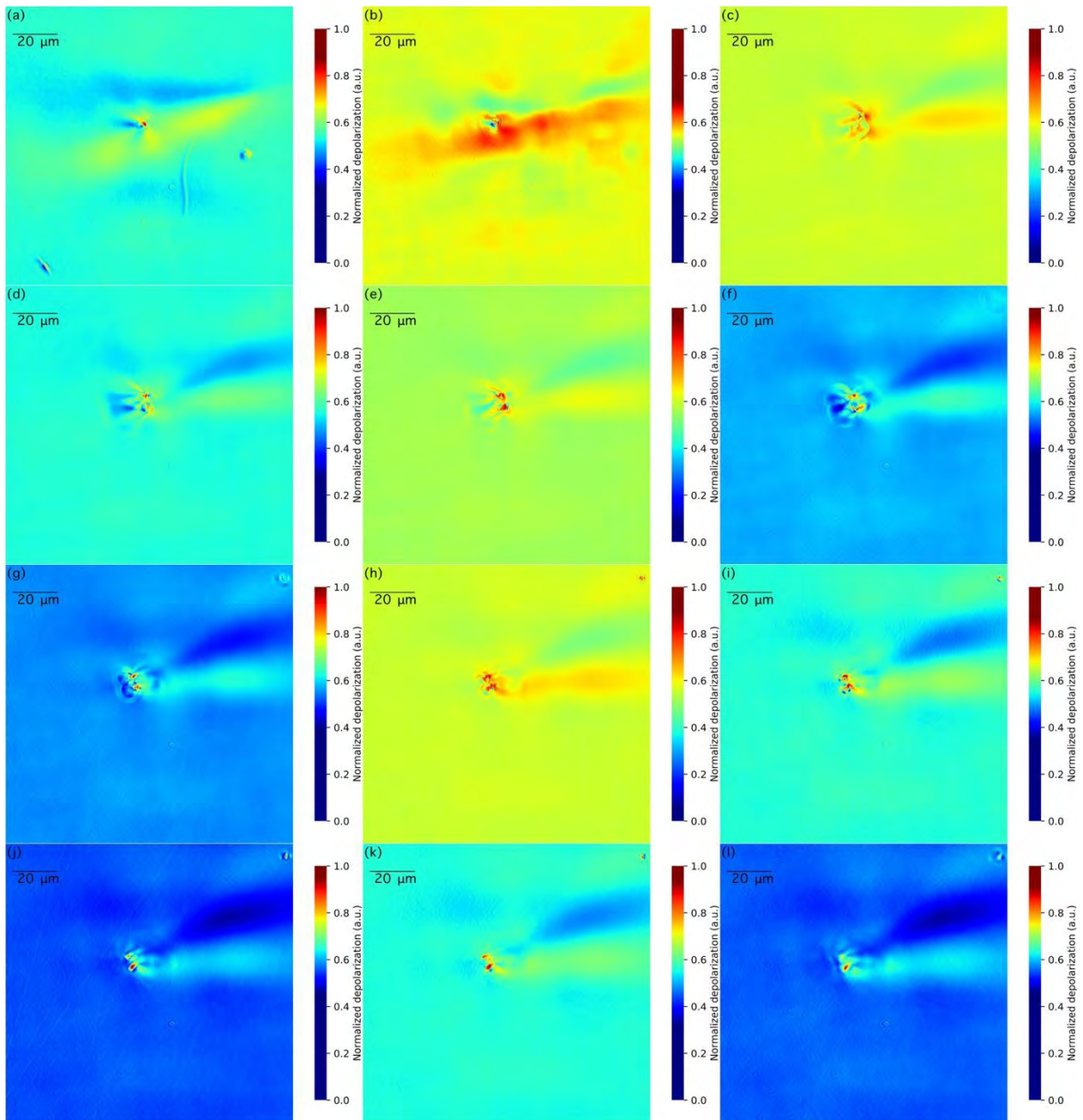


Figure 6.2.3.9 normalized depolarization of double micropipe in different focus positions

Figure 6.2.3.9 is the mapping of the normalized depolarization in different focus positions. A special characteristic of the structure is a red head with three yellow tails in Fig. 6.2.3.10d. A tip should exist at the position of the red head for a strong scattering, the depolarization is about 0.9 at the tip. From the direction of the tail, we can judge the convergence direction of the tip. At the twisted position, shown in Fig. 6.2.3.9f and Fig. 6.2.3.9g, the little tip is in the middle, it is divergence in both side of the tips. At the position shown from Fig. 6.2.3.9j to

Fig. 6.2.3.9l, the tip is on the left side and the tail is on the right side.

In conclusion, the double micropipe is distributed over a certain depth in the SiC. They are twisted and rotated. At the boundary of the hole, the linear polarization changes to an elliptical polarization. The tilt degree of the micropipe influences the mapping structure of parameters related to the phase difference, such as V , V/I , χ , δ and $\sin(\delta)$. The shape of the micropipe, such as the divergence or the convergence or the twist, can be detected through the mapping structure of Q , U , Q/I , U/I . In the image of the dP/I , the tilt degree of the micropipe and the shape of the micropipe can be observed together. azimuth angle can detect the shape of a tube, it represents as a structure in red and blue together, the azimuth angle of the polarization rotates in two direction at the two side of the wall of a tube.

6.2.4 Image of single micropipes in focus position

Figure 6.2.4.1 is the mapping of the Stokes parameters in a focus position with a largest diameter. The intensity, shown in Fig. 6.2.4.1a, inside of the hole is smallest and with a two tail on left and right side, respectively. The Q , shown in Fig. 6.2.4.1b, is zero inside the hole but with three rays on the left and right side, respectively. The mapping of U , shown in Fig. 6.2.4.1c is similar to the mapping of Q . While the mapping of V is different, shown in Fig. 6.2.4.1d, four rays with negative value is distributed on the top of the image, four rays with positive value are distributed at the bottom of the image.

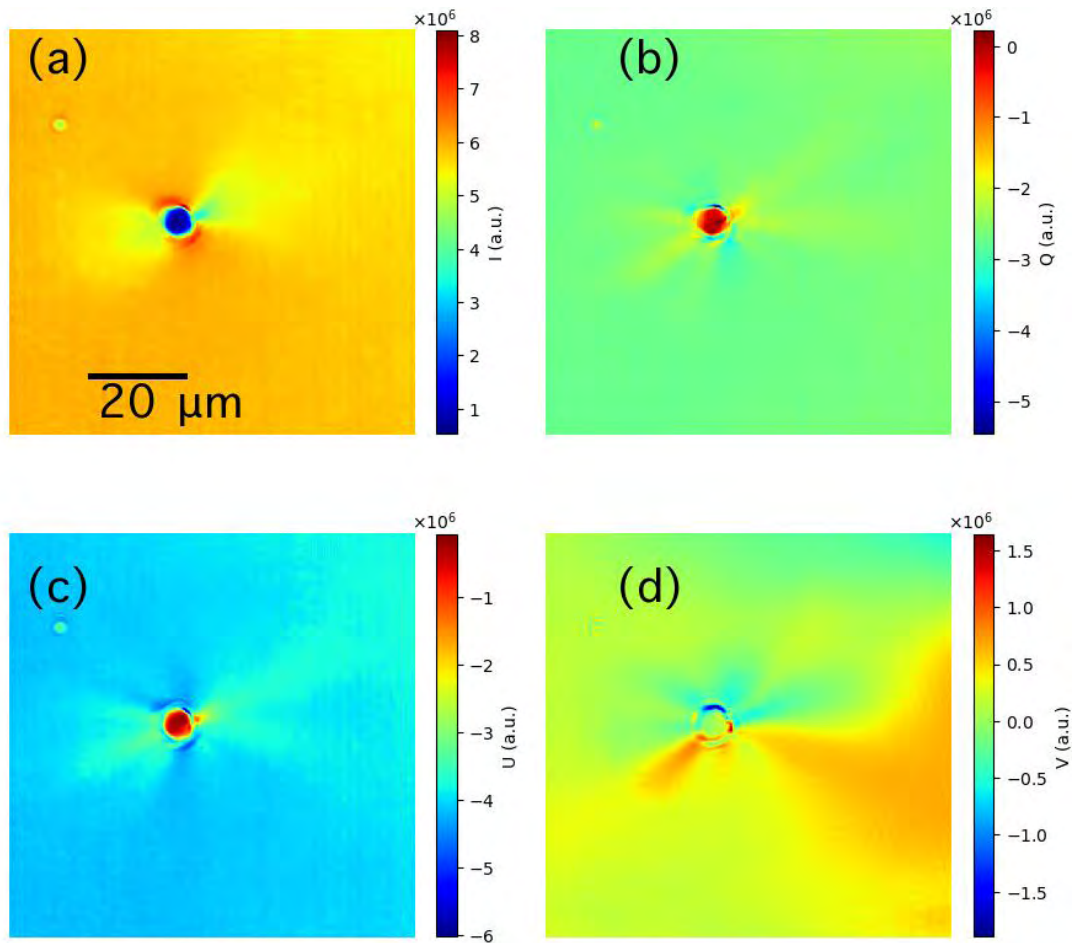


Figure 6.2.4.1 Image of contrast of the Stokes parameters at a single micropipe: (a) Intensity, (b) Stokes parameter Q , (c) Stokes parameter U , (d) Stokes parameter V

Figure 6.2.4.2 is the mapping of normalized signal. The normalized depolarization (dP/I) shown in Fig. 6.2.4.2a has eight rays on the side of the hole. The dP/I near to 1 inside of the micropipe and outside the wall of the micropipe. The dP/I is about 0.4 on the wall of the micropipe. The eight-ray structure is still present on the other three parameters, Q/I , U/I , V/I , shown from Fig. 6.2.4.2b to Fig. 6.2.4.2d, respectively. The Q/I at the wall of the micropipe is same to that on surrounding area; while, the Q/I outside the wall of the micropipe decreases to -0.8; and the Q/I inside the micropipe divided into two parts, -0.2 on the top of the hole and 0.2 on the bottom of the hole, respectively. The U/I at the wall of the

micropipe keeps the same to that on the surrounding area; while, the U/I outside of the wall of the micropipe increase to -0.5; and the Q/I inside of the micropipe divided into two parts, -0.1 on the top of the hole and -0.8 at the bottom of the hole, respectively. The trend of the Q/I is in contrast to that of U/I . The rays of the micropipe are negative on the top of the image of V/I and positive at the bottom of the image of V/I . The V/I reaches 0.3 inside the micropipe on the bottom of the hole. The structure of the micropipe looks like a screw rotated clockwise into the paper.

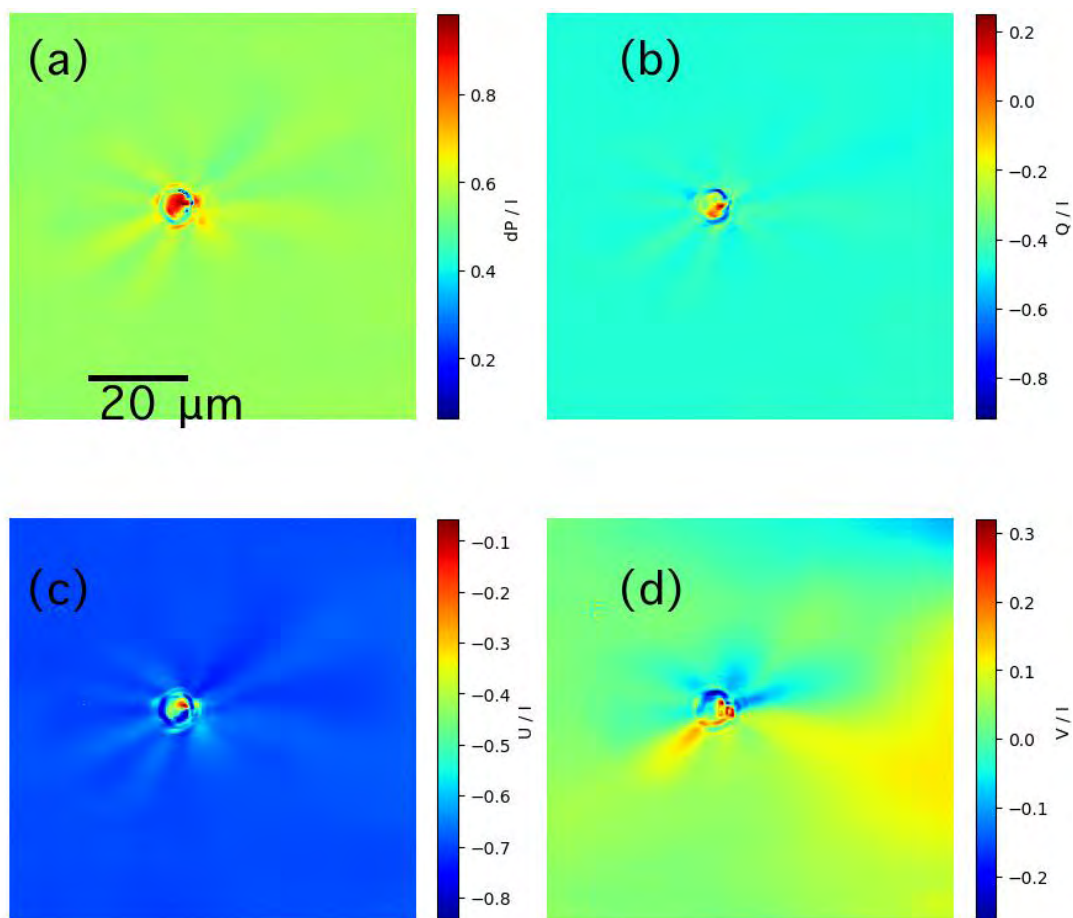


Figure 6.2.4.2 The image of at a single micropipe (a) normalized depolarization dP/I , (b) normalized Stokes parameter Q/I , (c) normalized Stokes parameter U/I , and (d) normalized Stokes parameter V/I

Figure 6.2.4.3 shows the mapping of particular angles describing the polarization. The elliptical angle χ , phase difference δ , and $\sin(\delta)$ are related to the V/I component, so the

mapping structure of the three parameter is similar. The trend of the mapping of the χ is in contrast to the mapping of δ . The azimuth angle ψ after interaction with the sample keeps the same with the polarization angle (about 120°) in general; however, the ψ decrease to 100° outside the wall of micropipe and decrease to the 50° on the bottom of hole. $\sin(\delta)$ listed here to compare the result of Ouisse (Ouisse, Chaussende, & Auvray, 2009).

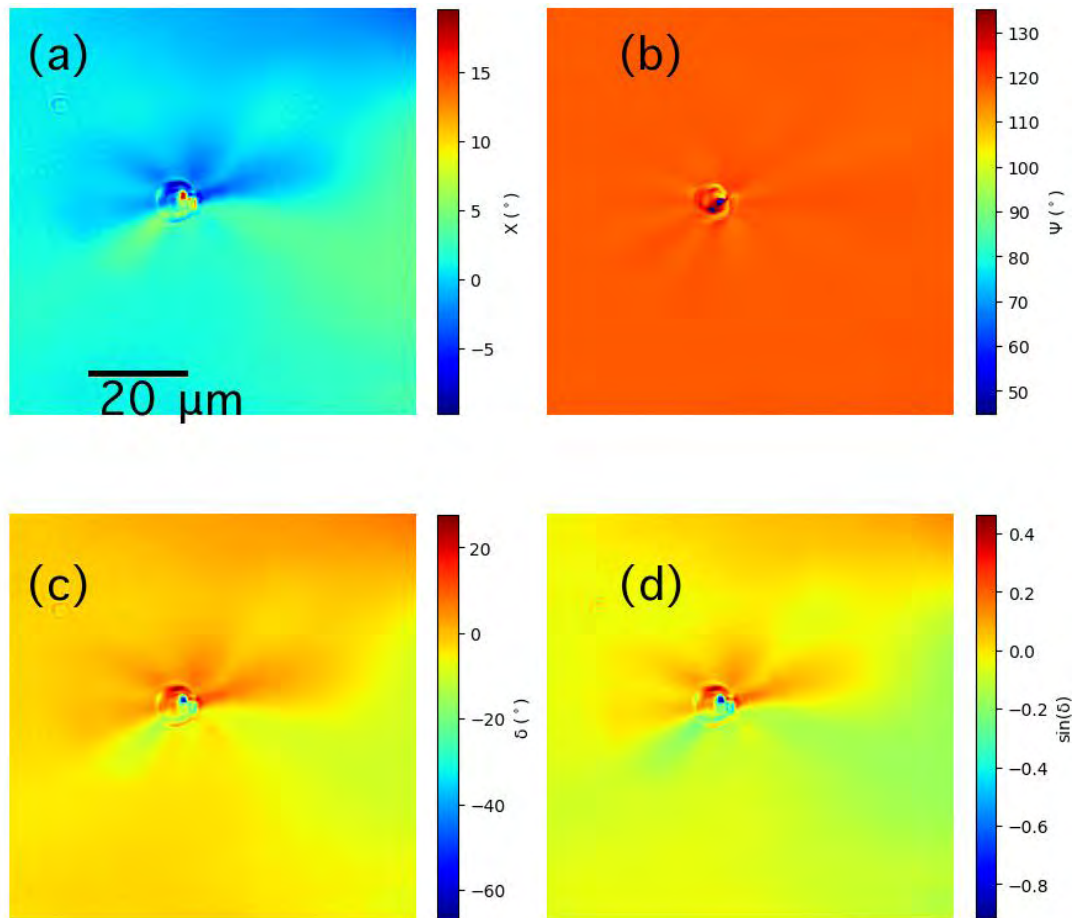


Figure 6.2.4.3 The contrast image of at a single micropipe (a) the elliptical angle χ , (b) the azimuth angle ψ , (c) the retardation of phase δ , and (d) the $\sin(\delta)$.

In conclusion, a set of polarization mapping images of a single micropipe is acquired. Eight rays existed on the range of the micropipe. On the wall of the micropipe, the value of Q/I , U/I , V/I , and I_{dp}/I keep the same with that on the surrounding area. A Ray structure exists outside the wall of the micropipe in different Stokes parameters images. Inside the micropipe, the mapping of Stokes parameters is different. On the images related with the signal V , such

as χ , δ , $\sin(\delta)$, a diving line between positive value and negative value existed, which is along the azimuth angle of the polarization of incident light.

6.2.5 Image of single micropipe in different focus positions

Figure 6.2.5.1 shows the overlapped image of the intensity of the micropipe at different focus planes. This micropipe is a tube-like structure with the maximum diameter in the middle.

This micropipe is about $30\mu\text{m}$ long and tilted grown in the substrate.

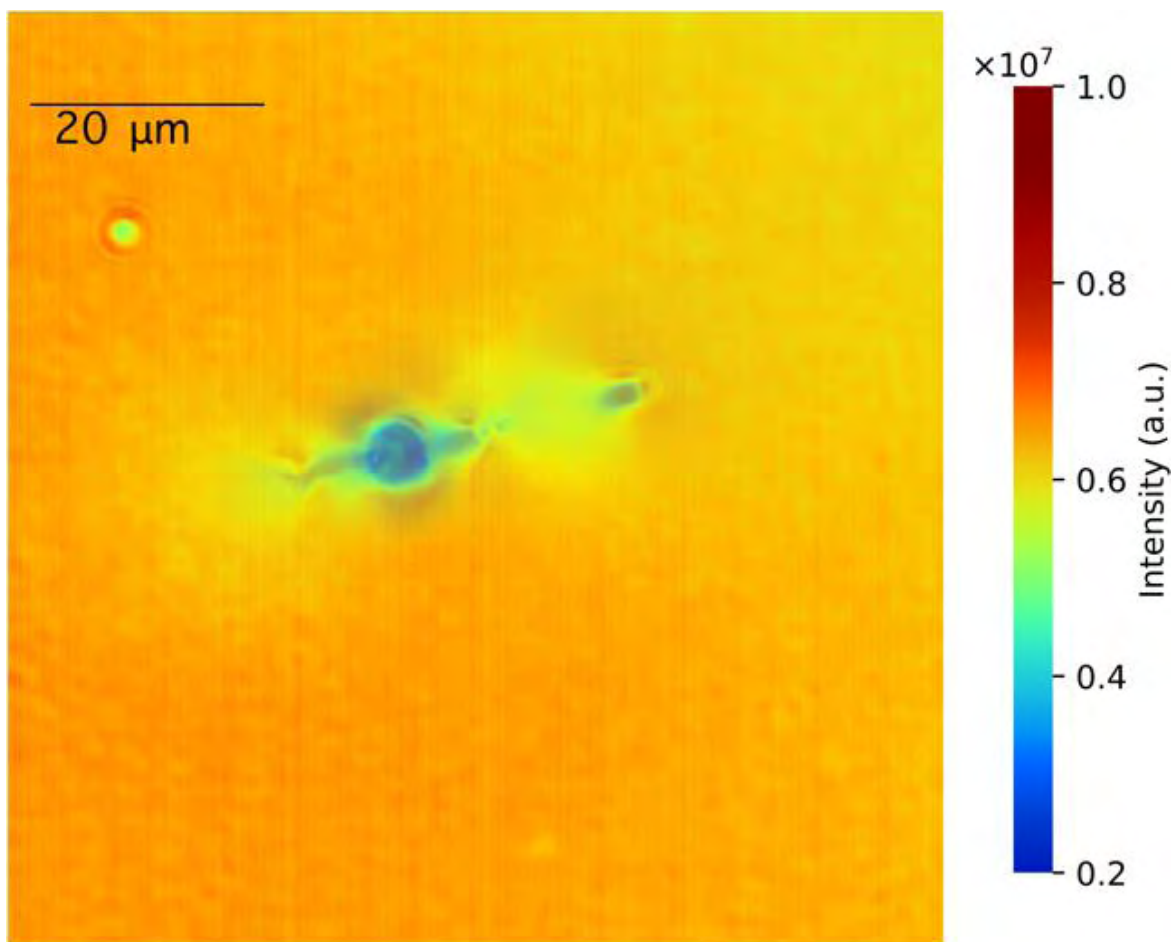


Figure 6.2.5.1 The overlapping image of the mapping of the intensity of the single micropipe. From Fig. 6.2.5.2, the phase difference δ is divided into positive part and negative part along the wall of the micropipe. The same situation exists in the image of V , such as χ , $\sin(\delta)$. I will not list here for the simple of the thesis.

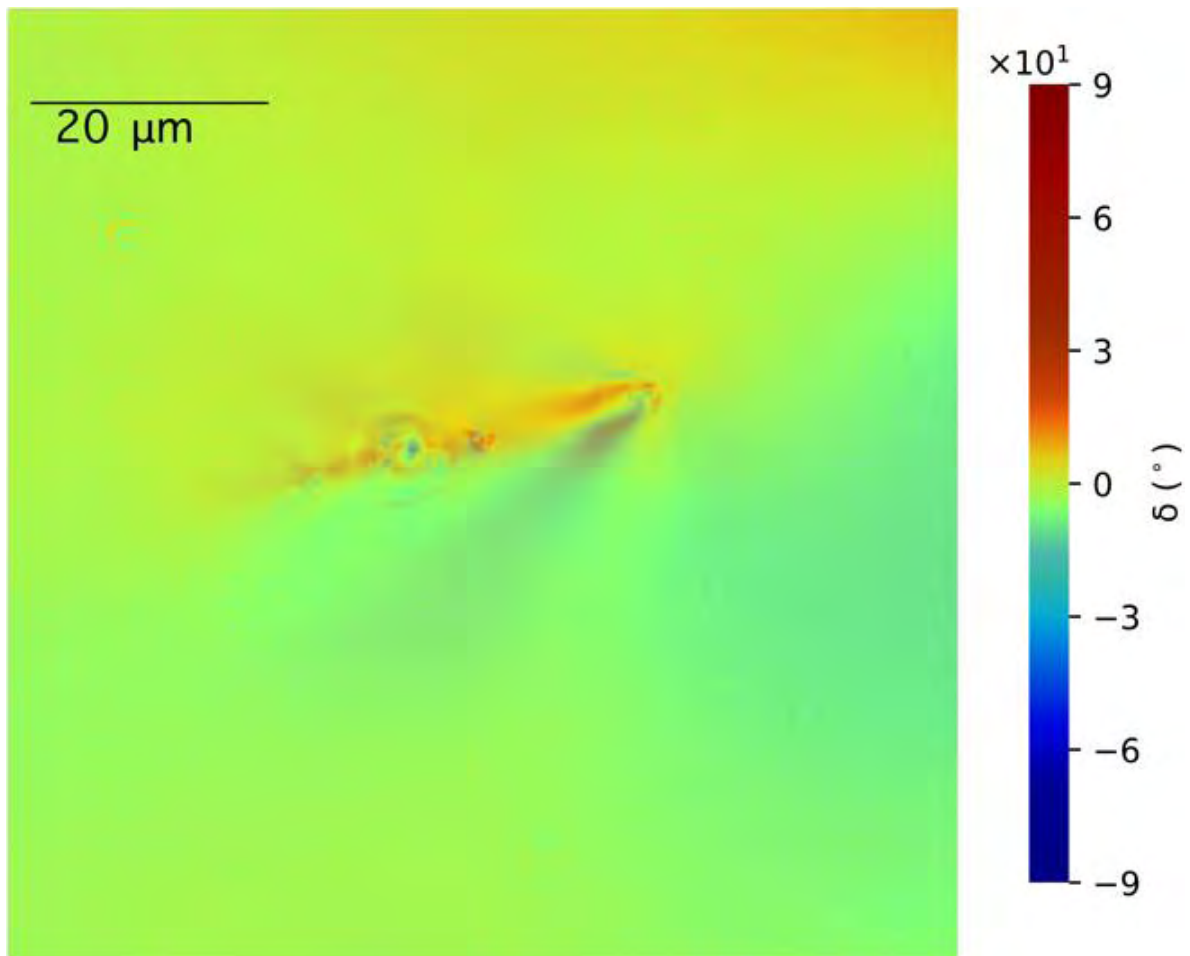


Figure 6.2.5.2 The overlapping image of the mapping of the phase difference δ of the single micropipe

Figure 6.2.5.3 is the intensity of the micropipe at different focus positions. The lobes in green on the left side and the right side of the micropipe implies a hollow position existed at the position of the lobes, which can be seen clearly after adjusting the focus position of the microscope.

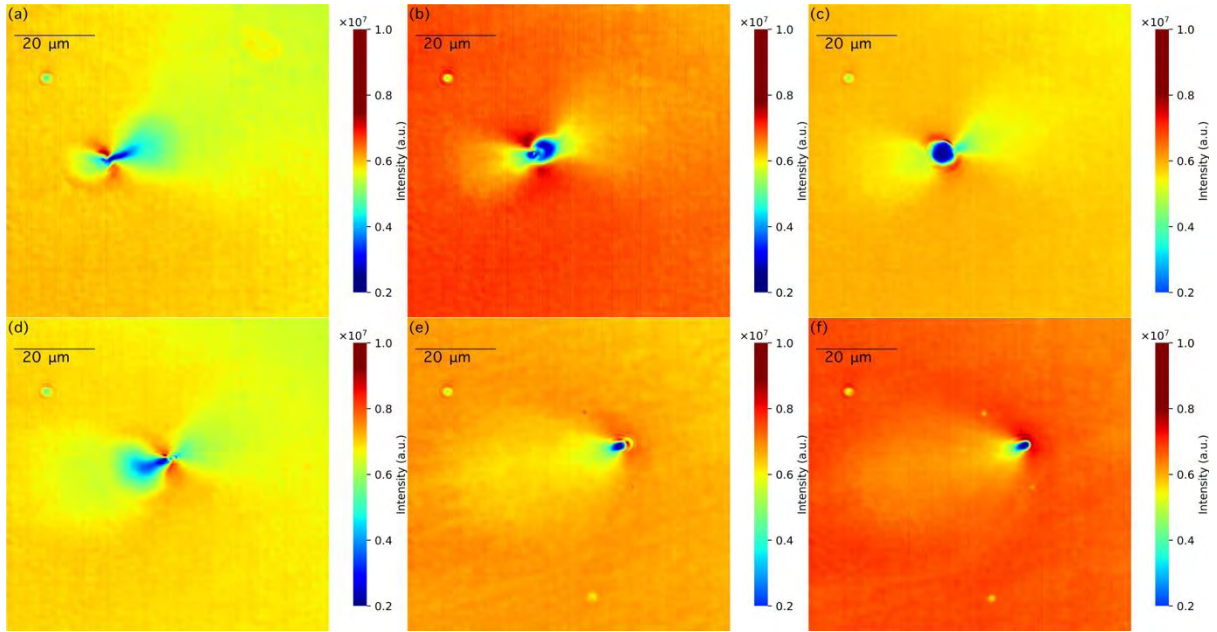


Figure 6.2.5.3 The mapping of the intensity of the single micropipe at different focus position

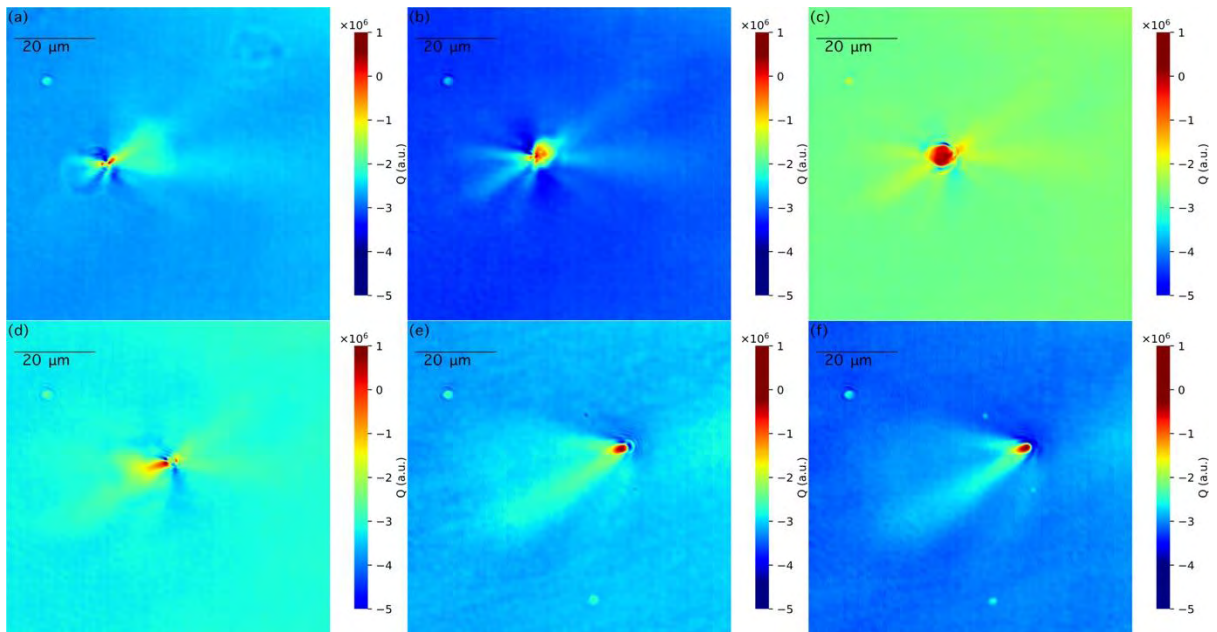


Figure 6.2.5.4 The mapping of Stokes parameter Q of the single micropipe in different focus positions

The mapping of Q is different in different positions, shown in Fig. 6.2.5.4. The eight-ray structure only exists when the micropipe is perpendicular to the surface of the substrate, shown in Fig. 6.2.5.4c. In the position where the micropipe is tilted, on Fig. 6.2.5.4e and Fig. 6.2.5.4f, only two rays left and some interference patterns on the other side. Fig. 6.2.5.4a and

Fig. 6.2.5.4d shows the mapping at a twist position.

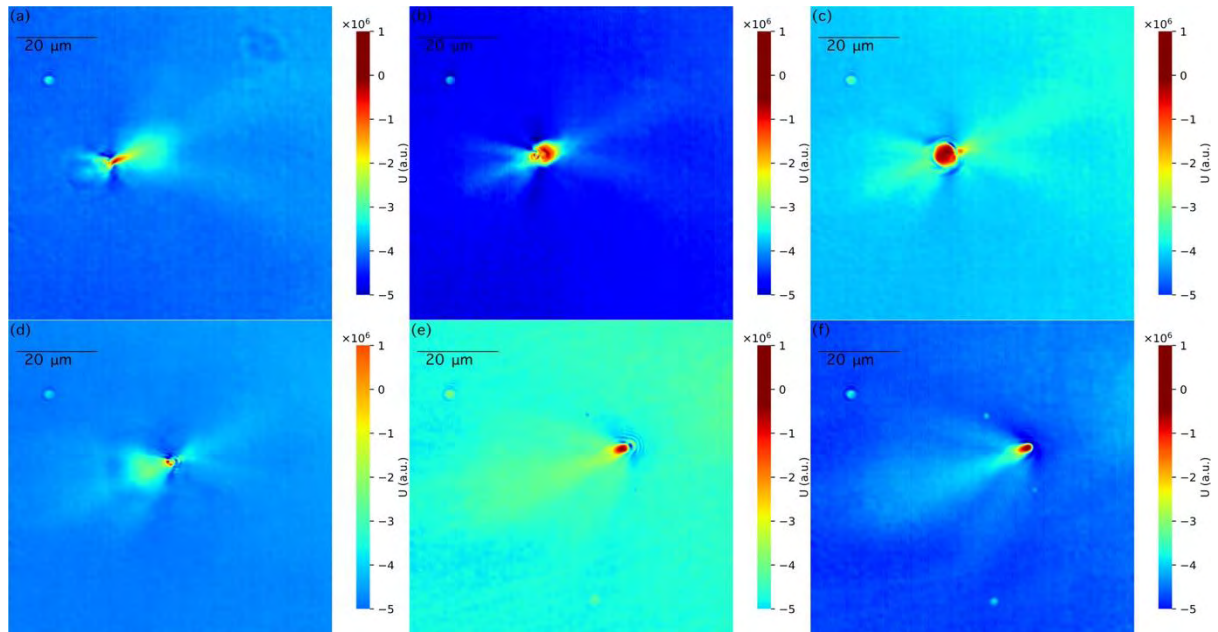


Figure 6.2.5.5 The mapping of Stokes parameter U of the single micropipe in different focus positions

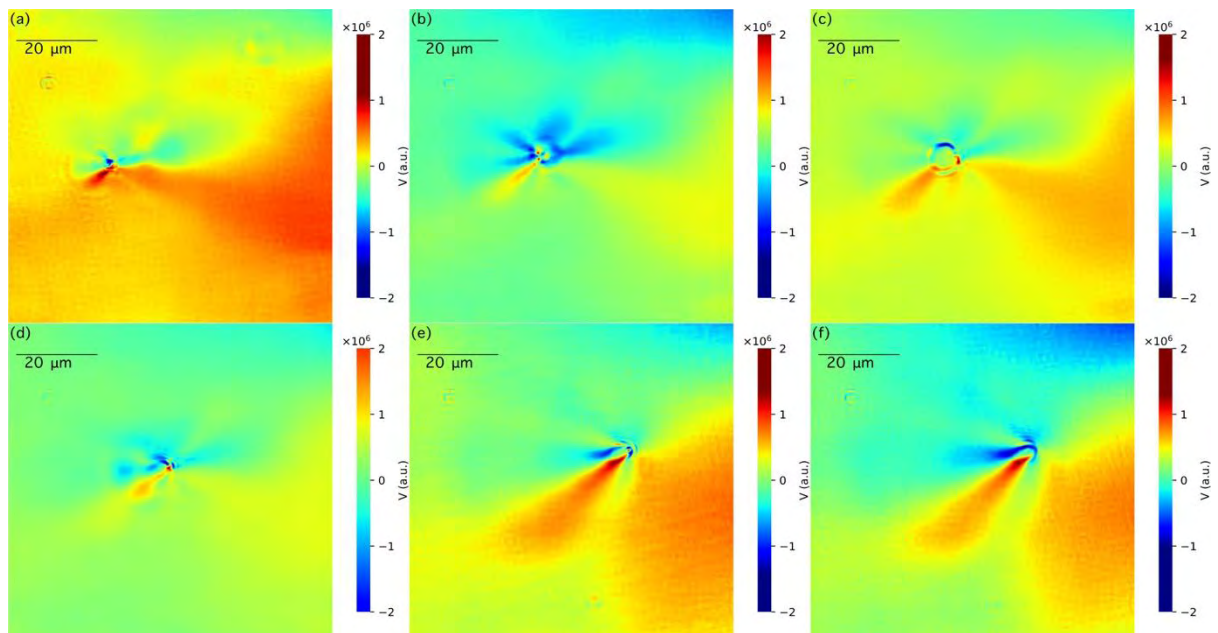


Figure 6.2.5.6 The mapping of Stokes parameter V of the single micropipe in different focus positions

Figure 6.2.5.5 shows the mapping of the U in different focus position. the structure of mapping in Fig. 6.2.5.5 is similar to that in Figure 6.2.5.4, but with a little different. The

distribution of the rays in Fig. 6.2.5.5 is in contrast to that in Fig. 6.2.5.4.

Figure 6.2.5.6 shows the mapping of the V of the micropipe in different focus positions. The upper side of the images is negative, and the lower side of the images is positive.

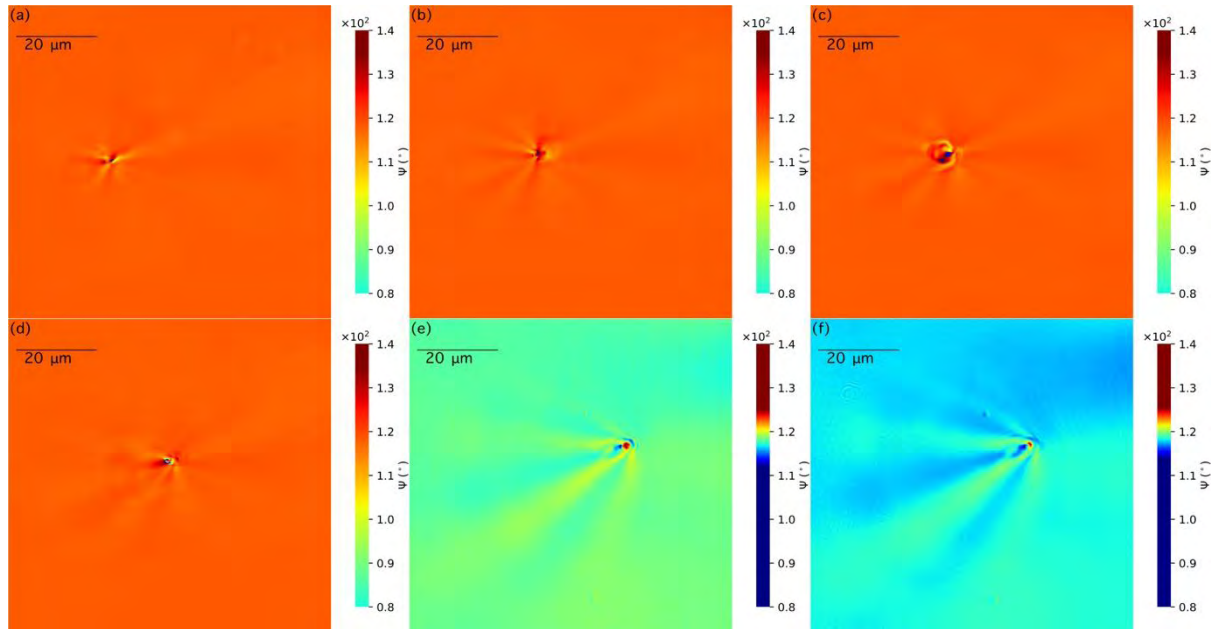


Figure 6.2.5.7 The mapping of azimuth angle ψ of the single micropipe in different focus positions

The azimuth angle in Fig 6.2.5.7 is changed sharply only at the position of micropipe. The variation of the rays is only about 5° .

Fig. 4.6.5-8 is the mapping of $\sin(\delta)$ in different focus position. In Fig. 6.2.5.8d, the variation of $\sin(\delta)$ is smaller than the other positions because this position is a twist position.

Fig. 6.2.5.9 is the mapping of normalized Q/I of single micropipe in different focus positions.

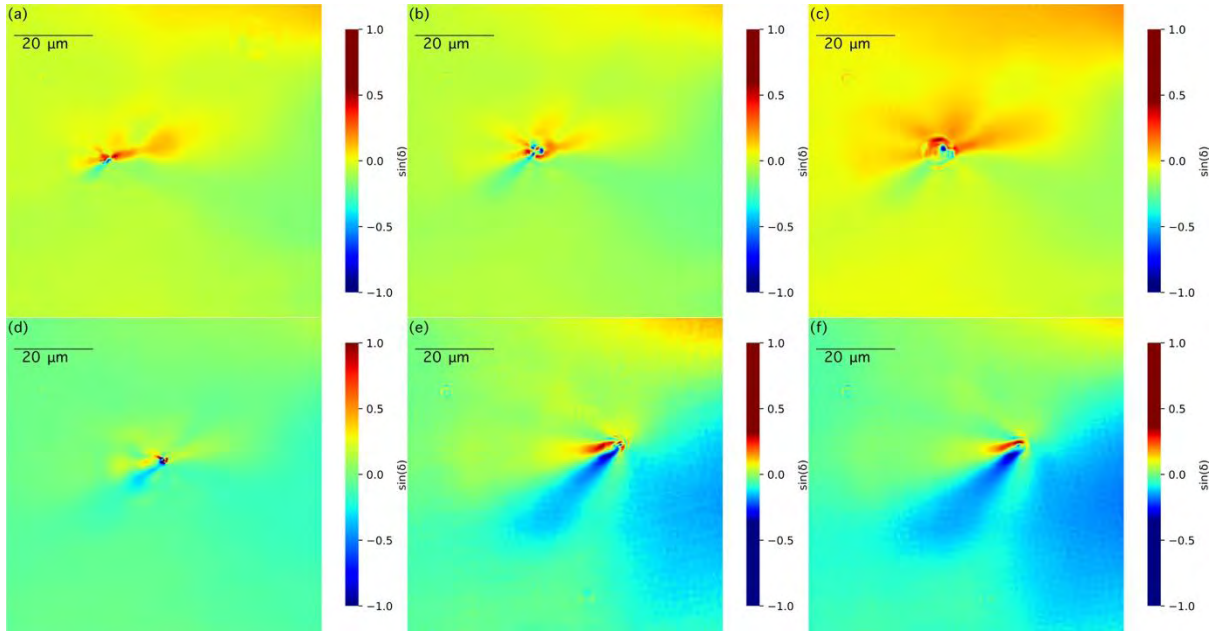


Figure 6.2.5.8 the mapping of $\sin(\delta)$ of the single micropipe in different focus positions

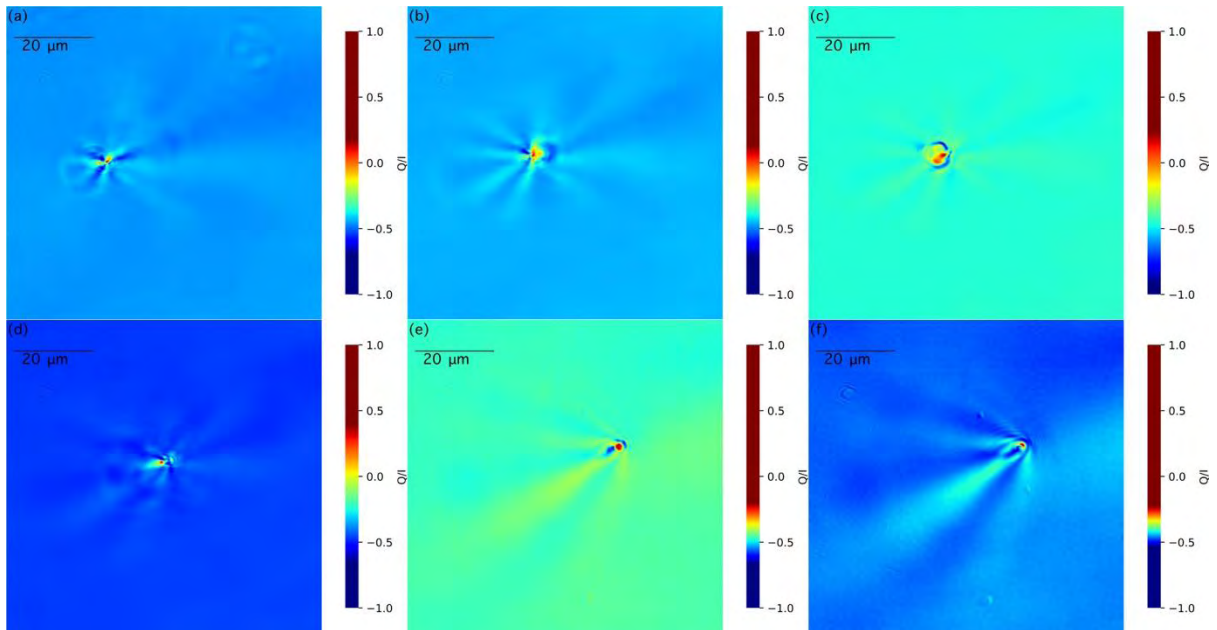


Figure 6.2.5.9 The mapping of normalized Stokes parameter Q/I of the single micropipe in different focus positions.

Figure 6.2.5.10 is the mapping of the normalized U/I in different focus position. An interference pattern existed on the right side of the hole in Fig. 6.2.5.10e and Fig. 6.2.5.10e.

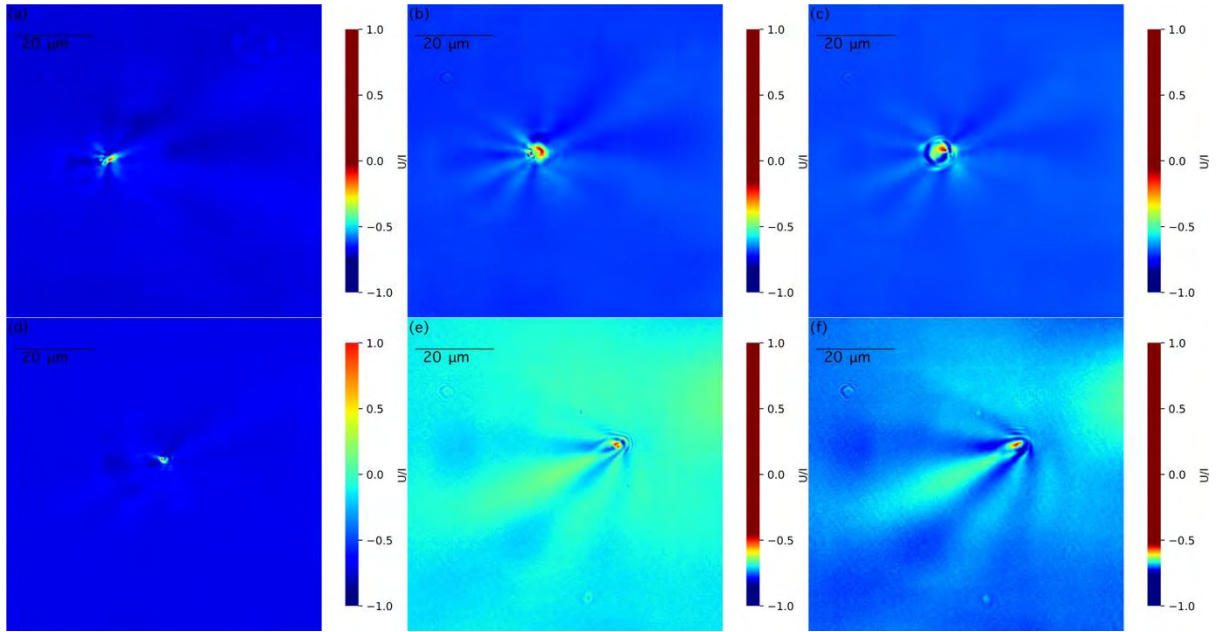


Figure 6.2.5.10 The mapping of normalized Stokes parameter U/I of the single micropipe in different focus positions

Figure 6.2.5.11 is the mapping of the normalized Stokes parameter V/I in different focus positions. The interference pattern can be seen at the end of the micropipe in Fig. 6.2.5.11e.

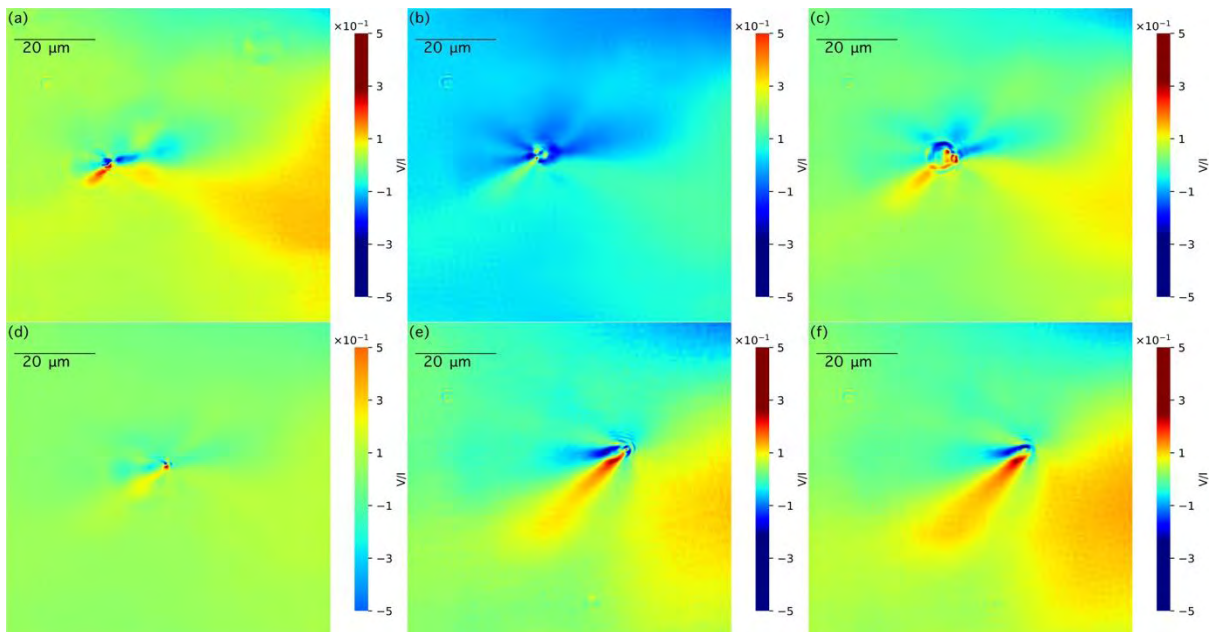


Figure 6.2.5.11 The mapping of normalized Stokes parameter V/I of the single micropipe in different focus positions

Figure 6.2.5.12 is the mapping of the normalized depolarization I_{dP}/I in different focus positions. The I_{dP}/I is near to 1 in the centre of the hole. On the wall of the hole, the I_{dP}/I is

0.5, which is similar to that on the substrate. Outside of the wall of the micropipe, there are eight rays when the micropipe is sited perpendicular to the substrate surface. The eight-ray structure outside the micropipe decreases to three rays when the micropipe is sited tilted in the substrate shown in Fig. 6.2.5.12f.

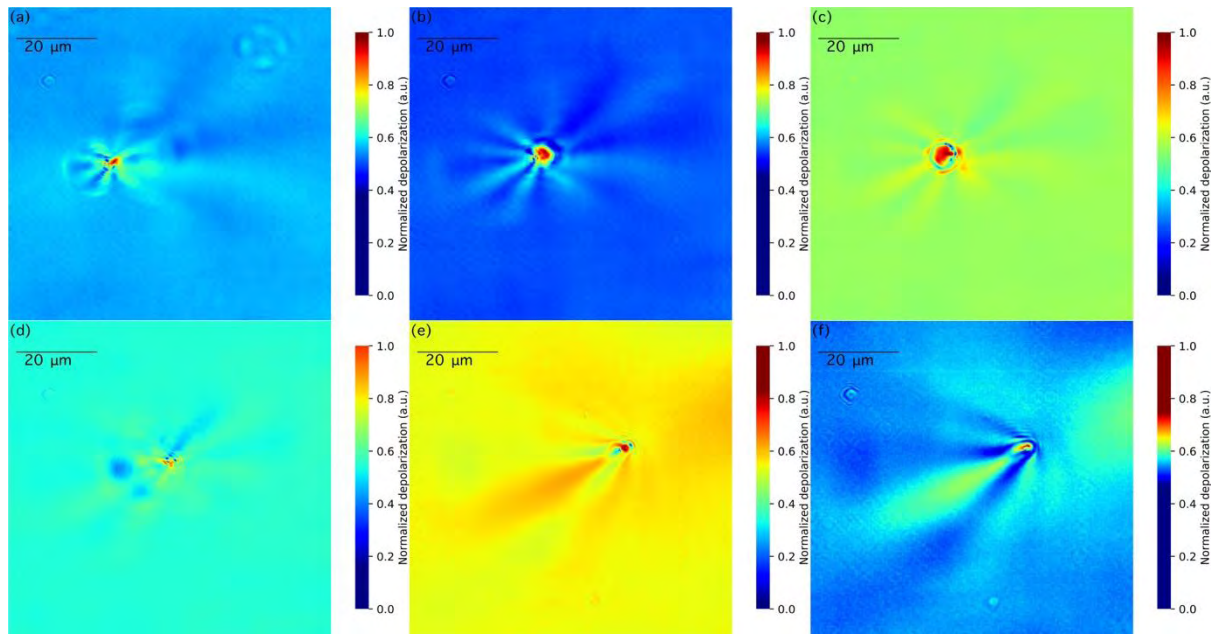


Figure 6.2.5.12 The mapping of normalized depolarization I_{dP}/I of the single micropipe in different focus positions.

In conclusion, an eight-ray structure existed around the micropipe when the micropipe is sited perpendicular to the surface of the substrate. When the micropipe is tilted within the substrate, a three-ray structure distributed on one side of the micropipe is observed. An interference pattern exists at the end of the micropipe.

6.2.6 Additional defects

This section introduces three other defects which are smaller than the two defects discussed above. Figure 6.2.6.1 shows the Stokes parameters. Unlike the situation in section 6.2.4, Fig. 6.2.6.2d shows the positive and negative division line is along two different orientations, although the polarizer is set at the same position (120°).

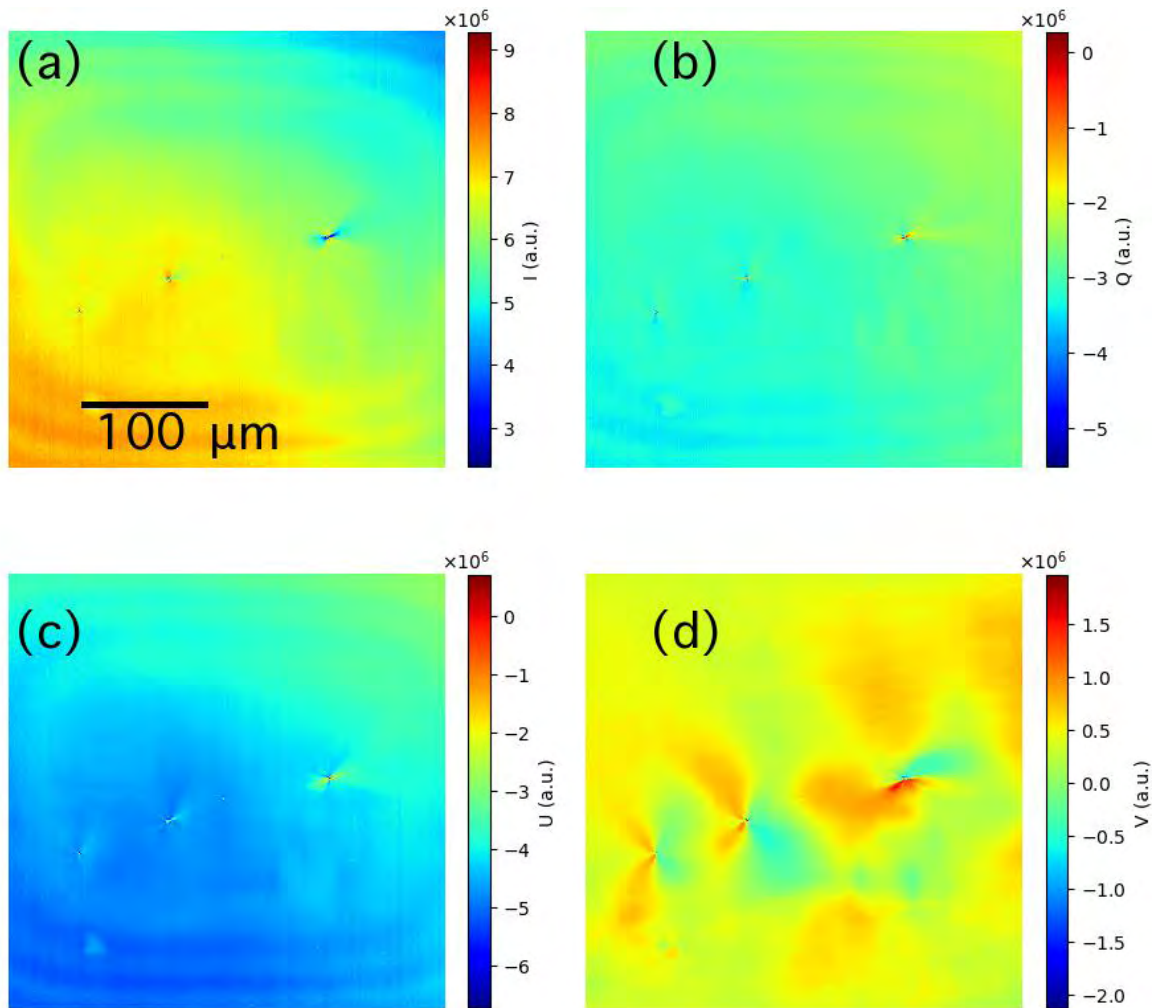


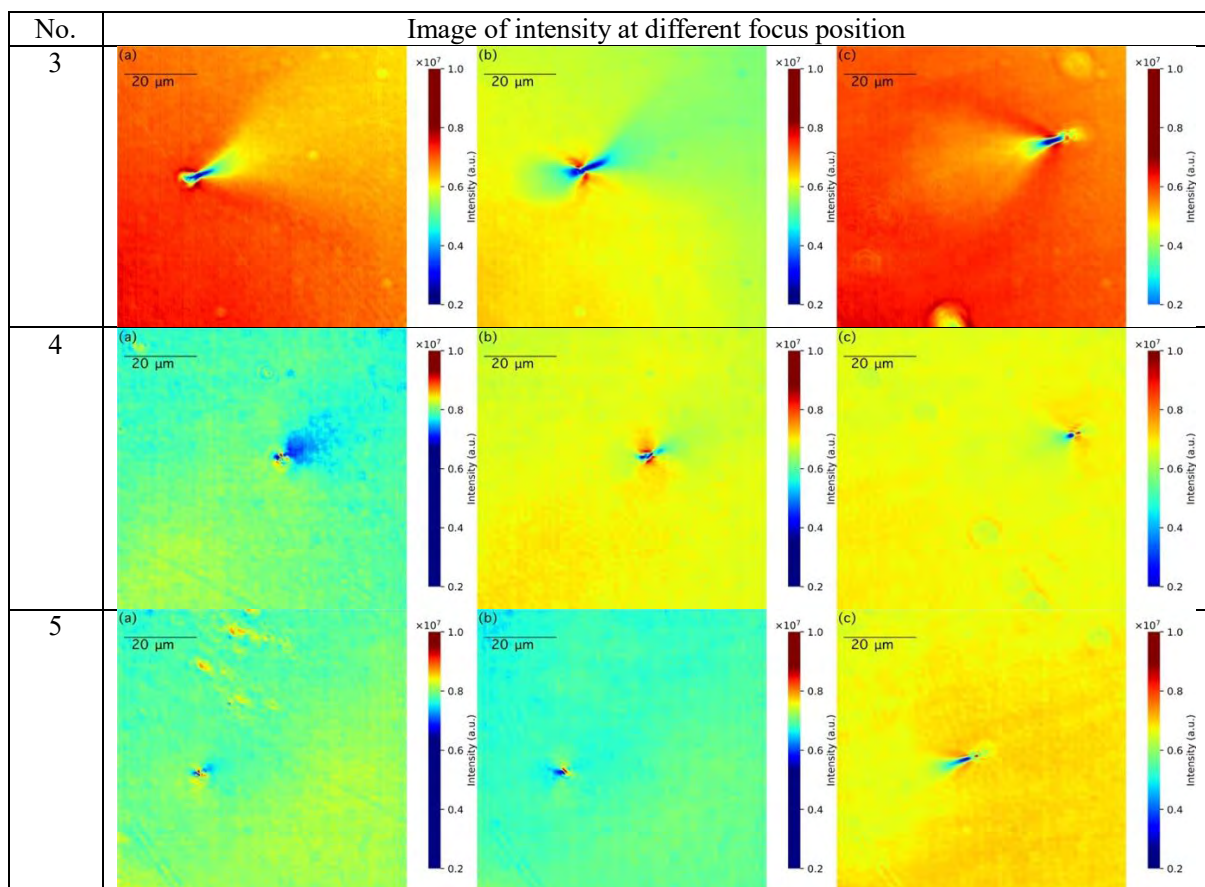
Figure 6.2.6.1 Image of contrast of the Stokes parameters at three micropipe: (a) Intensity, (b) Stokes parameter Q , (c) Stokes parameter U , (d) Stokes parameter V

In conclusion, the division line of positive and negative V for three defects are different. To clarify the situation, the three defects are magnified and observed at different focus positions.

in table 6.2.6.1. The image marked c is at the end of the micropipe. The focus position is moved from the surface (marked a) of the sample to the inside of the sample (marked c). A pipe structure is tilted located in the substrate from a to c. A tail structure is on the left of the defect in image c and on the right of the defect in image a. It may be from the hollow position of the micropipe. The image marked b is a position with two tails. It looks like a waist of the micropipe.

The image of V of the three defects is listed in table 6.2.6.2. The deviation of the positive region and negative region of the three defect is different. An interference pattern existed in the image marked c of defect 3, which be the end of the defect 3. The interference patten is not observed in the image marked a. The similar structure is seen in the image of V/I , χ , δ , and $\sin\delta$. The image of the intensity of the three defects 3, 4, and 5 at different focus position are listed in table 6.2.6.1.

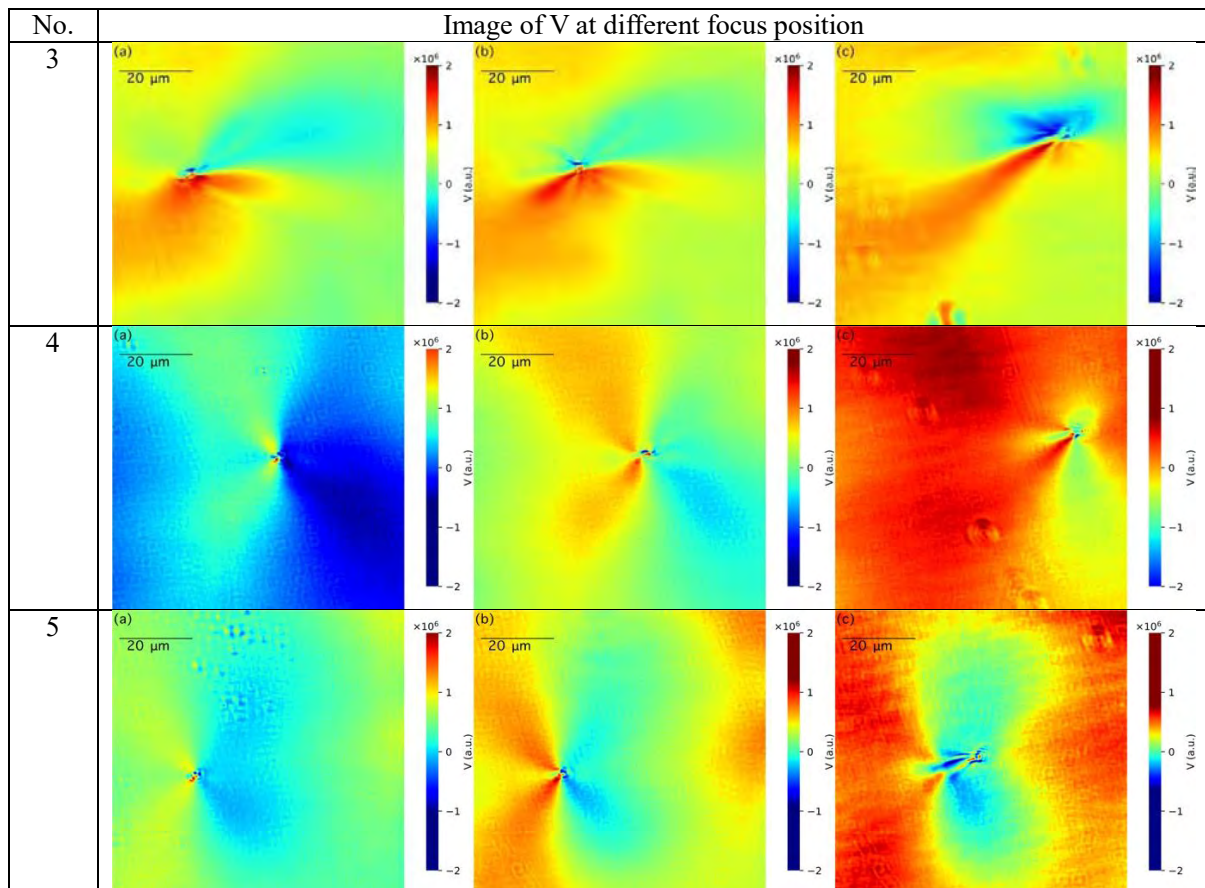
Table 6.2.6.1 The figures of intensity of defects 3, 4 and 5 at different focus position



The image of azimuth angle of the three defects is organized in the table 6.2.6.3. A tail structure is seen at the position of a hollow micropipe, shown in image marked a and c. The azimuth angle is not change generally. There is $2^\circ - 5^\circ$ variation to show the tail structure

existed at the position of a micropipe. While, the interference pattern is existed on the side of the termination of the micropipe. The micropipe of defect 5 is nearly perpendicular to the surface of the substrate but with a little tilt, that make the division line between positive and negative elliptical angle along 70° reference to the laboratory coordinate. Five rays exist near to the end of the micropipe, later, three rays exist further, shown in the image marked c of defect 5. The similar structure is existed in the image of Q , U , I_{dP} , and I_{dP}/I .

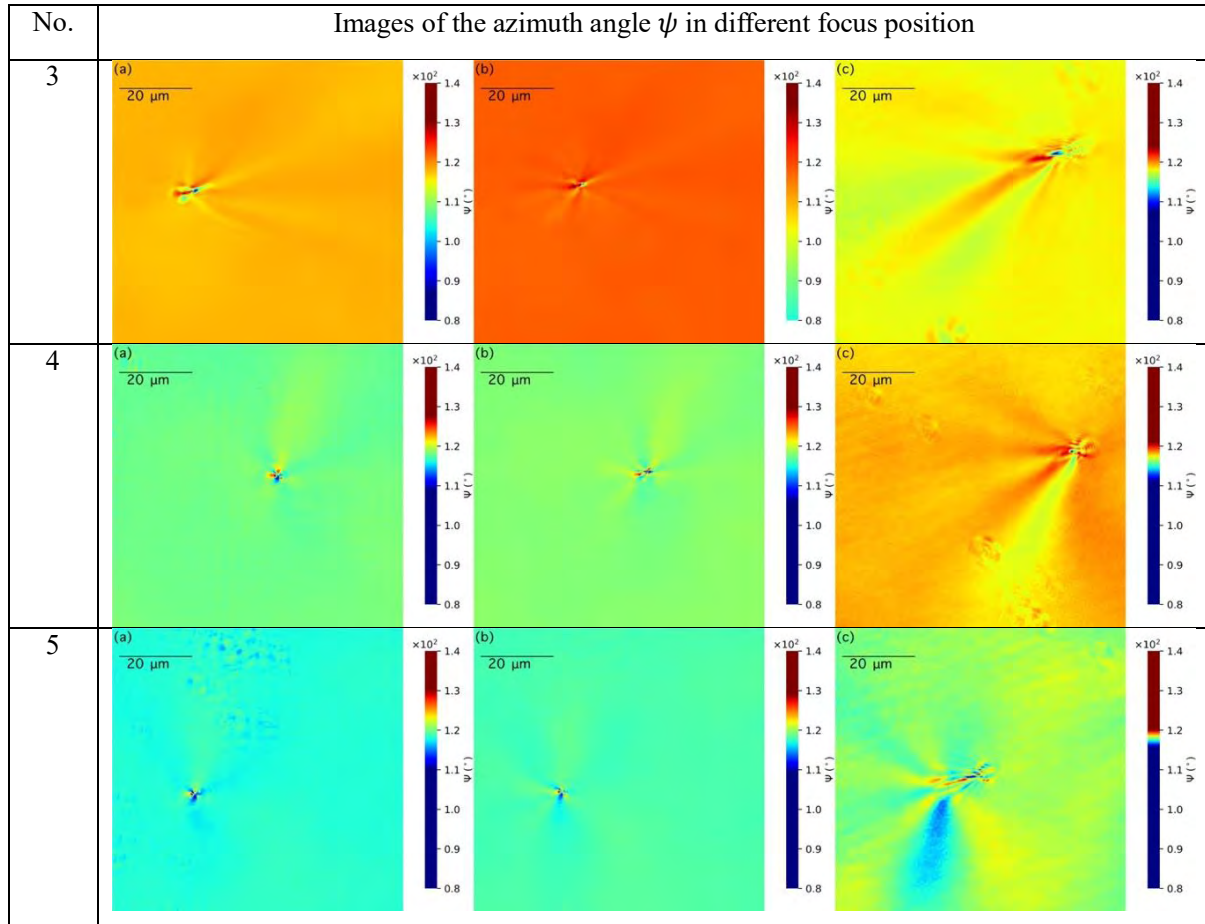
Table 6.2.6.2 The figures of Stokes parameter V of defects 3, 4 and 5 at different focus position



In conclusion, the background of the images is smooth. The defect 3 is a tube liked structure with a knot in the middle. The interference pattern exists on the right side of the termination of the micropipe on the image of V and ψ . The division line between positive V and negative V depends the defect itself. The defect 4 and defect 5 are different from the defects1, defect2,

and defect3 because of the different image of V. A tail structure existed at the position with a hollow micropipe structure on the image of ψ .

Table 6.2.6.3 The figures of azimuth angle ψ of defects 3, 4 and 5 at different focus position



6.3 Summary

Anisotropy of the structure can be observed through the polarization measurement. The non-uniformity of the substrate is detected through the Stokes polarimetric microscope. Based on the Stokes polarimetry microscope, the mapping of the polarization parameters is acquired.

Five defects are researched here. Eight rays' structure is existed on a micropipe perpendicular to the surface of the substrate. Three rays' structure is existed on a micropipe tilted along the surface of the substrate. An interference pattern existed at the termination of the micropipe.

The convergence or divergence of the micropipe can be judged through the directions of the

three rays. The normalized depolarization is near to 1 on the position of micropipe; and keeps 0.55 in most area of the substrate (which is that reflective and scattering process exist together). A flat background of the Stokes parameters can be acquired in this measurement.

Reference

Allia, P., Oldano, C., & Trossi, L. (1988). Linear optics: matrix methods. In I.-C. Khoo & F. Simoni (Eds.), *Physics of Liquid Crystalline Materials: based on lectures delivered at the summer school on the physics of liquid Crystals* (pp. 339). Italy: Gordon and Breach Science Publisher.

Hibberd, M. T., Frey, V., Spencer, B. F., Mitchell, P. W., Dawson, P., Kappers, M. J., . . .

Graham, D. M. (2016). Dielectric response of wurtzite gallium nitride in the terahertz frequency range. *Solid State Communications*, 247, 68-71. doi:10.1016/j.ssc.2016.08.017

Huard, S. (1997). *Polarization of light* (G. VACCA, Trans.). France: John Wiley & Sons Ltd.

J. Pedrós, F. C., and J. Grajal, R. J. Jiménez Riobóo, Y. Takagaki and K. H. Ploog, Z.

Bougrioua. (2005). Anisotropy-induced polarization mixture of surface acoustic waves in GaN/c-sapphire heterostructures. *Physical Review B*, 72, 075306.

Kliger, D. S., James W, L., & Randall, C. E. (Eds.). (1990). *Polarized light in optics and spectroscopy* (Vol. Appendix I). London: Academic Press Limited.

Misra, P. (2005). *Optical polarization anisotropy in nonpolar GaN thin films due to crystal symmetry and anisotropic strain*. (PhD thesis).

Misra, P., Sun, Y. J., Brandt, O., & Grahn, H. T. (2005). Polarization anisotropy and filtering for M-plane GaN films. In M. Stutzmann (Ed.), *Physica Status Solidi C - Conferences and Critical Reviews*, Vol 2, No 7 (Vol. 2, pp. 2704-2707). Weinheim: Wiley-V C H Verlag

GmbH.

Oliver Brandt, P. M., Timur Flissikowski, and Holger T. Grahn. (2013). Excitation polarization anisotropy of the spontaneous emission from an M-plane GaN film:

Competition between hole relaxation and exciton recombination. *Physical Review B*, 87, 165308.

Omae, K., Flissikowski, T., Misra, P., Brandt, O., Grahn, H. T., Kojima, K., & Kawakami, Y. (2005). Dynamic polarization filtering in anisotropically strained M-plane GaN films.

APPLIED PHYSICS LETTERS, 86(19). doi:10.1063/1.1927271

Pham, T.-T.-H., & Lo, Y.-L. (2012). Extraction of effective parameters of turbid media utilizing the Mueller matrix approach: study of glucose sensing. *Journal of Biomedical Optics*, 17(9), 097002.

Phama, T.-T.-H., & Lo, Y.-L. (2012). Extraction of effective parameters of anisotropic optical materials using a decoupled analytical method. *Journal of Biomedical Optics*, 17(2), 025006.

Zhuang, Z., Li, Y., Liu, B., Guo, X., Dai, J. P., Zhang, G. G., . . . Zhang, R. (2015). Optical polarization characteristics of c-plane InGaN/GaN asymmetric nanostructures. *Journal of Applied Physics*, 118(23). doi:10.1063/1.4938119

Chapter 7 Investigation of the polarisation characteristics of light in the vicinity of a pinhole

A pinhole is the simplest scattering system; and has been studied in theory and experiment for diffraction phenomenon. Using the polarimetric microscope to observe the pinhole helps to understand the diffraction theory of a pinhole. In this chapter, the vector field of the pinhole diffraction is measured first.

7.1 The experiment

7.1.1 The experiment of pinhole

A pinhole is a structure composing a hole in a metal. The metal used a stainless steel and its thickness is about $1\mu\text{m}$. The diameter of the pinhole is $2.5\mu\text{m}$, which is measured using the SEM shown in Fig. 7.1.1.1a. Some bulge (the diameter is around $6\mu\text{m}$.) existed outside the pinhole arising from manufacturing process. Figure 7.1.1.1b is the image of the pinhole observed with the Stokes polarimetric microscope. The shape of the bulge outside of the pinhole is observed in the image of Q, although it is not seen as clearly as that shown in the image of SEM. The pinhole is a simple structure, for only a scattering and diffraction process occurs when a light goes through the pinhole, without a refraction process. In this experiment, a linearly polarized light beam with azimuth angle of 120° is used to detect the Stokes vector of the image.

The pinhole is measured many times to obtain a best resolution shown in table 7.1.1.1. The experiment using a $64\times$ lens is reported in this section. The air conditioner is kept at $21\pm 0.5^\circ\text{C}$ because this experiment is sensitive to the room temperature.

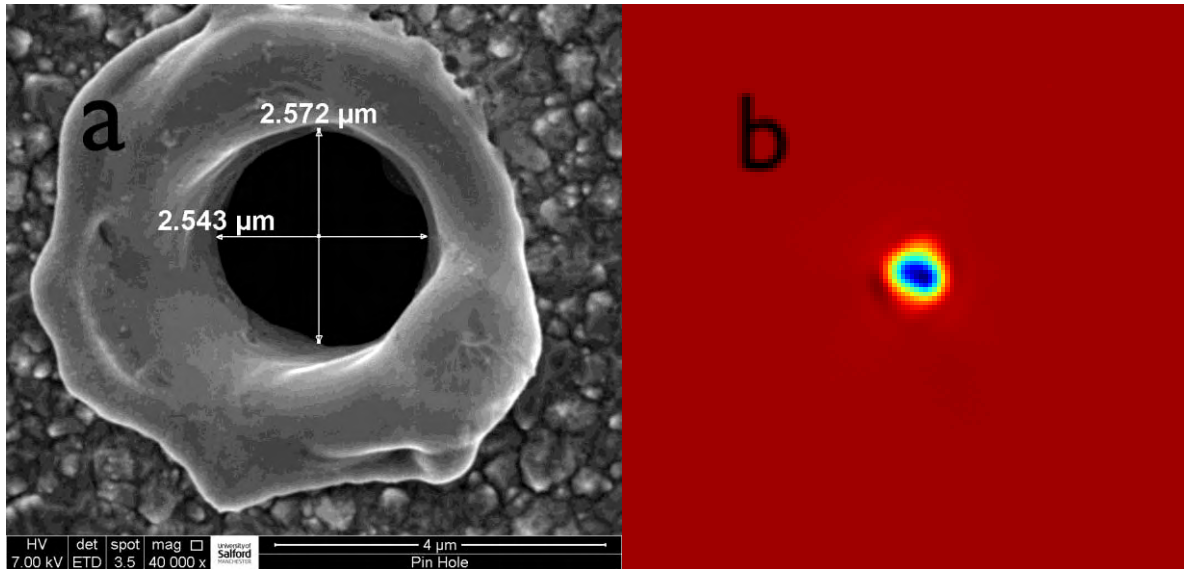


Figure 7.1.1.1 (a) the SEM picture of the pinhole used in the experiment; (b) the image of Q measured by Stokes Polarimetric microscope.

Table 7.1.1.1 the experiment of pinhole conducted using the microscope

Date	Sample	Magnification	Light	Configuration	Airconditioner	Temperature
2018/5/21	pinhole	40X	Laser	in focus or off focus		
2018/5/22	pinhole	40X	Laser	in focus/pangle change		
2019/2/8	pinhole	40X	LED	In focus	on	
2019/2/11	pinhole	40X	LED	In focus	on	
2019/2/13	Pinhole	40X	LED	In focus	on	
2019/2/15	Pinhole	40X	LED	in focus/circle	On	
2019/2/17	Pinhole	40X	LED	in focus or off focus	Off	24.2
2019/2/20	Pinhole	40X	LED	in focus or off focus	On	
2019/2/21	Pinhole	40X	LED	in focus or off focus	On	
2019/2/24	Pinhole	40X/64X	LED	in focus or off focus	On	

7.2 Results and discussion

7.2.1 Airy-like pattern from a circular aperture

The diffraction pattern of a pinhole is calculated and observed for many years. It is a good example to research the regulation of the imaging of the Stokes parameters. Adjusting the

objective lens, to choose the position of the focus plane, which is shown in Fig. 7.2.1.1. six position is chosen from the plane of the pinhole (marked a) to a position after pinhole of $5\mu\text{m}$ (marked f). All the figures marked with letters of an alphabet in next section are taken at the relevant position shown in Fig.7.2.1.1.

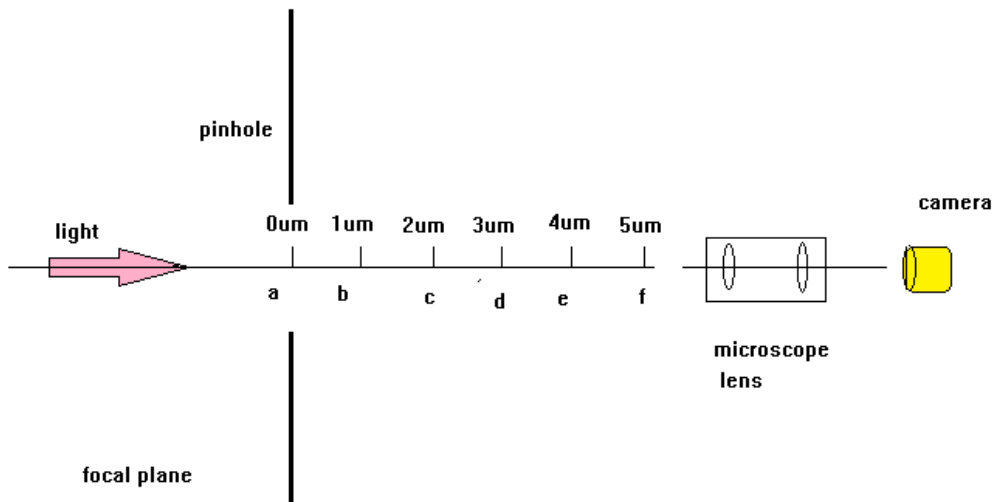


Figure 7.2.1.1 The configuration of the pinhole experiment

At the position of the light unfocused (b - f), the luminous flux decreased. The integration time is increase from b to f. The detail is shown in table 7.2.1.1.

Table 7.2.1.1 The exposure time of the images took at six planes (a-f)

Position	A	B	C	D	E	F
Exposure time (s)	0.3	0.3	0.3	0.6	0.7	0.9

Figure 7.2.1.2 shows the image of the intensity of the pinhole diffraction. It looks like Airy pattern but with a little difference, called Airy-like pattern here. In this experiment, the vector field of the light is measured. The intensity shown in Fig. 7.2.1.2 is normalized for convenience of the comparison between the image of the six position. Apparently, the intensity decreased from a to f for the defocusing process.

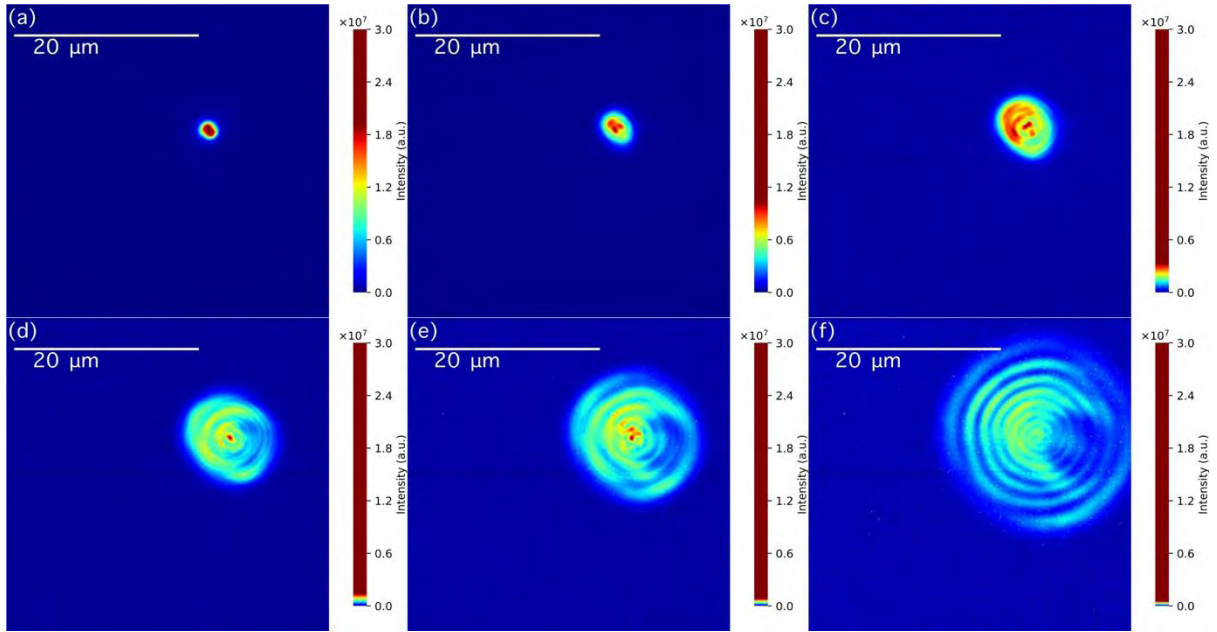


Figure 7.2.1.2 The Airy-like pattern of I for the pinhole after focus position: (a) $0 \mu\text{m}$, (b) $1 \mu\text{m}$, (c) $2 \mu\text{m}$, (d) $3 \mu\text{m}$, (e) $4 \mu\text{m}$, (f) $5 \mu\text{m}$

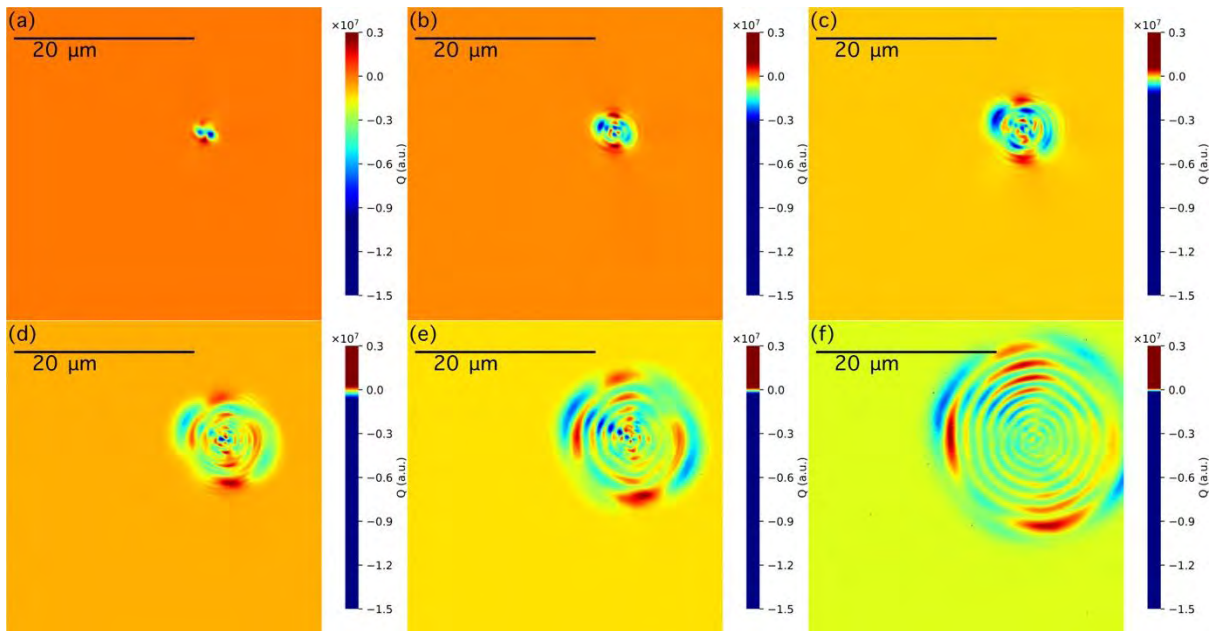


Figure 7.2.1.3 The Airy-like pattern of Q for the pinhole after focus position: (a) $0 \mu\text{m}$, (b) $1 \mu\text{m}$, (c) $2 \mu\text{m}$, (d) $3 \mu\text{m}$, (e) $4 \mu\text{m}$, (f) $5 \mu\text{m}$

Figure 7.2.1.3 to Fig. 7.2.1.5 shows the mapping of the Stokes parameters Q , U , and V . In the position between $0\mu\text{m}$ to $4\mu\text{m}$, the outside of the Airy-like pattern is an oval. The semi-minor axis is along the azimuth angle of the polarization, shown in the mapping of the I , Q , and U

from Fig. 7.2.1.3d to Fig. 7.2.1.5d. However, the mapping of the V keeps a circle in the position between $0\mu\text{m}$ to $4\mu\text{m}$. the division between positive and negative V is along the azimuth angle of the polarized light shown in Fig. 6.2.1.1.

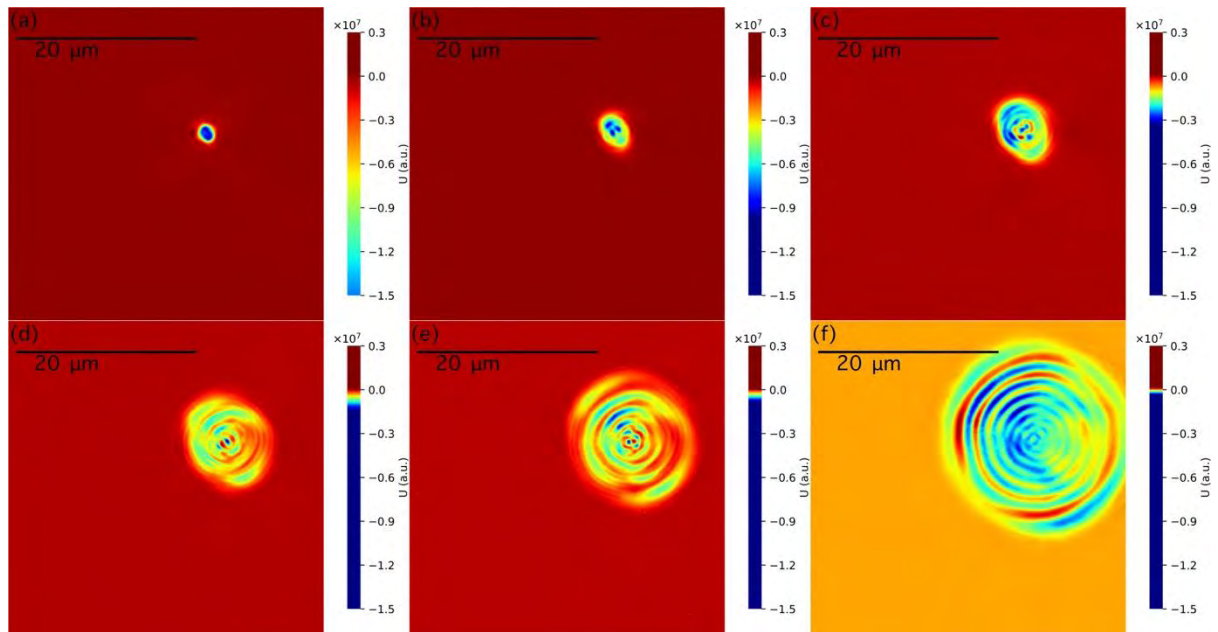


Figure 7.2.1.4 The Airy-like pattern of U for the pinhole after focus position: (a) $0\ \mu\text{m}$, (b) $1\ \mu\text{m}$, (c) $2\ \mu\text{m}$, (d) $3\ \mu\text{m}$, (e) $4\ \mu\text{m}$, (f) $5\ \mu\text{m}$

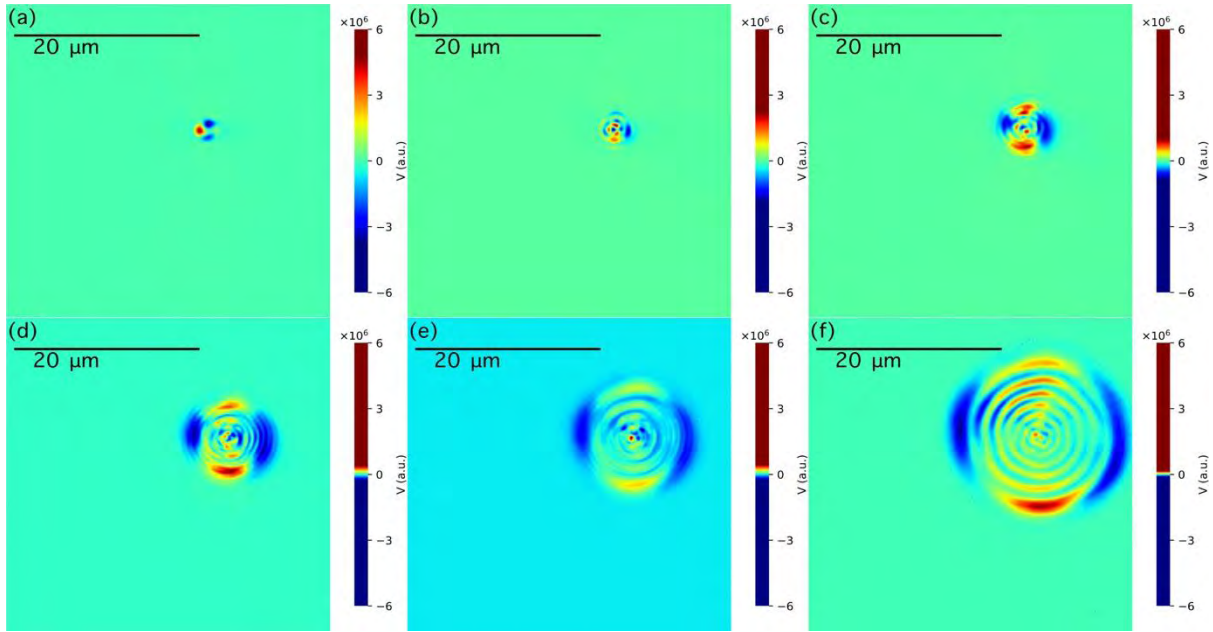


Figure 7.2.1.5 The Airy-like pattern of V for the pinhole after focus position: (a) $0 \mu\text{m}$, (b) $1 \mu\text{m}$, (c) $2 \mu\text{m}$, (d) $3 \mu\text{m}$, (e) $4 \mu\text{m}$, (f) $5 \mu\text{m}$

The elliptical angle of the pinhole is shown in Fig. 7.2.1.6. The response area of elliptical angle (the four rays structure shown in red and blue) kept between $0\mu\text{m}$ and $3\mu\text{m}$, shown from Fig. 7.2.1.6a to Fig. 7.2.1.6d; and in the position of $4\mu\text{m}$ and $5\mu\text{m}$, shown in Fig. 7.2.1.6e to Fig. 7.2.1.6f, the tail is absorbed into the Airy-like pattern. The diameter of the tail periphery keeps maximum, which is about $30\mu\text{m}$ in Fig. 7.2.1.6a; and that decrease to $20\mu\text{m}$ in Fig. 7.2.1.6d. The response areas of the mapping of the χ , ψ , δ , and $\sin\delta$, are the same, shown from Fig. 7.2.1.6 to Fig. 7.2.1.9. In position of $3\mu\text{m}$, Fig. 7.2.1.6d to Fig. 7.2.1.9d, a sub-fine structure exists with four lines in the outside circle of the Airy-like pattern. This sub-fine structure does not exist at the position of $5\mu\text{m}$ shown from Fig. 7.2.1.6f to Fig. 7.2.1.9f.

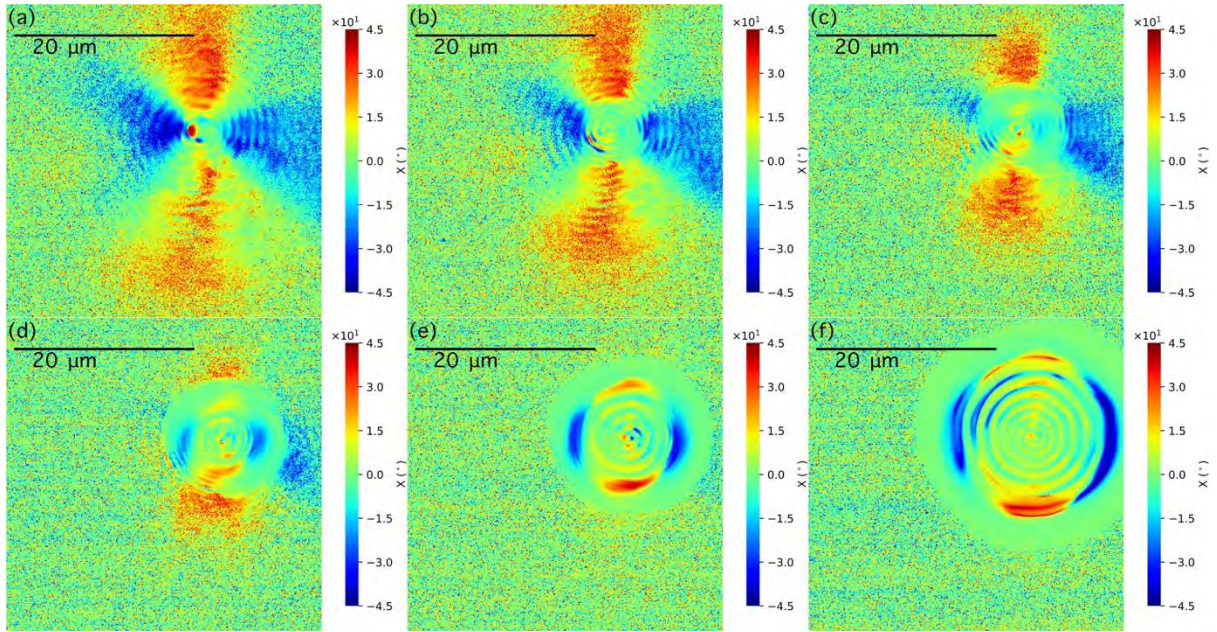


Figure 7.2.1.6 The Airy-like pattern of χ for the pinhole after focus position: (a) 0 μm , (b) 1 μm , (c) 2 μm , (d) 3 μm , (e) 4 μm , (f) 5 μm

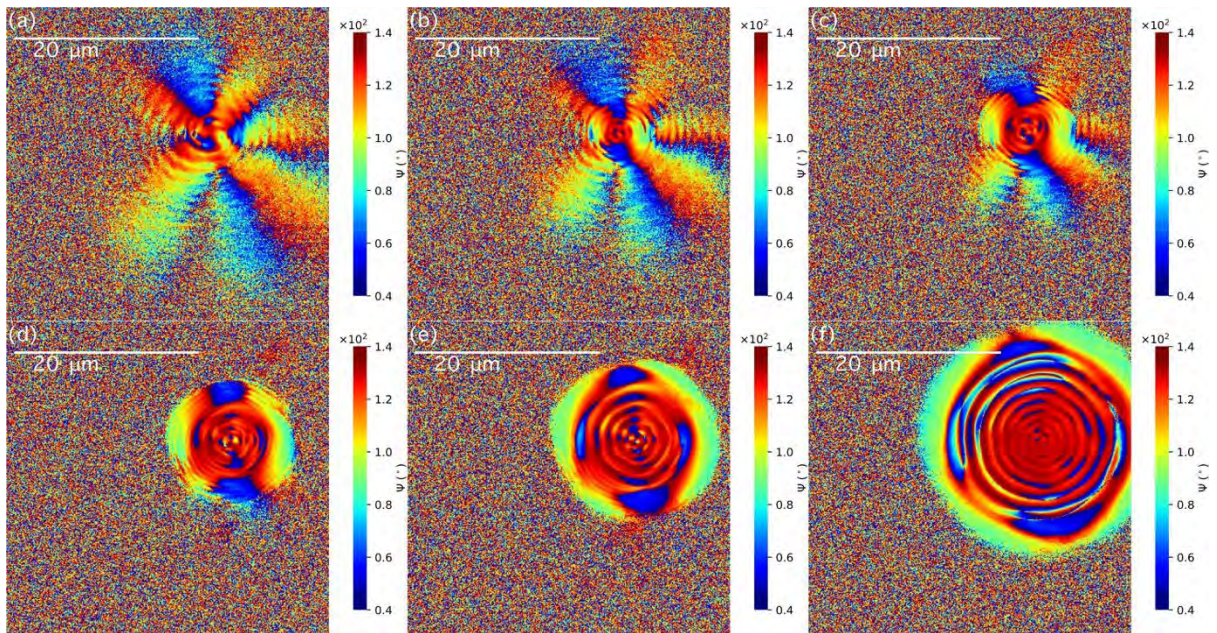


Figure 7.2.1.7 The Airy-like pattern of ψ for the pinhole after focus position: (a) 0 μm , (b) 1 μm , (c) 2 μm , (d) 3 μm , (e) 4 μm , (f) 5 μm

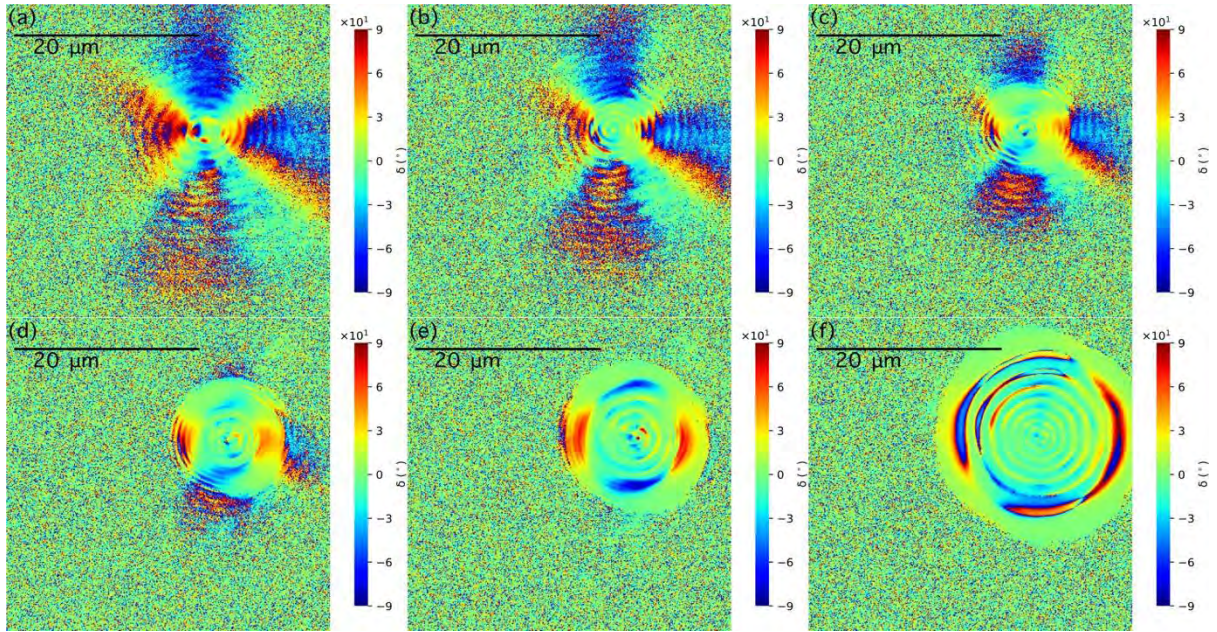


Figure 7.2.1.8 The Airy-like pattern of δ for the pinhole after focus position: (a) $0 \mu\text{m}$, (b) $1 \mu\text{m}$, (c) $2 \mu\text{m}$, (d) $3 \mu\text{m}$, (e) $4 \mu\text{m}$, (f) $5 \mu\text{m}$

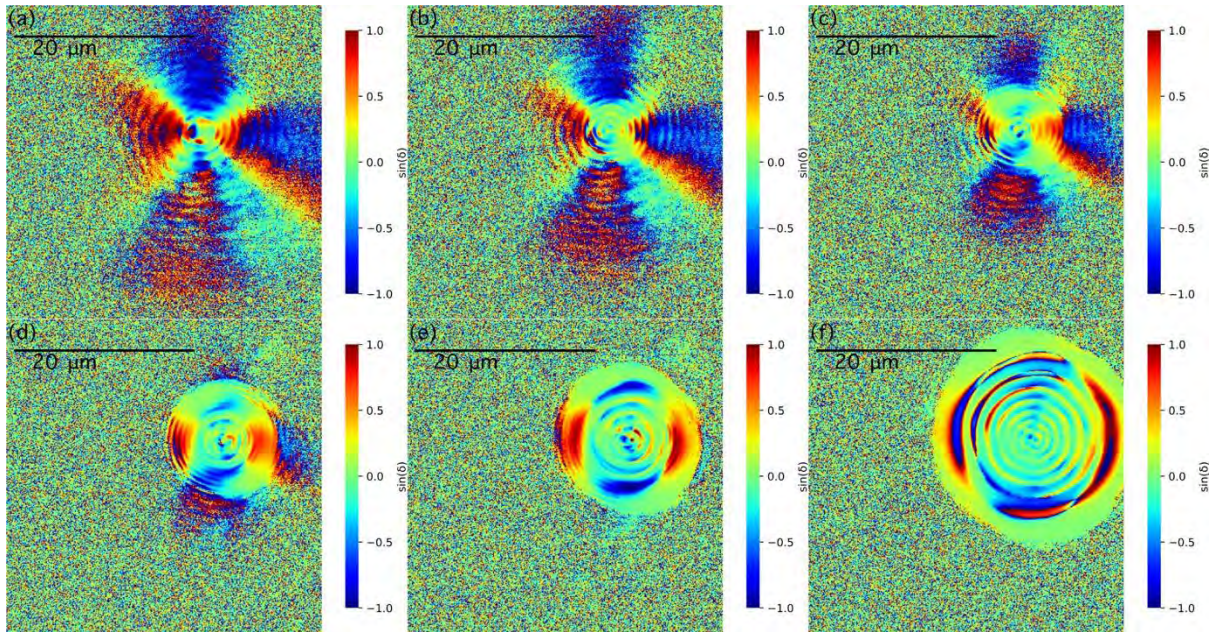


Figure 7.2.1.9 The Airy-like pattern of $\sin(\delta)$ for the pinhole after focus position: (a) $0 \mu\text{m}$, (b) $1 \mu\text{m}$, (c) $2 \mu\text{m}$, (d) $3 \mu\text{m}$, (e) $4 \mu\text{m}$, (f) $5 \mu\text{m}$

The image quality of the normalized Stokes parameter is very poor, because the intensity in the surrounding area of the pinhole is near to zero, which makes the normalized Stokes parameter an infinite number, which make the image of the normalized signal invisible.

Figure 7.2.1.10 to Fig. 7.2.1.13 are obtained through getting rid of the noise data. The Sign of Q/I and U/I are opposite.

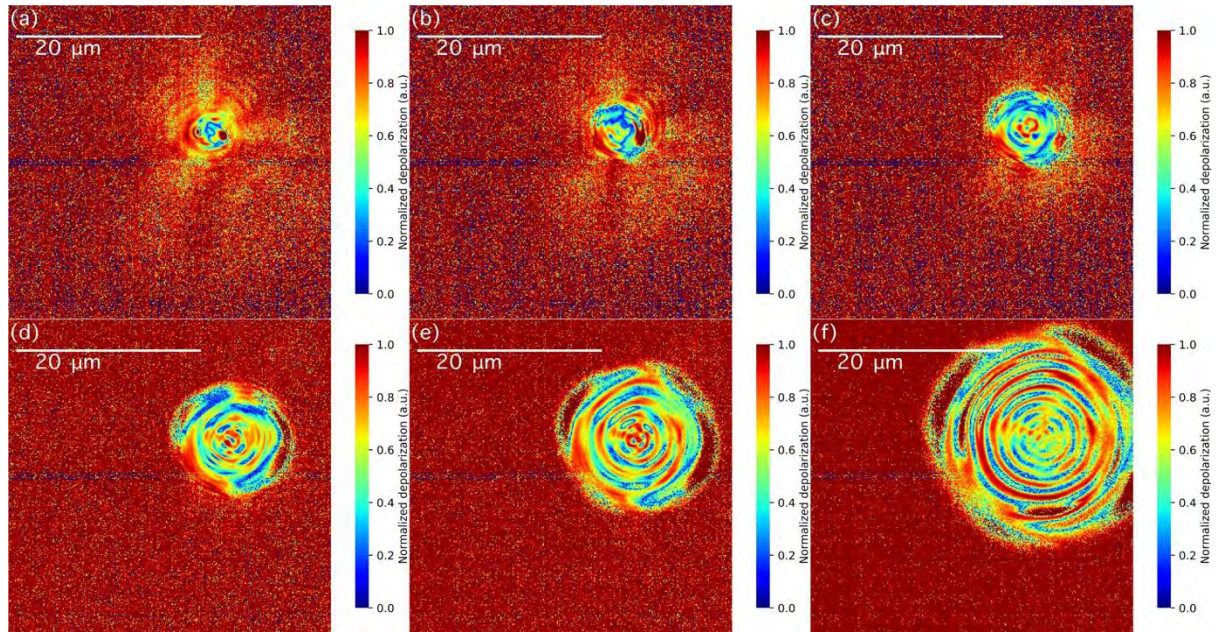


Figure 7.2.1.10 The Airy-like pattern of I_{dP}/I for the pinhole after focus position: (a) 0 μm, (b) 1 μm, (c) 2 μm, (d) 3 μm, (e) 4 μm, (f) 5 μm

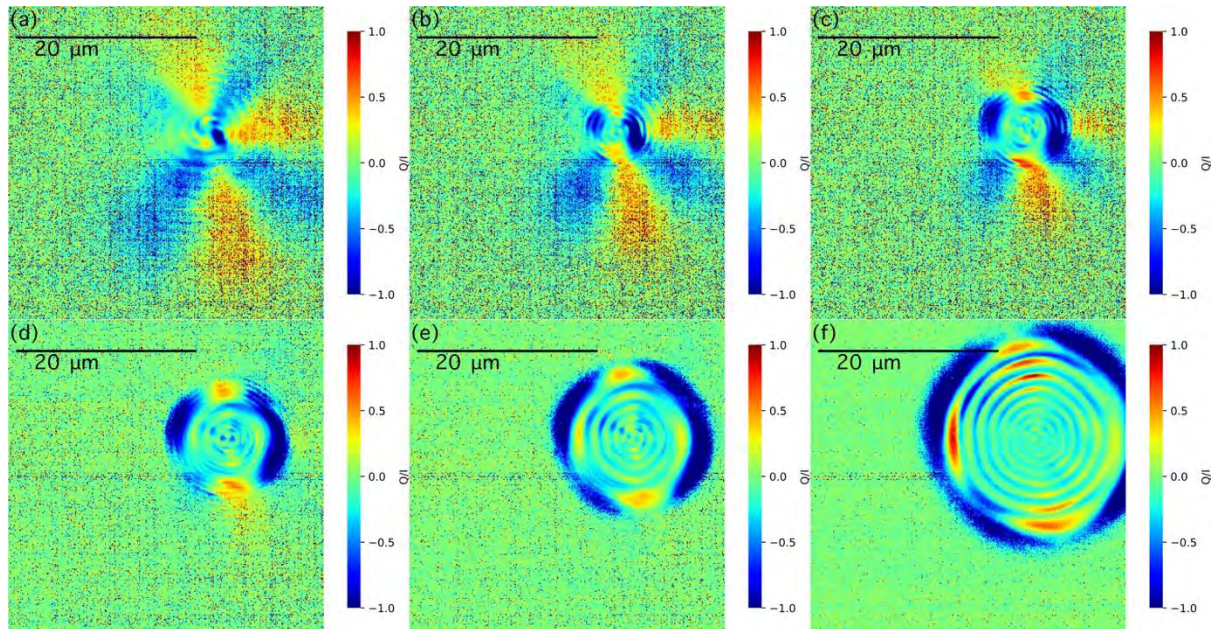


Figure 7.2.1.11 The Airy pattern of Q/I for the pinhole after focus position: (a) 0 μm, (b) 1 μm, (c) 2 μm, (d) 3 μm, (e) 4 μm, (f) 5 μm

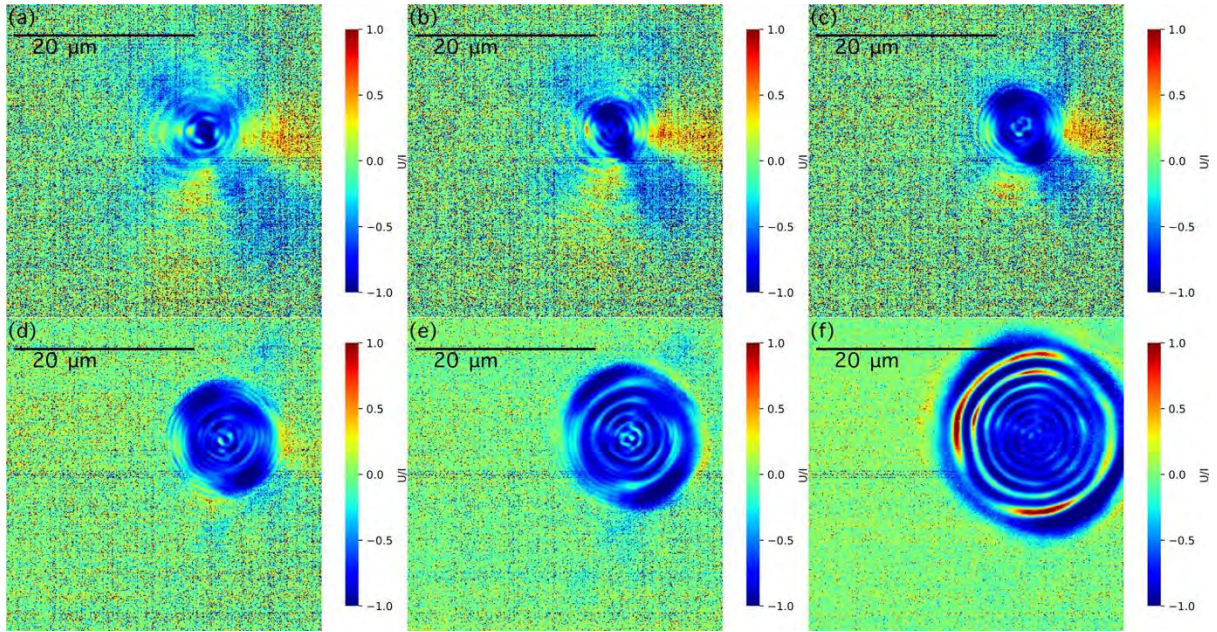


Figure 7.2.1.12 The Airy-like pattern of U/I for the pinhole after focus position: (a) $0 \mu\text{m}$, (b) $1 \mu\text{m}$, (c) $2 \mu\text{m}$, (d) $3 \mu\text{m}$, (e) $4 \mu\text{m}$, (f) $5 \mu\text{m}$

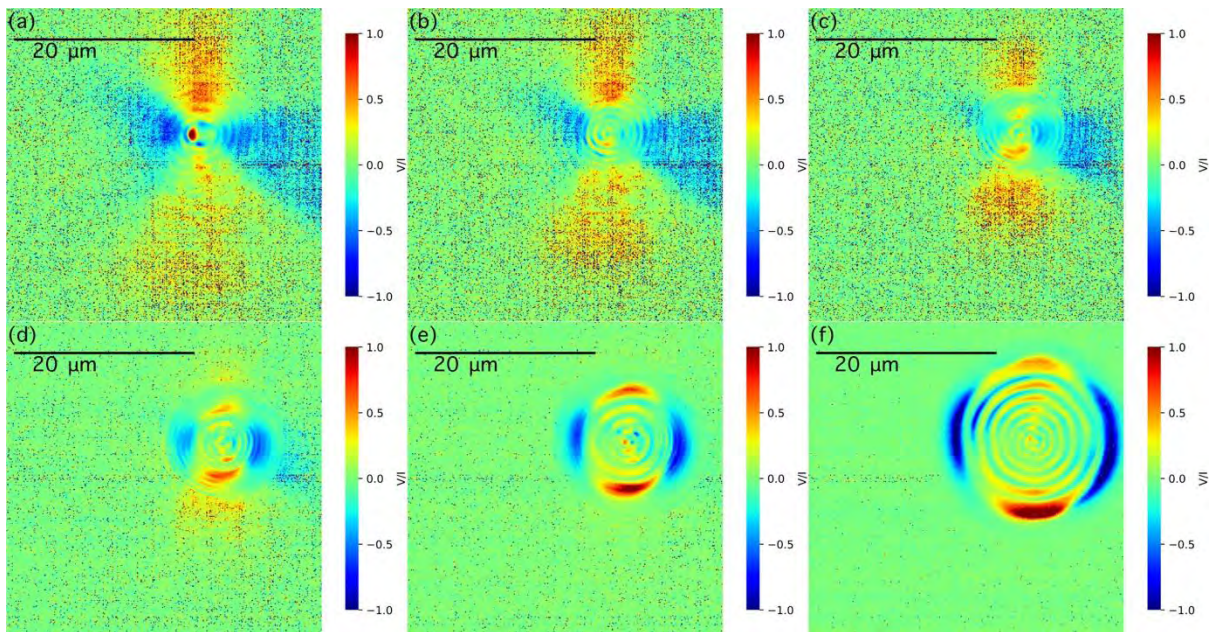


Figure 7.2.1.13 The Airy-like pattern of V/I for the pinhole after focus position: (a) $0 \mu\text{m}$, (b) $1 \mu\text{m}$, (c) $2 \mu\text{m}$, (d) $3 \mu\text{m}$, (e) $4 \mu\text{m}$, (f) $5 \mu\text{m}$

The local polarization states, a complex field vector, may be experimentally determined, assuming a plane wave normal incidence onto the sample. Figure 7.2.1.14 and Fig. 7.2.1.15 show the mapping of the modulus of the of electric filed $|E_x|$ and $|E_y|$: the distribution of patterns of $|E_x|$ and $|E_y|$ are complementary.

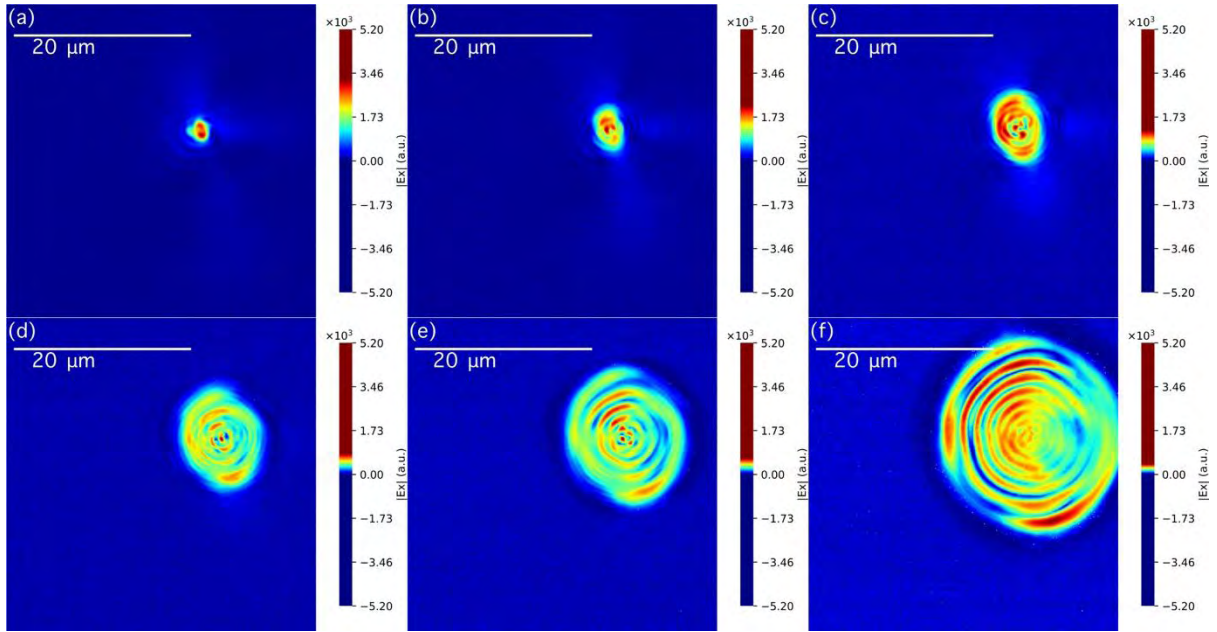


Figure 7.2.1.14 The Airy-like pattern of $|E_x|$ for the pinhole after focus position: (a) $0 \mu\text{m}$, (b) $1 \mu\text{m}$, (c) $2 \mu\text{m}$, (d) $3 \mu\text{m}$, (e) $4 \mu\text{m}$, (f) $5 \mu\text{m}$

A clockwise vortex structure is seen in Fig. 7.2.1.14b to Fig. 7.2.1.14e, which do not exist in Fig. 7.2.1.14f. This structure can't be seen in Fig. 7.2.1.15.

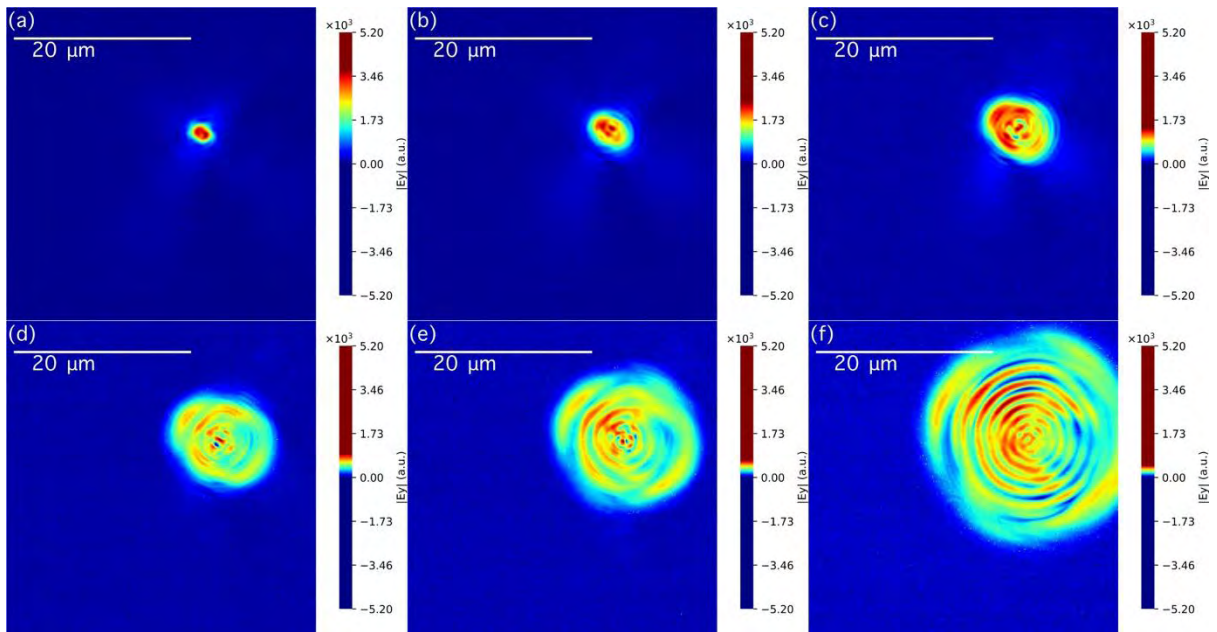


Figure 7.2.1.15 The Airy-like pattern of $|E_y|$ for the pinhole after focus position: (a) $0 \mu\text{m}$, (b) $1 \mu\text{m}$, (c) $2 \mu\text{m}$, (d) $3 \mu\text{m}$, (e) $4 \mu\text{m}$, (f) $5 \mu\text{m}$

The electric field is a complex number. The mapping of real part and imaginary part of the electric field E_y are shown in Fig.7.2.1.16 and Fig. 7.2.1.17.

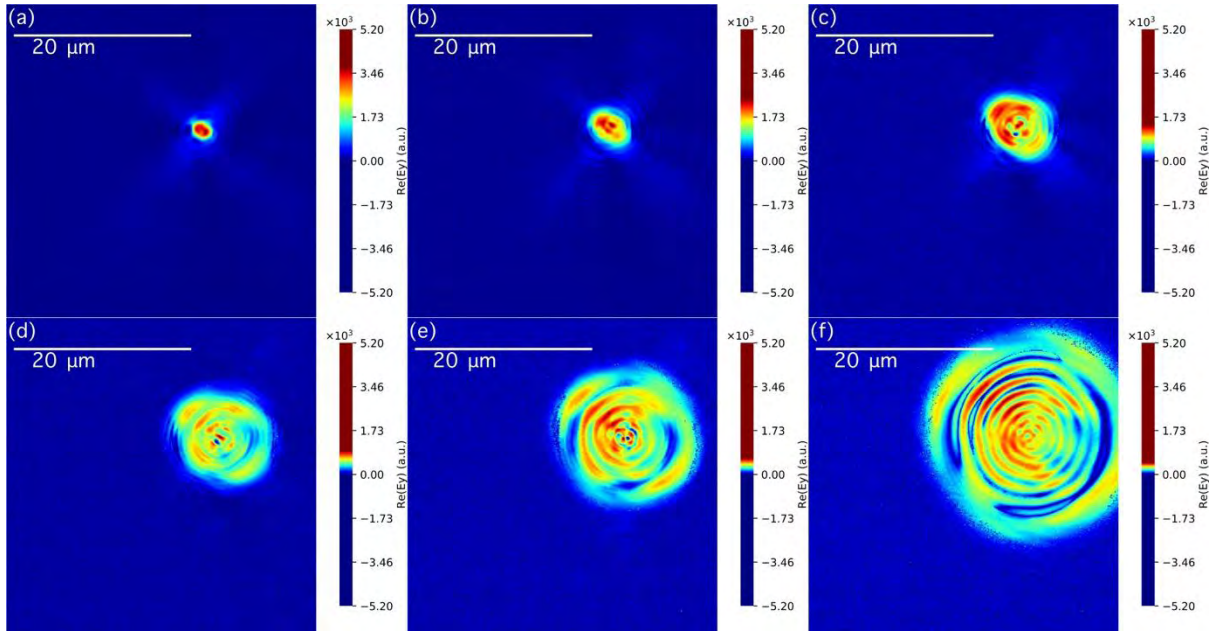


Figure 7.2.1.16 The Airy pattern of real part of E_y for the pinhole after focus position: (a) $0 \mu\text{m}$, (b) $1 \mu\text{m}$, (c) $2 \mu\text{m}$, (d) $3 \mu\text{m}$, (e) $4 \mu\text{m}$, (f) $5 \mu\text{m}$

The imaginary part shown in Fig. 7.2.1.17 is similar to that of V/I , but with the four lines of the sub-fine structure more visible. The position of $4 \mu\text{m}$ is a threshold position what the four lines sub-fine structure begins to disappear.

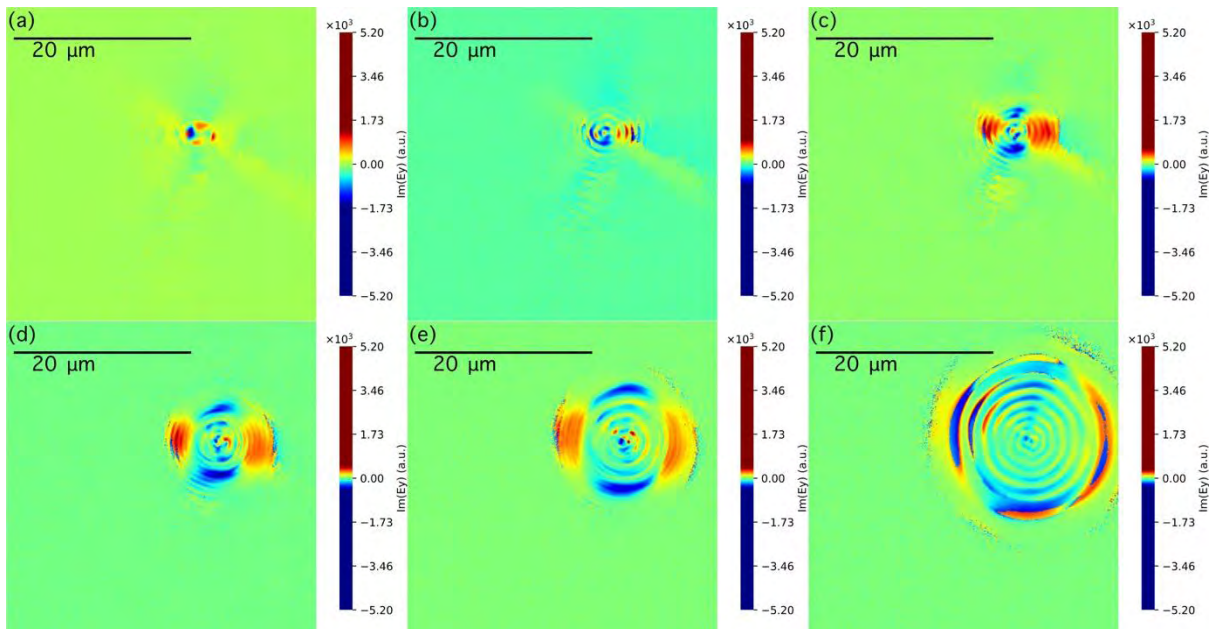


Figure 7.2.1.17 The Airy pattern of imaginary part of E_y for the pinhole after focus position: (a) $0 \mu\text{m}$, (b) $1 \mu\text{m}$, (c) $2 \mu\text{m}$, (d) $3 \mu\text{m}$, (e) $4 \mu\text{m}$, (f) $5 \mu\text{m}$

In conclusion, the response area of the mapping of the relevant angles on polarization

$(\chi, \psi, \delta, \sin\delta)$ is about $30\mu\text{m}$ for a pinhole whose diameter is about $2.5\ \mu\text{m}$. The range of the response area decreases with the increase of the distance from the pinhole. The image quality of the normalized Stokes parameters is poor because the intensity is very small on far from the pinhole. A four lines sub-fine structure exists between 0 to $3\ \mu\text{m}$ and disappears at $5\ \mu\text{m}$. At position of $4\ \mu\text{m}$, the sub-fine structure is starting to disappear. A clockwise vortex structure existed in the image of the modulus of the electrical field along x-axis.

7.2.2 Mapping of the polarization parameter before the pin hole

This section introduces the image before the pinhole. The rays structure exists, but no rings comparing the situation shown in section 7.2.1. I suppose the ray structure is from the scattering at the edge of the pinhole. The focal plane in this case is about $5\mu\text{m}$ before the pinhole. The image of relevant angles is shown in Fig. 7.2.2.1. The image of Stokes parameters is shown in Fig. 7.2.2.2. The image of V is special.

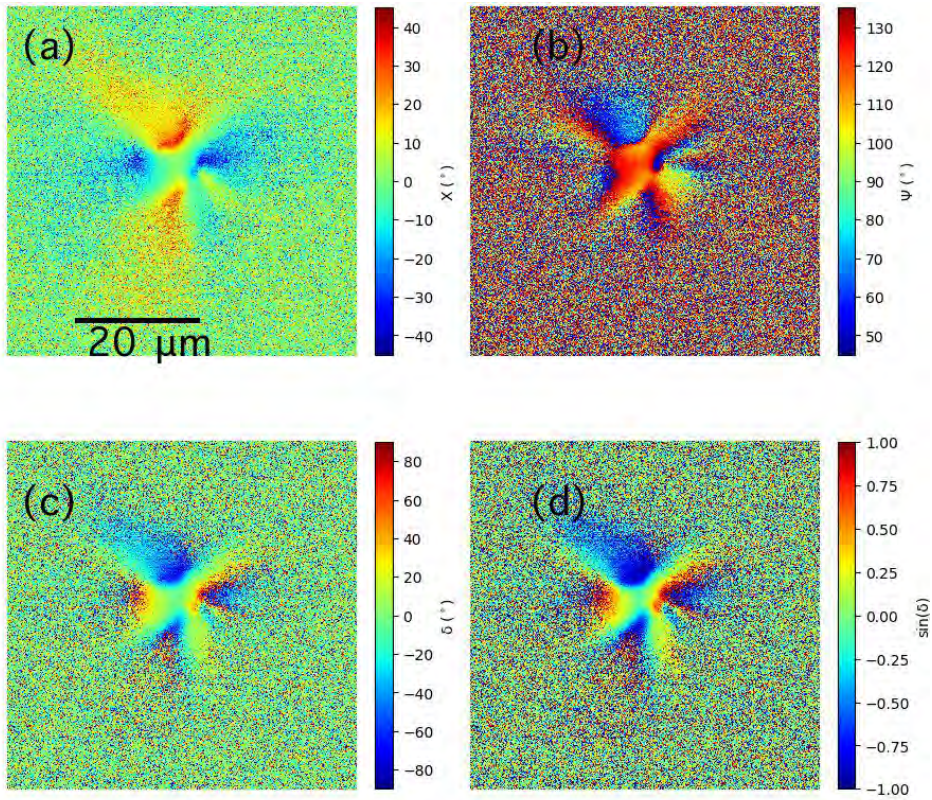


Figure 7.2.2.1 The contrast image of (a) the elliptical angle χ , (b) the azimuth angle ψ , (c) the retardation of phase δ , and (d) the $\sin(\delta)$.

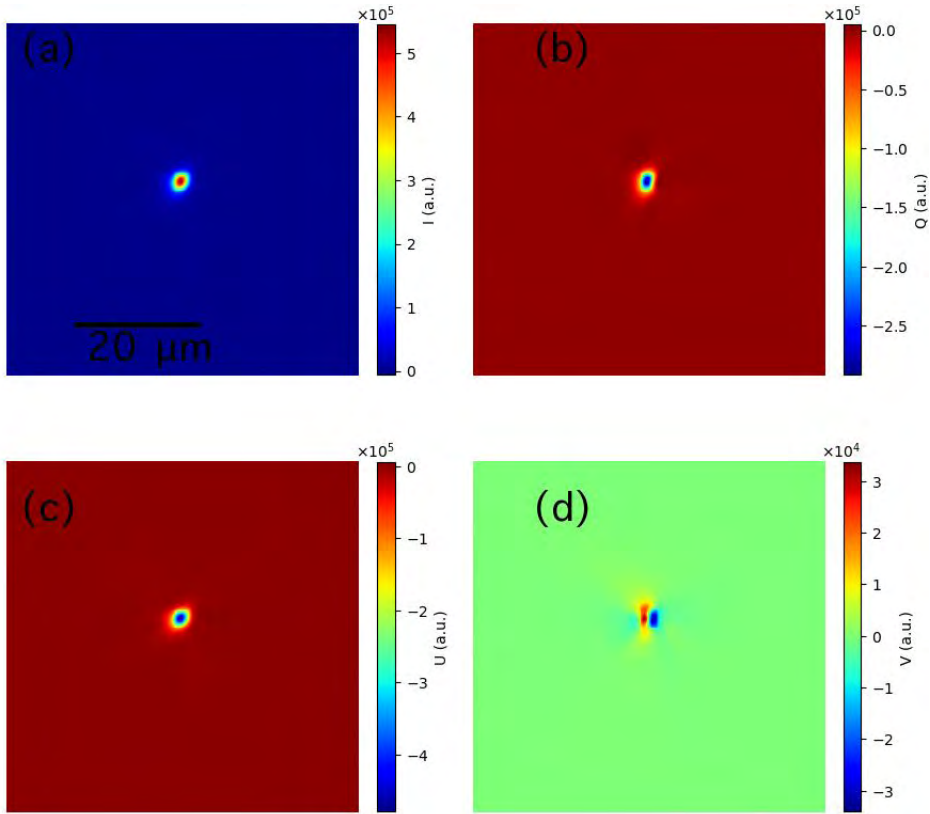


Figure 7.2.2.2 Image of contrast of the Stokes parameters on pinhole: (a) Intensity, (b) Stokes parameter Q , (c) Stokes parameter U , (d) Stokes parameter V .

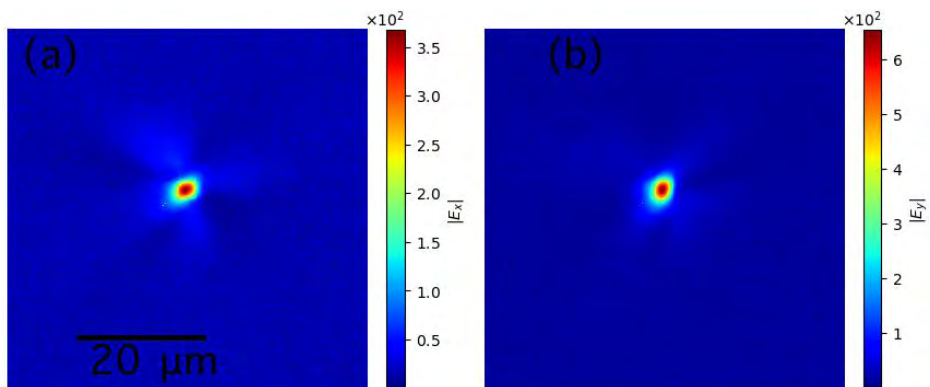


Figure 7.2.2.3 The modulus of the electric field with reference to the laboratory coordinate.

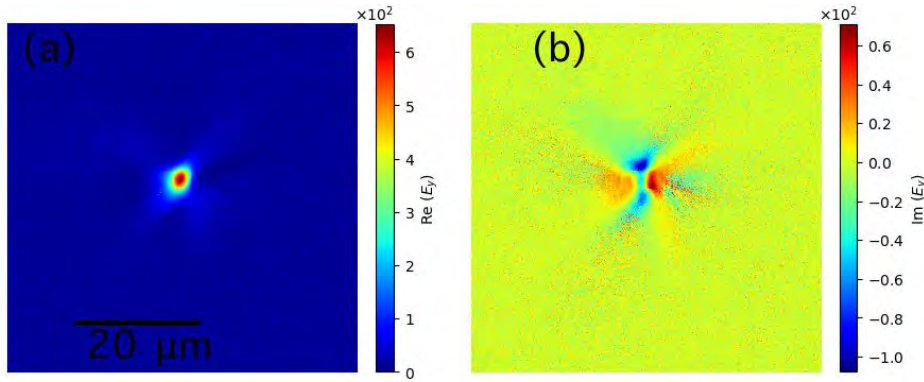


Figure 7.2.2.4 The electric field along y-axis: (a) real part and (b) the imaginary part.

In conclusion, the ray structure exists on both sides of the pinhole; while, the Airy pattern only exists after the pinhole. The ray structure may from the scattering of a bulge.

7.2.3 The situation in front of and behind the pinhole

It is interesting to observe the situation in front of the pinhole and behind the pinhole. This section compares the mapping of polarization parameters in the position near to the pinhole.

The shape of the mapping of intensity changes when the light going through, shown in Fig.

7.2.3.1. The shape on the focus is a circle only in the focused position, and an oval on the unfocused position. The semi-major axis of oval is along the azimuth angle in front of the pinhole and perpendicular to the azimuth angle behind the pinhole. The orthogonal

relationship of the semi-major axis of oval between the position in front of the pin hole and

behind the pinhole is also exist in the mapping of the Q and U in Fig. 7.2.3.2 and Fig. 7.2.3.3.

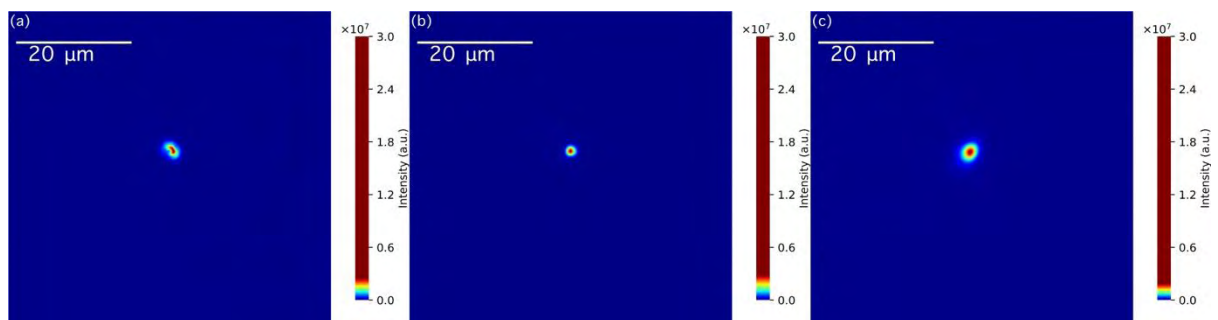


Figure 7.2.3.1 The mapping of I for the pinhole: (a) the object plane behind the pinhole; (b)

the object plane on the pinhole; (c) the object plane in front of the pinhole

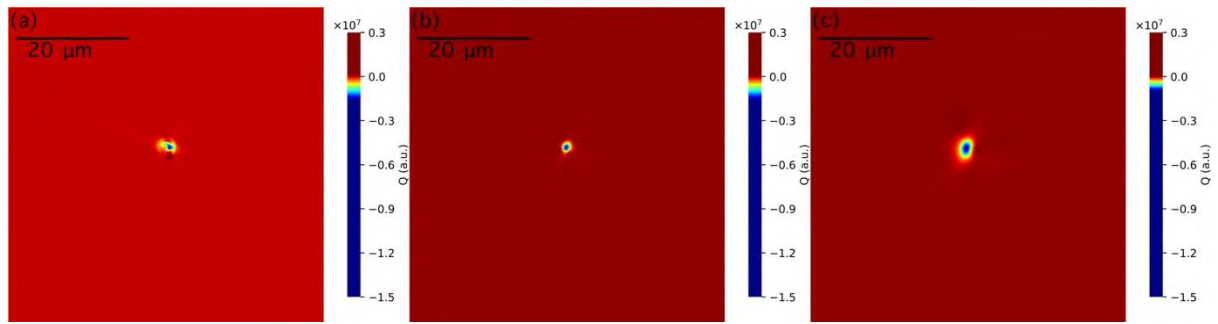


Figure 7.2.3.2 The mapping of Q for the pinhole: (a) the object plane behind the pinhole; (b) the object plane on the pinhole; (c) the object plane in front of the pinhole

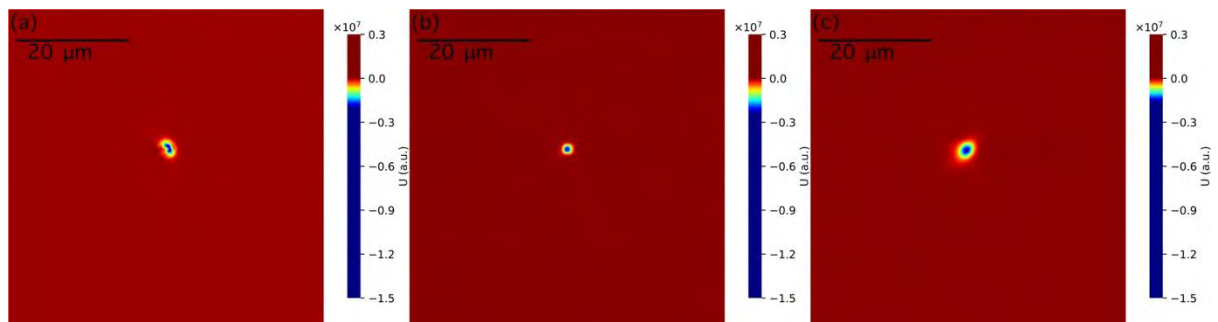


Figure 7.2.3.3 The mapping of U for the pinhole: (a) the object plane behind the pinhole; (b) the object plane on the pinhole; (c) the object plane in front of the pinhole

The mapping of V shown in Fig. 7.2.3.4b is a structure of four parts. The position near to the pinhole is divided into positive and negative along the azimuth angle. The V is negative on the left side of the azimuth angle, while, on the right side of the azimuth angle is positive.

The mapping of V in front of the pinhole is a structure double lines with positive and negative together and with an angle to the azimuth angle of polarization about 45° .

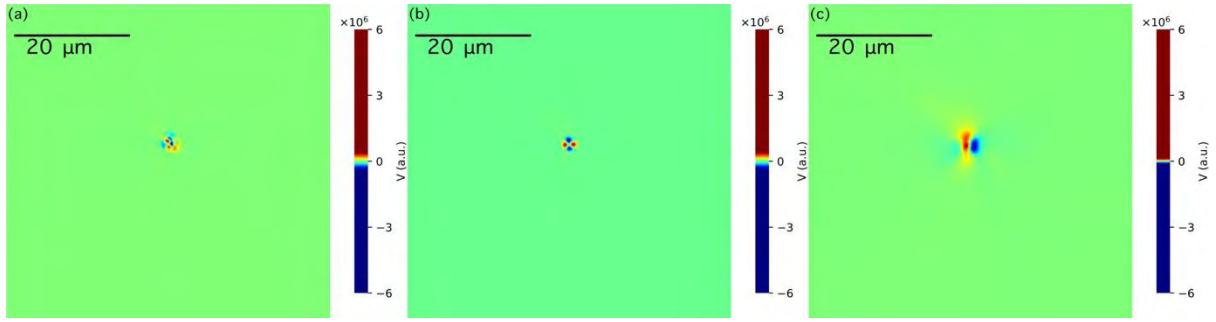


Figure 7.2.3.4 The mapping of V for the pinhole: (a) the object plane behind the pinhole; (b) the object plane on the pinhole; (c) the object plane in front of the pinhole;

The normalized depolarization keeps zero in the middle of the pinhole; and the shape of the ovals is same to the regulation of I , Q , and U . The rings and the rays can be seen on the position behind the pinhole, shown in Fig.7.2.3.5a, Fig.7.2.3.6a, and Fig.7.2.3.7a. However, only rays exist in front of the pinhole, shown in Fig.7.2.3.5c, Fig.7.2.3.6c, and Fig.7.2.3.7c. On the position of pinhole, the rays and four parts structure exist together, exist on the image of the normalized Stokes parameters.

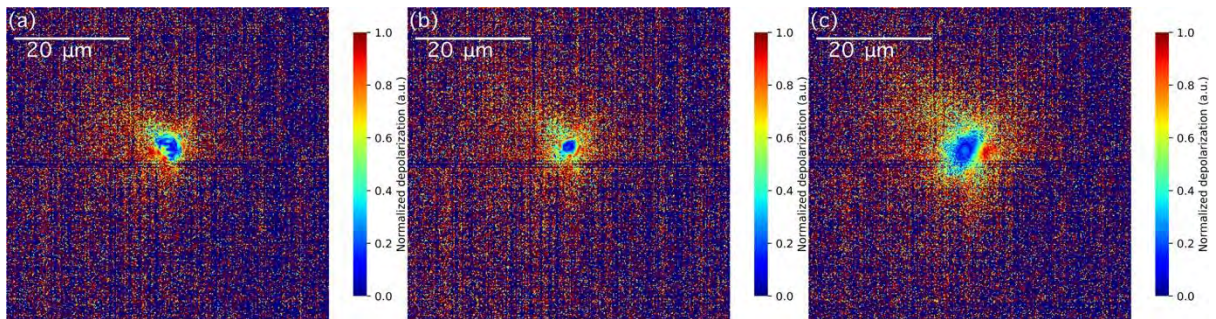


Figure 7.2.3.5 The mapping of I_{DP}/I for the pinhole: (a) the object plane behind the pinhole; (b) the object plane on the pinhole; (c) the object plane in front of the pinhole

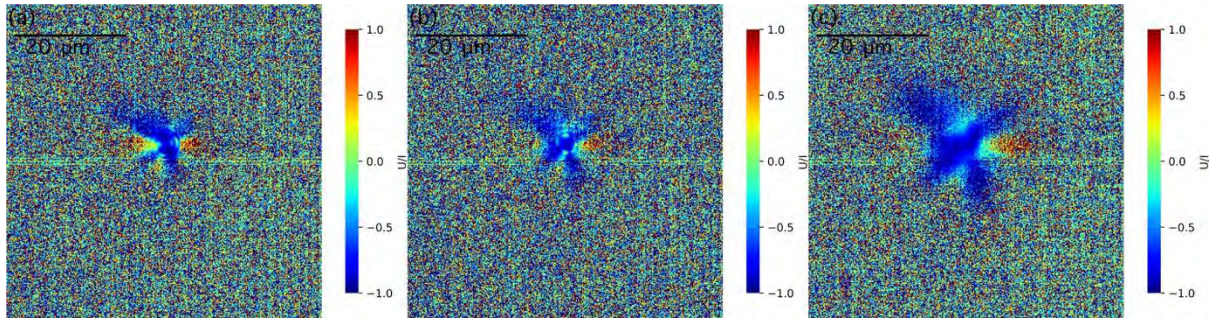


Figure 7.2.3.6 The mapping of U/I for the pinhole: (a) the object behind plane the pinhole; (b) the object plane on the pinhole; (c) the object plane in front of the pinhole

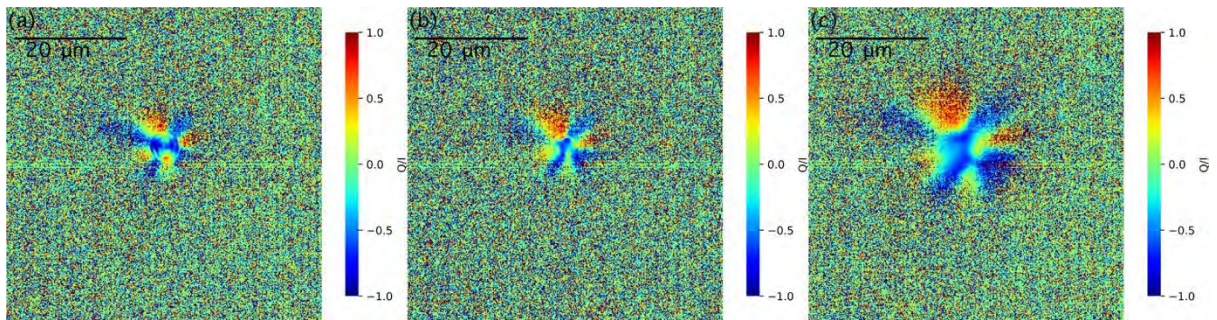


Figure 7.2.3.7 The mapping of Q/I for the pinhole: (a) the object behind plane the pinhole; (b) the object plane on the pinhole; (c) the object plane in front of the pinhole

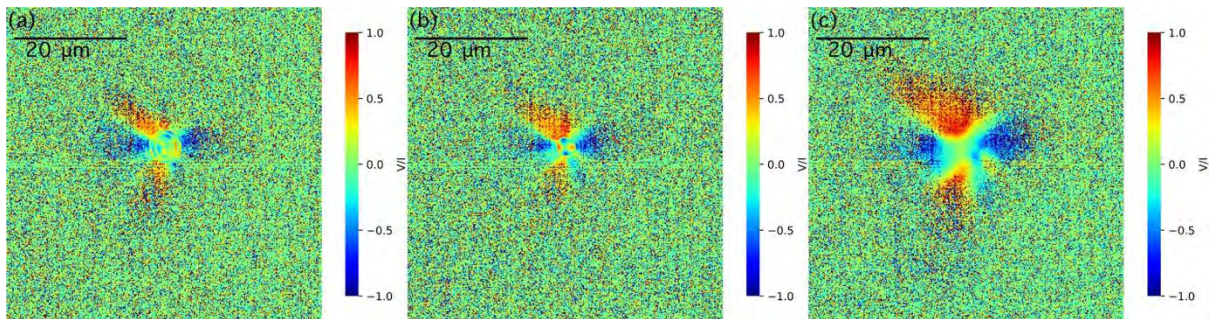


Figure 7.2.3.8 The mapping of V/I for the pinhole: (a) the object plane behind plane the pinhole; (b) the object plane on the pinhole; (c) the object plane in front of the pinhole

Figure 7.2.3.9 to Fig.7.2.3.11 are the relative angles in polarization characterization: elliptical angle χ , azimuth angle ψ , and phase difference δ . The structure is similar to that of V/I .

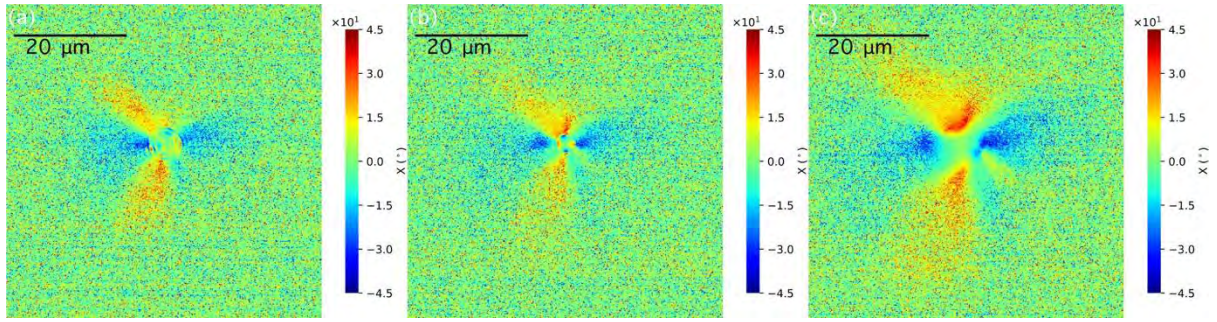


Figure 7.2.3.9 The mapping of χ for pinhole: (a) the object plane behind plane the pinhole; (b) the object plane on the pinhole; (c) the object plane in front of the pinhole

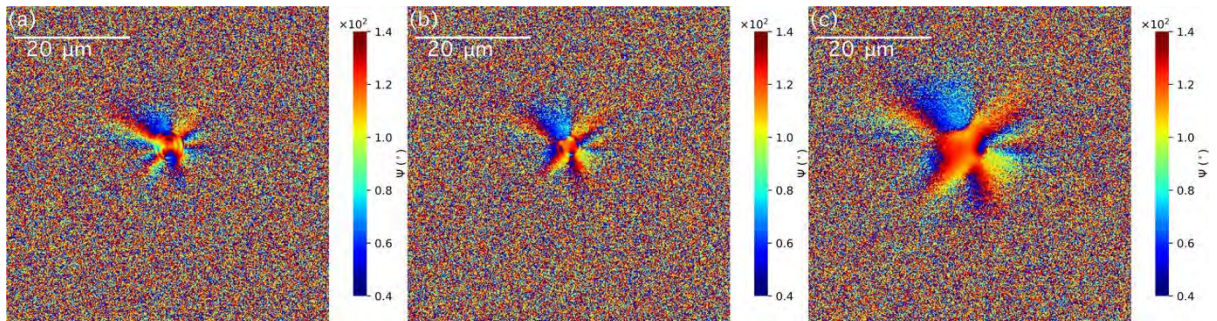


Figure 7.2.3.10 The mapping of ψ for the pinhole: (a) the object plane behind plane the pinhole; (b) the object plane on the pinhole; (c) the object plane in front of the pinhole

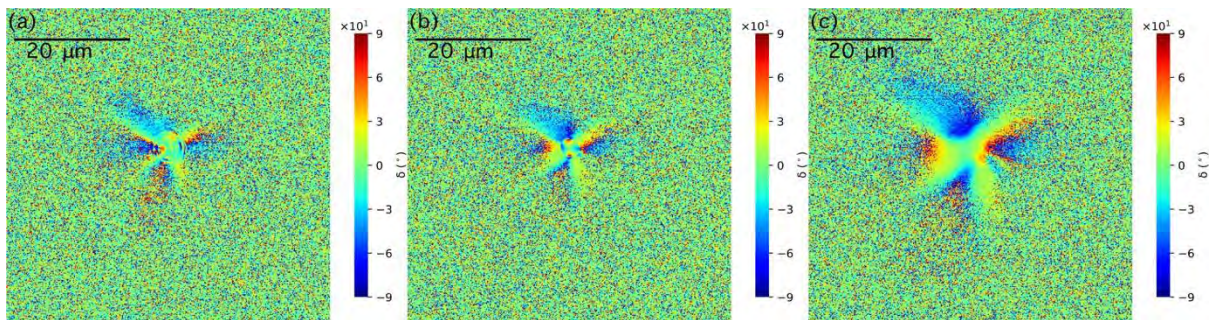


Figure 7.2.3.11 The mapping of δ for the pinhole: (a) the object plane behind plane the pinhole; (b) the object plane on the pinhole; (c) the object plane in front of the pinhole

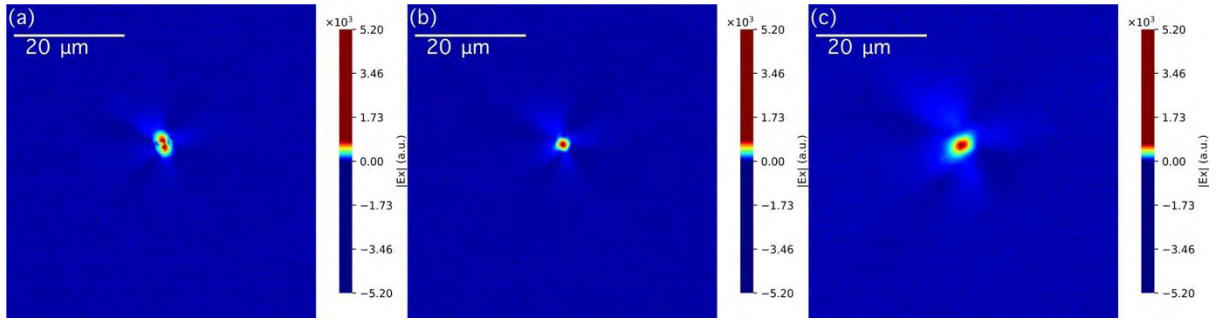


Figure 7.2.3.12 The mapping of $|E_x|$ for the pinhole: (a) the object plane behind plane the pinhole; (b) the object plane on the pinhole; (c) the object plane in front of the pinhole

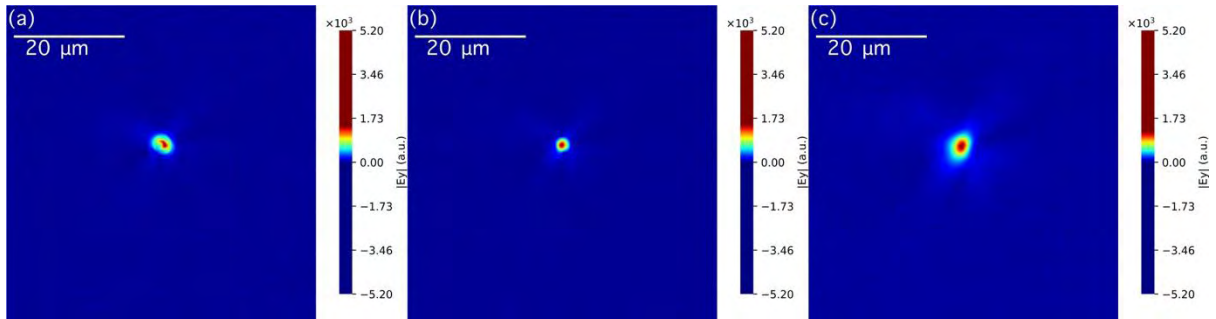


Figure 7.2.3.13 The mapping of $|E_y|$ for the pinhole: (a) the object plane behind plane the pinhole; (b) the object plane on the pinhole; (c) the object plane in front of the pinhole

The mapping of the modulus of the electric field ($|E_x|$ and $|E_y|$) is shown in Fig.7.2.3.12 and Fig.7.2.3.13. The azimuth angle of the semi-major axis of the oval of ($|E_x|$ rotates 45° clockwise comparing with the oval of $|E_y|$)

Figure 7.2.3.14 and Fig. 7.2.3.15 shows the mapping of the real part $\text{Re}(E_y)$ and imaginary part $\text{Im}(E_y)$ of electrical field E_y . The imaginary part includes the information of phase difference. An anti-clockwise vortex is shown in Fig. 7.2.3.16a.

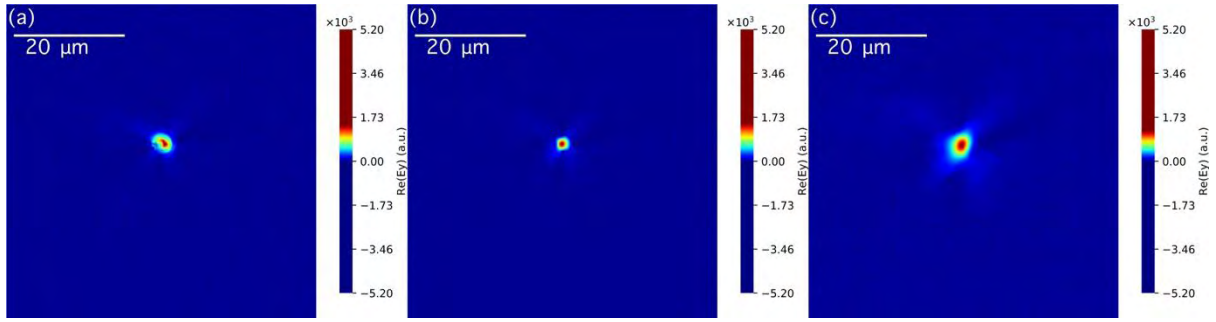


Figure 7.2.3.14 The mapping of $\text{Re}(E_y)$ for the pinhole: (a) the object plane behind plane the pinhole; (b) the object plane on the pinhole; (c) the object plane in front of the pinhole

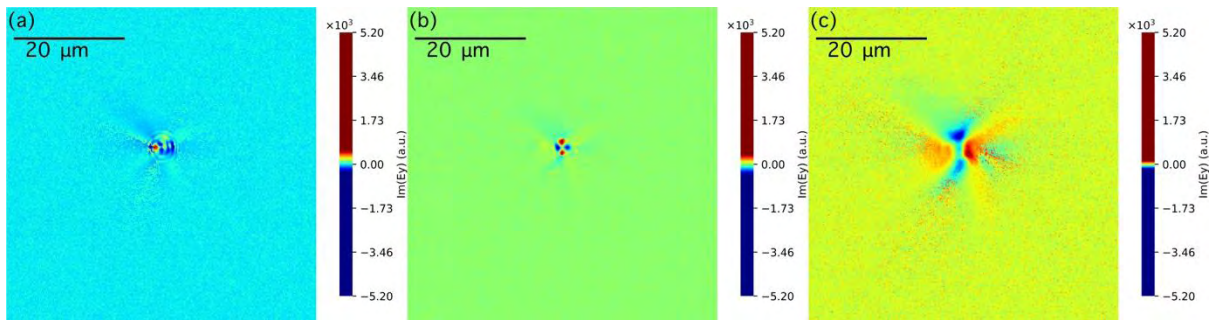


Figure 7.2.3.15 The mapping of $\text{Im}(E_y)$ for the pinhole: (a) the object plane behind plane the pinhole; (b) the object plane on the pinhole; (c) the object plane in front of the pinhole

In conclusion, the mapping of the intensity shows the shape of the polarized light is an oval in front of and behind the pinhole. The two ovals are orthogonal. The pin hole is a circle. The light is easily passing the pinhole along the edge which parallel to the azimuth angle of the polarized light; while, the light is stopped by the edge of the pinhole which perpendicular to the azimuth angle of the polarized light. The ray structure exists on both side of the pinhole within $3 \mu\text{m}$. The Airy-like patterns only exists on behind of the pinhole.

7.3 Theory model

7.3.1 The model of the scattering at a pin hole

Based on the experimental phenomena shown above. I extract a model shown in Fig. 7.3.1.1. The edge of the pinhole is a circle in Fig. 7.3.1.1. The orientation of the polarization is along the horizontal direction. The energy of the light is selected by the edge of the pinhole. On one

point of the circle o' , a new coordinate is established, $x'o'y'$. The coordinate $x'o'y'$ changed with the position of origin point o' . The angle between the polarization direction and the circular normal is C , shown on Fig. 7.3.1.1.

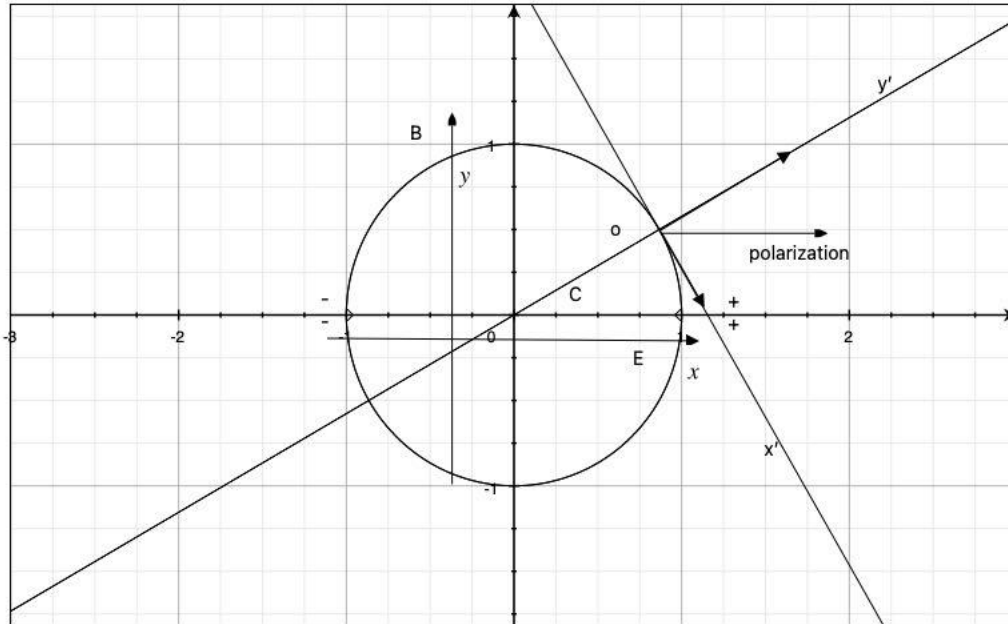


Figure 7.3.1.1 The interaction of the polarization at the edge of pin hole

The modulus of the incident polarization is marked as $|E|$. Electric field is divided into two components in two orthogonal directions which is shown as $o'x'$ and $o'y'$. We can establish the relationship shown in equation.

$$I_T = E^2 \sin^2 C. \quad (7.3.1.1)$$

$$I_R = E^2 \cos^2 C. \quad (7.3.1.2)$$

where, I_T represents the intensity around the edge passing through the pinhole, and, I_R represents the intensity around the edge in front of the pin hole. The interaction between polarization light and the pinhole, only includes the reflection and transmission. At the edge of the pinhole, no absorption existed. According to the wavelength of the probing light 670nm, the photon energy of the probing light is 1.85eV, which is less than the work function

of aluminium 4.28eV. The electrons on the metal around the pinhole are excited by the light absorbed at the edge.

1. $C = 0^\circ, I_T = 0, I_R = E^2$
2. $C = 180^\circ, I_T = 0, I_R = E^2$
3. $C = 90^\circ, I_T = E^2, I_R = 0$
4. $C = 270^\circ, I_T = E^2, I_R = 0$

This model can be used to explain why the semi-major axis of the oval in front of the pinhole and behind the pinhole are orthogonal.

7.4 Summary

In this chapter, a pinhole is studied using the Stokes polarimetric microscope. The Stokes polarimetric microscope is powerful to measure the near field vector field. A series of focus planes is chosen to obtain a series of Airy-like patterns. A ray structure is observed in the images of the Q, U and V both in front of and behind the pinhole. The diffraction pattern exists only behind the pinhole. The spot of the intensity in front of the pinhole and behind of the pinhole are ovals that whose semi-major axes orthogonal with each other. A clockwise vortex can be observed in the image of the $|E_x|$. We can measure Airy-like pattern quite well in the vicinity up to tens of microns away from the pinhole and broadly in line with what are known in literatures. The ‘decay’ in the signals are comparable and hence the ‘depth of focus’ would be expected in a similar manner.

Chapter 8 Liquid crystal droplets

This chapter researched four types of liquid crystal droplets, which have different interfaces inside the droplet, to show the advantage of microscope on the detection of the interface.

8.1 Experiment

8.1.1 The detail of four liquid crystal sample

The liquid crystal samples are provided by Bao Peng in Leeds University. We use our Stokes polarimetric microscope to investigate the liquid crystal sample. Four samples, which topographically is different, are researched. The experiment is done many times in different experimental states. The experimental detail is shown in table 8.1.1.1.

Table 8.1.1.1 The experiment parameter on liquid crystal droplet polarization observation

Date	sample1	sample2	sample3	sample4	light source
2018/5/17	PCPGE7 70 20	PCPGE7 no treatment	PVAE7	PVAS11FE-7-8	Laser
2018/5/24			PVAE7	PVAS11FE-7-8	Laser
2018/6/1				PVAS11FE-7-8	Laser
2018/6/6	E7PCPG treated	PCPGE7 notreatment	PVAE7	SDE7	Laser
2018/6/7				s1011-E7PVA	Laser
2018/6/8			PVAE7	s1011-E7PVA	Laser
2018/6/12				s1011-E7PVA	Laser
2018/6/13	E7PCPG treated	PCPGE7 notreatment		s1011-E7PVA	Laser
2018/6/21				PDMS2	Laser
2018/12/17	PCPGE7 1-1	PCPG-E7 1-1 75T	PVAE7	PVA chiral E7	LED
2018/12/19	PCPGE7 1-1	PCPG-E7 1-1 75T	PVAE7	PVA chiral E7	LED
2018/12/20			PVAE7		LED
2019/0222	PCPG-E7	PCPG-E7 1-1 75T	PVAE7	PVA chiral	LED

The liquid crystal droplets are produced by mixing several chemicals, such as E7, S1011, PVA (polyvinyl alcohol), and glycerol. The detail of the chemicals is shown below.

E7 (Merck): E7 is a commercially available nematic LC material, which is a mixture of four different liquid crystals, as shown in Fig. 8.1.1.1. (Cooper, n.d.).

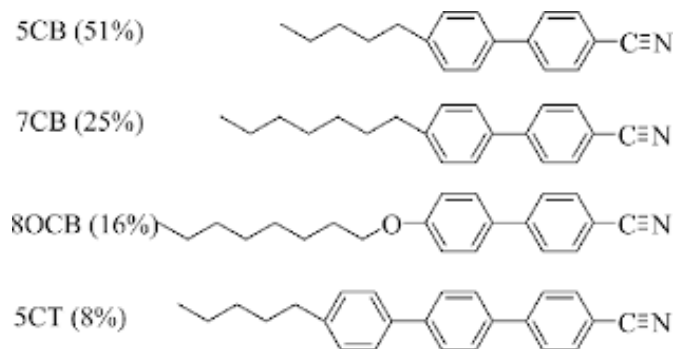


Figure 8.1.1.1 The chemical component of the E7 liquid crystals

S1011 is a chiral dopant (Merck), whose structure is shown in Fig. 8.1.1.2.

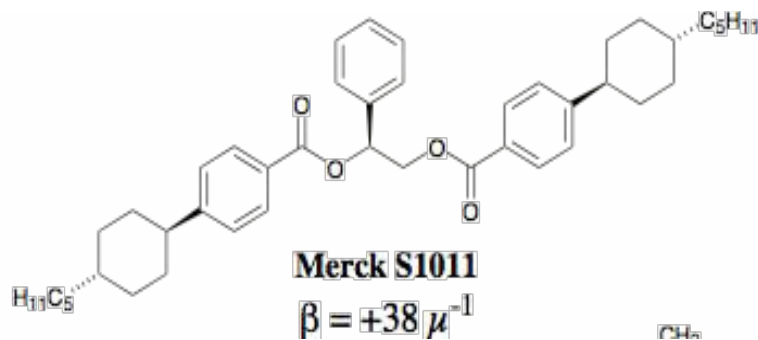


Figure 8.1.1.2 the molecular structure of the chiral solution S1011.

PVA (polyvinyl alcohol) is a water-soluble synthetic polymer. The structure is shown in Fig.8.1.1.3.

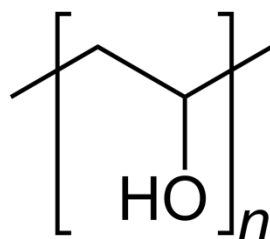


Figure 8.1.1.3 The structure of PVA

The structure of glycerol is shown in Fig. 8.1.1.4.

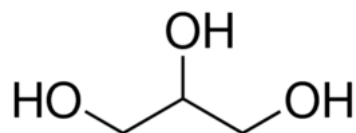


Figure 8.1.1.4 The structure of glycerol.

The nematic liquid crystal mixture E7 was purchased from Synthon Chemicals GmbH & Co. KG, Germany. The S1011 was purchased from Merck &co. Inc, USA. 1,2-Dioleoyl-*sn*-glycero-3-phosphocholine (DOPC), 1,2-dioleoyl-*sn*-glycero-3-phospho-rac-(1-glycerol) sodium salt (DOPG), PVA and glycerol were purchased from Sigma-Aldrich. The premium glass microscope slides were from Fisher Scientific (Pittsburgh, PA).

The production of LC droplets reference to P. Bao's paper (Bao et al., 2019): Monodisperse lipid-coated droplets (diameter = 17 μm) were produced using a flow focus droplet microfluidic device (Bao et al., 2019).

8.2 Results and discussions

8.2.1 Sample1

Sample1 is the DOPC/DOPG (1:1) coated E7 liquid crystal droplets (as produced). The polarization information of sample1 is shown in this section. Fig. 8.2.1.1 shows the image corresponding to different the Stokes parameters. There is no difference between the three samples in image of I, but in the image of Q, U and V. The difference of the image can be seen in the centre of the ball. One pattern is the laevo and the other is the dextro. A two layers structure can be observed in the image of V.

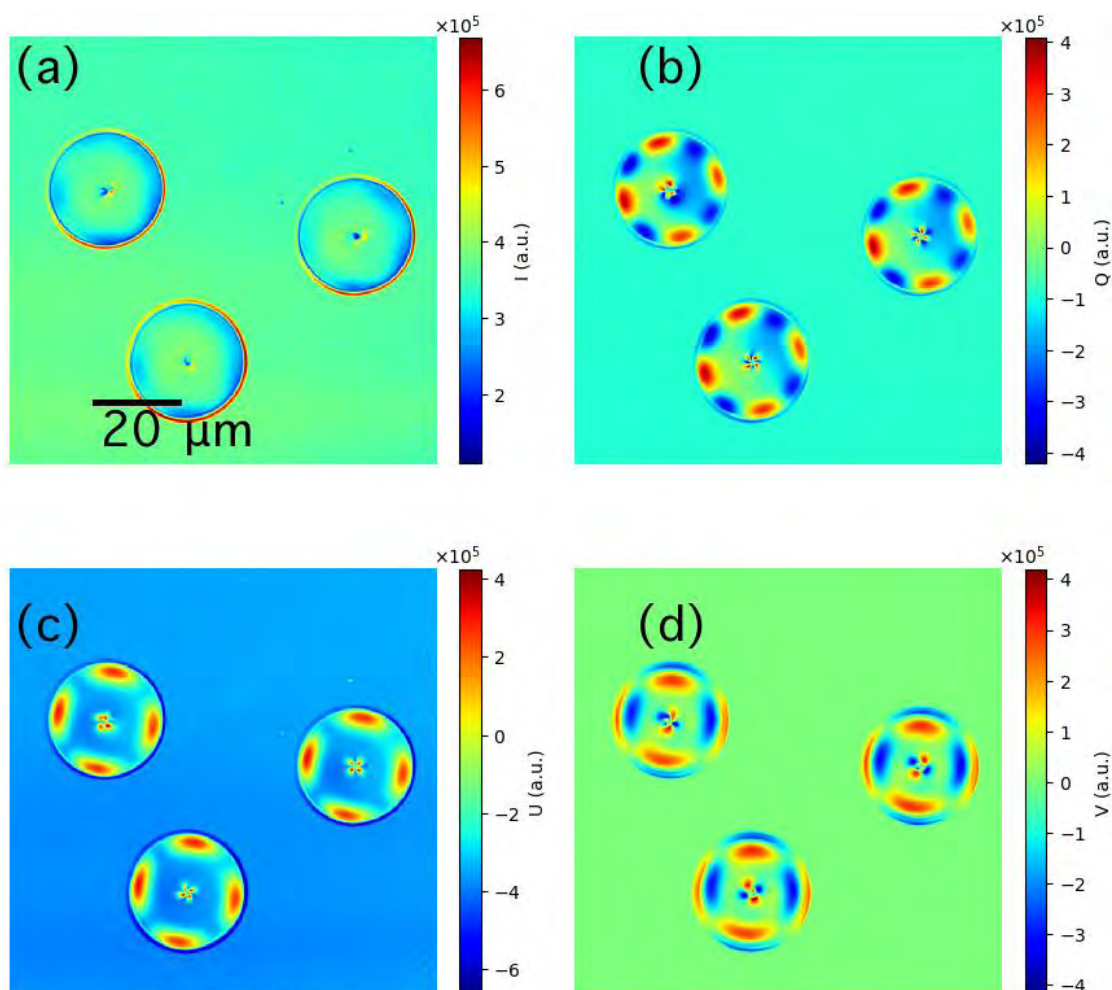


Figure 8.2.1.1 Image of contrast of the Stokes parameters on LCD sample1: (a) Intensity, (b) Stokes parameter Q, (c) Stokes parameter U, (d) Stokes parameter V.

Fig. 8.2.1.2 shows the relevant angles of the polarization. The azimuth angle of the incident probe light is 128° , shown in Fig. 8.2.1.2b. The optical axis of the polarizer is just the 180° rotation axis of the symmetry-axis of the shell of the droplet, which is a round structure, reference to the laboratory coordinate shown in Fig. 6.2.1.1.

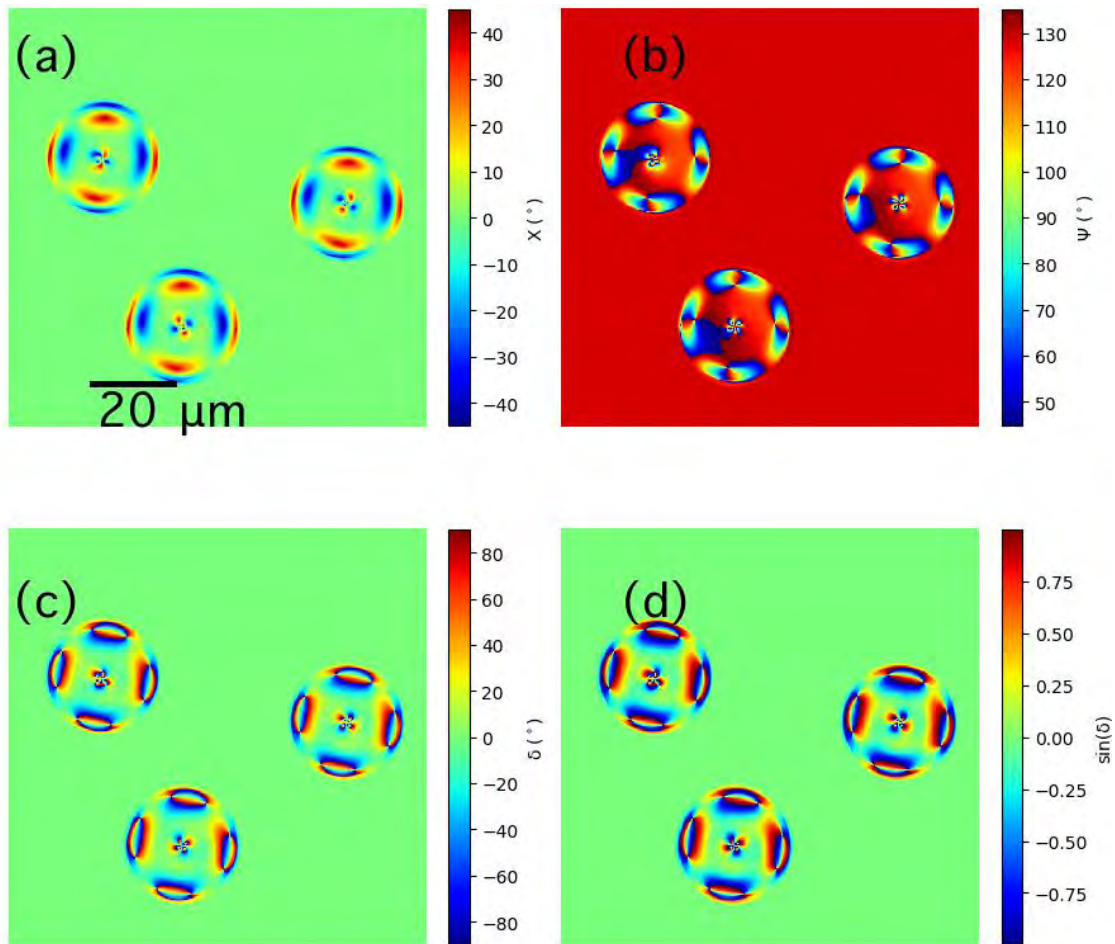


Figure 8.2.1.2 The contrast image of (a) the elliptical angle χ , (b) the azimuth angle ψ , (c) the retardation of phase δ , and (d) the $\sin(\delta)$ on LCD sample1.

Figure 8.2.1.3 shows the normalized depolarization and Stokes parameters. The structure is seen more clearly in the image of normalized Stokes parameters. The image is different from that of the image of the pinhole, which background is very rough. That is because the interaction between the light and the sample includes refraction in the liquid crystal system. The light can go through the sample that makes the intensity detected in the image

background is not zero.

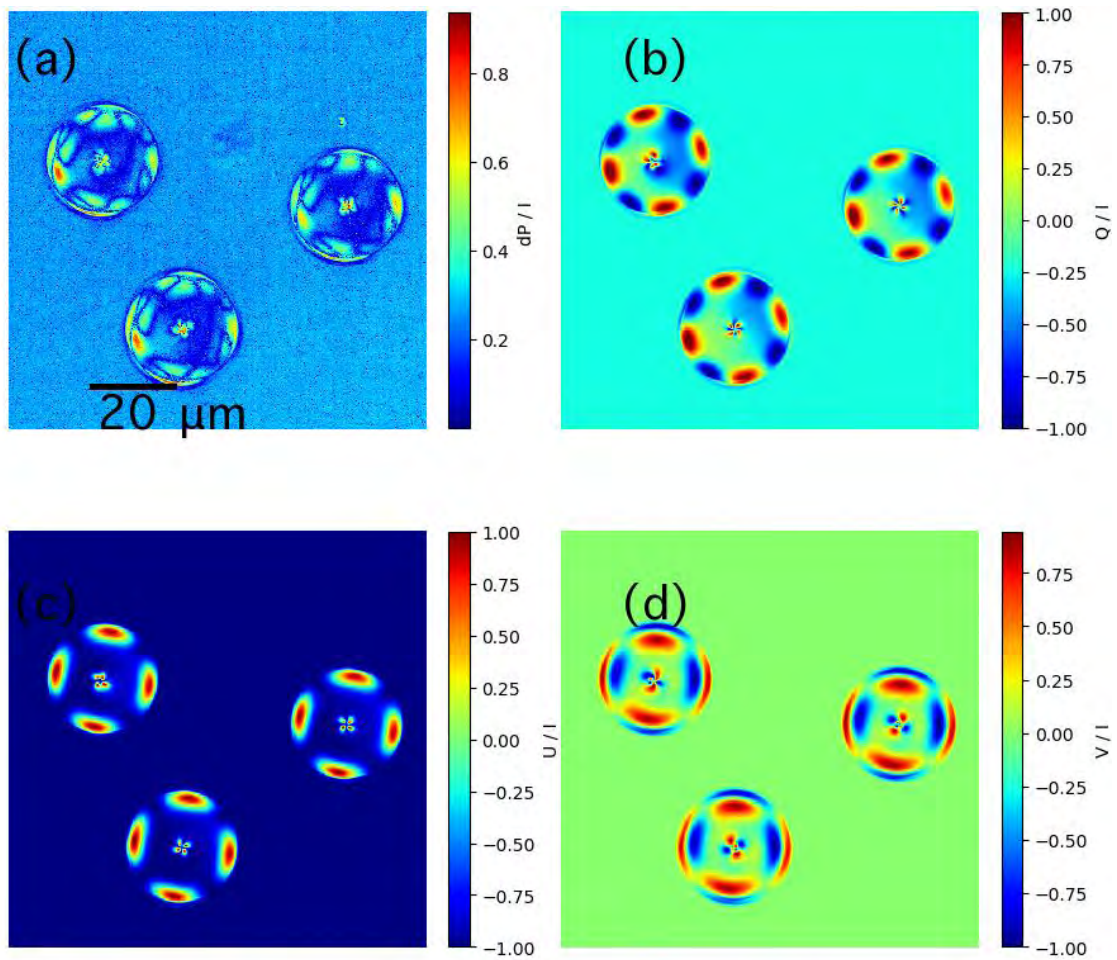


Figure 8.2.1.3 The image of (a) normalized depolarization, (b) normalized Stokes parameter Q/I , (c) normalized Stokes parameter U/I , and (d) normalized Stokes parameter V/I on LCD sample1.

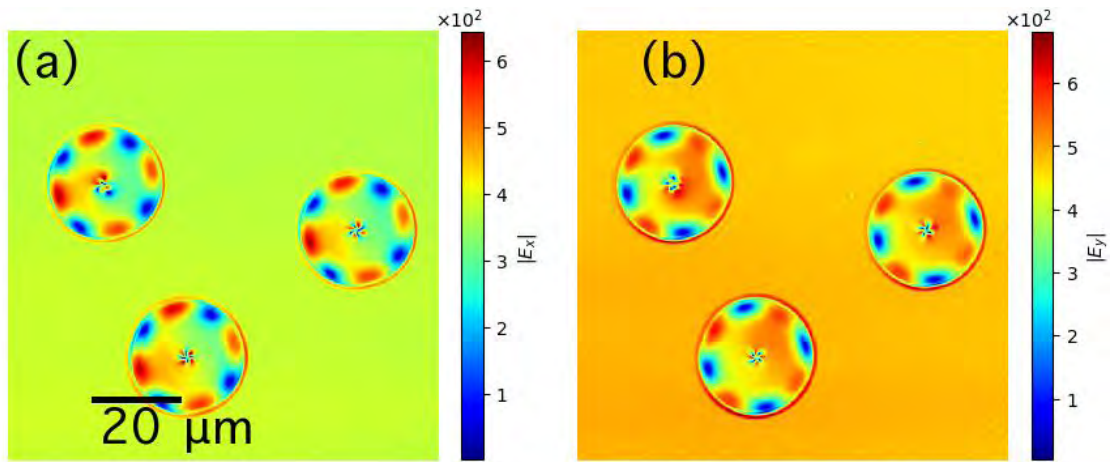


Figure 8.2.1.4 The modulus of the electric field of the LCD sample1 with reference to the laboratory coordinate (a) $|E_x|$ and (b) $|E_y|$

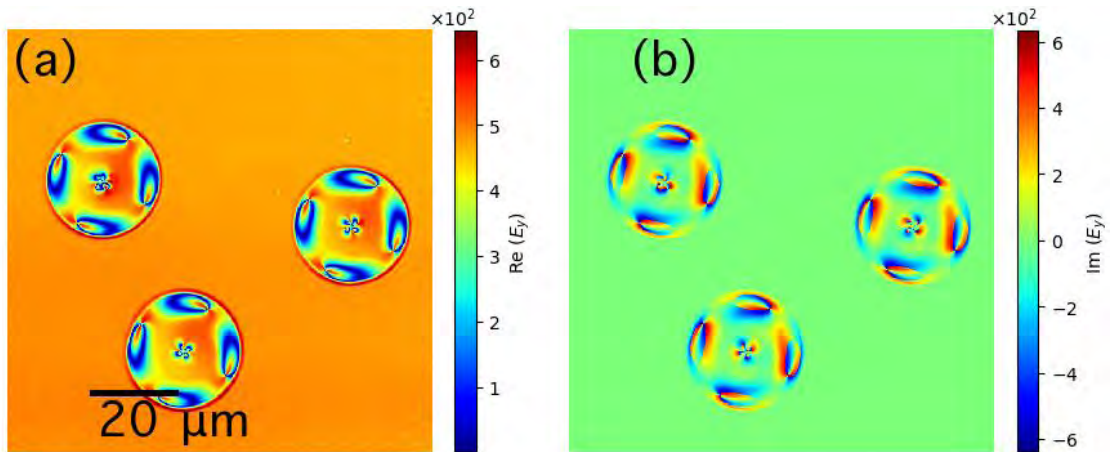


Figure 8.2.1.5 The electric field of the LCD sample1 along y-axis: (a) real part and (b) the imaginary part.

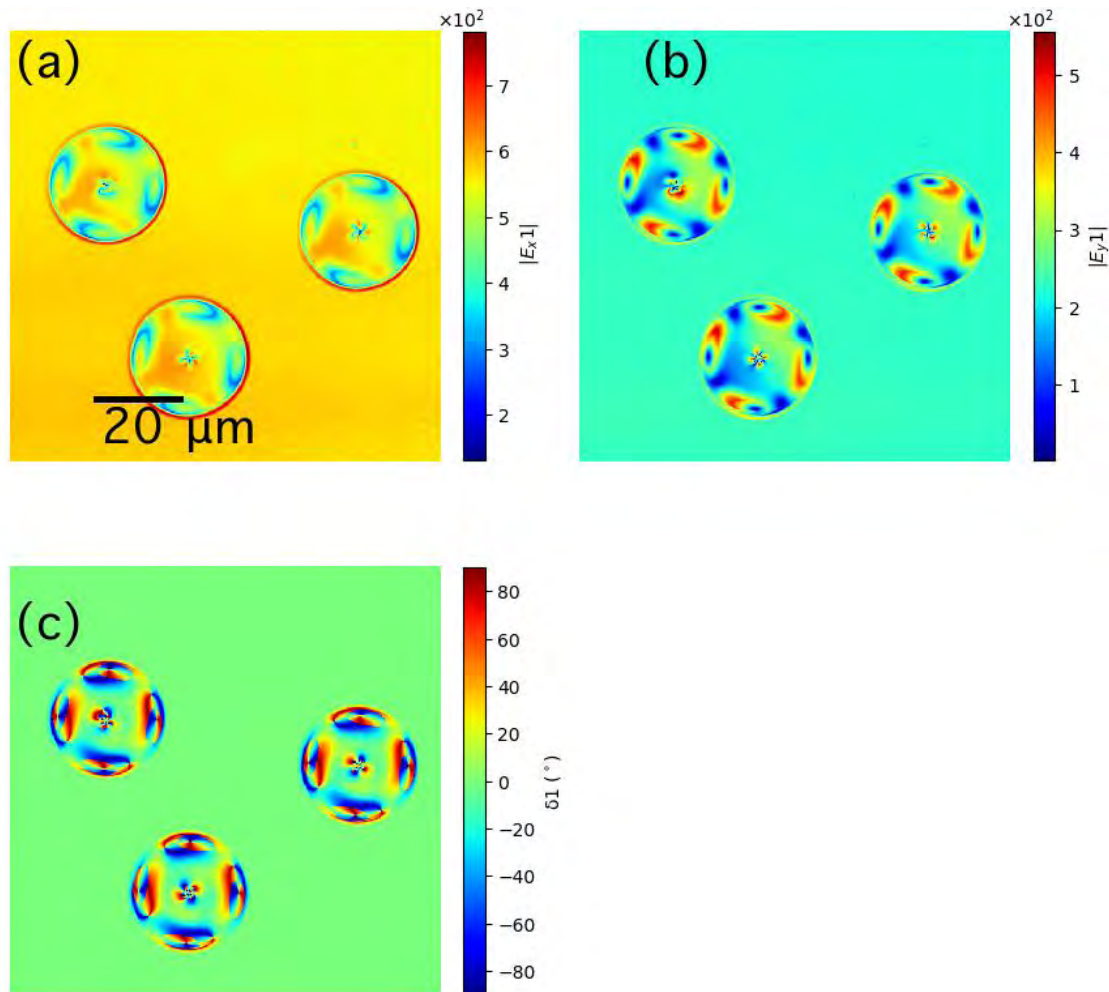


Figure 8.2.1.6 The modulus of the electric field of the LCD sample1 with reference to the polarizer coordinate: (a) modulus of electric field along x_1 , (b) modulus of electric field along y_1 , and (c) the retardation of phase δ_1

The modulus of the electric field with reference to the laboratory coordinate is shown in Fig. 8.2.1.4. The structure of $|E_x|$ and $|E_y|$ is complementary. The real part and the imaginary part of the electrical field along y -axis is shown in Fig. 8.2.1.5. The modulus of the electric field along x_1 and y_1 , which are the axis of the polarization coordinate, are shown in Fig. 8.2.1.6. δ_1 is the phase difference between the y_1 -axis and x_1 -axis, Fig. 8.2.1.6c.

In conclusion, the interface of the LCD is seen in the image of the Stokes parameters. The polarizer axis is a symmetric axis of the image of the Stokes parameters. Stokes polarimetric microscope is powerful to distinguish the dextrorotation and laevorotation.

8.2.2 Sample 2

Sample 2: DOPC/DOPG (1:1) coated E7 liquid crystal droplets (heated to 70 °C, held for 20min, then cooled to RT), which gives a radial alignment. The structure of sample 2 is shown in Fig. 8.2.2.1.

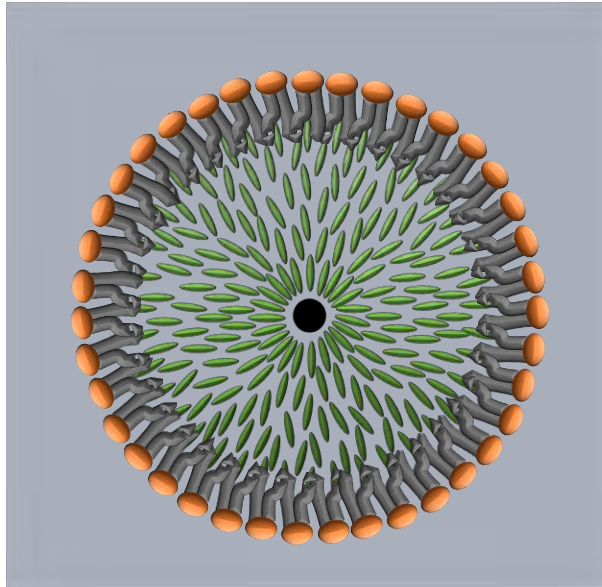


Figure 8.2.2.1 the structure of the sample2

Figure 8.2.2.2 shows the Stokes parameters of the sample. The four parts structure should be produced by the boundary of a circle, which can be observed in every droplet. But the inter-layer structure is characteristic of the sample, which is shown in the image of Q, U and V. This multilayer structure is more clearly in the image of the relevant angles, shown in Fig. 8.2.2.3. The biggest droplet has a five-layer shell structure. Some small droplets have a double shell structure which is same that shown in Fig. 8.2.2.1. Some small droplet does not have any inner structure. The polarization probing is a good way to distinguish the inner structure of the droplet, which cannot be seen in the image of the intensity.

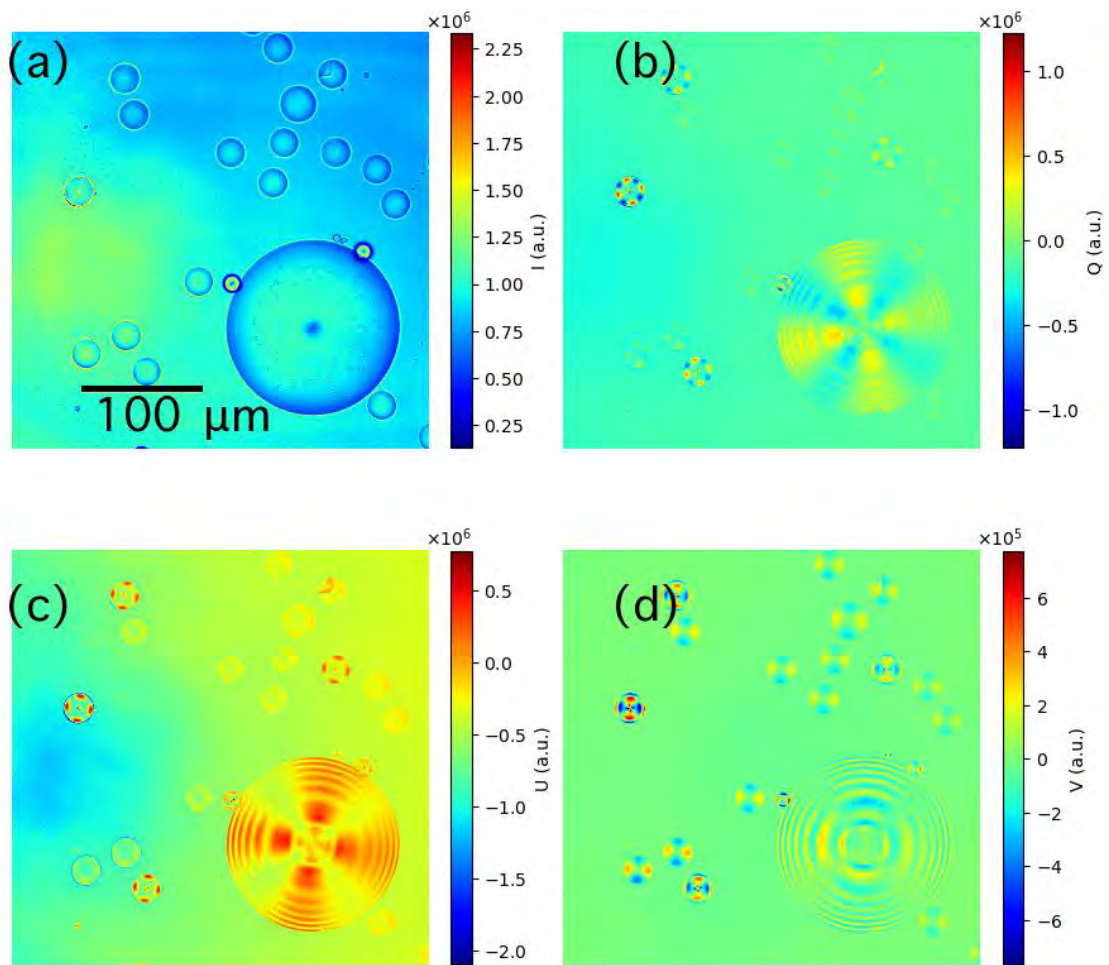


Figure 8.2.2.2 Image of contrast of the Stokes parameters on LCD sample 2 : (a) Intensity, (b) Stokes parameter Q , (c) Stokes parameter U , and (d) Stokes parameter V .

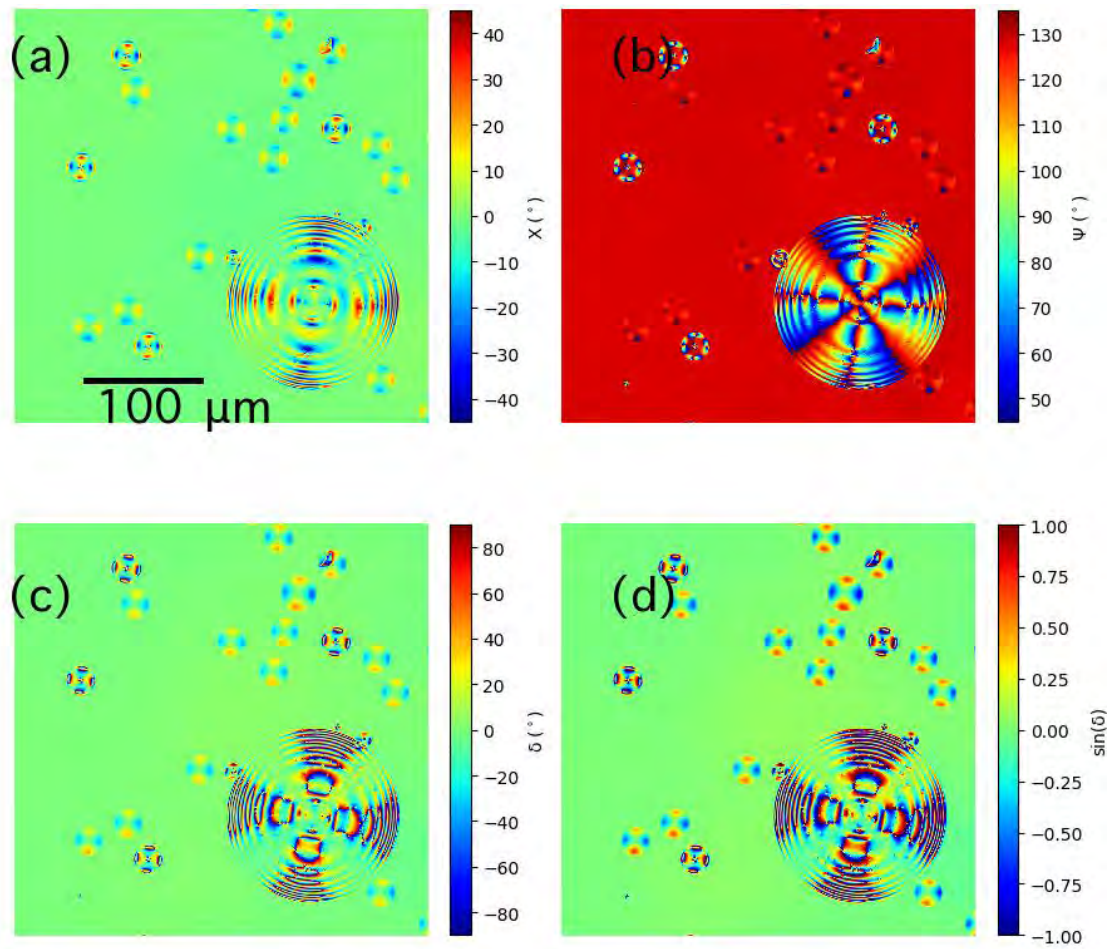


Figure 8.2.2.3 The contrast image of (a) the elliptical angle χ , (b) the azimuth angle ψ , (c) the retardation of phase δ , and (d) the $\sin(\delta)$ on LCD sample2.

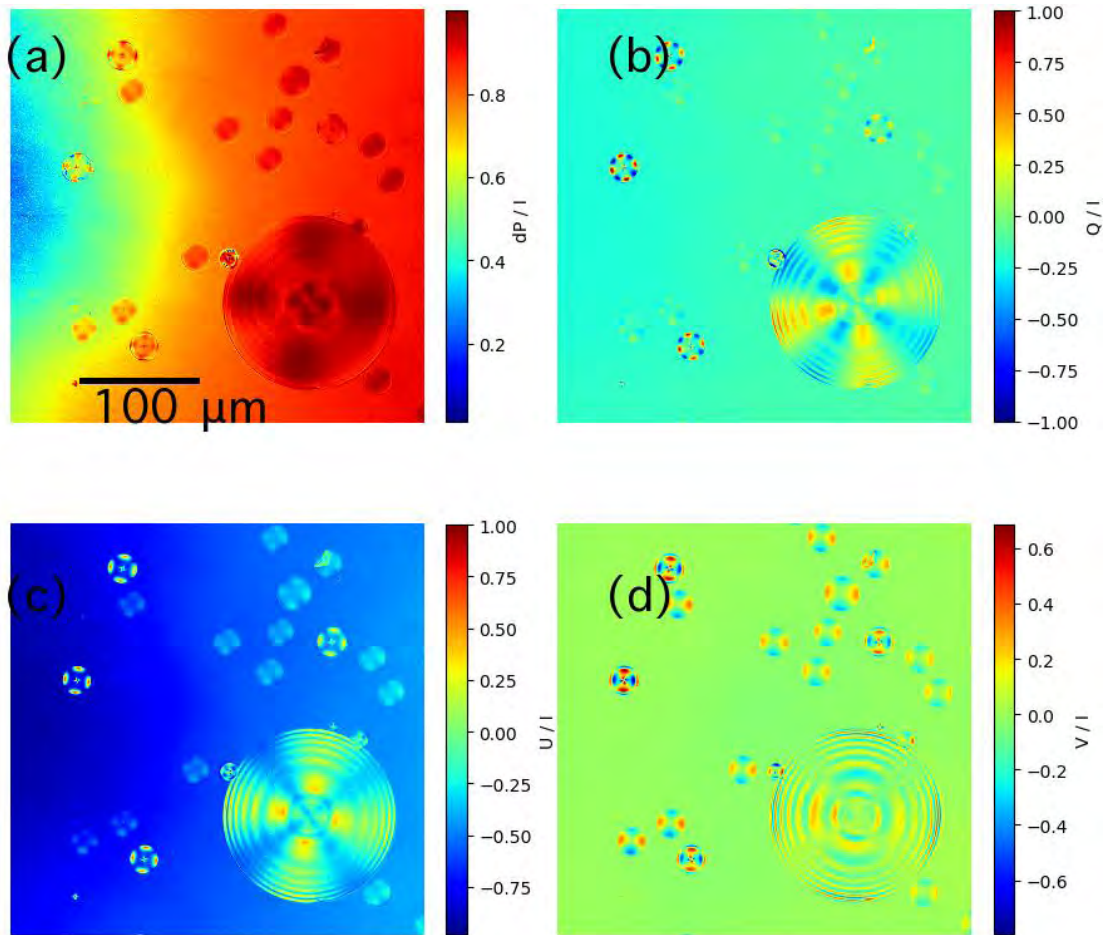


Figure 8.2.2.4 The image of (a) normalized depolarization, (b) normalized Stokes parameter Q/I , (c) normalized Stokes parameter U/I , and (d) normalized Stokes parameter V/I on LCD sample2.

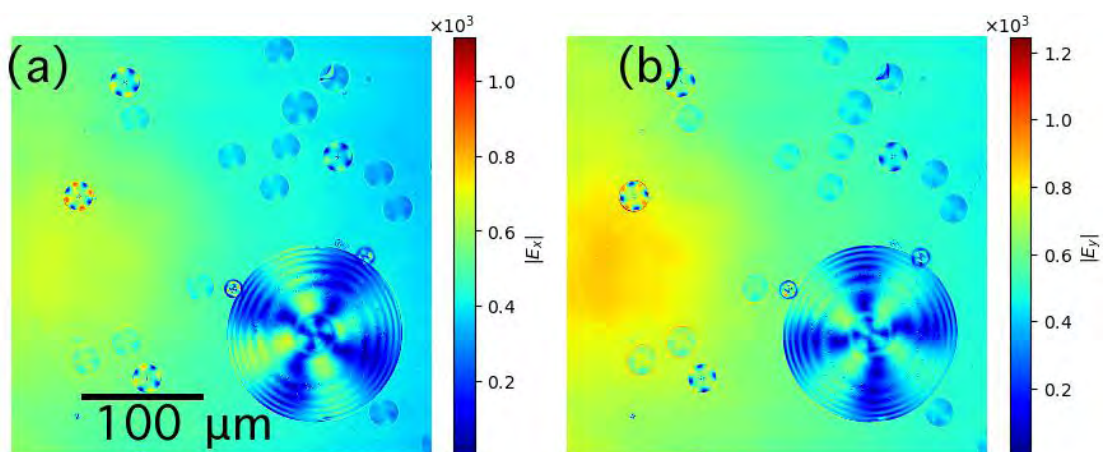


Figure 8.2.2.5 The modulus of the electric field of the LCD sample2 with reference to the laboratory coordinate (a) x-axis and (b) y-axis.

The background of the normalized depolarization is not uniform in Fig. 8.2.2.4a because this

azimuth angle (128°) is not in the best position (120°). Some light reflected from the surface of the sample is reflected back to the sample as part of the illumination for the microscope. A phase difference exists between the original light and the reflected light. It cannot be got rid of when the polarizer is not crossed with the analyzer.

The modulus of the electric field with reference to the laboratory coordinate is shown in Fig. 8.2.2.5.

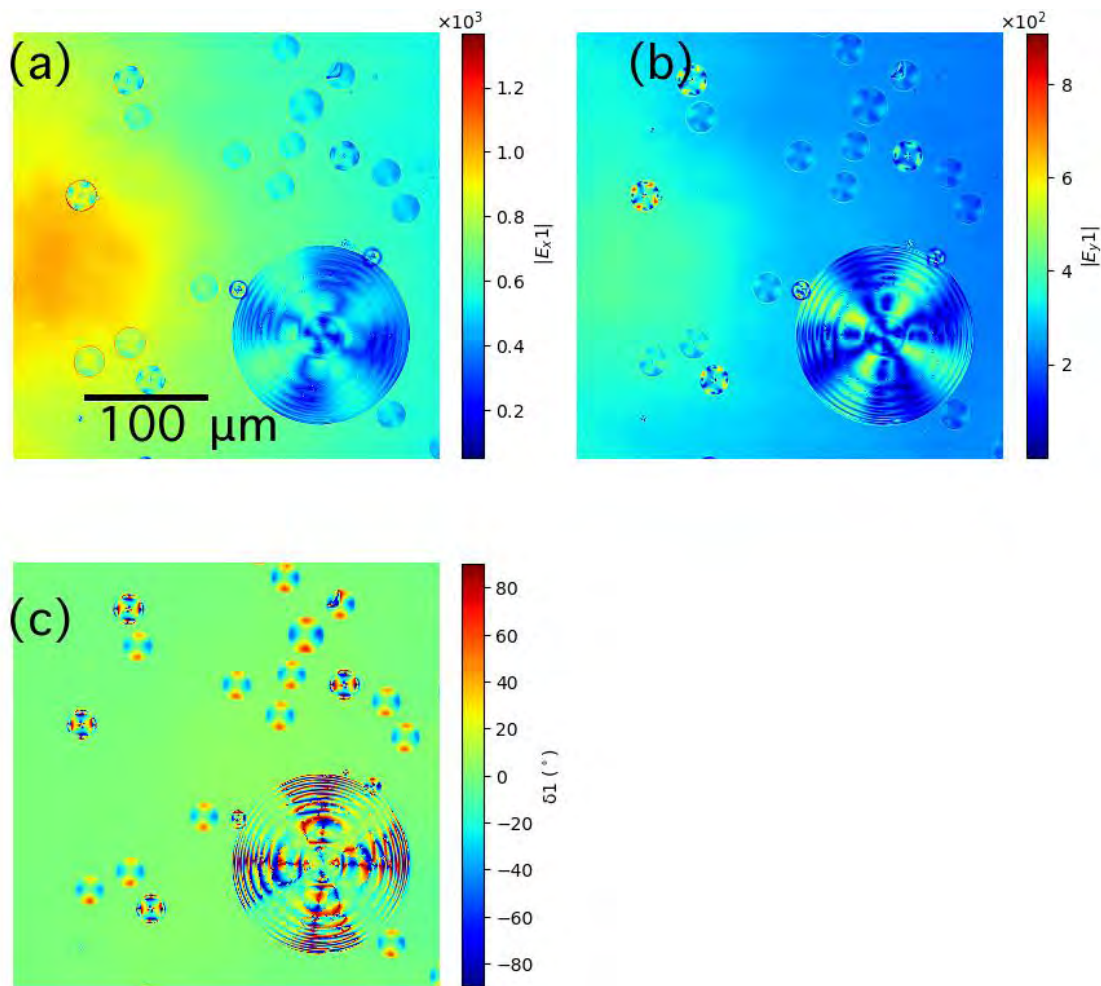


Figure 8.2.2.6 The modulus of the electric field of the LCD sample 2 with reference to the polarizer coordinate: (a) modulus of electric field along x_1 , (b) modulus of electric field along y_1 , and (c) the retardation of phase δ_1

Fig. 8.2.2.6 is the modulus of the electric field along the polarization coordinates and the phase difference between two axes.

Another structure of sample 2 is magnified, shown in Fig. 8.2.2.7 and Fig. 8.2.2.8.

Apparently, no inner structure exists in this liquid crystal.

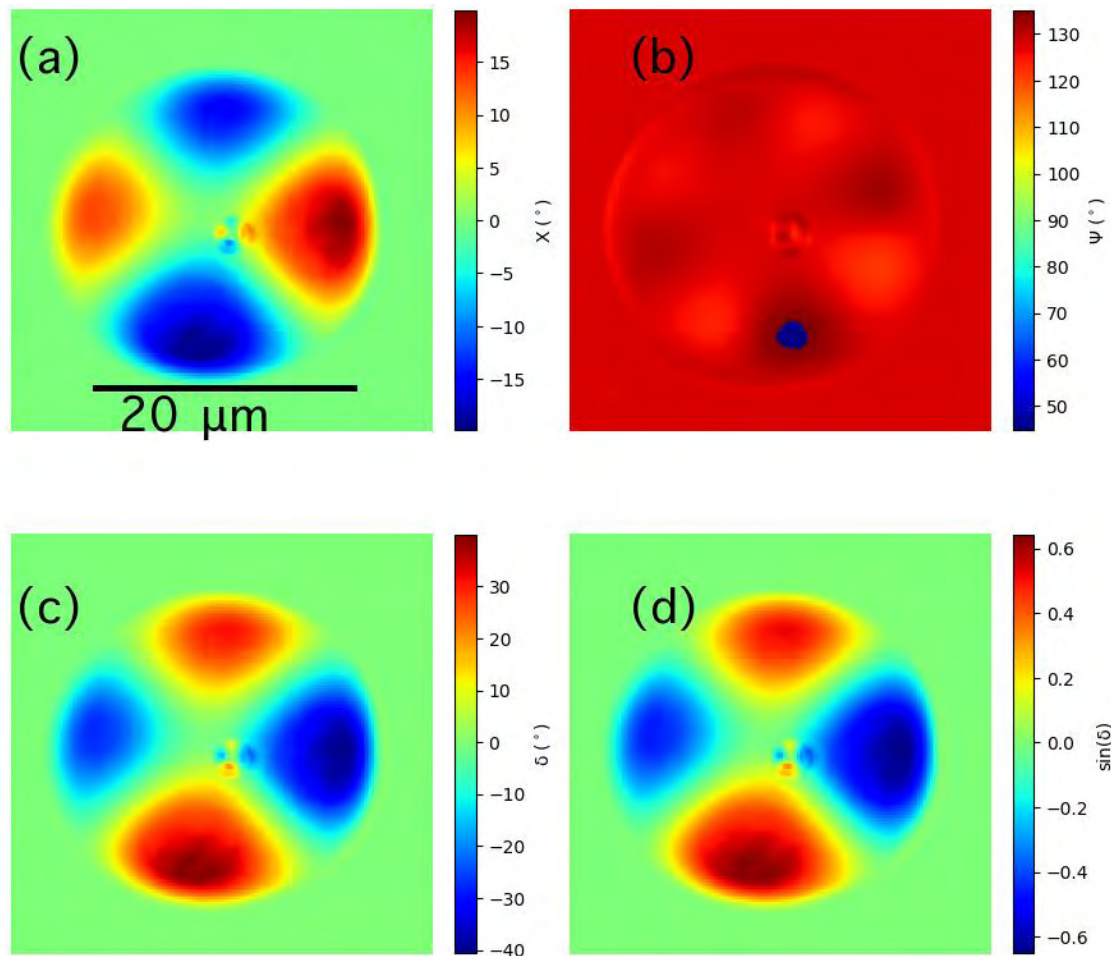


Figure 8.2.2.7 The contrast image of (a) the elliptical angle χ , (b) the azimuth angle ψ , (c) the retardation of phase δ , and (d) the $\sin(\delta)$ at another position of LCD sample2.

In conclusion, the 180° symmetric structure exists in every round edge uniform material, such as the pinhole, micropipe and the liquid crystal (except sample3). The two -degree symmetric structure can be recognized as a characteristic of a uniform round sample. The reflection passing through the edge of the hole is p-polarization and s-polarization in two orthogonal direction respectively, according to the Fresnel Equations. But sample 3 is different, it is a bipolar structure. The density in two poles is different, that makes the intensity passing through the material is different.

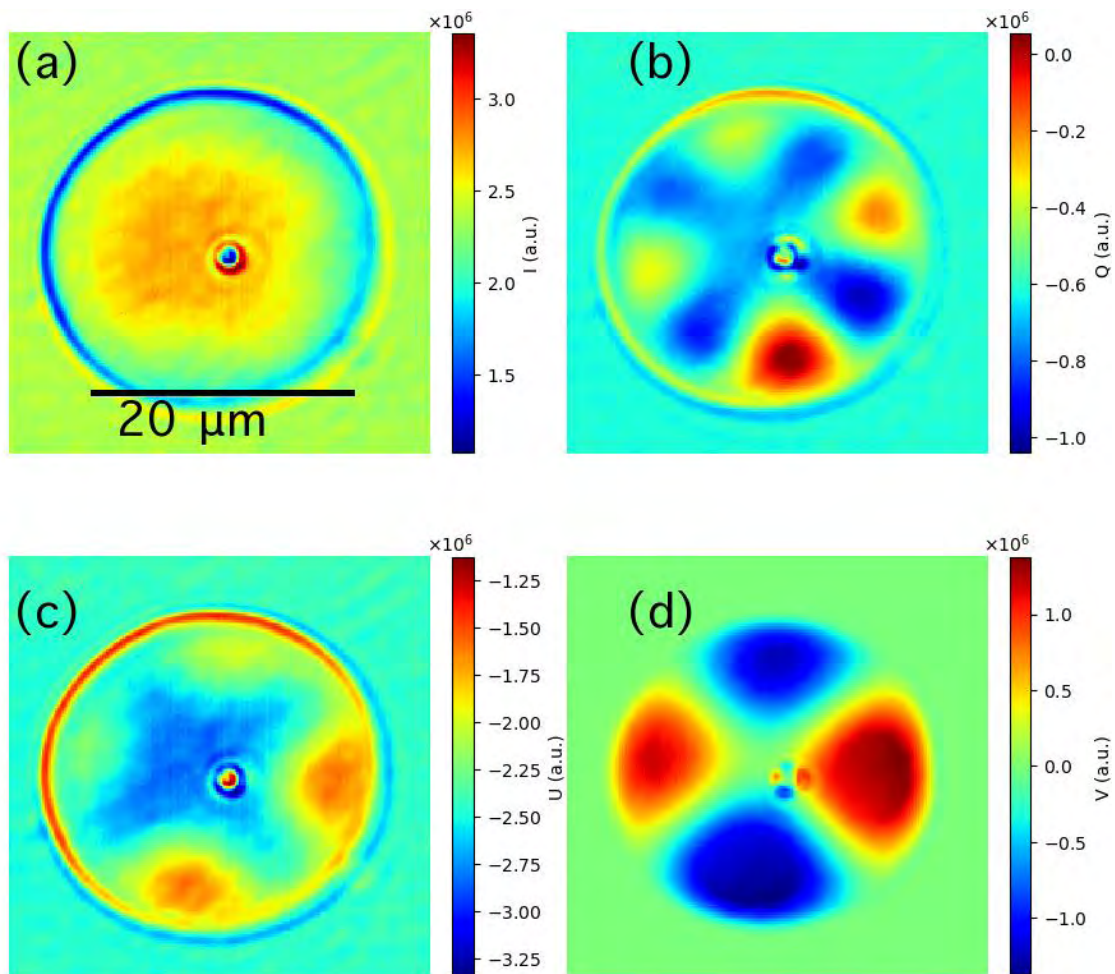


Figure 8.2.2.8 Image of contrast of the Stokes parameters on another position of LCD sample 2 : (a) Intensity, (b) Stokes parameter Q , (c) Stokes parameter U , and (d) Stokes parameter V .

8.2.3 Sample 3

Sample 3: PVA coated E7 liquid crystal droplets, which give a planar alignment. The production method of PVA coated LC droplets is similar to sample 1 and 2. The only difference is that the buffer used is 15% glycerol with 1w% of PVA. The structure of the sample 3 is shown in 8.2.3.1.



Figure 8.2.3.1 the structure of sample 3

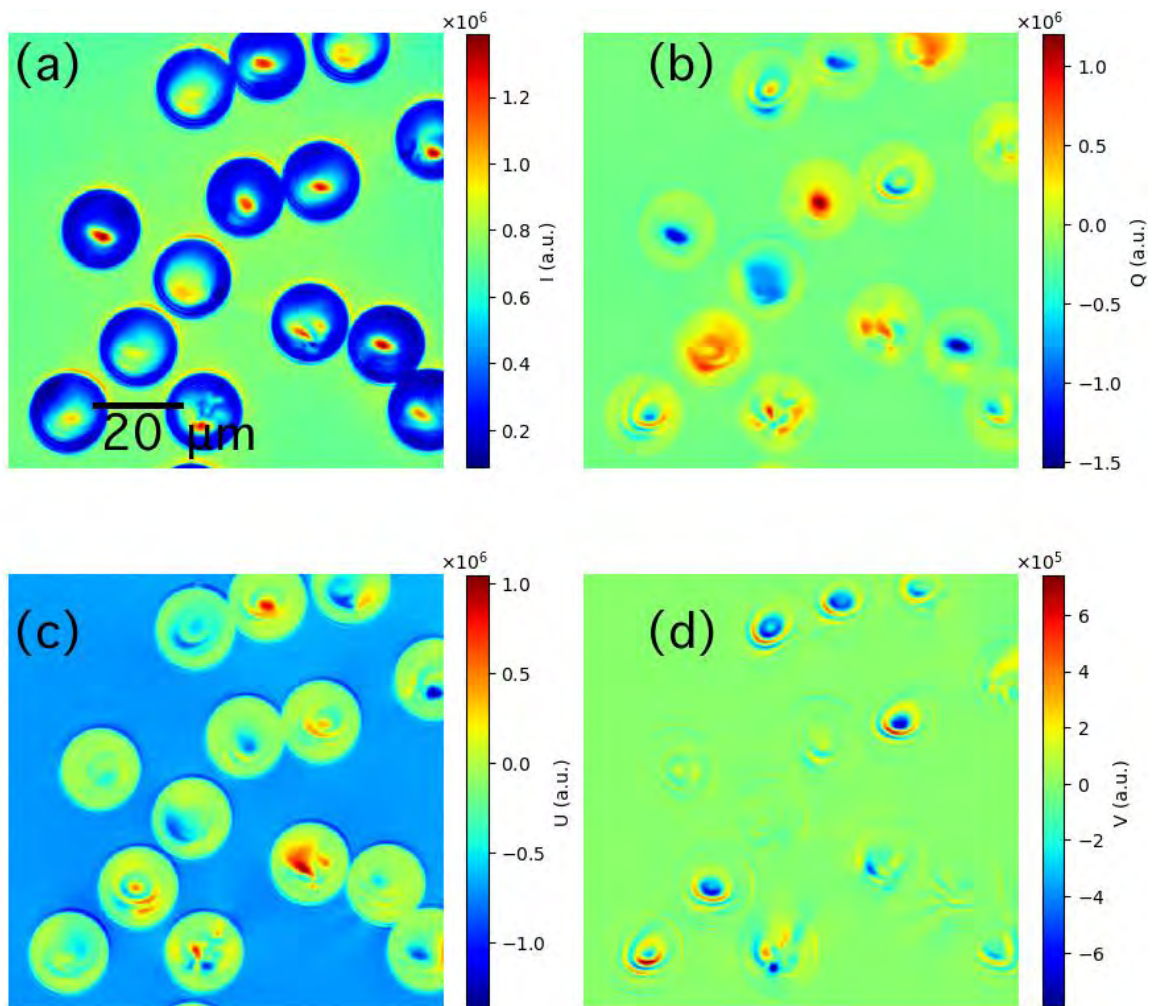


Figure 8.2.3.2 Image of contrast of the Stokes parameters on LCD sample3 : (a) Intensity, (b) Stokes parameter Q, (c) Stokes parameter U, and (d) Stokes parameter V.

The information of the polarization angles is more clearly than that on Stokes parameters,

which is shown in Fig.8.2.3.2. The PVA coated shell can be seen in the image of Stokes parameters, but not clearly. The image of the relevant angles, shown in Fig. 8.2.3.3, shows more clearly the layers on the shell. The response distance of the elliptical angle and azimuth angle is bigger than the Q and U. So, the interior the droplet is detected in the image of the relevant angles in Fig. 8.2.3.2.

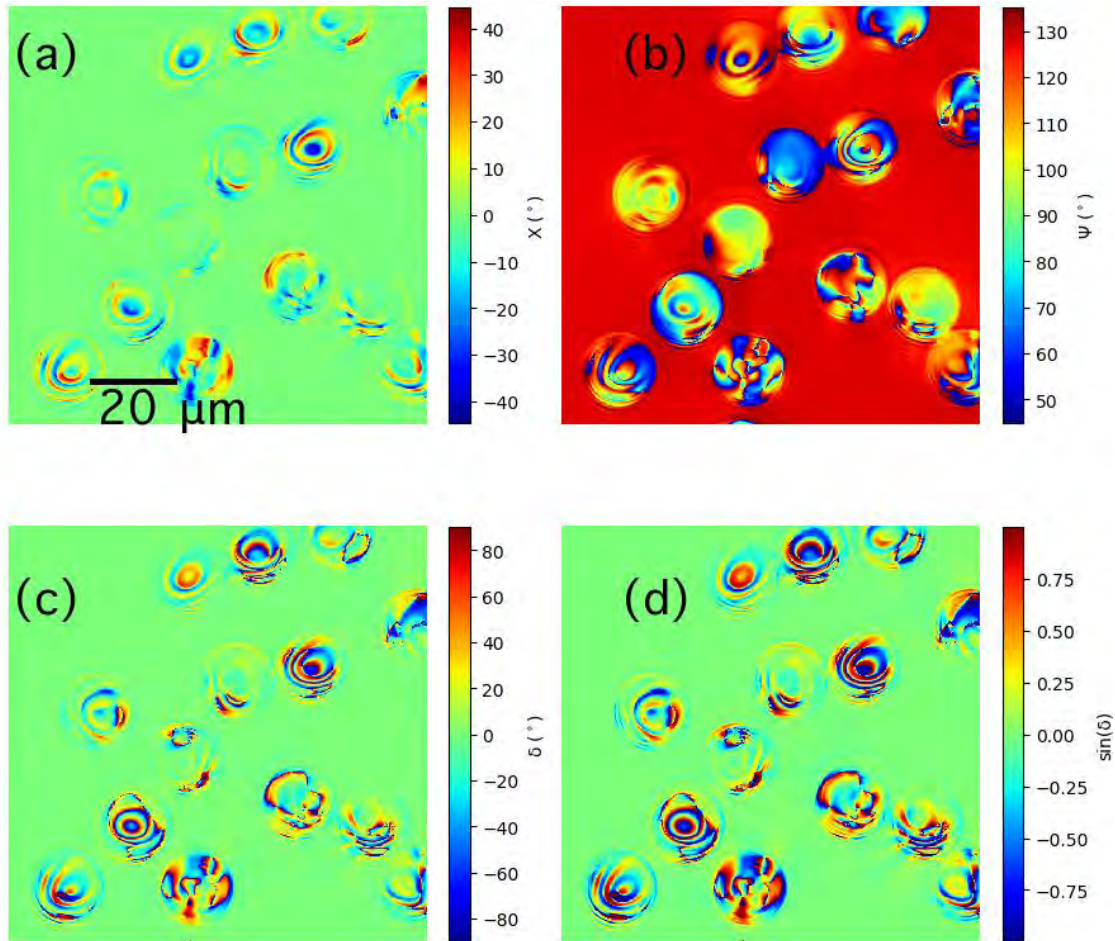


Figure 8.2.3.3 The contrast image of (a) the elliptical angle χ , (b) the azimuth angle ψ , (c) the retardation of phase δ , and (d) the $\sin(\delta)$ on LCD sample3.

The normalized depolarization and the normalized Stokes parameters are shown in Fig.

8.2.3.4. The PVA shell produced a big depolarization of the light, shown in Fig. 8.2.3.4a.

Some non-uniformity on the shell of the droplet is detected, which cannot be seen in the

image of the intensity. The modulus of the electric field with reference to the laboratory

coordinate is shown in Fig. 8.2.3.5. The images of $|E_x|$ and $|E_y|$ are complementary, shown

in Fig. 8.2.3.5. The real part and the imaginary part of the E_y is shown in Fig. 8.2.3.6. The

modulus of the electric field along x_1 -axis and y_1 -axis, which are the axis of the polarization coordinate, are shown in Fig. 8.2.3.7. δ_1 is the phase difference between the y_1 -axis and x_1 -axis, Fig. 8.2.3.7c.

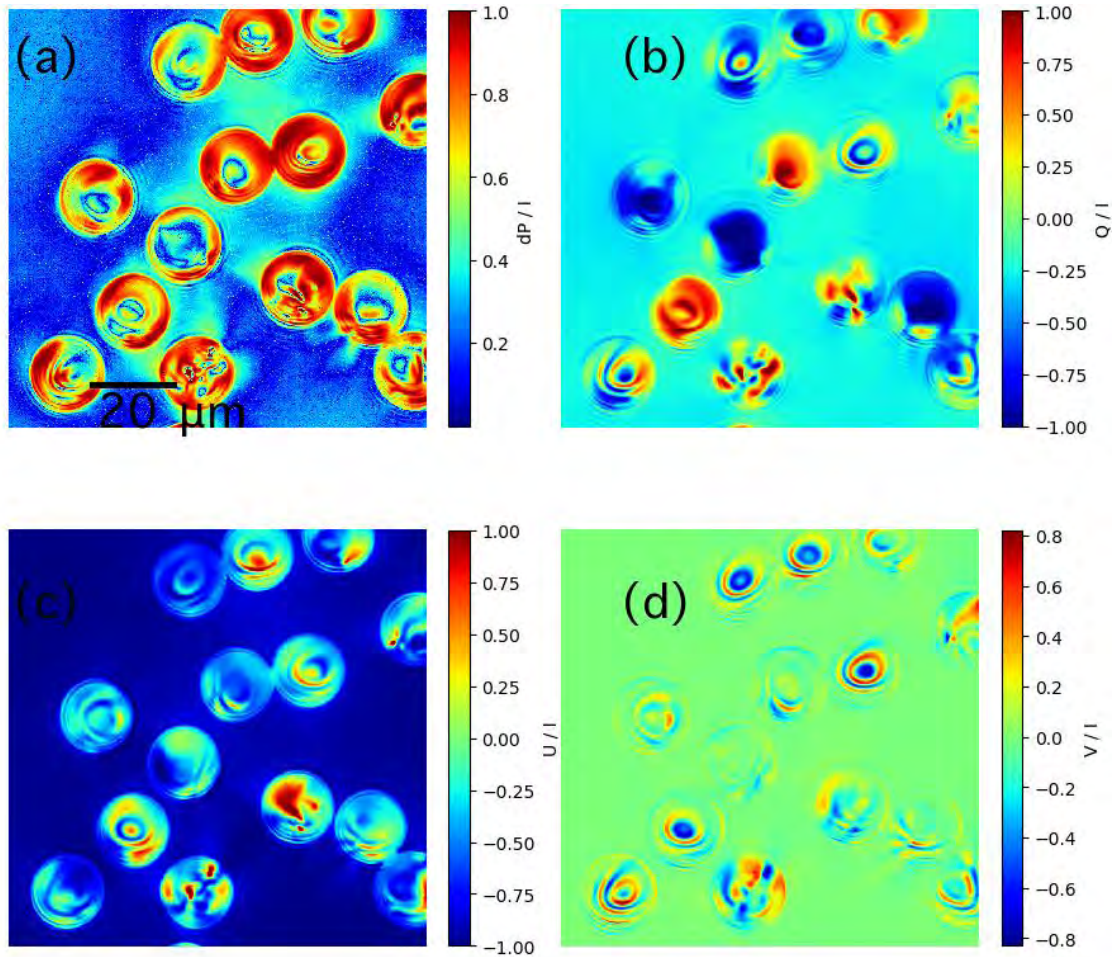


Figure 8.2.3.4 The image of (a) normalized depolarization, (b) normalized Stokes parameter Q/I , (c) normalized Stokes parameter U/I , and (d) normalized Stokes parameter V/I on LCD sample3.

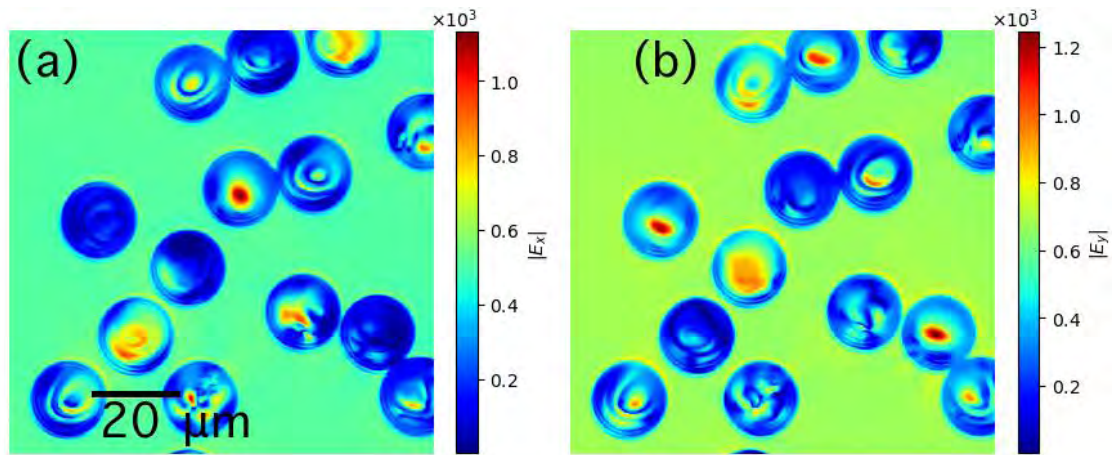


Figure 8.2.3.5 The modulus of the electric field of the LCD sample 3 with reference to the laboratory coordinate (a) x-axis and (b) y-axis.

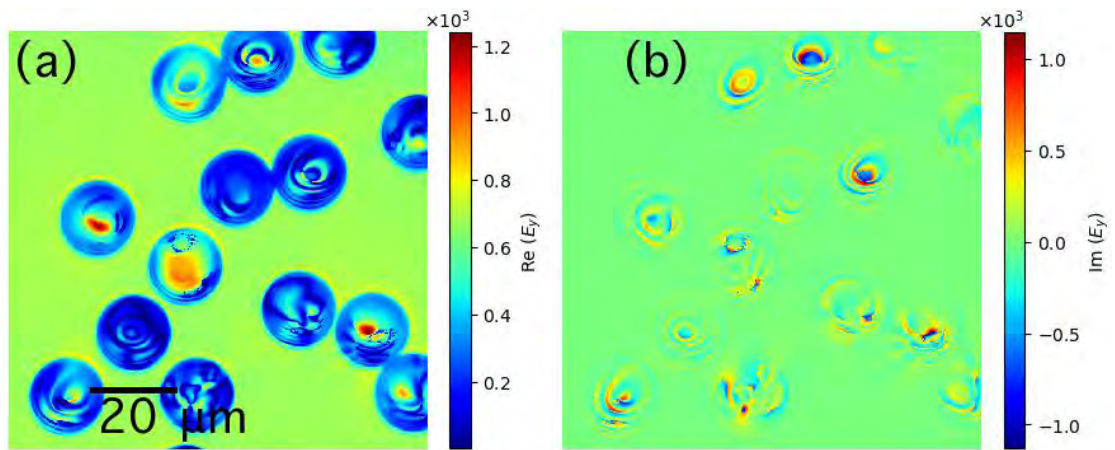


Figure 8.2.3.6 The electric field of the LCD sample 1 along y-axis: real part (a) and the imaginary part (b).

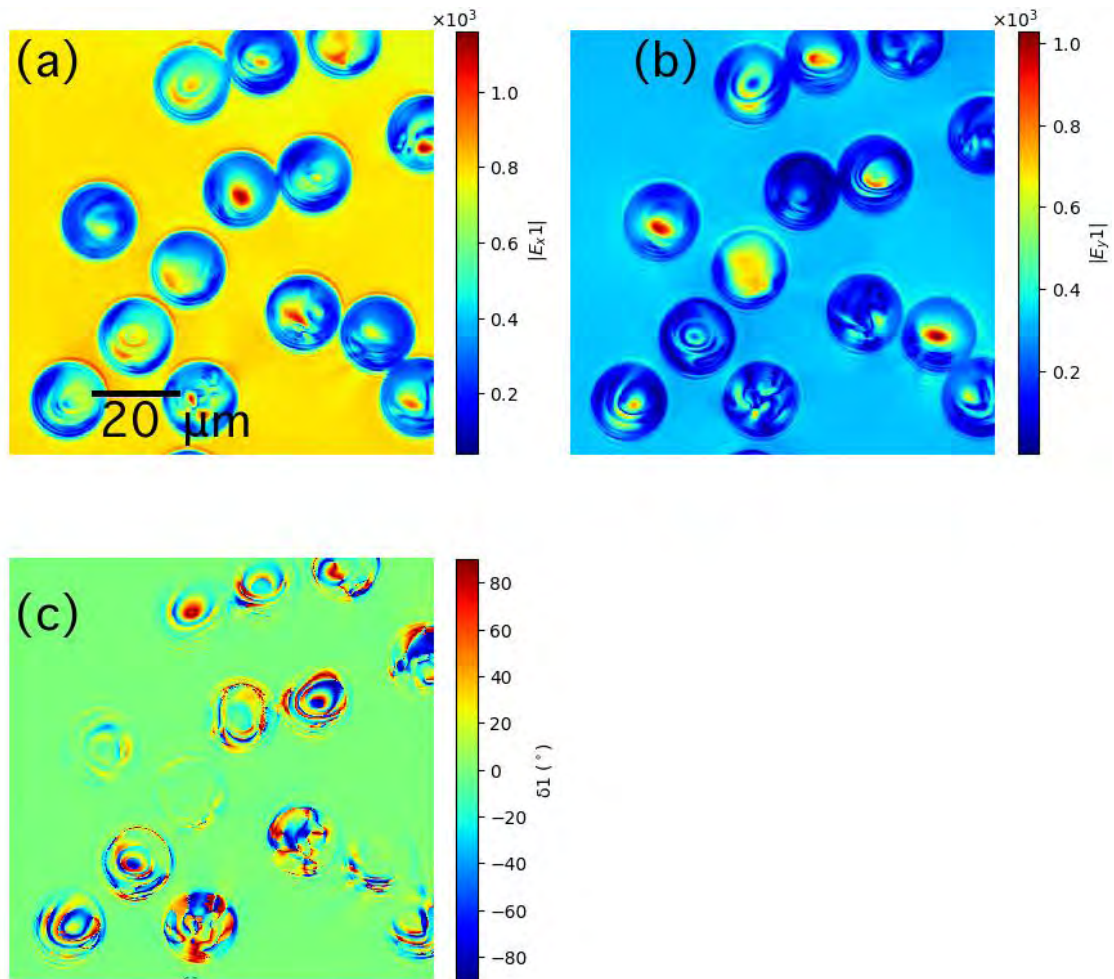


Figure 8.2.3.7 The modulus of the electric field of the LCD sample3 referenced to the polarizer coordinate: (a) modulus of electrical field along x1-axis, (b) modulus of electrical field along y1-axis, and (c) the retardation of phase δ_1

In conclusion, the structural information inside the droplet can be acquired in the image of the elliptical angle, azimuth angle, and V/I , which has big response scale. Also, it relates to the structure and material of the sample. When the structure is non uniform, the four parts structure cannot be seen as shown in sample 2. The microscope is a good way to detect the inner structure of a sample.

8.2.4 Sample4

Sample 4: PVA coated E7/S1011 (7.8 w%) liquid crystal droplets, which gives a planar alignment. The production of PVA coated LC droplets is same as sample 3.

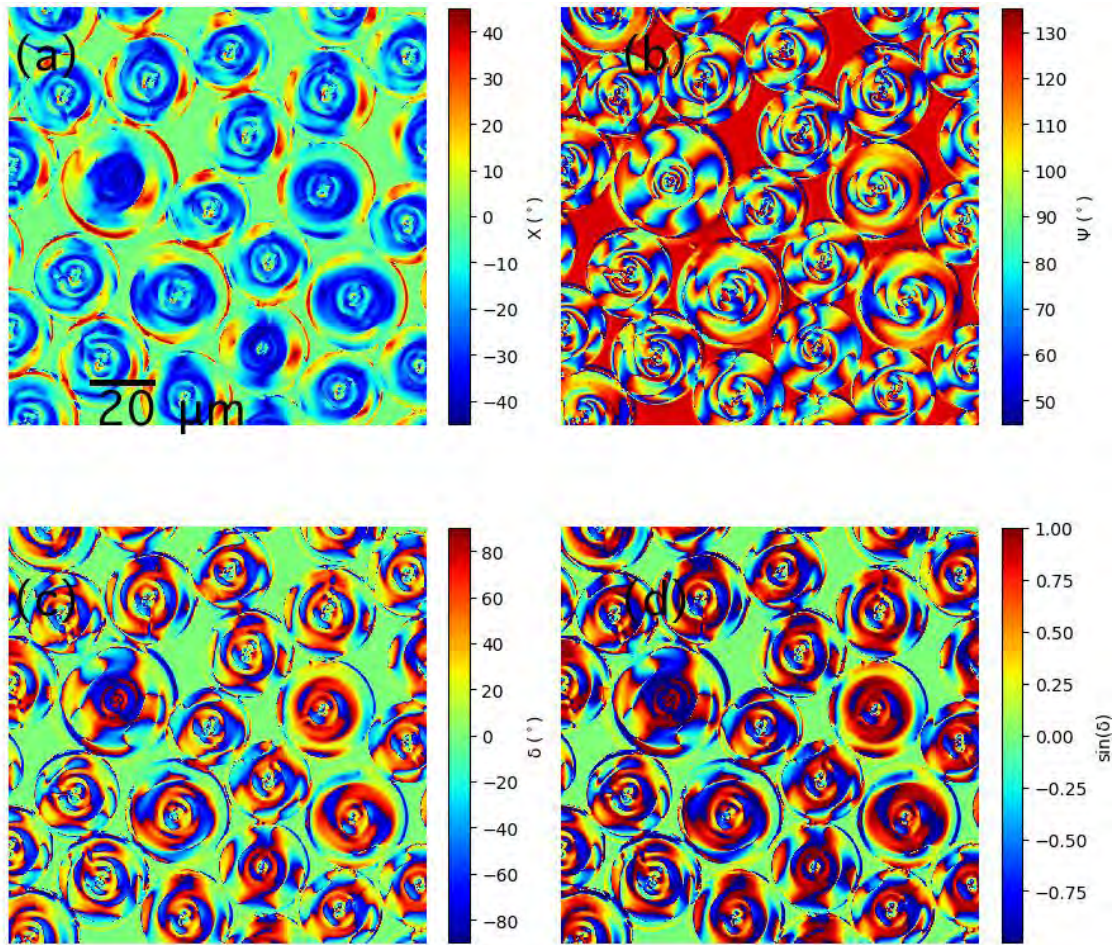


Figure 8.2.4.1 The contrast image of (a) the elliptical angle χ , (b) the azimuth angle ψ , (c) the retardation of phase δ , and (d) the $\sin(\delta)$ on LCD sample 4.

The polarization information is shown from Fig. 8.2.4.1 to Fig. 8.2.4.6. A defect line exists in the liquid crystal of sample 4. Two structures exist, shown in elliptical angle (Fig. 8.2.4.1a), the chirality is different. Figure 8.2.4.2b (image of Q) shows the difference of the structures more clearly. The difference of the two structures can also be observed in the image of the U and V.

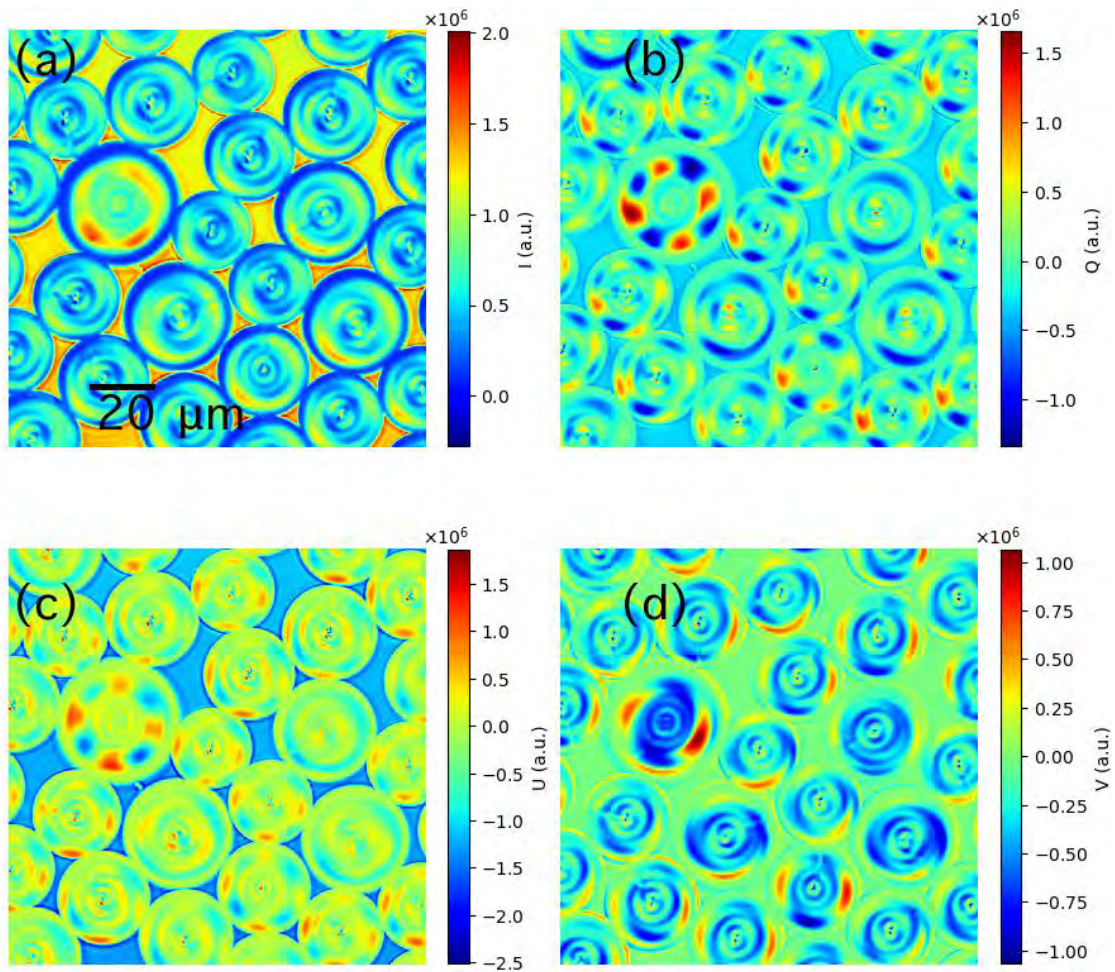


Figure 8.2.4.2 Image of contrast of the Stokes parameters on LCD sample4 : (a) Intensity, (b) Stokes parameter Q, (c) Stokes parameter U, and (d) Stokes parameter V.

The movement of the LCD makes the image of the normalized depolarization (Fig. 8.2.4.3a) very poor. The defect line in the LCD is very clear in the image of normalized Stokes parameter (Fig. 8.2.4.3c and Fig. 8.2.4.3d).

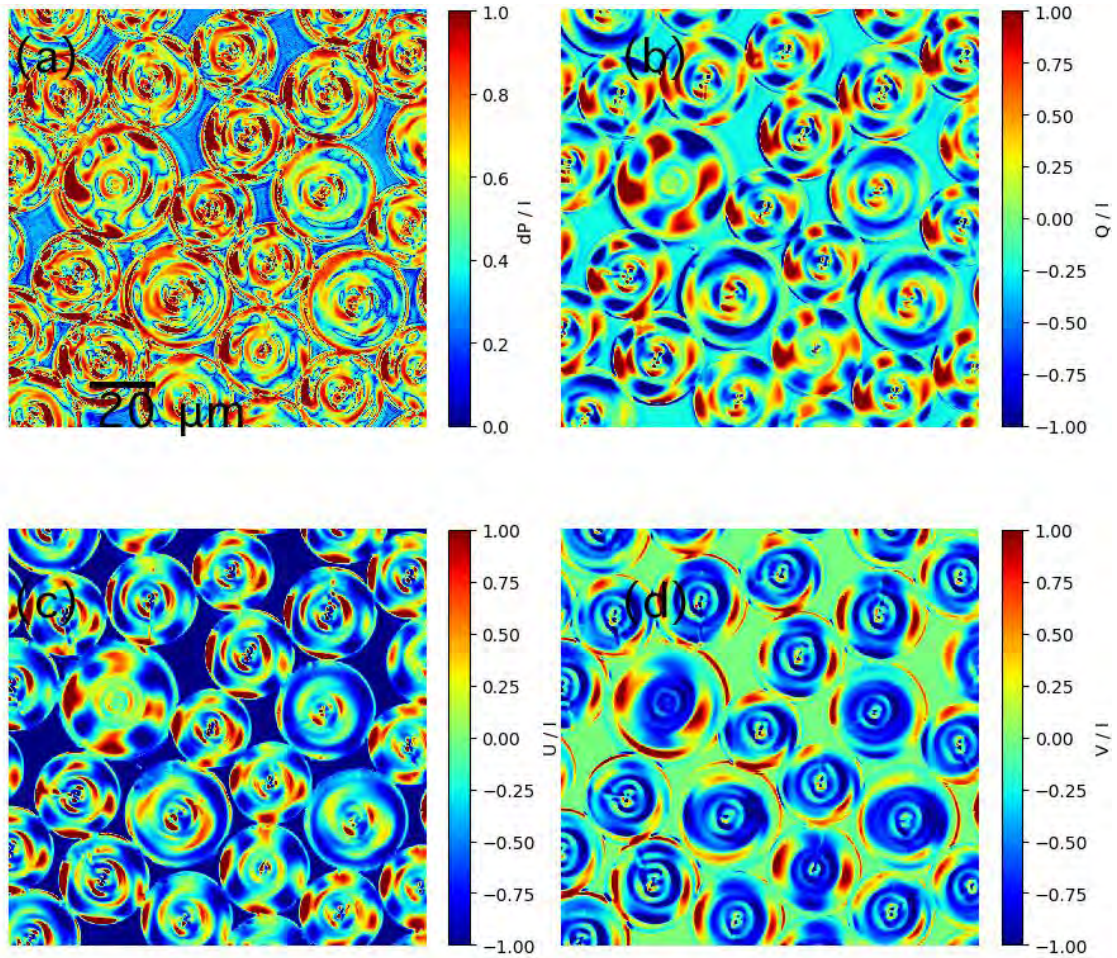


Figure 8.2.4.3 The image of (a) normalized depolarization dP/I , normalized Stokes parameters (b) Q/I , (c) U/I , and (d) V/I on LCD sample4.

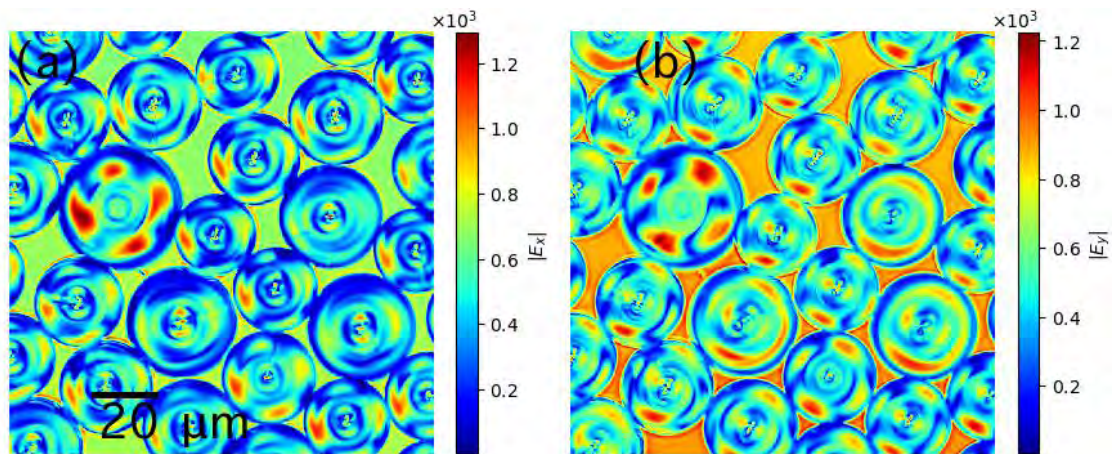


Figure 8.2.4.4 The modulus of the electric field of the LCD sample4 referred to the laboratory coordinate (a) x-axis and (b) y-axis.

The modulus of the electric field with reference to the laboratory coordinate is shown in Fig.

8.2.4.4. The real part and the imaginary part of the electrical field along y-axis is shown in Fig. 8.2.4.5. The movement of the droplet produces more effect on the image of the imaginary part of E_y .

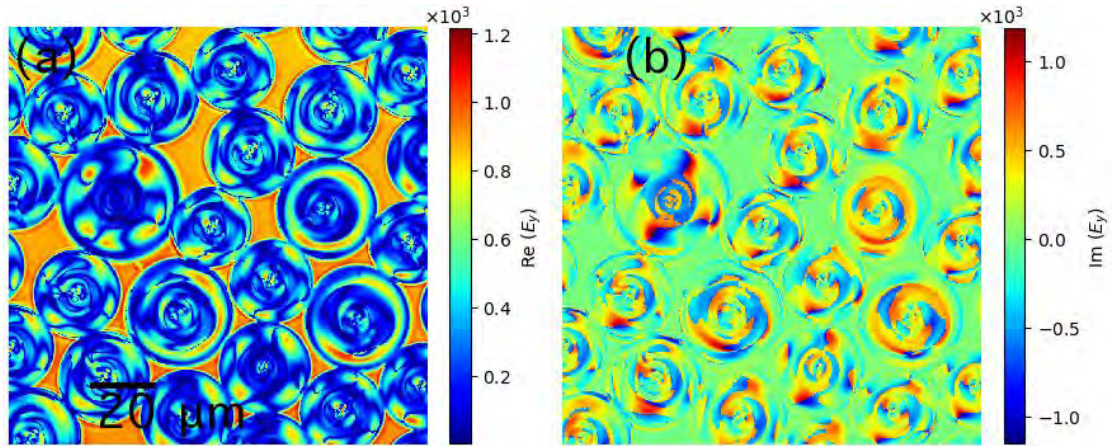


Figure 8.2.4.5 The electric field of the LCD sample4 along y-axis: (a) real part and (b) the imaginary part.

The modulus of the electric field along x_1 -axis and y_1 -axis, which are the axes of the polarization coordinate, are shown in Fig. 8.2.4.6. δ_1 is the phase difference between the y_1 -axis and x_1 -axis, Fig. 8.2.4.6c.

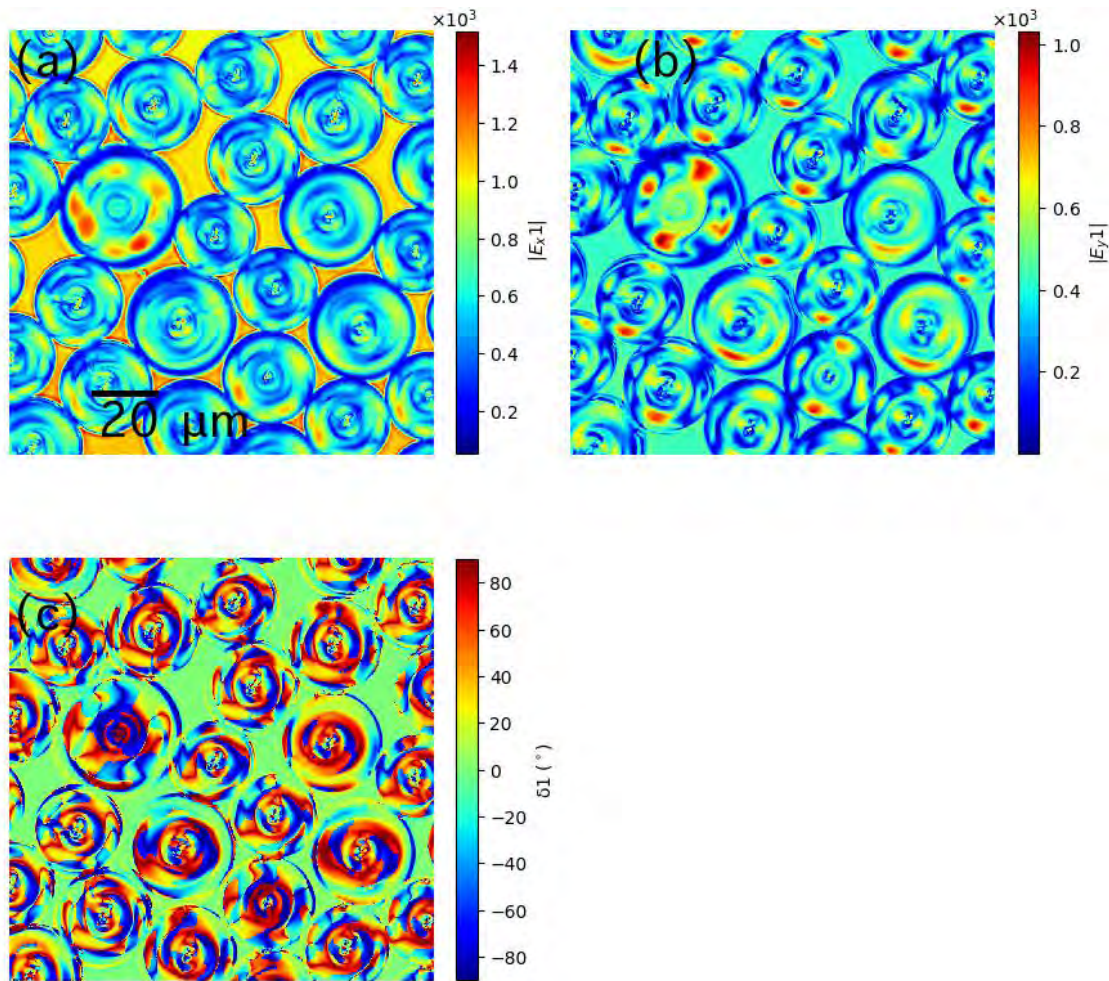


Figure 8.2.4.6 The modulus of the electric field of the LCD sample4 referred to the polarizer coordinate: (a) modulus of electric field along x_1 , (b) modulus of electrical field along y_1 , and (c) the retardation of phase δ_1

In summary, the defect in the chiral structure can be seen in the image of Stokes parameters.

The movement of the sample makes the image quality worse, because the data acquisition process of images is an accumulation process.

8.2.5 The movement of liquid crystal

To capture the images continually in a special time interval, I updated the controller program (version 7 in section 5.2.3). This set of data is acquired on liquid crystal sample 2 in a time interval of 1s. Fig. 8.2.5.1 is the intensity of LCD sample2; just a slight movement can be seen. The situation is similar in image of Q, U, and V, although they are not shown here. A

slight rotation of the LCD can be observed in the image of depolarization which is shown in Fig. 8.2.6-2. The normalized depolarization and the image of the $|E_{x1}|$ and $|E_{y1}|$ has the similar information but not significant. I am not going to show them here.

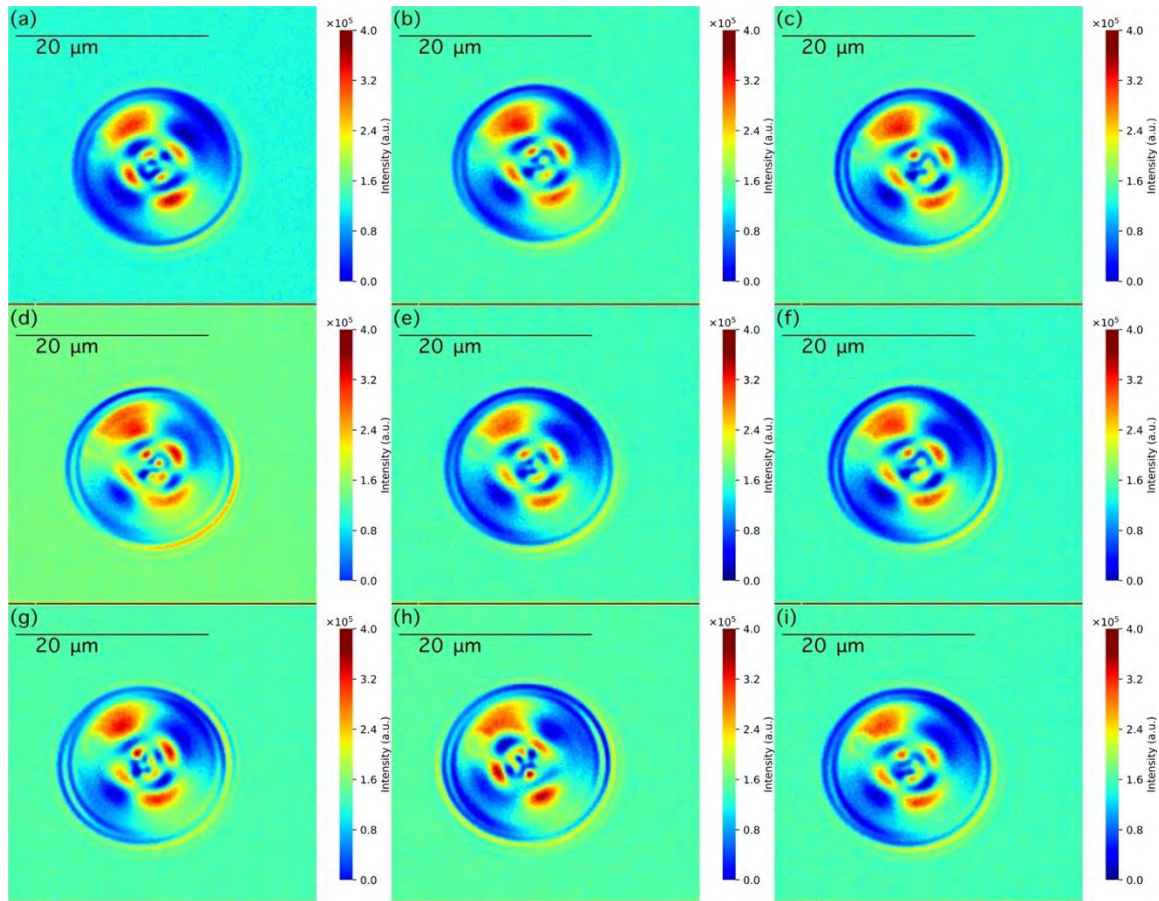


Figure 8.2.5.1 The mapping of I for the LCD sample2 tested in different time intervals, when the polarization azimuth angle sited at 128° and sample stage sited in 147° , sample number: (a) 0s, (b) 1s, (c) 2s, (d) 3s, (e) 4s, (f) 5s, (g) 6s, (h) 7s, (i) 8s

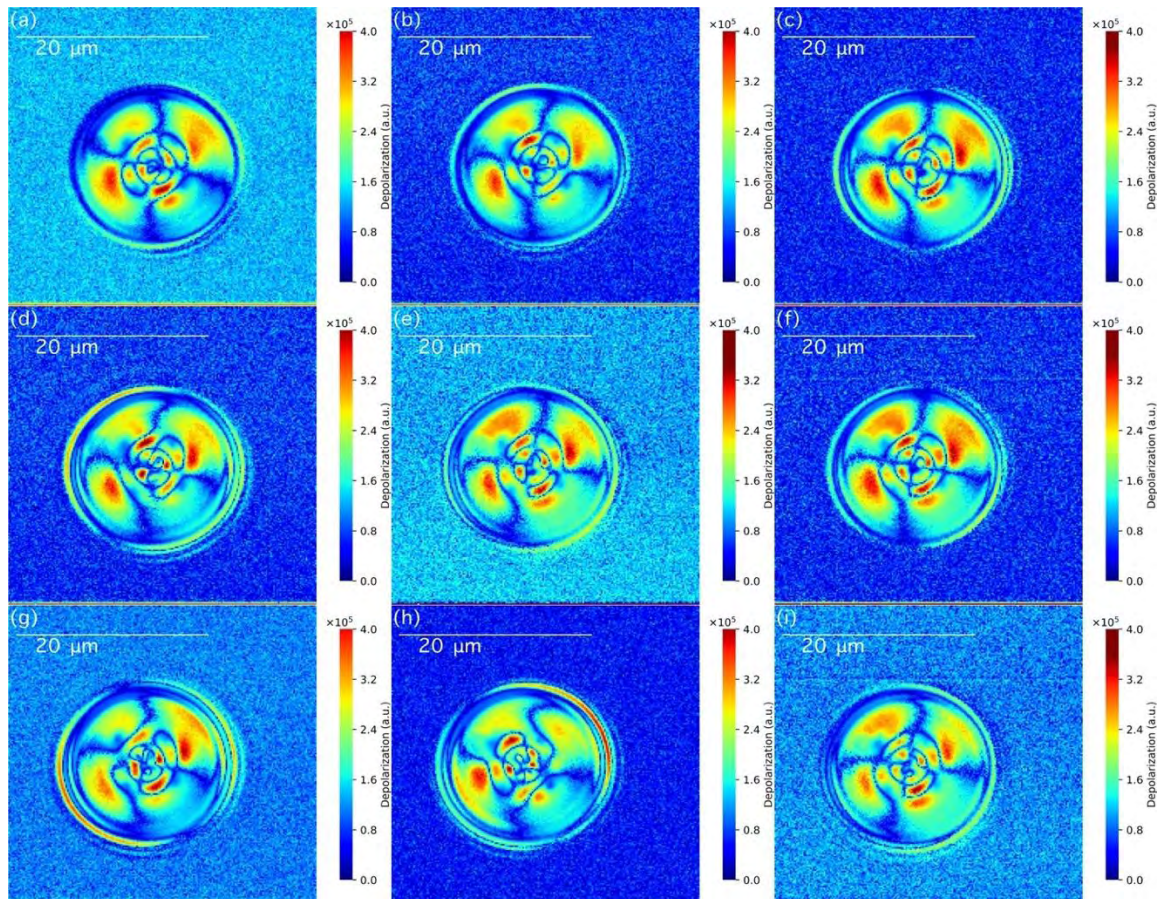


Figure 8.2.5.2 The mapping of I_{dP} for the LCD sample2 tested in different time intervals, when the polarization azimuth angle sited at 128° and sample stage sited in 147° , sample number: (a) 0s, (b) 1s, (c) 2s, (d) 3s, (e) 4s, (f) 5s, (g) 6s, (h) 7s, (i) 8s

In summary, the microscope can be used to observe the movement of the sample. The depolarization has more information than the intensity. It can be used to detect the revolve of a ball on its own axis.

8.3 Summary

The liquid crystal droplet, which is a ball, is studied, for its future application in the laser mode generation. The polarization pattern is sensitive to the inner structure of the liquid structure, that cannot be observed on the intensity image. The rotation and movement of the liquid crystal are observed in the depolarization image. The 180° symmetry is a characteristic of uniform matter with a circular boundary. The Stokes polarization measurement provides

more information on structure of the material that need to be researched further.

Reference

Bao, P., Paterson, D. A., Harrison, P. L., Miller, K., Peyman, S., Jones, J. C., ... Gleeson, H.

F. (2019). Lipid coated liquid crystal droplets for the on-chip detection of antimicrobial peptides. *Lab on a Chip*. <https://doi.org/10.1039/C8LC01291A>

Cooper, J. (n.d.). *Compositional Analysis of Merck E7 Liquid Crystal Intermediates Using UltraPerformance Convergence Chromatography (UPC 2) with PDA Detection*.

Retrieved from <https://www.waters.com/webassets/cms/library/docs/720004814en.pdf>

Humar, M., & Muševič, I. (2010). 3D microlasers from self-assembled cholesteric liquid-crystal microdroplets. *Optics Express*, *18*(26), 26995–27003.

<https://doi.org/10.1364/OE.18.026995>

Iib, S. (2016). Materials for soft matter photonics, (May), 11. Retrieved from

[http://mafija.fmf.uni-](http://mafija.fmf.uni-lj.si/seminar/files/2015_2016/Materials_for_soft_matter_photonics.pdf)

[lj.si/seminar/files/2015_2016/Materials_for_soft_matter_photonics.pdf](http://mafija.fmf.uni-lj.si/seminar/files/2015_2016/Materials_for_soft_matter_photonics.pdf)

Krakhalev, M. N., Gardymova, A. P., Prishchepa, O. O., Rudyak, V. Y., Emelyanenko, A. V,

Liu, J.-H., & Zyryanov, V. Y. (2017). Bipolar configuration with twisted loop defect in chiral nematic droplets under homeotropic surface anchoring. *Scientific Reports*, *7*(1),

14582. <https://doi.org/10.1038/s41598-017-15049-6>

Yoshioka, J., & Araoka, F. (2018). Topology-dependent self-structure mediation and efficient energy conversion in heat-flux-driven rotors of cholesteric droplets. *Nature*

Communications, *9*(1), 432. <https://doi.org/10.1038/s41467-018-02910-z>

Chapter 9 Research of the nanograters

The Polarimetric microscope can measure the vector field of the electromagnetic wave near to the sample. Due to a kind of nonlinear metamaterial (nanograter) is response to electrical field along two orthogonal directions (the optical axis of a polarizer and the direction perpendicular to the optical axis) in different way; the research using the polarimetric microscope to measure the electrical field around the nanograter is interesting and important.

experiment of the nanograter

9.1 Experiment

9.1.1 Experiment of nanograter

In the research of nanograter, three sample stage is used. A sample rotation stage (sample stage 3) is the best one, which is mounted on the microscope shown in Fig. 9.1.1.1a. Figure 9.1.1.1b show the detail of the sample stage 3. Sample stage 3 include two dial circle on the polarizer and the sample stage that can realizes the accurate controlling the angle of the polarizer and the sample.

Nanograter sample is provided by the Institute of Physics, Chinese Academy of Sciences, China. The nanograter samples are marked in a series of numbers, which is shown in Fig. 9.1.1.2. The shape of the nanograter unit is U-shape, Flower shape, square sjape, and rectangle shape. The experiment did on nanograter is shown in Table 9.1.1.1. The U-shape structure is measured in two ways, polarizer rotation and the sample stage rotation. To increase the quality of the imaging, an antireflection polarizer is used in the later stage of the experiment.

In the experiment of fix the azimuth angle of polarization at 122° , a new coordinate called polarizer coordinate is defined here, which is x_1Oy_1 . The axis of x_1 keeps an angle ϑ with the

x-axis of the laboratory coordinate about 30° . The configuration of two coordinate is shown in Fig. 9.1.1.3.

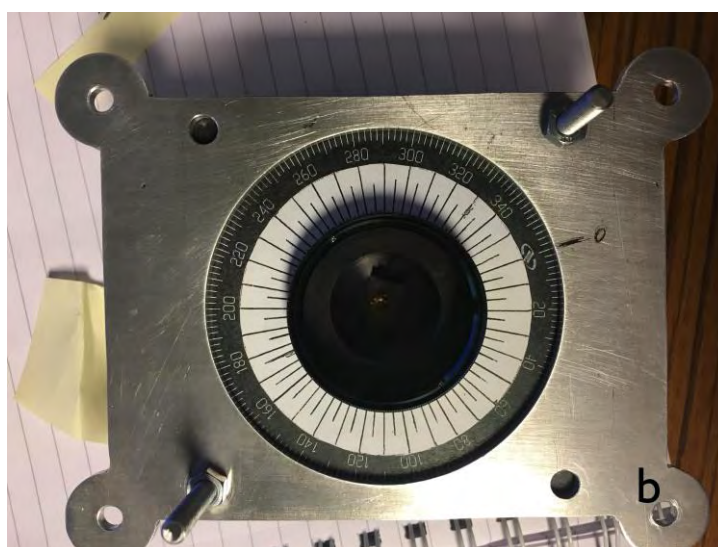
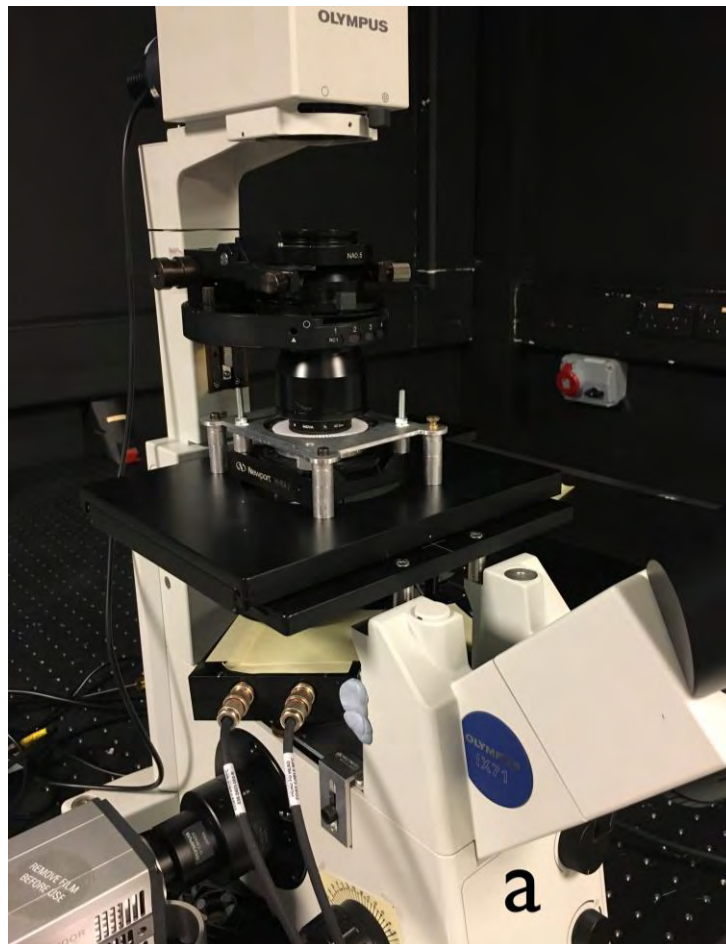


Figure 9.1.1.1 The configuration of the experiment: (a) the sample stage 3 mounted on the

microscope; (b) the sample stage 3



Figure 9.1.1.2 The number of the nanograting samples

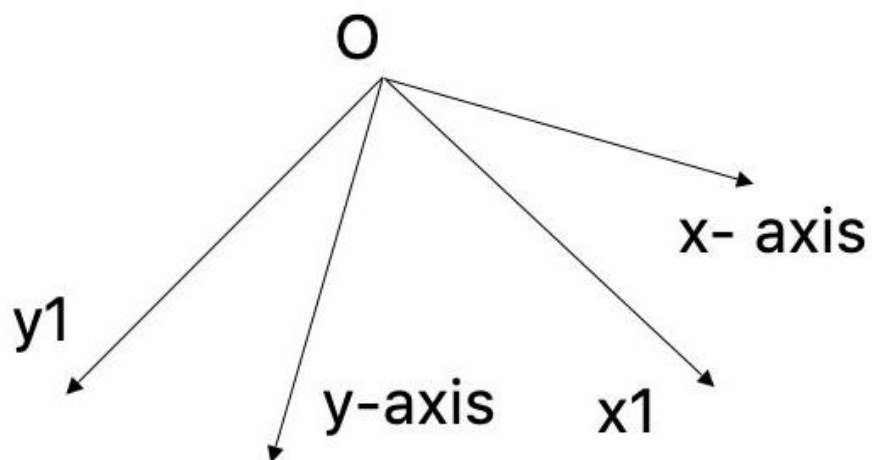


Figure 9.1.1.3 the diagram of the polarization coordinate and the laboratory coordinate

Because the image of elliptical angle is divided into positive and negative along the azimuth angle of the polarization. It is reasonable to detect the electrical field along the azimuth angle of the polarization (the x_1 -axis and y_1 -axis).

The coordinate transformation of the electrical field between the laboratory coordinate and polarization coordinate is rely on the equation shows below.

$$a_0 = |E_y|^2 \quad (9.1.1.1)$$

$$b_0 = |E_x|^2 \quad (9.1.1.2)$$

$$a' = a_0 \cos^2 \vartheta + b_0 \sin \vartheta \cos \vartheta + c_0 \sin^2 \vartheta \quad (9.1.1.3)$$

$$c' = a_0 \sin^2 \vartheta - b_0 \sin \vartheta \cos \vartheta + c_0 \cos^2 \vartheta \quad (9.1.1.4)$$

$$|E_{x1}| = \sqrt{c'} \quad 9.1.1.5)$$

$$|E_{y1}| = \sqrt{a'} \quad (9.1.1.6)$$

$$\delta_1 = \sin^{-1} \left(\sqrt{(a_0 c_0) / (a' c')} \sin \delta \right) \quad (9.1.1.7)$$

Table 9.1.1.1 the experiment of nanograter performed on the microscope: “┘” means the protrusion of the nanograter facing the light source; “└” means the protrusion of nanograter is facing the camera

Date	sample number	Lens	polarizer (°)	sample stage (°)	Configuration	Polarizer	Sample	Orientation
2019/2/21	7,8,9	40	120			Normal	sample stage 1	┘
2019/2/25	1	64	07 – 357		Focused	Normal	sample stage 1	┘
2019/2/27	1	64	297		Unfocused	Normal	sample stage 1	┘
2019/3/1	1,2-3,4-5,7,8	64	152		Focused	Normal	sample stage 2	┘
2019/3/4	9, ---, 27	64	152		Focused	Normal	sample stage 2	┘
2019/3/5	28, ---, 45, 2,3,4,5	64	152		Focused	Normal	sample stage 2	┘
2019/3/11	1, ---, 12	64	110	101	Focused	antireflection	sample stage 3	┘
2019/3/12	13, ---, 32	64	110	101	Focused	antireflection	sample stage 3	┘
2019/3/13	34, ---, 47	64	110	101	Focused	antireflection	sample stage 3	┘
	4, ---, 12	64	110	191	Focused	antireflection	sample stage 3	┘
2019/3/14	1, 2, 3, 13, ---, 33	64	110	191	Focused	antireflection	sample stage 3	┘
2019/3/15	34, ---, 47	64	110	191	Focused	antireflection	sample stage 3	┘
	13, 14, 15	64	110	146	Focused	antireflection	sample stage 3	┘
2019/3/18	1, 2	64	110	146	Focused	antireflection	sample stage 3	┘
	2	64	110	144	Focused	antireflection	sample stage 3	┘
	1,2, 8, 9, 10	64	110	148	Focused	antireflection	sample stage 3	┘
2019/3/19	2, ---, 7, 11, ---, 40	64	110	148	Focused	antireflection	sample stage 3	┘
2019/3/20	1	64	110	58, 238, 328	Focused	antireflection	sample stage 3	┘
	1	64	20	328	Focused	antireflection	sample stage 3	┘
	1	64	20	148	Focused	antireflection	sample stage 3	┘
	2, ---, 6	64	20	148	Focused	antireflection	sample stage 3	┘
2019/3/21	7,8,9,10, 11-12	64	20	148	Focused	antireflection	sample stage 3	┘
	1, ---, 32	64	20	328	Focused	antireflection	sample stage 3	┘
2019/3/22	31-47	64	20	328	Focused	antireflection	sample stage 3	┘
	15	64	20	328	Unfocused	antireflection	sample stage 3	┘
	1	64	20	304, 214, 124	Focused	antireflection	sample stage 3	└
2019/3/25	1	64	20	124, 34	Focused	antireflection	sample stage 3	└
	1	64	110	34, 304	Focused	antireflection	sample stage 3	└
	1	64	110	304	Unfocused	antireflection	sample stage 3	└
	10,20,19,17,35,32, 24	64	110	304	Focused	antireflection	sample stage 4	└

9.2 Results and discussion

9.2.1 Polarizer rotation experiment

A linear polarizer is rotated, when measuring the U-shape nanograter, with the intervals of 10° from 007° to 357° . The polarization angle is reference to the laboratory coordinate shown in Fig. 6.2.1.1. The calculation of the azimuth angle is according to the equation 2.1.2.11 in chapter 2 to make sure the azimuth angle measured follow the setting of the polarizer. The protrusion of the nanograter is facing the light source. The measured pattern is varied with the rotation of polarizer. The mapping of intensity is shown in Fig. 9.2.1.1. The mapping of Stokes parameter Q shown in Fig. 9.2.1.2, is depending on the rotation of the polarizer. It is the same to the U and V, shown in Fig. 9.2.1.3 and Fig. 9.2.1.4. Generally, there are four type patterns in the image of V shown in Fig. 9.2.1.4. The normalized depolarization and Stokes parameters are shown in Fig. 9.2.1.5, Fig. 9.2.1.6, Fig. 9.2.1.7, and Fig. 9.2.1.8. Because the nanograter is a scattering system, much scattering exists in this process, so much noise existed in the image of normalized signals. The position in red means the normalized depolarization is near to 1, shown in Fig. 9.2.1.5. From Fig. 9.2.1.6, we can know the periodicity of the polarizer rotation should be 180° . That is correspondence to the property of the polarizer. Fig.9.2.1.9 to Fig. 9.2.1.12 shows the mapping of related angles in the polarization measurement, such as, elliptical angle χ , azimuth angle ψ , phase difference δ , and $\sin \delta$. The mapping of the azimuth angle of the polarization shown in Fig. 9.2.1.10. A rotation happened on a linear polarization when the light going through the nanograter. In the position of the space between U-shape hole, the azimuth angle of the polarization is same to the incident polarized light. A variation of azimuth angle happens at the position of the nanograter. The range of the variation changes with the rotation of the polarizer. A minimum variation is sited at 217° in Fig. 9.2.1.10. In the two positions, the U-shape hole can't be seen. That means the polarization rotation only happens on the protrusion of the nanograter. A

minimum variation of azimuth angle at 57° . This is not existed on the 180° symmetric position at 237° .

δ is the phase difference of the electrical field between y-axis and x-axis. The mapping of δ is shown in Fig. 9.2.1.11. In some special configuration, such as 337° and 157° shown in Fig. 9.2.1.11, the δ near to zero. The mapping of $\sin(\delta)$ is shown in Figure 9.2.1.12. The variation is same to δ in Figure 9.2.1.11.

Figure 9.2.1.13 and Fig. 9.2.1.14 shows the modulus of the electrical field along x-axis and y-axis shown in Fig. 9.1.1.3. The electrical field along y-axis E_y is an imaginary number. Its real part and imaginary part are shown in Fig. 9.2.1.15 and Fig. 9.2.1.16.

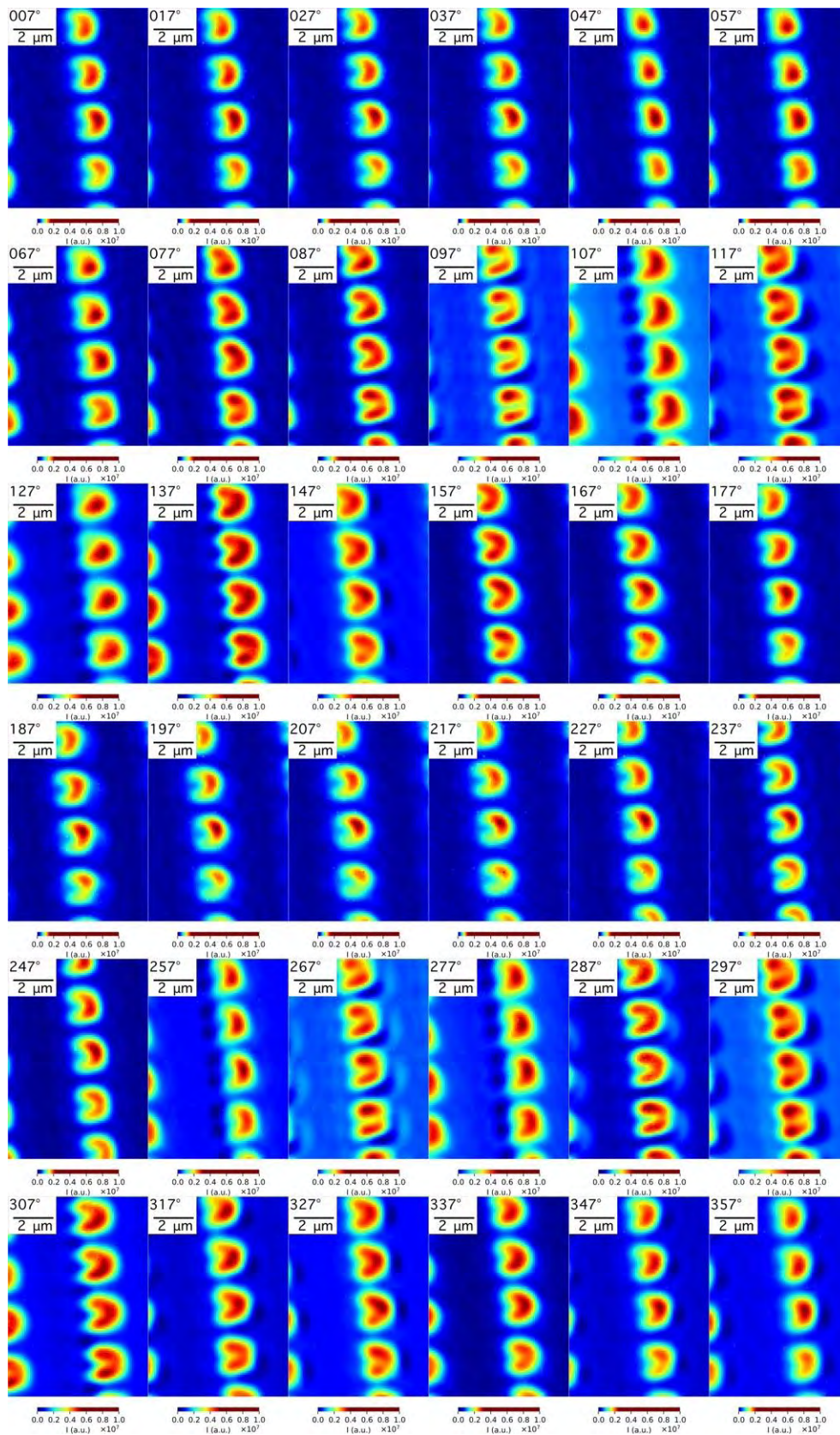


Figure 9.2.1.1 The mapping of I for the nanograting tested at different polarization angles reference to the laboratory coordinate

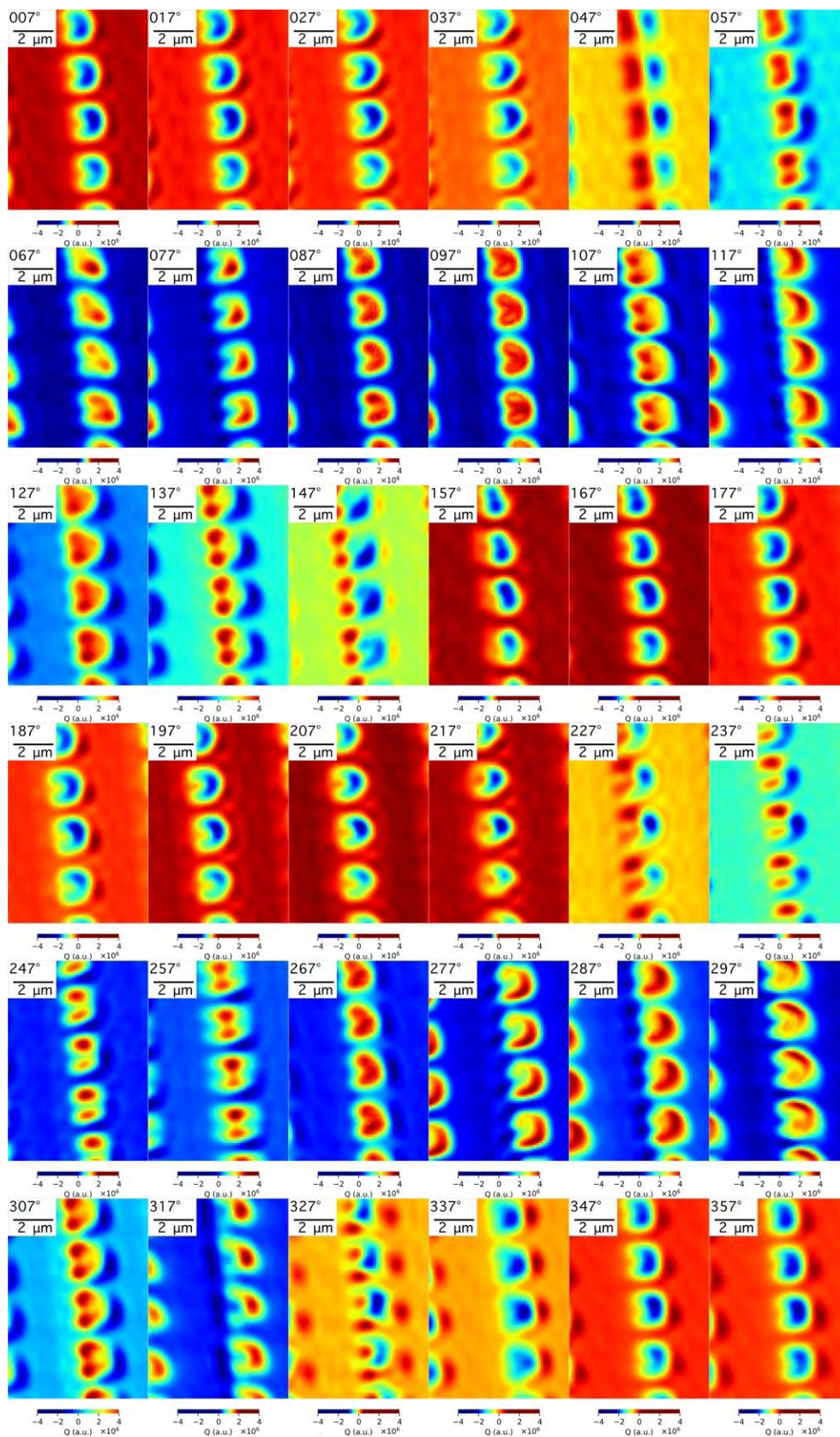


Figure 9.2.1.2 The mapping of Q for the nanograting tested at different polarization angles reference to the laboratory coordinate.

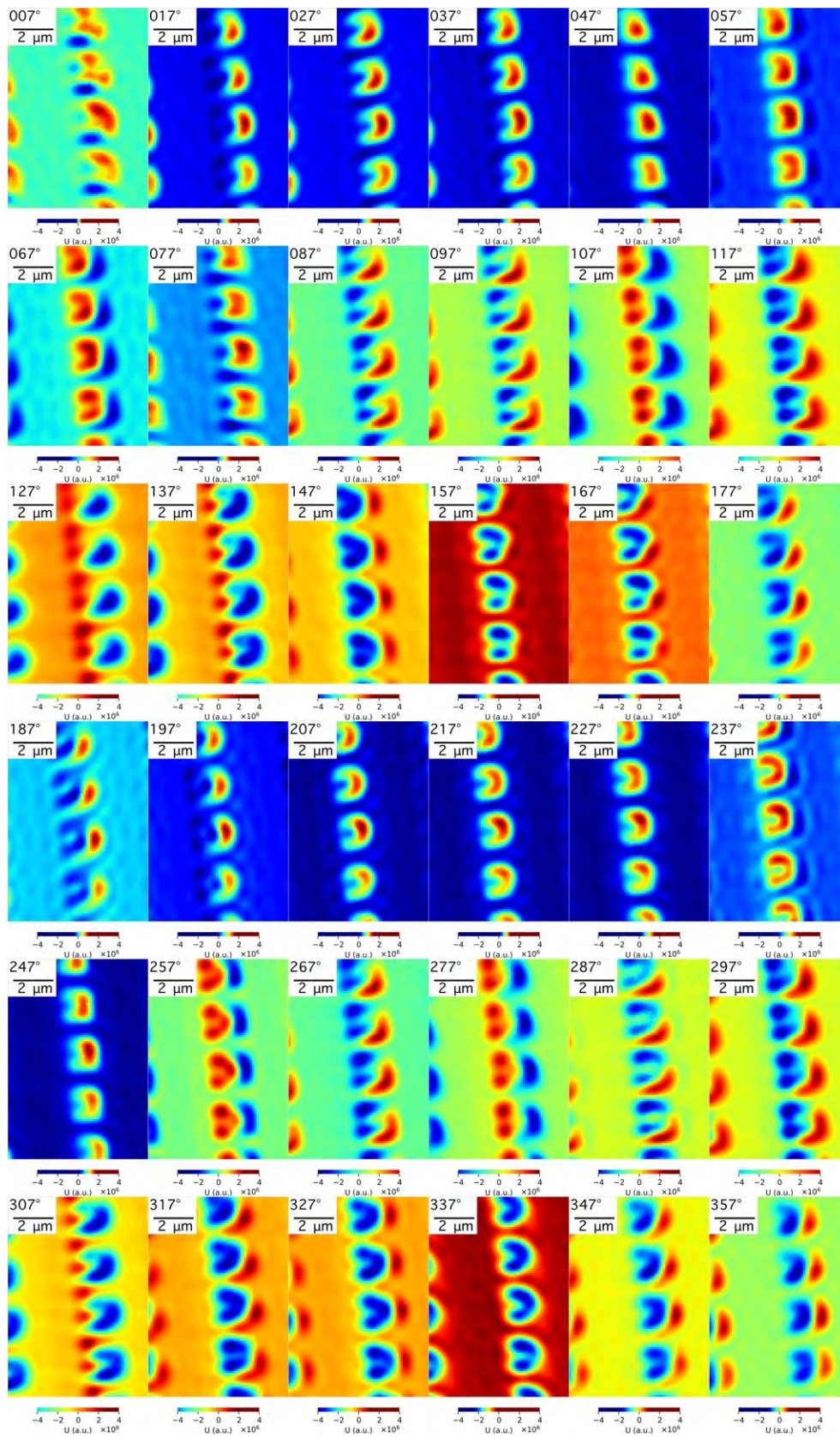


Figure 9.2.1.3 The mapping of U for the nanograting tested at different polarization angles reference to the laboratory coordinate.

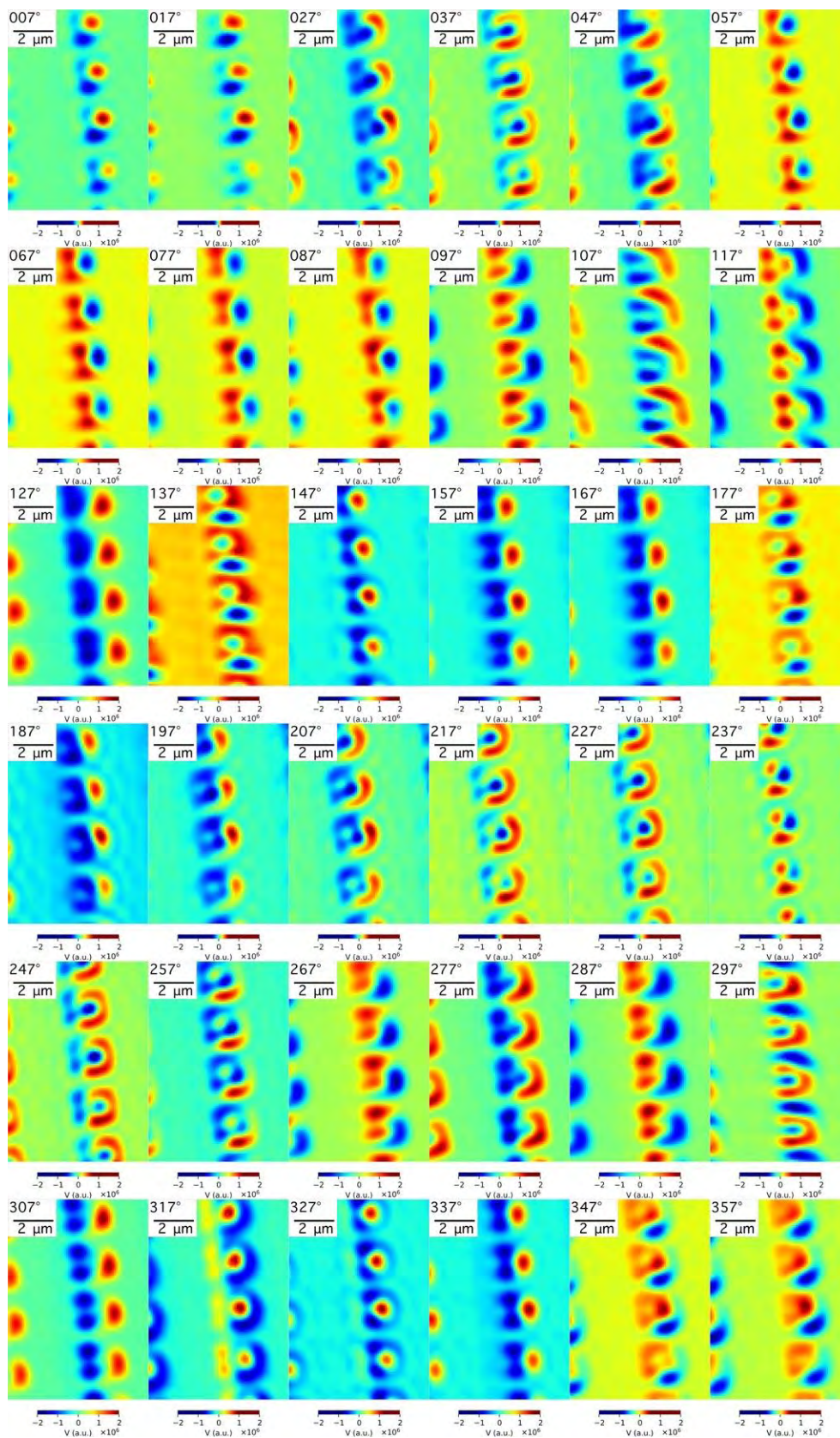


Figure 9.2.1.4 The mapping of V for the nanograting tested at different polarization angles reference to the laboratory coordinate.

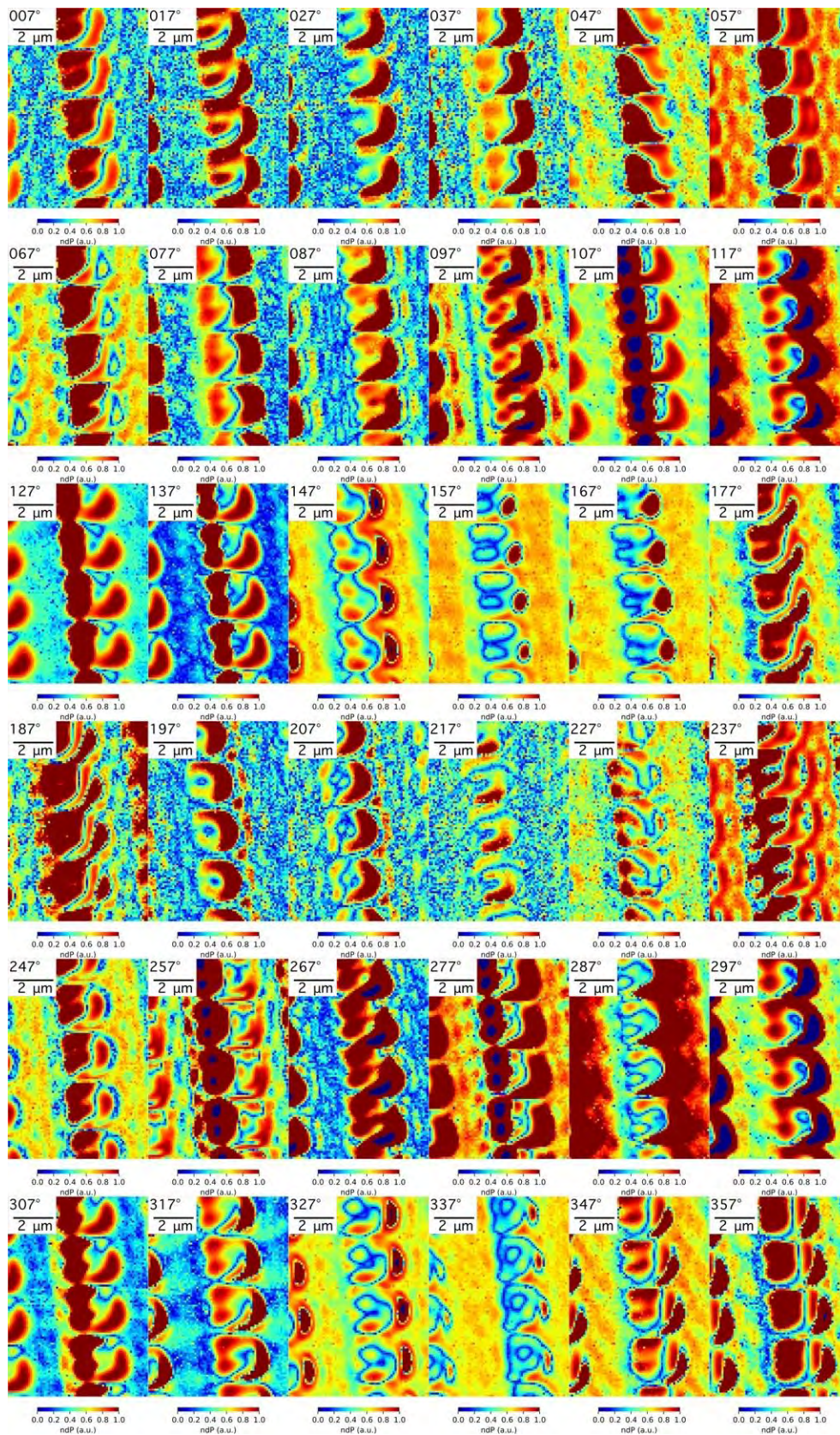


Figure 9.2.1.5 The mapping of I_{DP}/I for the nanograter tested at different polarization angles reference to the laboratory coordinate.

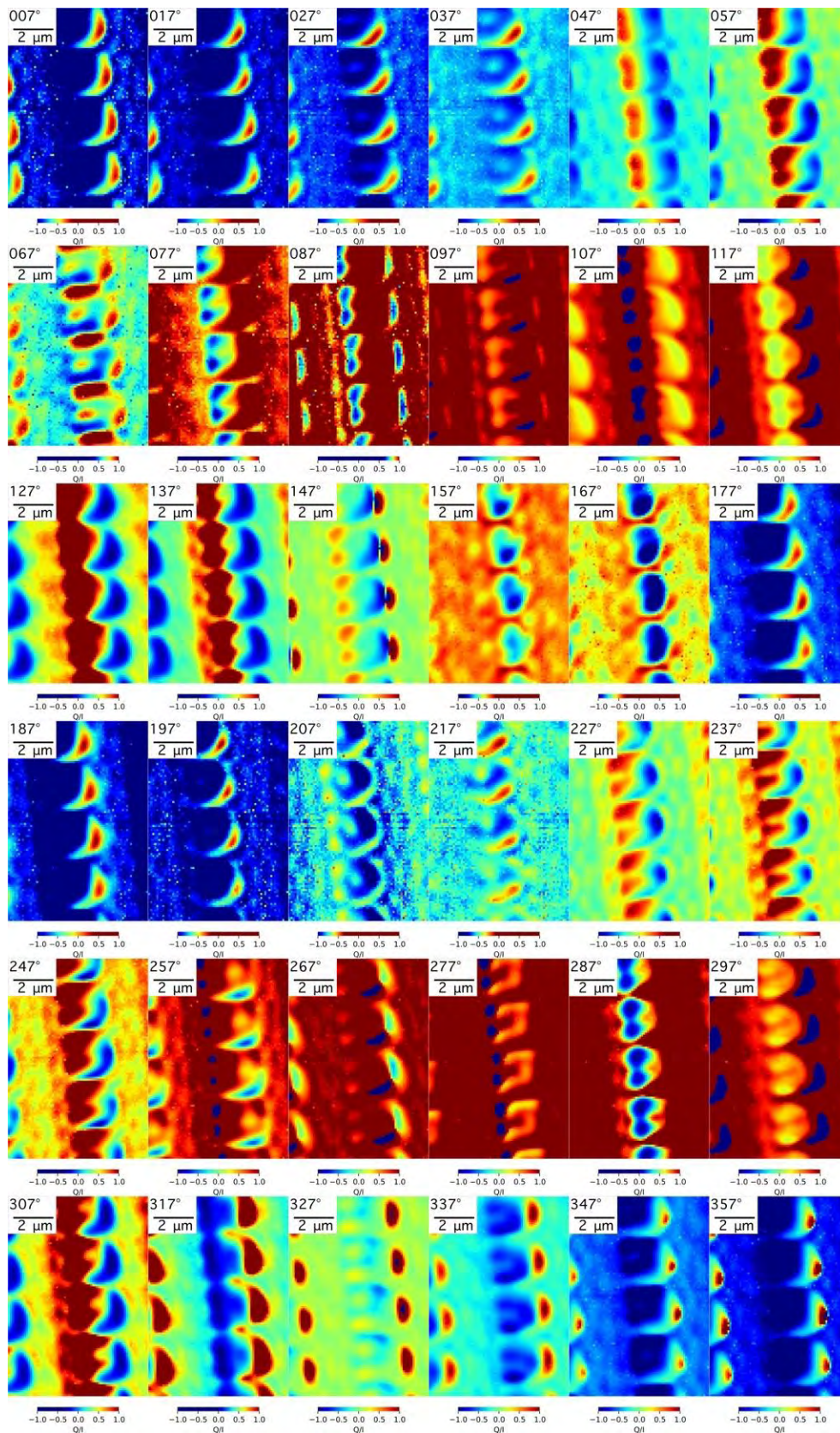


Figure 9.2.1.6 The mapping of Q/I for the nanograting tested at different polarization angles reference to the laboratory coordinate.

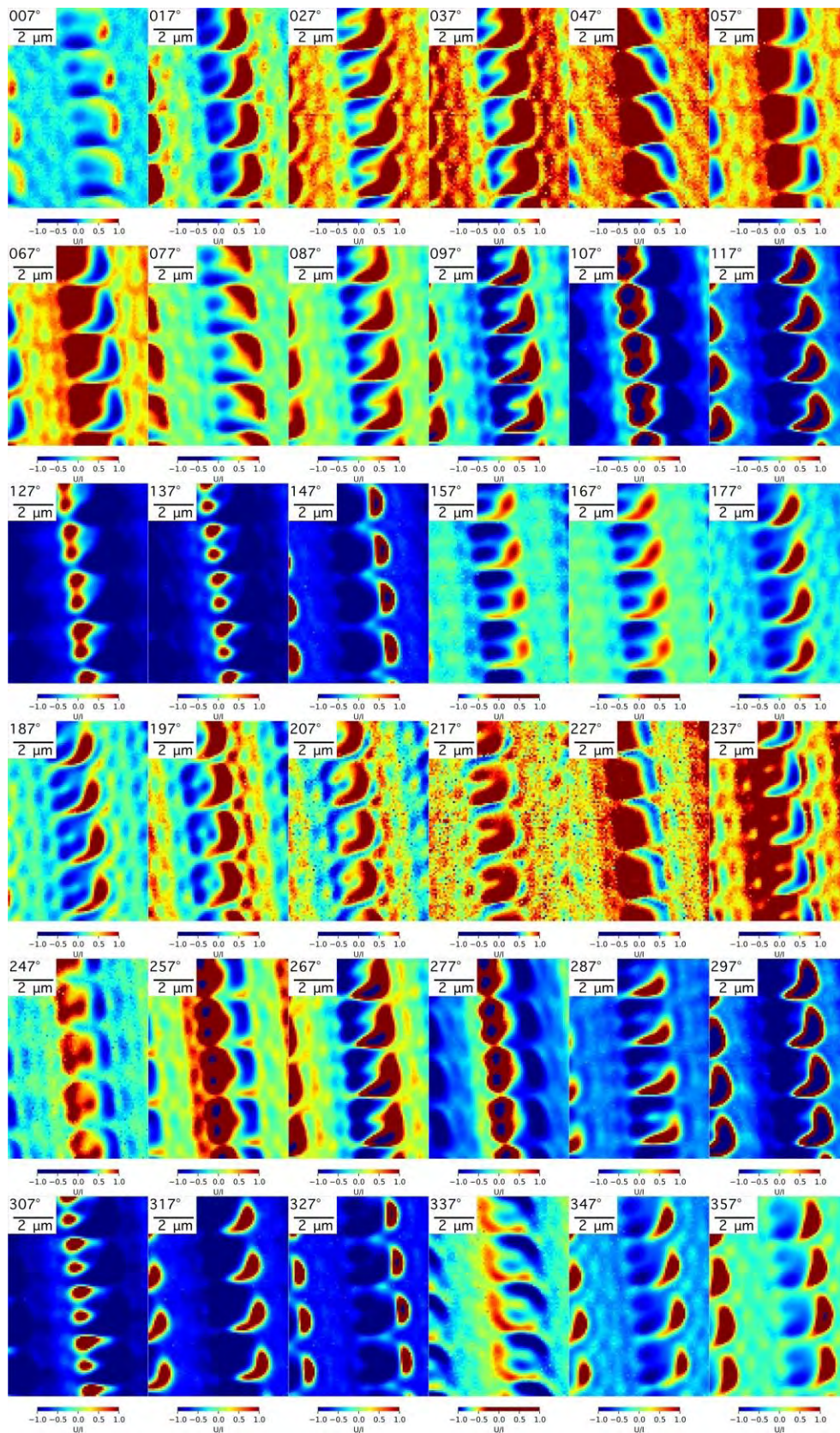


Figure 9.2.1.7 The mapping of U/I for the nanograting tested at different polarization angles reference to the laboratory coordinate.

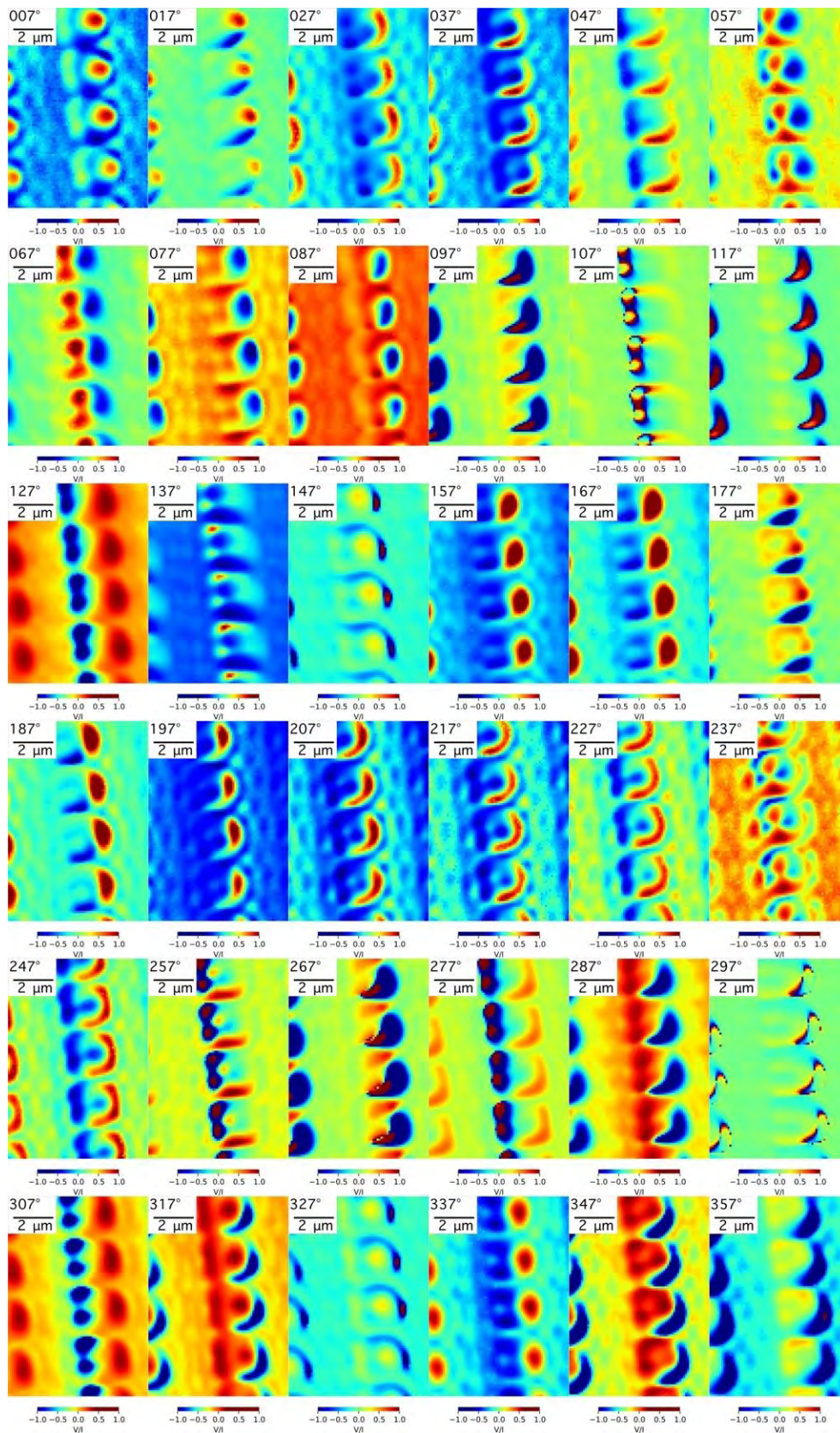


Figure 9.2.1.8 The mapping of V/I for the nanograting tested at different polarization angles reference to the laboratory coordinate.

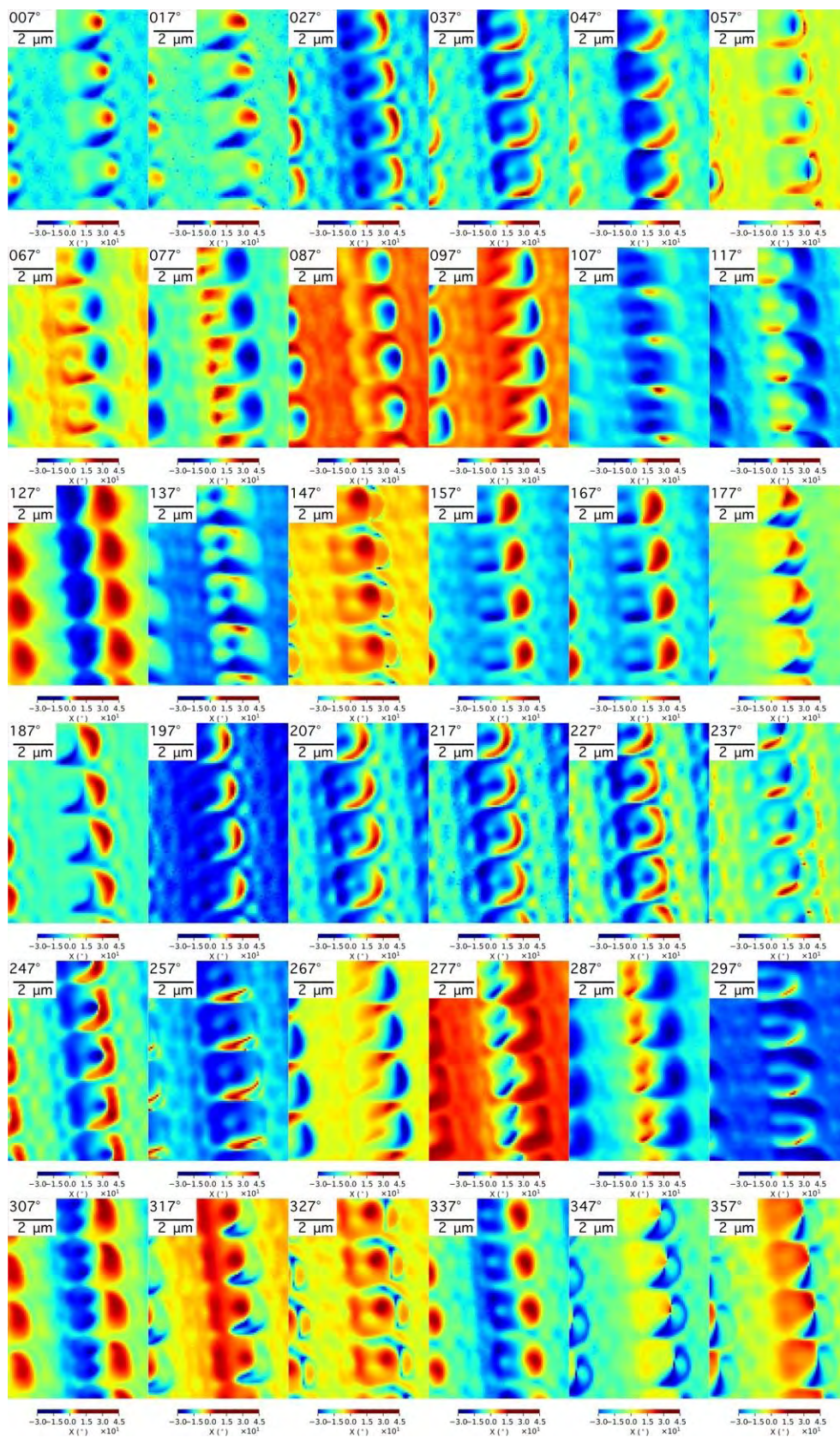


Figure 9.2.1.9 The mapping of χ for the nanograting tested at different polarization angles reference to the laboratory coordinate.

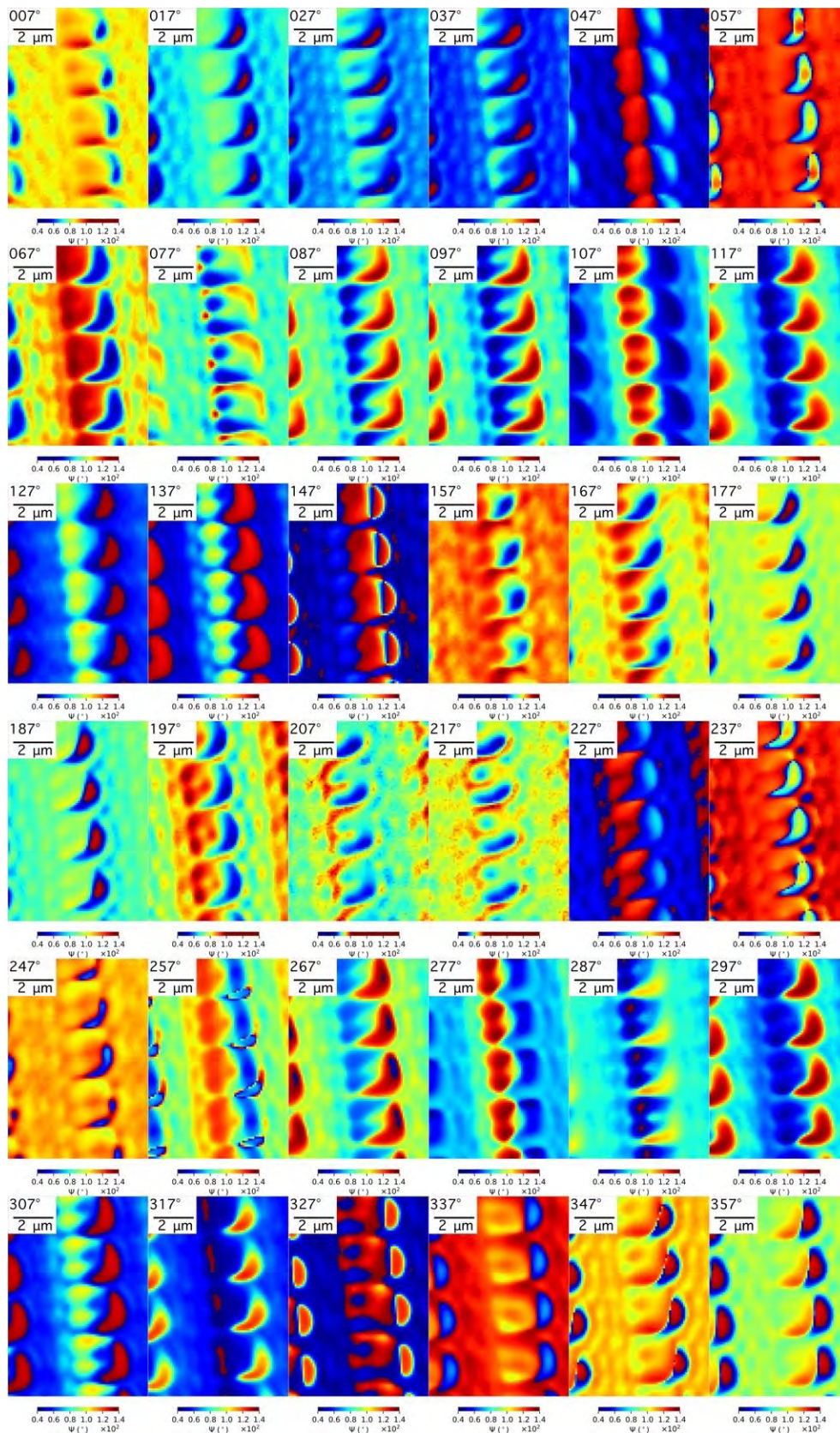


Figure 9.2.1.10 The mapping of ψ for the nanograter tested at different polarization angles reference to the laboratory coordinate.

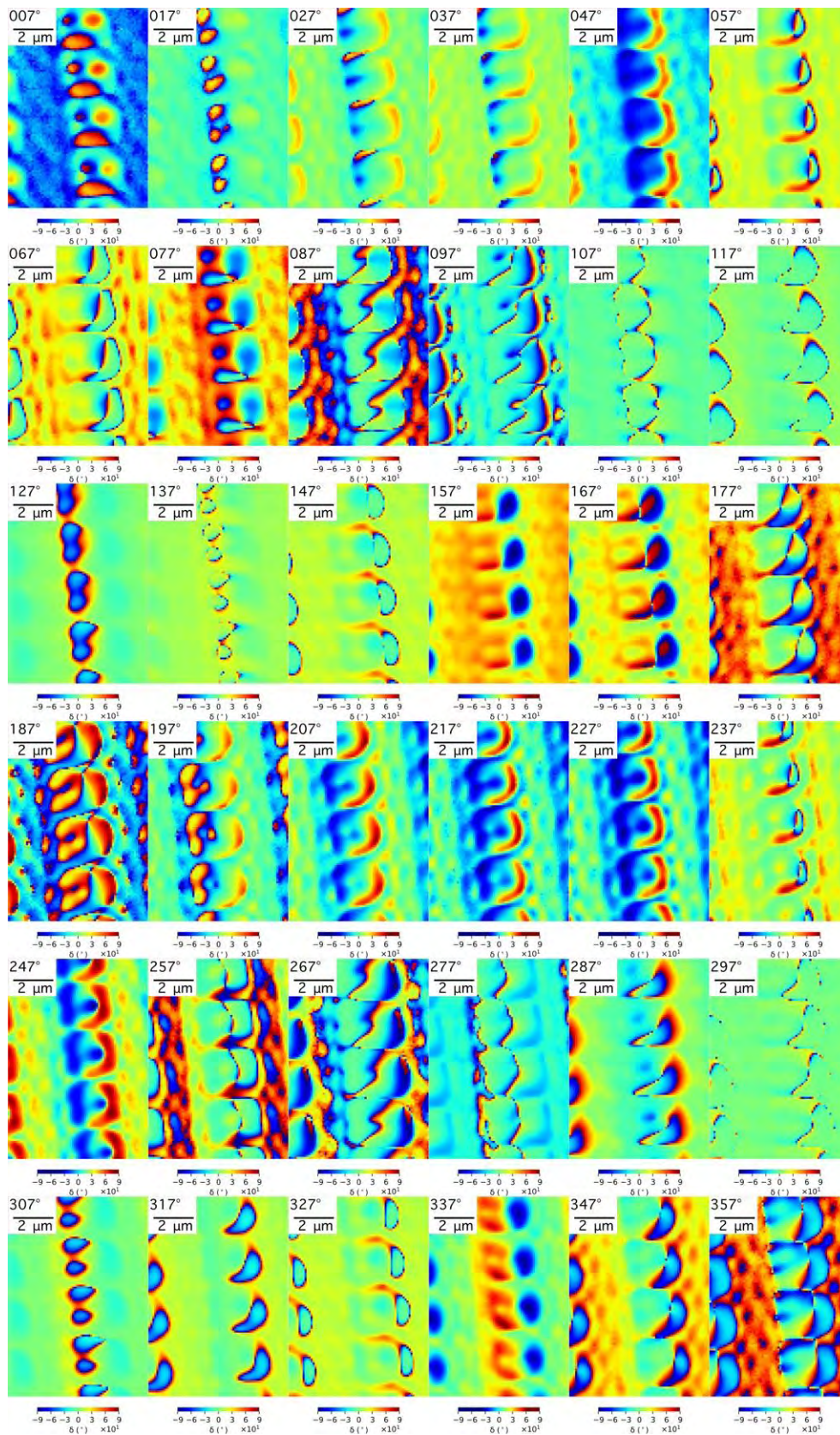


Figure 9.2.1.11 The mapping of δ for the nanograting tested at different polarization angles reference to the laboratory coordinate.

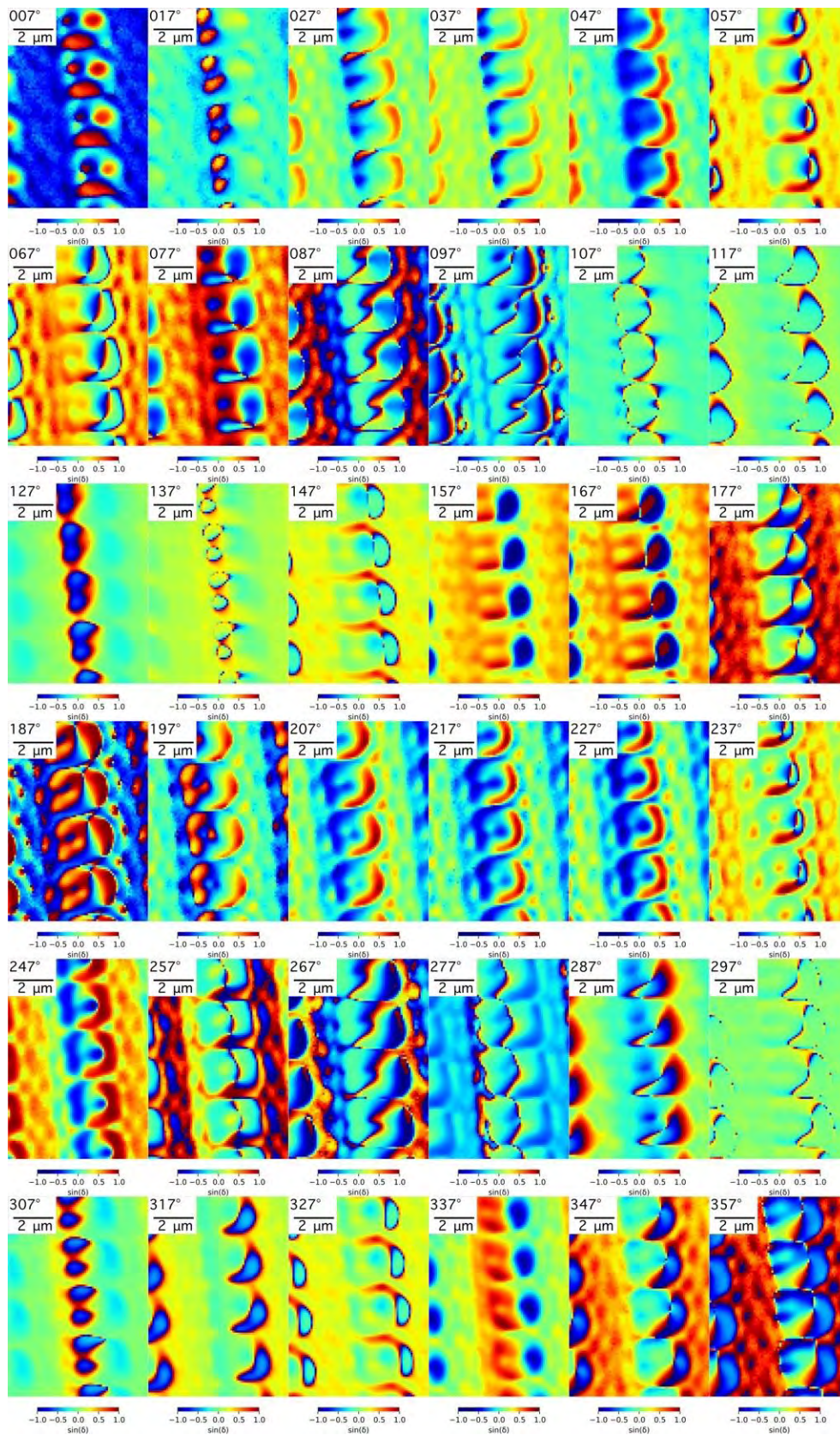


Figure 9.2.1.12 The mapping of $\sin(\delta)$ for the nanograting tested at different polarization angles reference to the laboratory coordinate.

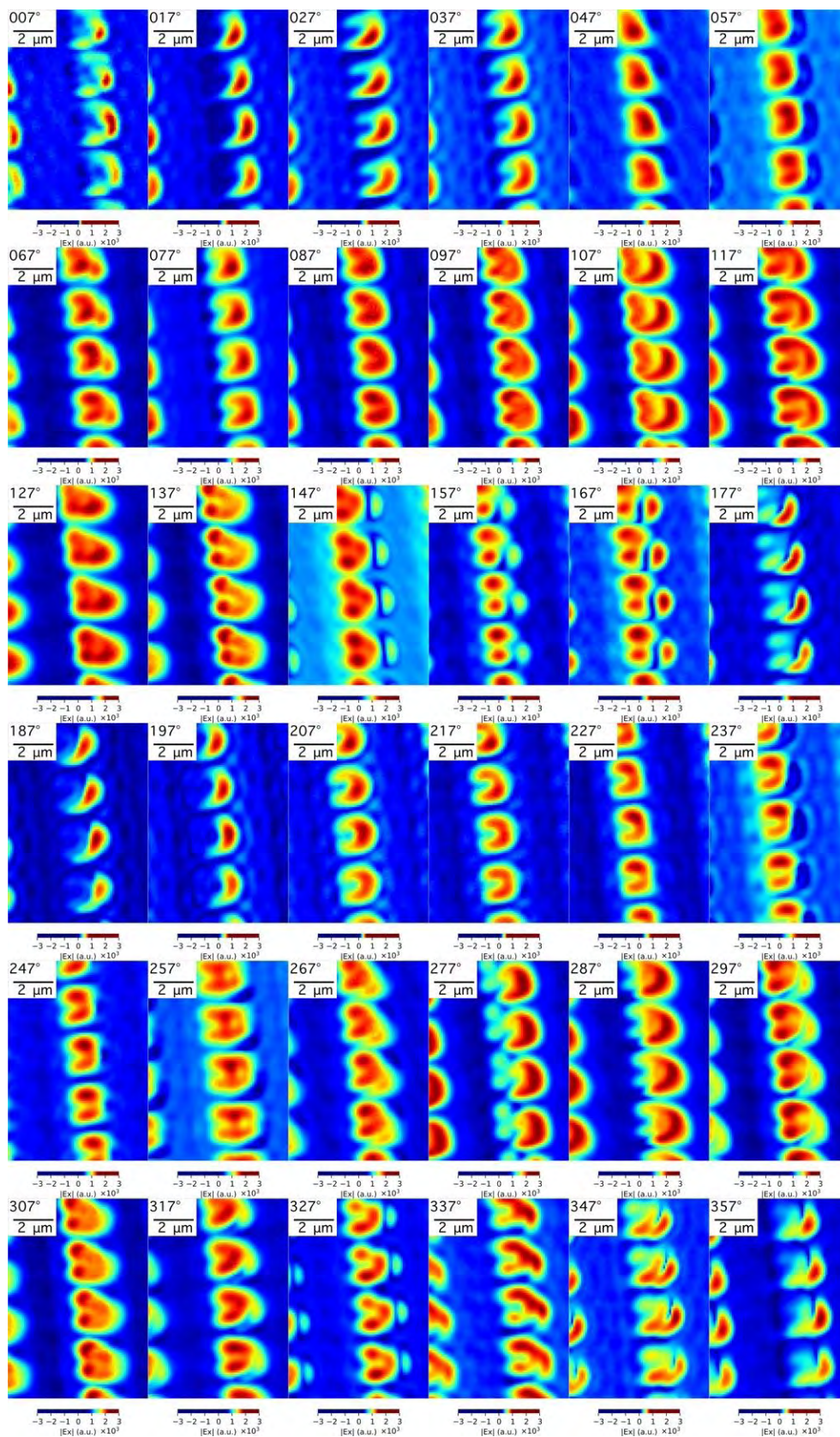


Figure 9.2.1.13 The mapping of $|E_x|$ for the nanograting tested at different polarization angles reference to the laboratory coordinate.

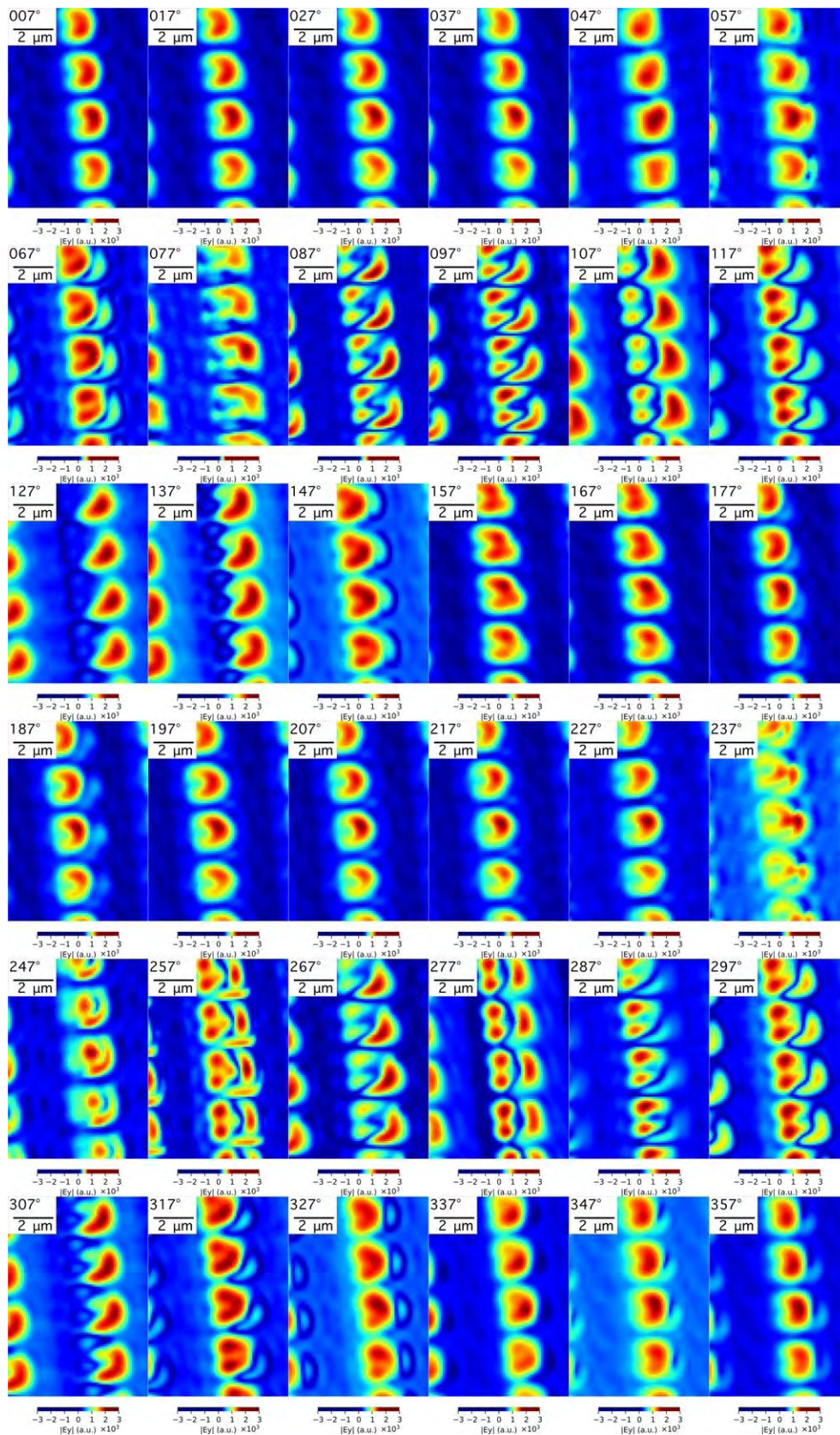


Figure 9.2.1.14 The mapping of $|E_y|$ for the nanograting tested at different polarization angles reference to the laboratory coordinate.

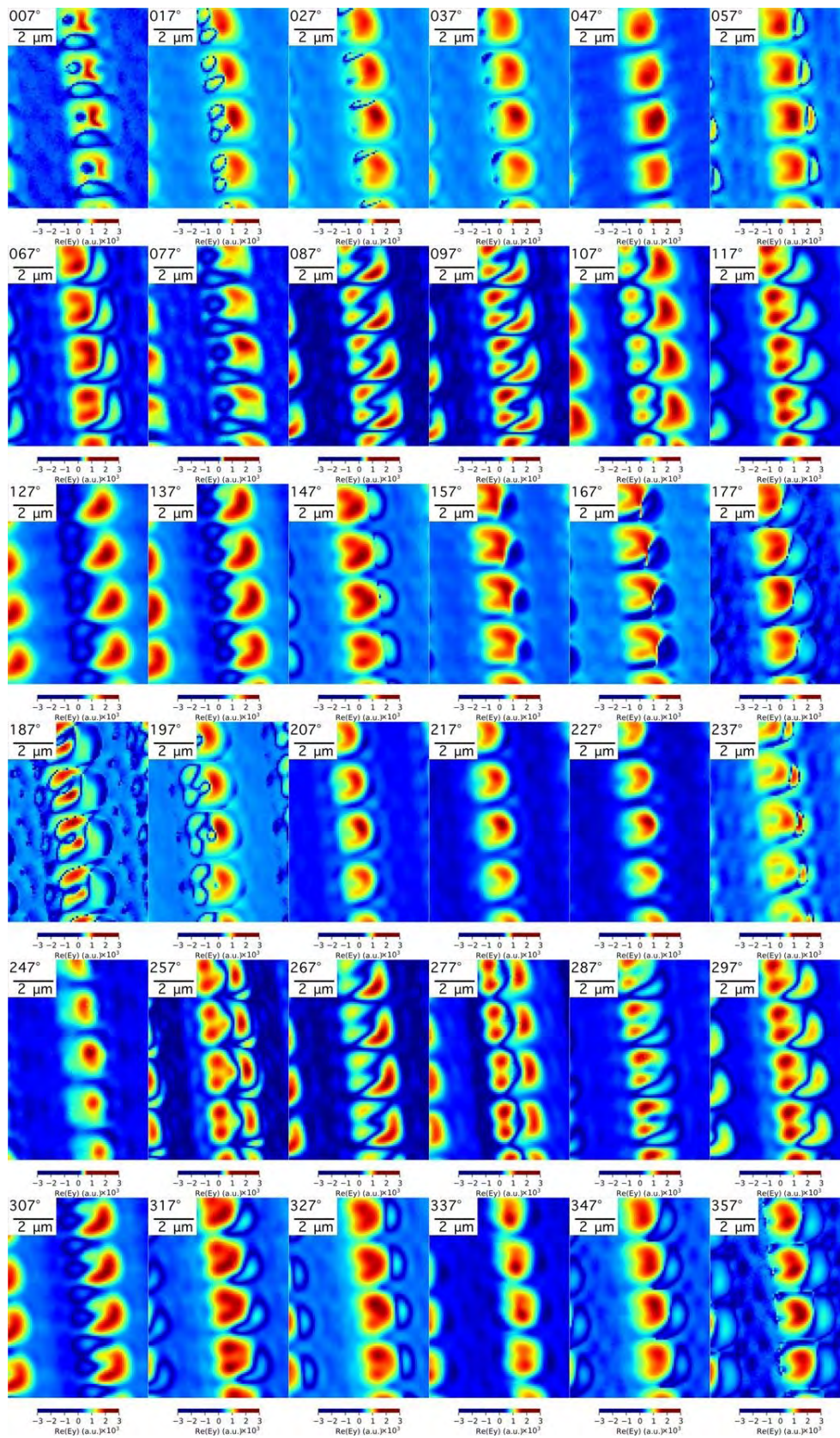


Figure 9.2.1.15 The mapping of $\text{Re}(E_y)$ for the nanograting tested at different polarization angles reference to the laboratory coordinate.

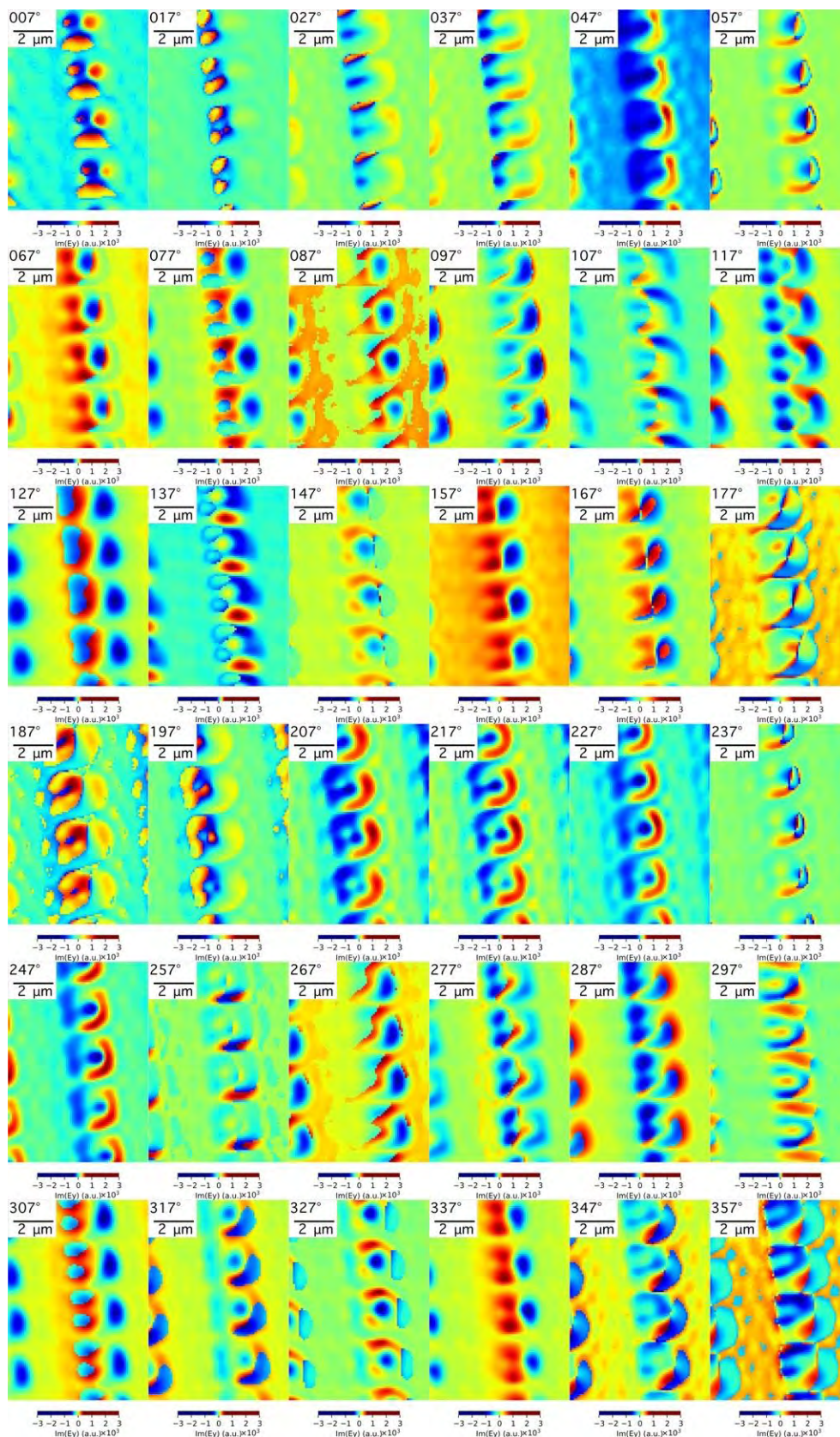


Figure 9.2.1.16 The mapping of $\text{Im}(E_y)$ for the nanograting tested at different polarization angles reference to the laboratory coordinate.

In this section, the polarization mapping of the U-shaped nanograting is measured with the

rotation of polarizer. The polarizer is rotated from 7° to 357° . The pattern of the mapping is depending on the polarizer rotation angle. A special position is sited on 337° that the variation of signal V is the minimum. This is not existed on the 180° symmetric position at 157° . The variation of azimuth angle is the minimum at 57° and 67° . This is not existed on the 180° symmetric position at 237° . The measurement relates with polarizer angles closely. So, I developed the sample stage 3 in the later experiment to pinpoint the configuration of the polarizer and the sample stage.

9.2.2 Sample rotation experiment with the protrusions facing the light source

From last section, the relative angle between the symmetrical axis of the sample (A) and the polarizer fast axis (P) is sensitive to the mapping pattern of the nanograter from last section. Because a background of the microscope is sensitive to the azimuth angle of the polarization discussed in chapter 5. To ensure the measurement is reliable, I do the experiment of fixing the polarizer at a special angle (The azimuth angle is about 122° reference to the laboratory coordinate) of the flattest background, shown in table 9.2.2.1, and rotate the sample stage.

The reading of angle of the sample stage is chosen at 58° , 148° , 238° , 328° , 102° , and 192° .

According to the laboratory coordinate shown in Fig.9.1.1.3, the configuration of the polarizer and the sample stage is shown in Table 9.2.2.1. The configuration $P \parallel A$ is shown in Fig.9.2.2.1a. The configuration $P \perp A$, is shown in Fig.9.2.2.1b. The angle of 102° , and 192° is the situation between Fig.9.2.2.1a and Fig.9.2.1.1b. A protrusion existed on one side of the U-shape nanograter shown on Fig. 9.2.2.1c. The sample stage rotated anticlockwise.

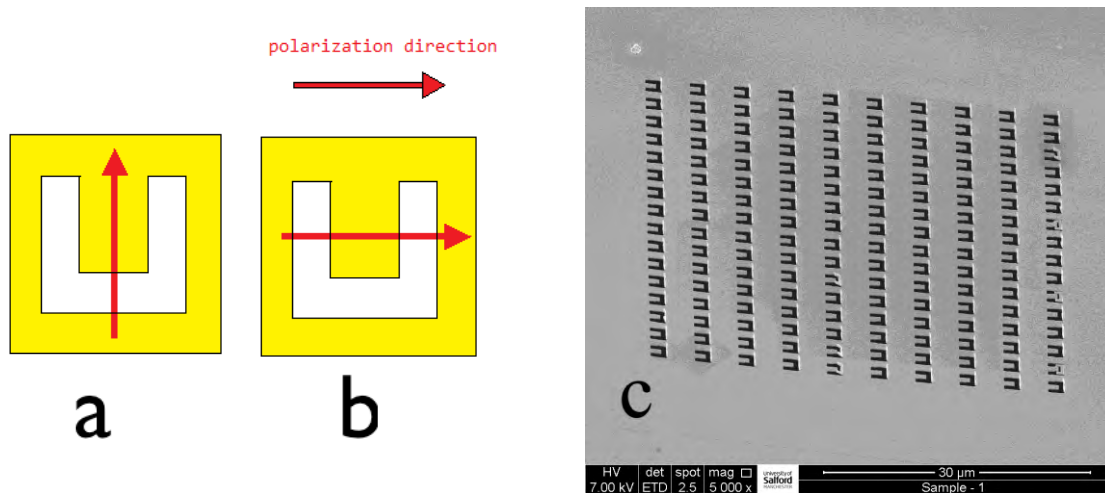


Figure 9.2.2.1 The configuration of the polarization and the nanograter: (a) polarization along the symmetrical plane of the nanograter; (b) polarization perpendicular to the symmetrical plane of the nanograter. (c) the SEM image of the nanograter.

Table 9.2.2.1 The configuration of the axis of polarizer (P) and the axis of nanograter (A)

Polarization angle	Sample stage angle (°)					
	58 ($P \perp A$)	148 ($P \parallel A$)	238 ($P \perp A$)	328 ($P \parallel A$)	102	192
122°						

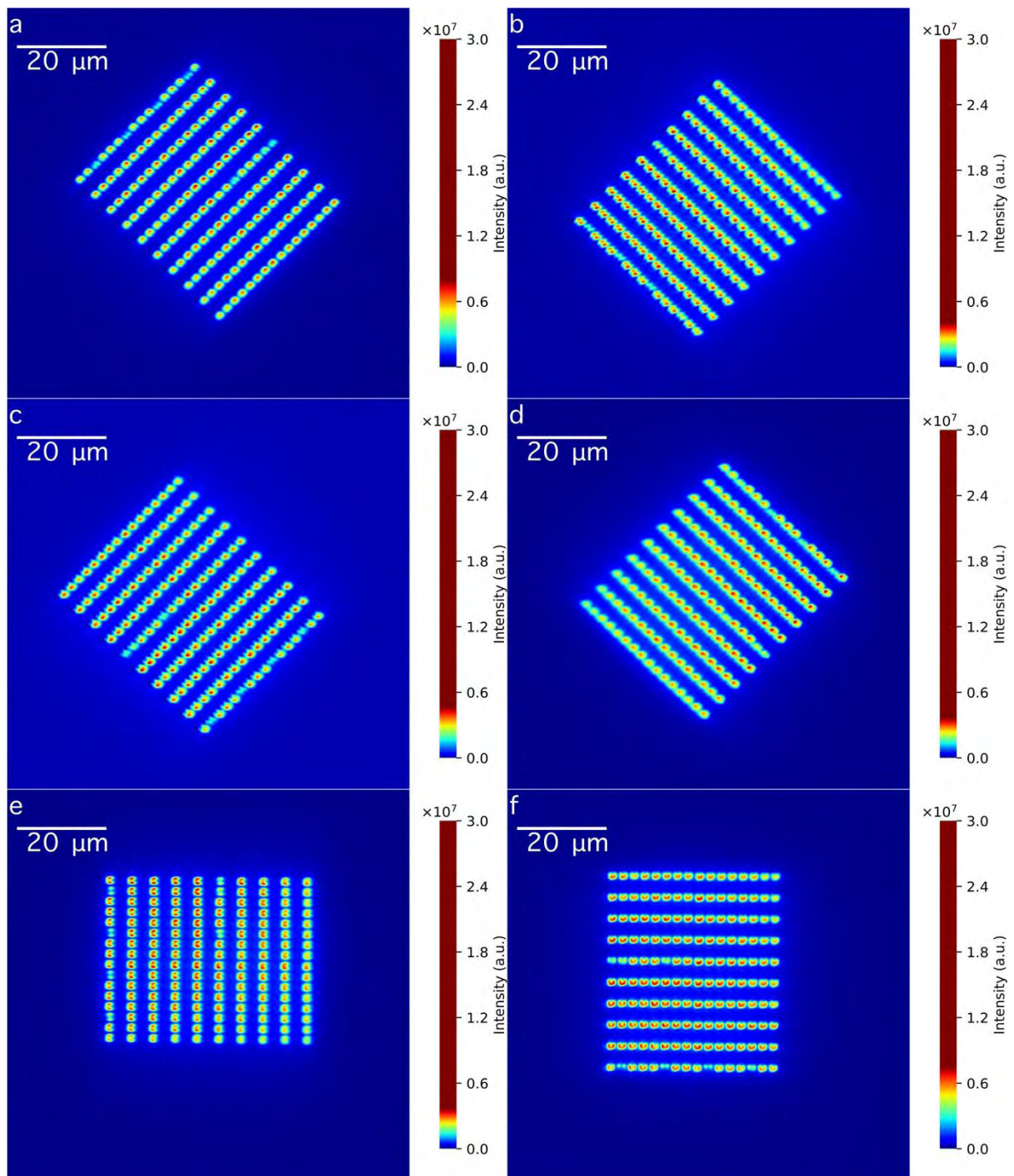


Figure 9.2.2.2 The mapping of I for the nanograting sited at angles: (a) 58° , (b) 148° , (c) 238° , (d) 328° , (e) 102° , (f) 192°

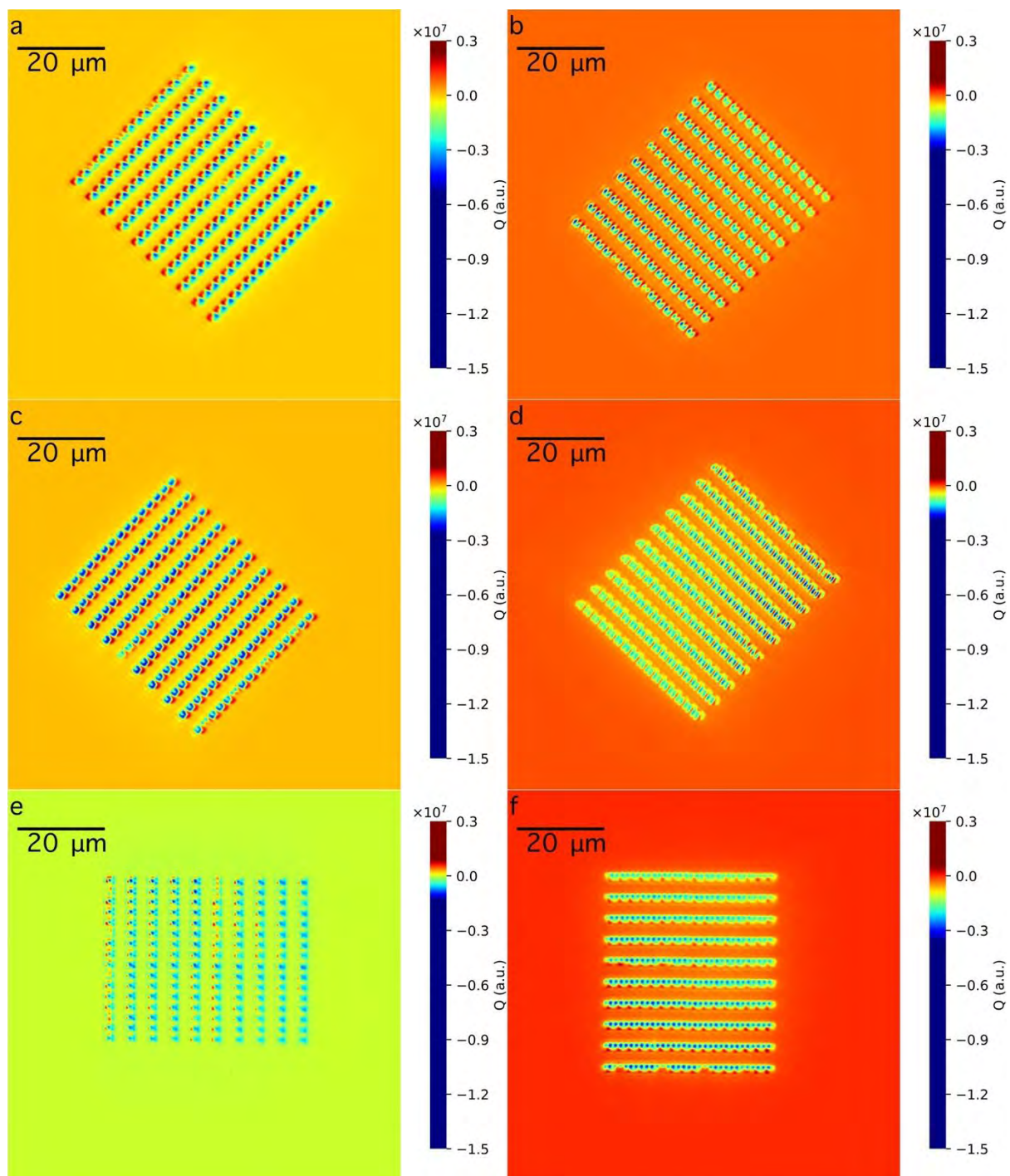


Figure 9.2.2.3 The mapping of Q for the nanograting sited at angles reference to the laboratory coordinate: (a) 58° , (b) 148° , (c) 238° , (d) 328° , (e) 102° , (f) 192°

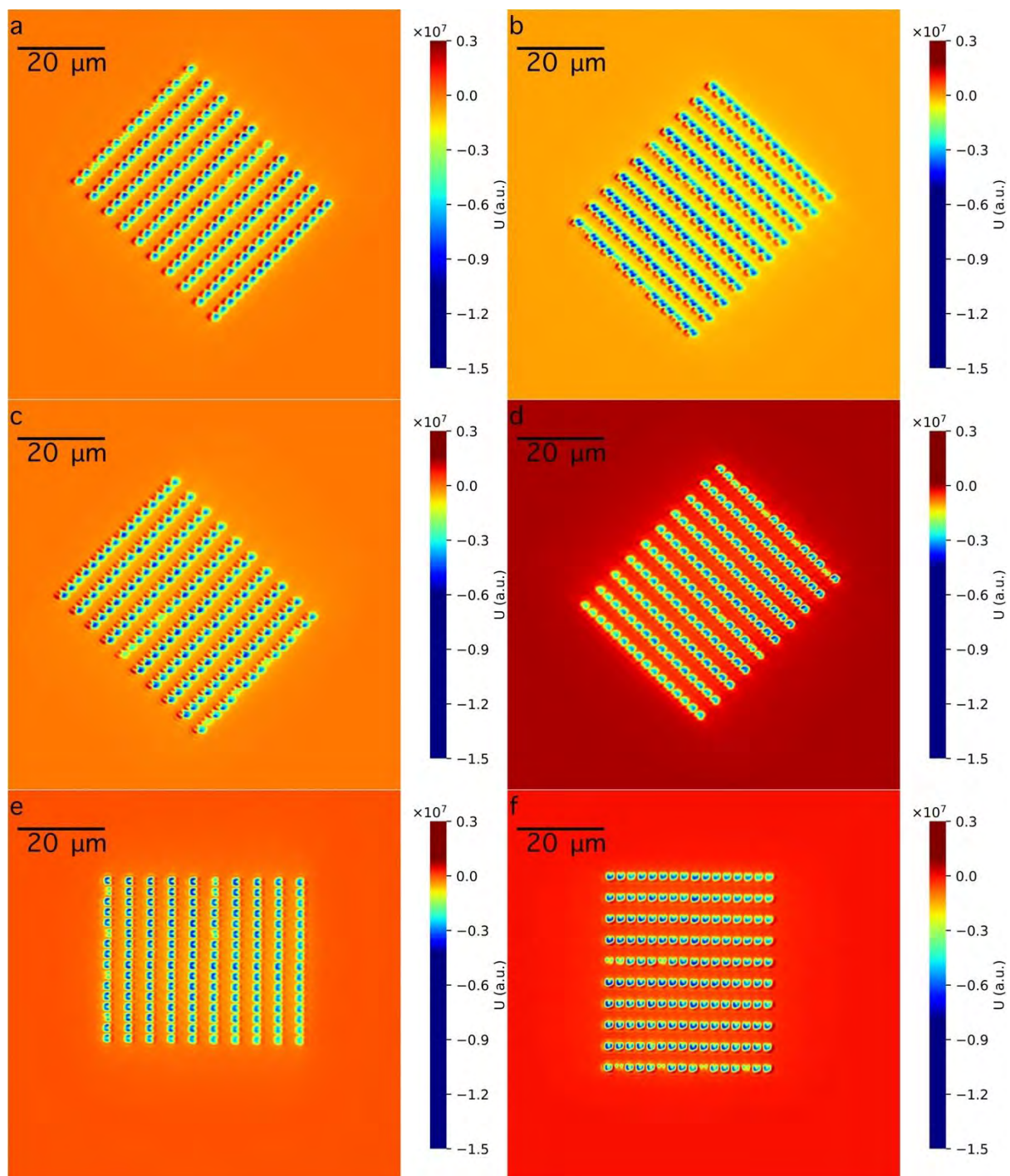


Figure 9.2.2.4 The mapping of U for the nanograting sited at angles: (a) 58° , (b) 148° , (c) 238° , (d) 328° , (e) 102° , (f) 192°

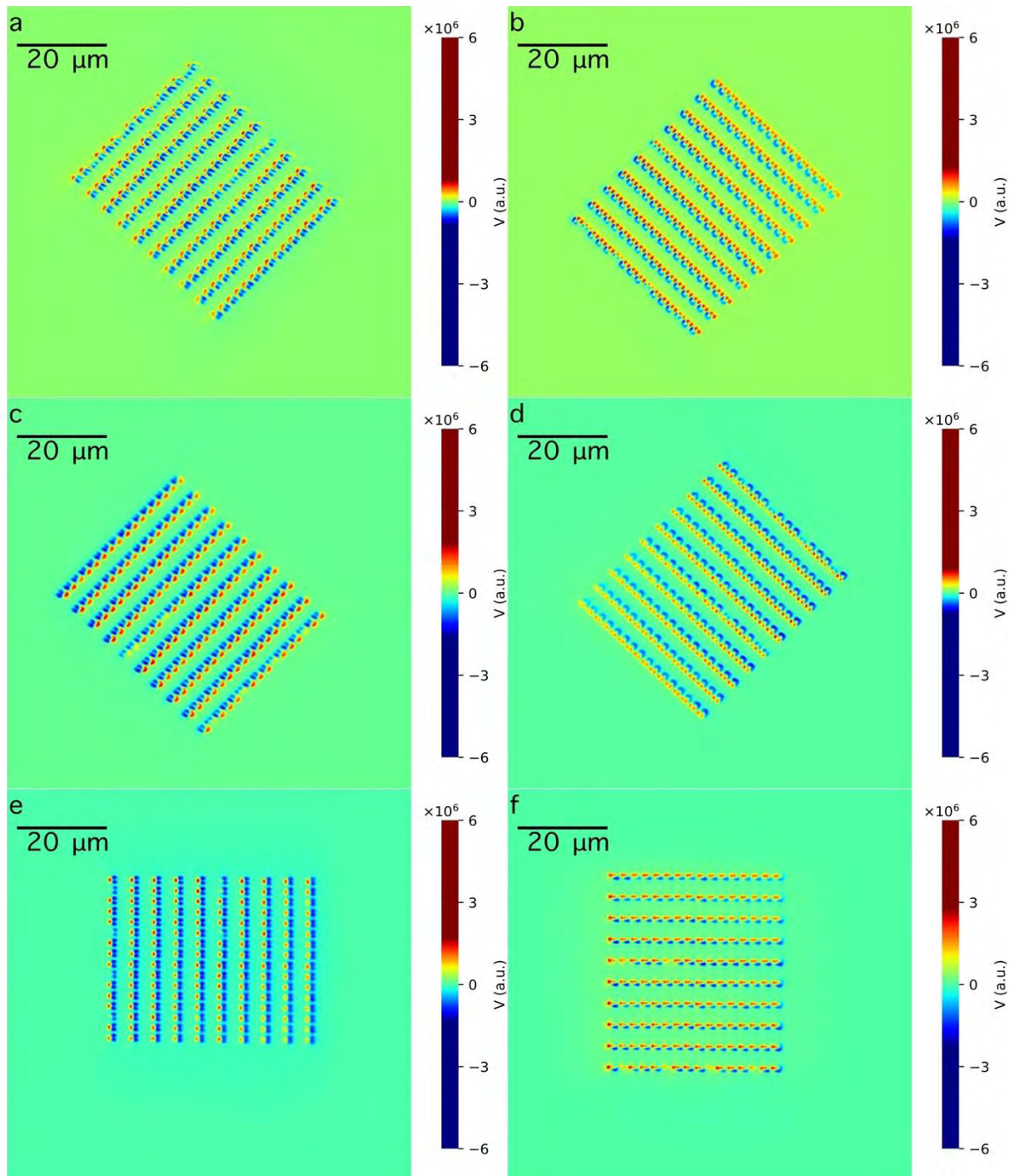


Figure 9.2.2.5 The mapping of V for the nanograting sited at angles: (a) 58° , (b) 148° , (c) 238° , (d) 328° , (e) 102° , (f) 192°

The pattern is varied with the relative angle of P and A. The Stokes parameters is shown in Fig. 9.2.2.1 to Fig. 9.2.2.4. The normalized depolarization is shown in Fig. 9.2.2.6. The image quality is poor because the strongly scattering exists in this system. In the configuration of 58° , 148° , 238° , and 328° , the depolarization is strong on the nanograting unit,

but weak in the surrounding area of the nanograter, shown in Fig. 9.2.2.6. In the configuration of 102° and 192° , the depolarization is strong in the surrounding area of the nanograter, but weak on the nanograter unit.

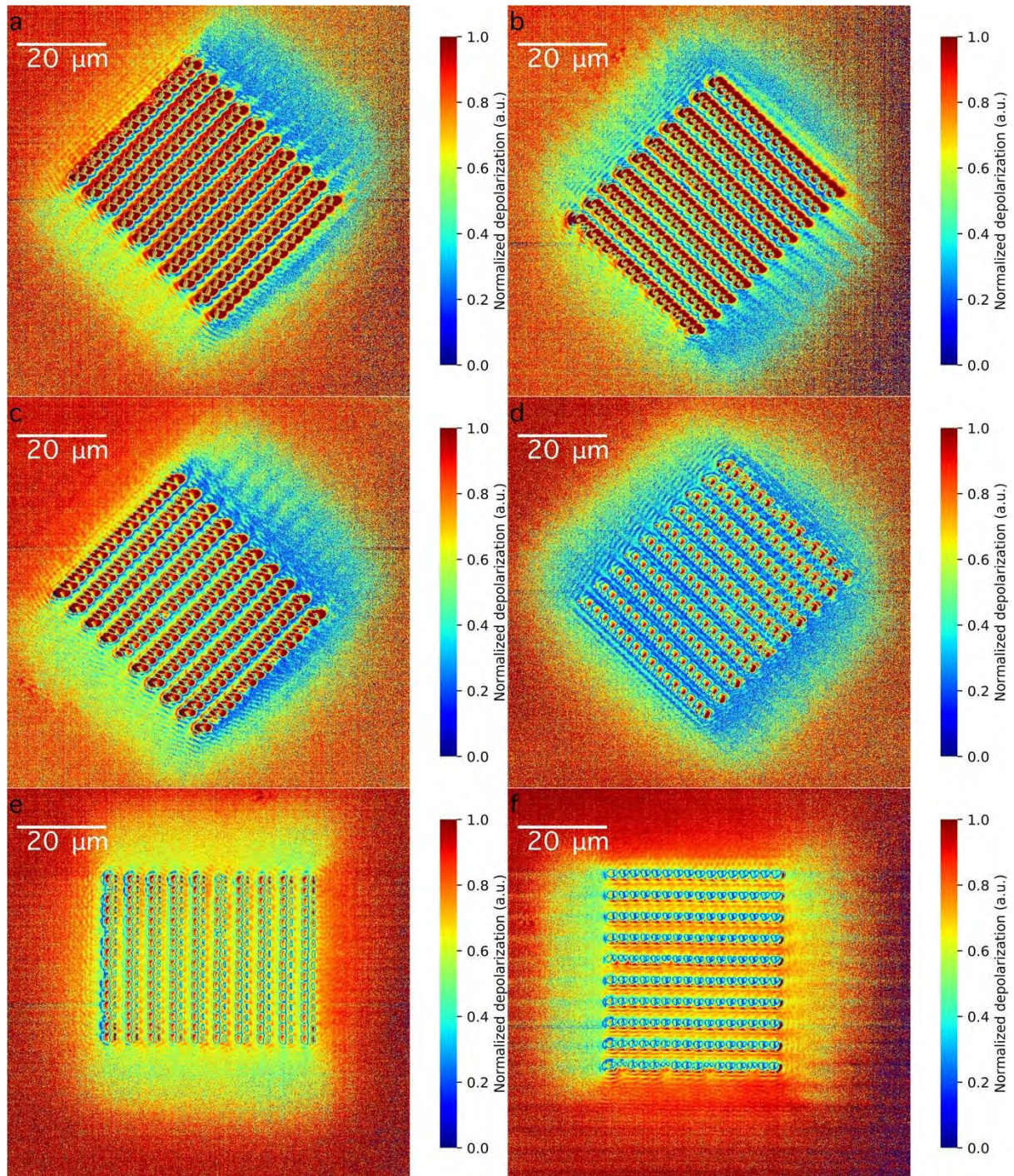


Figure 9.2.2.6 The mapping of dP/I for the nanograter sited at angles: (a) 58° , (b) 148° , (c) 238° , (d) 328° , (e) 102° , (f) 192°

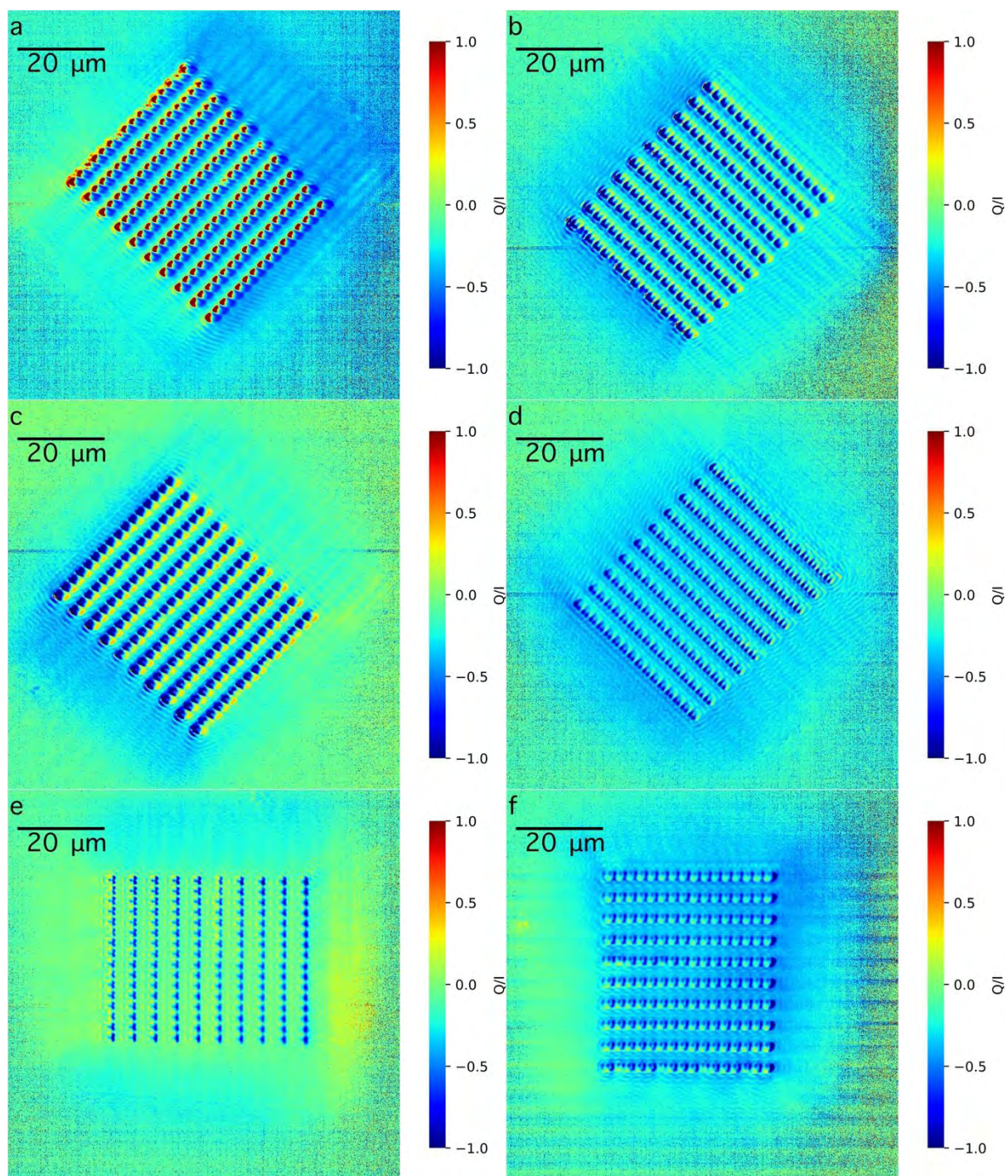


Figure 9.2.2.7 The mapping of Q/I for the nanograting sited at angles: (a) 58° , (b) 148° , (c) 238° , (d) 328° , (e) 102° , (f) 192°

The surrounding of P_2 is near to -1 when the sample stage is sited on 58° , 148° , 238° , 328° ; while the surrounding of P_2 is about -0.6 at 102° and 192° , shown in Fig.9.2.2.8.

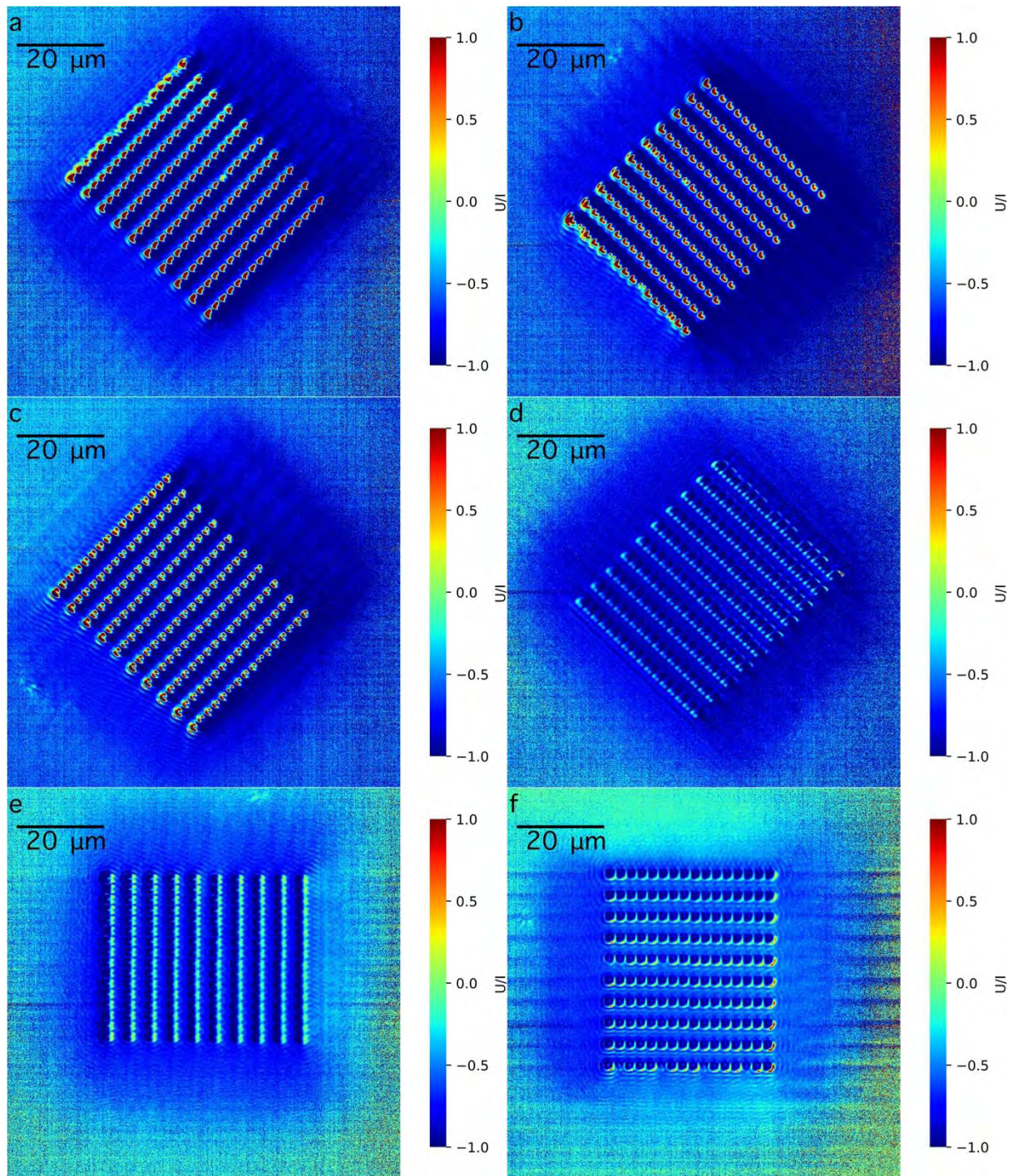


Figure 9.2.2.8 The mapping of U/I for the nanograting sited at angles: (a) 58° , (b) 148° , (c) 238° , (d) 328° , (e) 102° , (f) 192°

In the surrounding of the nanograting, the V/I is near to zero in the configuration of 58° , 148° , 238° , and 328° ; and the variation of V/I is localized at the position of the nanograting, shown

in Fig. 9.2.2.9 a, Fig. 9.2.2.9b, Fig. 9.2.2.9c, and Fig. 9.2.2.9d; while, the surrounding area of V/I is anisotropy, in the configuration of 102° and 192° , shown in Fig. 9.2.2.9 a, Fig. 9.2.2.9b.

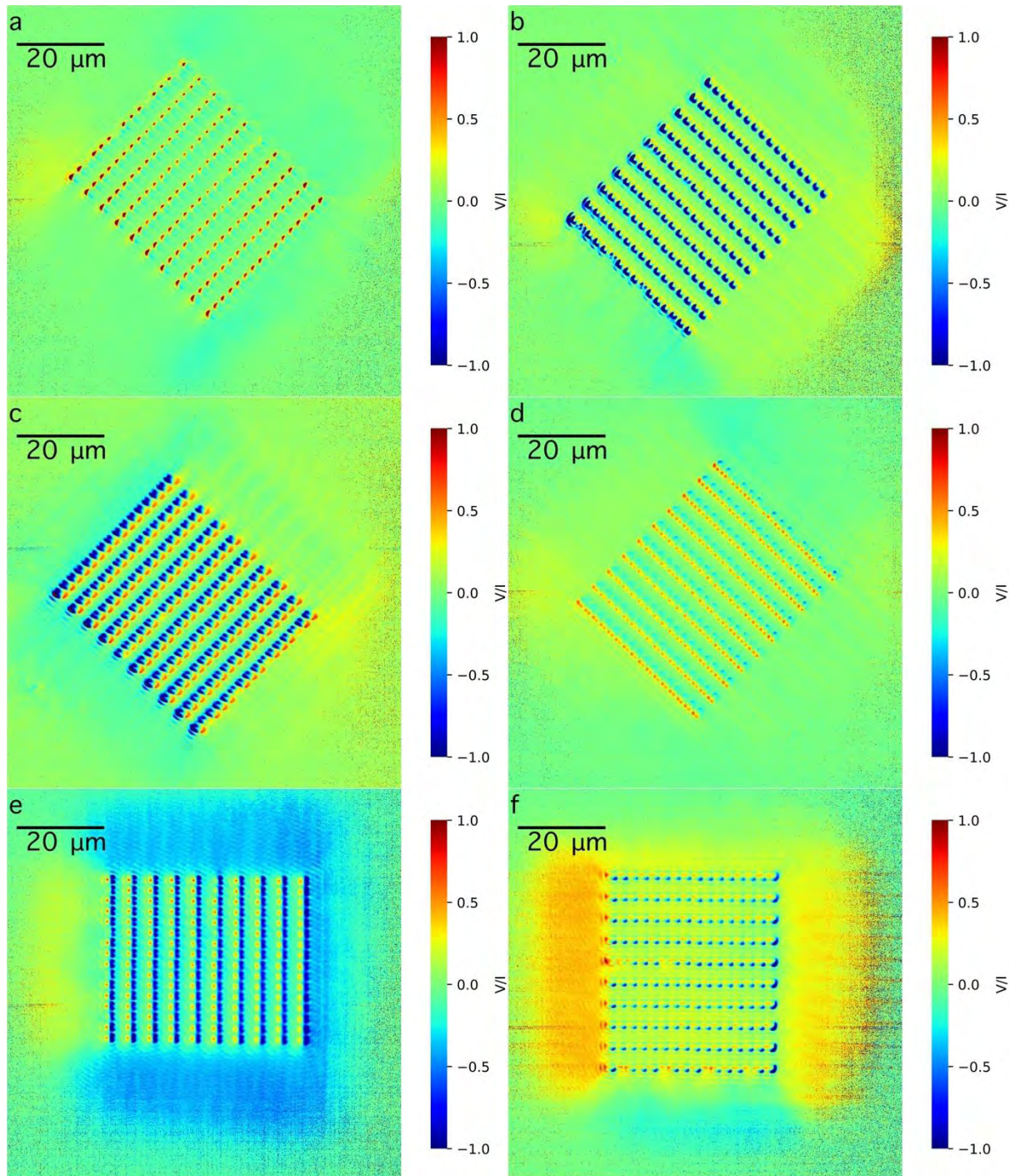


Figure 9.2.2.9 The mapping of V/I for the nanograting sited at angles: (a) 58° , (b) 148° , (c) 238° , (d) 328° , (e) 102° , (f) 192°

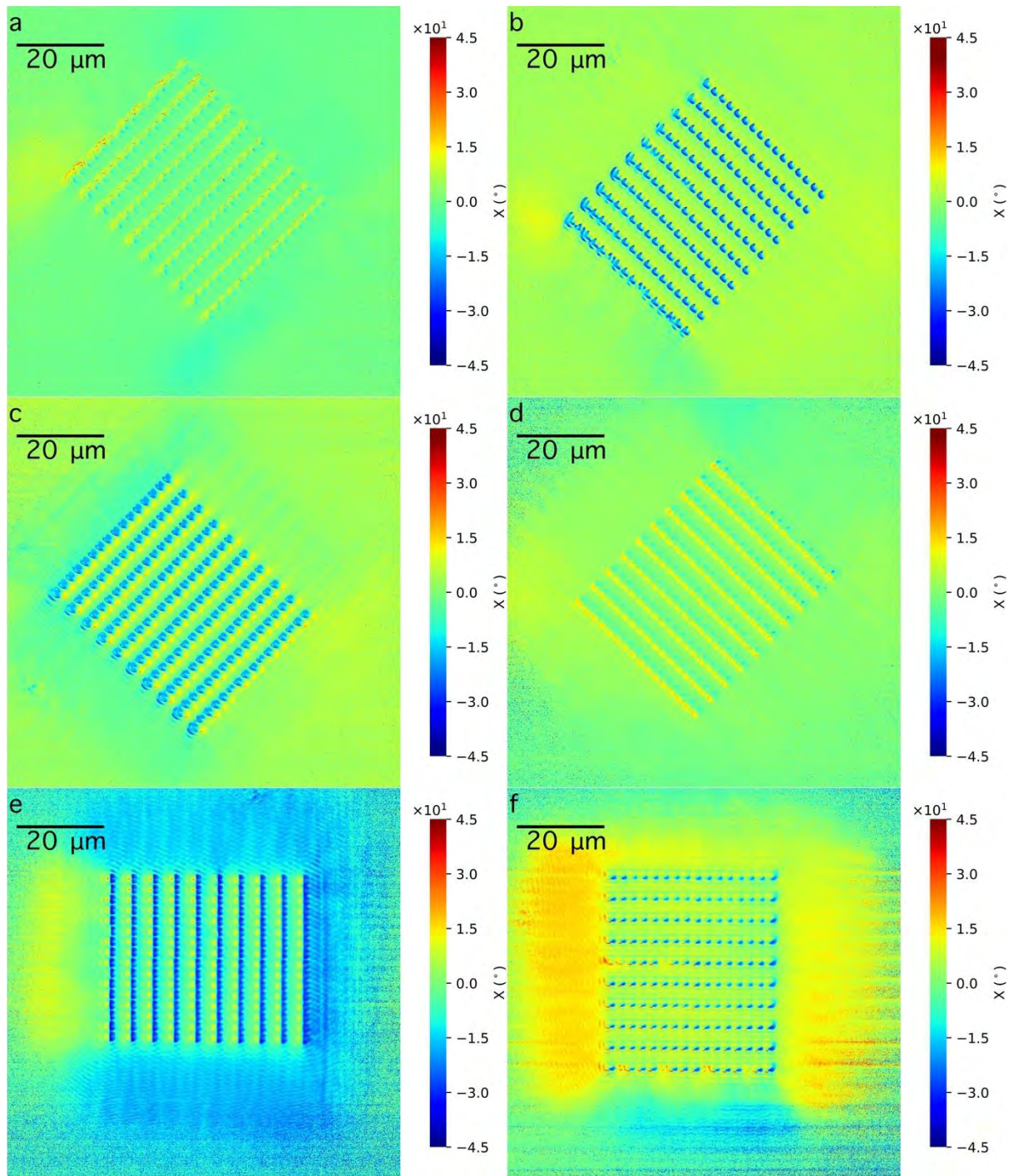


Figure 9.2.2.10 The mapping of elliptical angle χ for the nanograting sited at angles: (a) 58° , (b) 148° , (c) 238° , (d) 328° , (e) 102° , (f) 192°

The distribution of elliptical angle χ behaves similar to the V signal. The variation of χ is between 10° and 0° at the angle of 58° and 328° in $P \perp A$, while, that is between -20° to 0° at the angle between 148° and 238° in $P \parallel A$, shown in Fig. 9.2.2.10. The surrounding area in

orthogonal position (58° , 328° , 148° and 238°) is zero; while, the surrounding area in oblique position (102° and 192°) is about -20° and 20° , respectively.

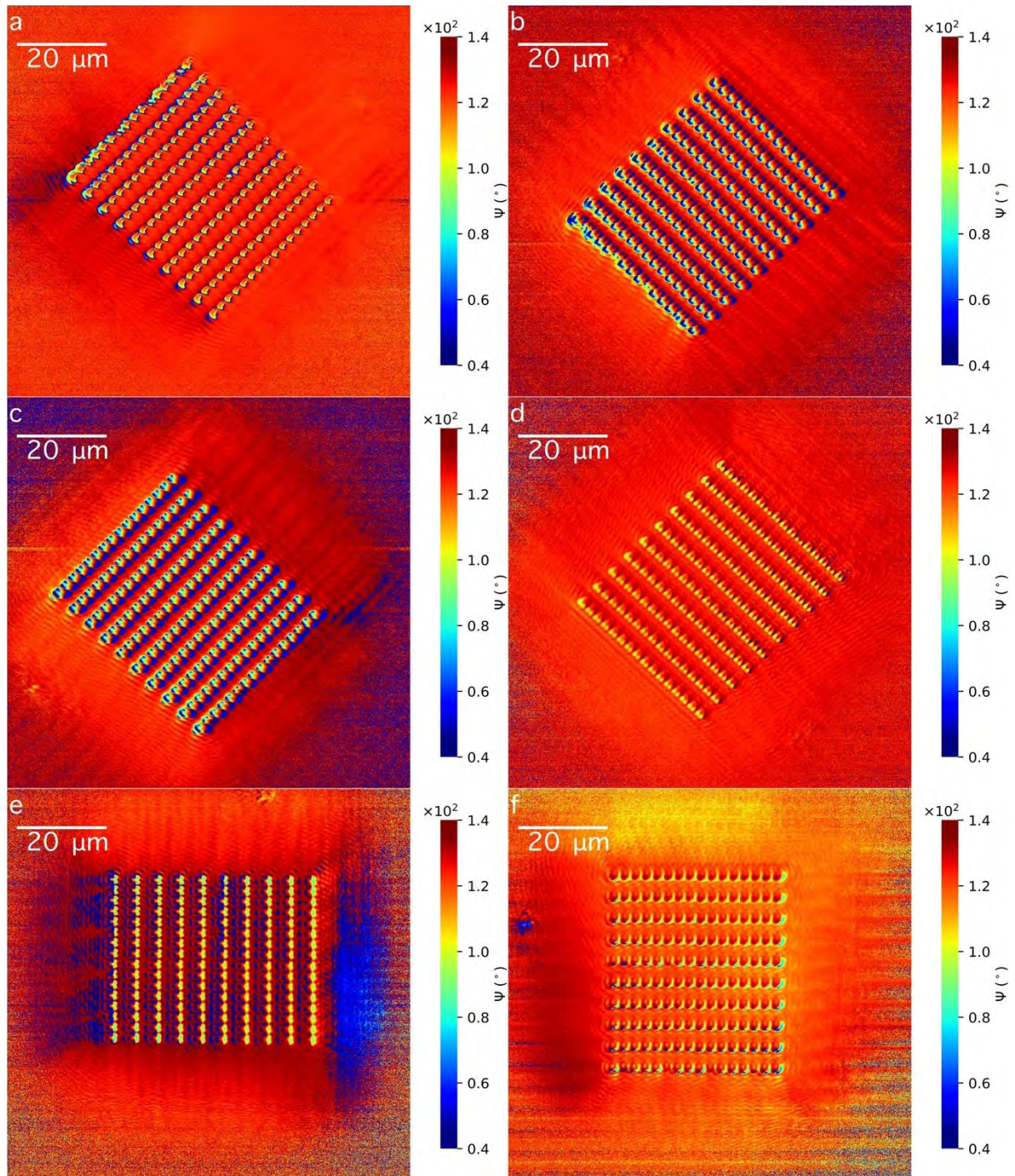


Figure 9.2.2.11 The mapping of azimuth angle ψ for the nanograter sited at angles: (a) 58° , (b) 148° , (c) 238° , (d) 328° , (e) 102° , (f) 192°

Figure 9.2.2.11 is the mapping of azimuth angle ψ sited at different angles. The surrounding

area of the nanograter is uniform in orthogonal position (58° , 148° , 238° , 328°). The surrounding area is not uniform when the polarizer fast axis tilt to the edge of the nanograter (102° and 192°). Big variation of azimuth angle on the nanograter patterns is sited on the position of 148° , 102° , and 238° ; while, small variation of azimuth angle is sited on the position of 58° , 192° , and 328° .

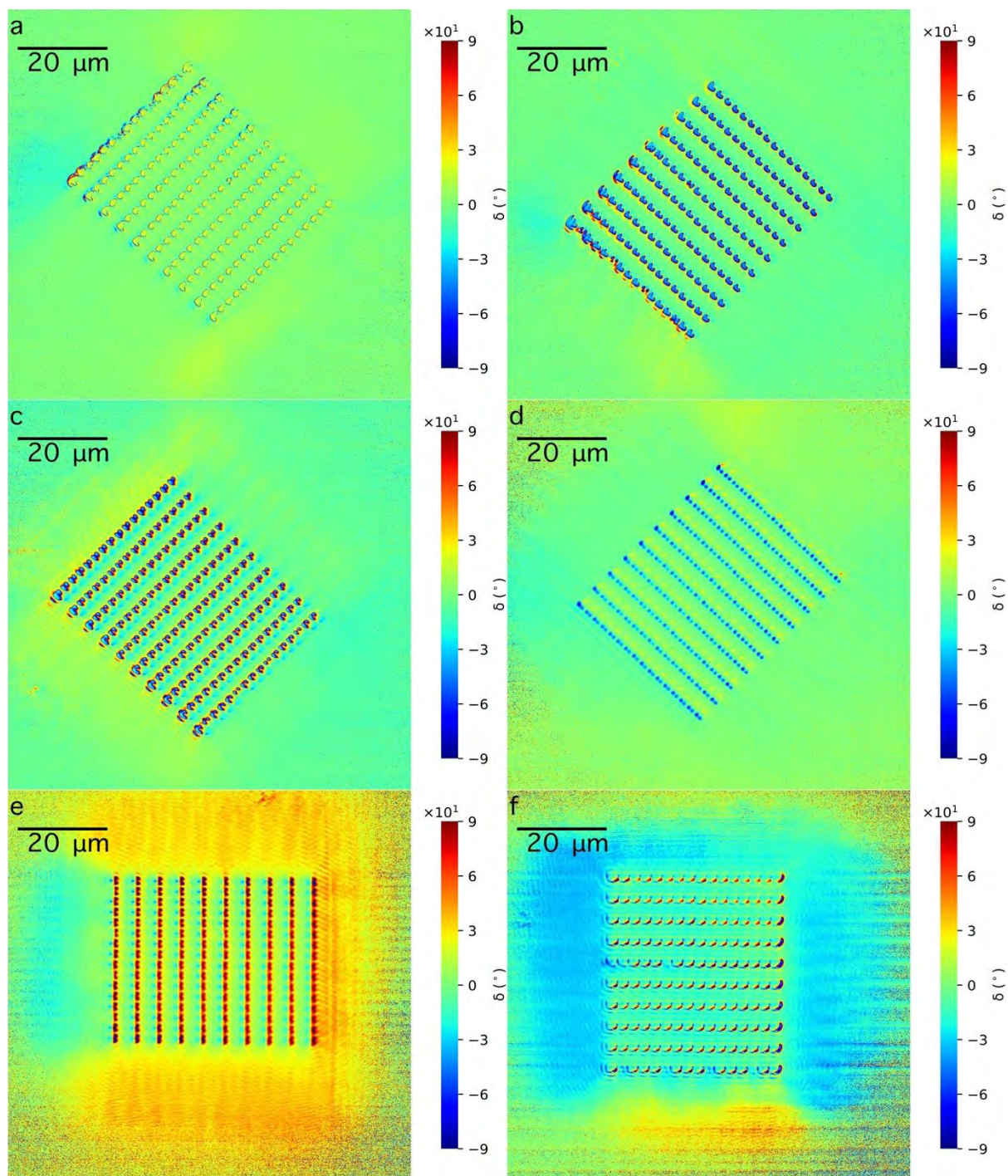


Figure 9.2.2.12 The mapping of δ for the nanograting sited at angles: (a) 58°, (b) 148°, (c) 238°, (d) 328°, (e) 102°, (f) 192°

The phase difference δ of y-axis and x-axis in the laboratory coordinate is shown in Fig.

9.2.2.12. Figure 9.2.2.12a shows δ is the minimum and the variation of δ is localized at the position of the edge of the protrusion.

The variation of $\sin(\delta)$ in Fig. 9.2.2.13 is same to the variation of δ in Fig. 9.2.2.12.

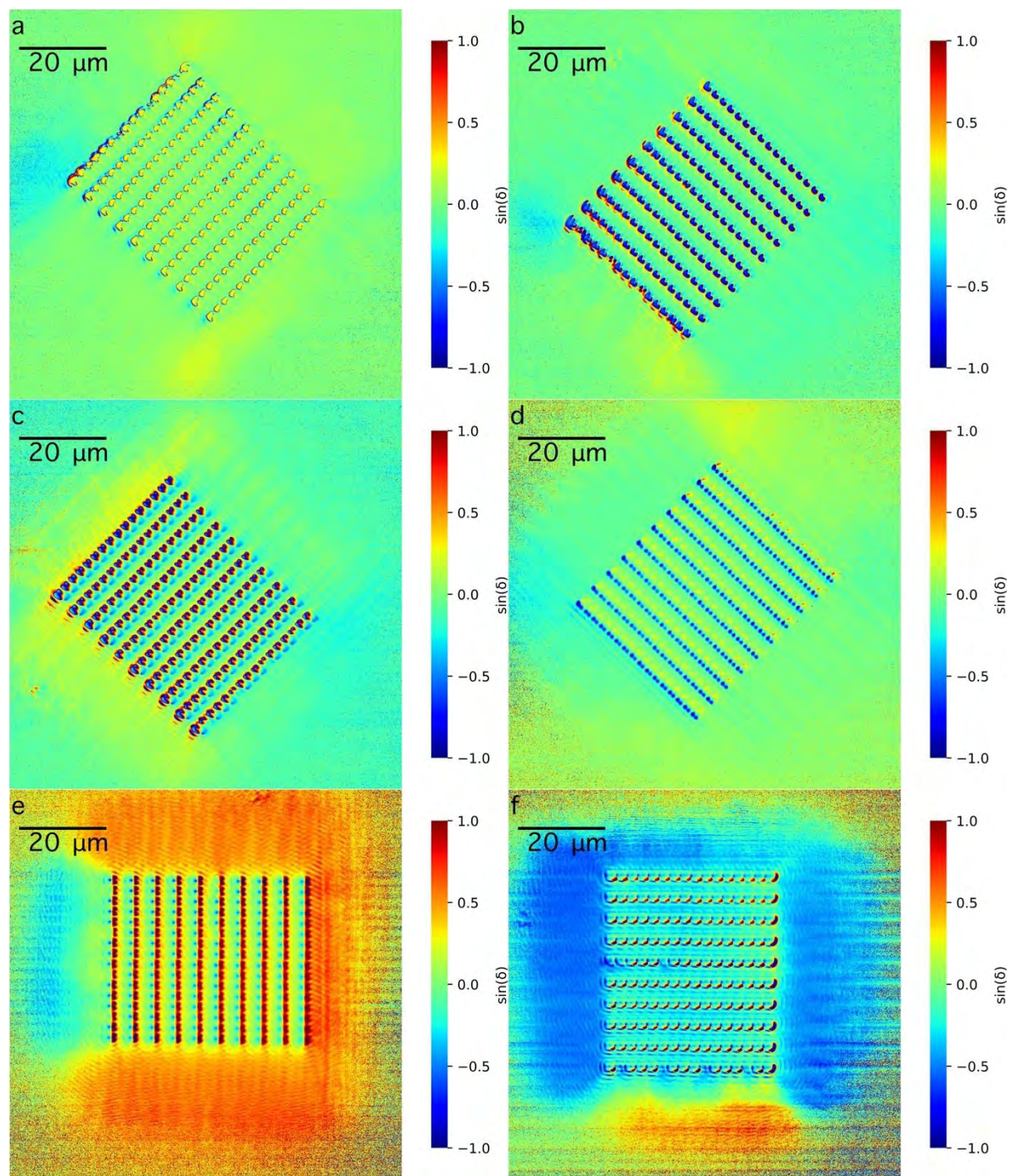


Figure 9.2.2.13 The mapping of $\sin(\delta)$ for the nanograting sited at angles: (a) 58°, (b) 148°, (c) 238°, (d) 328°, (e) 102°, (f) 192°

The mapping of the modulus of electrical field $|E_x|$ and $|E_y|$ is shown in Fig. 9.2.2.14 and Fig. 9.2.2.15.

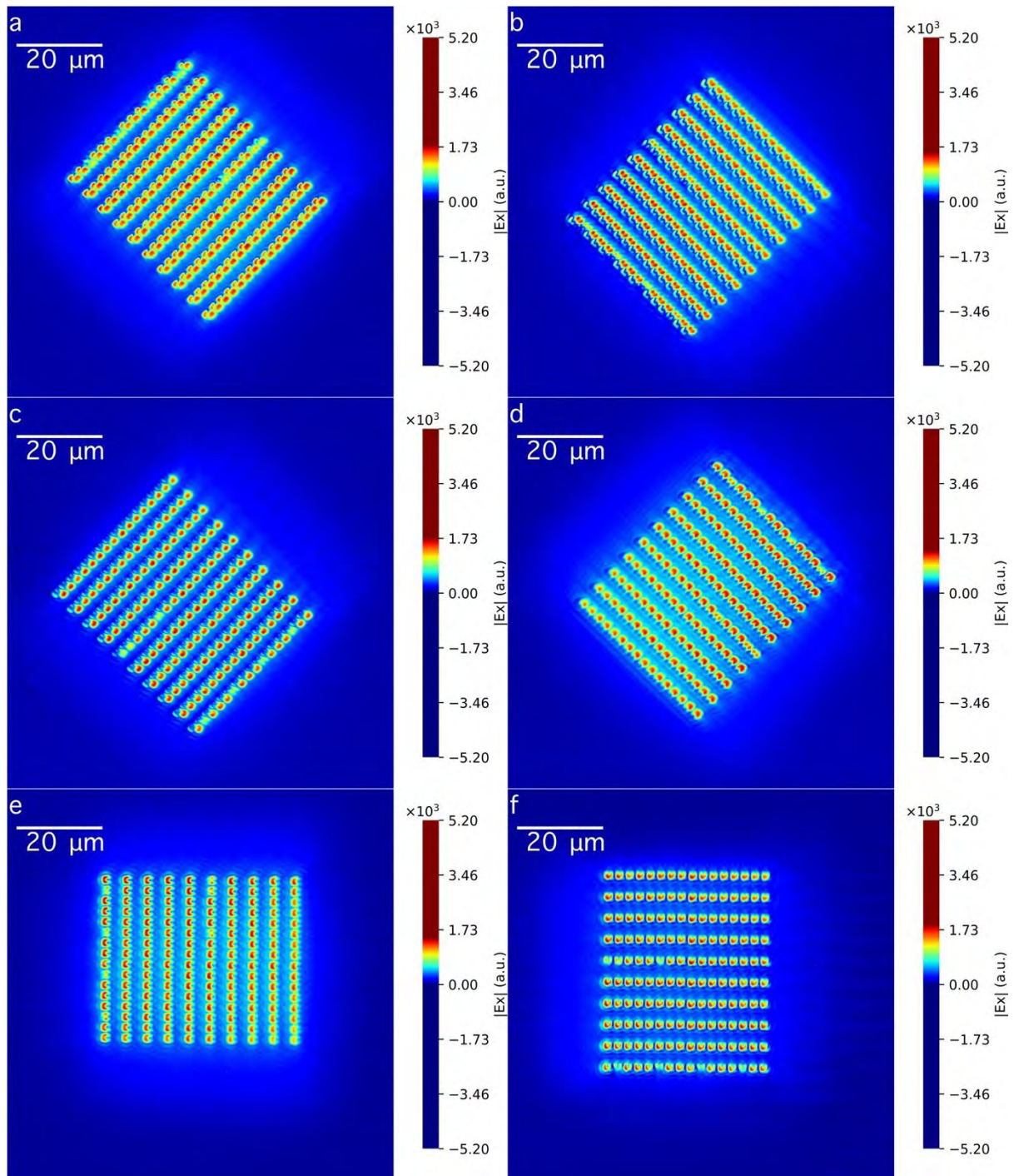


Figure 9.2.2.14 The mapping of $|E_x|$ for the nanograting sited at angles: (a) 58°, (b) 148°, (c) 238°, (d) 328°, (e) 102°, (f) 192°

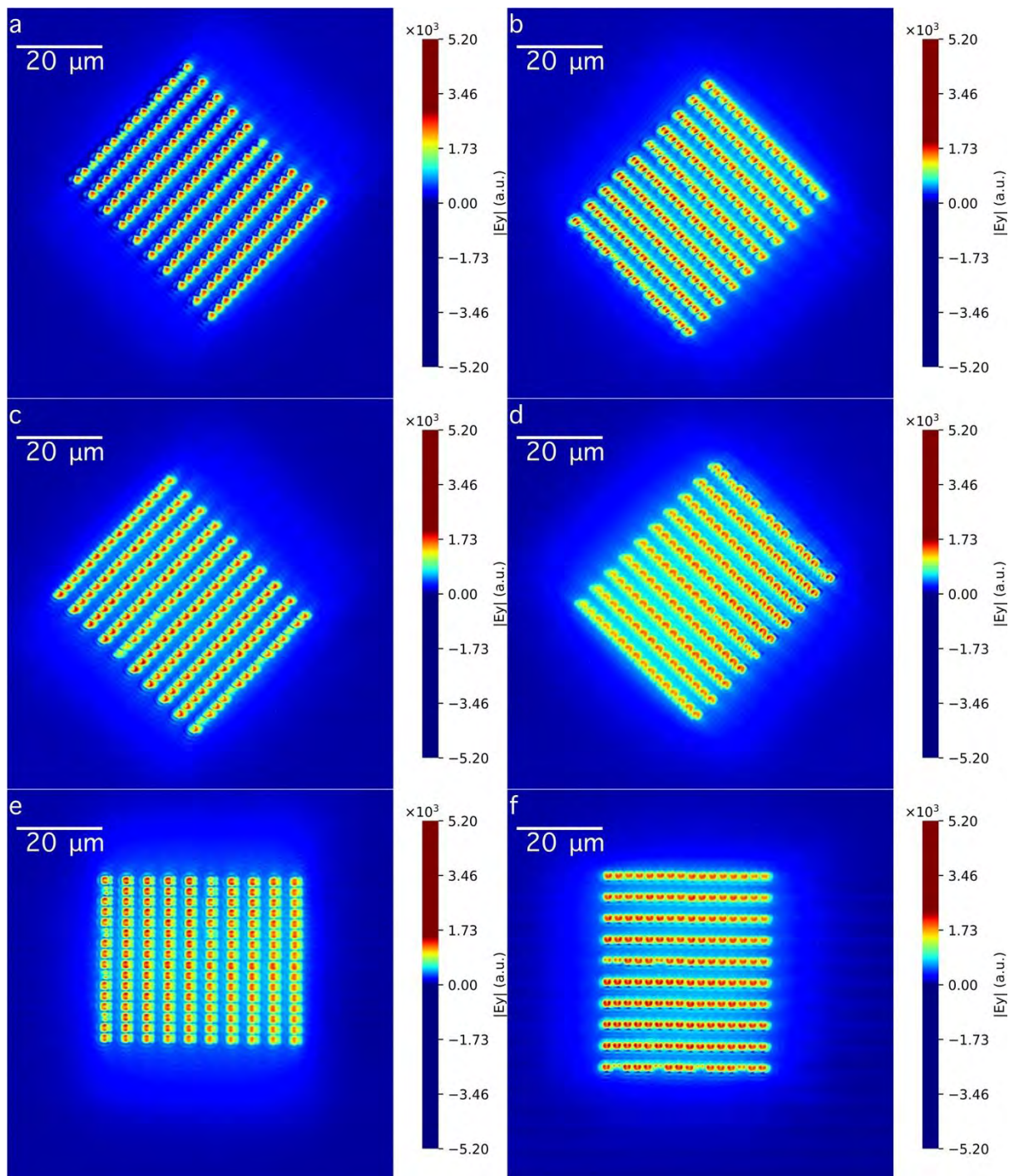


Figure 9.2.2.15 The mapping of $|E_y|$ for the nanograting site at: (a) 58° , (b) 148° , (c) 238° , (d) 328° , (e) 102° , (f) 192°

The real part and real part $Re(E_y)$ of the electrical field E_y are shown in Fig. 9.2.2.16.

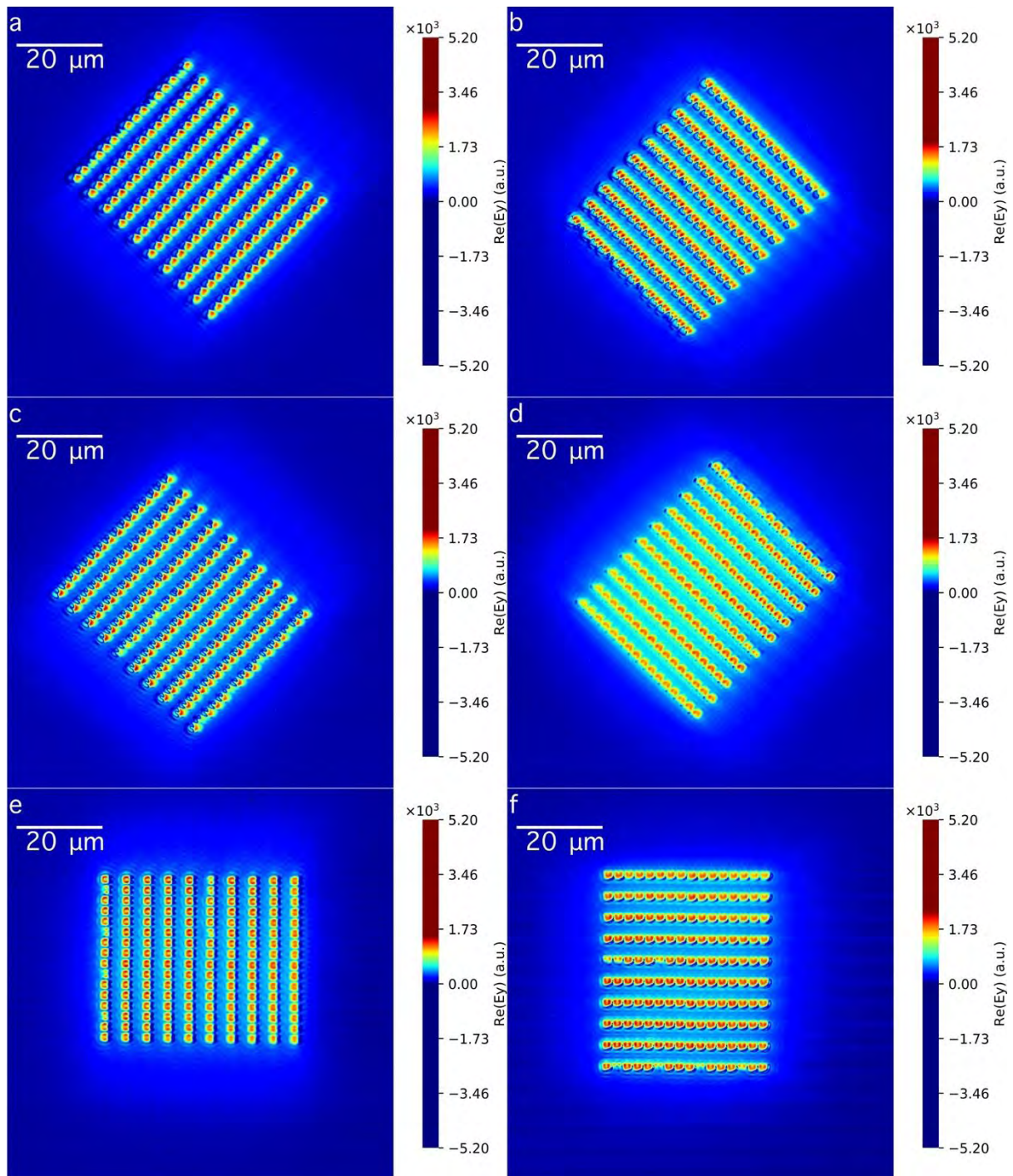


Figure 9.2.2.16 The mapping of $Re(E_y)$ for the nanograting sited at angles (a) 58°, (b) 148°, (c) 238°, (d) 328°, (e) 102°, (f) 192°

The variation of imaginary part of E_y is the smallest in the Fig. 9.2.2.17a.

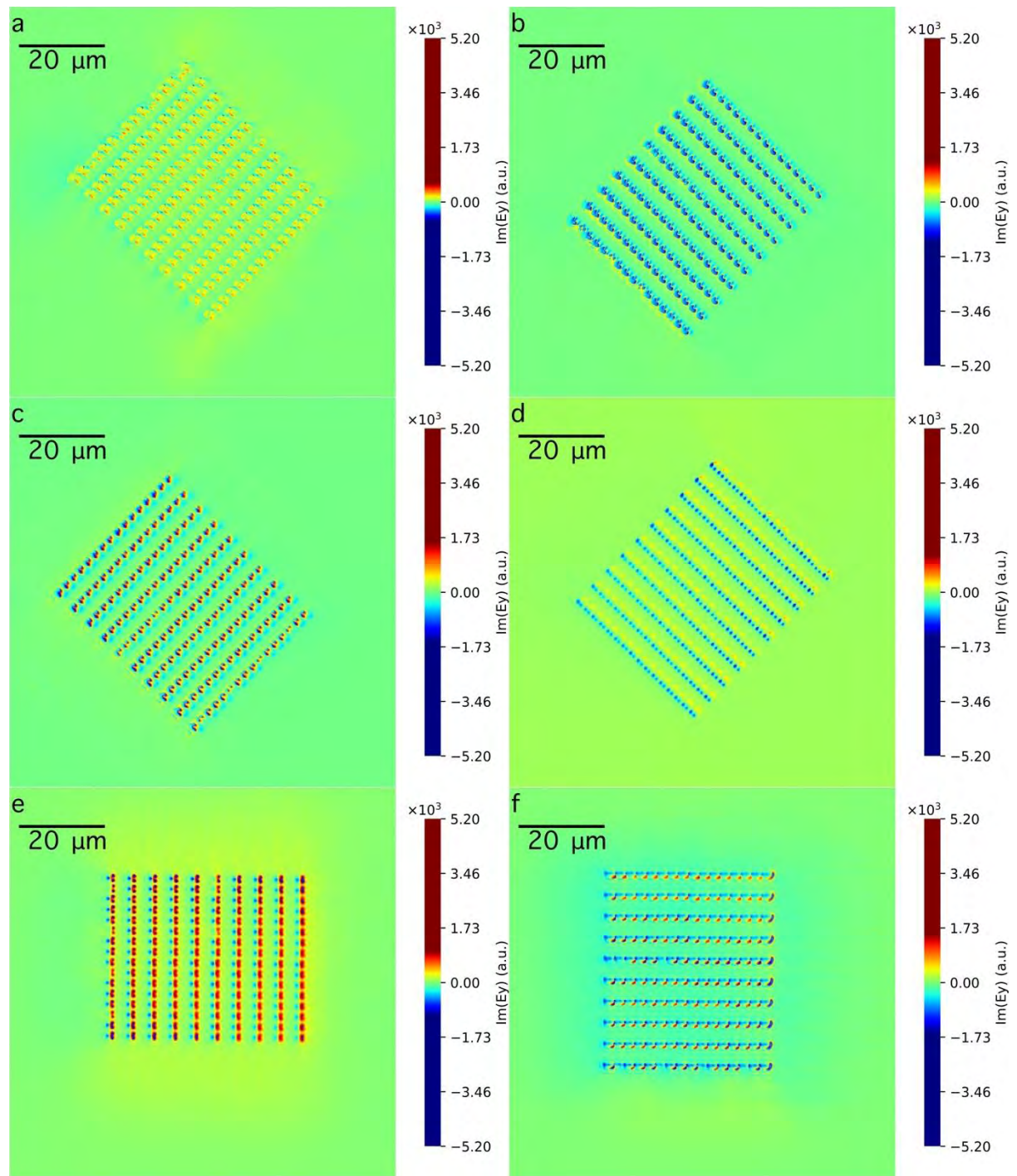


Figure 9.2.2.17 The mapping of $Im(E_y)$ for the nanograter sited at angles: (a) 58° , (b) 148° , (c) 238° , (d) 328° , (e) 102° , (f) 192°

The mapping of modulus of the electrical field along the x_1 axis (which is parallel to A shown in Fig. 9.1.1.3 and y_1 axis (which is perpendicular to A shown in Fig. 9.1.1.3 are shown in Fig. 9.2.2.18 and Fig. 9.2.2.19. The phase difference δ_1 between y_1 -axis and x_1 -

axis is shown in Fig. 9.2.2.20. The red heart, about 2.5×10^3 a.u. on Fig. 9.2.2.18a should be related with the U-shape hole on the nanograter sample1; while, the blue dot, about 1.2×10^3 a.u. should be related to the protrusion of the nanograter sample1.

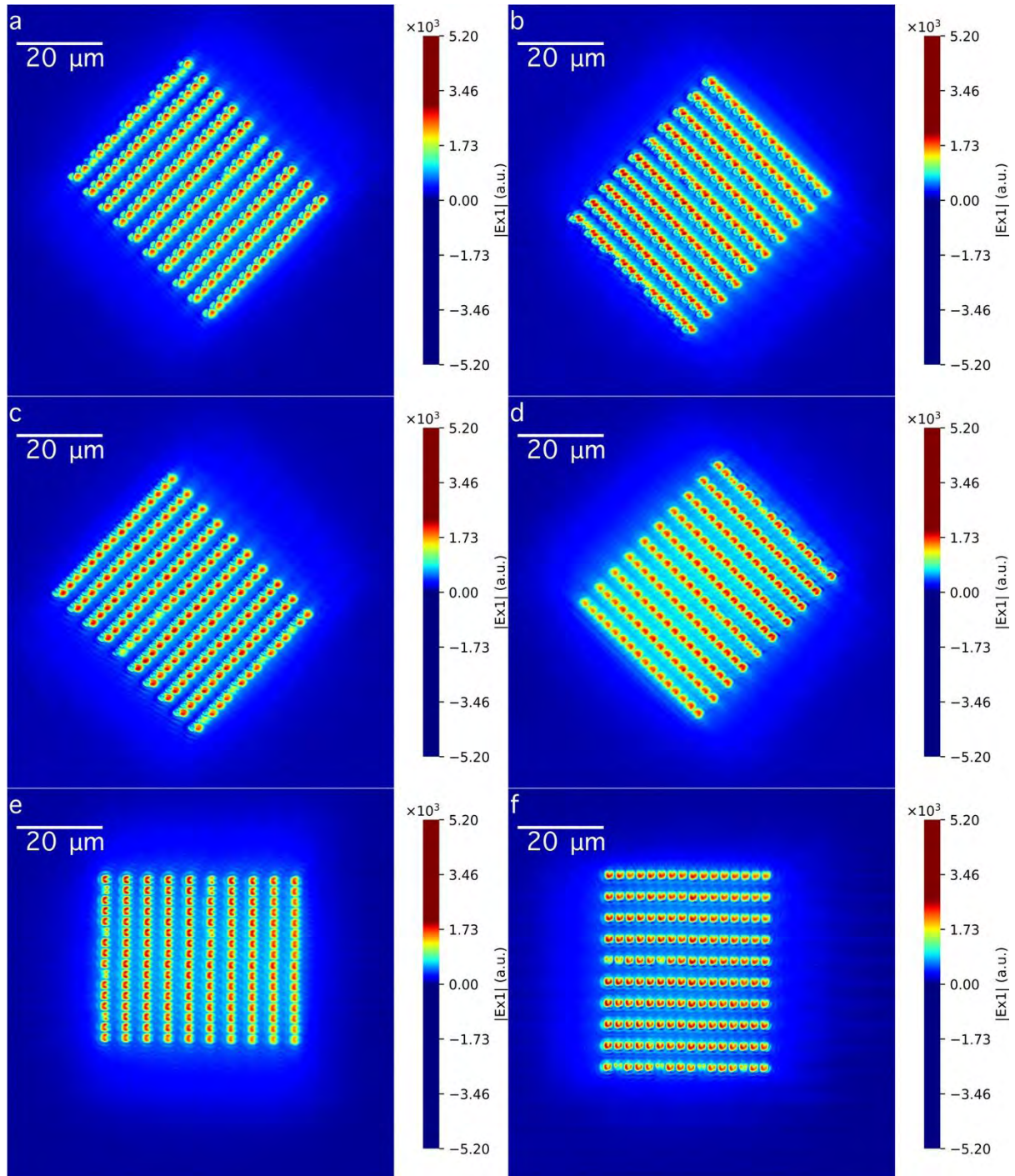


Figure 9.2.2.18 The mapping of $|E_{x1}|$ for the nanograter sited at angles: (a) 58°, (b) 148°, (c) 238°, (d) 328°, (e) 102°, (f) 192°

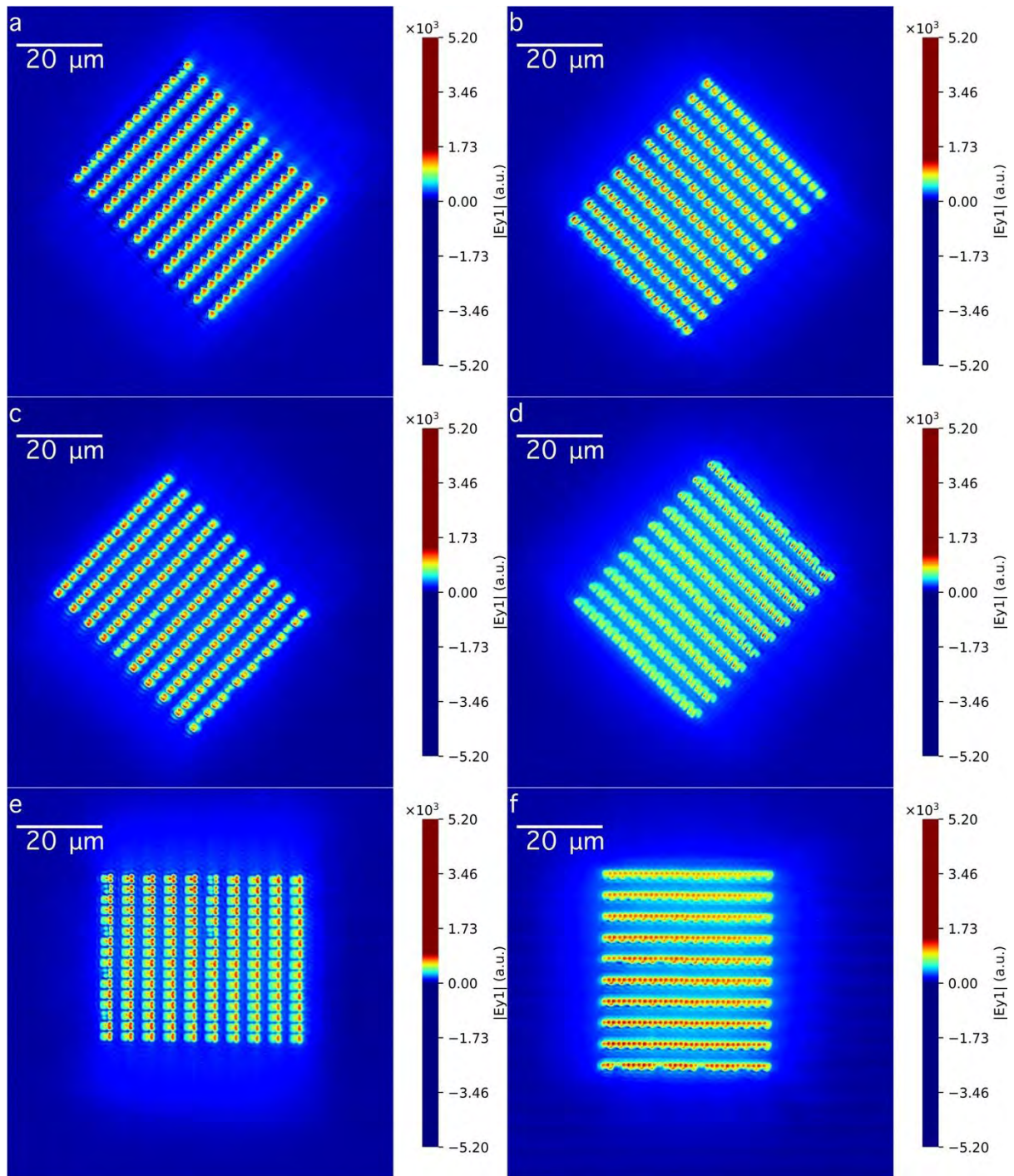


Figure 9.2.2.19 The mapping of $|E_{y1}|$ for the nanograting sited at angles: (a) 58° , (b) 148° , (c) 238° , (d) 328° , (e) 102° , (f) 192°

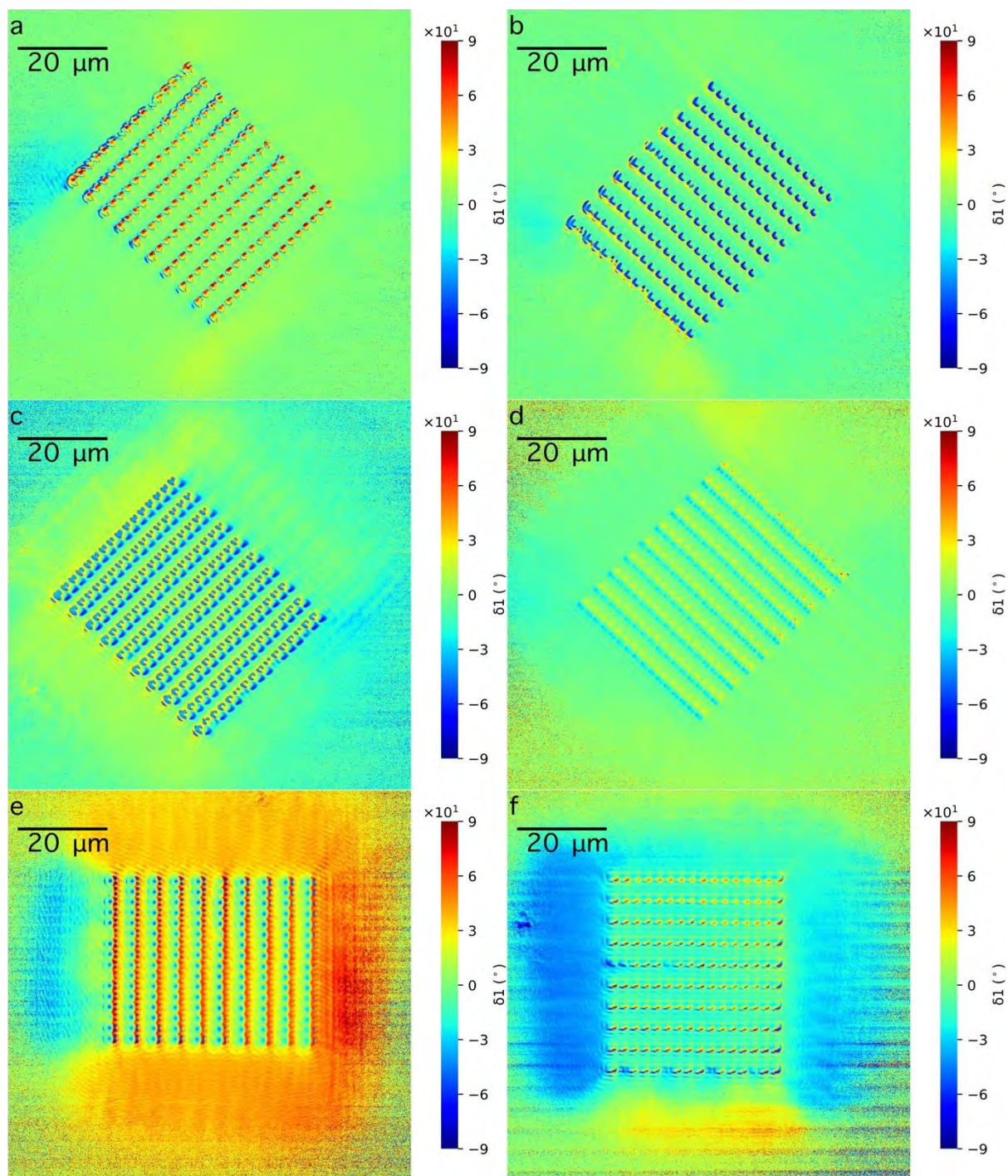


Figure 9.2.2.20 The mapping of δ_1 for the nanograting sited at angles: (a) 58° , (b) 148° , (c) 238° , (d) 328° , (e) 102° , (f) 192°

The relative angle between the polarizer fast axis and the nanograting edge can adjust the mapping of polarization component. The nonuniform background is removed in the sample rotation experiment. Orthogonal to the edge of the nanograting will make the surrounding area of the elliptical angle, azimuth angle and phase difference is uniform; while, tilt to the edge of

the nanograter will make the surrounding area of that parameters is nonuniform. At a special position 58° , the phase difference is near to zero in general.

9.2.3 sample rotation experiment with the protrusions facing the camera

Nanograter is a three-dimension structure. Despite the symmetrical characteristic in a plane discussed in section 9.2.2, another symmetrical characteristic outside of the plane is important, the protrusions' orientations, facing the light source or the camera. The situation of protrusion facing the light source is discussed in last section. The situation of protrusion facing the camera is going to be introduced in this section. Table 9.2.3.1 shows the configuration between the polarizer and the nanograter in the experiment of the protrusion facing to the camera.

Table 9.2.3.1 the configuration of the sample stage rotation experiment—the protrusion facing to the camera.

Polarization angle ($^\circ$)	Sample stage angle ($^\circ$)			
110 (122)	34 ($P \perp A$)	124 ($P \parallel A$)	214($P \perp A$)	304($P \parallel A$)
20 (32)	34 ($P \parallel A$)	124($P \perp A$)	214($P \parallel A$)	304($P \perp A$)

The experiment of the polarization angle (32°) is done for cross reference. I only list the situation of polarization at 122° in my thesis for significance.

Although the sample is flipped over, the symmetrical characteristic in plane is similar to the that in the last section. In the situation of $P \parallel A$, the V varied with the relative angle between P and A , for A is a vector, too. The polarization is strongly depolarized in the configuration of $P \perp A$ than that in the configuration of $P \parallel A$.

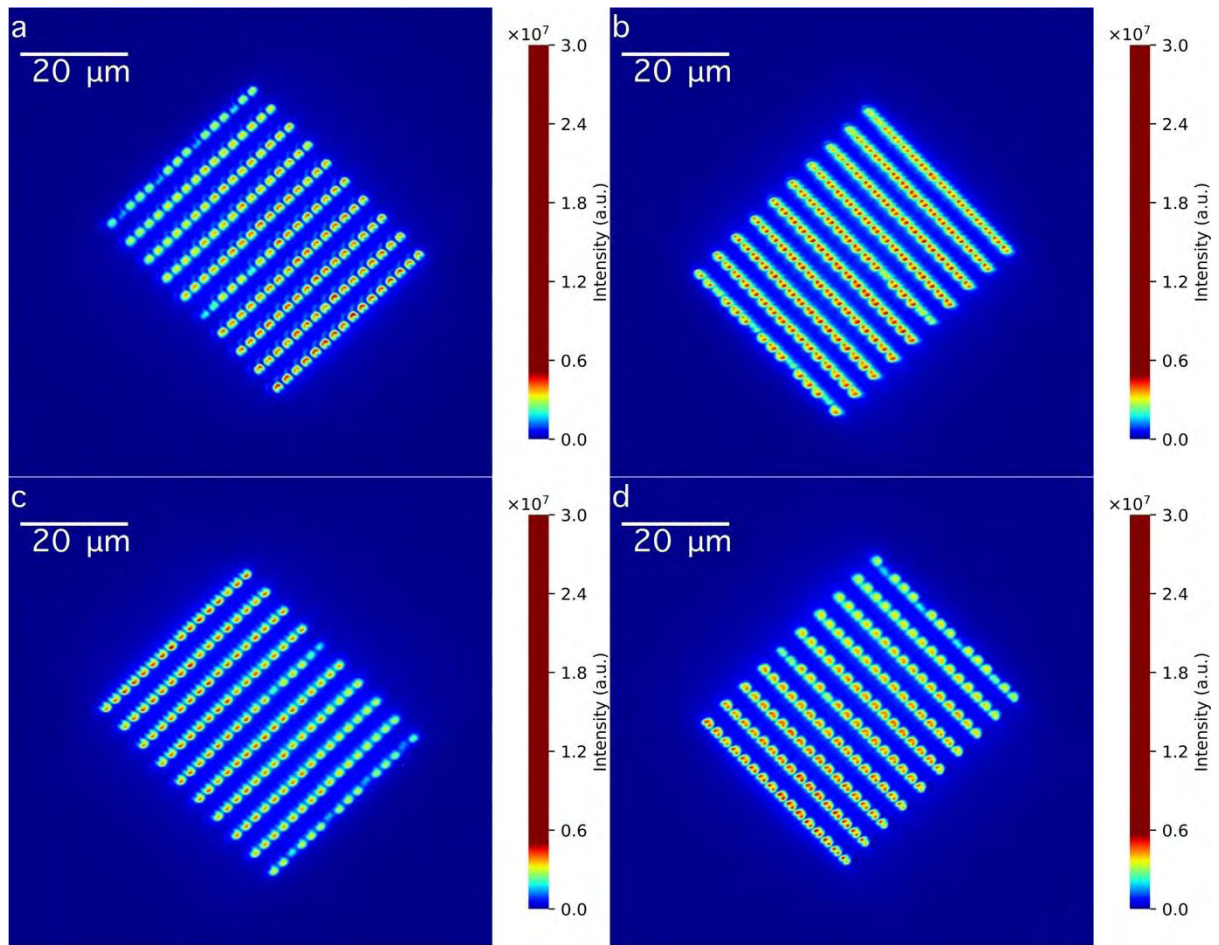


Figure 9.2.3.1 The mapping of I for the nanograting protrusion facing to the camera, when the polarizer sited at 122° : (a) 34° , (b) 124° , (c) 214° , (d) 304°

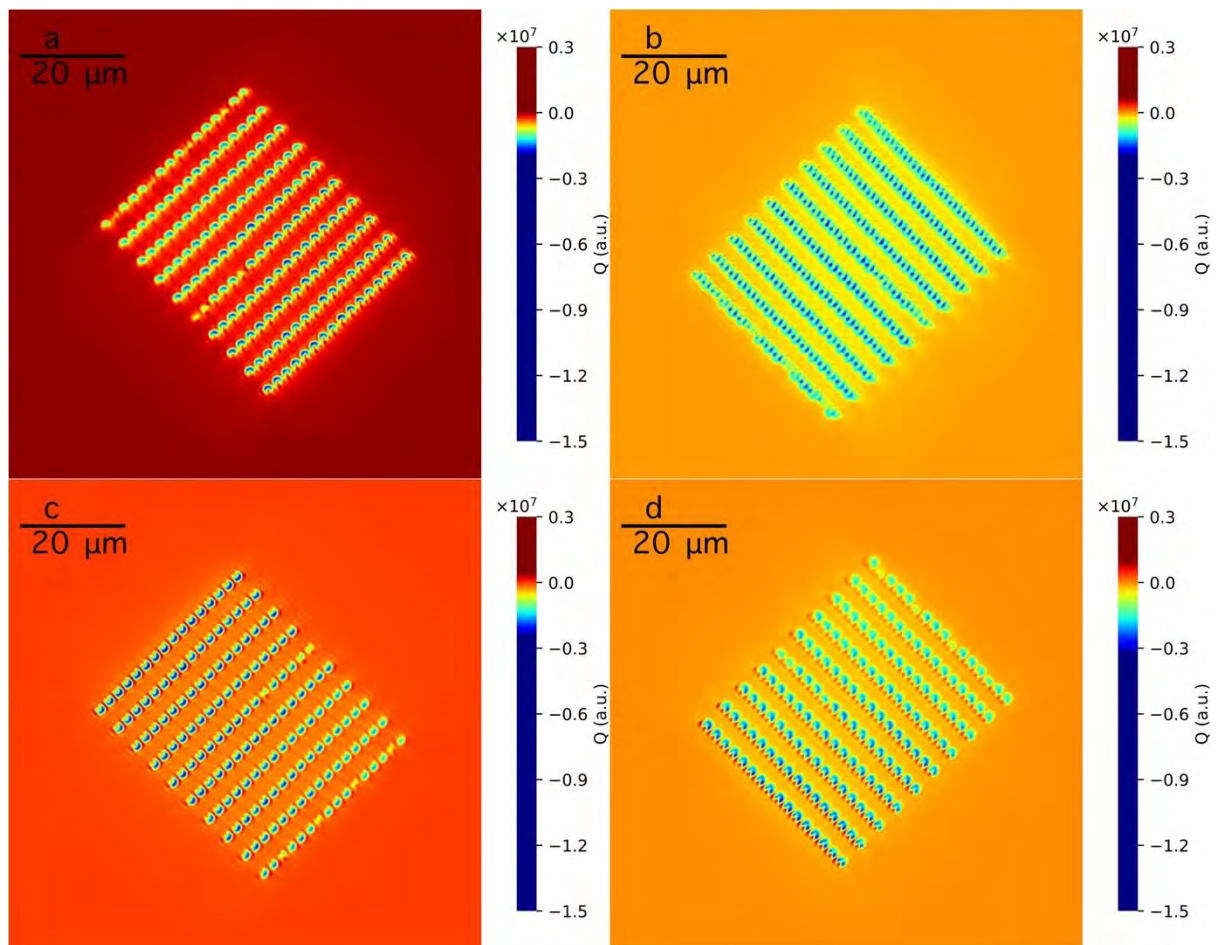


Figure 9.2.3.2 The mapping of Q for the nanograting protrusion facing to the camera, when the polarizer sited at 122° : (a) 34° , (b) 124° , (c) 214° , (d) 304°

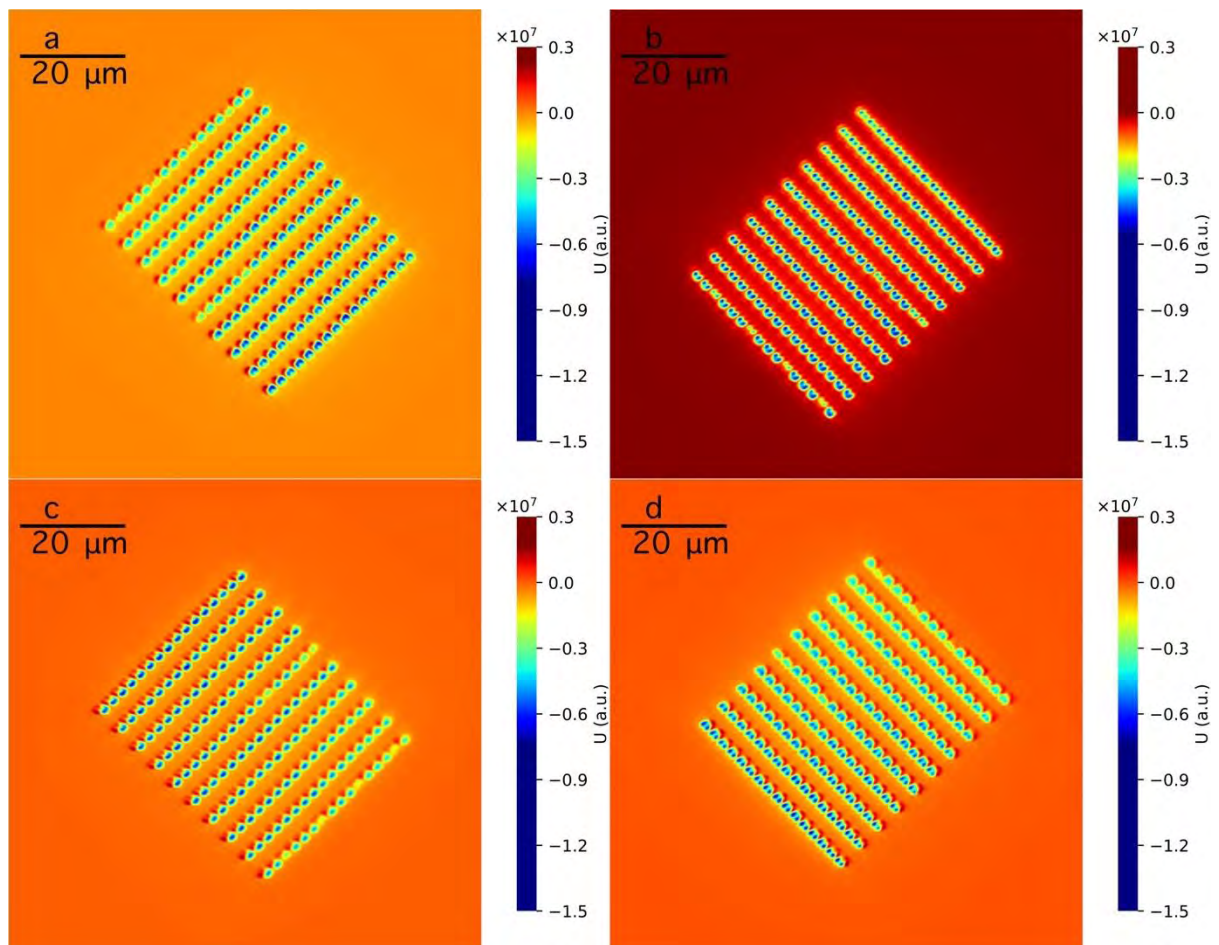


Figure 9.2.3.3 The mapping of U for the nanograter protrusion facing to the camera, when the polarizer is sited at 122° : (a) 34° , (b) 124° , (c) 214° , (d) 304°

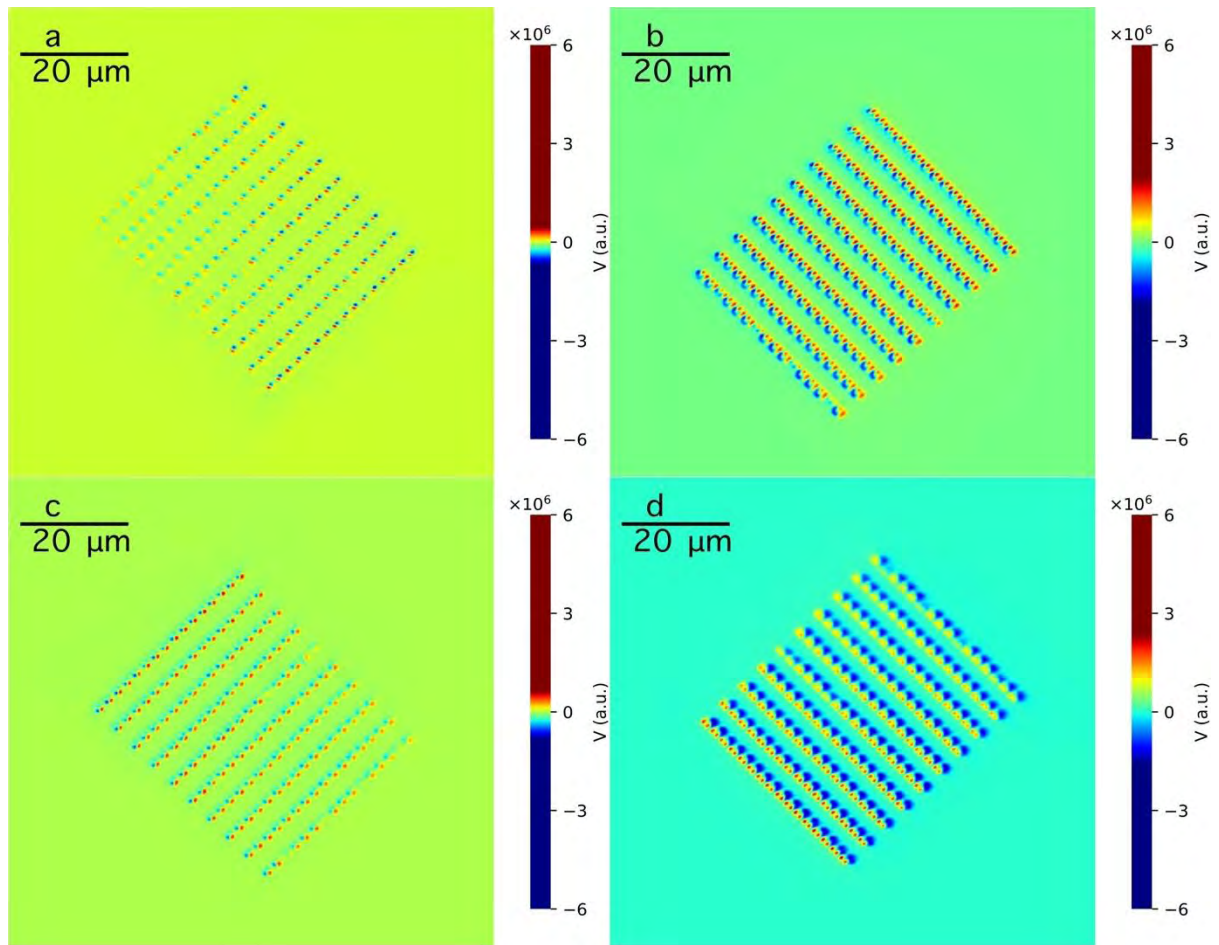


Figure 9.2.3.4 The mapping of V for the nanograting protrusion facing to the camera, when the polarizer is sited at 122° : (a) 34° , (b) 124° , (c) 214° , (d) 304°

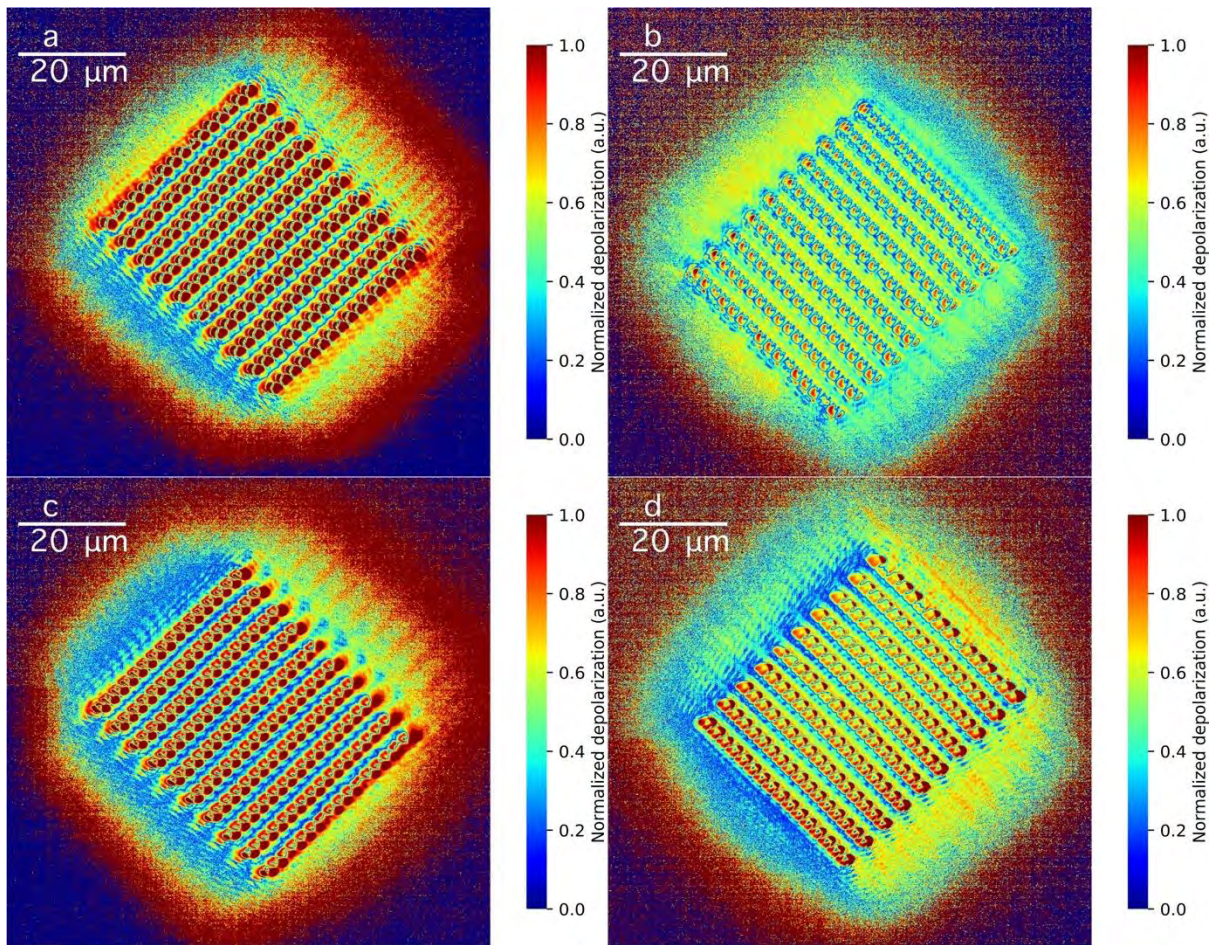


Figure 9.2.3.5 The mapping of I_{dP}/I for the nanograting protrusion facing to the camera, when the polarizer sited at 122° : (a) 34° , (b) 124° , (c) 214° , (d) 304°

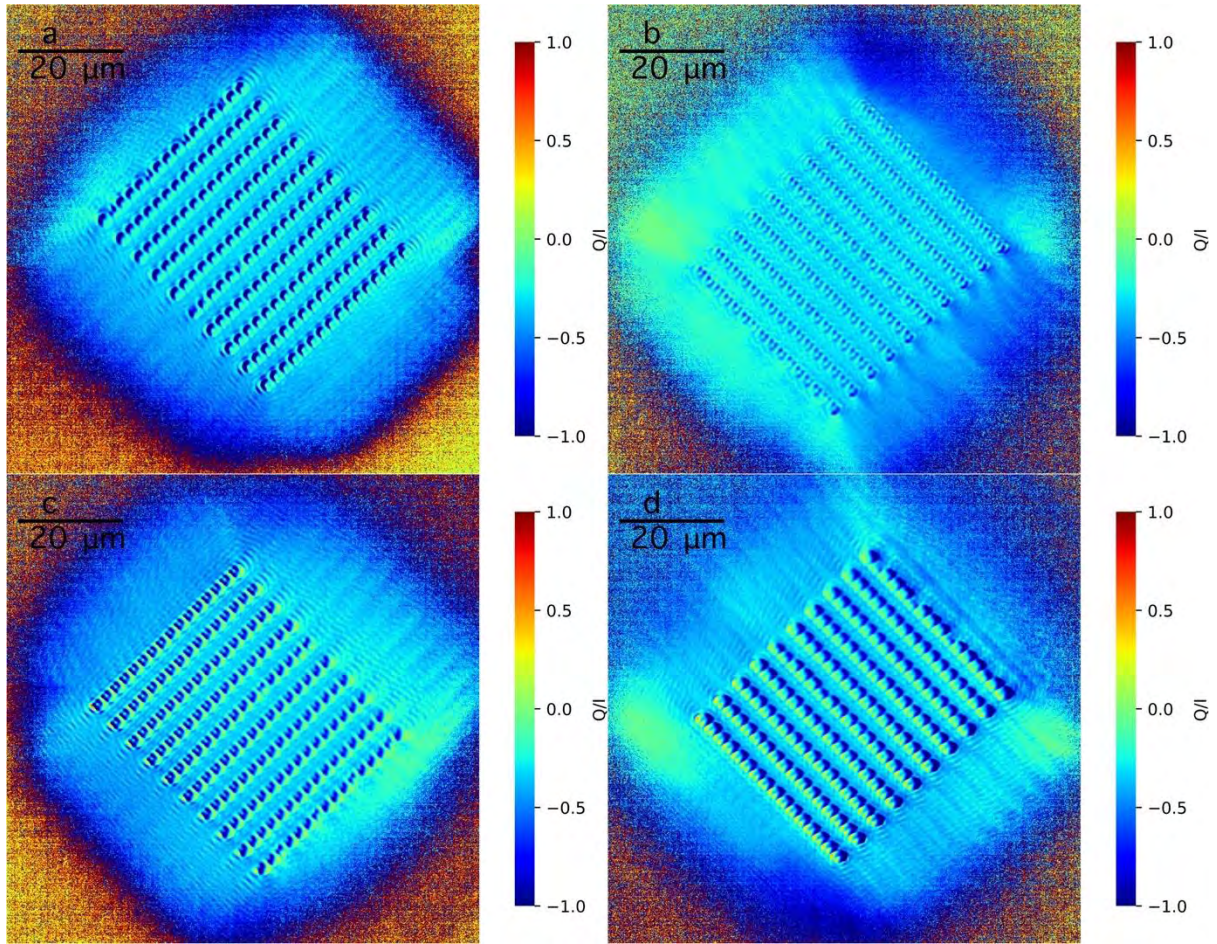


Figure 9.2.3.6 The mapping of Q/I for the nanograting protrusion facing to the camera, when the polarizer sited at 122° : (a) 34° , (b) 124° , (c) 214° , (d) 304°

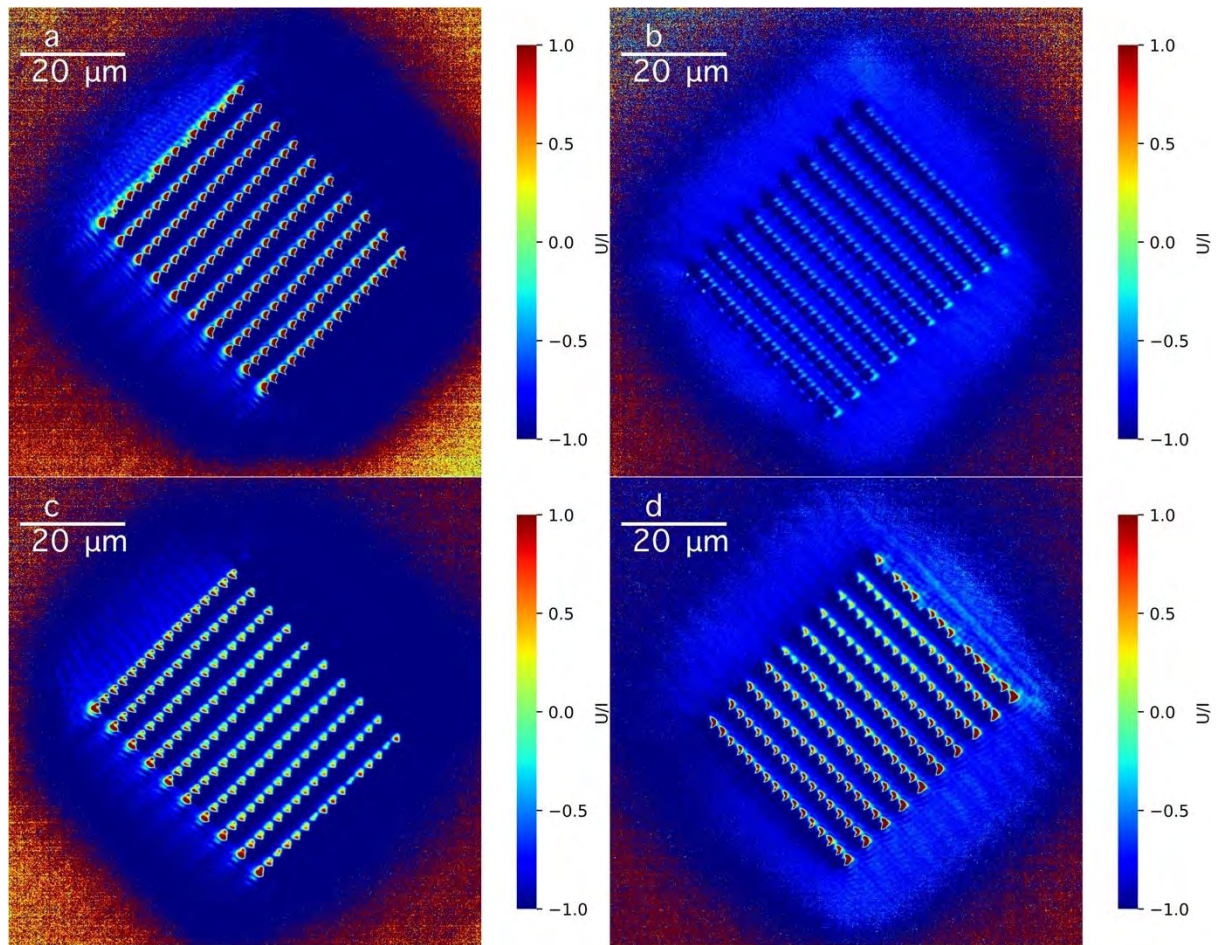


Figure 9.2.3.7 The mapping of U/I for the nanograting protrusion facing to the camera, when the polarizer sited at 122° : (a) 34° , (b) 124° , (c) 214° , (d) 304°

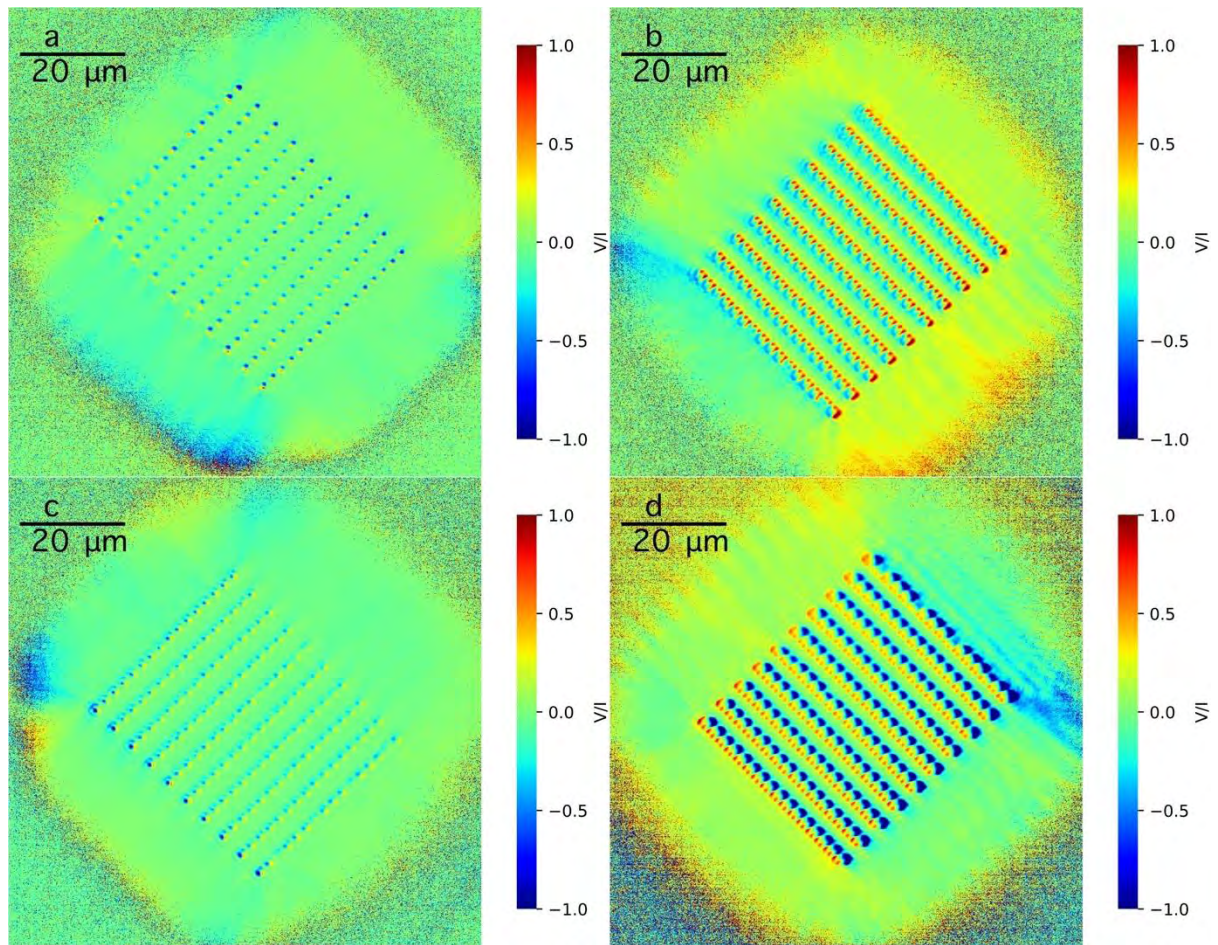


Figure 9.2.3.8 The mapping of V/I for the nanograter protrusion facing to the camera, when the polarizer sited at 122° : (a) 34° , (b) 124° , (c) 214° , (d) 304°

In the image of the elliptical angle, the image of the protrusion is can be seen, but the image of the U- shape can't be seen, when the $P \perp A$.

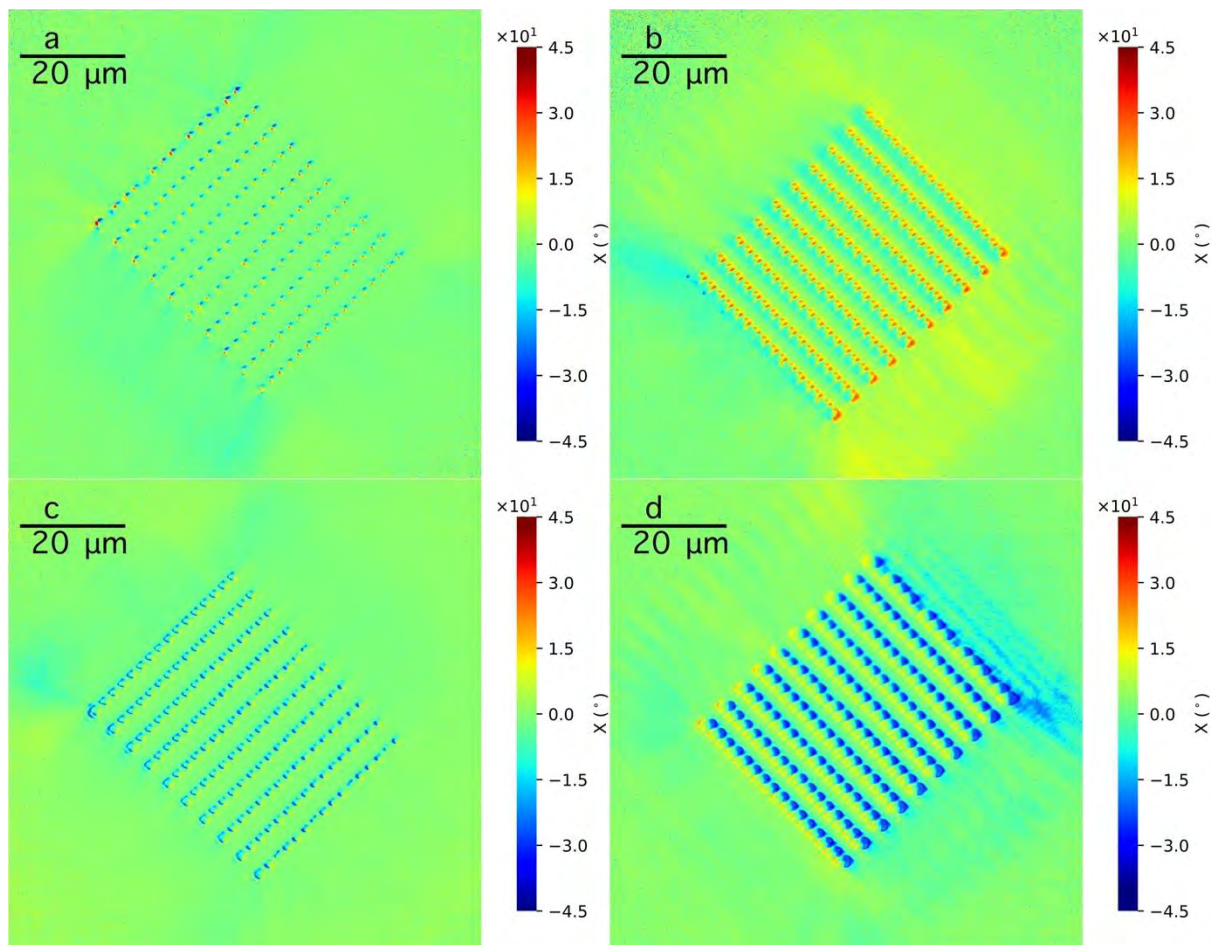


Figure 9.2.3.9 The mapping of χ for the nanograting protrusion facing to the camera, when the polarizer sited at 122° : (a) 34° , (b) 124° , (c) 214° , (d) 304°

When polarization rotate much in the situation of $P \perp A$, and it is nearly not change when the $P \parallel A$, shown in the image of azimuth angle. Although in the image d $P \parallel A$, the little error may produce the $P \nparallel A$.

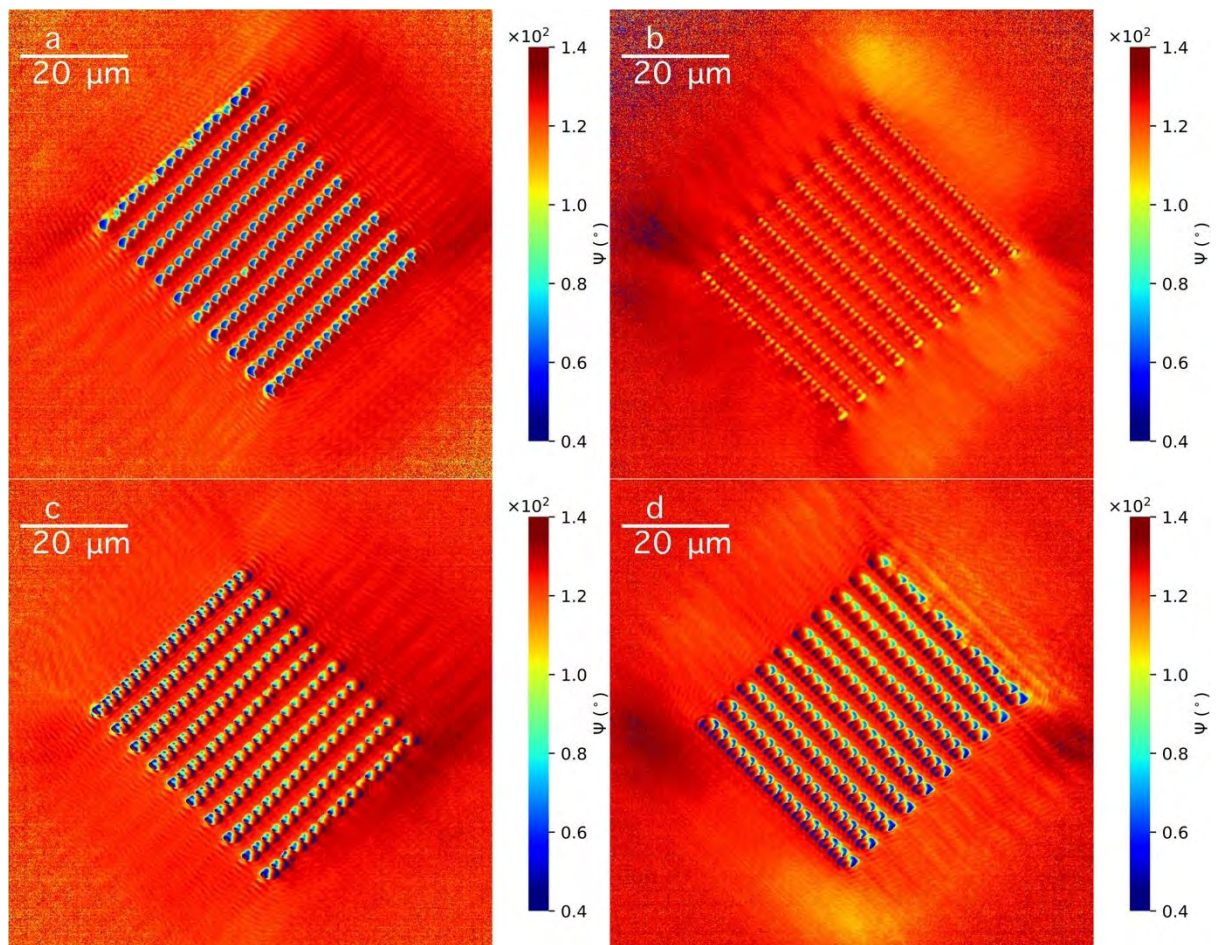


Figure 9.2.3.10 The mapping of ψ for the nanograting protrusion facing to the camera, when the polarizer sited at 122° : (a) 34° , (b) 124° , (c) 214° , (d) 304°

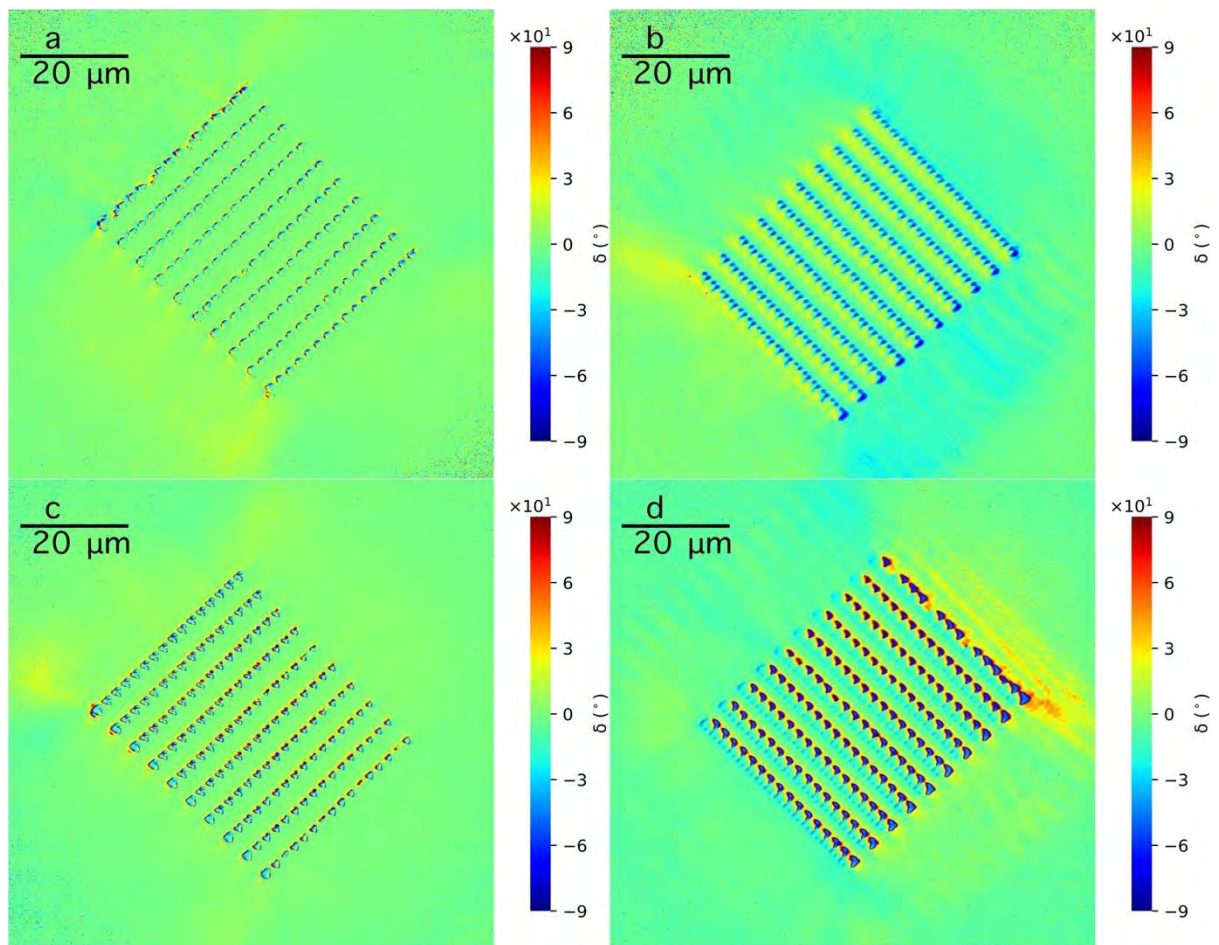


Figure 9.2.3.11 The mapping of δ for the nanograting protrusion facing to the camera, when the polarizer sited at 122° : (a) 34° , (b) 124° , (c) 214° , (d) 304°

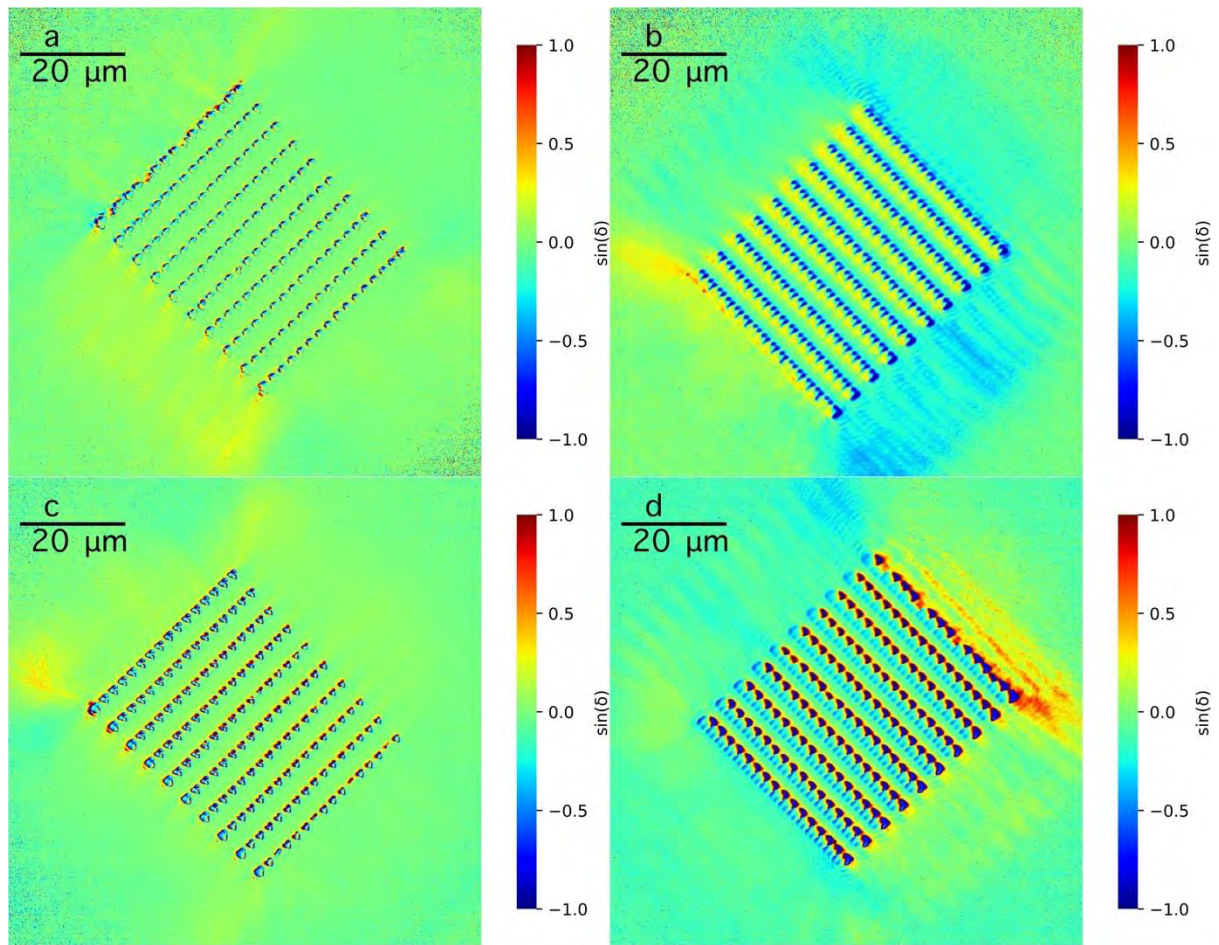


Figure 9.2.3.12 The mapping of $\sin(\delta)$ for the nanograter protrusion facing to the camera, when the polarizer sited at 122° : (a) 34° , (b) 124° , (c) 214° , (d) 304°

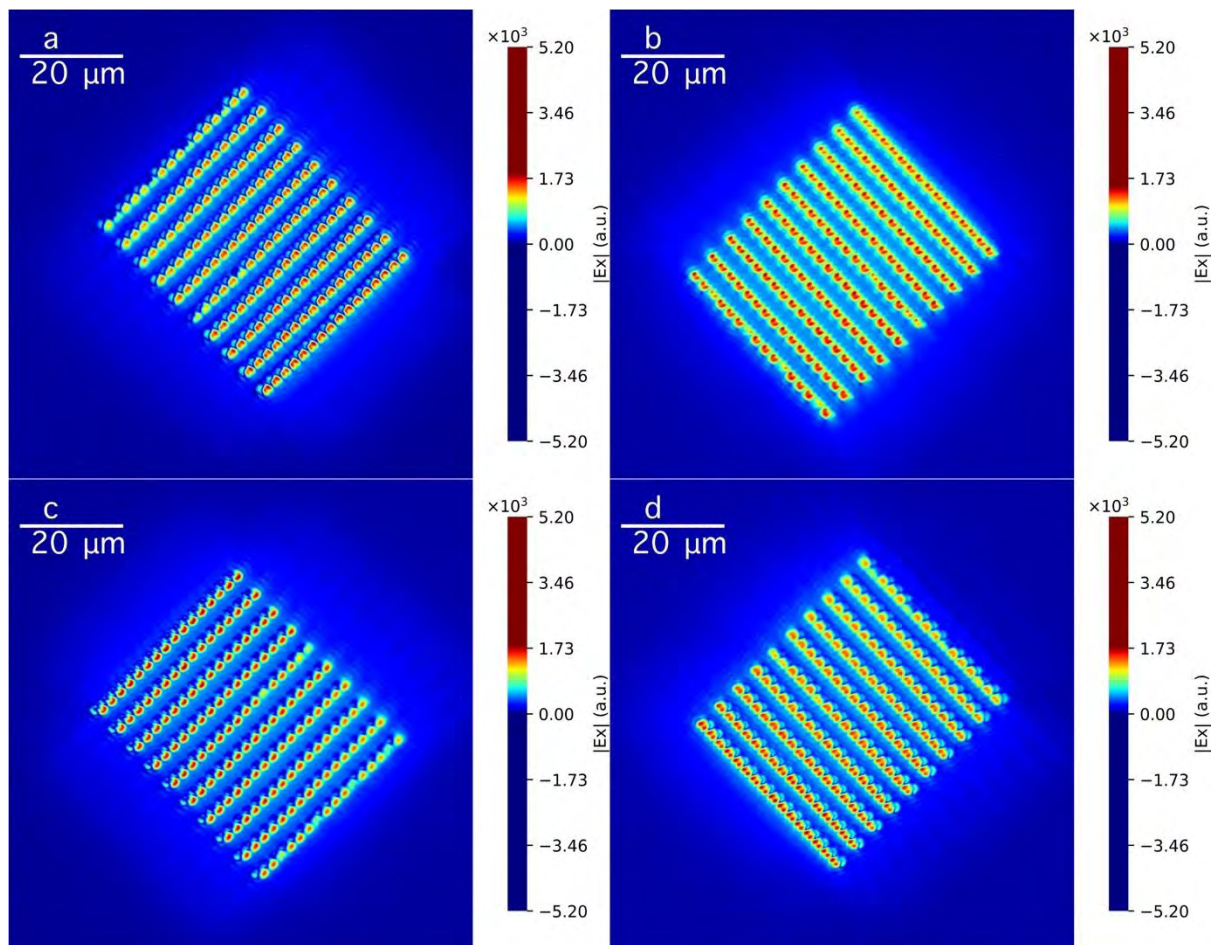


Figure 9.2.3.13 The mapping of $|E_x|$ for the nanograter protrusion facing to the camera, when the polarizer sited at 122° : (a) 34° , (b) 124° , (c) 214° , (d) 304°

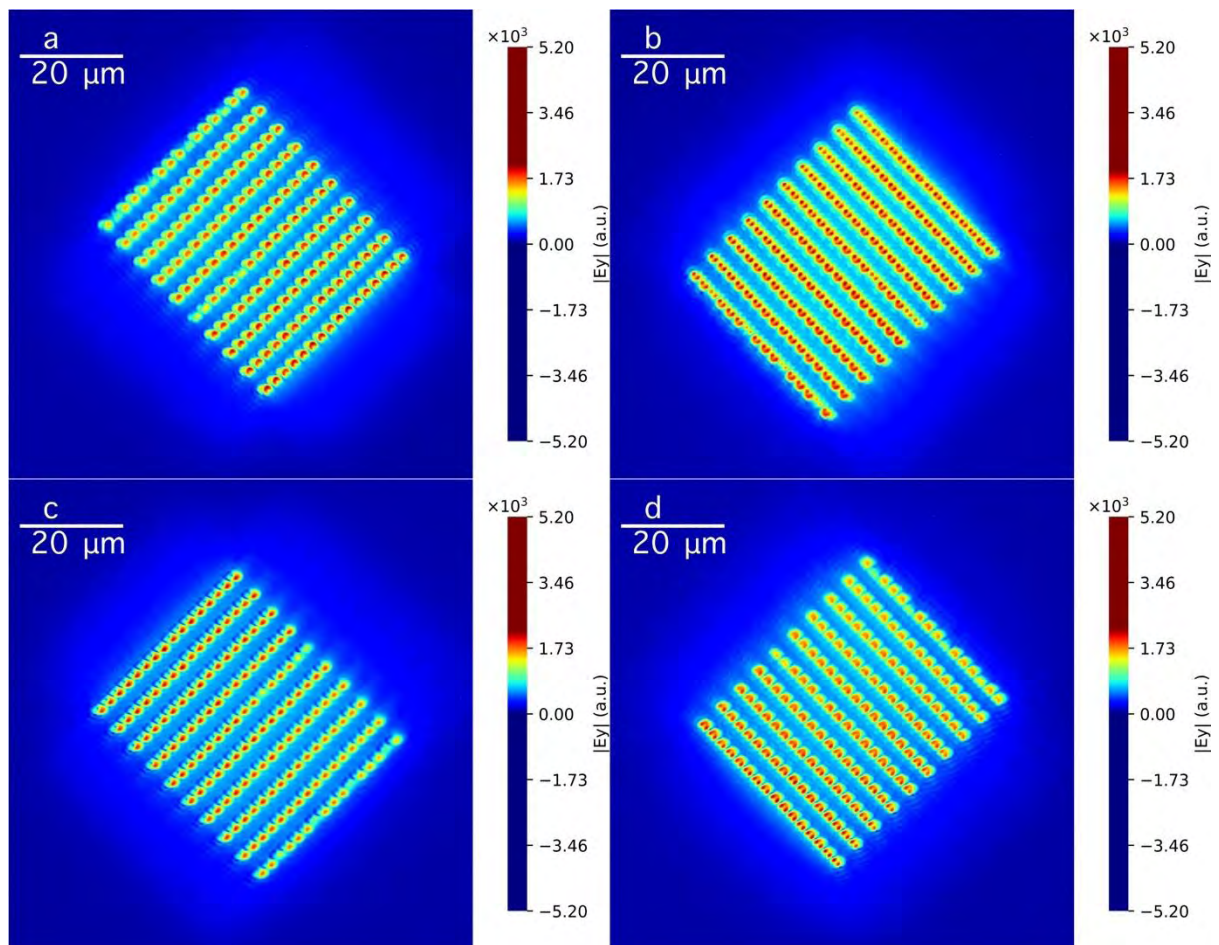


Figure 9.2.3.14 The mapping of $|E_y|$ for the nanograting protrusion facing to the camera, when the polarizer sited at 122° : (a) 34° , (b) 124° , (c) 214° , (d) 304°

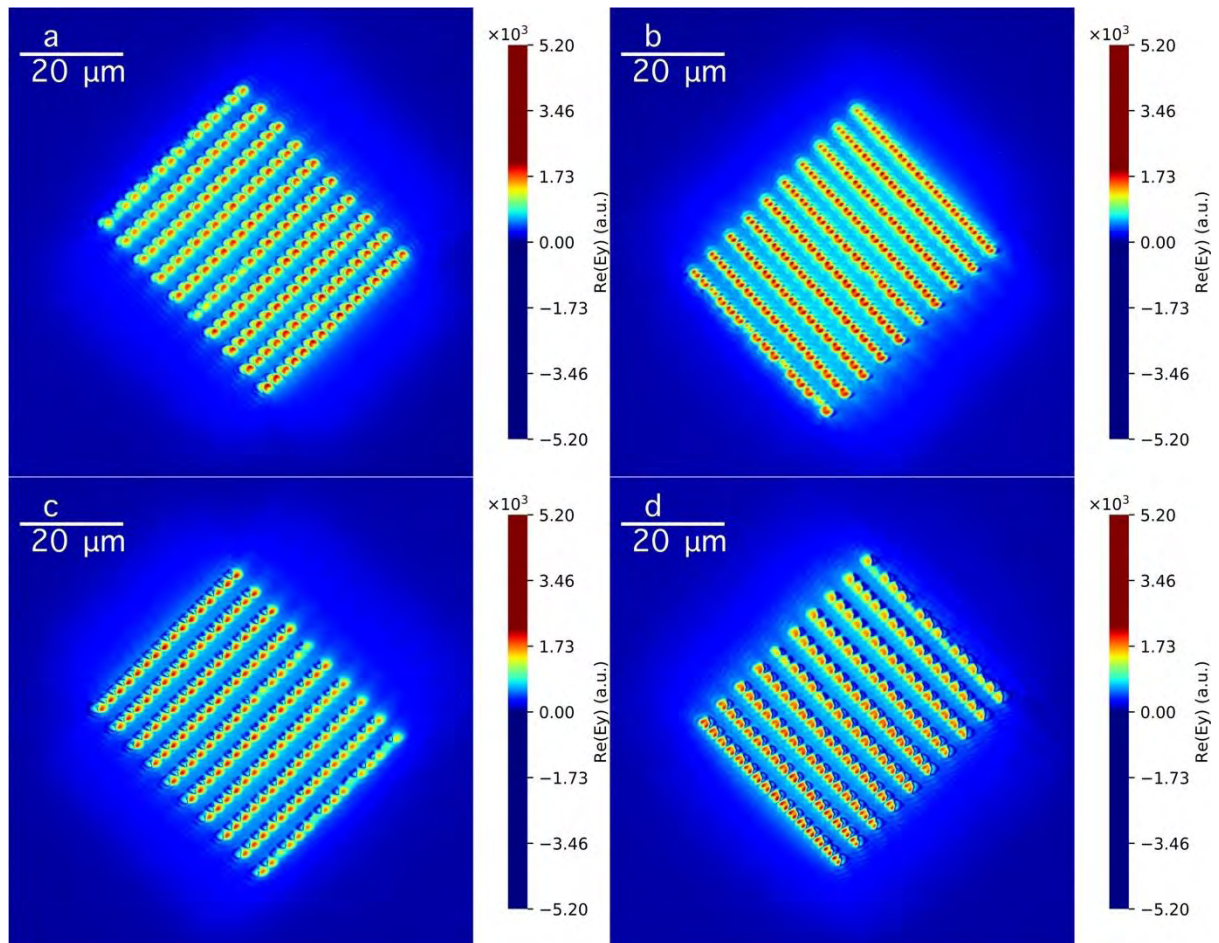


Figure 9.2.3.15 The mapping of $Re(E_y)$ for the nanograting protrusion facing to the camera, when the polarizer sited at 122° : (a) 34° , (b) 124° , (c) 214° , (d) 304°

The imaginary part of E_y can't provide an image of the protrusion when the $P \perp A$, although the protrusion is in front of the U-shape hole. At the position the U-shape is blocked by the protrusion, reference to the SEM image in Fig. 9.2.2.1c, the $\text{Im}(E_y)$ is no signal.

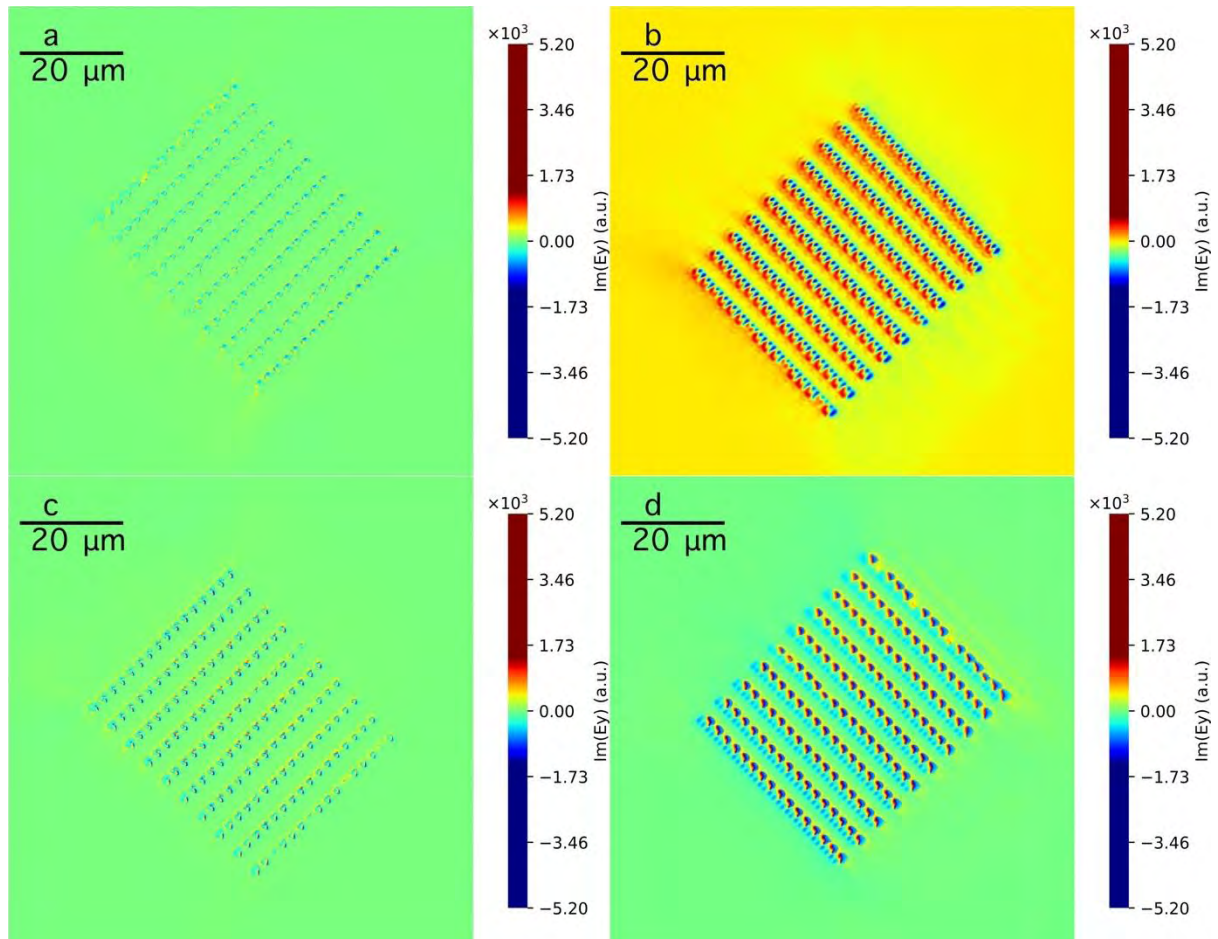


Figure 9.2.3.16 The mapping of $\text{Im}(E_y)$ for the nanograting protrusion facing to the camera, when the polarizer sited at 122° : (a) 34° , (b) 124° , (c) 214° , (d) 304°

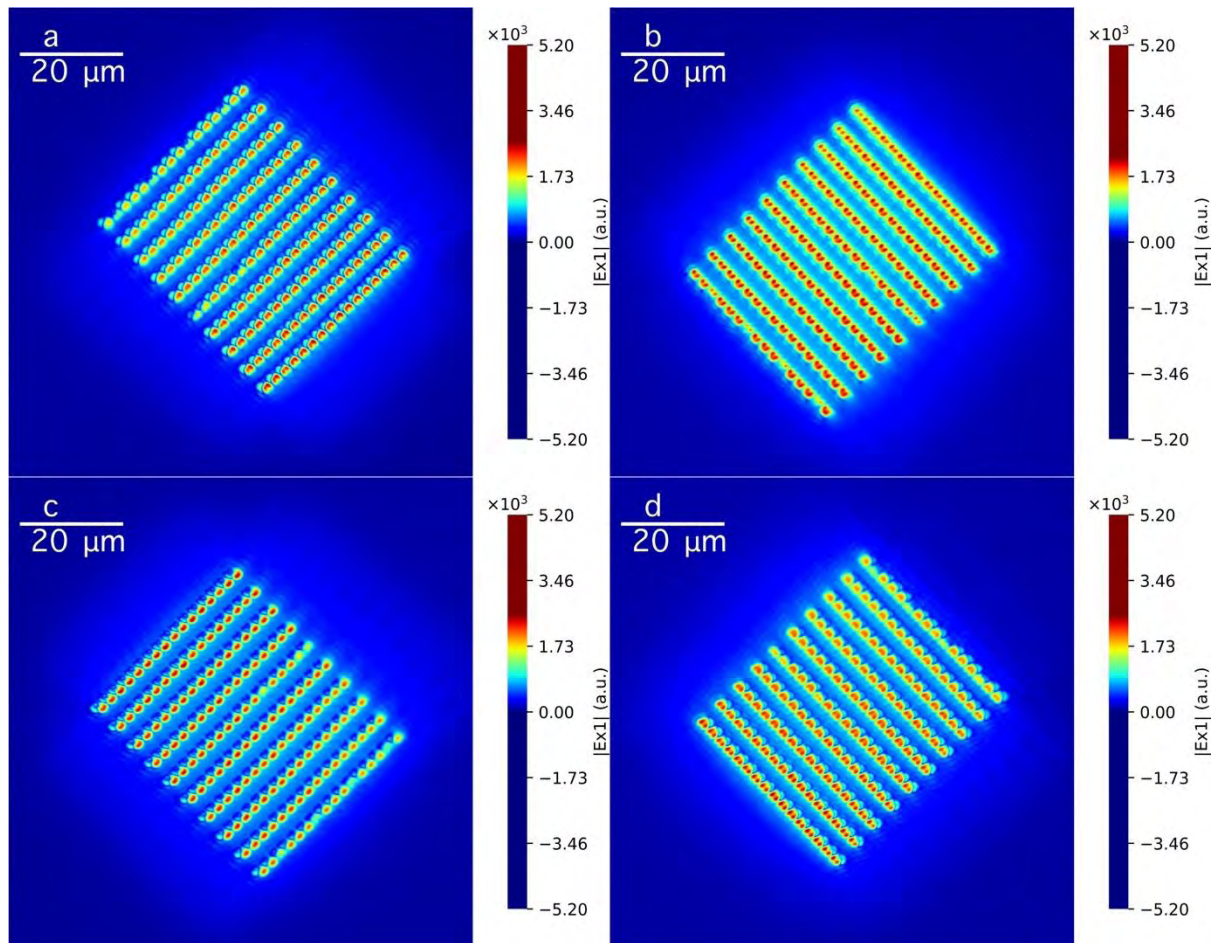


Figure 9.2.3.17 The mapping of $|E_{x1}|$ for the nanograting protrusion facing to the camera, when the polarizer sited at 122° : (a) 34° , (b) 124° , (c) 214° , (d) 304°

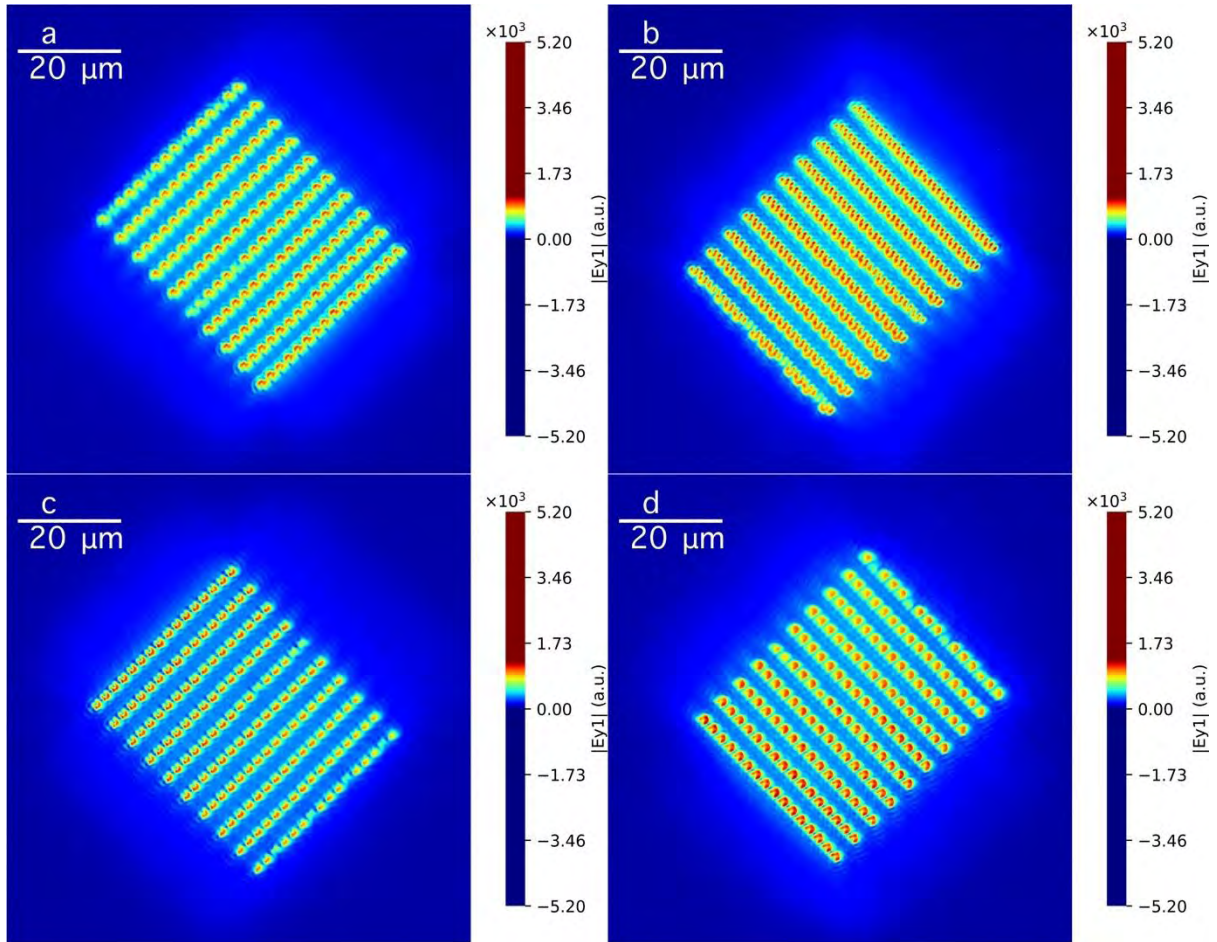


Figure 9.2.3.18 The mapping of $|E_{y1}|$ for the nanograting protrusion facing to the camera, when the polarizer sited at 122° : (a) 34° , (b) 124° , (c) 214° , (d) 304°

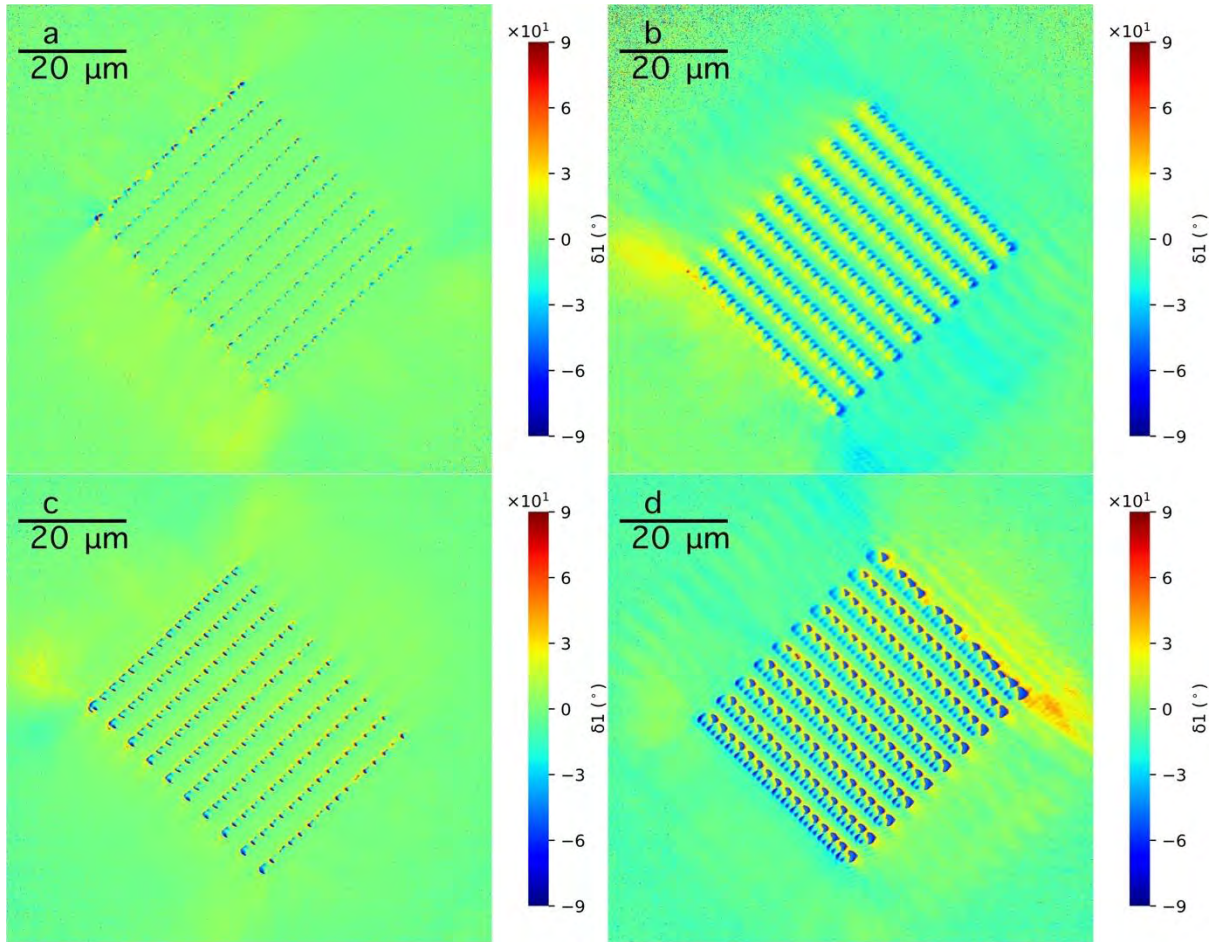


Figure 9.2.3.19 The mapping of δ_1 for the nanograting protrusion facing to the camera, when the polarizer sited at 122° : (a) 34° , (b) 124° , (c) 214° , (d) 304°

In conclusion, the patterns in configuration $P \perp A$ and $P \parallel A$ is different. The pattern of protrusion facing the camera and that facing the light source is different, too. The signal of phase difference is stronger in configuration of $P \parallel A$ than that in configuration of $P \perp A$. To analysis this phenomenon carefully, I sum up the pictures in configuration $P \perp A$ and $P \parallel A$ in next two sections, to analysis the influence of the protrusion facing.

9.2.4 The optical axis of polarizer perpendicular to the axis of the nanograting

The intensity is a bigger when the protrusion facing the light source than that facing the camera, shown in Fig.9.2.4.1. Both the protrusion and the U-shape hole can be seen in the image of the $|E_{x1}|$, shown in Fig.9.2.4.2. The U-shape hole is clear in Fig.9.2.4.3b, and the

protrusion is shown in image of $|E_{y1}|$, shown in Fig.9.2.4.3a. The phase difference $|\delta_1|$ is nearly zero when the protrusion facing the camera, shown in Fig.9.2.4.4a; while, the U-shape hole can be seen when the protrusion facing the light source, in Fig.9.2.4.4b. Both the protrusion and the U-shape hole can be seen in the image of semi-major axis a, but looks different, shown in Fig.9.2.4.5. The image of semi-minor axis b shows the protrusion and the U-shape hole, in Fig.9.2.4.5. The image of a and b is swapped when the sample is flipped over.

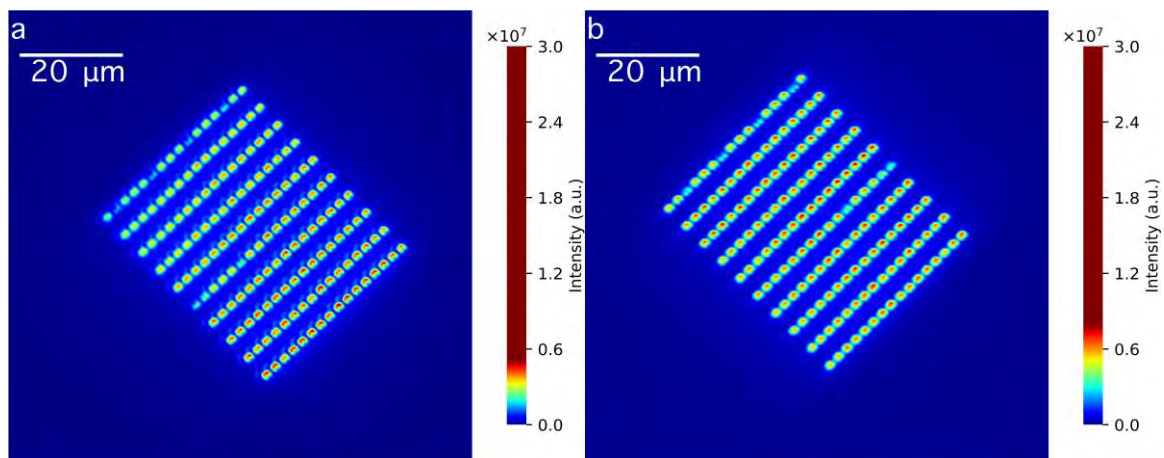


Figure 9.2.4.1 The mapping of I for the nanograting protrusion facing to (a) the camera, (b) the light source, when $P \perp A$, polarizer sited at 122°

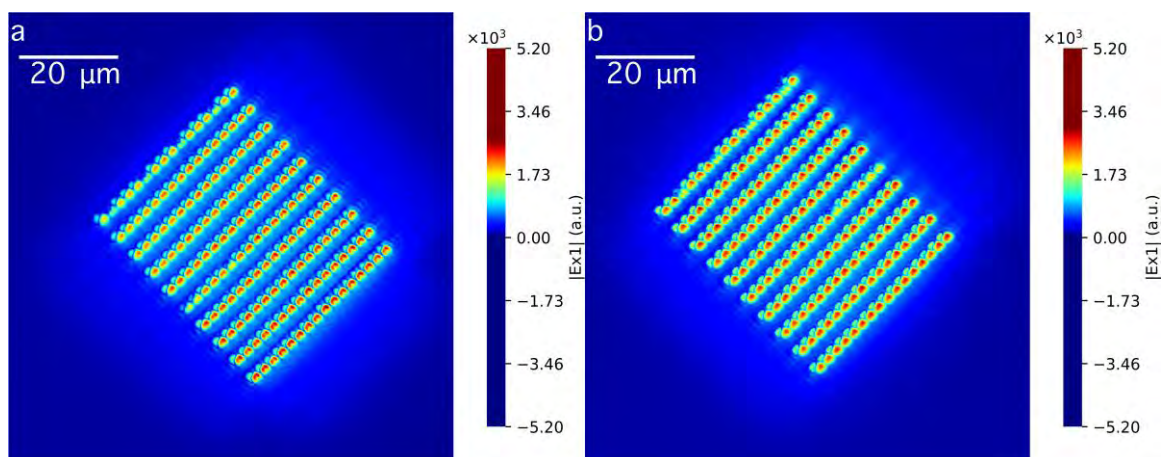


Figure 9.2.4.2 The mapping of $|E_{x1}|$ for the nanograting protrusion facing to (a) the camera, (b) the light source, when $P \perp A$, polarizer sited at 122°

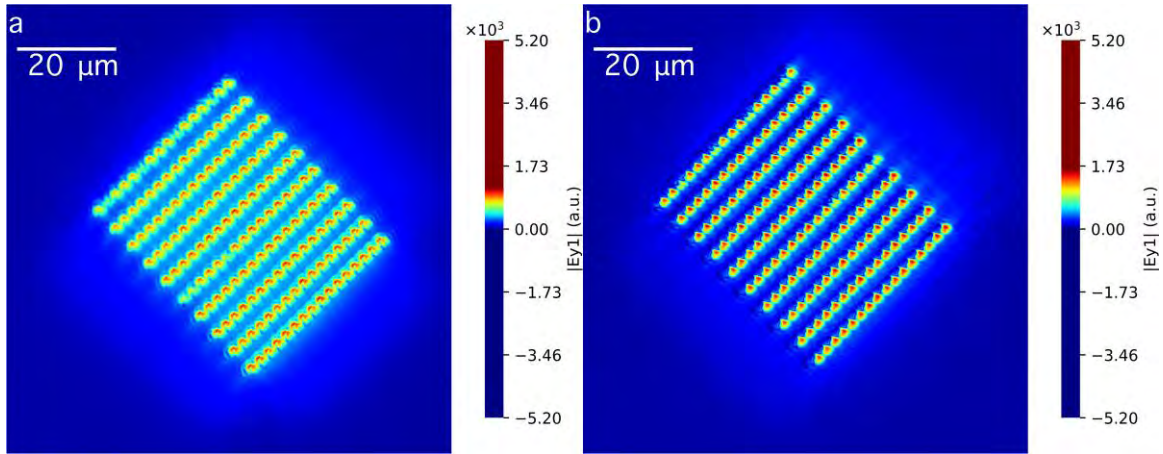


Figure 9.2.4.3 The mapping of $|E_{y1}|$ for the nanograting protrusion facing to (a) the camera, (b) the light source, when $P \perp A$, polarizer sited at 122°

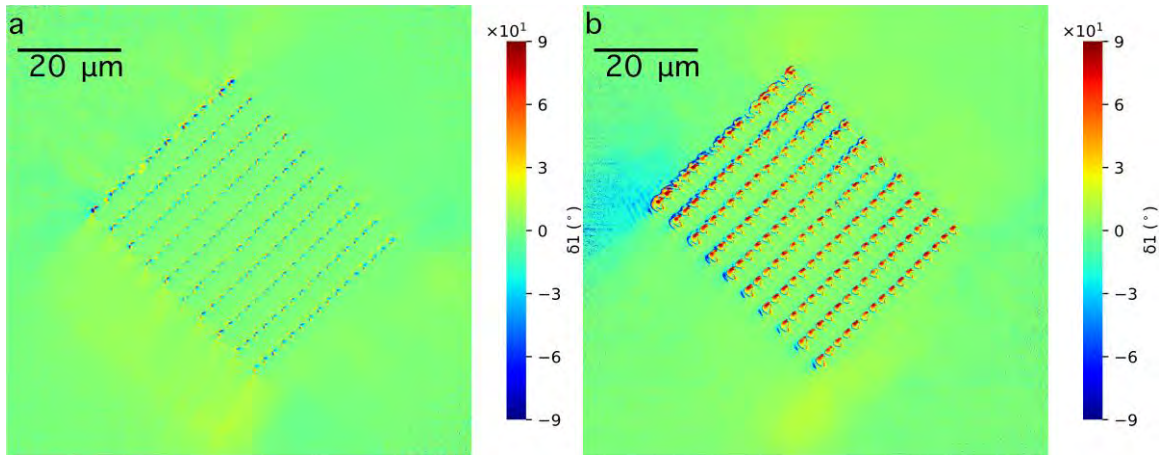


Figure 9.2.4.4 The mapping of δ_1 for the nanograting protrusion facing to (a) the camera, (b) the light source, when $P \perp A$, polarizer sited at 122°

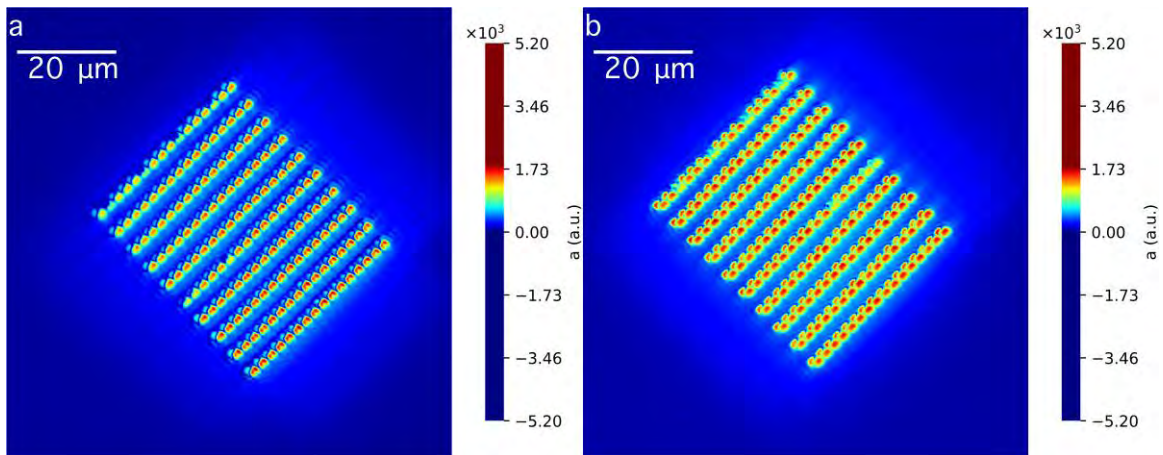


Figure 9.2.4.5 The mapping of semi-major axis of the polarization a for the nanograting protrusion facing to (a) the camera, (b) the light source, when $P \perp A$, polarizer sited at 122°

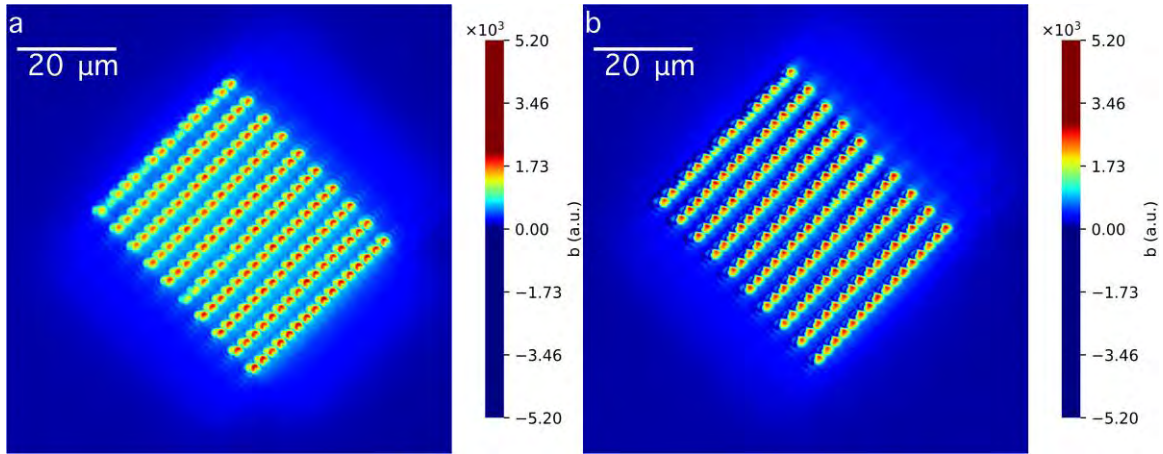


Figure 9.2.4.6 The mapping of semi-major axis of the polarization b for the nanograting protrusion facing to (a) the camera, (b) the light source, when $P \perp A$, polarizer sited at 122°

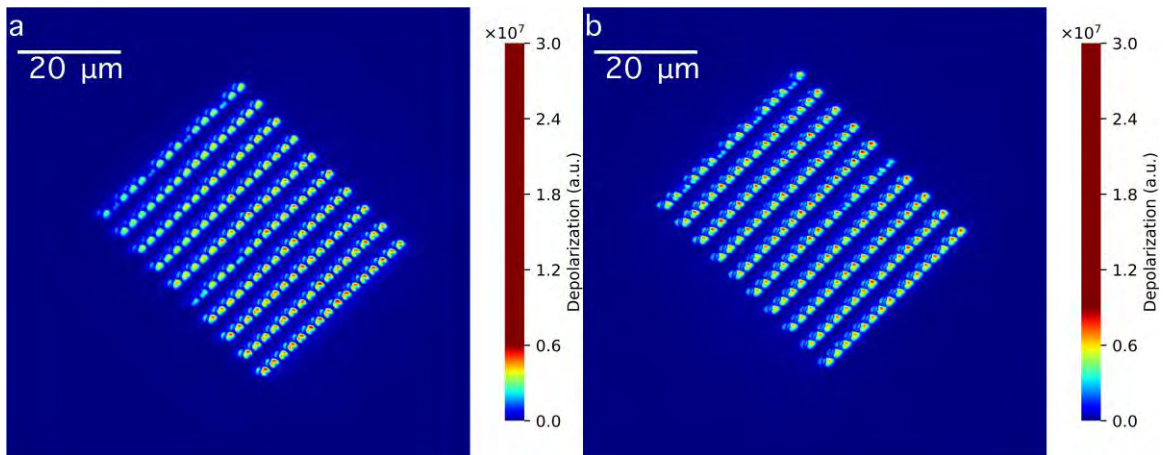


Figure 9.2.4.7 The mapping of I_{dP} for the nanograting protrusion facing to (a) the camera, (b) the light source, when $P \perp A$, polarizer sited at 122°

Both the protrusion and the U-shape hole can be seen in the image of I_{dP} , shown in Fig.9.2.4.7. In the image of $Im(E_y)$, shown in Fig.9.2.4.8, the U-shape hole is blurred when the protrusion facing the camera, and both the U-shape hole and the protrusion can be seen when the protrusion is facing the light source. $Im(E_y)$ may be useful to detect the information shadowed by a metal.

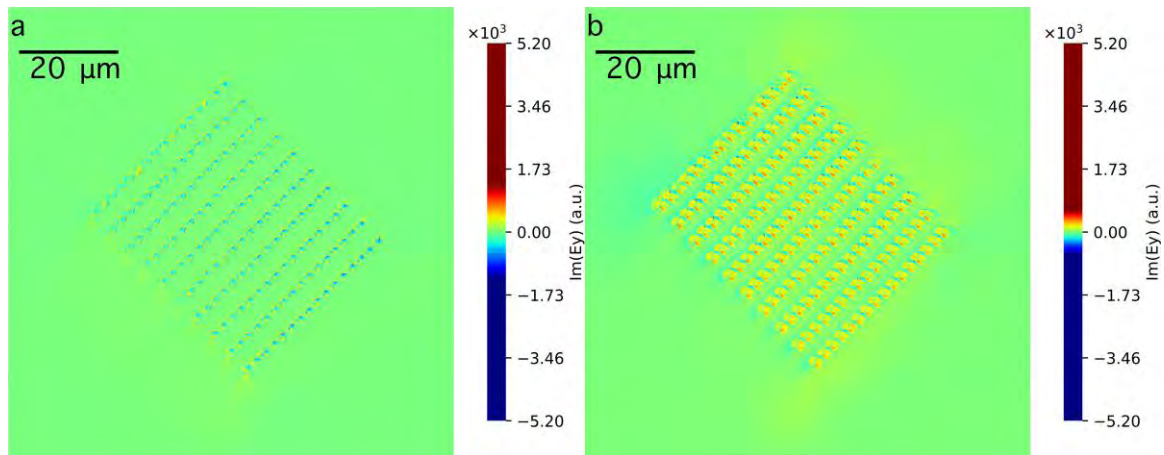


Figure 9.2.4.8 The mapping of $Im(E_y)$ for the nanograting protrusion facing to (a) the camera, (b) the light source, when $P \perp A$, polarizer sited at 122°

Only the protrusion can be seen in the image of the elliptical angle χ , both in Fig. 9.2.4.9a and in Fig. 9.2.4.9b. The azimuth angle variation is localized at the position of the protrusion. But the variation of azimuth angle is changing from negative to positive when the nanograting is flipped over, in Fig. 9.2.4.10.

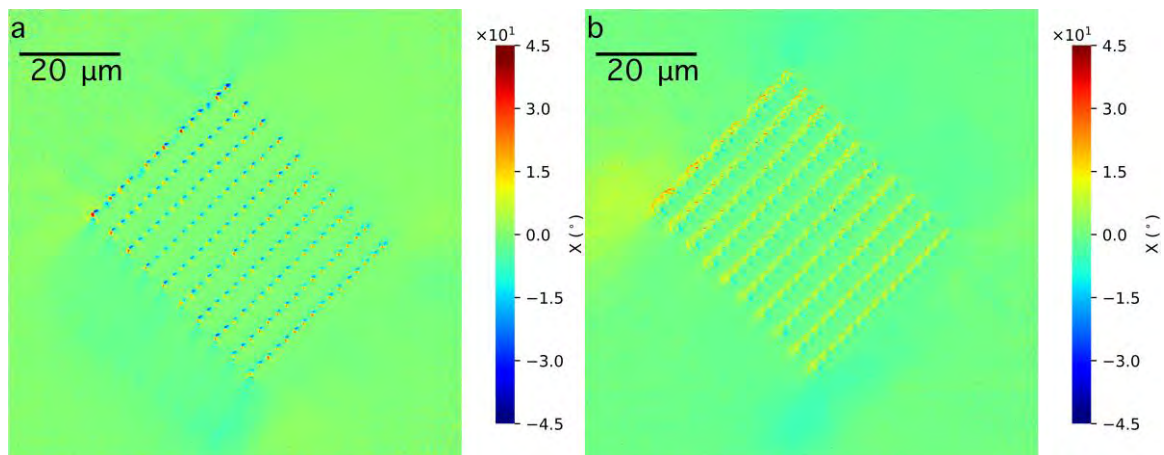


Figure 9.2.4.9 The mapping of χ for the nanograting protrusion facing to (a) the camera, (b) the light source, when $P \perp A$, polarizer sited at 122°

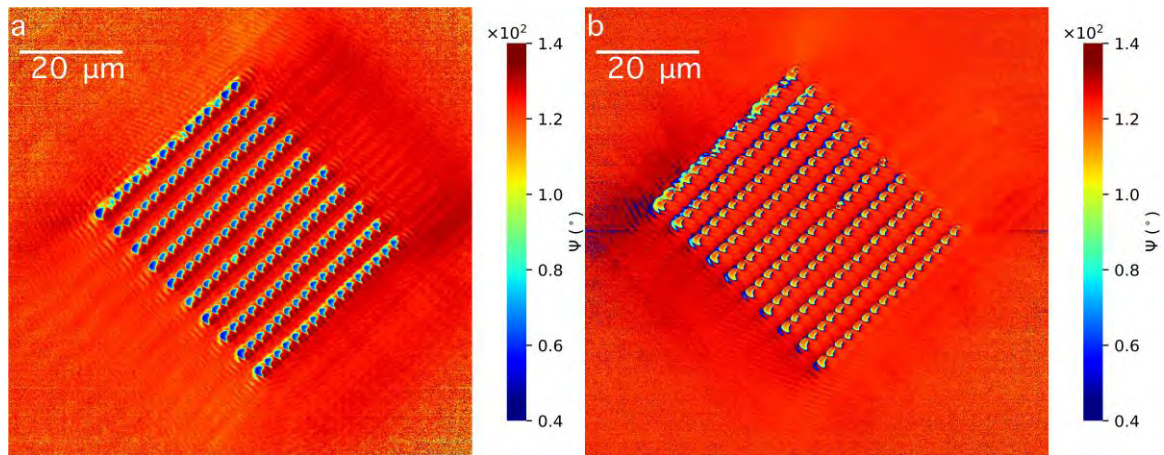


Figure 9.2.4.10 The mapping of ψ for the nanograter protrusion facing to (a) the camera, (b) the light source, when P \perp A, polarizer sited at 122°

In configuration of P \perp A: the protrusion can produce a localized rotation of the azimuth angle of polarization; the elliptical angle is nearly not changed. The rotation of azimuth angle is localized at the position of the protrusion. The variation of elliptical angle is localized at the juncture of the plane of the protrusion and the mainplane of U-shape hole. The image of the semi-major axis (a) of the polarization is swapped with the image of the semi-minor axis (b) when the nanograter is flipped over. The image of $|E_{x1}|$ is not changed with the flip over of the nanograter, but the image of $|E_{y1}|$ is the complementary in two side of the nanograter.

9.2.5 The axis of polarizer parallel to the axis of the nanograter

The intensity is bigger at the position of the U-shape hole, shown in Fig. 9.2.5.1.

Both the protrusion and the U-shape hole can be seen in the image of $|E_{x1}|$ shown in Fig. 9.2.5.2, when the protrusion facing to the light source, while, the image of protrusion is indistinct when the protrusion facing to the camera.

The image of $|E_{y1}|$ shown in Fig. 9.2.5.3 include the information of the protrusion and the U-shape hole when the protrusion is facing the camera; while, the information of the protrusion

is blurred when the protrusion is facing the light source.

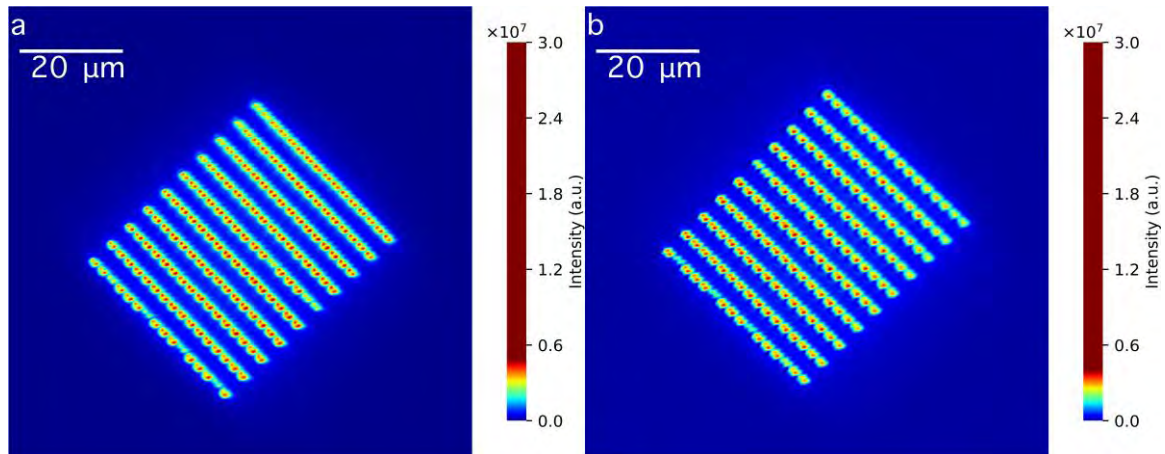


Figure 9.2.5.1 The mapping of I for the nanograting protrusion facing to (a) the camera, (b) the light source, when $P \parallel A$, polarizer sited at 122°

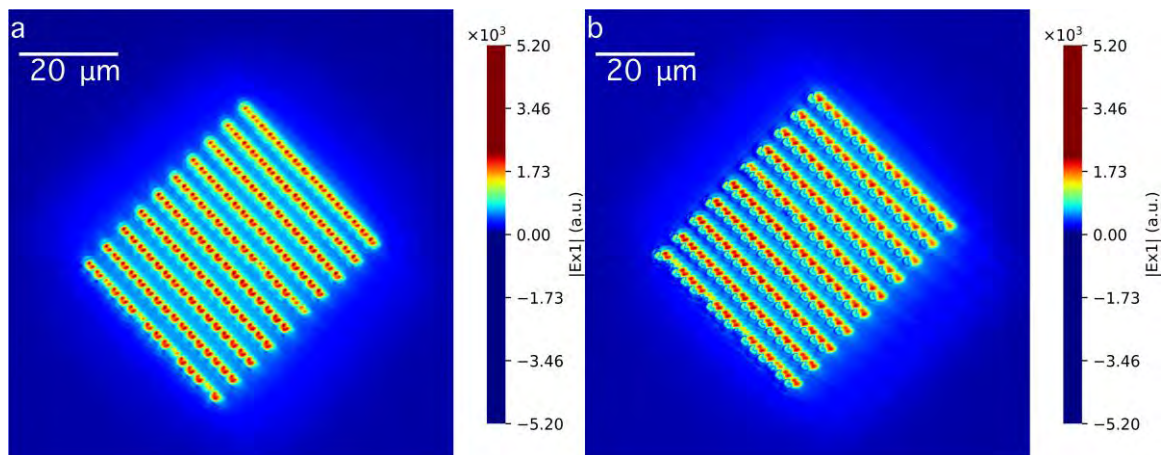


Figure 9.2.5.2 The mapping of $|E_{x1}|$ for the nanograting protrusion facing to (a) the camera, (b) the light source, when $P \parallel A$, polarizer sited at 122°

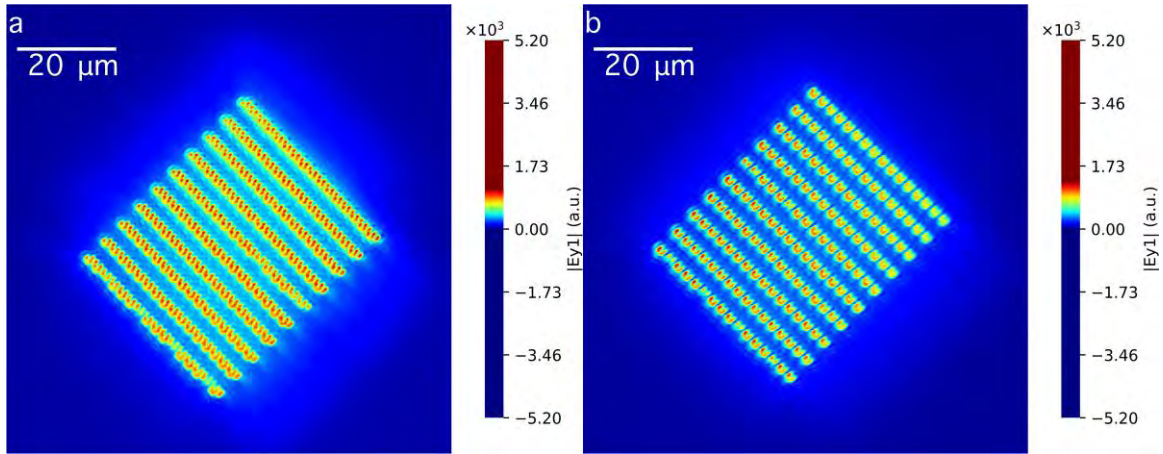


Figure 9.2.5.3 The mapping of $|E_{y1}|$ for the nanograting protrusion facing to (a) the camera, (b) the light source, when $P \parallel A$, polarizer sited at 122°

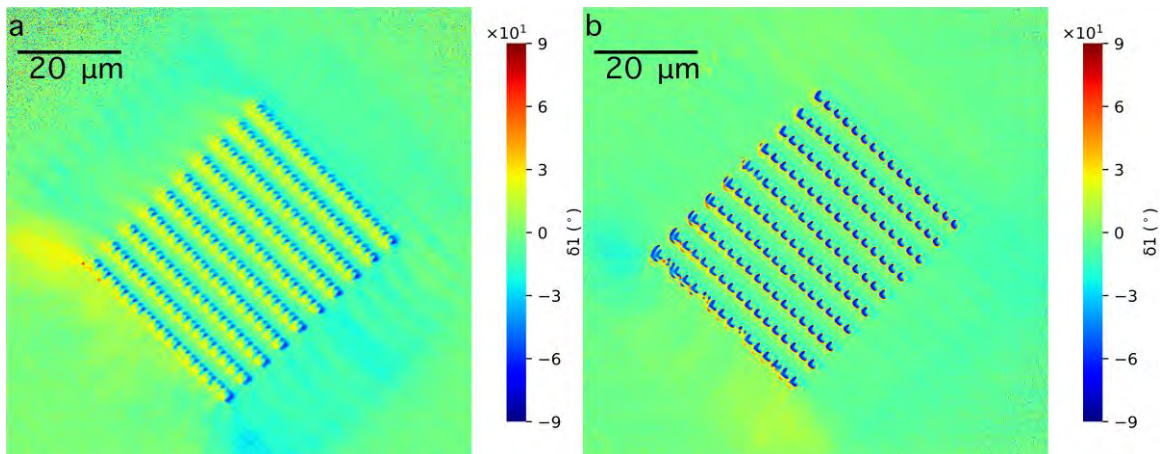


Figure 9.2.5.4 The mapping of $\delta 1$ for the nanograting protrusion facing to (a) the camera, (b) the light source, when $P \parallel A$, polarizer sited at 122°

Both the protrusion and the U-shape hole can be seen in the image of $\delta 1$, shown in Fig. 9.2,5.4, when the protrusion is facing the camera; while, only the U-shape hole can be seen when the protrusion is facing the light source.

Both the protrusion and the U-shape hole is clear in the image of a when the protrusion is facing the light source, shown in Fig.9.2.5.5b; while, the image of protrusion is blurred when the protrusion is facing the camera, shown in Fig.9.2.5.5a. An information behind the plane of nanograting sample can be seen in the image of semi-major axis a. The situation for semi-minor axis b shown in Fig.9.2.5.6 is similar to that of the semi-major axis shown in Fig.

9.2.5.5.

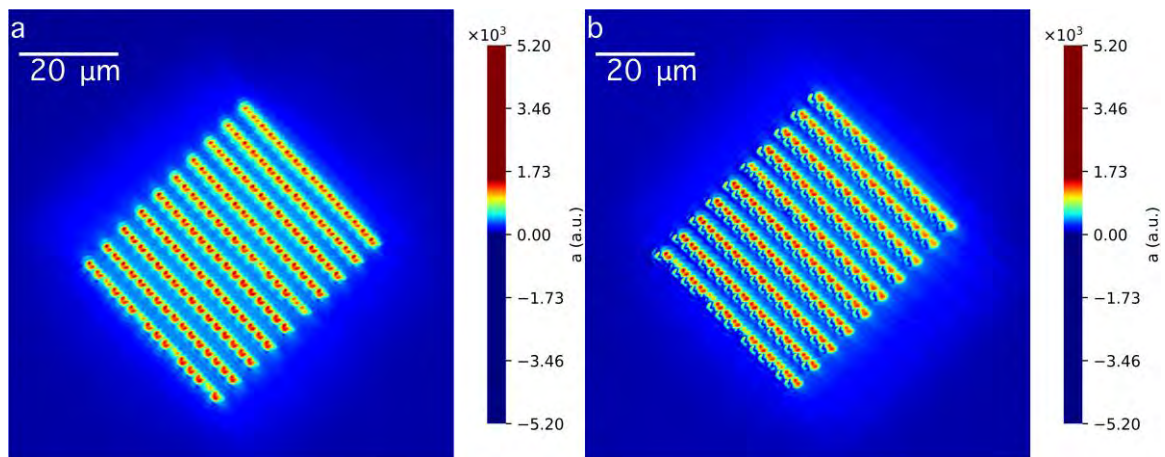


Figure 9.2.5.5 The mapping of semi-major axis of the polarization a for the nanograting protrusion facing to (a) the camera, (b) the light source, when $P \parallel A$, polarizer sited at 122°

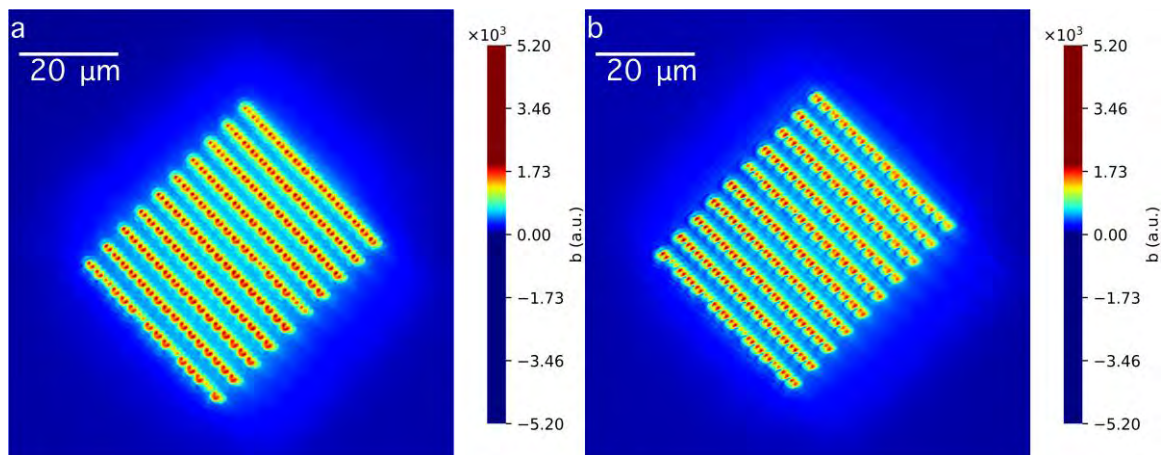


Figure 9.2.5.6 The mapping of semi-minor axis of the polarization b for the nanograting protrusion facing to (a) the camera, (b) the light source, when $P \parallel A$, polarizer sited at 122°

A big depolarization is existed at the position of U-shape hole when the protrusion is facing the camera, shown in Fig.9.2.5.7a. Both the protrusion and the U-shape hole can be seen in the image of depolarization when the protrusion is facing the light source, shown in Fig.9.2.5.5b.

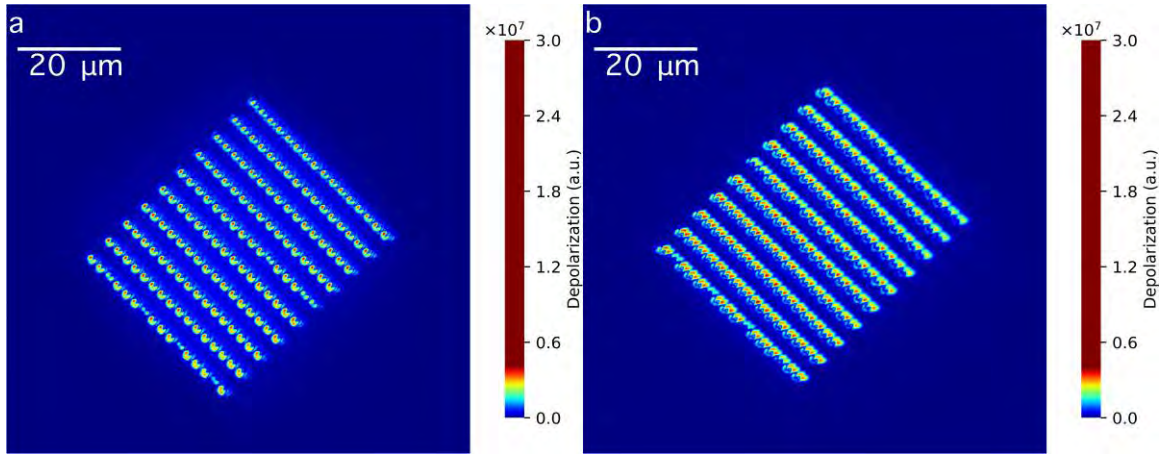


Figure 9.2.5.7 The mapping of I_{DP} for the nanograting protrusion facing to (a) the camera, (b) the light source, when $P \parallel A$, polarizer sited at 122°

The imaginary part of E_y is bigger when the protrusion is facing the camera than that facing the light source, shown in Fig.9.2.5.8.

The elliptical angle varied positively at the U-shape position when the protrusion is facing the camera, shown in Fig.9.2.5.9a; while, that varied negatively at the protrusion when the protrusion is facing the light source, shown in Fig.9.2.5.9b.

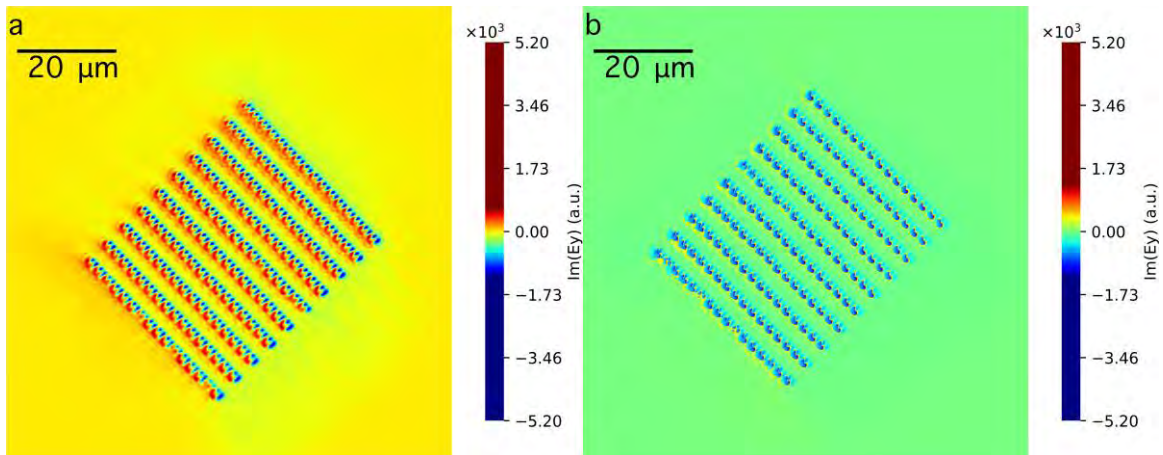


Figure 9.2.5.8 The mapping of $Im(E_y)$ for the nanograting protrusion facing to (a) the camera, (b) the light source, when $P \parallel A$, polarizer sited at 122°

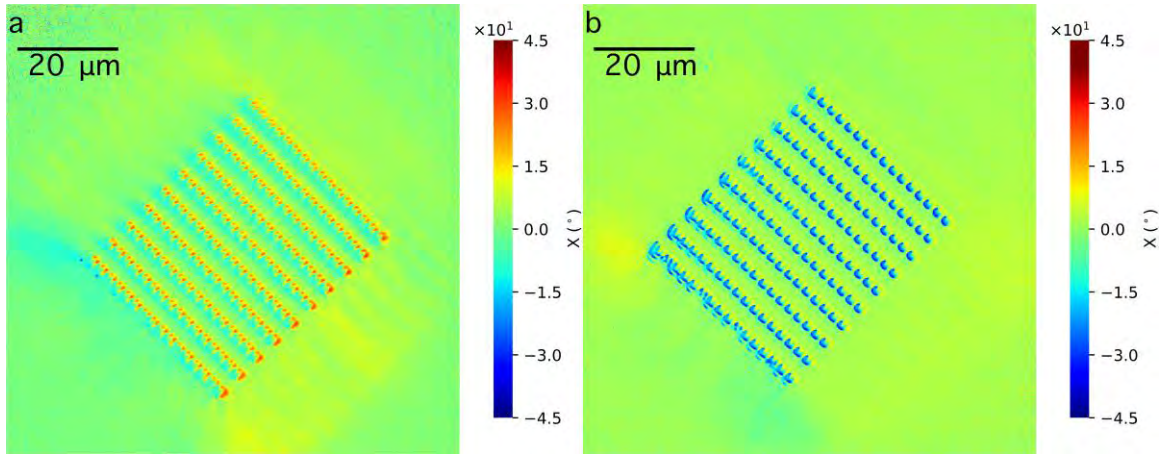


Figure 9.2.5.9 The mapping of χ for the nanograting protrusion facing to (a) the camera, (b) the light source, when $P \parallel A$, polarizer sited at 122°

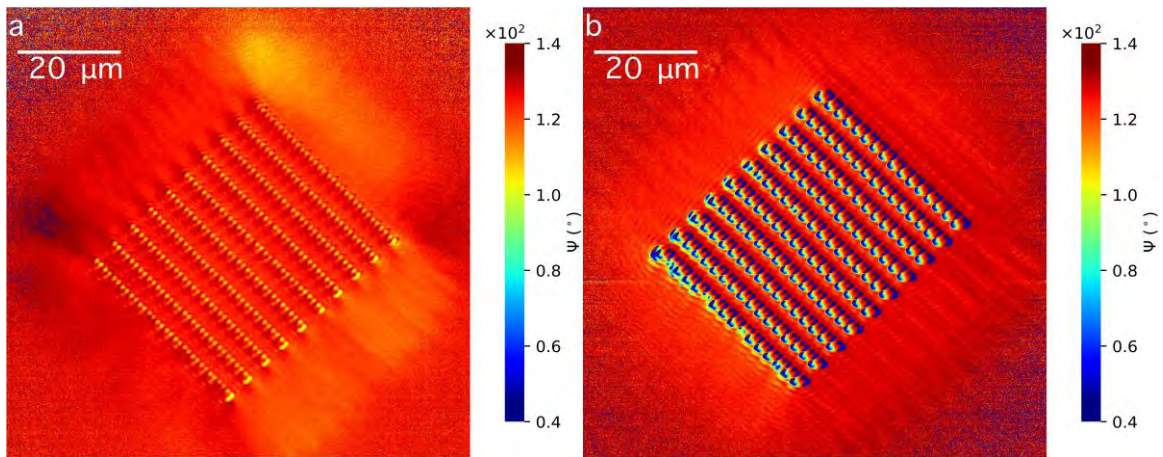


Figure 9.2.5.10 The mapping of ψ for the nanograting protrusion facing to (a) the camera, (b) the light source, when $P \parallel A$, polarizer sited at 122°

The azimuth angle is varied more when the protrusion is facing the light source than that when the protrusion is facing the camera, shown in Fig.9.2.5.10.

Table 9.2.5.1 summarized the pictures listed in section 9.2.4 and 9.2.5. The line in vertical represents the U-shape hole on nanograting. The line in horizontal represents the protrusion. The dash line ‘...’ represents that it can’t be seen in the relevant image. The solid line ‘—’ represents that it can be seen in the relevant image.

Table 9.2.5.1 The table of showing the visible part and the invisible part in the image of Physical quantity (‘|’ represent the U-shape hole; ‘—’ represent the protrusion)

Physical quantity	Configuration $P \perp A$		Configuration $P \parallel A$	
	Camera	Light source	Camera	Light source
$ E_{y1} $				
$ E_{x1} $				
δ_1				
a				
b				
dP				
$Im(E_y)$				
χ				
ψ				

To sum up, the characteristic of protrusion and the U-shape hole under four configurations are summarized in table 9.2.5.1.

9.2.6 The influence of the angle of the protrusion to the polarization patterns

To research the effect of the angle of the protrusion of the nanograter to the polarization adjustment, different protrusion angle samples are measured. The SEM images are shown in Figure 9.2.6.1. The information of the samples is listed in table 9.2.6.1. The polarization azimuth angle sited at 122° and sample stage sited in 148° . The configuration between the axis of polarizer and the symmetric axis of the nanograter is $P \parallel A$.

Table 9.2.6.1 The name of the samples and the relevant angles

Sample number	4	12	22	29	31	32	33
Protrusion angle	No	90	120	45	0	30	100
Protrusion angle	--	80	116.3	40	5.6	27.2	90
Figure name	g	d	f	c	a	b	E

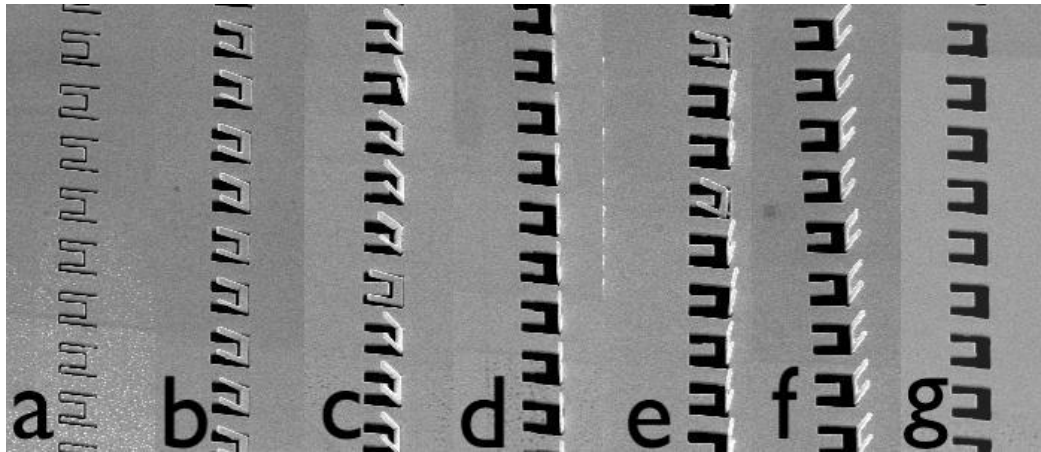


Figure 9.2.6.1 The SEM image of the U-shape nanograter with different angles.

The protrusion angle reference to the published paper (Liu et al., 2016). The angle of protrusion influences the intensity of the image in Fig.9.2.6.2.

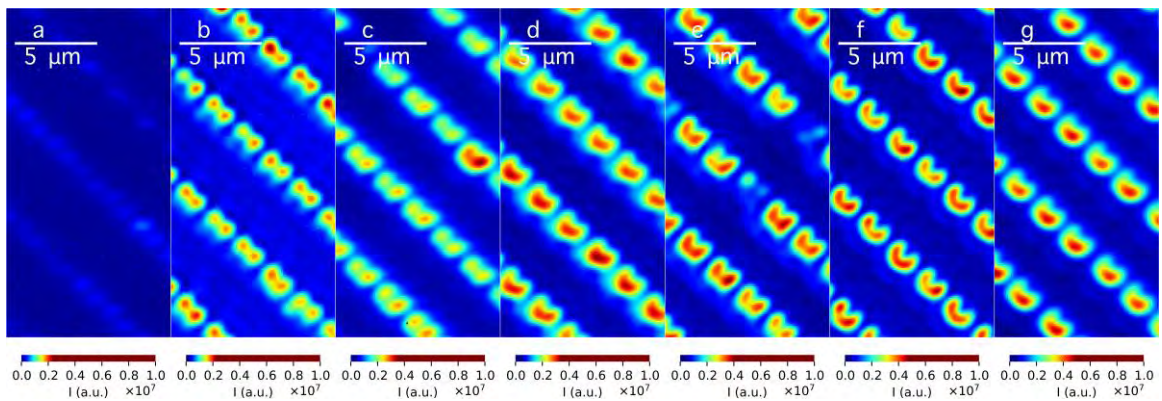


Figure 9.2.6.2 The mapping of I for the nanograter that protrusion in different angles: (a) 5.6° , (b) 27.2° , (c) 40° , (d) 80° , (e) 90° , (f) 116.3° , (g) no protrusions, when $P \parallel A$, polarizer sited at 122° and sample stage sited in 148° .

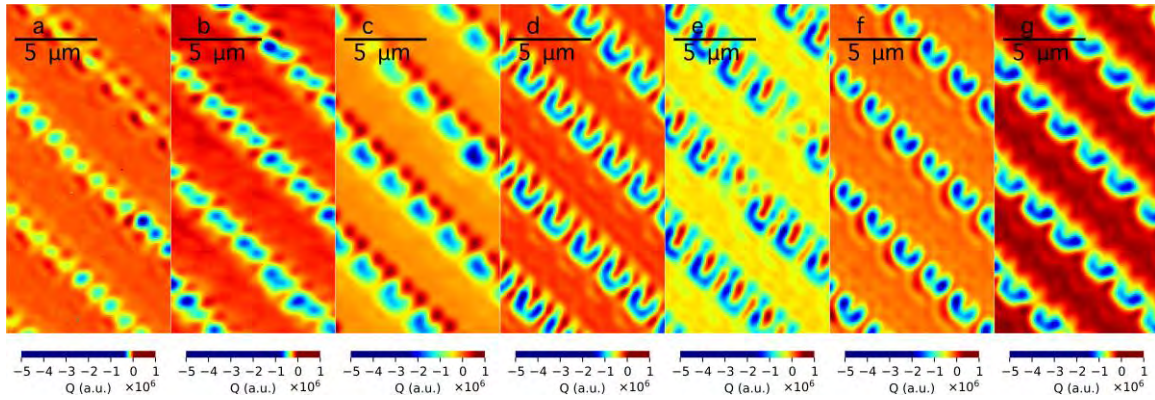


Figure 9.2.6.3 The mapping of Q for the nanograting that protrusion in different angles: (a) 5.6° , (b) 27.2° , (c) 40° , (d) 80° , (e) 90° , (f) 116.3° , (g) no protrusions, when $P \parallel A$, polarizer sited at 122° and sample stage sited in 148° .

The image of Q varied with the angle of protrusions, shown in Fig. 9.2.6.3. It is same to that of U and V , shown in Fig.9.2.6.4 and Fig. 9.2.6.5 respectively.

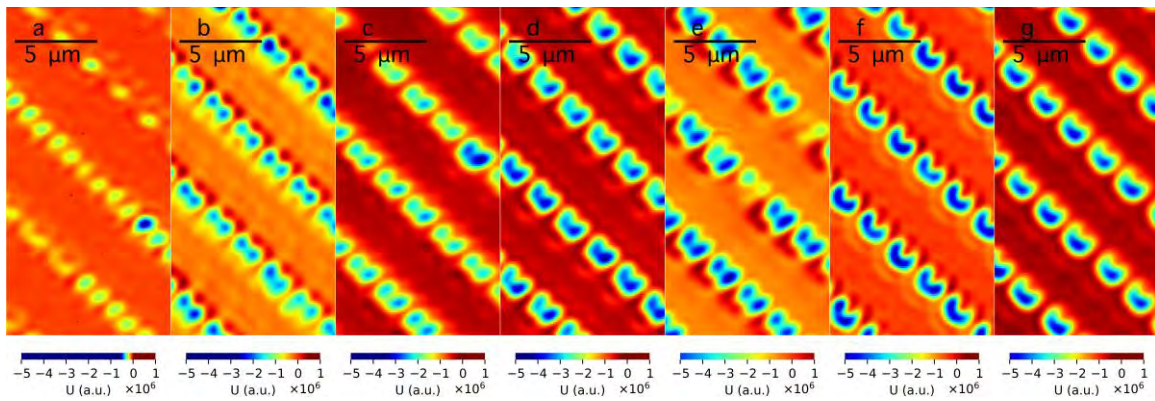


Figure 9.2.6.4 The mapping of U for the nanograting that protrusion in different angles: (a) 5.6° , (b) 27.2° , (c) 40° , (d) 80° , (e) 90° , (f) 116.3° , (g) no protrusions, when $P \parallel A$, polarizer sited at 122° and sample stage sited in 148° .

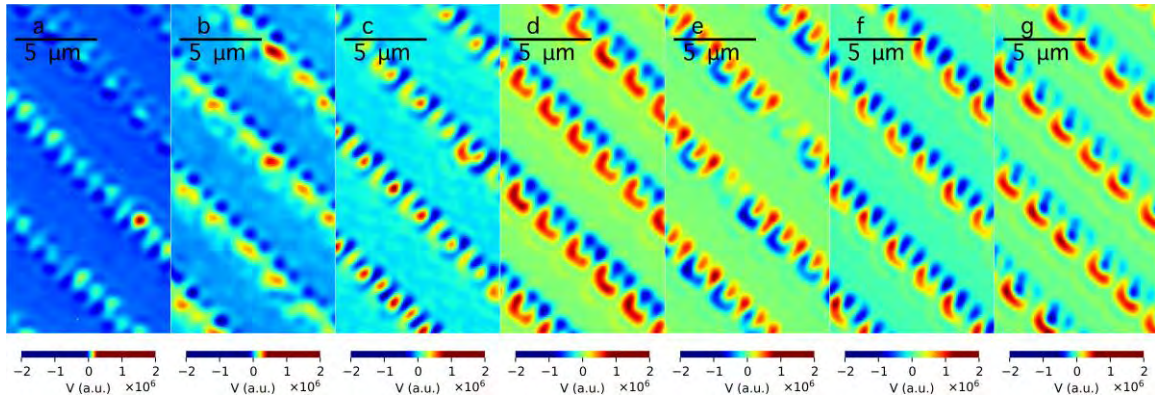


Figure 9.2.6.5 The mapping of V for the nanograting that protrusion in different angles: (a) 5.6° , (b) 27.2° , (c) 40° , (d) 80° , (e) 90° , (f) 116.3° , (g) no protrusions, when $P \parallel A$, polarizer sited at 122° and sample stage sited in 148° .

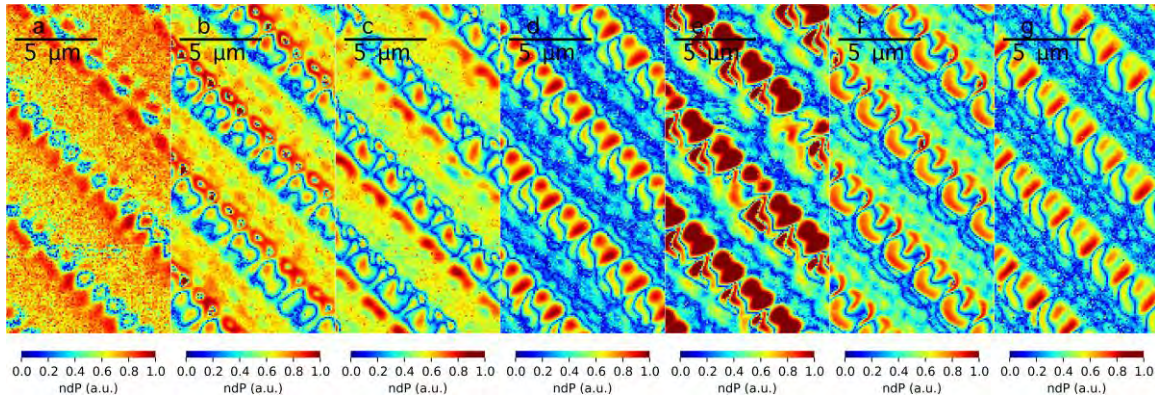


Figure 9.2.6.6 The mapping of dP/I for the nanograting that protrusion in different angles: (a) 5.6° , (b) 27.2° , (c) 40° , (d) 80° , (e) 90° , (f) 116.3° , (g) no protrusions, when $P \parallel A$, polarizer sited at 122° and sample stage sited in 148° .

Only the image e in Fig.9.2.6.6 is different with the others with a maximum depolarization at the position of the nanograting, which angle is 90° . The P_1 , P_2 , V/I also varied with the angles, shown in Fig. 9.2.6.7, Fig. 9.2.6.8, and Fig. 9.2.6.9.

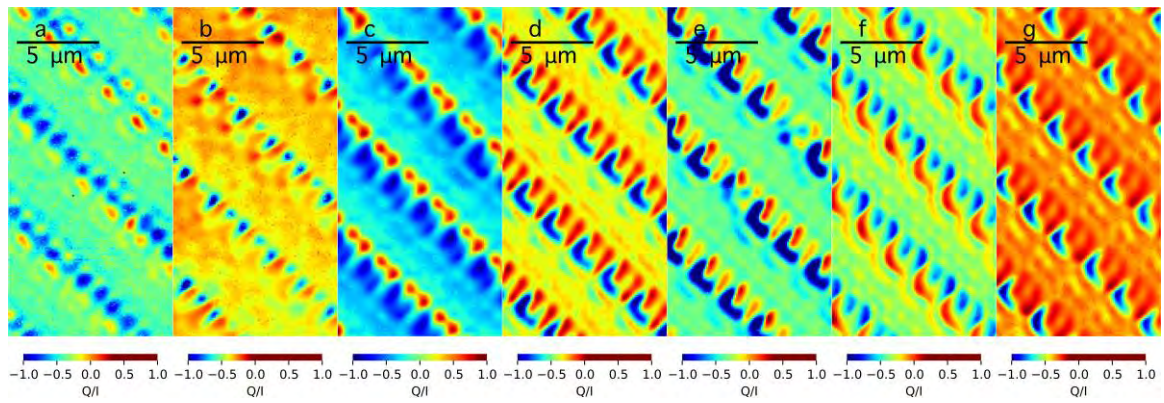


Figure 9.2.6.7 The mapping of Q/I for the nanograting that protrusion in different angles: (a) 5.6° , (b) 27.2° , (c) 40° , (d) 80° , (e) 90° , (f) 116.3° , (g) no protrusions, when $P \parallel A$, polarizer sited at 122° and sample stage sited in 148° .

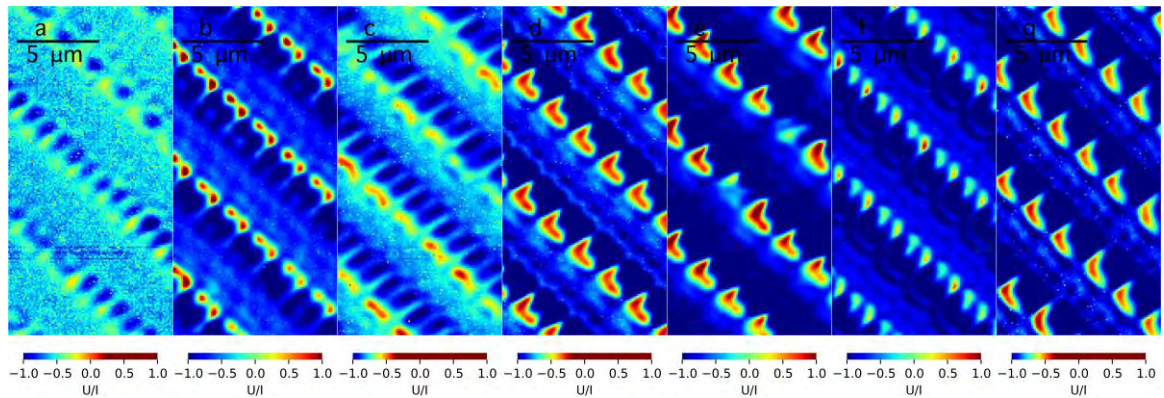


Figure 9.2.6.8 The mapping of U/I for the nanograting that protrusion in different angles: (a) 5.6° , (b) 27.2° , (c) 40° , (d) 80° , (e) 90° , (f) 116.3° , (g) no protrusions, when $P \parallel A$, polarizer sited at 122° and sample stage sited in 148° .

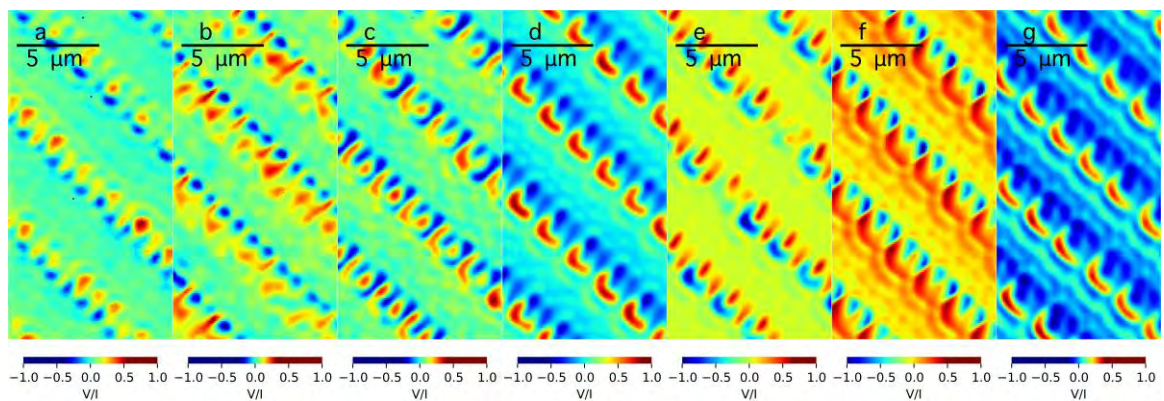


Figure 9.2.6.9 The mapping of V/I for the nanograting that protrusion in different angles: (a) 5.6° , (b) 27.2° , (c) 40° , (d) 80° , (e) 90° , (f) 116.3° , (g) no protrusions, when $P \parallel A$, polarizer sited at 122° and sample stage sited in 148° .

The elliptical angle χ varied with the protrusion angles too, shown in Fig. 9.2.6.10. The

variation of ψ is shown in Fig. 9.2.6.11.

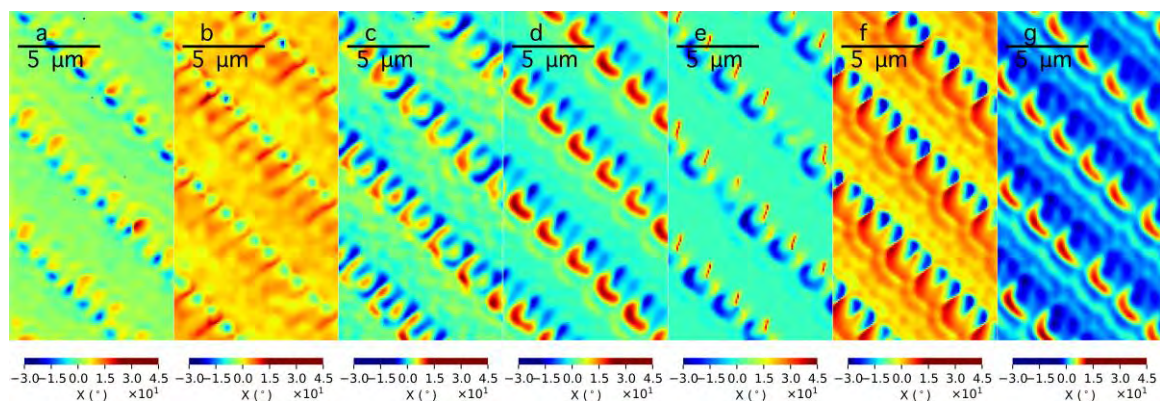


Figure 9.2.6.10 The mapping of χ for the nanograting that protrusion in different angles: (a) 5.6° , (b) 27.2° , (c) 40° , (d) 80° , (e) 90° , (f) 116.3° , (g) no protrusions, when $P \parallel A$, polarizer sited at 122° and sample stage sited in 148° .

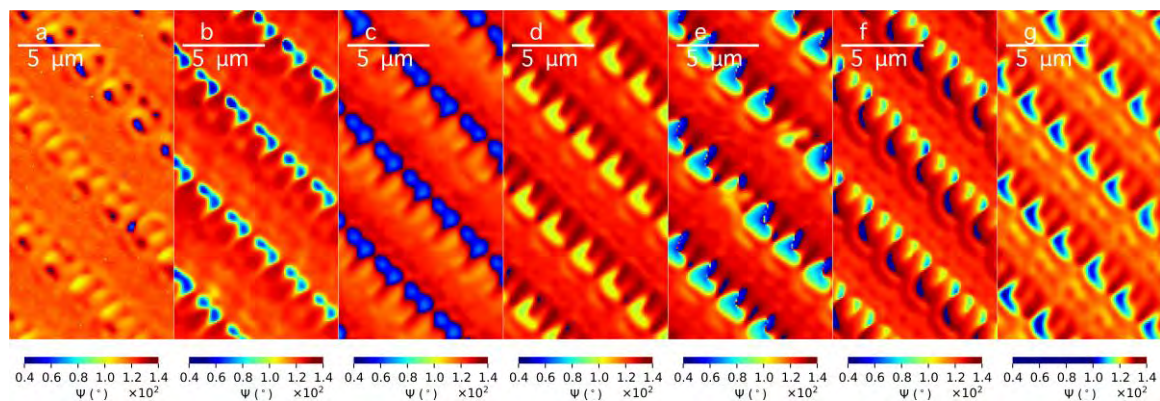


Figure 9.2.6.11 The mapping of ψ for the nanograting that protrusion in different angles: (a) 5.6° , (b) 27.2° , (c) 40° , (d) 80° , (e) 90° , (f) 116.3° , (g) no protrusions, when $P \parallel A$, polarizer sited at 122° and sample stage sited in 148° .

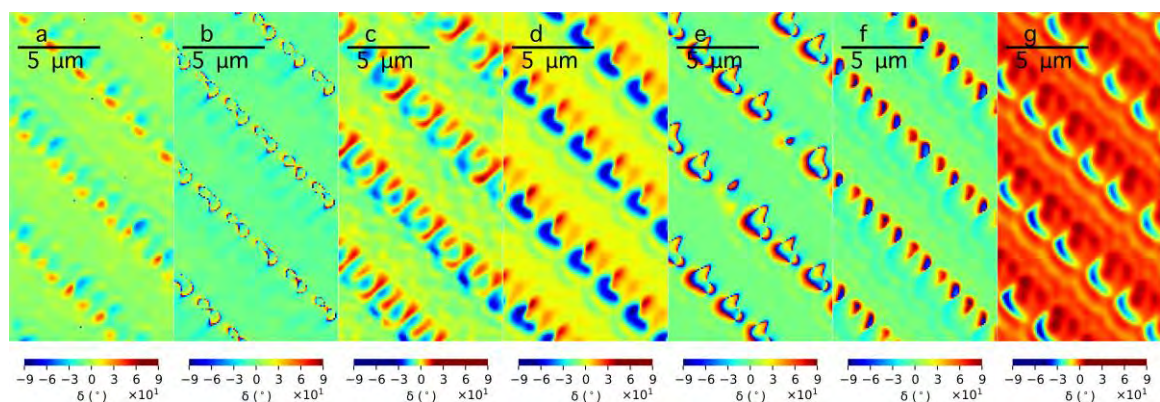


Figure 9.2.6.12 The mapping of δ for the nanograting that protrusion in different angles: (a) 5.6° , (b) 27.2° , (c) 40° , (d) 80° , (e) 90° , (f) 116.3° , (g) no protrusions, when $P \parallel A$, polarizer

sited at 122° and sample stage sited in 148° .

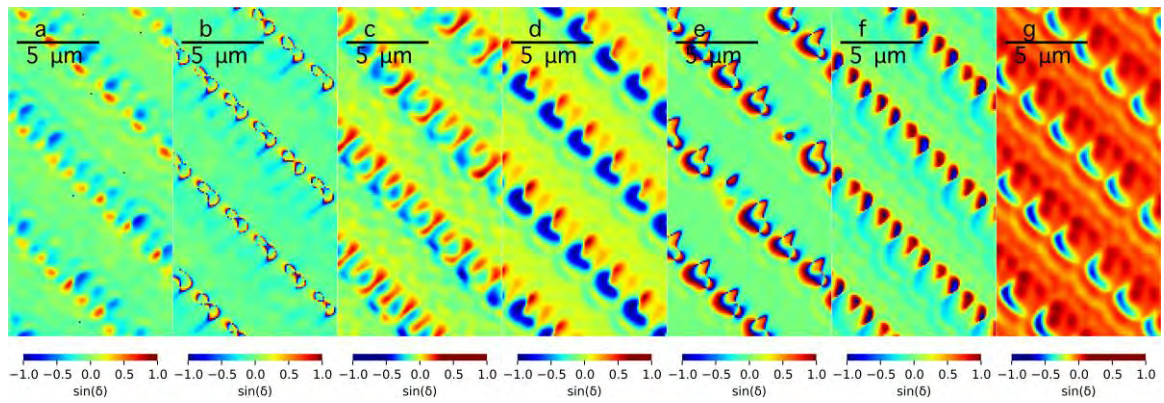


Figure 9.2.6.13 The mapping of $\sin\delta$ for the nanograting that protrusion in different angles: (a) 5.6° , (b) 27.2° , (c) 40° , (d) 80° , (e) 90° , (f) 116.3° , (g) no protrusions, when $P\parallel A$, polarizer sited at 122° and sample stage sited in 148° .

The variation of δ and $\sin\delta$ are shown in Fig. 9.2.6.13 and Fig.9.2.6.13, respectively.

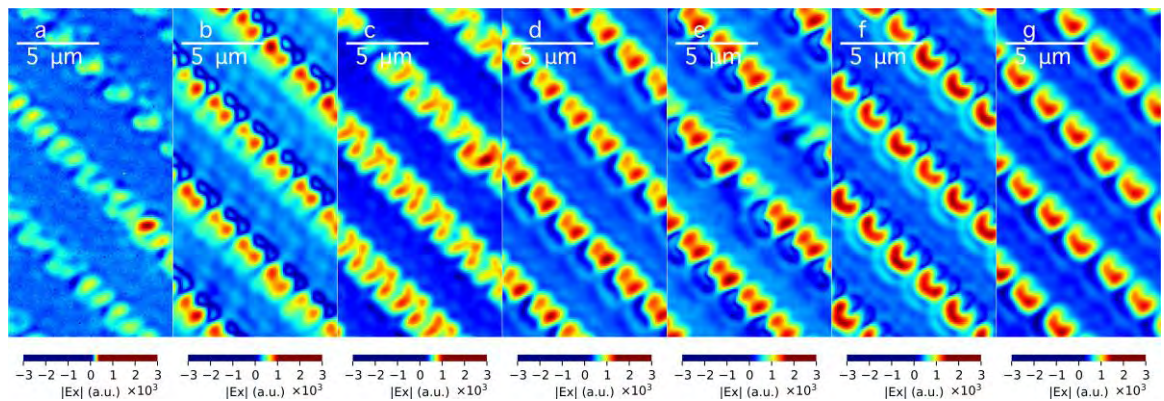


Figure 9.2.6.14 The mapping of $|E_x|$ for the nanograting that protrusion in different angles: (a) 5.6° , (b) 27.2° , (c) 40° , (d) 80° , (e) 90° , (f) 116.3° , (g) no protrusions, when $P\parallel A$, polarizer sited at 122° and sample stage sited in 148° .

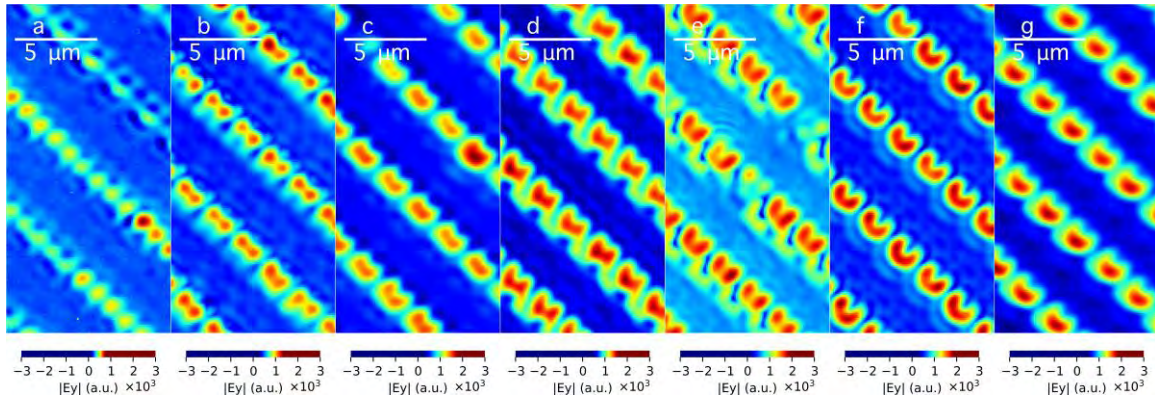


Figure 9.2.6.15 The mapping of $|E_y|$ for the nanograting that protrusion in different angles: (a) 5.6° , (b) 27.2° , (c) 40° , (d) 80° , (e) 90° , (f) 116.3° , (g) no protrusions, when $P \parallel A$, polarizer sited at 122° and sample stage sited in 148° .

The image of $|E_x|$ and $|E_y|$ are shown in Fig. 9.2.6.14 and Fig.9.2.6.15, respectively.

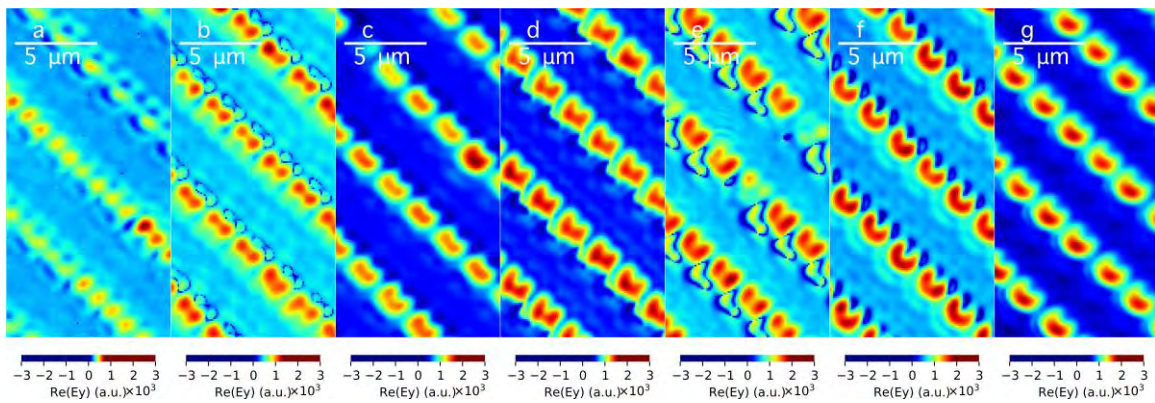


Figure 9.2.6.16 The mapping of $Re(E_y)$ for the nanograting that protrusion in different angles: (a) 5.6° , (b) 27.2° , (c) 40° , (d) 80° , (e) 90° , (f) 116.3° , (g) no protrusions, when $P \parallel A$, polarizer sited at 122° and sample stage sited in 148° .

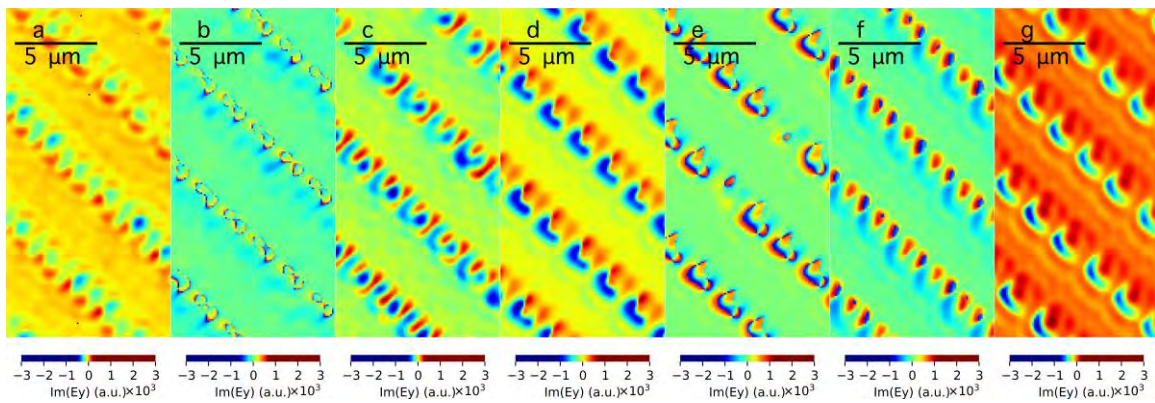


Figure 9.2.6.17 The mapping of $Im(E_y)$ for the nanograting that protrusion in different angles:

(a) 5.6° , (b) 27.2° , (c) 40° , (d) 80° , (e) 90° , (f) 116.3° , (g) no protrusions, when $P \parallel A$, polarizer sited at 122° and sample stage sited in 148° .

The real part and the imaginary part of E_y is shown in Fig. 9.2.6.16 and Fig. 9.2.6.17.

respectively. The spot in Fig. 9.2.6.16e is from the scattering light in the system, but it does

not exist in Fig. 9.2.6.17e. The mapping of $|E_{x1}|$ and $|E_{y1}|$ are shown in Fig.9.2.6.18 and

Fig.9.2.6.19. The image of $|E_{y1}|$ is similar to that of the Q shown in Fig. 9.2.6.19. The image

of δ_1 in Fig. 9.2.6.20 is similar to that of the $Im(E_y)$ in Fig.9.2.6.17, but the signal of $Im(E_y)$

is stronger.

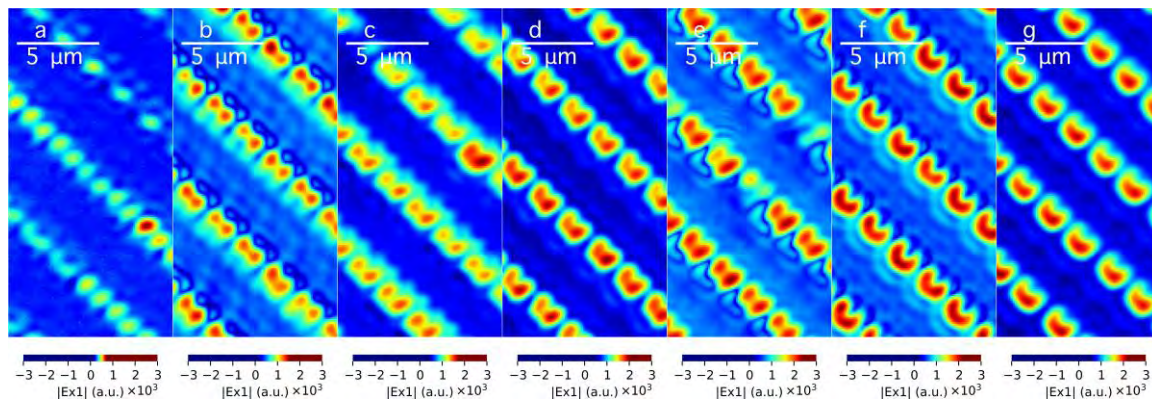


Figure 9.2.6.18 The mapping of $|E_{x1}|$ for the nanograting that protrusion in different angles: (a) 5.6° , (b) 27.2° , (c) 40° , (d) 80° , (e) 90° , (f) 116.3° , (g) no protrusions, when $P \parallel A$, polarizer sited at 122° and sample stage sited in 148° .

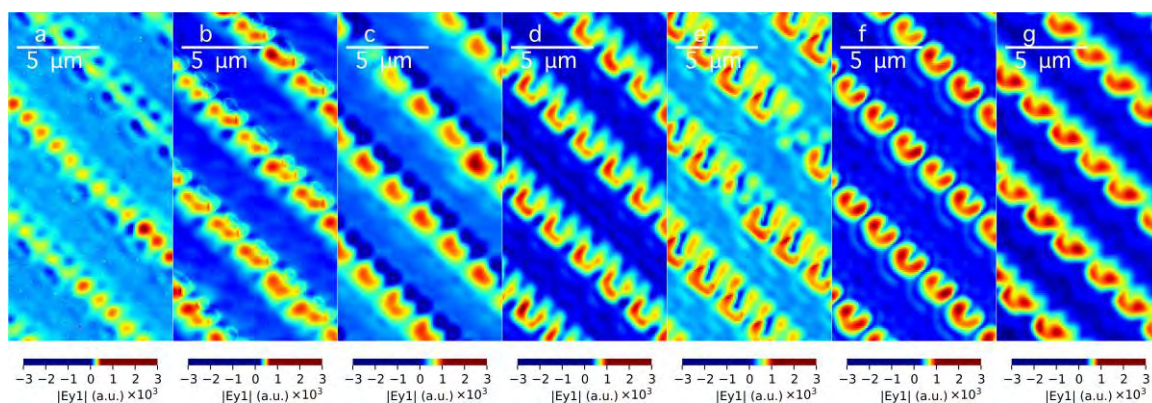


Figure 9.2.6.19 The mapping of $|E_{y1}|$ for the nanograting that protrusion in different angles: (a) 5.6° , (b) 27.2° , (c) 40° , (d) 80° , (e) 90° , (f) 116.3° , (g) no protrusions, when $P \parallel A$, polarizer sited at 122° and sample stage sited in 148° .

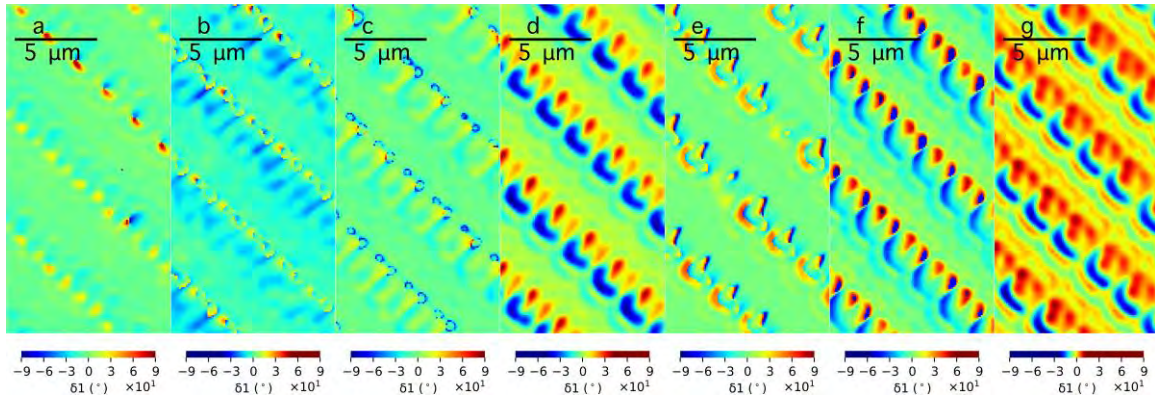


Figure 9.2.6.20 The mapping of δ_1 for the nanograting that protrusion in different angles: (a) 5.6° , (b) 27.2° , (c) 40° , (d) 80° , (e) 90° , (f) 116.3° , (g) no protrusions, when $P \parallel A$, polarizer sited at 122° and sample stage sited in 148° .

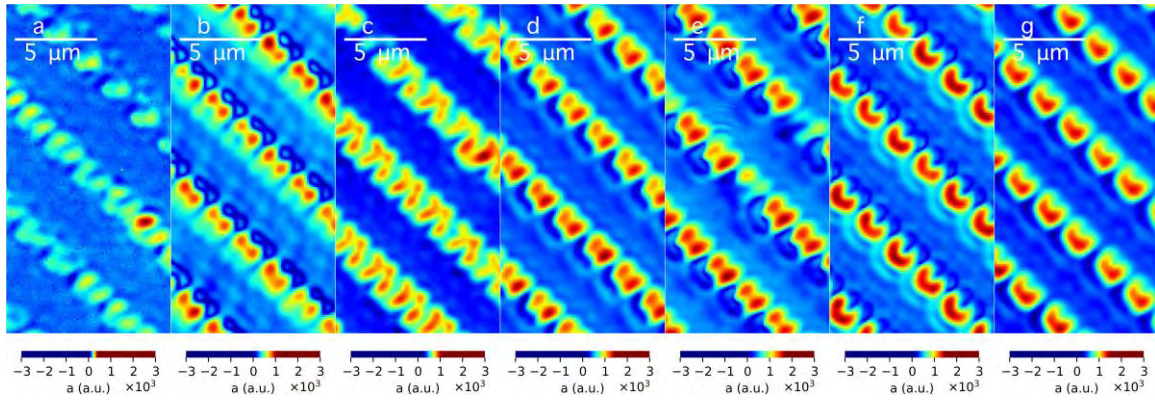


Figure 9.2.6.21 The mapping of a for the nanograting that protrusion in different angles: (a) 5.6° , (b) 27.2° , (c) 40° , (d) 80° , (e) 90° , (f) 116.3° , (g) no protrusions, when $P \parallel A$, polarizer sited at 122° and sample stage sited in 148° .

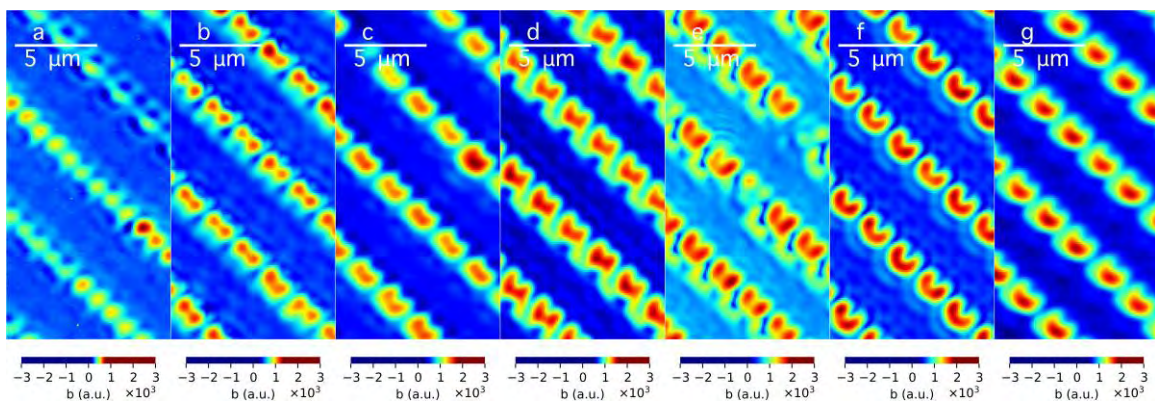


Figure 9.2.6.22 The mapping of b for the nanograting that protrusion in different angles: (a) 5.6° , (b) 27.2° , (c) 40° , (d) 80° , (e) 90° , (f) 116.3° , (g) no protrusions, when $P \parallel A$, polarizer sited at 122° and sample stage sited in 148° .

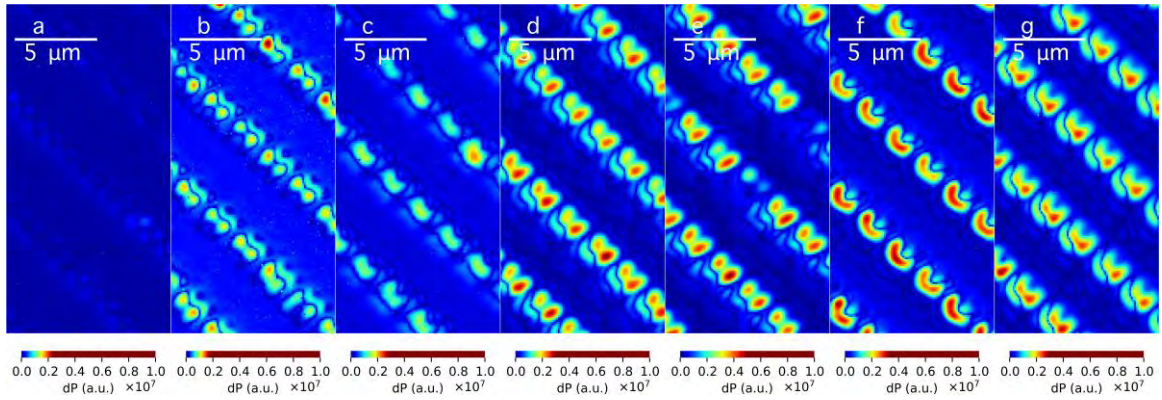


Figure 9.2.6.23 The mapping of dP for the nanograting that protrusion in different angles: (a) 5.6° , (b) 27.2° , (c) 40° , (d) 80° , (e) 90° , (f) 116.3° , (g) no protrusions, when $P \parallel A$, polarizer sited at 122° and sample stage sited in 148° .

The image of semi-major axis a , semi-minor axis b , and I_{dP} are shown in Fig. 9.2.6.21, Fig.9.2.6.22, and Fig. 9.2.6.23, respectively.

In conclusion, the angle of the protrusion influences the patterns of the polarization image.

All the image is shown in this section. The 90° can produce biggest depolarization in the configuration of $P \parallel A$. The signal of $Im(E_y)$ is similar to that of the δ , $\sin\delta$ and δ^1 . The Q is similar to that of the $|E_{y1}|$.

9.2.7 Other types of nanograting

Despite the U-shape nanograting, there are other type of the nanograting, I list the typical of them in this section.

9.2.7.1 Rectangle shape

Without a U-shape protrusion, just a rectangle protrusion sits beside a rectangle hole or not,

The SEM image is shown in Fig. 9.2.7.1.

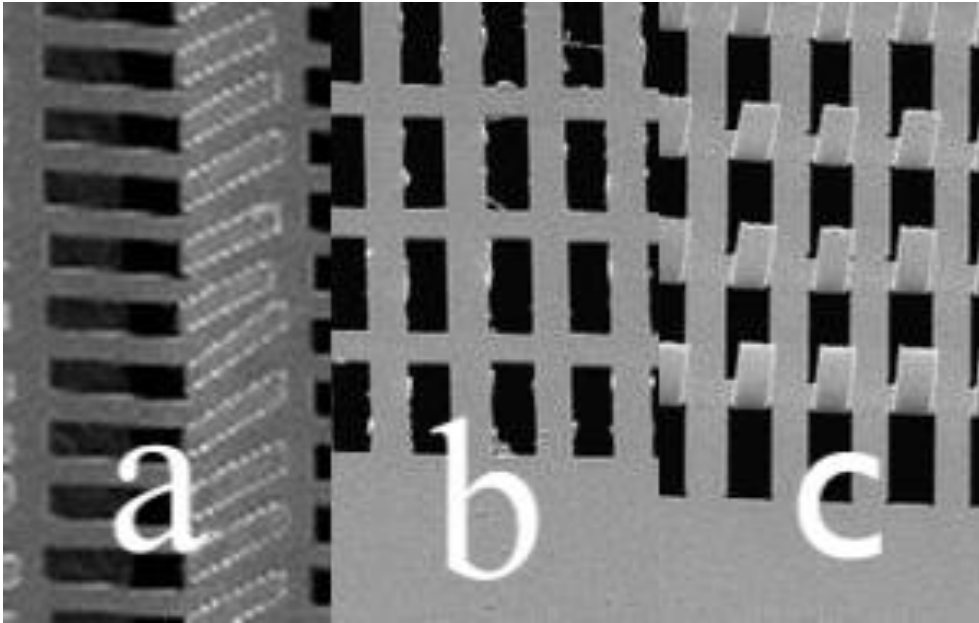


Figure 9.2.7.1 SEM image of rectangle nanograting: (a) sample: 20, (b) sample 34, (c) sample 36

Without a protrusion, the image is significantly different from that of with a protrusion, shown in Fig.9.2.7.2. The δ_1 is divided into positive and negative in a protrusion exist structure, shown in Fig.9.2.7.4a and Fig. 9.2.7.4c. A big variation on δ_1 existed when the protrusion is removed, shown in Fig. 9.2.7.4b. The pattern of $|E_{x1}|$ and $|E_{y1}|$ of sample 20 and sample 34 are coincident, while, that of sample 36 is complementary, shown in Fig. 9.2.7.2 and Fig. 9.2.7.3. All the image of δ_1 in Fig.9.2.7.4 is complementary with the image of $|E_{y1}|$ in Fig. 9.2.7.3.

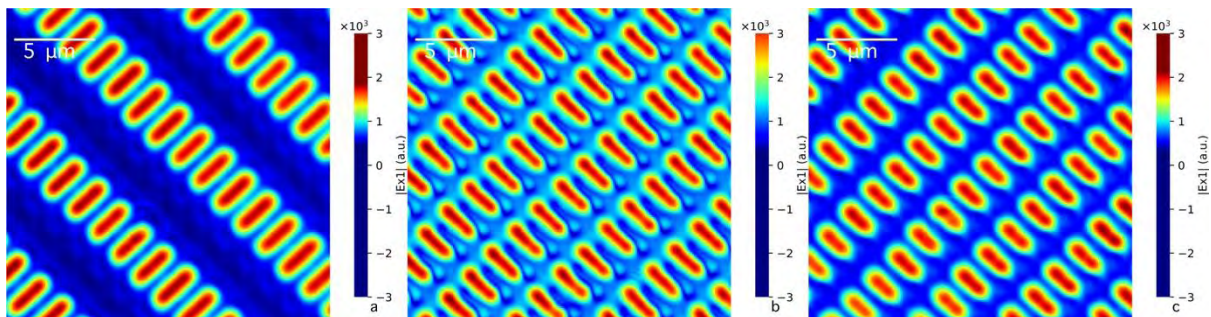


Figure 9.2.7.2 The mapping of $|E_{x1}|$ for the nanograting that protrusion in different direction, when the polarization azimuth angle sited at 122° and sample stage sited in 148° : (a) sample 20, protrusion along the azimuth angle of polarization ($P \parallel A$); (b) sample 34, no protrusion;

(c) sample36, protrusion perpendicular to the azimuth angle of polarization ($P \perp A$)

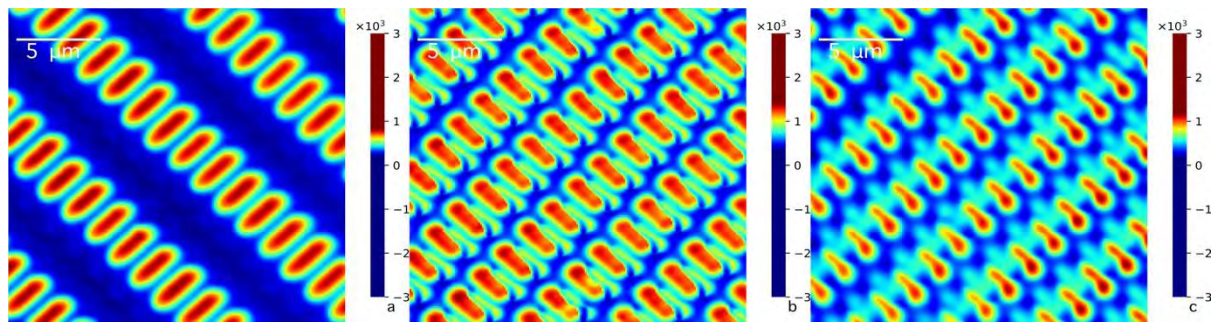


Figure 9.2.7.3 The mapping of $|E_{y1}|$ for the nanograter that protrusion in different direction, when the polarization azimuth angle sited at 122° and sample stage sited in 148° : (a) sample 20, $P \parallel A$; (b) sample 34, no protrusion; (c) sample36, $P \perp A$

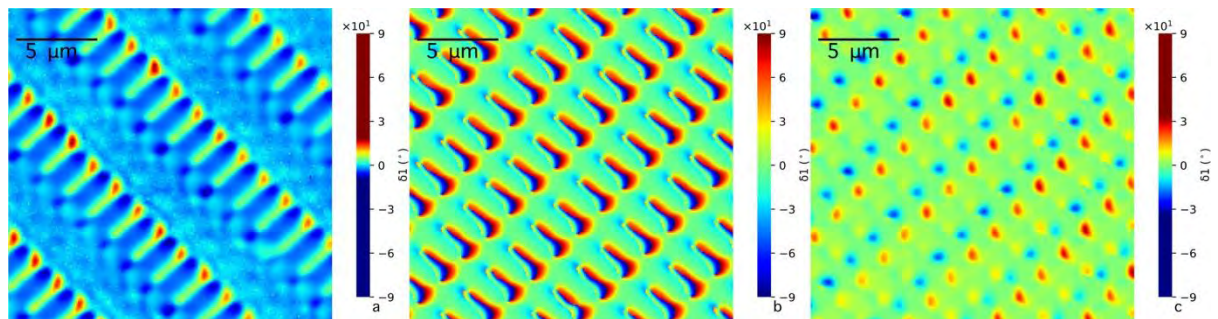


Figure 9.2.7.4 The mapping of δ_1 for the nanograter that protrusion in different direction, when the polarization azimuth angle sited at 122° and sample stage sited in 148° : (a) sample 20, $P \parallel A$; (b) sample 34, no protrusion; (c) sample36, protrusion perpendicular to the azimuth angle of polarization $P \perp A$

9.2.7.2 Square shape

A square shape structure hole and U-shape protrusion structure typical structure is listed in this section, which SEM image is shown in Fig.9.2.7.5. The protrusion is on the left and on the right on sample 26.

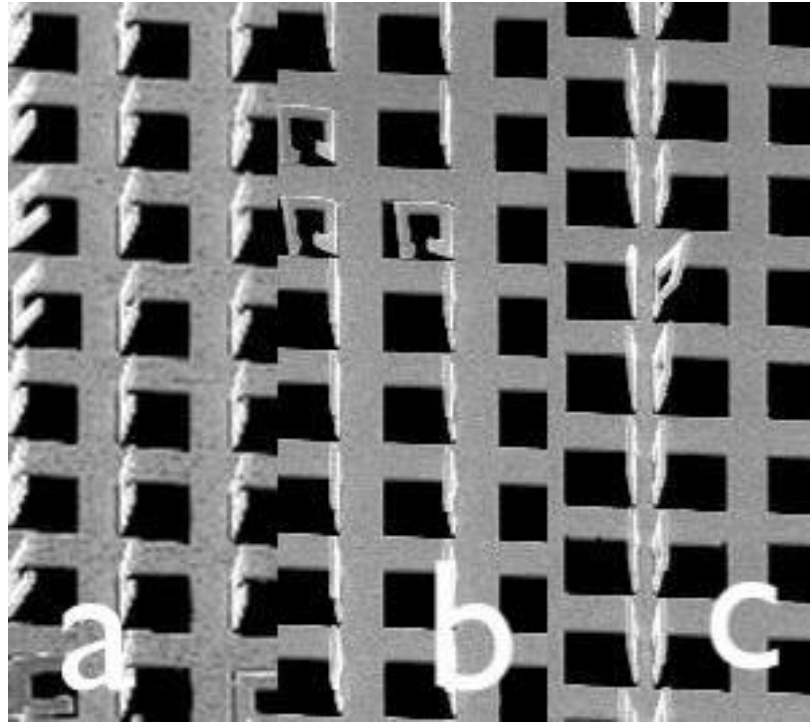


Figure 9.2.7.5 SEM image of (a) sample 24, (b) 25 and (c) 26

The image of $|E_{x1}|$ and $|E_{y1}|$ are coincidence in the three samples 24, 25 and 26 shown in Fig.9.2.7.6 and Fig.9.2.6.7. Sample 26 produce big variation on δ_1 shown in Fig. 9.2.6.8. The image of $|E_{y1}|$ and δ_1 are complementary on sample 24 and 25 in Fig. 9.2.7.7 and Fig. 9.2.7.8, while that on sample 26 is coincidence in range but the shape changed a little.

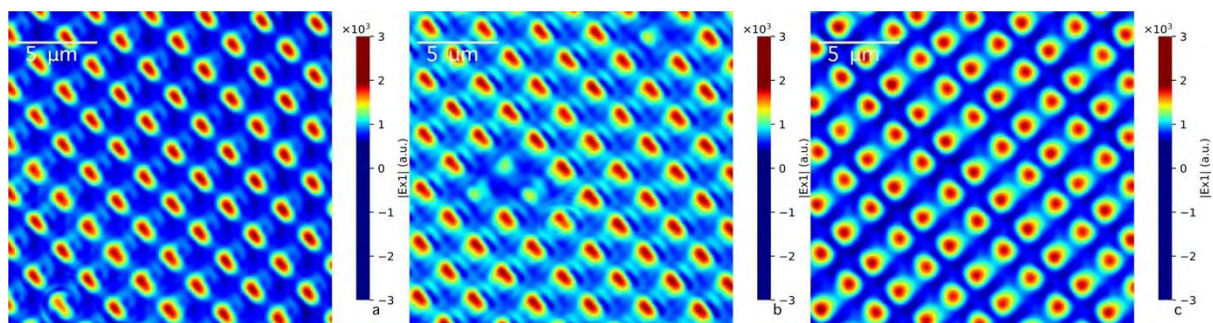


Figure 9.2.7.6 The mapping of $|E_{x1}|$ for the square-nanograting that protrusion in different angles, when the polarization azimuth angle sited at 122 and sample stage sited in 148 , sample number: (a) 24, (b) 25, c) 26

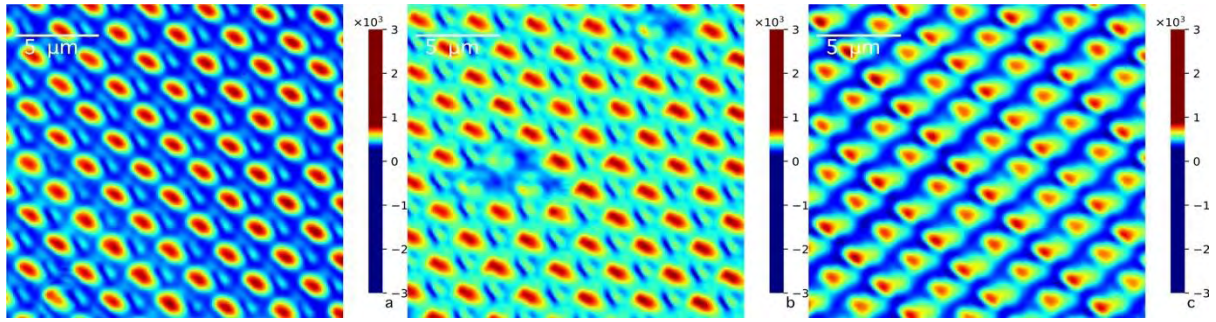


Figure 9.2.7.7 The mapping of $|E_{y1}|$ for the square-nanograter that protrusion in different angles, when the polarization azimuth angle sited at 122° and sample stage sited in 148° , sample number: (a) 24, (b) 25, (c) 26

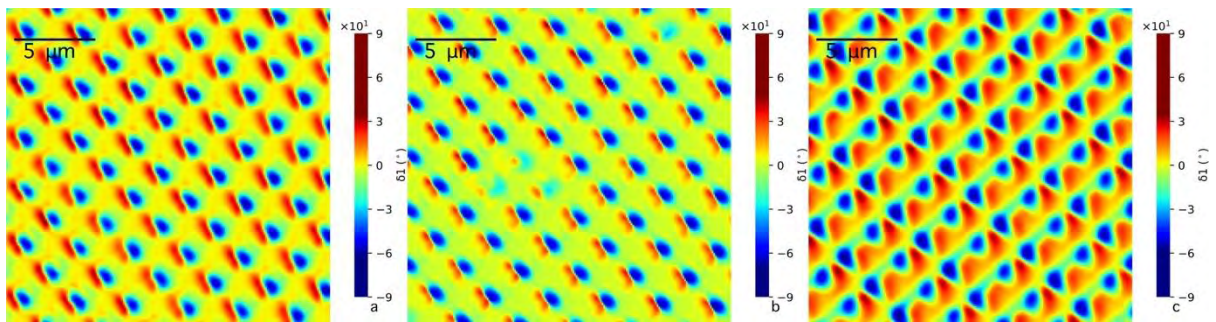


Figure 9.2.7.8 The mapping of δ_1 for the square-nanograter that protrusion in different angles, when the polarization azimuth angle sited at 122° and sample stage sited in 148° , sample number: (a) 24, (b) 25, (c) 26

9.2.7.3 Flower shape

This set of samples compare the influence of the shape of the protrusion, because the shape of the hole is the same, a square hole quaternity (flower shape), shown in Fig. 9.2.7.9.

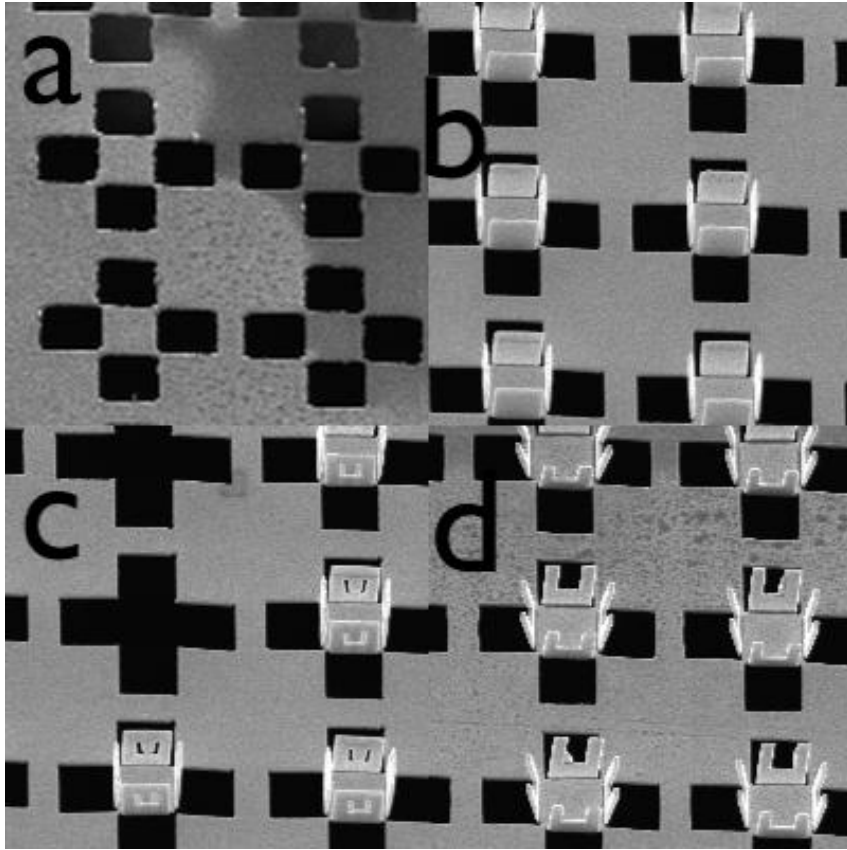


Figure 9.2.7.9 SEM image of flower-shape nanograting, sample number: (a) 13, (b) 14 (c) 15, (d) 19

The blue spot around the red spot in the image of $|E_{x1}|$, shown in Fig. 9.2.7.10b and Fig. 9.2.7.10d, should be from the protrusion. The red spot is from the square hole. The U-shape protrusion produce bigger effect than square-shape protrusion on $|E_{y1}|$, shown in Fig. 9.2.7.11. The square hole doesn't produce a variation of $|E_{y1}|$ shown in Fig. 9.2.7.11a. The U-shape hole protrusion on sample 15 produce a pattern of δ_1 , which is significantly different from the others, shown in Fig. 9.2.7.12. A square hole can produce a division on δ_1 shown in Fig. 9.2.7.12a, but the distribution of positive δ_1 and negative δ_1 is localized with a existence of the protrusion (square shape in Fig. 9.2.7.12b and U-shape in Fig.9.2.7.12d) and diffused because of the protrusion (U-shape hole in Fig. 9.2.7.12c).

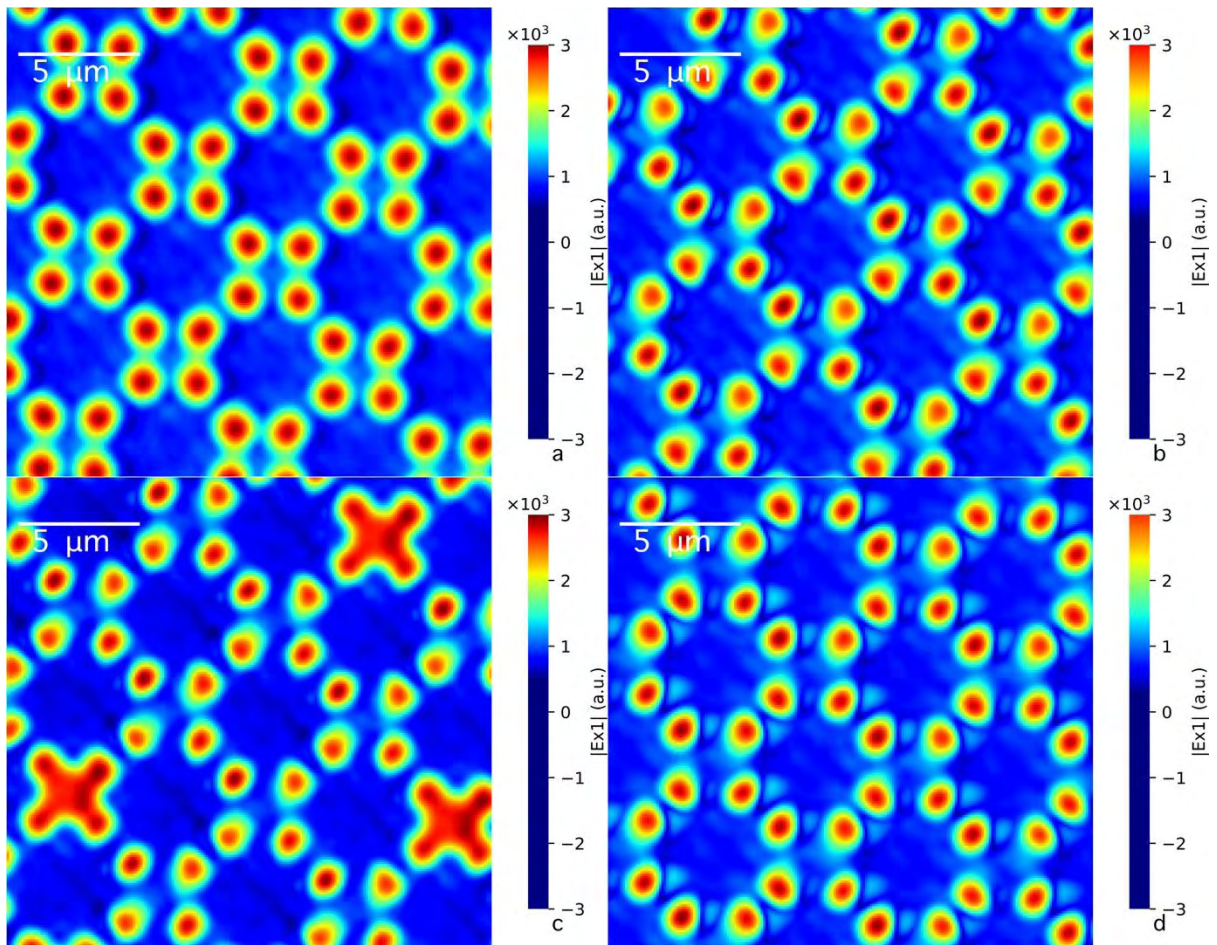


Figure 9.2.7.10 The mapping of $|E_{x1}|$ for the nanograter that protrusion in different angles, when the polarization azimuth angle sited at 122° (sample stage sited in 146° for sample 13, 14, 15 and 148° for sample 19), sample number: (a) 13, (b) 14 (c) 15, (d) 19

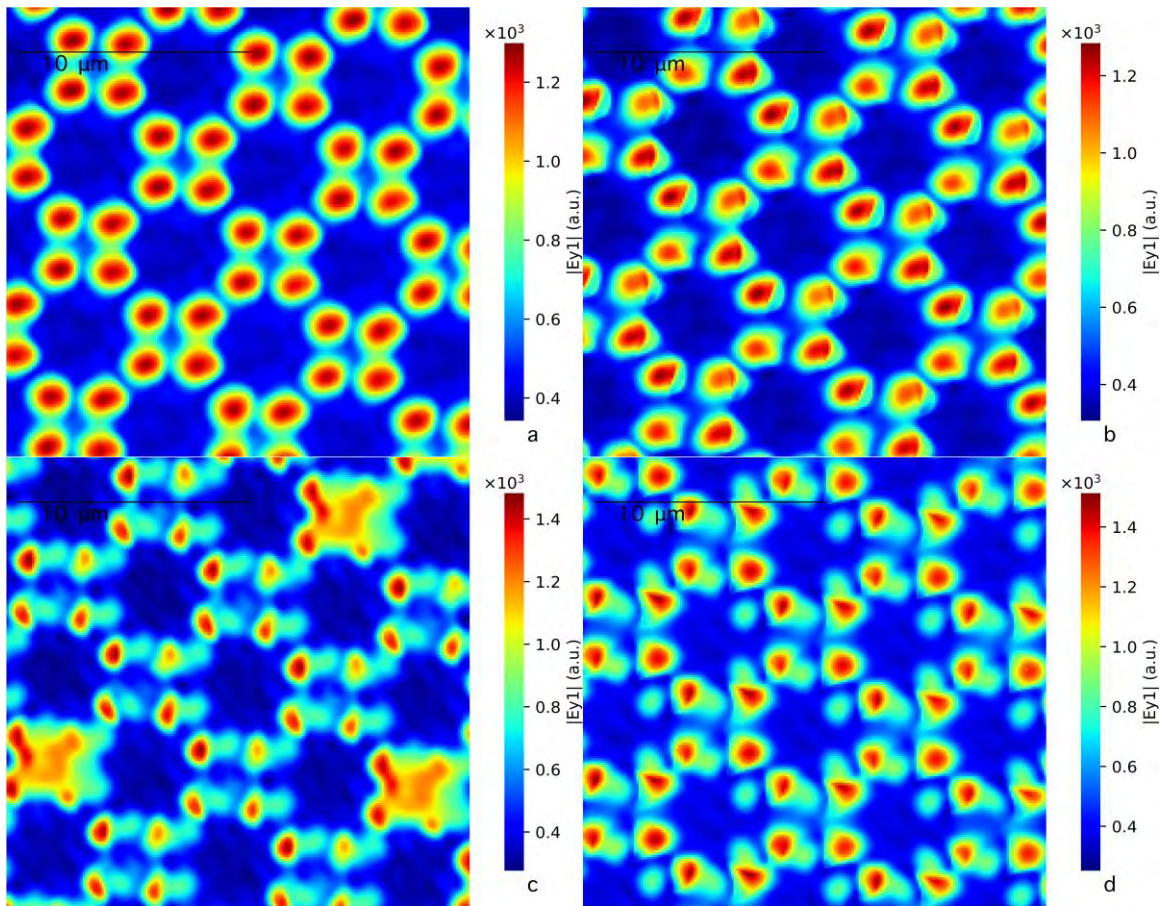


Figure 9.2.7.11 The mapping of $|E_{y1}|$ for the nanograter that protrusion in different angles, when the polarization azimuth angle sited at 122° (sample stage sited in 146° for sample 13, 14° , 15° and 148° for sample 19), sample number: (a) 13, (b) 14 (c) 15, (d) 19

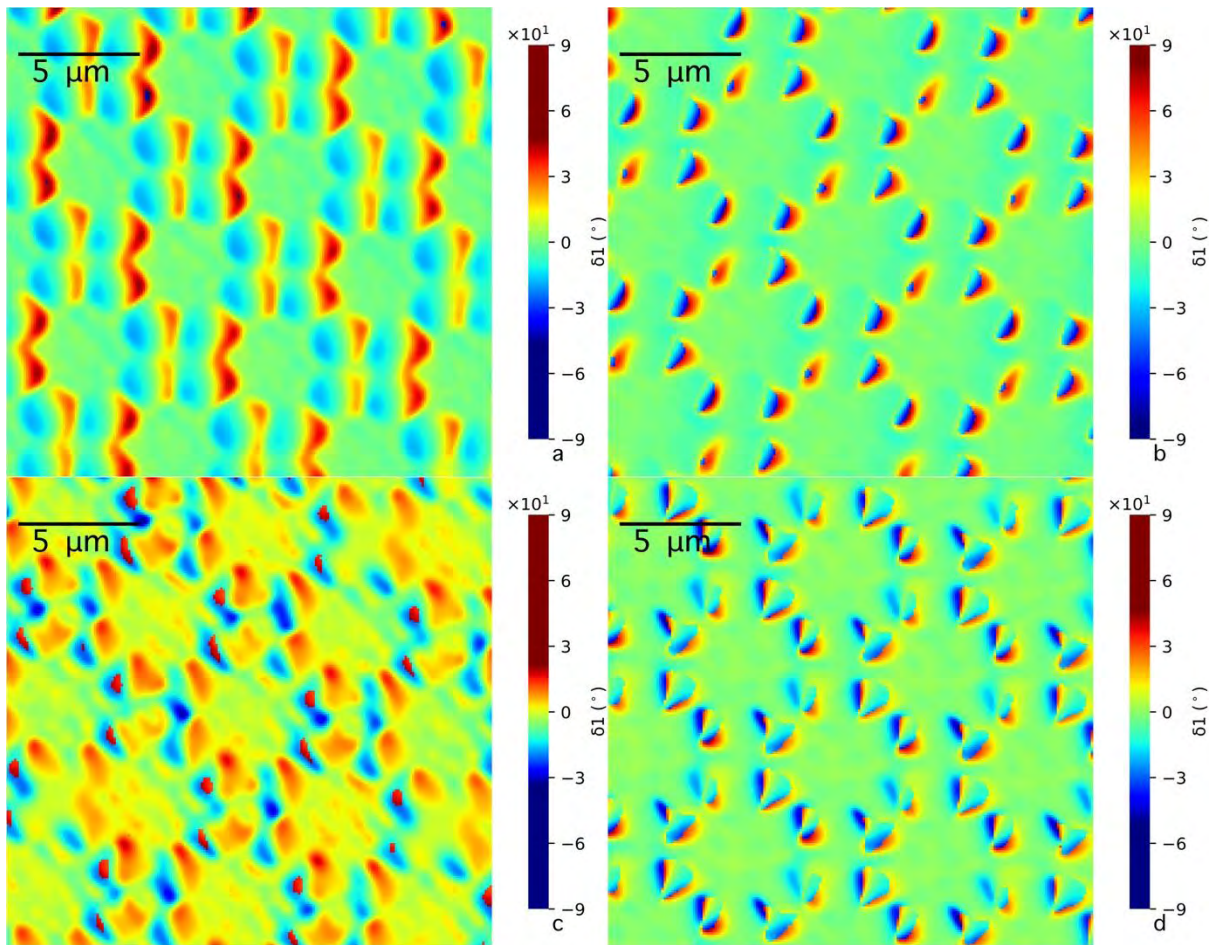


Figure 9.2.7.12 The mapping of δ_1 for the nanograting that protrusion in different angles, when the polarization azimuth angle sited at 122° (sample stage sited in 146° for sample 13, 14, 15 and 148° for sample 19), sample number: (a) 13, (b) 14 (c) 15, (d) 19

9.3 Summary

The nanograting is a 3D material. The symmetrical characteristic is broken. The Stokes polarimetric microscope can detect the information of a vector field. So, Abundant image with different patterns is obtained and reported in this chapter. The pattern is sensitive to the angle between the symmetric axis of the nanograting and the polarization directions. The different polarization component is sensitive to the protrusion or the hole-structure; so, the information of the protrusion or the hole-structure can be observed separately in different polarization image. The rectangle hole can produce a localized variation of δ_1 when the short edge is parallel with the optical axis of the polarization. The square hole can't localize the

variation of δ_1 , the protrusion structure can manipulate the distribution of the δ_1 . This result can provide a reference for the electromagnetic wave manipulation design in future.

Reference

Liu, Z., Gong, Z., Li, H., Xia, X., Shen, T. H., Li, J., ... Cui, A. (2016). Spatially oriented plasmonic “nanograting” structures. *Scientific Reports*, 6, 28764.

<https://doi.org/doi:10.1038/srep28764>

Chapter 10 Summarize and future work

In my PhD scheme, I realized Stokes polarization imaging. I developed the control software for the microscope in high speed acquisition. To acquire a high resolution, I optimized the experiment process. Firstly, I find the error on channel 9 and channel 10 in my calibration experiment and optimize the 12-channel method to 6-channel method. Secondly, I find the room temperature influences the measurement of signal V strongly and find out a special temperature to keep the accuracy of the experiment. Thirdly, I find the best position to acquire a parallel light. Fourthly, we aligned the microscope in a best position to acquire a uniform background image. And at last, I used an antireflection coated polarizer to improve the quality of the images.

The reflection light back to the light source is the reason of the uniform background of the polarization signal because the light path to the sample is different for the reflected back light and the original light. The phenomenon is found in the experiment using the parallel light without a condenser. In the process of microscope imaging, a condenser must be used to obtain the high luminescence. A parallel light is not available anymore, so the cross of the polarizer and the analyser is the optimized position to get rid of the reflected light to the light source. The parallel light source and the cross position of polarizer and the analyser are both needed in the experiment to acquire a uniform background. Under this equipment configuration, a high resolution is obtained.

Based on the experiment technique we developed, I researched four material systems, micropipe, pinhole, liquid crystal, and nanograting. The image of micropipe can be compared with that acquired by Metripol apparatus (Ouisse, Chaussende, & Auvray, 2009) and crossed polarizer method, but with much higher resolution. In our image, no blank area, which is much different with the image acquired by Metripol apparatus. The image of micropipe is

sensitive the configuration of the micropipe in the silicon carbide. Abundant images are reported in chapter six.

The vector field of the pinhole diffraction is reported in chapter seven. An Airy-like pattern in a vector field is published. The information of elliptical angle and azimuth angle has a response area of $20\mu\text{m}$, which is much higher than that of the intensity $2\mu\text{m}$. The four-ray structure is from the scattering of the edge of the pinhole; it exists in front of the pinhole and behind the pinhole.

The liquid crystal is a good sample to be researched on the Stokes polarimetric microscope, because it has interface inside the liquid crystal with different style. Four type of liquid crystal is researched, the interface inside the liquid crystal can be seen clearly. Also, some feature is because of the round edge of the liquid crystal droplet.

Nanograter is a kind of metamaterial to manipulate the light. The pattern of the polarization is relative to the angle between the optical axis of the polarizer and the symmetric axis of the nanograter. The electrical field along and orthogonal to the polarisation is deduced in chapter nine. The protrusion or the U-shape hole may be indistinct in the image of a special polarization. The angle of the protrusion also influences the image of the polarization. The shape of the hole can influence the distribution of the polarization, too. The shape of the protrusion can influence the distribution of the phase difference.

Beside this, I realized the six-polarization measurement on the optical bench and developed calculation program of the polarization extraction in our lab. I put it in the appendix because it may influence the coherence of the whole thesis. Also, the relationship between the polarization and the anisotropy of the structure is clarified in this thesis in chapter two.

However, many problems are not been solved and need to be done in future.

Because of the magnification of our microscope, some nanograter pattern is too small to see the details, a big magnification lens is needed in future to research them. The faulty of the channel 9 and channel 10 on the equipment needs to be modified. The six-channel method cannot get the information of the phase angle, which is only can be acquired using twelve-channel method. The measurement of intensity needs to be modified too.

Appendix A

A.1 Calibration experiment -- Alignment

The calibration experiment is used to establish the relationship between actual signals and Stokes parameters. The Matrix K is solved through calibration process. A proper alignment is the basement of the right calibration parameters.

The alignment process follows these steps:

1. Set the Polarizer and the Analyzer cross, where we got an extinction;
2. Put the PEM2 between the Polarizer and the Analyzer and got an extinction;
3. Put the PEM1 between the Polarizer and the Analyzer and got an extinction;
4. Set axis of PEM2 to be the laboratory coordinate;
5. Under the right-hand coordinate, rotate the analyzer clockwise 22.5° to make sure the axis of the analyzer ($\beta = 22.5^\circ$)
6. Rotate the PEM1 clockwise 45° to make sure the axis of the PEM1 along the direction ($\alpha = 45^\circ$)
7. To acquire a circular polarization, a retarder with the right wavelength was installed after the polarizer.

A linear calibration and circular calibration are done separately. The retarder (waveplate) is only needed when the process of a circular calibration.

Appendix B: Optical component extraction deduction

This chapter presents a description of the state of polarization of light and the related mathematical method. Details of the matrix inversion technique to determine the optical characteristic of the sample relevant to the measurement of polarization with Stokes polarimetry are also presented.

B.1 Mueller matrix of different optical component

Mueller matrix is a good way to represent the effect of an optical component on the light. However, sometimes optical properties are a hybrid effect which need further analysis. To extract the optical parameters, the hybrid Mueller matrix is treated as a product of Mueller matrix of different optical components. The Mueller matrix of every significant optical property is shown in the following sections.

The optical property of a material is classified into five parts: linear birefringence, circular birefringence, linear dichroism, circular dichroism, and depolarization. The definition of the effective parameters is shown in table B.1-1.

Table B.1-1 Symbols and definitions of effective parameters (where, LB is linear birefringence; CB is circular birefringence; LD is linear dichroism; CD is circular dichroism (Pham & Lo, 2012b, 2012a))

Name	Symbol	Range	Definition
Orientation angle of fast axis of LB	α	$[0^\circ, 180^\circ]$	
Linear birefringence of LB	δ	$[0^\circ, 360^\circ]$	$2\pi(n_s - n_f) l/\lambda$
Optical rotation angle of CB	γ	$[0^\circ, 180^\circ]$	$2\pi(n_- - n_+) l/\lambda$
Orientation angle of LD	θ_d	$[0^\circ, 180^\circ]$	
Linear dichroism of LD	D	$[0, 1]$	$2\pi(\mu_s - \mu_f) l/\lambda$
Circular dichroism of CD	R	$[-1, 1]$	$2\pi(\mu_- - \mu_+) l/\lambda$
Linear depolarization	e1 and e2	$[-1, 1]$	
Circular depolarization	e3	$[-1, 1]$	
Depolarization index	Δ	$[0, 1]$	

B.1.1 Mueller Matrix of linear birefringence

The Mueller Matrix of linear birefringence with an orientation angle α and phase retardance δ is expressed as follows (Kliger et al., 1990, p.287)

$$M_{lb} = \begin{pmatrix} 1 & 0 & 0 & 0 \\ 0 & \cos(4\alpha) \sin^2(\delta/2) + \cos^2(\delta/2) & \sin(4\alpha) \sin^2(\delta/2) & -\sin(2\alpha) \sin(\delta) \\ 0 & \sin(4\alpha) \sin^2(\delta/2) & -\cos(4\alpha) \sin^2(\delta/2) + \cos^2(\delta/2) & \cos(2\alpha) \sin(\delta) \\ 0 & \sin(2\alpha) \sin(\delta) & -\cos(2\alpha) \sin(\delta) & \cos(\delta) \end{pmatrix} \quad (B.1.1.1)$$

B.1.2 Mueller Matrix of circular birefringence sample

The Mueller Matrix of circular birefringence with an optical rotation angle γ is expressed as follows (Huard, 1997, p.313)

$$M_{cb} = \begin{pmatrix} 1 & 0 & 0 & 0 \\ 0 & \cos(2\gamma) & \sin(2\gamma) & 0 \\ 0 & -\sin(2\gamma) & \cos(2\gamma) & 0 \\ 0 & 0 & 0 & 1 \end{pmatrix} \quad (B.1.2.1)$$

B.1.3 Mueller Matrix for a linear dichroism material

The Mueller Matrix of linear dichroism with an optical rotation angle θ_d and linear dichroism D is expressed as follows (Pham & Lo, 2012a)

$$M_{ld} = \begin{pmatrix} \frac{1}{2}\left(1 + \frac{1-D}{1+D}\right) & \frac{1}{2}\cos(2\theta_d)\left(1 - \frac{1-D}{1+D}\right) & \frac{1}{2}\sin(2\theta_d)\left(1 - \frac{1-D}{1+D}\right) & 0 \\ \frac{1}{2}\cos(2\theta_d)\left(1 - \frac{1-D}{1+D}\right) & \frac{1}{4}\left[\left(1 + \sqrt{\frac{1-D}{1+D}}\right)^2 + \cos(4\theta_d)\left(1 - \sqrt{\frac{1-D}{1+D}}\right)^2\right] & \frac{1}{2}\sin(4\theta_d)\left(1 - \sqrt{\frac{1-D}{1+D}}\right)^2 & 0 \\ \frac{1}{2}\sin(2\theta_d)\left(1 - \frac{1-D}{1+D}\right) & \frac{1}{2}\sin(4\theta_d)\left(1 - \sqrt{\frac{1-D}{1+D}}\right)^2 & \frac{1}{4}\left[\left(1 + \sqrt{\frac{1-D}{1+D}}\right)^2 - \cos(4\theta_d)\left(1 - \sqrt{\frac{1-D}{1+D}}\right)^2\right] & 0 \\ 0 & 0 & 0 & \sqrt{\frac{1-D}{1+D}} \end{pmatrix} \quad (B.1.3.1)$$

B.1.4 Mueller Matrix of a circular dichroism material

The Mueller Matrix of circular dichroism R is expressed as follows(Pham & Lo, 2012a)

$$M_{cd} = \begin{pmatrix} 1 + R^2 & 0 & 0 & 2R \\ 0 & 1 - R^2 & 0 & 0 \\ 0 & 0 & 1 - R^2 & 0 \\ 2R & 0 & 0 & 1 + R^2 \end{pmatrix} \quad (B.1.4.1)$$

B.1.4 Mueller Matrix of the property of depolarization

Considering the existence of the solution of the matrix decomposition proved by Lu and Chipman(Ossikovski, De Martino, & Guyot, 2007), two types of depolarizer matrix form are used in the calculation. The Mueller Matrix of depolarization in forward family² M_{Δ} is shown in formula (B.1.5-1) and the Mueller matrix of depolarization in reverse family $M_{\Delta r}$ is shown in formula (B.1.5-2) (Ossikovski et al., 2007). Ossikovski proved that the decomposition process has a solution only using the right style of Mueller matrix of depolarization in its corresponding family (Ossikovski et al., 2007).

$$M_{\Delta} = \begin{bmatrix} 1 & 0 & 0 & 0 \\ p_1 & e_1 & 0 & 0 \\ p_2 & 0 & e_2 & 0 \\ p_3 & 0 & 0 & e_3 \end{bmatrix} \quad (B.1.4.1)$$

$$M_{\Delta r} = \begin{bmatrix} 1 & d_1 & d_2 & d_3 \\ 0 & e_1 & 0 & 0 \\ 0 & 0 & e_2 & 0 \\ 0 & 0 & 0 & e_3 \end{bmatrix} \quad (B.1.4.2)$$

where p_1, p_2, p_3 are the polarize; d_1, d_2, d_3 are diattenuation; e_1, e_2 , are the degree of linear depolarization, and e_3 is the circular depolarization.

B.2 Deduction of the effective optical parameters

The interaction between sample and polarization is represented by a Mueller Matrix M . The status of polarization before interaction with the sample is represented as S , and the status of

² Because the matrix multiplication is not commutative, the Mueller matrix of retarder M_b , diattenuator M_d , and depolarizer M_{Δ} are order dependent(Lu & Chipman, 1996). The forward family means the M_{Δ} on the left of the M_b and M_d (Ossikovski et al., 2007). The reverse family means the means the M_{Δ} on the right of the M_b and M_d (Ossikovski et al., 2007).

polarization after interaction with the sample is represented as S' . The relationship is shown in equation 2.1.3-1.

In a complex situation, matrix M includes many kinds of optical effect, such as CD, LD, CB, LB, and depolarization. The matrix M is decomposed as a product of Mueller matrices of different optical effect. The algorithm of the decomposition of the Mueller matrix is shown by Cloude in 1986 (Cloude, 1986). Lu et. al. proves any Mueller matrix can be decomposed into a diattenuator, retarder, and a depolarizer (Lu & Chipman, 1996). Chipman also declared the problem of the order dependence of the matrix multiplication (Lu & Chipman, 1996). Ossikovski et al. had pointed out a symmetry existed between the two order of decomposition: forward and reverse family (Ossikovski et al., 2007).

B.2.1 Testing method

Stokes polarimeter is used in our experiment to test the Stokes parameters. Six different polarization states ($\hat{S}_{0^\circ}, \hat{S}_{45^\circ}, \hat{S}_{90^\circ}, \hat{S}_{135^\circ}, \hat{S}_{LHC}, \hat{S}_{RHC}$), explained in section 1.3.5, are used as input polarization, whose Stokes parameters are acquired without a sample in the way of light propagation. The polarization ($\hat{S}'_{0^\circ}, \hat{S}'_{45^\circ}, \hat{S}'_{90^\circ}, \hat{S}'_{135^\circ}, \hat{S}'_{LHC}, \hat{S}'_{RHC}$) is used as an output polarization, whose Stokes parameters is acquired with a sample mounted between retarder and PEM1. The Mueller matrix of the sample is acquired through the calculation method shown in section B.2.5. The data acquired is calculated through a program written by MATLAB to get the Mueller matrix of the sample.

B.2.2 Situation without regard to depolarization

In some systems, the depolarization effect is very small. The depolarization effect is not considered. Assuming the order of the optical components is CD, LD, CB, and LB.

According to the Mueller Matrix shown in section B.2.2, the Mueller matrix tested is the product of these Mueller matrices, which is shown in equation (B.2.2-1). From derivation

shown below, the polarization parameters under the situation without depolarization is obtained.

$$M = M_{cd}M_{ld}M_{cb}M_{lb} \quad (B.2.2.1)$$

$$M_{cd}M_{ld} = \begin{bmatrix} A_{11} & A_{12} & A_{13} & A_{14} \\ A_{21} & A_{22} & A_{23} & A_{24} \\ A_{31} & A_{32} & A_{33} & A_{34} \\ A_{41} & A_{42} & A_{43} & A_{44} \end{bmatrix} \quad (B.2.2.2)$$

$$M_{cd}M_{ld}M_{cb} = \begin{bmatrix} A_{11} & A_{12} & A_{13} & A_{14} \\ A_{21} & A_{22} & A_{23} & A_{24} \\ A_{31} & A_{32} & A_{33} & A_{34} \\ A_{41} & A_{42} & A_{43} & A_{44} \end{bmatrix} \begin{bmatrix} 1 & 0 & 0 & 0 \\ 0 & \cos 2\gamma & \sin 2\gamma & 0 \\ 0 & -\sin 2\gamma & \cos 2\gamma & 0 \\ 0 & 0 & 0 & 1 \end{bmatrix}$$

$$= \begin{bmatrix} A_{11} & A_{12}\cos 2\gamma - A_{13}\sin 2\gamma & A_{12}\sin 2\gamma + A_{13}\cos 2\gamma & A_{14} \\ A_{21} & A_{22}\cos 2\gamma - A_{23}\sin 2\gamma & A_{22}\sin 2\gamma + A_{23}\cos 2\gamma & A_{24} \\ A_{31} & A_{32}\cos 2\gamma - A_{33}\sin 2\gamma & A_{32}\sin 2\gamma + A_{33}\cos 2\gamma & A_{34} \\ A_{41} & A_{42}\cos 2\gamma - A_{43}\sin 2\gamma & A_{42}\sin 2\gamma + A_{43}\cos 2\gamma & A_{44} \end{bmatrix}$$

$$= \begin{bmatrix} B_{11} & B_{12} & B_{13} & B_{14} \\ B_{21} & B_{22} & B_{23} & B_{24} \\ B_{31} & B_{32} & B_{33} & B_{34} \\ B_{41} & B_{42} & B_{43} & B_{44} \end{bmatrix} \quad (B.2.2.3)$$

$$M_{lb} = \begin{bmatrix} 1 & 0 & 0 & 0 \\ 0 & h_1 & h_2 & h_3 \\ 0 & h_4 & h_5 & h_6 \\ 0 & h_7 & h_8 & h_9 \end{bmatrix} \quad (B.2.2.4)$$

$$M_{cd}M_{ld}M_{cb}M_{lb} = \begin{bmatrix} B_{11} & B_{12} & B_{13} & B_{14} \\ B_{21} & B_{22} & B_{23} & B_{24} \\ B_{31} & B_{32} & B_{33} & B_{34} \\ B_{41} & B_{42} & B_{43} & B_{44} \end{bmatrix} \begin{bmatrix} 1 & 0 & 0 & 0 \\ 0 & h_1 & h_2 & h_3 \\ 0 & h_4 & h_5 & h_6 \\ 0 & h_7 & h_8 & h_9 \end{bmatrix}$$

$$= \begin{bmatrix} B_{11} & h_1B_{12} + h_4B_{13} + h_7B_{14} & h_2B_{12} + h_5B_{13} + h_8B_{14} & h_3B_{12} + h_6B_{13} + h_9B_{14} \\ B_{21} & h_1B_{22} + h_4B_{23} + h_7B_{24} & h_2B_{22} + h_5B_{23} + h_8B_{24} & h_3B_{22} + h_6B_{23} + h_9B_{24} \\ B_{31} & h_1B_{32} + h_4B_{33} + h_7B_{34} & h_2B_{32} + h_5B_{33} + h_8B_{34} & h_3B_{32} + h_6B_{33} + h_9B_{34} \\ B_{41} & h_1B_{42} + h_4B_{43} + h_7B_{44} & h_2B_{42} + h_5B_{43} + h_8B_{44} & h_3B_{42} + h_6B_{43} + h_9B_{44} \end{bmatrix}$$

$$= \begin{bmatrix} C_{11} & C_{12} & C_{13} & C_{14} \\ C_{21} & C_{22} & C_{23} & C_{24} \\ C_{31} & C_{32} & C_{33} & C_{34} \\ C_{41} & C_{42} & C_{43} & C_{44} \end{bmatrix} = M. \quad (B. 2.2.5)$$

From equation (B.2.2-2) to (B.2.2-5), we can obtain

$$C_{11} = B_{11} = A_{11}, C_{21} = B_{21} = A_{21}, C_{31} = B_{31} = A_{31}, C_{41} = B_{41} = A_{41} \quad (B. 2.2.6)$$

where, matrix M is acquired by Stokes polarimetry experimentally. So, the C_{11} , C_{21} , C_{31} , and C_{41} are known number from the experiment. From the matrix of the linear dichroism (B.1.3-1) and circular dichroism (B.1.4-1), A_{11} , A_{21} , A_{31} , and A_{41} are acquired.

From formula B.2.2-6, we can obtain the formula of C_{11} , C_{21} , C_{31} , and C_{41} .

$$C_{11} = \frac{1}{2}(1 + R^2) \left(1 + \frac{1 - D}{1 + D}\right) \quad (B. 2.2.. 1)$$

$$C_{21} = \frac{1}{2} \cos(2\theta_d) \left(1 - \frac{1 - D}{1 + D}\right) (1 - R^2) \quad (B. 2.2.. 2)$$

$$C_{31} = \frac{1}{2} \sin(2\theta_d) \left(1 - \frac{1 - D}{1 + D}\right) (1 - R^2) \quad (B. 2.2. 3)$$

$$C_{41} = R \left(1 + \frac{1 - D}{1 + D}\right) \quad (B. 2.2. 4)$$

From equation (B.2.2-7) to (B.2.2-10), the D , R , and θ_d are acquired.

$$\theta_d = \tan^{-1} \left(\frac{C_{31}}{C_{21}} \right) \quad (B. 2.2. 5)$$

$$D = \sqrt{\frac{C_{21}^2 + C_{31}^2}{C_{11}^2 - C_{41}^2}} \quad (B. 2.2. 6)$$

$$R = \frac{\sqrt{C_{11} - C_{41}} - \sqrt{C_{11} + C_{41}}}{\sqrt{C_{11} - C_{41}} + \sqrt{C_{11} + C_{41}}} \quad (\text{B.2.2.7})$$

According to the formula (B.2.2-11) to (B.2.2-13), the Mueller matrix of dichroism

$M_d = M_{cd}M_{ld}$ is obtained. The Mueller matrix of birefringence $M_b = M_{cb}M_{lb}$ is acquired through the formula shown below

$$M_b = M_d^{-1} \cdot M = \begin{bmatrix} D_{11} & D_{12} & D_{13} & D_{14} \\ D_{21} & D_{22} & D_{23} & D_{24} \\ D_{31} & D_{32} & D_{33} & D_{34} \\ D_{41} & D_{42} & D_{43} & D_{44} \end{bmatrix} \quad (\text{B.2.2.8})$$

From formula (B.1.2-1) and (B.2.2-4), we can obtain

$$M_b = M_{cb}M_{lb} =$$

$$\begin{bmatrix} 1 & 0 & 0 & 0 \\ 0 & h_1 \cos 2\gamma + h_4 \sin 2\gamma & h_2 \cos 2\gamma + h_5 \sin 2\gamma & h_3 \cos 2\gamma + h_6 \sin 2\gamma \\ 0 & -h_1 \sin 2\gamma + h_4 \cos 2\gamma & -h_2 \sin 2\gamma + h_5 \cos 2\gamma & -h_3 \sin 2\gamma + h_6 \cos 2\gamma \\ 0 & h_7 & h_8 & h_9 \end{bmatrix} \quad (\text{B.2.2.9})^F$$

From matrix (B.1.1-1), we can obtain

$$h_3 = -h_7 = -\sin(2\alpha)\sin(\delta), \text{ and } h_6 = -h_8 = \cos(2\alpha)\sin(\delta) \quad (\text{B.2.2.10})$$

$$D_{22} = h_1 \cos 2\gamma + h_4 \sin 2\gamma = \sin^2 \frac{\delta}{2} \cos(4\alpha - 2\gamma) + \cos^2 \frac{\delta}{2} \cos 2\gamma. \quad (\text{B.2.2.11})$$

$$\begin{aligned} D_{33} &= -h_2 \cos 2\gamma + h_5 \sin 2\gamma \\ &= -\sin^2 \frac{\delta}{2} \cos(4\alpha - 2\gamma) + \cos^2 \frac{\delta}{2} \cos 2\gamma \end{aligned} \quad (\text{B.2.2.12})$$

$$D_{23} = h_2 \cos 2\gamma + h_5 \sin 2\gamma = \sin^2 \frac{\delta}{2} \sin(4\alpha - 2\gamma) + \cos^2 \frac{\delta}{2} \sin 2\gamma. \quad (\text{B.2.2.13})$$

$$\begin{aligned} D_{32} &= -h_1 \cos 2\gamma + h_4 \sin 2\gamma \\ &= \sin^2 \frac{\delta}{2} \sin(4\alpha - 2\gamma) - \cos^2 \frac{\delta}{2} \sin 2\gamma. \end{aligned} \quad (\text{B.2.2.14})$$

Comparing the formula (B.2.2-14) and (B.2.2-15), we can acquire the formula of these optical parameters

$$\alpha = -\frac{1}{2} \tan^{-1} \left(\frac{D_{42}}{D_{43}} \right) \quad (\text{B. 2.2. 15})$$

$$\delta = \cos^{-1}(D_{44}/D_{11}) \quad (\text{B. 2.2. 16})$$

$$\gamma = \frac{1}{2} \tan^{-1} \left(\frac{D_{23} - D_{32}}{D_{22} + D_{33}} \right) \quad (\text{B. 2.2. 17})$$

According to the derivation above, the parameters α , δ , γ , θ_d , D , R are obtained for the Mueller matrix of the sample being measured.

B.2.3 Situation with regard to depolarization

In the situation with regard to the depolarization, the Mueller matrix of depolarization is involved in the calculation. According to the paper of Ossikovski (Ossikovski et al., 2007), the Mueller matrix of a reverse family is used here. This is very important, because it make the decomposition process easily solved.

$$\begin{aligned} M_{db\Delta} = M_d M_b M_{\Delta r} &= \begin{bmatrix} C_{11} & C_{12} & C_{13} & C_{14} \\ C_{21} & C_{22} & C_{23} & C_{24} \\ C_{31} & C_{32} & C_{33} & C_{34} \\ C_{41} & C_{42} & C_{43} & C_{44} \end{bmatrix} \begin{bmatrix} 1 & d_1 & d_2 & d_3 \\ 0 & e_1 & 0 & 0 \\ 0 & 0 & e_2 & 0 \\ 0 & 0 & 0 & e_3 \end{bmatrix} \\ &= \begin{bmatrix} C_{11} & d_1 C_{11} + C_{12} e_1 & d_2 C_{11} + C_{13} e_2 & d_3 C_{11} + C_{14} e_3 \\ C_{21} & d_1 C_{21} + C_{22} e_1 & d_2 C_{21} + C_{23} e_2 & d_3 C_{21} + C_{24} e_3 \\ C_{31} & d_1 C_{31} + C_{32} e_1 & d_2 C_{31} + C_{33} e_2 & d_3 C_{31} + C_{34} e_3 \\ C_{41} & d_1 C_{41} + C_{42} e_1 & d_2 C_{41} + C_{43} e_2 & d_3 C_{41} + C_{44} e_3 \end{bmatrix} \\ &= \begin{bmatrix} E_{11} & E_{12} & E_{13} & E_{14} \\ E_{21} & E_{22} & E_{23} & E_{24} \\ E_{31} & E_{32} & E_{33} & E_{34} \\ E_{41} & E_{42} & E_{43} & E_{44} \end{bmatrix} \quad (\text{B. 2.3. 1}) \end{aligned}$$

From relationship in (B.2.3-1) and (B.2.2-3), we can obtain the formula below

$$E_{11} = C_{11} = B_{11} = A_{11}, E_{21} = C_{21} = B_{21} = A_{21}, E_{31} = C_{31} = B_{31} = A_{31}, E_{41} = C_{41} = B_{41} = A_{41} \quad (\text{B. 2.3. 2})$$

According to the formula (B.2.2-11) to (B.2.2-13) in section B.2.2, the polarization parameters are solved.

$$\theta_d = \tan^{-1} \left(\frac{E_{31}}{E_{21}} \right) \quad (\text{B. 2.3. 3})$$

$$D = \frac{\sqrt{E_{21}^2 + E_{31}^2}}{\sqrt{E_{11}^2 - E_{41}^2}} \quad (\text{B. 2.3. 4})$$

$$R = \frac{\sqrt{E_{11} - E_{41}} - \sqrt{E_{11} + E_{41}}}{\sqrt{E_{11} - E_{41}} + \sqrt{E_{11} + E_{41}}} \quad (\text{B. 2.3. 5})$$

The diattenuation matrix $M_d = M_{cd}M_{ld}$ is acquired through (0-4) to (0-6), (B.1.3-1) and (B.1.4-1).

The Mueller matrix of retarder and depolarizer $M_{b\Delta}$ is acquired through the formula (B.2.2-9).

$M_{Db\Delta}$ is the Mueller matrix tested by Stokes polarimetry in the experiment.

$$M_{b\Delta} = M_b M_{\Delta r} = M_d^{-1} M_{db\Delta} \quad (\text{B.2.3.6})$$

$$M_{b\Delta} = \begin{bmatrix} D_{11} & 0 & 0 & 0 \\ 0 & D_{22} & D_{23} & D_{24} \\ 0 & D_{32} & D_{33} & D_{34} \\ 0 & D_{42} & D_{43} & D_{44} \end{bmatrix} \begin{bmatrix} 1 & d_1 & d_2 & d_3 \\ 0 & e_1 & 0 & 0 \\ 0 & 0 & e_2 & 0 \\ 0 & 0 & 0 & e_3 \end{bmatrix}$$

$$= \begin{bmatrix} 1 & 0 & 0 & 0 \\ 0 & h_1 \cos 2\gamma + h_4 \sin 2\gamma & h_2 \cos 2\gamma + h_5 \sin 2\gamma & h_3 \cos 2\gamma + h_6 \sin 2\gamma \\ 0 & -h_1 \sin 2\gamma + h_4 \cos 2\gamma & -h_2 \sin 2\gamma + h_5 \cos 2\gamma & -h_3 \sin 2\gamma + h_6 \cos 2\gamma \\ 0 & h_7 & h_8 & h_9 \end{bmatrix} \begin{bmatrix} 1 & d_1 & d_2 & d_3 \\ 0 & e_1 & 0 & 0 \\ 0 & 0 & e_2 & 0 \\ 0 & 0 & 0 & e_3 \end{bmatrix}$$

$$= \begin{bmatrix} 1 & & & \\ 0 & (h_1 \cos 2\gamma + h_4 \sin 2\gamma)e_1 & (h_2 \cos 2\gamma + h_5 \sin 2\gamma)e_2 & (h_3 \cos 2\gamma + h_6 \sin 2\gamma)e_3 \\ 0 & (-h_1 \sin 2\gamma + h_4 \cos 2\gamma)e_1 & (-h_2 \sin 2\gamma + h_5 \cos 2\gamma)e_2 & (-h_3 \sin 2\gamma + h_6 \cos 2\gamma)e_3 \\ 0 & h_7 e_1 & h_8 e_2 & h_9 e_3 \end{bmatrix}$$

$$= \begin{bmatrix} 1 & & & \\ 0 & (\sin^2 \frac{\delta}{2} \cos(4\alpha - 2\gamma) + \cos^2 \frac{\delta}{2} \cos 2\gamma)e_1 & (\sin^2 \frac{\delta}{2} \sin(4\alpha - 2\gamma) - \cos^2 \frac{\delta}{2} \sin 2\gamma)e_2 & (\sin \delta \sin(2\gamma - 2\alpha))e_3 \\ 0 & (\sin^2 \frac{\delta}{2} \sin(4\alpha - 2\gamma) + \cos^2 \frac{\delta}{2} \sin 2\gamma)e_1 & (-\sin^2 \frac{\delta}{2} \cos(4\alpha - 2\gamma) + \cos^2 \frac{\delta}{2} \cos 2\gamma)e_2 & (\sin \delta \cos(2\gamma - 2\alpha))e_3 \\ 0 & \sin 2\alpha \cdot \sin \delta \cdot e_1 & -\cos 2\alpha \cdot \sin \delta \cdot e_2 & \cos \delta \cdot e_3 \end{bmatrix}$$

$$= \begin{bmatrix} F_{11} & F_{12} & F_{13} & F_{14} \\ 0 & F_{22} & F_{23} & F_{24} \\ 0 & F_{32} & F_{33} & F_{34} \\ 0 & F_{42} & F_{43} & F_{44} \end{bmatrix} \quad (\text{B. 2.3.7})$$

According to B.2.3-7, the equation B.2.3-8 acquired,

$$\begin{bmatrix} 1 & & & \\ 0 & \overset{d_1}{(\sin^2 \frac{\delta}{2} \cos(4\alpha - 2\gamma) + \cos^2 \frac{\delta}{2} \cos 2\gamma)e_1} & \overset{d_2}{(\sin^2 \frac{\delta}{2} \sin(4\alpha - 2\gamma) - \cos^2 \frac{\delta}{2} \sin 2\gamma)e_2} & \overset{d_3}{(\sin \delta \sin(2\gamma - 2\alpha))e_3} \\ 0 & (\sin^2 \frac{\delta}{2} \sin(4\alpha - 2\gamma) + \cos^2 \frac{\delta}{2} \sin 2\gamma)e_1 & (-\sin^2 \frac{\delta}{2} \cos(4\alpha - 2\gamma) + \cos^2 \frac{\delta}{2} \cos 2\gamma)e_2 & (\sin \delta \cos(2\gamma - 2\alpha))e_3 \\ 0 & \sin 2\alpha \cdot \sin \delta \cdot e_1 & -\cos 2\alpha \cdot \sin \delta \cdot e_2 & \cos \delta \cdot e_3 \end{bmatrix}$$

$$= \begin{bmatrix} F_{11} & F_{12} & F_{13} & F_{14} \\ 0 & F_{22} & F_{23} & F_{24} \\ 0 & F_{32} & F_{33} & F_{34} \\ 0 & F_{42} & F_{43} & F_{44} \end{bmatrix} \quad (\text{B. 2.3.8})$$

Using normalized Stokes parameter to solve the equation, the diattenuation is eliminated.

$$M_{\Delta b} = \begin{bmatrix} 1 & 0 & 0 & 0 \\ p_1 & e_1 & 0 & 0 \\ p_2 & 0 & e_2 & 0 \\ p_3 & 0 & 0 & e_3 \end{bmatrix} \begin{bmatrix} D_{11} & 0 & 0 & 0 \\ 0 & D_{22} & D_{23} & D_{24} \\ 0 & D_{32} & D_{33} & D_{34} \\ 0 & D_{42} & D_{43} & D_{44} \end{bmatrix}$$

$$= \begin{bmatrix} D_{11} & 0 & 0 & 0 \\ p_1 D_{11} & D_{22} e_1 & D_{23} e_2 & D_{24} e_3 \\ p_2 D_{11} & D_{32} e_1 & D_{33} e_2 & D_{34} e_3 \\ p_3 D_{11} & D_{42} e_1 & D_{43} e_2 & D_{44} e_3 \end{bmatrix}$$

$$= \begin{bmatrix} 1 & 0 & 0 & 0 \\ p_1 & e_1 & 0 & 0 \\ p_2 & 0 & e_2 & 0 \\ p_3 & 0 & 0 & e_3 \end{bmatrix} \begin{bmatrix} 1 & 0 & 0 & 0 \\ 0 & h_1 \cos 2\gamma + h_4 \sin 2\gamma & h_2 \cos 2\gamma + h_5 \sin 2\gamma & h_3 \cos 2\gamma + h_6 \sin 2\gamma \\ 0 & -h_1 \sin 2\gamma + h_4 \cos 2\gamma & -h_2 \sin 2\gamma + h_5 \cos 2\gamma & -h_3 \sin 2\gamma + h_6 \cos 2\gamma \\ 0 & h_7 & h_8 & h_9 \end{bmatrix}$$

$$= \begin{bmatrix} 1 & 0 & 0 & 0 \\ p_1 & (h_1 \cos 2\gamma + h_4 \sin 2\gamma) e_1 & (h_2 \cos 2\gamma + h_5 \sin 2\gamma) e_2 & (h_3 \cos 2\gamma + h_6 \sin 2\gamma) e_3 \\ p_2 & (-h_1 \sin 2\gamma + h_4 \cos 2\gamma) e_1 & (-h_2 \sin 2\gamma + h_5 \cos 2\gamma) e_2 & (-h_3 \sin 2\gamma + h_6 \cos 2\gamma) e_3 \\ p_3 & h_7 e_1 & h_8 e_2 & h_9 e_3 \end{bmatrix}$$

$$= \begin{bmatrix} 1 & 0 & 0 & 0 \\ p_1 & (h_1 \cos 2\gamma + h_4 \sin 2\gamma) e_1 & (h_2 \cos 2\gamma + h_5 \sin 2\gamma) e_2 & (h_3 \cos 2\gamma + h_6 \sin 2\gamma) e_3 \\ p_2 & (-h_1 \sin 2\gamma + h_4 \cos 2\gamma) e_1 & (-h_2 \sin 2\gamma + h_5 \cos 2\gamma) e_2 & (-h_3 \sin 2\gamma + h_6 \cos 2\gamma) e_3 \\ p_3 & -h_3 e_1 & -h_6 e_2 & h_9 e_3 \end{bmatrix}$$

$$= \begin{bmatrix} 1 & 0 & 0 & 0 \\ p_1 & (\sin^2 \frac{\delta}{2} \cos(4\alpha - 2\gamma) + \cos^2 \frac{\delta}{2} \cos 2\gamma) e_1 & (\sin^2 \frac{\delta}{2} \sin(4\alpha - 2\gamma) - \cos^2 \frac{\delta}{2} \sin 2\gamma) e_2 & (\sin \delta \sin(2\gamma - 2\alpha)) e_3 \\ p_2 & (\sin^2 \frac{\delta}{2} \sin(4\alpha - 2\gamma) + \cos^2 \frac{\delta}{2} \sin 2\gamma) e_1 & (-\sin^2 \frac{\delta}{2} \cos(4\alpha - 2\gamma) + \cos^2 \frac{\delta}{2} \cos 2\gamma) e_2 & (\sin \delta \cos(2\gamma - 2\alpha)) e_3 \\ p_3 & \sin 2\alpha \cdot \sin \delta \cdot e_1 & -\cos 2\alpha \cdot \sin \delta \cdot e_2 & \cos \delta \cdot e_3 \end{bmatrix} \quad (B.2.3.9)$$

$$D_{11} = E_{11} = 1. \quad (B.2.3.10)$$

$$p_1 = \frac{E_{21}}{D_{11}} \quad (\text{B. 2.3. 11})$$

$$p_2 = \frac{E_{31}}{D_{11}} \quad (\text{B. 2.3. 12})$$

$$p_3 = \frac{E_{41}}{D_{11}} \quad (\text{B. 2.3. 13})$$

$$e_1 = \frac{E_{22}}{D_{22}} \quad (\text{B. 2.3. 14})$$

$$e_2 = \frac{E_{33}}{D_{22}} \quad (\text{B. 2.3. 15})$$

$$e_3 = \frac{E_{44}}{D_{44}} \quad (\text{B. 2.3. 16})$$

$$\alpha = -\frac{1}{2} \tan^{-1} \left(\frac{D_{42}}{D_{43}} \right) = -\frac{1}{2} \tan^{-1} \left(\frac{E_{42}/e_1}{E_{43}/e_2} \right) \quad (\text{B. 2.3. 17})$$

$$\delta = \cos^{-1} \left(\frac{D_{44}}{D_{11}} \right) = \cos^{-1} \left(\frac{E_{44}/e_3}{E_{11}} \right) \quad (\text{B. 2.3. 18})$$

$$\gamma = \frac{1}{2} \tan^{-1} \left(\frac{D_{23} - D_{32}}{D_{22} + D_{33}} \right) = \frac{1}{2} \tan^{-1} \left(\frac{E_{23}/e_2 - E_{32}/e_1}{E_{22}/e_1 + E_{33}/e_2} \right) \quad (\text{B. 2.3. 19})$$

$$\gamma = \frac{1}{2} \sin^{-1} \left(\frac{D_{34}D_{42} - D_{24}D_{43}}{D_{42}^2 + D_{43}^2} \right) = \frac{1}{2} \sin^{-1} \left(\frac{(E_{34}/e_3)(E_{42}/e_1) - (E_{24}/e_3)(E_{43}/e_2)}{(E_{42}/e_1)^2 + (E_{43}/e_2)^2} \right) \quad (\text{B. 2.3. 20})$$

$$\gamma = \frac{1}{2} \cos^{-1} \left(\frac{E_{22}/e_1 + E_{33}/e_2}{1 + E_{44}/e_3} \right) \quad (\text{B. 2.3. 21})$$

B.2.4 Acquisition of the Mueller matrix of a sample

Suppose the Mueller matrix of the sample to be a matrix M , the Stokes parameter before interaction with the sample is input Stokes parameter (S), and the Stokes parameter after interaction with the sample is output Stokes parameter (S'). The relationship of input Stokes parameters and output parameters is shown in equation 1.1.3.1.

The Mueller matrix of a sample is determined through the measurement of Stokes parameters at special polarization (Chen, Lo, Yu, Lin, & Yang, 2009; Liao & Lo, 2013; Pham & Lo, 2012a, 2012b). Usually, using six different input polarizations to do the measurement (Pham & Lo, 2012a): $\hat{S}_{0^\circ} = [1 \ 1 \ 0 \ 0]^T$, $\hat{S}_{90^\circ} = [1 \ -1 \ 0 \ 0]^T$, $\hat{S}_{45^\circ} = [1 \ 0 \ -1 \ 0]^T$, $\hat{S}_{135^\circ} = [1 \ 0 \ -1 \ 0]^T$, $\hat{S}_{LHC} = [1 \ 0 \ 0 \ -1]^T$, and $\hat{S}_{RHC} = [1 \ 0 \ 0 \ -1]^T$. Then the output polarization shows below.

Using M_S represent the Mueller Matrix of a sample,

$$M_S = M_{db\Delta} = \begin{bmatrix} E_{11} & E_{12} & E_{13} & E_{14} \\ E_{21} & E_{22} & E_{23} & E_{24} \\ E_{31} & E_{32} & E_{33} & E_{34} \\ E_{41} & E_{42} & E_{43} & E_{44} \end{bmatrix} \quad (\text{B. 2.4. 1})$$

We can obtain the relationship

$$M_S \begin{bmatrix} 1 \\ 1 \\ 0 \\ 0 \end{bmatrix} = \begin{bmatrix} E_{11} + E_{12} \\ E_{21} + E_{22} \\ E_{31} + E_{32} \\ E_{41} + E_{42} \end{bmatrix} \quad (\text{B. 2.4. 2})$$

$$M_S \begin{bmatrix} 1 \\ -1 \\ 0 \\ 0 \end{bmatrix} = \begin{bmatrix} E_{11} - E_{12} \\ E_{21} - E_{22} \\ E_{31} - E_{32} \\ E_{41} - E_{42} \end{bmatrix} \quad (\text{B. 2.4. 3})$$

$$M_s \begin{bmatrix} 1 \\ 0 \\ 1 \\ 0 \end{bmatrix} = \begin{bmatrix} E_{11} + E_{13} \\ E_{21} + E_{23} \\ E_{31} + E_{33} \\ E_{41} + E_{43} \end{bmatrix} \quad (B.2.4.4)$$

$$M_s \begin{bmatrix} 1 \\ 0 \\ -1 \\ 0 \end{bmatrix} = \begin{bmatrix} E_{11} - E_{13} \\ E_{21} - E_{23} \\ E_{31} - E_{33} \\ E_{41} - E_{43} \end{bmatrix} \quad (B.2.4.5)$$

$$M_s \begin{bmatrix} 1 \\ 0 \\ 0 \\ 1 \end{bmatrix} = \begin{bmatrix} E_{11} + E_{14} \\ E_{21} + E_{24} \\ E_{31} + E_{34} \\ E_{41} + E_{44} \end{bmatrix} \quad (B.2.4.6)$$

$$M_s \begin{bmatrix} 1 \\ 0 \\ 0 \\ -1 \end{bmatrix} = \begin{bmatrix} E_{11} - E_{14} \\ E_{21} - E_{24} \\ E_{31} - E_{34} \\ E_{41} - E_{44} \end{bmatrix} \quad (B.2.4.7)$$

According to formula B.2.4-2 to B.2.4-7, the Mueller matrix of a sample is determined.

$$E_{11} = \frac{1}{6} (S_{0^\circ}(S_0) + S_{90^\circ}(S_0) + S_{45^\circ}(S_0) + S_{135^\circ}(S_0) + S_{RHC}(S_0) + S_{LHC}(S_0)) \quad (B.2.4.8)$$

$$E_{12} = \frac{1}{2} (S_{0^\circ}(S_0) - S_{90^\circ}(S_0)) \quad (B.2.4.9)$$

$$E_{13} = \frac{1}{2} (S_{45^\circ}(S_0) - S_{135^\circ}(S_0)) \quad (B.2.4.10)$$

$$E_{14} = \frac{1}{2} (S_{RHC}(S_0) - S_{LHC}(S_0)) \quad (B.2.4.11)$$

$$E_{21} = \frac{1}{6} (S_{0^\circ}(S_1) + S_{90^\circ}(S_1) + S_{45^\circ}(S_1) + S_{135^\circ}(S_1) + S_{RHC}(S_1) + S_{LHC}(S_1)) \quad (B.2.4.12)$$

$$E_{22} = \frac{1}{2}(S_{0^\circ}(S_1) - S_{90^\circ}(S_1)) \quad (B.2.4.13)$$

$$E_{23} = \frac{1}{2}(S_{45^\circ}(S_1) - S_{135^\circ}(S_1)) \quad (B.2.4.14)$$

$$E_{24} = \frac{1}{2}(S_{RHC}(S_1) - S_{LHC}(S_1)) \quad (B.2.4.15)$$

$$E_{31} = \frac{1}{6}(S_{45^\circ}(S_2) + S_{135^\circ}(S_2) + S_{RHC}(S_2) + S_{LHC}(S_2) + S_{0^\circ}(S_2) + S_{90^\circ}(S_2)) \quad (B.2.4.16)$$

$$E_{32} = \frac{1}{2}(S_{0^\circ}(S_2) - S_{90^\circ}(S_2)) \quad (B.2.4.17)$$

$$E_{33} = \frac{1}{2}(S_{45^\circ}(S_2) - S_{135^\circ}(S_2)) \quad (B.2.4.18)$$

$$E_{34} = \frac{1}{2}(S_{RHC}(S_2) - S_{LHC}(S_2)) \quad (B.2.4.19)$$

$$E_{41} = \frac{1}{6}(S_{RHC}(S_3) + S_{LHC}(S_3) + S_{45^\circ}(S_3) + S_{135^\circ}(S_3) + S_{0^\circ}(S_3) + S_{90^\circ}(S_3)) \quad (B.2.4.20)$$

$$E_{42} = \frac{1}{2}(S_{0^\circ}(S_3) - S_{90^\circ}(S_3)) \quad (B.2.4.21)$$

$$E_{43} = \frac{1}{2}(S_{45^\circ}(S_3) - S_{135^\circ}(S_3)) \quad (B.2.4.22)$$

$$E_{44} = \frac{1}{2}(S_{RHC}(S_3) - S_{LHC}(S_3)) \quad (B.2.4.23)$$

Reference

- Chen, P.-C., Lo, Y.-L., Yu, T.-C., Lin, J.-F., & Yang, T.-T. (2009). Measurement of linear birefringence and diattenuation properties of optical samples using polarimeter and Stokes parameters. *Optics Express*, *17*(18), 15860–15884.
<https://doi.org/10.1364/oe.17.015860>
- Cloude, S. R. (1986). Group theory and polarisation algebra. *Optik(Stuttgart)*, *75*, 26–36.
- Huard, S. (1997). *Polarization of light*. (G. Vacca, Ed.). Paris: John Wiley & Sons, Masson.
- Kliger, D. S., Lewis, J. W., & Randall, C. E. (1990). *Polarized light in optics and spectroscopy*. London: Academic Press.
- Liao, C.-C., & Lo, Y.-L. (2013). Extraction of anisotropic parameters of turbid media using hybrid model comprising differential- and decomposition-based Mueller matrices. *Optics Express*, *21*(14), 16831–16853. <https://doi.org/10.1364/oe.21.016831>
- Lu, S.-Y., & Chipman, R. (1996). Interpretation of Mueller matrices based on polar decomposition. *Journal of Optical Society of America*, *13*(5), 1106–1113.
- Ossikovski, R., De Martino, A., & Guyot, S. (2007). Forward and reverse product decompositions of depolarizing Mueller matrices. *Optics Letters*, *32*(6), 689–691.
<https://doi.org/10.1364/OL.32.000689>
- Pham, T.-T.-H., & Lo, Y.-L. (2012a). Extraction of effective parameters of anisotropic optical materials using a decoupled analytical method. *Journal of Biomedical Optics*, *17*(2), 097002. Retrieved from [http://internal-pdf/\[31\]Extraction of effective parameters of-](http://internal-pdf/[31]Extraction of effective parameters of-)

1665496578/[31]Extraction of effective parameters of.pdf

Pham, T.-T.-H., & Lo, Y.-L. (2012b). Extraction of effective parameters of turbid media utilizing the Mueller matrix approach: study of glucose sensing. *Journal of Biomedical Optics*, *17*(9), 97002.